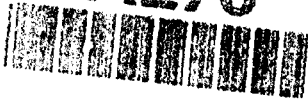


AD-A276 170



①

DTIC
ELECTE
FEB 22 1994

S A

Proceedings
of the
Sixth International Symposium
on
Interaction of Nonnuclear Munitions
with Structures

This document has been approved
for public release and sale; its
distribution is unlimited.

Panama City Beach, Florida
May 3-7, 1993

REPORT DOCUMENTATION PAGEForm Approved
OMB No. 0704-0188

Public reporting burden for this collection of information is estimated to average 1 hour per response, including the time for reviewing instructions, searching existing data sources, gathering and maintaining the data needed, and completing and reviewing the collection of information. Send comments regarding this burden estimate or any other aspect of this collection of information, including suggestions for reducing this burden, to Washington Headquarters Services, Directorate for Information Operations and Reports, 1215 Jefferson Davis Highway, Suite 1204, Arlington, VA 22202-4302, and to the Office of Management and Budget, Paperwork Reduction Project (0704-0188), Washington, DC 20503.

1. AGENCY USE ONLY (Leave blank)		2. REPORT DATE May 1993	3. REPORT TYPE AND DATES COVERED Symposium Proceedings May 3-7, 1993	
4. TITLE AND SUBTITLE Proceedings of the Sixth International Symposium on Interaction of Nonnuclear Munitions with Structures			5. FUNDING NUMBERS F08635-93-C-0020	
6. AUTHOR(S) R			8. PERFORMING ORGANIZATION REPORT NUMBER	
7. PERFORMING ORGANIZATION NAME(S) AND ADDRESS(ES) Applied Research Associates, Inc. Post Office Box 40128 Bldg 1142, Mississippi Road Tyndall AFB FL 32403				
9. SPONSORING / MONITORING AGENCY NAME(S) AND ADDRESS(ES) Wright Laboratories Flight Dynamic Directorate Vehicle Subsystems Division Air Base Systems Branch Tyndall AFB FL 32403-6001			10. SPONSORING / MONITORING AGENCY REPORT NUMBER WL-TR-93-3521	
11. SUPPLEMENTARY NOTES				
12a. DISTRIBUTION / AVAILABILITY STATEMENT Approved for public release; Distribution unlimited.			12b. DISTRIBUTION CODE	
13. ABSTRACT (Maximum 200 words)				
14. SUBJECT TERMS			15. NUMBER OF PAGES 55	
			16. PRICE CODE	
17. SECURITY CLASSIFICATION OF REPORT Unclassified		18. SECURITY CLASSIFICATION OF THIS PAGE Unclassified	19. SECURITY CLASSIFICATION OF ABSTRACT Unclassified	20. LIMITATION OF ABSTRACT

GENERAL INSTRUCTIONS FOR COMPLETING SF 298

The Report Documentation Page (RDP) is used in announcing and cataloging reports. It is important that this information be consistent with the rest of the report, particularly the cover and title page. Instructions for filling in each block of the form follow. It is important to stay *within the lines* to meet optical scanning requirements.

Block 1. Agency Use Only (Leave blank).

Block 2. Report Date. Full publication date including day, month, and year, if available (e.g. 1 Jan 88). Must cite at least the year.

Block 3. Type of Report and Dates Covered. State whether report is interim, final, etc. If applicable, enter inclusive report dates (e.g. 10 Jun 87 - 30 Jun 88).

Block 4. Title and Subtitle. A title is taken from the part of the report that provides the most meaningful and complete information. When a report is prepared in more than one volume, repeat the primary title, add volume number, and include subtitle for the specific volume. On classified documents enter the title classification in parentheses.

Block 5. Funding Numbers. To include contract and grant numbers; may include program element number(s), project number(s), task number(s), and work unit number(s). Use the following labels:

C - Contract	PR - Project
G - Grant	TA - Task
PE - Program Element	WU - Work Unit Accession No.

Block 6. Author(s). Name(s) of person(s) responsible for writing the report, performing the research, or credited with the content of the report. If editor or compiler, this should follow the name(s).

Block 7. Performing Organization Name(s) and Address(es). Self-explanatory.

Block 8. Performing Organization Report Number. Enter the unique alphanumeric report number(s) assigned by the organization performing the report.

Block 9. Sponsoring/Monitoring Agency Name(s) and Address(es). Self-explanatory.

Block 10. Sponsoring/Monitoring Agency Report Number. (If known)

Block 11. Supplementary Notes. Enter information not included elsewhere such as: Prepared in cooperation with...; Trans. of...; To be published in.... When a report is revised, include a statement whether the new report supersedes or supplements the older report.

Block 12a. Distribution/Availability Statement. Denotes public availability or limitations. Cite any availability to the public. Enter additional limitations or special markings in all capitals (e.g. NOFORN, REL, ITAR).

DOD - See DoDD 5230.24, "Distribution Statements on Technical Documents."

DOE - See authorities.

NASA - See Handbook NHB 2200.2.

NTIS - Leave blank.

Block 12b. Distribution Code.

DOD - Leave blank.

DOE - Enter DOE distribution categories from the Standard Distribution for Unclassified Scientific and Technical Reports.

NASA - Leave blank.

NTIS - Leave blank.

Block 13. Abstract. Include a brief (Maximum 200 words) factual summary of the most significant information contained in the report.

Block 14. Subject Terms. Keywords or phrases identifying major subjects in the report.

Block 15. Number of Pages. Enter the total number of pages.

Block 16. Price Code. Enter appropriate price code (NTIS only).

Blocks 17. - 19. Security Classifications. Self-explanatory. Enter U.S. Security Classification in accordance with U.S. Security Regulations (i.e., UNCLASSIFIED). If form contains classified information, stamp classification on the top and bottom of the page.

Block 20. Limitation of Abstract. This block must be completed to assign a limitation to the abstract. Enter either UL (unlimited) or SAR (same as report). An entry in this block is necessary if the abstract is to be limited. If blank, the abstract is assumed to be unlimited.

TABLE OF CONTENTS

DEFENCE IN THE AGE OF PRECISION GUIDED MUNITIONS Werner Heierli and Arthur Eiff, Heierli Consulting Engineers, SWITZERLAND	1	IMPACT OF PROJECTILES ON HARD LAYERS T. Fries and D. Favarger, Defence Technology and Procurement Agency, SWITZERLAND; and M. Koller, Résonance SA, SWITZERLAND	39
MODELING OF PROJECTILE PENETRATION INTO GEOLOGIC TARGETS BASED ON ENERGY TRACKING AND MOMENTUM IMPULSE PRINCIPLE Ali Amini, UTD, Incorporated; and Jon Anderson, Wright Laboratory Airbase Systems Branch	6	RESISTANCE OF CONCRETE AND REINFORCED CONCRETE STRUCTURES IMPACTED BY CU AND TA PROJECTILES Vladimir M. Gold, James C. Pearson and Joseph P. Turci, US Army ARDEC	44
ANALYSIS OF ROCK-RUBBLE OVERLAY PROTECTION OF STRUCTURES BY THE FINITE BLOCK METHOD Joseph M. Gebara and Austin D. Pan, Purdue University; and Jon B. Anderson, Wright Laboratory Airbase Systems Branch	12	PENETRATION COUNTERMEASURES James M. Underwood, Applied Research Associates, Inc.; and Michael K. Westmoreland, Wright Laboratory Airbase Systems Branch	50
A SIMPLY COUPLED PENETRATION TRAJECTORY/STRUCTURAL DYNAMICS MODEL Mark D. Adley, US Army Engineer Waterways Experiment Station	18	LEAKAGE PRESSURES BEHIND BLAST WALLS T. A. Rose, P. D. Smith and G. C. Mays, Royal Military College of Science, UNITED KINGDOM	56
DEVELOPMENT OF INSTRUMENTATION TECHNIQUES TO INVESTIGATE HIGH VELOCITY PROJECTILE PENETRATION INTO CONSTRUCTION MATERIALS Jeffrey Peters, William F. Anderson and Alan J. Watson, University of Sheffield, UNITED KINGDOM	23	ENVIRONMENTS FROM INTERNAL DETONATION OF WARHEADS James A. Keller, University of Denver	62
AN EMPIRICAL EQUATION FOR PENETRATION DEPTH OF OGIVE-NOSE PROJECTILES INTO CONCRETE TARGETS M. J. Forrestal and B. S. Altman, Sandia National Laboratories; J. D. Cargile, US Army Engineer Waterways Experiment Station; and S. J. Hanchak, University of Dayton Research Institute	29	BLAST IN TUNNELS AND ROOMS FROM CYLINDRICAL HE-CHARGES OUTSIDE THE TUNNEL ENTRANCE G. Scheklinski-Glück, Ernst-Mach- Institut, GERMANY	68
SUBSCALE PENETRATION TESTS WITH BOMBS AND ADVANCED PENETRATORS AGAINST HARDENED STRUCTURES Helga Langheim, Eberhard Schmolinske and Alois J. Stilp, Ernst-Mach-Institut, GERMANY; and Hermann Pahl, NATO Headquarters, BELGIUM	33	BLAST VALVES - A SUPERFLUOUS INVESTMENT? J. Hasler, LUWA Ltd., SWITZERLAND	74
		PREDICTION OF IN-STRUCTURE SHOCK Ph. van Dongen and J. Weerheijm, TNO Prins Maurits Laboratory, THE NETHERLANDS	80
		STOCHASTIC SIMULATION OF IN- STRUCTURE SHOCK DUE TO CONVENTIONAL WEAPON EFFECTS Erwin Kessler and Bernard Anet, Laboratory Spiez, SWITZERLAND	84

SUB SURFACE BARRIERS FOR GROUND SHOCK ATTENUATION: NUMERICAL TECHNIQUES TO MODEL EXPERIMENTAL RESULTS	89	TEST OF CIVIL DEFENCE CONTROL CENTRE, RC 90	128
Leslie J. Kennedy, Royal Military College of Science, UNITED KINGDOM; Frederick G. Hulton, Defence Research Agency, UNITED KINGDOM; and Michael C. R. Davies, University of Wales, UNITED KINGDOM		Tommy Wirén, Swedish Rescue Services Board, SWEDEN	
MATERIALS FOR EXTERNAL SHOCK MITIGATION	95	COUNTER TERRORIST FORTIFICATIONS IN NORTHERN IRELAND	134
Larry C. Muszynski and Michael A. Rochefort, Applied Research Associates, Inc.		R. Watt, 62 CRE Royal Engineers, UNITED KINGDOM; and M. G. Richardson, 523 Specialist Team Royal Engineers, UNITED KINGDOM	
SHOCK TEST FACILITIES FOR HIGH SHOCK TESTS	100	RESPONSE OF PILE FOUNDATIONS IN SATURATED SOIL	140
Ronald Kaufmann, Armed Forces Office, GERMANY; and Fritz Rischbieter, Battelle Motor and Vehicle Technology, GERMANY		Barry L. Bingham, Robert E. Walker and Scott E. Blouin, Applied Research Associates, Inc.	
PRACTICAL STRENGTHENING MEASURES FOR EXISTING STRUCTURES TO INCREASE THEIR BLAST RESISTANCE - WALLS AND CEILINGS	105	RESPONSE OF SATURATED AND PARTIALLY SATURATED SOILS TO HIGH EXPLOSIVE LOADINGS - NUMERICAL ANALYSIS	146
Reuben Eytan, Eytan Building Design Ltd., ISRAEL; and Arkadi Kolodkin, Hardening Consultant, ISRAEL		R. E. Walker and S. E. Blouin, Applied Research Associates, Inc.	
PRACTICAL STRENGTHENING MEASURES FOR EXISTING STRUCTURES TO INCREASE THEIR BLAST RESISTANCE - WINDOWS AND DOORS	109	FIBER-REINFORCED CONCRETE IN HARDENED SHELTER CONSTRUCTION	152
Arkadi Kolodkin, Hardening Consultant, ISRAEL; and Reuben Eytan, Eytan Building Design Ltd., ISRAEL		David L. Read and Larry C. Muszynski, Applied Research Associates, Inc.	
FULL SCALE TESTS ON STRENGTHENING MEASURES FOR EXISTING STRUCTURES	113	A COMBINATION OF STEEL FIBERS AND CONVENTIONAL REINFORCEMENT IN PROTECTIVE CONCRETE STRUCTURES SUBJECTED TO NEAR MISS EXPLOSIONS, CONTACT EXPLOSIONS, DIRECT HITS, AND EXPLOSIONS AFTER PENETRATION	158
Yitzhak Fouks, Israeli Defense Forces, ISRAEL		G. Naeyaert, Infrastructure Dep., MOD BELGIUM; A. H. Verhagen, Royal Military Academy, THE NETHERLANDS; and T. Türker, UNITEK Consult, Eng., TURKEY	
CONVENTIONAL EXPLOSIVE AIRBLAST EFFECTS WITHIN COMPARTMENTED STRUCTURES	116	EXPEDIENT REPAIR OF MISSION-CRITICAL STRUCTURAL FACILITIES	166
M. Rosenblatt, D.W. Hatfield and H. D. Zimmerman, Titan Corporation		David L. Read and Douglas H. Merkle, Applied Research Associates, Inc.	
STRUCTURAL RESPONSE TO MULTIPLE PULSE BLAST LOADING	122	IMPACT COMPRESSION PROPERTIES OF CONCRETE	172
Mark G. Whitney, Darrell D. Barker and Johnny H. Wacławczyk, Jr., Wilfred Baker Engineering, Inc.		D. E. Grady, Sandia National Laboratories	
		HIGH LOADING RATE EFFECTS ON STRUCTURAL CONCRETE RESPONSE UNDER IMPULSIVE LOADS	176
		D. Chandra and T. Krauthammer, Pennsylvania State University	

DYNAMIC COMPRESSIVE BEHAVIOUR OF CONCRETE AT STRAIN RATES UP TO 10^3 /S - COMPARISON OF PHYSICAL EXPERIMENTS WITH HYDROCODE SIMULATIONS	182	JOINT SERVICES PROGRAM FOR THE DESIGN AND ANALYSIS OF HARDENED STRUCTURES TO CONVENTIONAL WEAPONS EFFECTS	220
A. D. Pullen and J. B. Newman, Imperial College, UNITED KINGDOM; and A. J. Sheridan, Defence Research Agency, UNITED KINGDOM		J. E. Walter, Defense Nuclear Agency	
USE OF LARGE DIAMETER HOPKINSON BAR TO INVESTIGATE THE STRESS PULSE GENERATED DURING HIGH VELOCITY PROJECTILE PENETRATION INTO CONSTRUCTION MATERIALS	188	CENTRIFUGE MODELLING TESTING TO INVESTIGATE THE USE OF BARRIERS TO MITIGATE BLAST EFFECTS ON BURIED STRUCTURES	224
J. Peters, W.F. Anderson and A.J. Watson, University of Sheffield, UNITED KINGDOM		M. C. R. Davies and A. J. Williams, University of Wales College of Cardiff, UNITED KINGDOM; and K. J. Claber, DRA, UNITED KINGDOM	
LOAD RATE EFFECTS ON CONCRETE COMPRESSIVE STRENGTH	194	FROUDE-SCALED TESTS OF EXPLOSIVELY LOADED BURIED STRUCTURES USING A SOIL SIMULANT	229
J. W. Tedesco, Auburn University; C. Allen Ross, University of Florida; and M. L. Hughes, Wright Laboratory Airbase Systems Branch		Maynard A. Plamondon, Daniel E. Chitty, Robert L. Guice and Douglas H. Merkle, Applied Research Associates, Inc.	
FRACTURE ENERGY OF CONCRETE UNDER DYNAMIC TENSILE LOADING	200	IMPACT LOADING OF PLATES - A COMPARISON BETWEEN NUMERICAL SIMULATIONS AND EXPERIMENTAL RESULTS	235
J. Weerheijm and J.C.A.M. van Doormaal, TNO Prins Maurits Laboratory, THE NETHERLANDS; and L. J. Sluys, Delft University of Technology, THE NETHERLANDS		Magnus Langseth, Torodd Berstad and Per Kr. Larsen, The Norwegian Institute of Technology, NORWAY; and Arnfinn Jenssen, Norwegian Defence Construction Service, NORWAY	
A NUMERICAL SIMULATION OF STRESS WAVE PROPAGATION IN CONCRETE AND ITS EFFECT ON SPALL AND BREACH IN SCALED TESTS	205	DESIGN PROCEDURE FOR PREFABRICATED ROOF BEAMS FOR BLAST-RESISTANT SHELTERS	241
Charles J. Oswald, Kirk A. Marchand and Ben H. Thacker, Southwest Research Institute		Larry M. Bryant, Paul F. Mlakar and Brian Campbell, JAYCOR; and Richard Reid, Wright Laboratory Airbase Systems Branch	
CUMULATIVE DAMAGE ALGORITHMS DEVELOPMENT FOR REINFORCED CONCRETE	211	PROTECTIVE CONSTRUCTION WITH REINFORCED EARTH	247
Robert W. Cilke and Frank A. Maestas, Applied Research Associates, Inc.; and Marvis Adams, Aeronautical Systems Directorate		Christopher Y. Tuan, Applied Research Associates, Inc.	
EXPERIMENTAL/ANALYTICAL PROGRAM FOR CONSTRUCTING MODELS FOR THE DYNAMIC RESPONSE OF CONCRETE MATERIALS	215	RESPONSE OF GEOGRID-REINFORCED SOIL SUBJECTED TO BLAST LOADING	253
John A. Collins, Wright Laboratory; Frank A. Maestas and Barry L. Bingham, Applied Research Associates, Inc.; and James A. Keller and W. Russ Seebaugh, University of Denver		Richard A. Reid, Wright Laboratory Airbase Systems Branch; and Robert C. Bachus, Kara L. Olen and Richard Fragaszy, GeoSyntec Consultants	
		DIMENSIONING OF HIGH EXPLOSIVE DETONATIONS ON CONCRETE STRUCTURES	259
		D. Kraus and J. Rötzer, University of German Armed Forces, GERMANY	

THE EFFECTS OF HIGH EXPLOSIVES IN CONTACT WITH REINFORCED CONCRETE SLABS	262	HOW TO SELECT A DESIGN FRAGMENT FOR PROTECTIVE STRUCTURE DESIGN WITH CONSISTENT RELIABILITY	311
Lena Lönnqvist, National Defence Research Establishment, SWEDEN		Robert H. Sues and Lawrence A. Twisdale, Applied Research Associates, Inc.	
ON MODELLING OF SHAPED CHARGE JET INTERACTION WITH SPACED PLATES	267	RELIABILITY-BASED SAFETY FACTORS FOR GROUND SHOCK LOADS IN PROTECTIVE CONSTRUCTION	317
Pierre Y. Chanteret, French-German Research Institute of Saint-Louis, FRANCE		R. H. Sues, J. L. Drake and L. A. Twisdale, Applied Research Associates, Inc.	
OPTIMIZATION OF SHAPED CHARGES AGAINST CONCRETE TARGETS	273	RELIABILITY-BASED DESIGN METHODS FOR THE PROTECTIVE CONSTRUCTION DESIGN MANUAL	323
Hermann Rösner, Deutsche Aerospace AG, GERMANY		L. A. Twisdale, R. H. Sues and F. M. Lavelle, Applied Research Associates, Inc.	
RESPONSIVE CHARACTERISTICS OF BURIED STRUCTURES SUBJECTED TO IMPULSIVE LOADINGS	277	DYNAMIC PROPERTIES OF NOVEL THERMOPLASTIC HONEYCOMB CORE MATERIAL	329
Fang Qin, Nanjing Engineering Institute, PEOPLE'S REPUBLIC OF CHINA		R. L. Sierakowski, Ohio State University; and C. A. Ross, University of Florida	
FEM IN SATURATED SOIL UNDER EXPLOSIVE LOADING	282	COMPOSITE MATERIALS - THE FUTURE OF AIRMOBILE SHELTERS	332
QiHu Qian and Mingyang Wang, Nanjing Engineering Institute, PEOPLE'S REPUBLIC OF CHINA		Robert J. Majka, Applied Research Associates, Inc.	
MATERIAL PROPERTIES DATABASE SEARCH AND RETRIEVAL PROGRAM	289	AIRMOBILE SHELTER CONCEPT SELECTION METHODOLOGY	335
B. R. Phillips, D. E. Barnes and A. E. Jackson, Jr., US Army Engineer Waterways Experiment Station; and T. R. Slawson and R. E. Walker, Applied Research Associates, Inc.		Francis M. Lavelle and Lawrence A. Twisdale, Applied Research Associates, Inc.	
EFFECTIVE STRESS CONSTITUTIVE MODELS FOR SATURATED & PARTIALLY SATURATED SOILS	294	RESEARCH TO DEVELOP CONCEPTS FOR A NEW FAMILY OF AIRMOBILE SHELTERS	341
H. D. Zimmerman, Y. M. Ito and J. A. Carney, Titan Corporation		Lawrence A. Twisdale, Francis M. Lavelle and Robert A. Frank, Applied Research Associates, Inc.	
STRAIN-RATE EFFECTS IN UNSATURATED SOILS	300		
George E. Veyera, University of Rhode Island; Wayne A. Charlie, Colorado State University; and C. Allen Ross, University of Florida			
EFFECTS OF ENHANCED CONSTITUTIVE MODELS ON CALCULATED FREE-FIELD GROUND SHOCK	305		
H. D. Zimmerman, Y. M. Ito and J. A. Carney, Titan Corporation; and J. E. Windham, US Army Engineer Waterways Experiment Station			

AUTHOR INDEX

- Adams, M., 211
 Adley, M. D., 18
 Altman, B. S., 29
 Amini, A., 6
 Anet, B., 84
 Anderson, J. B., 6, 12
 Anderson, W. F., 23, 188
 Bachus, R. C., 253
 Barker, D. D., 122
 Barnes, D. E., 289
 Berstad, T., 235
 Bingham, B. L., 140, 215
 Blouin, S. E., 140, 146
 Bryant, L. M., 241
 Campbell, B., 241
 Cargile, J. D., 29
 Carney, J. A., 294, 305
 Chandra, D., 176
 Chanteret, P. Y., 267
 Charlie, W. A., 300
 Chitty, D. E., 229
 Cilke, R. W., 211
 Claber, R. E., 224
 Collins, J. A., 215
 Davies, M. C. R., 89, 224
 Drake, J. L., 317
 Eiff, A., 1
 Eytan, R., 105, 109
 Favarger, D., 39
 Forrestal, M. J., 29
 Fouks, Y., 113
 Fragaszy, R., 253
 Frank, R. A., 341
 Fries, T., 39
 Gebara, J. M., 12
 Gold, V. M., 44
 Grady, D. E., 172
 Guice, R. L., 229
 Hanchak, S. J., 29
 Hasler, J., 74
 Hatfield, D. W., 116
 Heierli, W., 1
 Hughes, M. L., 194
 Hulton, F. G., 89
 Ito, Y. M., 294, 305
 Jackson, A. E., Jr., 289
 Jenssen, A., 235
 Kaufmann, R., 100
 Keller, J. A., 62, 215
 Kennedy, L. J., 89
 Kessler, E., 84
 Koller, M., 39
 Kolodkin, A., 105, 109
 Kraus, D., 259
 Krauthammer, T., 176
 Langheim, H., 33
 Langseth, M., 235
 Larsen, P. K., 235
 Lavelle, F. M., 323, 335, 341
 Lonnqvist, L., 262
 Maestas, F. A., 211, 215
 Majka, R. J., 332
 Marchand, K. A., 205
 Mays, G. C., 56
 Merkle, D. H., 166, 229
 Mlakar, P. F., 241
 Muszynski, L. C., 95, 152
 Naeyaert, G., 158
 Newman, J. B., 182
 Olen, K. L., 253
 Oswald, C. J., 205
 Pahl, H., 33
 Pan, A. D., 12
 Pearson, J. C., 44
 Peters, J., 23, 188
 Phillips, B. R., 289
 Plamondon, M. A., 229
 Pullen, A. D., 182
 Qian, O. H., 282
 Qin, F., 277
 Read, D. L., 152, 166
 Reid, R. A., 241, 253
 Richardson, M. G., 134
 Rischbieter, F., 100
 Rochefort, M. A., 95
 Rose, T. A., 56
 Rosenblatt, M., 116
 Rösner, H., 273
 Ross, C. A., 194, 300, 329
 Rötzer, J., 259
 Schmolinske, E., 33
 Schelinski-Glück, G., 68
 Seebaugh, W. R., 215
 Sheridan, A. J., 182
 Sierakowski, R. L., 329
 Slawson, T. R., 289
 Sluys, L. J., 200
 Smith, P. D., 56
 Stilp, A. J., 33
 Sues, R. H., 311, 317, 323
 Tedesco, J. W., 194
 Thacker, B. H., 205
 Tuan, C. Y., 247
 Turci, J. P., 44
 Türker, T., 158
 Twisdale, L. A., 311, 317, 323, 335, 341
 Underwood, J. M., 50
 van Dongen, P., 80
 van Doormaal, J.C.A.M., 200
 Verhagen, A. H., 158
 Veyera, G. E., 300
 Wacławczyk, J. H., Jr., 122
 Walker, R. E., 140, 146, 289
 Wang, M., 282
 Watson, A. J., 23, 188
 Watt, R., 134
 Weerheijm, J., 80, 200
 Welter, J. E., 220
 Westmoreland, M. K., 50
 Whitney, M. G., 122
 Williams, A. J., 224
 Windham, J. E., 305
 Wiren, T., 128
 Zimmerman, H. D., 116, 294, 305

Defence in the Age of Precision Guided Munitions

Werner Heierli
Arthur Eiff

Heierli Consulting Engineers
CH-8033 Zurich, Switzerland

ABSTRACT

Images of the pinpoint destruction of Iraq's military infrastructure in 1991, broadcast to every corner of the world, have left the impression that there is no defence against this "new," non-nuclear weapons threat. Certainly, the defence of key infrastructure has been made more difficult. However, there remain many defensive options that, when properly applied, can offset some of this threat. The Gulf War also illustrated that the line between "civilian" and "military" infrastructure targets in today's modern, centralized economy is no longer distinct. Therefore, true defence becomes "total defence." Attacks with precision guided weapons against political, military and industrial facilities can, in principle, deprive a country not only of the possibilities of effective military defense - thereby exposing it to the possibly disastrous effects of enemy occupation - but also of the nation's survival in the aftermath of war. Defense is incomplete and ineffective if it cannot achieve the reasonably 'uninjured' survival of the population during, and after, the war.

INTRODUCTION

"To be able to foresee events, one has to consider the past, since the actors on the stage of this world - men - always had the same passions and, therefore, the same cause will always produce the same effect".

Niccolò Machiavelli (1469-1527)

Until less than a century ago, conquering a country required physically crossing borders and carrying a surface attack into a nation's heartland. Defense meant the prevention of such action, and the Great Wall in China, Roman frontier fortifications in Central Europe ("limes") and the Maginot line bear witness to this concept. The one other way to indirectly influence a country's resistance was blockade or embargo.

Historically, however, embargoes alone have seldom succeeded in bringing a nation to the point of surrender since there always seem to be ways to overcome them. Today, the former Yugoslavia and Iraq serve to illustrate this point.

World War I, with its first applications and modest successes in air warfare, changed the practice to think in terms of frontiers and fronts and tempted strategists to contend that air attacks against cities could alone and of themselves deal crippling blows to a defender and quickly subdue him. Indeed, in World War II, both Germany and the Allies believed that air warfare against cities could be a decisive means of overcoming the enemy. As few are aware, this belief did not prove to be true in actual practice; neither did Hitler win the "Battle of Britain" by attacking British cities, nor were the Allies able to bring Germany to its knees by countless massive 1000-bomber attacks against German cities. In fact, war production in Germany peaked in the fall of 1944. Only concentrated attacks against transportation facilities (including coal hydration plants for gasoline synthetization) curbed German armament and, finally, the country had to be conquered almost square mile by square mile.

With the advent of large nuclear weapons and means for their intercontinental delivery, many people were convinced that nuclear weapons employed against cities could decide a war. Fortunately, we have not really seen this concept put to the test. Who knows the reasons for this? Fear of a retaliatory blow was certainly one of them; the prospect of destroying the industrial potential of the country to be conquered probably was another. Possibly, responsible politicians and generals had the insight that, while nuclear weapons had tremendous effects, they could not completely wipe out the defenses of an entire country. It was certainly realized that, while protection cannot be afforded at the very center of the attack, survival of the military and the entire population can be assured quite close to it - in the area of collateral damage - through a reasonable shelter program.

Now that the nuclear weapons threat has moved from

the limelight, precision guided weapons have, in some ways, taken their place. While hundreds of attacks and thousands of bombs were needed to destroy a specific target in World War II, precision guided weapons have now reduced the magnitude of resources necessary for successful attack. They have enabled an attacker to target, hit and eliminate specific facilities deep in the defender's territory with ever-increasing efficiency. It is now imaginable to cripple a country's military installations, its centers of government and its many nodes of vulnerable peacetime infrastructure to such an extent that the country would be left defenseless - even helpless - in regard to the day-to-day necessities for survival. The Gulf War has given a prelude to a scenario in which decisive air blows almost exclude coordinated defense efforts and render the necessary supplies to the population critically difficult to attain.

The presentation's aim is to analyze, in a very general way, whether - and how - a **defending country** can thwart the evolving strategy of crippling precision guided weapons attacks against political, military and economic nerve centers. The fact that neither the air war strategies of World War I, World War II nor of the Cold War yielded convincing results makes one hope that options might exist which can render this type of attack inefficient. If there were no way of doing so, one would face considerable world instability because any attacker could arm himself with the appropriate weapons and at least intimidate other countries with the threat to wipe out, for example, a few hundred vital facilities quickly, efficiently and without the stigma of directly attacking the

population. The attacker might even formally remain, so to speak, within the international conventions governing warfare.

The viewpoint taken is that of a small to medium sized country as the defender - not a superpower. The options of a preemptive strike or second (counter) strike are not considered in this presentation in spite of their possible reasonableness and probable cost-effectiveness.

DEFENCE OPTIONS

1. PROTECTION AGAINST DIRECT HITS

The very character of precision attacks requires an attacker to select a limited number of targets; targets whose destruction decisively degrades the defensive capabilities of those who are attacked. Today, many countries have not, or not yet, hardened or otherwise protected their selection of **important** defense facilities to the extent necessary. The graph below helps illustrate the order of magnitude of protective layers that are - among many other measures - required to survive under the effects of modern precision guided standard or penetration weapons.

The graph shows concrete thicknesses required to avoid penetration or heavy damage by the weapons listed. The spread shown illustrates uncertainty due to the application of the various penetration formulae. Two salient features should be highlighted:

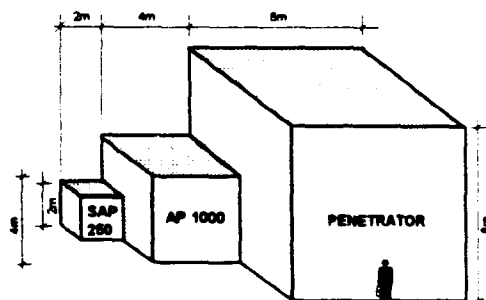
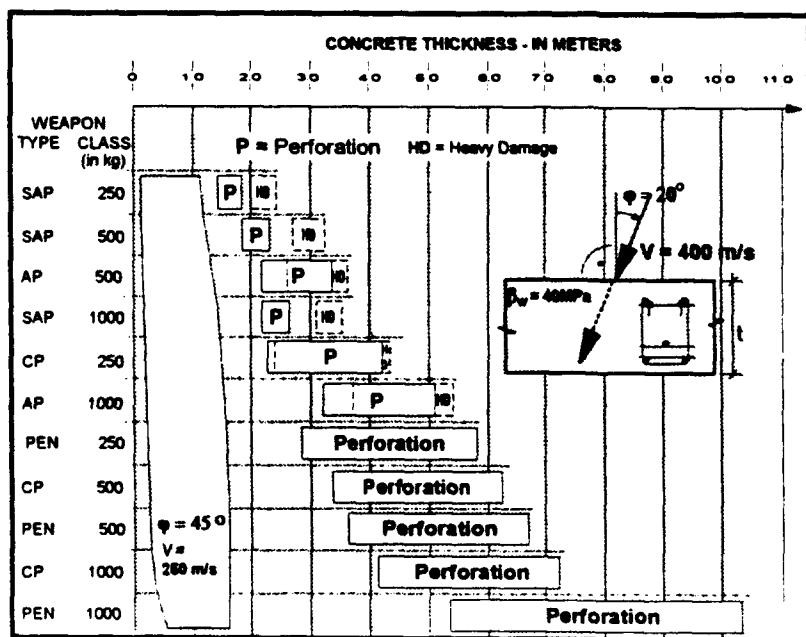


Figure 1: Concrete Thicknesses At Which Failure Occurs

- As expected, angles of attack of 20° and less, and impact velocities of 400 m/s (or more), lead to required concrete thicknesses far in excess of those for more "traditional" angles of 45° and impact velocities of 250 m/s.
- Solid layers of shaped blocks of rock with joints fully filled with mortar substantially reduce the necessary protective thicknesses, making the hardening measures more feasible.

Another indirect consequence of these thickness determinations is that facilities in rock - provided rock is available at some reasonable distance - soon become a viable alternative if attacks with heavier weapons are to be assumed.

All facilities - concrete or rock - remain vulnerable at their exits and other aboveground connections, thus requiring additional protective measures, among which are redundancies.

2. RELOCATION TUNNELS

In the 1991 Gulf War, fixed Scud facilities were quickly destroyed because their location was known and they were not hardened. Mobile Scuds, however, posed a significant problem for the coalition forces because they could not be reliably tracked. They were hidden anywhere - in underpasses, under bridges, in garages - and the hideouts were randomly changed (relocation).

Relocation tunnels are a combination of three factors of effective defence - dispersal, concealment, hardening - that use road and rail tunnels, and other rock facilities, as alternative "hideouts" for defensive resources.

The tactic of relocation is not new, but its combination with hardening in traffic tunnels and systematic use for avoiding modern precision guided weapons could be. Many functions can be organized such that they are road or rail transportable. Modern containers could help greatly; their use as "mobile homes" for many defense functions brings many advantages:

- Containers can be used for road and rail transport.
- "Defense Containers" are difficult to tell from "normal" containers.
- Containers can be designed as "protective structures" against chemical warfare agents and could even offer some fragment protection.
- Containers can be easily driven to and into their hideouts.

- Containers can be standardized and maintained at central yards at low cost in peacetime.

By using relocation tunnels (and many other facilities like basements, underground car parks, etc., defensive assets have a multitude of places where they cannot only hide, but where they are protected from attacks even if their location was known. It should be mentioned that tunnels may even offer significant NEMP protection. All traffic tunnels - road and rail - are easily and quickly accessible for containers. Changing from rail to road is achieved quickly. Traffic tunnels, especially in rock, offer an ideal combination and synergy of accessibility, concealment, and protection. The concept can be expanded by providing certain key facilities in the tunnels: facilities like data links (communications), power, food and water.

3. PROTECTION AGAINST COLLATERAL EFFECTS

To survive in a war, everyone living in an area of possible weapons engagement needs protection against collateral effects of those weapons, especially if the risk of nuclear and chemical weapons cannot be excluded. Unless protection against such effects is provided, the defender risks losing what he is fighting for - the survival of the population. After all, survival is still the first aim in war, even before freedom and democracy. War history and analysis show that the collateral effects of nuclear, chemical and conventional weapons require only relatively modest countermeasures for survival. This analysis is shown in Figure 2 which illustrates the risk distribution for a typical war scenario in Europe, including nuclear, chemical and conventional threats.

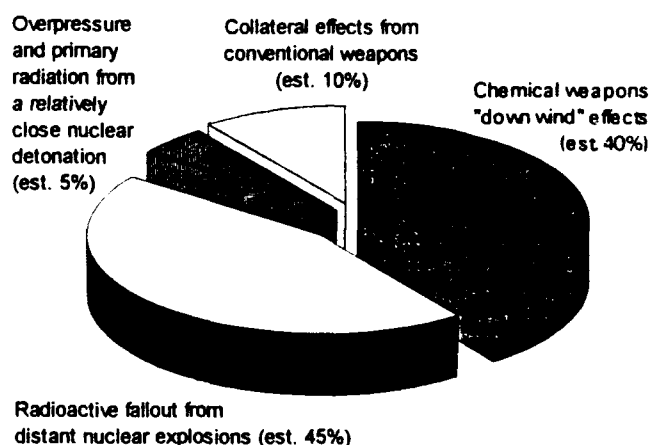


Figure 2: Typical Risk Distribution

The "risk pie" shows us that it is not the exact number of bars of overpressure that matters, but rather the balanced protection against all, predominately the chemical and radiological, effects.

4. ECONOMY

If the population can survive the direct effects of the attacks themselves - a matter of days or weeks - but not the aftermath of them, the defensive task is not fulfilled. Several wars, including the 1991 Gulf War, have illustrated how much the prolonged survival of the population - months to years - depends on the minimal functioning of a small but essential part of the economy. The destruction of a few key points - electricity generation and distribution, communication, traffic nodes, etc. - is sufficient to create tremendous supply problems for the population. After the Gulf war there were about 70,000 civilian casualties due to the absence of a sufficient supply of water, food and medication - compared to only about 2,000 civilian deaths as a result of immediate weapons effects during air attacks. This and other examples show where protective measures can spare lives.

The threat to eliminate a few key points of our vulnerable modern economy can become decisive, whether it be as blackmail to invoke surrender, or as part of a "world police call to order and peace" of, for example, the United Nations or a similar organization.

The threat to modern economies urges one to find an answer. It would not make much sense to prepare for the defense of a country without providing the basis for prolonged survival - months to years. Due to the complexity of modern economies, it would be almost impossible to try to harden their key installations. Instead, it is believed that there is a viable approach that is proposed below. The main tasks are to provide:

- Protection against weapons effects (Figure 2) and inclement weather. The solution is to provide a shelter space for each inhabitant. No heat is required, even in winter, due to the heat generated by shelterees (assuming an area of about 1 m²/person). Long shelter stays, with occasional short periods outside, are viable, as history and experiments have shown.
- A Supply of water. This task is solved with relative ease in most climates by reducing water consumption from peacetime levels of 500 to 1000 liters/day per person to the long term survival standard of 5 to 10 liters/day per person. Further, impure water can be purified easily.
- Communications. Experience shows the great need of information and communication in an emergency. Basic systems, independent of peacetime electrical supply and cable networks, are one technical solution, together with establishing a trained service able to use these technical means.

- Food. This is the big problem, as seen more than enough in former Yugoslavia, in Iraq, the Sudan, Somalia and earlier in many other parts of the world. From peace-time standards, one can reduce water consumption by a factor of 100, but food consumption only by a factor of about 2. In the course of years, one may be able to bring agriculture up to speed to replace food imports, but with the dependence of modern farming on electricity, pesticides, storage, transportation, fuel and communication, emergency agriculture will not be a reliable short to medium term supplier for the period of months to years after the onset of an attack. This, of course, always assumes that no outside supplies from other sources can be brought in.

A viable solution, therefore, seems to be long term food storage. The questions, however, are:

- **What to store:** Food that keeps for years - sugar (keeps indefinitely), cereals, pasta, potato powder, milk powder, rare elements and vitamins. Whereas the latter must be changed periodically, other items can be stored at normal temperature, with special packaging, for so long - years to many decades - that change-out will not be a major consideration. This simplifies food storage.
- **Where to store:** In order not to be dependent on vulnerable means of transportation, food storage should be regionally based, close enough to the consumer that it can be distributed with little or no use of trucks, cars or rail lines. These requirements, together with population density, will define the **size of the food storage**.
- **How to store:** It is expected that modern airtight food packaging does not require dry or cooled rooms, just simple below ground, or partly below ground, storage rooms. If change-out of food can be largely eliminated through very long durability, available space can be used almost exclusively for storage. Little space is required for access.
- **How much to store:** For the period of time it takes to reestablish normal supply lines (i.e., months to years).

5. DIRECT EFFECTS OF ENEMY OCCUPATION

One of the saddest lessons of war history is that the effects of enemy occupation, not the direct effects of combat, often take most of the lives in the

surrendering defender's country. This has been true from the times of Caesar to those of Mongolian Warlord Genghis Khan in the 13th century and on to modern times, with memorable exceptions such as the Western Allied occupation of Europe at the end of World War II. Fewer lives were lost in all European air attacks in World War II than in the concentration camps. We now witness the genocide or fratricide in former Yugoslavia that seems to confirm the lessons of the overwhelming negative effects of enemy occupation. Sadly enough, the conventions of Geneva and the Hague have not been effective enough in the past. A defensive strategy without sufficient protection against the effects of occupation is therefore not acceptable.

The only reliable means of avoiding losses under enemy occupation seem to be to prevent the attacker from crossing the borders - a means only achieved if a sound military organization is available. Peace movements intentionally (or not) ignore this fact; they either pass or misunderstand the lessons of history, or their intention is not that of true and lasting peace. Peace efforts, without avoiding the often devastating physical and moral effects of enemy occupation, are clearly incomplete. Peace marches and initiatives against defensive military forces are, therefore, bound to be as potentially destructive as the weapons of the attacker.

CONCLUSION

Precision guided attacks against political, military and industrial facilities can, in principle, not only deprive a country of its military defense capabilities (and protection against enemy occupation), but also expose the population to the lack of water and food in the aftermath of war. Defense is incomplete and ineffective if it cannot achieve the 'uninjured' survival of the population, both during and after the war.

The 20th century has given birth to several strategies of air war aimed at speedy victories over a defender. These strategies have at least partially failed for several reasons; reasons like inadequacy of means of attack, hardening of defense installations and preparations that halfway enable the population to survive war's indirect effects. It would, therefore, seem that precision guided weapons systems, while providing an attacker with the capability to deal enormous blows, are not the epilogue of the defense of small to medium countries in general. Defense certainly has a chance. While precision guided weapons - and maybe active defense systems - will play an important part in that defence, the following measures and precautions form an integral part of the modern "total" defense:

- protection of static defense installations by sufficiently hardening their key elements. The surviving functions must be able to perform the necessary minimal role of defense. Concrete, rock masonry and tunnels/cavities are part of the answer. In most cases, today's existing hardened facilities will require considerable upgrading if they are not to become an easy prey to modern air attacks.
- survival of "movable" defense facilities, whereby basements of modern large structures - and especially traffic tunnels - will play a key role. Combining rock traffic tunnels with mobility (containers) promises an especially efficient alternative to fixed facilities.
- immediate survival of the population under the collateral weapons effects of modern war; protection not only against conventional attack, but also against the collateral effects of nuclear and chemical/biological weapons. Treaties banning such weapons do not sufficiently protect us against those nations that, by their sheer intention to violate another nation's existence, show they lack the intention to abide by modern international law and standards.
- extended survival of the population, *after* precision guided and other attacks have crippled the *normal, modern economy that can hardly be protected*. Apart from shelter against inclement weather and weapons effects, and apart from some simple means of communication, one needs minimum supplies of water, food and medicine during an extended period of time at, or close to, where the population lives. These supplies, and their distribution, must not rely on modern technical facilities like electricity and modern road traffic. The methods and resources can be primitive, but they must be able to survive a war lasting months to years.

Finally, while civil defense and "economic defense" are important, active defenses remain indispensable in keeping an attacker at bay - away from one's population. The suffering of men, women and children under enemy occupation throughout the ages should be sufficient cause for the governments, politicians and the population to maintain an active defense.

The research work underlying this presentation was organized and sponsored by KASKO, the Swiss Federal Committee responsible for advising the government on the protection of military, civilian and economic facilities.

MODELING OF PROJECTILE PENETRATION INTO GEOLOGIC TARGETS BASED ON ENERGY TRACKING AND MOMENTUM IMPULSE PRINCIPLE

Ali Amini*
Jon Anderson**

* UTD, Incorporated, Newington, VA
** HQ AFCEA/RACS, Tyndall AFB, FL

ABSTRACT

Projectile penetration into geologic materials was investigated by analyzing the penetration problem in various stages. Governing equations were either selected or derived using lower-bound and upper-bound solution techniques. These equations can be generalized to model non-normal penetration into layered geologic targets. The lower-bound solution is based on force equilibrium and failure conditions in the target material, whereas the upper-bound solution uses energy tracking to satisfy kinematics in the target material adjacent to the projectile. The momentum-impulse principle was used to track the momentum of the projectile as a function of time. This resulted in displacement, velocity, and deceleration history of the projectile in space and time domains. The model was compared with two field experiments in Thirsty Canyon Tuff and Antelope Tuff.

INTRODUCTION

An effective means for protecting structures against earth penetrating projectiles is to build a protective layered structure in the path of the projectile. The layered structure can be designed to deflect and force the projectile away from the structure. A layered protection may consist of a concrete screen, an air gap, and a soil backfill. The concrete screen absorbs the initial impact energy and deflects the projectile, and the soil backfill absorbs the remaining energy of the projectile and stops it before it hits the protected structure.

In order to design an effective protective structure, it is necessary to model the path of the projectile in a layered material. For this purpose one needs a model that incorporates the most important parameters that affect penetration. These parameters are the deformation and strength properties of the protective layers, impact pressure wave propagation in the target and subsequent target material degradation, and layering interface effects. In most cases, the path of the projectile in the target will deviate from normal penetration (90° angle of

penetration). As a result the model has to include non-normal penetration in its solution algorithms.

Projectile penetration into geologic targets has been studied by numerous investigators in the past thirty years, leading to various models for predicting depth or path of penetration. These models are either empirical, analytical or numerical in nature, [1]. Empirical methods predict depth of penetration based on numerous experiments in homogenous soil and rock targets and normal penetration. They have also been incorporated into computer programs for prediction of the path of projectiles in layered structures. As a common deficiency, these models do not explicitly describe impact wave interaction with the projectile and are not reliable for non-normal penetration (penetration angles different from 90°). Analytic models are often based on cavity expansion theories (cylindrical and spherical) in an elastic or elasto-plastic material. Because of symmetry requirements and the fact that interfacial friction between projectile and the target is not included in the solution scheme, cavity expansion theories are not suitable for non-normal penetration modeling in layered targets. Numerical models used for projectile penetration analysis include Finite Difference (FD), and Finite Element (FE), codes. These are general purpose main frame codes which require extensive constitutive material parameters for each layer of the target. Because of this and the time involved to generate the input files and interpret the output files, the use of numerical models is only justified in final design stages.

The study presented here is a theoretical model that when completed will be used for predicting the path of projectiles in layered materials. The model overcomes the shortcomings associated with existing methods and provides a relatively simple way of optimizing the design for a layered protective structure.

STAGES OF PENETRATION AND GOVERNING EQUATIONS

At the moment of hitting a hard target, the projectile generates a shockwave in the target material.

This shockwave propagates ahead of the projectile and interacts with the target first. This interaction may change the properties of the traversed material. In addition, some of the energy of the shockwave is reflected back towards the projectile when the shockwave impinges on an interface in the target. Depending on the intensity of the shockwave and the strength of the target material, a pulverized and fractured zone develops which is limited to a certain radius. The projectile, then instead of penetrating into an intact material will penetrate into a material with residual strength.

The projectile penetrates into the target (intact or fractured) by creating a zone of highly stressed material around its nose. Because of high stresses, the material in this zone is pulverized or heavily fractured. Due to the geometry of the nose, before the full penetration of the nose, the highly stressed target material around the nose is restrained from large movements. However, when the entire length of the projectile is embedded in the target, the pulverized material starts flowing around the aft body into the void created in its wake. If the projectile has a pusher plate attached to its tail, upon impact of the pusher plate on the target surface, the plate is stripped off and the energy associated with this impact travels down the path of projectile and further degrades the target material ahead of the projectile. Figure 1 shows four stages of penetration. The first stage occurs during nose penetration when the target material is restrained from large movements; the second stage is the partially restrained penetration due to chipping and cratering at the point of impact, which allows larger movements of material around the projectile; the third stage occurs when the projectile is fully embedded and the pusher plate hits the target and strips off; and finally, the fourth stage occurs when the full length of the projectile is penetrating in the target and the target material flows around the projectile into the wake cavity behind the projectile.

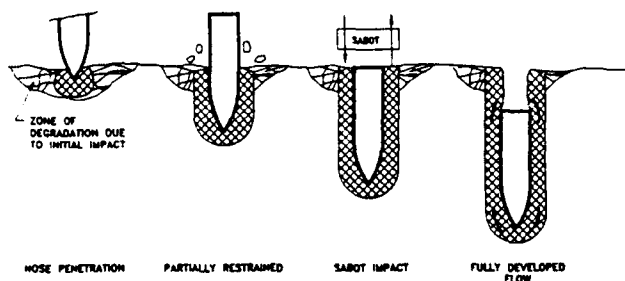


Figure 1. The four stages of penetration.

Resisting stresses acting on the projectile at each stage of penetration can be quantified through equations suitable for each stage. But before these equations can be used, the extent of material degradation due to initial impact has to be determined. For this purpose, the magnitude of the initial impact stress is calculated as:

$$\sigma_i = \rho \cdot u \cdot c_p \quad (1)$$

where ρ = target material density,
 u = particle velocity imparted to the target,
 and c_p = seismic wave velocity in target material.

Assuming that σ_i is attenuated inversely proportionally to the distance from the point of impact (r), the radial stress at any radius r , σ_r , is:

$$\sigma_r = \frac{r_0}{r} \sigma_i \quad (2)$$

where r_0 = the initial penetration radius (shown in Fig. 1),

and the tangential stress, σ_θ , is:

$$\sigma_\theta = K \cdot \sigma_r \quad (3)$$

where K = Coefficient of Lateral Pressure.

The radial and tangential stresses are the major and minor principal stresses and at the boundary of the failed material around the point of impact they can be related through the linear Mohr-Coulomb failure theory as:

$$\sigma_r = q_u + \sigma_\theta \tan^2 \left(45 + \frac{\phi}{2} \right) \quad (4)$$

where q_u = unconfined compressive strength of the target material,

and ϕ = angle of internal friction of the target material.

Substituting Eqs. (2) and (3) in Eq.(4), and solving for r , the following equation is obtained for the radius of failed material due to initial impact:

$$r = r_0 \frac{\sigma_i}{q_u} \left[1 - K \tan^2 \left(45 + \frac{\phi}{2} \right) \right] \quad (5)$$

Within distance r , the residual properties of the target material will be used in calculating resisting stresses acting on the projectile, whereas outside of r , the intact properties will be used.

The resisting stresses acting on the projectile are due to generation of a pulverized or highly deformed region around the nose of the projectile and the inertia of the material in this region as it is pushed away from the nose. They can be quantified by calculating static resistance to penetration of the nose and adding the inertial effects as dynamic stresses.

The subject of static resistance to penetration (slow penetration) has been investigated extensively in

the field of drilling. There are two solution schemes that are usually followed. The first is a lower-bound solution where only equilibrium and yield (or material failure) are considered, with no consideration of kinematics, [2]. The second solution scheme is an upper-bound solution where the velocity (kinematics) and strain boundary conditions are satisfied and resisting stresses are determined by equating the rate of work done by the penetrator to the rate of energy dissipation on slip surfaces, [3]. In this study during the restrained penetration stage of penetration, a lower-bound solution is used. During the fully developed flow, an upper-bound solution is utilized.

Lower-bound solution

The lower-bound solution used in this study is that developed by Pariseau, and Fairhurst, [4]. In their analysis of wedge penetration in a plastic material they derived the following equation for resisting stresses, P_s :

$$P_s = q_u \left\{ \frac{1 + \cos 2\theta (1 + \cot \beta \tan 2\theta) \sin \phi}{1 + \sin \phi} \exp(2\xi \tan \phi) - \tan^2 \mu \right\} \frac{\tan \beta}{2 \tan \phi \tan \mu} \quad (6)$$

where the angles θ , β , μ , and ξ are shown in Figure 2.

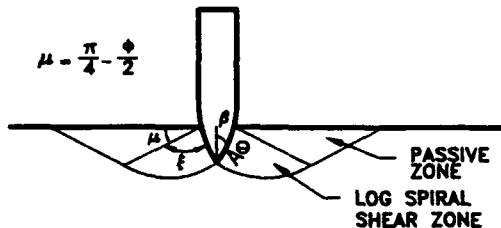


Fig.2. Slip line field around the nose of the projectile.

θ is related to the angle of interfacial friction ϕ' through the following equation, [5]:

$$2(\theta - \alpha) = \phi' + \arcsin \left[\left(1 - \frac{C}{\sigma} \right) \frac{\sin \phi'}{\sin \phi} \right] \quad (7)$$

where

C	=	cohesion of the target material,
ϕ'	=	friction angle between projectile and target material,
σ	=	mean stress in the plastic material, and
α	=	$\frac{\pi}{2} - \beta$

Upper-bound solution

An upper-bound solution based on the Prandtl mechanism is derived here, [6]. Figure 3 shows this mechanism adjacent to the nose of the projectile. The mechanism consists of a log-spiral shear zone (ACD), and a constant stress passive zone (ADE). The resisting stress, P_s can be calculated by setting the rate of work done by the projectile, \dot{W}_p equal to the rate of energy dissipation in the target material:

$$\dot{W}_p = \dot{E}_f + \dot{E}_{ls} + \dot{E}_{pz} + \dot{W}_g \quad (8)$$

where

- \dot{E}_f = Rate of energy dissipation due to friction along the nose length, AC.
- \dot{E}_{ls} = Rate of energy dissipation along the log-spiral zone, CD.
- \dot{E}_{pz} = Rate of energy dissipation along the passive zone, DE.
- \dot{W}_g = Rate of work done to move pulverized material up around the aft body.

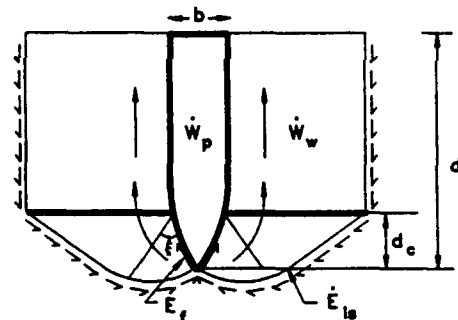


Fig. 3. Assumed slip line field and velocity diagram.

Expanding each term of Eq. (8) and simplifying leads to the following equation for pressure acting normal to the surface of projectile:

$$P_s = C \frac{N_\phi}{N_\beta} + (d - d_c) \cdot \gamma \cdot N_\gamma \quad (9)$$

where

$$N_\phi = \exp(2\xi \tan \phi) (\cos \phi + \cot \phi) - \cot \phi, \quad (10)$$

$$N_\beta = \frac{\sin \beta}{\sin \beta + \cos \beta \tan \phi'} - \frac{\tan \phi'}{\tan \beta + \tan \phi'}, \quad (11)$$

and

$$N_r = \left(\frac{2 \exp(\xi \tan \phi) \sin\left(\frac{\pi}{4} - \frac{\phi}{2}\right)}{\sin \beta} - \frac{1}{2} \right) \times \exp(\xi \tan \phi) \cos\left(\frac{\pi}{4} - \frac{\phi}{2}\right) \quad (12)$$

Dynamic Stresses

Dynamic stresses are generated due to inertia of the target material as it is pushed aside by the nose. The magnitude of dynamic stresses can be calculated through the impulse-momentum principle applied to the material around the nose of the projectile:

$$P_D = \rho \cdot u \cdot c_p (1 + \tan \phi' \cot \beta) \quad (13)$$

where P_D = dynamic stress normal to the nose of the projectile,
 u = projectile velocity normal to the nose surface.

The dynamic stress of Eq. (13) is added to static stress of Eq. (6) or (9) in order to calculate the total resisting stress on the nose of the projectile.

CALCULATION OF PROJECTILE PENETRATION

The resisting force acting on the projectile can be calculated by integrating static and dynamic stresses over the contact area of the nose and the aft body. The resisting force equations for various stages of penetration will then be used to calculate depth, velocity, and deceleration of the projectile in the target as a function of time. For this purpose the solution is carried out in time domain incrementally, and in each time increment, Δt , the principal of impulse-momentum is utilized to calculate the change in penetration velocity, deceleration and depth.

The incremental calculations are carried out until the kinetic energy of the projectile is exhausted, i.e., ΔV , approaches zero.

COMPARISON WITH FIELD EXPERIMENTS

Two normal penetration experiments in tuff were selected for application of the penetration model described in this paper. The first experiment was carried out in a Thirsty Canyon Tuff target, and the second experiment was in Antelope tuff. Material properties of interest for the two targets are shown in Table 1.

Table 1. Material properties for Thirsty Canyon and Antelope Tuffs.

	Thirsty Canyon	Antelope
Angle of Internal Friction, ϕ	22°	25°
Angle of Interface Friction, ϕ'	2°	2°
Seismic Velocity of Intact Rock, C_p	2,865 m/s	1,346 m/s
Seismic Velocity of Shock Conditioned Rock, C_p	1,270 m/s	610 m/s
Target Material Density, ρ	1,928 kg/m ³	1,714 kg/m ³
Unconfined Compressive Strength, q_u	63.0 MPa	15.0 MPa
Cohesion, C	10.4 MPa	5.0 MPa

Dimensions of the projectiles for the two events are shown in Figure 4. The coefficient of interfacial friction for the rock-projectile interface was assumed to have a low value of 0.03 ($\tan \phi' = .03$) due to melting that occurs at the interface. This value was selected based on a numerical study of sliding friction, experimental observations, and a thermodynamic analysis of the rubbing contact at the nose. The thermodynamic analysis indicated that the heat generated around the nose during penetration at velocities higher than 30 m/s was larger than the ability of the steel to transfer heat away from the contact surface. The temperature rise due to this excess heat at the nose-rock interface was larger than the melting point of steel and resulted in a thin melt layer. At velocities smaller than 30 m/s the rate of heat generation at the interface dropped to a lower value and heat transfer away from the interface became large enough to cause the temperature of the steel to drop below its melting point. As a result, during the final stages of penetration the thin melt layer starts cooling down and solidifying and the coefficient of friction increases correspondingly. The sudden increase in the coefficient of friction brings the projectile to a halt rapidly.

Figures 5 and 6 show the results of model predictions with those measured experimentally. Overall, the model predicts the trends observed experimentally. In both figures the model predicts a sharp rise in deceleration up to full nose penetration. Then there is a steady state penetration phase up to full penetration of the projectile. The steady state phase is disrupted by the pusher plate impact. At this point there is a spike in deceleration when the pusher plate strips off from the

projectile, resulting in a smaller mass for the projectile. After the pusher plate impact, the deceleration falls continuously, tending towards another steady state phase corresponding to a fully developed flow condition around the aft body. This is clearly visible in Fig. 6, where due to lower strength of the rock, the projectile traveled longer and reached a greater depth of penetration. Another phenomenon observed in experimental data of Figures 5 and 6 is the sudden deceleration increase just before penetration stopped. As discussed earlier, this may be due to an increase in coefficient of friction at lower velocities. In the present model when the projectile velocity dropped below 30 m/s, it was assumed that an increase in coefficient of friction occurred resulting in a sudden halt in further penetration. This is shown in Figures 5 and 6 as deceleration spikes at the end of penetration.

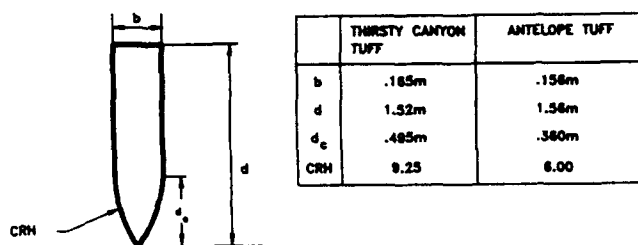


Figure 4. Projectile profiles in Thirsty Canyon, and Antelope Tuff.

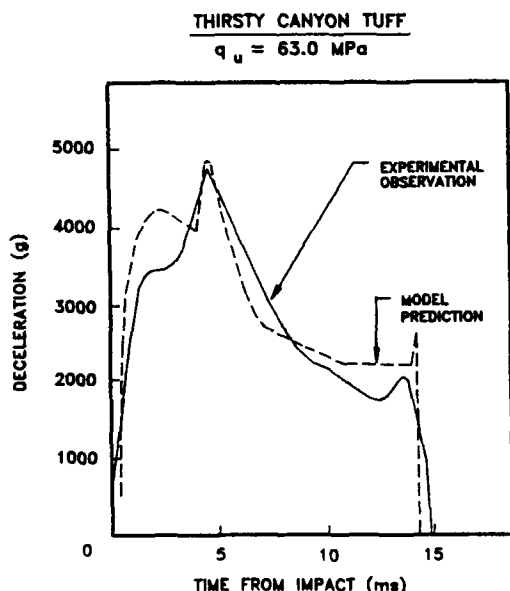


Figure 5. Model predictions in Thirsty Canyon Tuff.

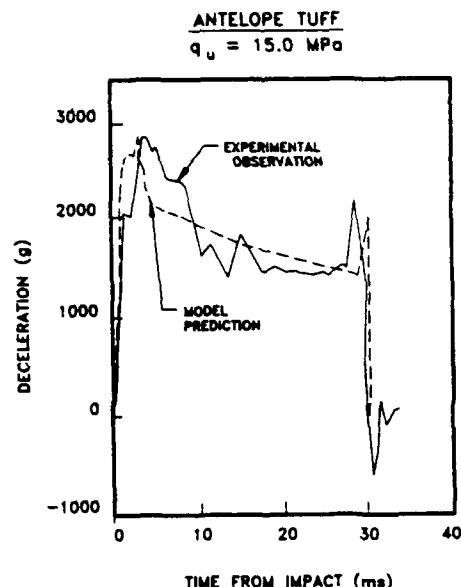


Figure 6. Model predictions in Antelope Tuff.

NON-NORMAL PENETRATION IN LAYERED TARGET

The theoretical model presented above has to be refined further in order to predict the non-normal path of projectile in a layered target. The lower and upper bound solutions can be readily generalized for non-normal penetration by including the angle of incidence of the projectile into the equations for slip surfaces. As shown in Figure 7, slip surface AB will have a longer length than slip surface AC. This will result in larger static and dynamic pressures on AB than on AC. As a result, "J" hooking of the projectile, defined as deviation of the path of projectile from its path at the time of impact (change in angle ω shown in Fig. 7) will result. This can be calculated by obtaining the sum of resisting forces in the x and y directions (F_x and F_y), and taking their moments (M) about the center of mass of the projectile. The angular acceleration $\ddot{\omega}$ can then be calculated as:

$$\ddot{\omega} = \frac{M}{I_m} \quad (14)$$

where I_m = Mass moment of inertia of the projectile.

The change in angle ω over Δt is then equal to:

$$\omega = \frac{1}{2} \ddot{\omega} \cdot (\Delta t)^2 \quad (15)$$

The effects of layering interfaces on projectile penetration are caused by the reflected waves that travel back towards the projectile. In targets that have relatively thin layers like concrete screens, the reflected waves may impart large enough forces on the projectile to cause additional deviation in the path of the projectile.

At present the lower and upper bound equations are being analyzed to include non-normal penetration. Wave propagation effects are also under study. The results of the final model will be presented in a future paper.

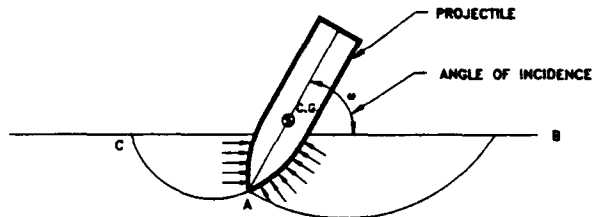


Figure 7. Slip surfaces in non-normal penetration.

CONCLUSIONS

A theoretical model was developed for prediction of projectile penetration in geologic materials based on energy tracking and the impulse-momentum principle. The model was developed by analyzing the various stages of penetration separately and then coupling them together to calculate resisting stresses on the projectile, and displacement, velocity and deceleration of the projectile as a function of time. The coupled model was then applied to two field experiments in different materials. The comparison indicated good agreement between predictions and experimental observations.

The governing equations were developed for normal penetration. However, the assumptions leading to these equations are also valid for non-normal penetration. As a result a procedure was developed for prediction of the projectile path in two dimensions. This procedure can be used with the governing equations presented in the paper after modifications are made to include the angle of attack, ω , in the equations.

ACKNOWLEDGEMENTS

UTD, Inc. expresses gratitude to the Tyndall AFB for sponsoring the work described in this paper. The contributions made by Drs. Eugene Foster and Steve Majtenyi of UTD are also acknowledged.

REFERENCES

- [1] Heuze, F. E., An Overview of Projectile Penetration Into Geologic Materials, with Emphasis on Rocks, Int. J. Rock Mech. Min. Sci. Vol. 27, No. 1, 1990.
- [2] Chen, W. F., and A. P. Pan, Finite Element and Finite Block Methods In Geomechanics, Purdue University, Civil Engineering Report CE-STR-90-20, p. 3, 1990.
- [3] Ibid, p. 4.
- [4] Pariseau, W. G., and C. Fairhurst, The Force Penetration Characteristic for Wedge Penetration Into Rock, Int. J. Rock Mech. & Min. Sci., Vol. 4, pp. 165 - 180, 1967.
- [5] Ibid, p. 170.
- [6] Chen, W. F., Developments in Geotechnical Engineering 7, Limit Analysis and Soil Plasticity, Elsevier Scientific Publishing Co., Amsterdam, 1975.

ANALYSIS OF ROCK-RUBBLE OVERLAY PROTECTION OF STRUCTURES BY THE FINITE BLOCK METHOD

Joseph M. Gebara¹, Austin D. Pan¹,
Jon B. Anderson²,

¹School of Civil Engineering, Purdue University, West Lafayette, IN 47907-1284

²HQ Air Force Civil Engineering Support Agency, Survivability Branch,
Tyndall Air Force Base, FL 32403-5519

ABSTRACT

Rock-rubble overlays have shown to be effective in stopping, deflecting, or breaking impacting projectiles. In this paper, the Finite Block Method, along with an energy approach to the dynamic fragmentation of rocks, is used to model the penetration problem. The Finite Block Method is a discrete element method based on the minimization of the total energy of the block system. The analysis follows fundamental physical principles and shows that the Finite Block Method is able to simulate a penetration problem with results comparable to experimental observations described in the literature.

INTRODUCTION

Burster slabs used to protect underground facilities from threatening penetrating projectiles are inordinately expensive and unable to be easily and quickly repaired after withstanding repeated hits. On the other hand, rock-rubble overlays (Fig. 1) have the potential to overcome the above mentioned drawbacks. However, more in-depth understanding of this defensive mechanism is needed, especially for categories II and III weapons, (see Table 1). Numerical, analytical, and empirical investigations have been conducted on rock-rubble overlay protection systems [1]-[2]. The numerical methods developed in the past are limited by using simplified fracturing schemes and by modeling the rock rubble as a uniform mesh of octagons [2]. A good numerical simulation of the penetration mechanism will save valuable time and resources from field experiments and provide insight for improving fortification design. In this paper, the Finite Block Method is introduced to model rock rubble penetration and rock fracture based on fundamental physical principles.

BACKGROUND

Rock-rubble overlays have been proposed as an alternative to burster slabs for protecting underground installations from high kinetic energy penetrating projectiles. To understand the effectiveness of the rock-rubble overlay it is important to start by identifying the threat weapon. Rohani [3] divided the weapons of interest into three categories, (Table 1). Where L , D , W , and A are respectively the length, the diameter, the weight, and the cross-sectional area of the penetrator. Whereas GP, AP, and SAP stand for general purpose, armor-piercing and semiarmor-piercing respectively.

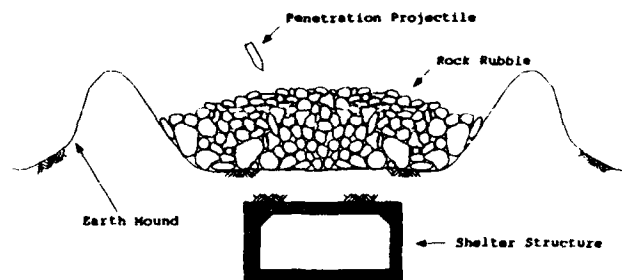


Figure 1: Typical example for the use of rock rubble

Experiments by: the Air force Civil Engineering Support Agency, Tyndal AFB, Florida; the U.S. Army Engineers Waterways Experiment Station, Vicksburg, Mississippi; the Naval Weapons Center, China Lake, California; and, the Air Force Armament Laboratory, Eglin AFB, Florida, have shown that the protective potential of the rock-rubble overlay depend to a great extent on the characteristics of the weapon against which the structure is to be protected. These characteristics include: length to diameter (L/D) ratio, sectional pressure (W/A), caliber or diameter (D), thickness of walls, material strength and fracture toughness of the case. Test results have also shown that the dominant mechanism of defeat depends on the characteristics of the boulder pile such as: rock size, rock unconfined strength, number of layers, and filler materials (sand and grout fillers have been tested).

Rock rubble overlays have proved to be effective in breaking up category I weapons due to triaxial loading or disarming them by fuze disruption. On the other hand, rock rubble overlays were less effective with category II and III weapons since they are unlikely to break because of their short L/D ratio and their high strength case. However, due to the short L/D , such projectiles may rotate significantly and tumble in the boulder pile. Therefore the function of the boulder screen in this case is to reduce the depth of penetration by increasing the rotation and tumbling of the penetrator.

The basic mechanisms involved in this defensive process are: the high probability of non-normal impacts will induce large obliquity and yaw angles which will cause the projectile to deflect from its original path; the fragmentation of rocks will result in a sudden increase in the stress fields that is resisting the projectile motion

Category	Weapon Type	Characteristics
I	GP weapons	Low to moderate L/D; Low W/A; Thin walls; Low strength; Low fracture toughness.
II	SAP weapons	Low to moderate L/D; Moderate W/A; Thick walls; Mild steel.
III	AP weapons	Moderate to high L/D; High W/A Thick walls; High strength; High fracture toughness

Table 1: Categories of weapons

thus promoting loss of velocity (thus loss of energy) and projectile rotation; the moving of boulders in different directions will also lead to the loss of energy. The above list of mechanisms is not inclusive but it shows that the rock-rubble overlay has good potential of defeating the penetrators.

THE FINITE BLOCK METHOD

Researchers have approached the solution of the above described penetration problem from three different techniques: analytical, empirical and numerical. The heterogeneous nature of rock rubbles and their complex constitutive behavior are definite obstructions to the application of analytical and empirical methods. Although these methods have been used with some measure of success, only numerical methods are credible in modeling structural analysis of rock-rubble overlays.

The method of Discrete Deformation Analysis (DDA) developed by Shi and Goodman [4] is the precursor of the Finite Block Method (FBM) which is a name coined by W.F.Chen [5] to better describe the present analysis. Chen recognized the essence of these computer-based methods in extending limit analysis [6] techniques to frictional materials.

Shi and Goodman [4] provides a complete kinematic theory that enables a large assemblage of blocks to undergo large deformations under loading or unloading conditions without the overlapping of one block onto another (Fig.2). A system of equilibrium equations for the block assemblage can then be derived through the minimization of the total energy of the system (i.e. potential, strain, frictional). These equations are solved iteratively in each time interval until the constraints of no-overlap and no-tension between blocks are satisfied. At the end of each iteration, external and internal equilibrium are satisfied for each block, and Coulomb's Law of friction is fulfilled at all contact points. A major advantage this procedure offers is its ease in modeling a discontinuous block medium as an assemblage of convex, concave or even multi-connected polygons.

The above characteristics of the Finite Block Method form the basis for choosing this method to simulate the penetration and fragmentation phenomena as opposed to other discrete element and finite element approaches. The rock-rubble boulder can be easily modeled by the Finite Block Method; and the method is energy-

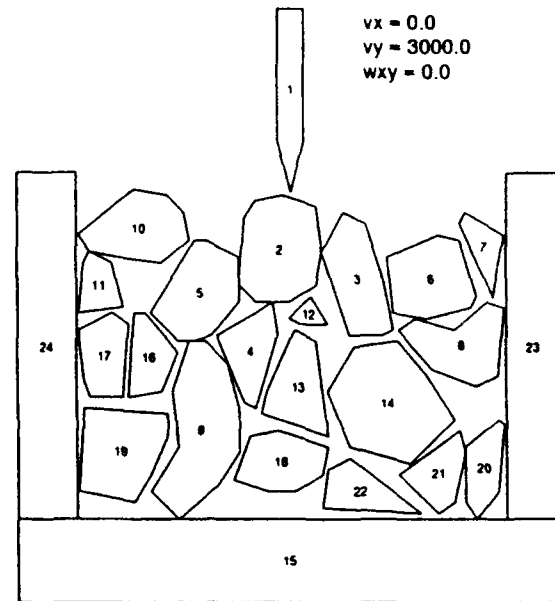


Figure 2: Finite Block Model

based and uses hard contacts which better represents the contact between rocks and between rocks and penetrator [7]. Moreover, the representation for the displacement and velocity vectors by FBM directly gives strains, strain-rates and stresses that are necessary for implementing a fracturing scheme which is a major contribution of the present work.

DYNAMIC FRACTURE OF ROCK

The concept of dynamic fracture of flawed brittle material such as rocks has been extensively studied by Grady and Kipp [9]. It is basic to this concept to distinguish between the response of a single crack and the response of a system of cracks to impulsive loading. Experimental studies of fracture under high strain rates have revealed unusual features associated with the fracture phenomenon, such as greatly enhanced material strength and fracture stress dependence on loading conditions. Grady and Kipp [9] discuss two theoretical descriptions of dynamic fragmentation which they describe as not compatible. The first is explicitly based on the concept of a distribution of flaws that act as points of fracture initiation. The second has no recourse to a flaw distribution; fragment size is based strictly on energy balance considerations. In the latter approach a tacit assumption of some sufficient flaw distribution is implied. For the rock rubble problem where rocks are mined from quarries this assumption is satisfied.

In his energy balance analysis Grady [10] states that it is reasonable to assume that if the material has sufficient flaws ("favorably disposed") a reasonable prediction of the dynamic spall strength (P_s), the time to failure (t_s), and the nominal fragment size (s) created in the spall event can be given by Eqs. (1)-(3.)

$$P_s = (3 \rho c_0 K_c^2 \dot{\epsilon})^{1/3} \quad (1)$$

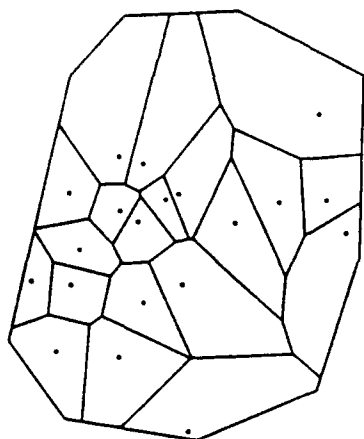


Figure 3: Example of Voronoi fragmentation

$$t_s = \frac{1}{c_0} \left[\frac{\sqrt{3} K_c}{\rho c_0 \dot{\epsilon}} \right]^{2/3} \quad (2)$$

$$s = 2 \left[\frac{\sqrt{3} K_c}{\rho c_0 \dot{\epsilon}} \right]^{2/3} \quad (3)$$

Experimental evidence shows [11] that under high strain rates these spall properties are less sensitive to microstructural details of the material, but depend more on a balance of the driving energy in the transient stress wave loading and some continuum measure of fracture dissipation such as fracture toughness, surface tension or flow stress.

In the present rock rubble problem, most rocks can be easily considered as "favorably disposed" for fracture and the impacting projectile will create high strain rates in the rocks. Thus the energy approach derived above is ideal for incorporation into the Finite Block Method.

DYNAMIC FRAGMENTATION

The geometric modeling of fragments is an important part of the present work since impact dynamics depends not only on the size and fracture toughness of the impacting bodies, but also on their shape. Unfortunately, the literature has focused more on achieving a better understanding of the distributions in particle size which result from severe fragmentation ([12]-[14]), and have tended to ignore any description of the shape of the fragments. In this section a brief overview of this work will be given from which the choice of the Voronoi construction approach for the present work will be explained.

Statistical and physical principles underlying the dynamic fragmentation process have been substantially explored in the literature [12]. Numerous ideas have been pursued which are clearly related to observed fragmentation phenomena. However, a complete theory of dynamic fragmentation is not yet available, and in many cases observed phenomena lack even a good explanation. Grady and Kipp [12] have focused on the statistical nature of

dynamic fragmentation and presented an excellent review of the background of important earlier works.

There appears to be general agreement over the application of geometric statistical fragmentation in one dimension — namely, the random distribution of points which partition the line into a distribution in fragment lengths. On an infinite line, the position of the points is a Poisson variate and the only parameter is the average number of points per unit length which is expected to relate to the intensity of the fracturing load. In contrast, there is apparently no agreement on the application of geometric statistics to the random partitioning of two and three dimensional bodies. Although it is generally agreed that the random placement in the space is Poisson, there are a variety of partitioning constructions which can be formed with these points. The theory of Mott [15], for example, differs fundamentally from that of Gilvarry [16] which also differs from that of Grady and Kipp [12], even though all of them start with a Poisson process. Other common constructions which have been explored extensively include the Voronoi and the Johnson-Mehl [12]. Such statistical fragmentation methods have been broadly applied in other areas of science including metallurgy, geology, and biology. Different statistical constructions have been found to provide different fragment size distributions and consequently it becomes necessary to rationalize a particular choice to each application.

In the present rock rubble study the Voronoi construction (Fig. 3) is chosen. The Voronoi construction uses perpendicular bisectors between the random points to partition the block area [17]. Although this construction produces strongly centered fragment sizes [12], with a lag of the larger and smaller fragments that are usually found in dynamic fragmentation, preliminary rock rubble penetration experiments appear to show that the fragment shapes are well represented by a Voronoi construction. Crain [18] noted that "the perimeter and area are highly correlated showing that the polygon shapes tend to be equant or quasicircular rather than elongated". Moreover, the Voronoi construction is extensively used for a wide range of applications including finite element mesh generation [19] and computer graphics [20].

PROPOSED FRAGMENTATION PROCESS

It is important to note that the size of the rocks considered in the rock rubble fortification problem is about three times the diameter of the penetrator; hence the analysis is different from a penetration problem where a projectile impacts a continuum which is relatively large in size and where upon impact the penetrator becomes embedded in the continuum. In the case of the system being analyzed, the projectile proceeds in a succession of impact and fracturing of rocks that come into its path of penetration. The velocity of the projectile ranges between 1 000 ft/sec and 2 500 ft/sec, thus upon impact a high stress level is reached in the rocks, leading some rocks to severe fragmentation.

Impact between two or more bodies is known to go through three stages. In the first stage, upon impact, each of the bodies will start to contract under a certain strain rate thus acquiring internal kinetic and elastic energy. The contraction will continue to the point of maximum deformation which is stage two where there is zero kinetic energy and maximum elastic energy. In the third stage, depending on the material properties and the strain rates, solid bodies will either regain their original shape, stay permanently deformed, or even fracture. It is worth noting that only in

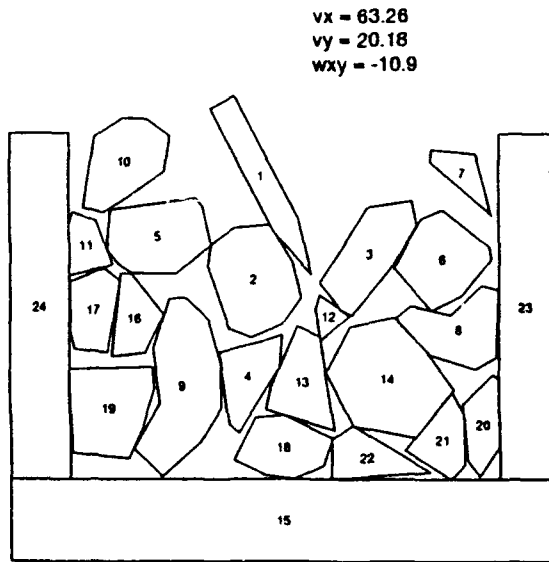


Figure 4: Finite Block Analysis without fragmentation

the case of perfectly elastic impact the total energy of the system is conserved. In the general case where elasto-plastic or plastic impact takes place, the coefficient of restitution is not unity, lost energy is transformed into creating new fracture surfaces, generating elastic waves within the colliding bodies, as well as generating heat.

Thus in the restitution period, failure or rupture of condensed rock may occur due to stresses in excess of the tensile strength — a process which is referred to as the spall process. The spall process becomes fairly complex under transient loads, especially when the load leads to high compression before the material is carried into tension. The material is thus in a state of tensile stress that is intrinsically unstable and small perturbations can lead to the opening of voids and initiation of the spall process.

The threshold tensile stress at which void nucleation occurs and spall fracture initiates, the time at which the threshold tensile stress is reached, and the nominal size of the fragments were derived by Grady [10] and are presented by Eqs. (1), (2) and (3), respectively.

In the rock rubble analysis, the Finite Block Method continues without fracture until contact between the penetrator and a boulder element occurs and a critical strain rate is reached. At this strain rate the strain energy density U_s needed for fracture is calculated using:

$$U_s = \frac{180\gamma}{62c_0t} \quad (4)$$

where t is the time after contact and $\gamma = K_c^2/(2\rho c_0^2)$ is the fracture surface energy density per unit area. In this process it is assumed that the strain rate in compression has the same order of magnitude of the strain rate in tension, thus the material will expand at the same strain rate as it was compressed. U_s is compared to the elastic energy density U found in the Finite Block elements which can be written as:

$$U = \frac{B_0 \epsilon^2 t^2}{2} \quad (5)$$

Fracture will occur when $U \geq U_s$. After checking for fracture,

the nominal fragment size created by the spall process is approximated by Eq. (3) and used to distribute N Poisson points inside the fractured block element. N being the ratio of the area of the fractured block to the nominal fragment area.

The Poisson points will form the basis of the Voronoi construction that partitions the fractured block into a collection of randomly shaped polygons. Each polygon is then given an initial velocity that results from the kinetic energy not used to fuel the fragmentation, referred to as the Kinetic Energy Difference. The Finite Block analysis of the system is then continued to the next contact, impact, and fracture progression. This process is continued until the projectile stalls or penetrates through the rubble layers.

The Kinetic Energy Difference can be calculated by noting that the total kinetic energy K.E. of a sphere expanding with a strain rate $\dot{\epsilon}$ can be represented by

$$K.E. = 8 \int_0^{\pi/2} \int_0^{\pi/2} \int_0^{s/2} \frac{1}{2} \rho \dot{\epsilon}^2 r^2 (r^2 \sin(\theta) dr d\theta d\phi) \quad (6)$$

which is equivalent to

$$K.E. = \frac{2\pi}{5} \rho \dot{\epsilon}^2 \left(\frac{s}{2}\right)^2 \quad (7)$$

Using the kinetic energy available for fracture from Eq. (8):

$$T = \frac{1}{120} \rho \dot{\epsilon}^2 s^2 \quad (8)$$

after multiplying it by the volume of the sphere since Eq. (8) represents the kinetic energy density, the product will give the Kinetic Energy Difference K.E.D. as:

$$K.E.D. = \frac{1}{90} \pi \dot{\epsilon}^2 s^5 \rho \quad (9)$$

The Kinetic Energy Difference is used to initiate the dispersion velocity of the fragments. By equating K.E.D. to $\left(\frac{1}{2} m v^2\right)$ the velocity v of each fragment can be calculated by:

$$v = \sqrt{\frac{2}{15}} \dot{\epsilon} s \quad (10)$$

This velocity is considered to have a direction along a line that joins the center of gravity of the fragment to the equivalent center of gravity of the fractured block.

ILLUSTRATIVE EXAMPLE AND DISCUSSION

To illustrate the fragmentation process, a penetrator ($E = 29 \times 10^6$ lb/in², $\nu = 0.30$, and $\rho = 0.28404$ lb/in³) with an initial velocity of 15000 in/sec impacts an igneous rock rubble that has the following material properties: $E = 14 \times 10^6$ lb/in², $\nu = 0.25$, $\rho = 0.102$ lb/in³, and $K_c = 7.764 \times 10^3$ lb/in^{3/2}.

Knowing that the spall process appears at strain rates that range between 10^1 /sec and 10^4 /sec, a strain rate of 10^3 /sec was used in Eq. (2) to approximate the spall fracture time for the igneous rock at 6μ sec. Thus a time step of the order of 1μ sec is needed for the analysis. A maximum displacement of 0.005 in. per time step and a contact spring stiffness of 10^9 lb/in were set for the Finite Block analysis. Note that fragmentation of the projectile was not considered and that double precision on a 32-bit SUN Sparcstation was used to minimize the effect of round-off errors.

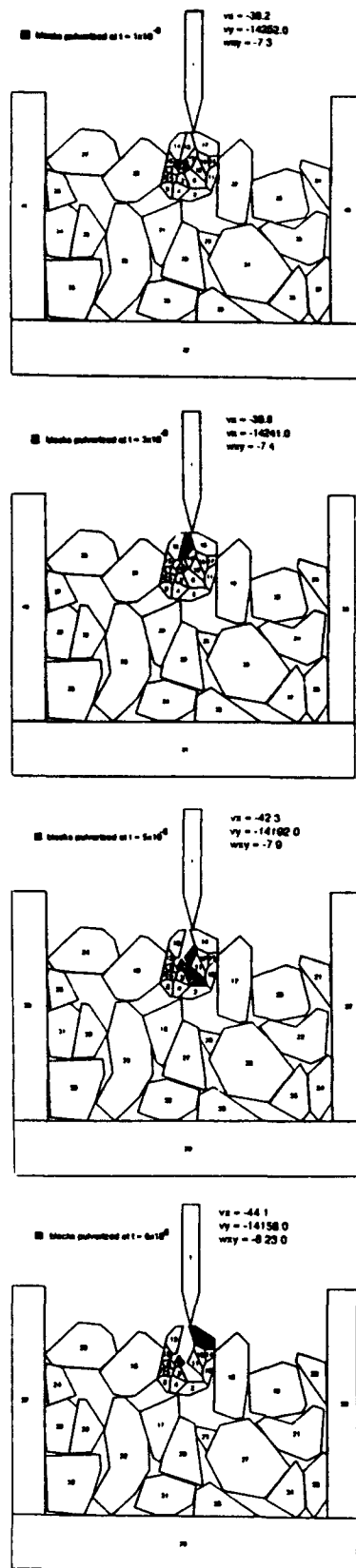


Figure 5: Example of the process of fragmentation and penetration

Even though a 2D cross section of a rock rubble is by no means compact, a compacted 2D finite block mesh was used in the analysis to reduce rigid body movements and to create the 3D effect of confinement (compare Fig. 2 with Fig. 5). The Finite Block code was modified to allow the input of initial velocities for each block and gravity acceleration which was used to settle the blocks into a confined rubble. Gravity loading was explicitly incorporated into the Finite Block Method by adding a new loading case to the forcing vector.

The example to follow is used to illustrate the fragmentation of a block at an intermediate stage of the penetration process when the velocity of the projectile is reduced to a point that fragmentation results in 19 new blocks (Fig. 5). At an initial velocity of impact ($v \approx 30\,000$ in/sec) rocks may reach strain rates of up to 10^4 /sec leading to more than 6 000 fragments according to the fracture calculations outlined. This phenomenon represents the pulverization of the blocks that the projectile initially impacts and has been actually observed.

In Fig. 5 the fracturing process is shown by the Finite Block output. At the first time step ($t = 1 \mu\text{sec}$) the fragmentation takes place. The initial velocity of the fragments is calculated according to Eq. (10) and stresses, strains, and strain rates are initialized to zero. The Finite Block analysis is then continued to the next time step ($t = 2 \mu\text{sec}$). The vertical velocity of the projectile is now reduced from 15 000 in/sec to 14 250 in/sec, and the horizontal and rotational velocities increase from zero to 39.2 in/sec and 7.3 rad/sec, respectively. Two interior fragments reach high strain rates that lead them to pulverize and are shown shaded in Fig. 5(a). The pulverized fragments are then removed since their effect is negligible. The sequence of pulverization and breakup is further shown by Figs. 5 and 6. Fig. 6 shows the projectile penetrating the fractured rock, with its vertical velocity now reduced to 14 150 in/sec, and its horizontal and rotational velocities increased to 44.2 in/sec and 26.8 rad/sec, respectively.

CONCLUSION

The Finite Block Method is used to analyze the impact of high kinetic energy penetrators into rock rubbles. An energy balance approach to the dynamic fragmentation of brittle material has been incorporated into the Finite Block Method that allows blocks to fracture at high strain rates. The analysis follows fundamental physical principles that govern the phenomena and realistic results are obtained when compared with experiments described in the literature. The fracture and fragmentation analysis is important in the penetration problem since without fracture, large and unrealistic deflection of the projectile path is simulated. The analysis results have also shown that high velocities, high strain rates, and small time steps can be used effectively in the Finite Block Method to model the pulverization and fragmentation of the rock rubble and to detect the change in velocity components of the projectile.

ACKNOWLEDGMENTS

The authors wish to acknowledge the support of the the U. S. Air force Civil Engineering Support Agency and the Purdue Research Foundation, as well as G.-H. Shi of the University of California at Berkeley; C. M. Hoffman and W. J. Bouma of the Department of Computer Science at Purdue University; and D. E. Grady and M.

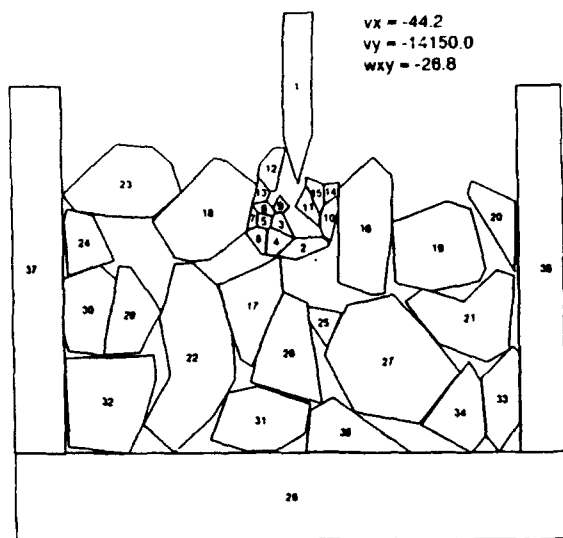


Figure 6: Penetrator before second contact is already starting to deflect

E. Kipp of Sandia National Laboratories for their encouragement and helpful discussions.

References

- [1] NELSON, R.B., ITO, Y.M., BURKS, D.E., MUKI, Y., California Research and Technology, Inc., and HOLLOWELL, J.A., MILLER, C.W., Avco systems Division, 'Numerical Analysis of Projectile Penetration into Boulder Screens,' WES MP SL-83-11, U.S. Army Engineer Waterways Experiment Station, Vicksburg, MS, (1983).
- [2] GELMAN, M.D., RICHARD, B.N., and ITO, Y.M., California Research and Technology, Inc., 'Impact of AP Projectile into array of Large Caliber Boulders,' U.S. Army Engineer Waterways Experiment Station, Vicksburg, MS, (1987).
- [3] ROHANI, Behzad, 'Penetration of Kinetic Energy Projectiles into Rock-Rubble/Boulder Overlays,' Report, U.S. Army Engineer Waterways Experiment Station, Vicksburg, Mississippi, (1987).
- [4] SHI, G.H., and GOODMAN, R.E., 'Generalization of Two Dimensional Discontinuous Deformation Analysis for Forward Modeling,' International Journal for Numerical and Analytical Method sin Geomechanics, **13**(4), pp. 359-380, (1989).
- [5] CHEN, W.F. and PAN, A.D., 'Finite Element and Finite Block Methods in Geomechanics,' Proceedings of the third International Conference on Constitutive Laws of Engineering Materials, Tuscon, Arizona, (1991).
- [6] CHEN, W.F. Limit Analysis in Soil Plasticity, Elsevier, Amsterdam, The Netherlands, 1975.
- [7] CUNDALL, A.P. and ROGER, D.H., 'Numerical Modeling of Discontinua,' Proc. of 1st U.S. Conference on Discrete Element Methods, Golden, Colorado, (1989).
- [8] SHI, G.H., 'Discontinuous Deformation Analysis: A New Numerical Model for the Statics and Dynamics of Block Systems,' Ph.D. Dissertation, Department of Civil Engineering, University of California at Berkeley, 1988.
- [9] GRADY, D.E., and KIPP, M.E., 'Mechanics of Dynamic Fragmentation Factors Governing Fragment Size,' Sandia National Laboratories, Rept. SAND 84-2304C, (1984).
- [10] GRADY, D.E., 'The Spall Strength Of Condensed Matter,' J. Mech. Phys. Solids, **36**(3), pp. 353-384, (1988).
- [11] GRADY, D.E., 'Analysis of Prompt Fragmentation in Explosively Loaded Uranium Cylindrical Shells,' Sandia National Laboratories, SAND 82-0140, (1982).
- [12] GRADY, D.E., and KIPP, M.E., 'Geometric statistics and dynamic fragmentation,' Journal of applied physics, **58**(3), pp. 1210-1222, (1985).
- [13] TAKAGI, Y., MIZUTANI, H., and KAWAKAMI, S., 'Impact Fragmentation Experiments of Basalts and Pyrophyllites,' Icarus, **59**, pp. 462-477, (1984).
- [14] FUJIWARA, A., KAMIMOTO, G., and TSUKAMOTO, A., 'Destruction of Basaltic Bodies by High-Velocity Impact,' Icarus, **31**, pp. 277-288, (1977).
- [15] MOTT, N.F. and LINFOOT, E.H., 'A Theory of Fragmentation,' Extra-Mural Research No. F72/80, Ministry of Supply, England, (1943).
- [16] GILVARRY, J.J., 'Fracture of Brittle Solids, I, Distribution Function for Fragment Size in Single Fracture (theoretical),' Journal of Applied Physics, **32**, pp. 391-399, (1961).
- [17] PREPARATA, F.P., and SHAMOS, M.I., COMPUTATIONAL GEOMETRY An Introduction, Springer-Verlag, New York, 1985.
- [18] CRAIN, I.K., 'The Monte Carlo Generation of Random Polygons,' Computers and geosciences, **4**, pp. 131-141, (1977).
- [19] GHOSH, S., and MUKHOPADHYAY, S.N., 'A Two Dimensional Automatic Mesh Generator for Finite Element Analysis for Random Composites,' Computers and Structures, **41**(2), pp. 245-256, (1991).
- [20] HOFFMAN, C.M., 'Computer Vision, Descriptive Geometry and Classical Mechanics,' Proc. of the Eurographics Workshop Computer Graphics and Mathematics, Genova, Italy, (1991).
- [21] MILES, R.E., 'On the homogeneous planar Poisson point process,' Math. Biosciences, **6**(1), pp. 85-127, (1970).

A SIMPLY COUPLED PENETRATION TRAJECTORY/STRUCTURAL DYNAMICS MODEL

Mark D. Adley
Research Civil Engineer

US Army Engineer Waterways Experiment Station
3909 Halls Ferry Road, Vicksburg, Mississippi, USA 39180-6199

ABSTRACT

The rigid-body penetration code PENC02D has been linked with the general-purpose analysis code ABAQUS* to provide a method of analyzing the structural response of projectiles subjected to impact/penetration loads. The logic and forcing functions of the trajectory code PENC02D are used as an ABAQUS DLOAD user subroutine to compute the loads experienced by the projectile during a penetration event. The computed penetration loads are a function of the material properties of the target and the velocity, position, and deformed shape of the projectile. The resulting simply coupled penetration trajectory/structural dynamics model can be used to analyze various normal and oblique impact/penetration problems. The time-history of the structural response, depth of penetration, velocity, and acceleration of the projectile is computed. The deformed shapes predicted by the PENC02D/ABAQUS** model compared well with the deformed shapes of projectiles which were tested at the US Army Engineer Waterways Experiment Station Projectile Penetration Test Facility.

INTRODUCTION

Projectiles and earth penetrators are designed to survive a specified range of impact and penetration events. For that reason, nonlinear finite element (FE) analyses are conducted to investigate the structural response of the projectile. Most impact/penetration problems are investigated by utilizing either a coupled or an uncoupled method of analysis. The coupled method of analysis involves the use of a special purpose computer code (Reference 1), such as EPIC or DYNA, which includes algorithms that allow the analyst to model the interaction between the target and the penetrator. The uncoupled method of analysis involves the use of a structural dynamics code (References 2 and 3), e.g. ABAQUS or NASTRAN, to determine the response of a projectile subjected to a loading history which is computed with a penetration trajectory code such as

SAMPL, PENDEPTH or PENC02D. Although these methods are useful for some impact/penetration analyses, their shortcomings make them a poor choice for many common penetration analyses.

Since the coupled method of analysis utilizes a code that allows the user to model the target as well as the projectile, the analyst does not have to conduct a separate penetration analysis to determine the loading history. The shortcomings of the coupled analysis method are that sliding surface algorithms are required to define the projectile/target boundary, computational techniques such as rezoning are usually required to handle the large deformations of elements located in the target, and constitutive models currently available are not adequate to accurately model many target materials. Also, since this approach requires that the target as well as the projectile be modeled, these problems generally involve very large numbers of elements. Because of the large size of the resulting models, and the aforementioned shortcomings, the coupled method of analysis can be very expensive and time consuming.

An uncoupled approach which uses a structural dynamics code and a penetration trajectory code greatly simplifies the size and complexity of the FE analysis. In this approach, the analyst must first conduct a penetration analysis to determine the time-history of the penetration loads on a rigid projectile and then use these loads as input to a structural dynamics code. A shortcoming of this approach is that the computed penetration loads are not a function of the projectile's structural response. Also, a significant amount of effort is often required to translate the load data generated by the rigid-body trajectory code into a format that is compatible with the selected FE code.

The impact/penetration model created by linking the rigid-body penetration code PENC02D (References 4 and 5) and the general-purpose FE code ABAQUS (References 6, 7 and 8) represents an alternative approach to penetration problems. This approach does not require modeling of the target or a separate analysis to determine the penetration loads and in many cases it is less time-consuming and less expensive than either of the two aforementioned approaches. Also, since the deformation of the projectile at a given time step is allowed to influence the loads obtained from the trajectory

*ABAQUS is available under license from Hibbitt, Karlsson and Sorensen, Inc.

**PENC02D/ABAQUS denotes the model created by using the logic and forcing functions of the trajectory code PENC02D as an ABAQUS DLOAD user subroutine; it is not a product of, and it is not endorsed by, Hibbitt, Karlsson and Sorensen, Inc.

code at the next time step, this approach represents a simply coupled method of analysis (Reference 9).

THE PENCO2D/ABAQUS PENETRATOR ANALYSIS MODEL

The PENCO2D computer code was developed to compute the trajectory and penetration loads of a rigid projectile due to impact with geologic and man-made targets such as soil, rock, and concrete (References 10 and 11). A description of the target and the shape, mass, moment of inertia, initial position, and initial velocity of the projectile are the input data required for a PENCO2D analysis. The projectile is divided into a mesh of differential area elements. At each time step of a PENCO2D analysis the equations of motion are integrated, and the position, velocity, and acceleration of the projectile's center of gravity are updated. The updated position and velocity of the projectile are then utilized in the empirical forcing functions to determine the magnitude of the force acting on each differential area element of the projectile. The forces acting on the differential area elements are then integrated to obtain the total forces and moments acting on the projectile. These forces and moments are used as applied loads for the next time step. PENCO2D also contains algorithms to account, in an approximate manner, for interface and free-surface effects.

The general-purpose FE code ABAQUS provides users with the option of linking their own FORTRAN subroutines with the ABAQUS code. ABAQUS provides several different interfaces; the interface utilized in this work is known as the DLOAD user subroutine. The DLOAD user subroutine consists of a user supplied FORTRAN subroutine that computes the magnitude of a non-uniform distributed load. The DLOAD user subroutine is called by ABAQUS at each load integration point where a non-uniform distributed load is applied. The PENCO2D/ABAQUS impact/penetration model described in this paper is created by utilizing segments of PENCO2D code, rewritten to provide compatibility with FE code, as the heart of an ABAQUS DLOAD user subroutine.

THE PROJECTILE FINITE ELEMENT MODEL

The nodal coordinates of the projectile FE model define the initial position and orientation of the projectile. The element type and connectivity define the structural shape of the projectile, and the position and orientation of the projectile's surface. The correct mass, center of gravity, and mass moment of inertia of the projectile can be obtained by utilizing several materials which are identical except for the value of their densities. Thus, the mass of internal components is accounted for by utilizing these artificial density values.

The initial (impact) velocity vector, and therefore the angle of attack, of the projectile is defined by specifying the initial velocity of the translational degrees of freedom at each nodal point of the FE model. The angle of attack and the angle of obliquity are defined in Figure 1. For a two-dimensional (2D) impact/penetration problem it is only necessary to develop a FE model of a 180-degree section of the projectile; of course this requires that symmetry boundary conditions be imposed on all

nodal points which lie on the plane of symmetry. For a general 3D impact/penetration problem the entire projectile is modeled and no boundary conditions are applied.

The projectile penetration analyses under consideration are nonlinear structural dynamics problems. To account for material nonlinearities an appropriate constitutive model must be utilized for the projectile material. The analysis presented in this paper utilized the ABAQUS PLASTIC option. This option is used to specify a Mises yield surface with associated plastic flow and isotropic hardening. To account for geometric nonlinearities the NLGEOM option must be specified in the ABAQUS solution procedure description.

PENCO2D/ABAQUS IMPACT/PENETRATION ANALYSES

EXAMPLE PROBLEM: OBLIQUE IMPACT INTO CONVENTIONAL-STRENGTH CONCRETE

The example problem investigates the structural response of a projectile as it impacts and penetrates a concrete half-space. The impact conditions are described by an angle of obliquity of 15 degrees, and an angle of attack of 15 degrees. The impact speed of the projectile is assumed to be approximately 12,000 in./sec. The projectile is composed of material that is assumed to obey an elastic-plastic material law with an initial yield stress of 192,000 psi. The concrete half-space is assumed to have an unconfined compressive strength of 7,000 psi, a mass density of 0.000225 lb-sec²/in.⁴, and a rigidity index of 350.

Figure 2 contains plots of the deformed shape of the projectile at 0.00, 3.01, 4.99 and 6.72 milliseconds (msec) after impact; a scale factor of 1.0 was used for this plot. Plots of FE analysis results presented in this paper were created with the post-processing module of the I-DEAS software package (I-DEAS is available under license from the Structural Dynamics Research Corporation, Milford, Ohio). The large flat element shown in Figure 2 represents the surface of the target. The vertical distance between the large element and the nose of the projectile represents the penetration depth at the timestep considered in the plot.

An examination of Figure 2 reveals that the magnitude of the predicted structural deformations is quite large, and leads to the conclusion that a projectile subjected to those impact conditions would sustain significant permanent damage, i.e. significant levels of plastic strains. The photograph in Figure 3 shows the posttest condition of a projectile that was subjected to the impact conditions used in the simulation. An examination of Figure 3 indicates that, as predicted by the PENCO2D/ABAQUS analysis, the projectile did sustain permanent large-scale bending deformation. A comparison of the predicted deformed shape and the photograph of Figure 3 indicates that the PENCO2D/ABAQUS prediction is very close to the actual deformed shape.

SUMMARY AND CONCLUSIONS

An impact/penetration model for the structural response analysis of deformable projectiles has been introduced. The model was created by linking the rigid-body trajectory code PENC02D with the general-purpose finite element code ABAQUS. The resulting weakly coupled impact/penetration model can be used to determine the time-history of the structural response, depth of penetration, velocity, and acceleration of deformable projectiles subjected to very general impact/penetration loading events.

The results of the example problem indicate that the PENC02D/ABAQUS impact/penetration model introduced herein represents a very effective method of determining the structural response of projectiles subjected to impact/penetration loading events. The method of analysis represented by the PENC02D/ABAQUS model makes very efficient use of both computer time and the analyst's time while still providing significant insight into, and a reasonably accurate estimate of, the time-history of the projectile's response.

ACKNOWLEDGEMENT

The research reported herein was conducted as a part of the US Army Corps of Engineers (USACE) Hardened Structures Work Package, Work Unit No. AT22-HS-003, "Performance of Projectiles Impacting Geologic/Structural Targets." The permission from the Office, Chief of Engineers, to publish this paper is gratefully acknowledged.

REFERENCES

1. Schwer, L.E. and Day, J. 1991. "Computational Techniques for Penetration of Concrete and Steel Targets by Oblique Impact of Deformable Projectiles," Nuclear Engineering and Design, Vol. 125, pp. 215-238.
2. Stronge, W.J. and Schulz, J.C. 1987. "Finite Element Analysis of Projectile Impact Response," in Finite Element Handbook, Kardestuncer, H., (ed.), McGraw-Hill.
3. Gelman, M.D. and Ito, Y.M. 1992. "Excalibur Code Analysis for Penetrator Structural Response," Technical Report SL-92-1, US Army Engineer Waterways Experiment Station, Vicksburg, MS.
4. Creighton, D. C. 1982. "Non-Normal Projectile Penetration in Soil and Rock: User's Guide for Computer Code PENC02D," Technical Report SL-82-7, US Army Engineer Waterways Experiment Station, Vicksburg, MS.
5. Creighton, D. C. 1991. "Three-Dimensional Projectile Penetration in Soil and Rock: User's Guide for Computer Code PENC03D," Technical Report SL-91-13, US Army Engineer Waterways Experiment Station, Vicksburg, MS.
6. Hibbitt, Karlson and Sorensen, Inc., 1989. ABAQUS Users Manual, Version 4-8, Providence, RI.
7. Hibbitt, Karlson and Sorensen, Inc., 1989. ABAQUS Theory Manual, Version 4-8, Providence, RI.
8. Hibbitt, Karlson and Sorensen, Inc., 1989. ABAQUS Examples Manual, Version 4-8, Providence, RI.
9. Longcope, Donald B., Jr. 1990. "Coupled Bending/Lateral Loading Modeling of Earth Penetrators", Report SAND90-0789, Sandia National Laboratories, Albuquerque, NM.
10. Bernard, R.S. and Creighton, D.C. 1979. "Projectile Penetration in Soil and Rock: Analysis for Non-Normal Impact", Technical Report SL-79-15, U.S. Army Engineer Waterways Experiment Station, Vicksburg, MS.
11. Bernard, R.S. and Creighton, D.C. 1978. "Non-Normal Impact and Penetration: Analysis for Hard Targets and Small Angles of Attack", Technical Report S-78-14, U.S. Army Engineer Waterways Experiment Station, Vicksburg, MS.
12. Adley, M.D. 1992. "PENC02D/ABAQUS: A Simply Coupled Penetration Trajectory/Structural Dynamics Model for Deformable Projectiles", Technical Report SL-92-26, U.S. Army Engineer Waterways Experiment Station, Vicksburg, MS.
13. Cargile, J.D. and Tidwell, L.E. 1992. "Penetration of a Subscale Semi-Armor Piercing Projectile into Conventional-Strength and High-Strength Concrete Targets", Technical Report in Preparation, U.S. Army Engineer Waterways Experiment Station, Vicksburg, MS.
14. Young, C.W. 1972. "Empirical Equations for Predicting Penetration Performance in Layered Earth Materials for Complex Penetrator Configurations", Development Report No. SC-DR-72-0523, Sandia Laboratories, Albuquerque, NM.
15. Bathe, K.J. 1982. Finite Element Procedures in Engineering Analysis, Prentice-Hall.

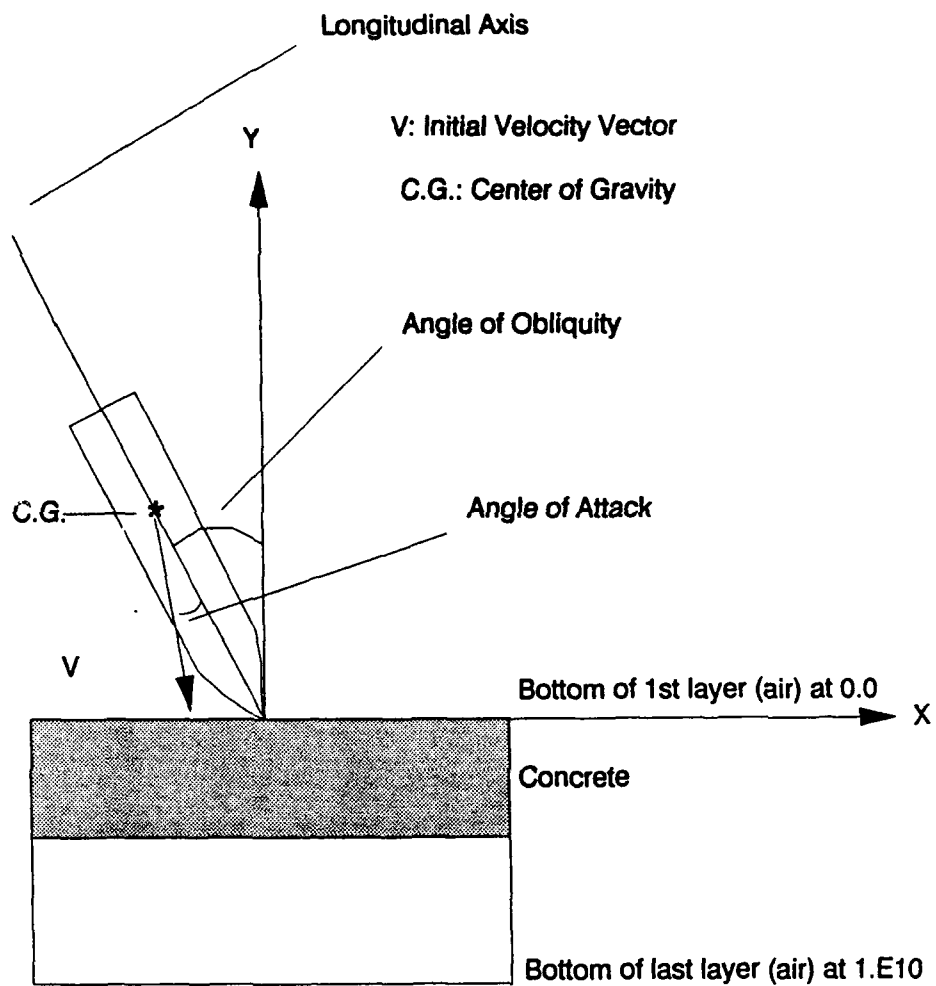


Figure 1. Illustration of initial projectile orientation for a 2-D impact/penetration example problem.

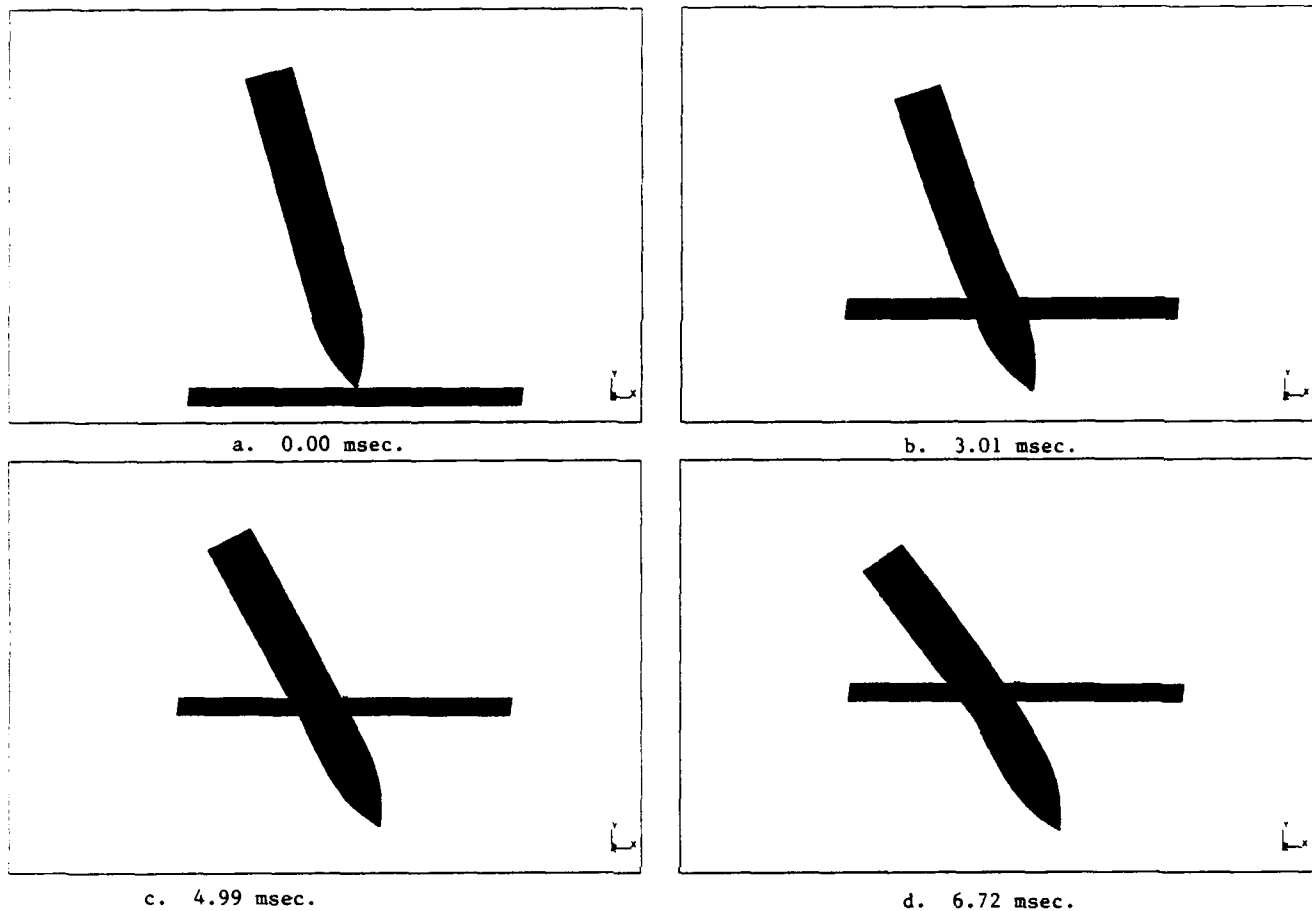


Figure 2. Deformed shape of projectile at (a) 0.00 msec, (b) 3.01 msec, (c) 4.99 msec, and (d) 6.72 msec, after impact (Scale Factor = 1).

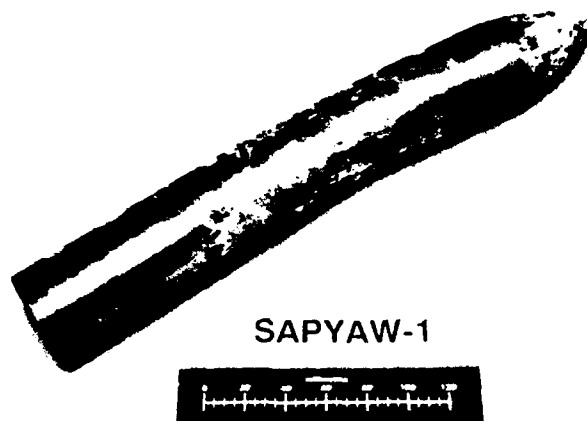


Figure 3. Photograph of the posttest condition of a projectile subjected to the oblique impact conditions considered in the example problem.

DEVELOPMENT OF INSTRUMENTATION TECHNIQUES TO INVESTIGATE HIGH VELOCITY PROJECTILE PENETRATION INTO CONSTRUCTION MATERIALS

Jeffrey Peters, William F Anderson, Alan J Watson

Department of Civil and Structural Engineering
University of Sheffield, UK

ABSTRACT

Instrumentation has been developed to examine in real time the complex mechanisms involved when a high velocity projectile impacts mortar or concrete. Bullet deceleration and propagation of a plastic cracked zone during bullet penetration are monitored using optical glass fibres and high speed photography. Cracking of the target and the arrival of stress waves at the back face of the target have been monitored using silver paint detectors and piezoguages respectively. A time history for the event is reported.

INTRODUCTION

There is a considerable amount of information published on projectile penetration into a wide range of materials. Homogeneous materials such as metals, heterogeneous composite materials such as concrete, particulate materials such as soil and layered materials such as laminates have all been studied using a number of approaches, i.e. empirical, analytical and numerical. Empirical approaches give little or no insight into the mechanisms involved when a projectile impacts and penetrates a target, and analytical and numerical methods require simplifying assumptions to be made before solutions may be obtained. All methods require validation by experiments and virtually all experimental data is obtained from post test examination of impacted targets.

When heterogeneous construction materials are impacted by small arms rounds post test damage consists of an impact face spall crater, a projectile burrow which is often found to deviate from a straight line continuation of the bullet flight path and, depending on the thickness and nature of the target, a back face scab crater. It is most unlikely that these damage features are produced independently and a complex sequence of events occurs. Anderson et al (1) reported that initial stages of a fundamental study to examine the interaction of events in real time when a small arms round impacts and penetrates

mortar targets. This work has progressed with experimental techniques refined and new methods developed to examine impact on both mortar and concrete.

TEST ARRANGEMENT

The projectiles being used are 7.62 armour piercing (AP) bullets with a bullet length of 32.7mm and average mass of 9.4g. They have a hardened steel core with length 23.8mm, diameter 5.75mm and a mass of 4.42g. These are fired from a 7.62mm proof barrel attached to a pressure housing incorporating a breech, firing pin, bolt and trigger mechanism with safety catch. The arrangement is mounted on a rigid steel frame bolted to the range floor. Firing is carried out by activating an 11.4 kgf solenoid with 18mm stroke length which is linked to the trigger. The solenoid is activated from a remote control room by a firing box with arming key either manually by pressing an off-biased switch or automatically by a high speed camera when it is at speed and is ready to photograph the event.

Twenty metres down range the target is held in a rigid frame with edge support only. Initially square targets were tested but in order to develop an axisymmetric situation most tests have been carried out with central impact on circular targets 450mm diameter and 125mm thick.

Projectile velocity prior to impact is measured using a laser based velocity measurement rig positioned up range of the target. The bullet passes through a laser "curtain" created by a narrow laser beam striking one of a pair of front silvered mirrors at an angle of about 20° to the normal resulting in a continuous triangular grid of beams reflected between the pair of mirrors. The beam is broken by the bullet and a timer is started when the beam is re-established, the bullet having passed through. A similar system a fixed distance away stops the timer. Further details may be found in Anderson et al (1).

The velocities measured for the batch of rounds used in these tests has been fairly consistent with a mean value of 864.8m/s and standard deviation of 13.2m/s.

INSTRUMENTATION

Instrumentation has been developed to monitor projectile deceleration within the target (optical glass fibre detectors), crack propagation (optical glass fibre detectors and silver paint circuits) and arrival of compressive waves at the target boundary (piezoelectric transducers). Using this instrumentation data is recorded either electronically (silver paint circuits, piezoelectric transducers) or photographically using a high speed camera in pseudo streak mode (optical glass fibre detectors). Fundamental to all measurements is a reliable datum, i.e. the time at which the projectile tip contacts the front surface of the target.

Impact Detector

Two methods of detecting impact, a tin foil "make" circuit and an optical glass fibre array were used in the early stages of the study(1), but it soon became apparent that inconsistent delays of up to 10 μ s could occur using the tin foil method and there were doubts about whether the projectile tip or shank broke the optical glass fibre array. A new method based on the successful laser "curtain" velocity rig was therefore developed. To protect the mirrors, laser and detector from spall debris when the target is impacted all parts of the new detector are mounted in a section of rolled steel channel 720mm long and 130mm wide with a central hole in it as shown in Fig. 1. After the target specimen is mounted in the target frame the steel channel is bolted to the front of the target holder.

A small collimated laser diode is mounted on the channel and the laser beam strikes one of a pair of parallel front silvered mirrors at an angle of about 20° to the normal.

The beam is reflected between the mirrors to form a laser "curtain". At the end of its passage between the mirrors the beam is launched down the end of a polymer fibre optic cable giving a datum which may be recorded photographically. A small semi-silvered area on one of the mirrors near the end of the beam passage allows some of the laser light to pass through the mirror while the remainder of the beam is reflected. The part of the beam which passes through the mirror strikes an optoschmitt detector and allows the time datum to be recorded electronically and optically simultaneously.

When the bullet hits the laser curtain the beam is broken. Because of the separation of the reflected paths of the beam and the ogive shape of the nose of the bullet there is uncertainty about what part of the bullet has broken the beam. However, the bullet has a flat back and as it completes its passage through the curtain the laser beam is re-established.

Optical Glass Fibre Detectors

Anderson et al (1) showed the potential of using optical glass fibre detectors as a non-invasive method of monitoring transient events and the technique has now been developed to the stage where optical glass fibres may be routinely cast in both mortar and concrete targets to monitor projectile deceleration or target cracking.

Target moulds are formed from 1.5mm thick steel sheet rolled to form 450mm diameter rings which are tig welded to give a smooth joint. The moulds have lifting lugs and restraining clips mounted on them. The latter are used to securely position the rings on a 620mm x 1200mm wooden base plate as shown in Fig. 2.

The 40 μ m diameter optical glass fibres are used in bundles of about 20 fibres cut to a length of 2.5 metres and each bundle is fed through a stainless steel tube (2.00mm i.d., 2.65mm o.d.) which goes through diametrically opposite holes drilled in the target mould (Fig. 2). Each target may

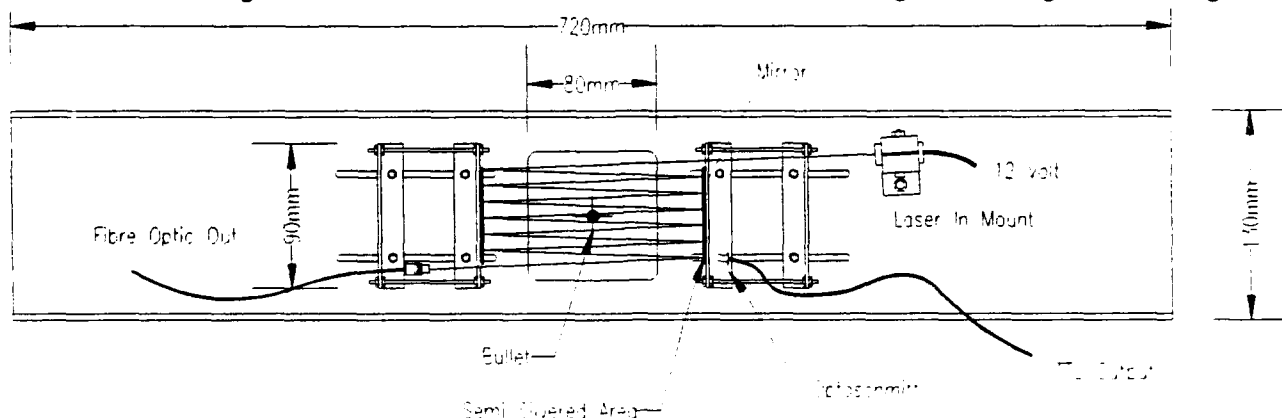


Fig. 1. Laser "curtain" impact detector.

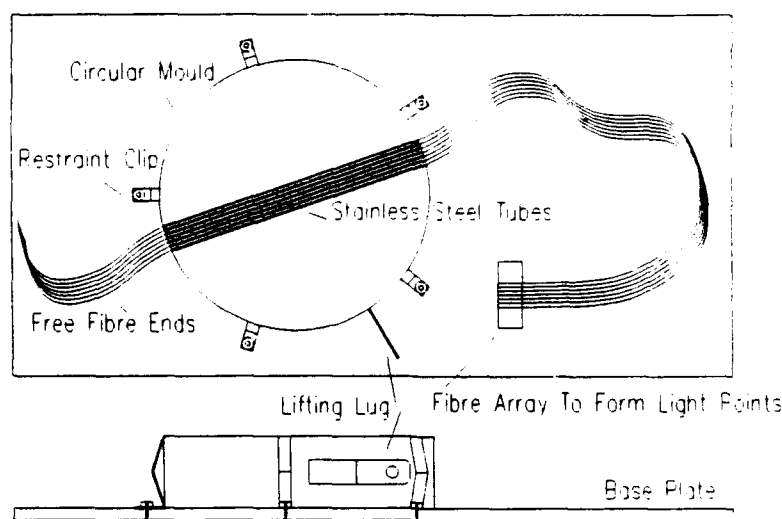


Fig. 2. Casting of optical glass fibres in targets.

have up to 30 separate bundles of fibres fed through steel tubes placed in arrays, the positioning of which depends on what is being examined.

In tests examining projectile deceleration the thirty bundles of fibres are arranged in six layers varying in width from 12mm at a depth of 15mm from the front of the target to nearly 40mm at a depth of 90mm, fibre bundle spacing being about 5mm. The divergence of fibre array width is to allow for deviation of the bullet within the target as it penetrated. The orientation of the arrays is varied to ensure that no planes of weakness are introduced into the targets. This arrangement gives a concentration of fibres around the centre of the target.

In tests examining crack propagation an identical technique is used but the number of layers in the array is reduced to three. Two layers are placed at depths of 30mm and 60mm from the front surface, each layer having thirteen bundles of fibres at spacings of 5-7mm to pick up cracks generated by the penetrating bullet. A third layer, only 15mm from the rear face of the target, consists of four bundles of fibres at 15mm spacing to detect rear face scabbing.

When all the bundles of fibres have been fed through the array of tubes the mortar or concrete, maximum aggregate size 10mm, is placed in the mould and vibrated. The steel tubes are carefully withdrawn from the mould leaving the fibres in position in the mortar or concrete, which is then vibrated again to ensure intimate contact with the fibres and a good bond when cured. Curing takes place under polythene sheeting for at least three weeks before impact testing is carried out. The targets, with the steel ring left in place to avoid damaging the fibres, are removed from the mould base plates and carefully mounted in the target frame.

The bundles of optical glass fibres are illuminated by butting them up against a back silvered 1000W projector bulb in a high intensity light box with reflective inner surfaces. At the other end the thirty bundles of fibres are glued to a serrated plate to form a horizontal array (Fig. 2) which, when the fibres are illuminated, gives thirty points of light on a straight line in the same plane. Breakage of a fibre bundle by the bullet or a crack results in that point of light being extinguished.

The extinguishing of light points is monitored using a high speed 16mm cine camera which has been modified to run in pseudo streak mode by optically bypassing the framing prism and projecting the image of the thirty light points directly onto the film through a 50mm lens. The film passes through the camera at a rate of approximately 6000 frames per second (45m/sec film speed) and each of the light points from the optical fibres forms a straight line streak on the film, the streak terminating when the light from a fibre bundle is extinguished as shown in Fig. 3.

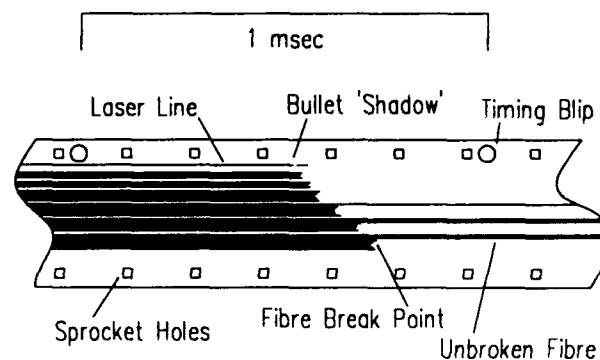


Fig. 3. Section of developed film.

The optical output from the laser "curtain" impact detector also marks the film as a streak which is broken and reformed as the bullet passes through the detector, and this allows fibre streak times from impact to be calculated when the film is examined using a Vanguard film analyser. The time resolution is $0.45 \mu\text{s}$.

For times to be converted into velocities it is necessary to accurately pick up the position of the fibre bundles within the target. This is done by sawing the target in half and illuminating the free ends of the fibres. The positions of the fibre bundles on the sawn faces of the concrete are easily identified as points of light on the sawn concrete face and the distances from the front face of the specimen measured to an accuracy of 0.1 mm using a modified digital vernier.

Silver Paint Crack Detectors

Breakage of silver lines painted on the surface of concrete specimens has been used previously (2) for detection of crack propagation during dynamic testing. For this project a preliminary study using a four point static load test on a concrete prism on which silver paint lines of varying width and thickness had been painted was carried out. This showed that open cracks can form in concrete without a break in continuity of the silver paint circuit because concentrations of silver paint around aggregate particles can stretch across gaps. Thus much higher strains are required to cause cracking in the silver paint than the concrete.

Great care was therefore taken in the preparation of silver paint lines. The fine colloidal silver paint was diluted considerably and a retarder added to allow the thinnest possible lines (2 mm wide), which still provided continuity for a circuit, to be drawn on the targets. For front and back face cracking 300 mm long paint lines were positioned as shown in Fig. 4, and the lines connected through a simple interface circuit, allowing the signal to go from "low" to "high" for better resolution, to digital storage oscilloscopes which were triggered by the optoschmitt output from the laser "curtain" impact detector.

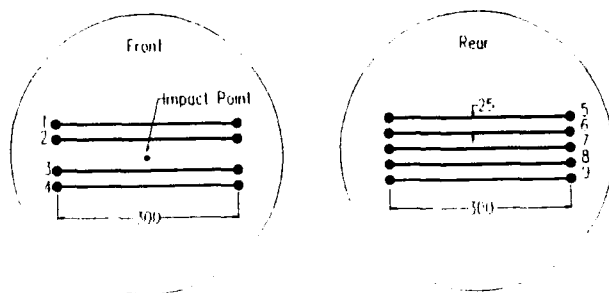


Fig. 4. Silver paint line positions.

Piezoelectric Transducers

The arrival at the target back face of the stress pulse generated by projectile impact on the front face has been monitored by piezoelectric transducers. The transducers are 15 mm diameter and 4 mm thick and, being effectively strain rate sensitive, allow detection of the first arrival of the stress pulse at the rear surface of the target. To ensure that each of the transducers was coupled to the specimen Swarfega was applied to the transducers before mounting them, but it was still necessary to preload the transducers against the specimen to ensure good contact. This was done by fixing the transducers in set positions on a plastic positioner as shown in Fig. 5. Each transducer was isolated from its neighbours by foam tape. The preload was applied using an elastic cord stretched over a wooden load spreader placed horizontally behind the transducers.

The transducers, being piezoelectric, required no input voltage nor signal conditioning and their output was fed directly to a digital storage oscilloscope which was triggered by the output from the impact detector optoschmitt.

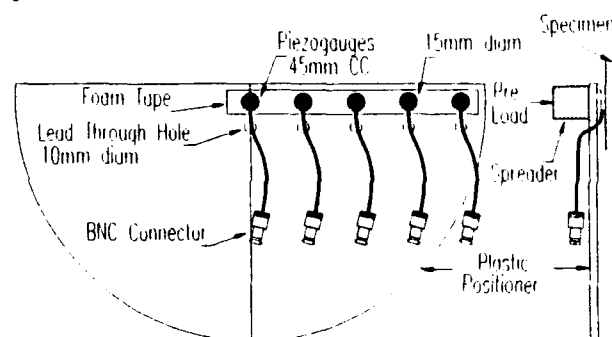


Fig. 5. Piezoelectric transducer positioning.

RESULTS AND DISCUSSION

Impact Detector

Fig. 3 is a representation of the streaks obtained on the high speed film. Examination of the laser line shows that the laser beam is broken as the bullet passes through the curtain. Of importance is when the beam is re-established after the "bullet shadow" break because this indicates the time at which the flat back face of the bullet has passed the detector. Knowing the length of the bullet, its velocity and the standoff from the front face of the target (Fig. 6) the impact time may be calculated with an accuracy of $1.0 \mu\text{s}$. The breaking up of the laser line after it has been reestablished on the film is due to target front face spall debris passing through the laser curtain after impact.

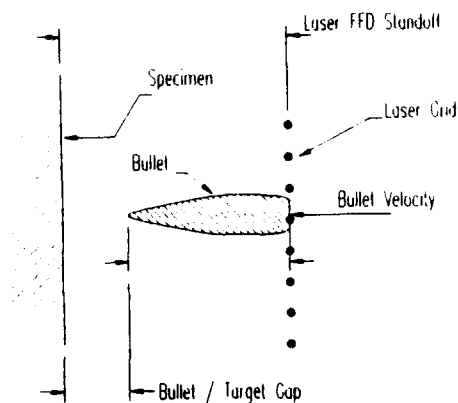


Fig. 6. Laser "curtain" standoff.

Bullet Deceleration

Fig. 3 also shows the way the streaks produced by the fibre optic light points terminate when bundles of fibres are broken. Each batch of streaks represents an array of fibre bundles at nominally the same depth from the front face of the target, with those closest to the front face being shown as the top array. It can be seen that within an array there is generally a variation in breakage time, with one of the central fibres breaking first indicating the arrival of the bullet at that array. The termination of a streak after the first arrival may indicate breakage by the bullet or by a crack as the projectile burrow enlarges. By plotting the first arrival time for each array of fibres against distance from the impact face as shown in Fig. 7, the deceleration profile for the bullet may be deduced.

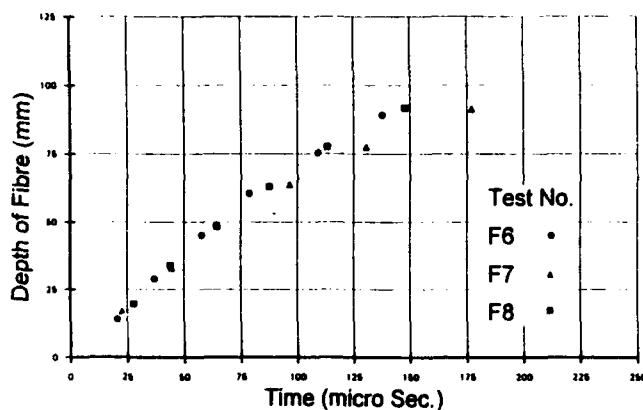


Fig. 7. Fibre depth v time (bullet deceleration).

In the initial work reported earlier by Anderson et al(1) the breakage of the optical fibres to monitor bullet deceleration gave a velocity higher than the impact velocity of the bullet, and it was argued that this could be due to crack propagation at a higher speed in front of the penetrating bullet. However, the inconsistent delays in the

"tin foil" impact detector used in early tests must cast some doubt on the accuracy of the early results. With the new laser curtain impact detector very consistent results have been obtained as shown for three tests in Fig. 7.

Stress Wave Velocity

Estimates of the stress wave velocities through concrete may be obtained from the arrival times at the target back face of stress waves produced by bullet impact on the front face. Fig. 8 shows a typical trace from one of the piezogauges mounted on the target back face. Initial examination would suggest that there is a little noise on the trace but that the large increase in voltage at time = 40 μ s signifies stress wave arrival. However, closer examination of the pulse shows that initial disturbance of the trace with a positive voltage rise occurs at 30 μ s. It could be argued that this is when the tip of the bullet contacts the target and it takes a further 10 μ s before a significant area of the bullet is in contact. Compressive stress wave velocity through the concrete used in these

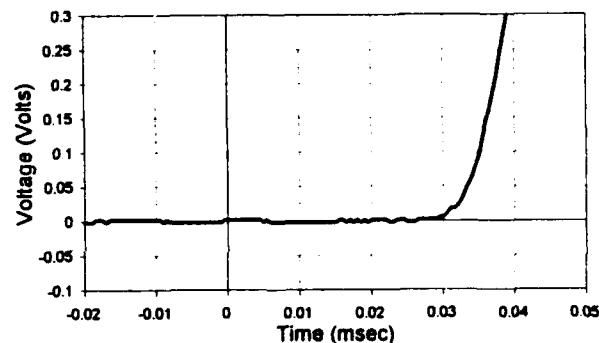


Fig. 8. Piezoelectric transducer output.

specimens based on the clear increase in voltage is 4280 m/s, and based on the first disturbance is a higher than expected 5130 m/s. This discrepancy needs further examination.

Crack Propagation Spalling and Scabbing

The wide arrays of embedded optical glass fibres and the silver paint circuits on the target surface allow times of arrival of cracks and crack propagation velocities to be deduced. Fig. 9 shows when breakages occur in arrays of optical glass fibres at depths of 30mm and 60mm from the target front face. It can be seen that cracking is first detected at 37.5 μ s after impact. The crack propagation velocity is difficult to determine because the crack length between breaks in adjacent optical glass fibres is unknown. However, if it is assumed that the cracks progress by the shortest distance between adjacent fibres the lines through the points representing fibres break points have a slope equal to the velocity of propagation of the cracks. It is interesting to note that the value of 919

Time(μ sec)	Event	Bullet Penetration (mm)	Bullet Velocity (mm/ μ sec)
T= -45	Tip of projectile breaks laser curtain.	-38.7	0.86
T= -10	Rear of projectile clears laser curtain (time datum established).	-8.6	0.86
T= 0	Tip of projectile touches target (stress waves start to propagate).	0	0.86
T= 22	First layer of fibres break	17	0.76
T= 25	First indication of stress wave arriving at rear surface. (125 mm depth)	19	0.76
T= 26	Front face silver paint shows first disturbance 25mm from impact point.	20	0.76
T= 33	Full stress wave arriving at rear surface.	25	0.76
T= 40	Front face silver paint shows clear break 25 mm from impact point	30	0.76
T= 44	Second layer of fibres break	36	0.76
T= 55	Rear Face silver paint shows first disturbance.	41	0.76
T= 61	Third layer of fibres breaks	49	0.72
T= 75	Rear Face silver paint shows shows clear break.	59	0.67
T= 82	Fourth layer of fibres breaks	65	0.64
T= 105	Fifth layer of fibres breaks	75	0.43
T= 143	Sixth layer of fibres breaks	94	0.27
T= 200	Projectile Stops.	113	0.0
T= 240	Internal rear face scab crack fractures rear fibres.	113	0.0

Table 1. Time history of 7.62 AP projectile penetrating cementitious material

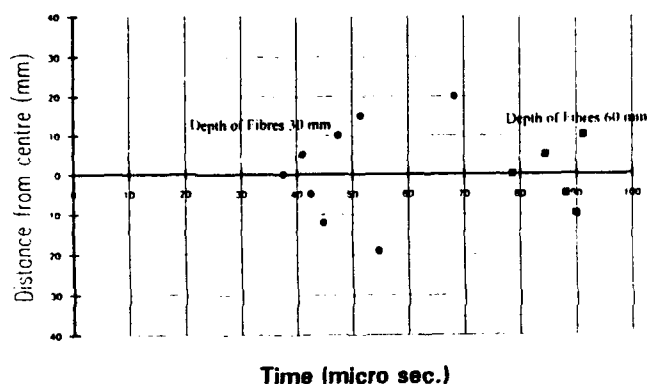


Fig. 9. Fibre radial distance v time (plastic crack zone)

m/s obtained from these slopes compares well with a theoretical value of 928 m/s(1).

Fig. 10 shows a typical silver paint circuit trace and it can be seen that by using a thin silver paint line a relatively clean break may be detected. The data from all the instrumentation allows a time history of the impact and penetration event to be postulated as given in Table 1.

CONCLUSIONS

1. A laser "curtain" provides a non-contact projectile impact detector which can produce simultaneously a photographic and electrical time datum for impact studies.
2. The instrumentation has allowed a time sequence of events to be postulated for projectile penetration into cementitious materials.

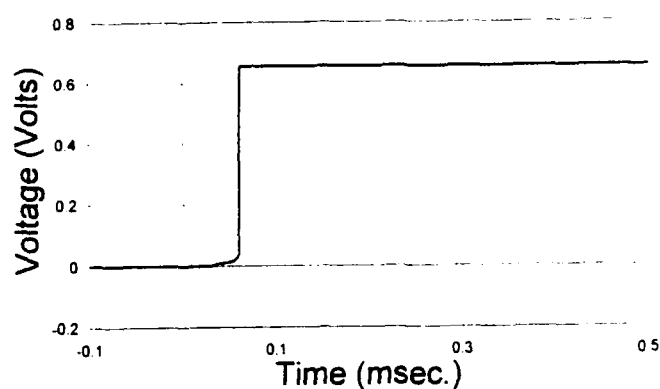


Fig. 10. Silver paint circuit output.

ACKNOWLEDGEMENTS

The authors would like to express their thanks to the Science and Engineering Research Council and the Ministry of Defence (DRA, Christchurch) who are jointly funding this work under Grant Number GR/F 20735. The assistance of A. Hindle in developing experimental techniques is gratefully acknowledged.

REFERENCES

1. Anderson, W.F., Watson, A.J. and Peters, J (1991), "High Velocity Projectile Penetration into Cementitious Materials". Proc. 5th Int. Symp. on Interaction of Conventional Munitions with Protective Structures, Mannheim, pp 381-287.
2. Watson, A.J., Anderson, W.F. and Archer, B. (1982) "Hypervelocity Impact of Concrete", Proc. Inter. Symposium on Concrete Structures under Impact and Impulsive Loading, Berlin, pp 188-201.

AN EMPIRICAL EQUATION FOR PENETRATION DEPTH OF OGIVE-NOSE PROJECTILES INTO CONCRETE TARGETS

M.J. Forrestal*, B.S. Altman*, J.D. Cargile†, S.J. Hanchak‡

*Sandia National Laboratories, Albuquerque, NM 87185-5800

†Waterways Experiment Station, Vicksburg, MS 39180-0631

‡University of Dayton Research Institute, Dayton, OH 45469-0182

ABSTRACT

We develop an empirical equation for penetration depth of ogive-nose projectiles penetrating concrete targets at normal impact. Our penetration equation contains a single, dimensionless empirical constant that depends only on the unconfined compressive strength of the target. We determine the empirical constant from penetration depth versus striking velocity data for targets with unconfined compressive strengths of nominally 14 MPa (2 ksi), 35 MPa (5 ksi), and 97 MPa (14 ksi). Predictions are in good agreement with six sets of penetration data for striking velocities between 250 and 800 m/s.

INTRODUCTION

Brown [1] presents an historical account of empirical equations for penetration and perforation of concrete targets. These empirical equations result from curve-fits with test data and do not provide physically based descriptions. In addition, the empirical equations in [1] are expressed in terms of specific units, so these equations are dimensionally dependent. In this paper, we develop a dimensionally consistent empirical equation for depth of penetration into concrete targets that contains the functional form of recently published, experimentally verified, analytical models [2,3,4].

MODEL FORMULATION

Forrestal and Luk [4] derive an analytical equation for penetration into soil targets that requires triaxial material data from samples cored from the target material. Unfortunately, most penetration studies lack the necessary triaxial test data required for input to analytical and computational models. Many experimental studies do, however, report the unconfined compressive strength f'_c for concrete targets. To use this data base, we develop an empirical penetration equation that describes the concrete targets in terms of unconfined compressive strength f'_c , a dimensionless empirical constant S that multiplies f'_c , and density.

The development of the empirical equation starts with the equation for force on the projectile nose given in [4]. For the analytical model in [4] and this empirical equation, we assume normal impact and that the projectile is a rigid body (nondeforming nose). Axial force is given by

$$F = \pi a^2 (\tau_0 A + NB\rho V^2) \quad (1a)$$

$$N = \frac{8\psi - 1}{24\psi^2} \quad (1b)$$

where the projectile has mass m , shank radius a , caliber-radius-head ψ , and rigid-body velocity V . The target is characterized by density ρ and the constants $(\tau_0 A)$ and B that involve only material parameters obtained from triaxial tests.

Previous studies [2,3,4] showed that B depends mostly on the compressibility of the target material and B has a narrow range; for example, $B = 1.1$ for aluminum targets [2,3], and $B = 1.2$ for soil targets [4]. By contrast, $(\tau_0 A)$ depends mostly on the shear strength of the target materials, and $(\tau_0 A)$ has a broad range. For this empirical equation, we take $B = 1$ and $(\tau_0 A) = Sf'_c$, where S is the dimensionless empirical constant that multiplies unconfined compressive strength. Thus, the empirical equation for axial force takes the form

$$F = \pi a^2 (Sf'_c + N\rho V^2), \quad z > 4a \quad (2)$$

where N is given by equation (1b). Equation (2) is limited to penetration depths $z > 4a$. For $z < 4a$, the process is dominated by surface cratering.

Post-test observations of soil and concrete targets show that the cavity left after penetration has a conical region with length about two projectile shank diameters ($4a$) followed by a circular cylinder with diameter nearly equal to the projectile shank diameter ($2a$). Thus, the cavity length $0 < z < 4a$ is called the crater region, and the cavity length $4a < z < P$ is called the tunnel region, where z is measured from the target surface and P is final penetration depth. For the soil penetration tests analyzed in [4], $P \approx 100a$; so the crater region was ignored. However, both the crater and tunnel regions must be taken into account in the analysis of the more resistant concrete targets.

Deceleration data [4] show a rise time during the crater region, followed by a decaying pulse during the tunnel region. For this model, we take force on the projectile nose as

$$F = cz, \quad 0 < z < 4a \quad (3a)$$

$$F = \pi a^2 (Sf'_c + N\rho V^2), \quad 4a < z < P \quad (3b)$$

where c is a constant. From Newton's second law

$$m \frac{d^2 z}{dt^2} = -cz, \quad 0 < z < 4a \quad (4)$$

With the initial conditions $z(t=0)=0$ and $V(t=0)=V_s$, equation (4) has the following solutions for projectile displacement, velocity, and acceleration:

$$z = \left(\frac{V_s}{\omega} \right) \sin \omega t, \quad 0 < z < 4a \quad (5a)$$

$$V = \frac{dz}{dt} = V_s \cos \omega t, \quad 0 < z < 4a \quad (5b)$$

$$\frac{d^2 z}{dt^2} = -\omega V_s \sin \omega t, \quad 0 < z < 4a \quad (5c)$$

$$\omega^2 = \frac{c}{m} \quad (5d)$$

We now define t_1 and V_1 as the time and rigid-body projectile velocity at $z=4a$. The unknowns t_1 , V_1 , and c are found from the conditions of continuity of force, velocity, and displacement at $z=4a$ and $t=t_1$.

From equations (3) and (5)

$$m\omega V_s \sin \omega t_1 = \pi a^2 (Sf'_c + N\rho V_1^2), \quad \text{at } z = 4a \quad (6a)$$

$$V_s \cos \omega t_1 = V_1, \quad \text{at } z = 4a \quad (6b)$$

$$\left(\frac{V_s}{\omega} \right) \sin \omega t_1 = 4a, \quad \text{at } z = 4a \quad (6c)$$

Substituting (6c) into (6a) gives

$$c = \frac{\pi a}{4} (Sf'_c + N\rho V_1^2) \quad (7a)$$

Squaring and then adding (6b) and (6c) give

$$c = \frac{m(V_s^2 - V_1^2)}{16a^2} \quad (7b)$$

Equating (7a) and (7b) gives the rigid-body velocity at $z=4a$ as

$$V_1^2 = \frac{mV_s^2 - 4\pi a^3 Sf'_c}{m + 4\pi a^3 N\rho} \quad (7c)$$

From (6b),

$$t_1 = \frac{\cos^{-1}\left(\frac{V_1}{V_s}\right)}{\left(\frac{c}{m}\right)^{\frac{1}{2}}} \quad (7d)$$

Values of t_1 , V_1 , and c can be determined with equations (7b), (7c), and (7d).

Depth of penetration in the tunnel region is found from

$$m \frac{d^2 z}{dt^2} = mV \frac{dV}{dz} = -\pi a^2 (Sf'_c + N\rho V^2), \quad 4a < z < P \quad (8)$$

Integrating (8) from V_1 to zero and $4a$ to P gives the final penetration depth

$$P = \frac{m}{2\pi a^3 \rho N} \ln \left(1 + \frac{N\rho V_1^2}{Sf'_c} \right) + 4a, \quad P > 4a \quad (9)$$

where V_1 is related to the striking velocity V_s in equation (7c).

DETERMINATION OF EMPIRICAL CONSTANT FROM PENETRATION DATA

We solve for S in equation (9) and obtain

$$S = \frac{N\rho V_s^2}{f'_c} \cdot \frac{1}{\left(1 + \frac{4\pi a^3 N\rho}{m} \right) \exp \left[\frac{2\pi a^2 (P - 4a) N\rho}{m} \right] - 1} \quad (10)$$

For each experiment, all terms on the right side of equation (10) are known, so we can calculate S for each data point. We take the average value of S for the data points in each data set and compare results from equation (9) and penetration data. This procedure produced accurate data fits for six sets of penetration data.

14 MPa (2 ksi) Grout Targets.

Hanchak and Forrestal [5] conducted depth-of-penetration experiments with 0.064 kg, 12.7-mm-diameter projectiles with 3.0 and 4.25 caliber-radius-head nose shapes into grout targets. Table 1 lists the other parameters for these experiments. The value of S in Table 1 is the average of the values calculated from equation (10) for each data point. Figure 1 shows the results from equation (9) with $S=21$ and the data sets with $\psi=3.0$ and $\psi=4.25$.

35 MPa (5 ksi) Concrete Targets.

Canfield and Clator [6] present depth-of-penetration data for full-scale (5.90 kg, 76.2-mm-diameter) and one-tenth scale (0.0059-kg, 7.62-mm-diameter) armor-piercing projectiles. Table 1 lists the other parameters for these experiments and the calculated value of S . Figures 2 and 3 show penetration data and results from equation (9) with $S=13$ for the full-scale projectile and $S=14$ for the one-tenth scale projectile.

Ehrgott and Cargile [7] conducted depth-of-penetration experiments with 0.90 kg, 26.9-mm-diameter projectiles. Table 1 lists the other parameters for these experiments and the calculated value of S . Figure 4 shows penetration data and results from equation (9) with $S=12$.

97 MPa (14 ksi) Concrete Targets.

Ehrgott and Cargile [7] conducted depth-of-penetration experiments with 0.90 kg, 26.9-mm-diameter projectiles. Table 1 lists the other parameters for these experiments with the calculated value of S . Figure 4 shows penetration data and results from equation (9) with $S = 7$.

An Estimate for S versus f'_c .

We obtained values of S for six data sets. For the two data sets with nominal 14 MPa (2 ksi) grout targets, $S = 21$; for the three data sets with nominal 35 MPa (5 ksi) concrete targets, $S = 12, 13$, and 14; and for the single data set with a nominal 97 MPa (14 ksi) concrete target, $S = 7$. The model prescribes that S depends only on f'_c , and equation (10) shows that S is proportional to $1/f'_c$. Figure 5 shows the calculated values of S and a curve-fit where S is proportional to $1/f'_c$.

SUMMARY

We present a dimensionally consistent empirical equation for penetration depth of ogive-nose projectiles penetrating concrete targets. This equation has a single, dimensionless empirical constant S that multiplies unconfined compressive strength f'_c . The empirical constant S depends only on the unconfined compressive strength of the concrete target and is independent of the projectile parameters and striking velocity. We note that the penetration equation is limited to normal impact and rigid projectiles (nondeforming nose). Most of the penetration data base is limited to $V_s < 800$ m/s, and for $V_s < 800$ m/s, the nose remained undeformed.

Acknowledgment - This work was sponsored by the Joint DoD/DOE Munitions Technology Development Program.

REFERENCES

1. S.J. Brown. Energy release protection for pressurized systems. Part II. Review of studies into impact/terminal ballistics. *Applied Mechanics Reviews*, Vol. 39, 1986.
2. M.J. Forrestal, N.S. Brar, and V.K. Luk. Penetration of strain-hardening targets with rigid spherical-nose rods. *Journal of Applied Mechanics*, Vol. 58, pp. 7-10, 1991.
3. M.J. Forrestal, V.K. Luk, Z. Rosenberg, and N.S. Brar. Penetration of 7075-T651 aluminum targets with ogival-nose rods. *International Journal of Solids and Structures*, Vol. 29, pp. 1729-1736, 1992.
4. M.J. Forrestal and V.K. Luk. Penetration into soil targets. *International Journal of Impact Engineering*, Vol. 12, pp. 427-444, 1992.
5. S.J. Hanchak and M.J. Forrestal. Penetration into grout targets with 0.064 kg, ogive-nose projectiles. Work in progress.
6. J.A. Canfield and I.G. Clator. Development of a scaling law and techniques to investigate penetration in concrete. NWL Report No. 2057, U.S. Naval Weapons Laboratory, Dahlgren, VA, 1966.
7. J.Q. Ehrgott and J.D. Cargile. Penetration into concrete targets. Work in progress.

Table 1. Penetration Parameters

Parameter	Ref. [5]	Ref. [5]	Ref. [6]
m (kg)	0.0642	0.0642	5.90
$2a$ (mm)	12.7	12.7	76.2
ψ	3	4.25	1.5
N	0.106	0.076	0.204
ρ (kg/m ³)	1960	1960	2310
f'_c (MPa)	13.5	13.5	35.1
S	21	21	13

Parameter	Ref. [6]	Ref. [7]	Ref. [7]
m (kg)	0.0059	0.906	0.904
$2a$ (mm)	7.62	26.9	26.9
ψ	1.5	2.0	2.0
N	0.204	0.156	0.156
ρ (kg/m ³)	2240	2370	2340
f'_c (MPa)	34.6	36.2	96.7
S	14	12	7

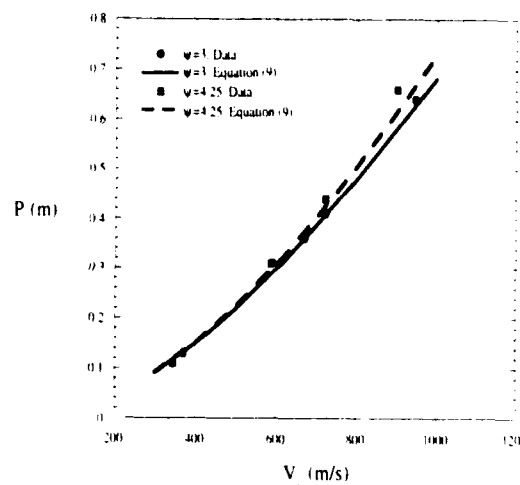


Figure 1. Penetration data [5] and model prediction for 0.064 kg, 12.7-mm-diameter projectile with $f'_c = 13.5$ MPa, $S=21$.

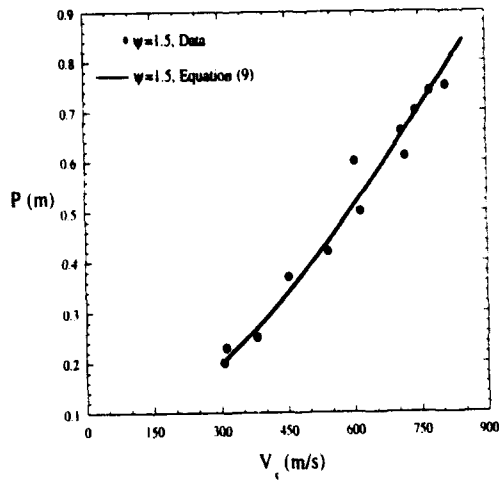


Figure 2. Penetration data [6] and model prediction for 5.9 kg, 76.2-mm-diameter projectile with $f'_c = 35.1$ MPa, $S=13$.

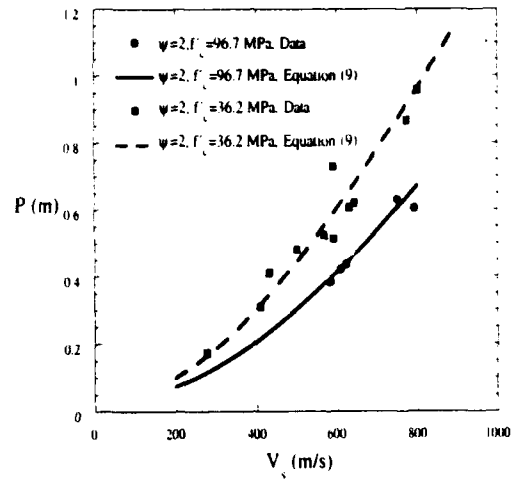


Figure 4. Penetration data [7] and model prediction for 0.904 kg, 26.9-mm-diameter projectile with $f'_c = 36.2$ MPa, $S=12$ and $f'_c = 96.7$ MPa, $S=7$.

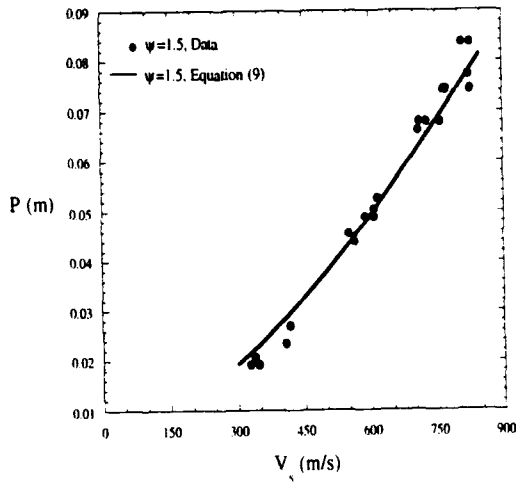


Figure 3. Penetration data [6] and model prediction for 0.0059 kg, 7.62-mm-diameter projectile with $f'_c = 34.6$ MPa, $S=14$.

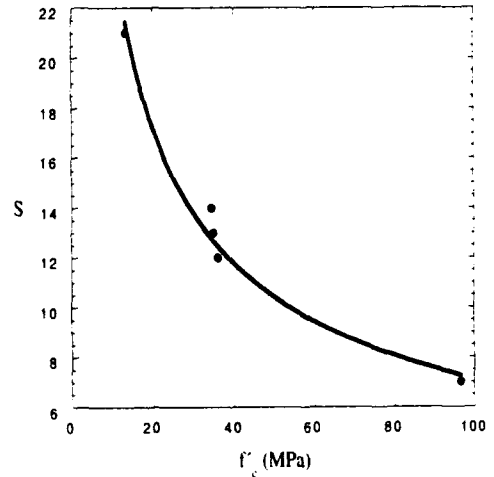


Figure 5. Dimensionless empirical constant versus unconfined compressive strength.

Subscale Penetration Tests with Bombs and Advanced Penetrators against Hardened Structures

Helga Langheim*
Hermann Pahl**
Eberhard Schmolinske*
Alois J. Stilp*

*Fraunhofer-Institut für Kurzzzeitdynamik,
Ernst-Mach-Institut, Freiburg i. Br.
**NATO Headquarters, Brussels

Abstract

Modern weapons with increased terminal velocities, high strength cases and with high length/diameter ratios delivered with pinpoint accuracy force the structural engineer to provide a structure with a higher level of protection. The current database for design is inadequate. Other data derived from model tests can therefore help. Model tests allow variations of parameters with regard to both potential threat and protective measures at affordable costs and time.

This paper describes the results of model tests carried out at the Ernst-Mach-Institut, where generic model bombs were fired against sections of a scaled protective structure. The sections consisted of a layer of grouted rock boulders which were backed by a reinforced concrete slab. The gap between the roof slab and the above-mentioned backing slab was filled with either asphalt or ashes. A scaled German WW II Armour Piercing Bomb PD 500 was chosen. The inert bombs struck the target at right angles to the surface in the high velocity range of 400 m/s and 500 m/s.

The penetration behaviour of the weapon is strongly dependent upon the yaw angle of the bomb. If a bomb strikes with a yaw angle, the penetration depth in the grouted rock rubble layer will be approximately twice the caliber. During the penetration process the bomb deflected and the casing underwent Euler buckling. Without the yaw the bomb perforated the rock rubble layer and penetrated into the reinforced slab. In all tests the backing slabs were practically undamaged and only small cracks could be observed.

From the results it can be concluded that a grouted rock boulder layer backed by a reinforced concrete slab offers a high level of protection against the effects of Armor Piercing bombs.

Tests with hard target penetrators against the same protective structure at velocities of 740 m/s resulted in penetrator failure in the rock rubble layer.

Objectives and Approach

With the development of sophisticated conventional weapons we have to consider an increased threat potential. Advanced conventional weapon threats, forecasted for the next 40 years, are characterized by the following terminal parameters (1):

- New high strength case material
- Improved case design
- Higher terminal velocities due to boosters (bombs up to 600 m/s, hypervelocity projectiles up to 1500 m/s)
- Greater cross section loads caused by higher length/diameter ratios (up to 16)
- More effective nose shapes
- Higher penetration performance through attitude control (yaw angle and impact velocity)
- Pinpoint accuracy with laser guide and infrared sensor
- Target identification with radar seekers
- Smart fuze and improved energy output

For future planning and design of new protective structures it is important to investigate the penetration mechanics of potential future weapons against targets of various designs with different protection systems.

The aim of these tests was to achieve an insight into the effectiveness of a grouted rock boulder layer, backed by reinforced concrete slabs against modern penetrating weapons. Two kinds of projectiles have been used:

1. A generic AP weapon with good penetration ability, chosen because it had been tested extensively against massive rock targets and for which resultant data is known.
2. A hard target penetrator (HTP).

It can be assumed that in the future modern HTP with greater penetration performance, resulting from greater cross sectional loads, higher terminal velocities, high strength alloys like special steel and tungsten-sinter alloys will be used against point targets. Earlier impact tests performed by the EMI (2) with KE penetrators against concrete demonstrated that the border line between normal penetration and hydrodynamic region (where reduced penetration depths were measured and where the data scatter) was reached at approximately 800 m/s. The border line between these effects depend on material properties and nose shapes. In the hydrodynamic range standard concrete penetration formulae cannot be used.

This paper describes the results of tests carried out at the EMI where generic model bombs and HTP were fired against generic targets. This test series was also a pilot project in an extensive near-future determination research program. The objective will be the evaluation of a database for the design of protected structures against modern bombs and advanced HTP.

Test Parameter

Target

The model target consists of a reinforced concrete slab which is protected by single or multiple layers of grouted rock boulders, backed by a reinforced concrete slab. The gap between the roof slab and the backing slab was either filled with asphalt or ashes. In accordance with the similarity laws the model had geometric similarity and consisted of the same material with the same material properties as the full scale prototype target. All the lateral dimensions of the target layers, thickness as well as the diameter, and the spacing of the reinforcing bars need to be scaled. The scaling factor is equally valid for the size of concrete aggregates.

Figure 1 shows the two types of layered target construction. Thicknesses are: quartzit boulders in concrete - 30 cm; burster slab - 26 cm; ash layer - 25 cm (type A), asphalt - 7.5 cm (type B); roof slab - 35 cm. The rock layer had a thickness of 30 cm for the tests with bombs impacting at 400 m/s. The rock layer was doubled for the PD 500 at 500 m/s. For the tests with HTP the rock thickness was tripled to 90 cm. The compressive strength of the quartzit boulders was 250 MN/m² and the density 2.5 g/cm³. The boulders had a maximum edge length of 25 cm and the interstices between the boulders were filled with B 35 concrete. All layers were bonded together with prestressed steel rods.

Projectile

Bomb

The German WWII Armor Piercing Bomb PD 500 was chosen as a prototype threat weapon. AP bombs have heavy cases of alloy steel which resist deformation when striking heavily protected targets. The prototype bomb - figure 2 - with mass 500 kg, explosive mass 30 kg, Caliber 280 mm, L/D 5.6 was in this case scaled 1:4 in the main dimensions. The model bombs were made from high strength steel, tensile strength 1000 N/mm². The mass was 7.81 kg and caliber 69 mm. Figure 3 shows the model bomb with sabot. The inert model bombs impacted normally to the target surface at velocities of 400 m/s.

Penetrator

In addition to using the PD 500 bomb, the effectiveness of high velocity penetrators was also evaluated. For these tests penetrators were made from tungsten sinter alloy, shown in figure 4 with sabot having the following material properties: density: 17.7 g/cm³, hardness: 429 HV10, tensile strength R_m : 1230 N/mm², stress $R_{p0.2}$: 1090 N/mm² and percentage elongation after fracture A_5 : 18%. The mass was 1.13 kg, caliber is 25 mm and the L/D ratio is 9.3.

Test Facility and Experimental Set-up

The impact tests were performed at the ERNST-MACH-Institute proving ground, Wintersweiler. The range building itself has a total length of 46 m and covers an area of 670 m including offices, machine shops, conference room, dark room, control room, instrumentation rooms and a target preparation and storage area. Figure 5 shows a floor plan of the facility. The range itself consists of rooms for the launcher system and the blast tanks resp. Here flash X-ray tubes and shadowgraph stations are installed, whereas the impact bunker is surrounded by an instrumentation area, so that several X-ray channels, a ruby laser stroboscope, optics for holography and a radar technique can be employed.

The impact bunker is a 67 m large chamber made of 75 cm thick walls consisting of high reinforced concrete. The bunker is constructed for 9 bars overpressure, so one can handle around 1 kg HE at ambient pressure and about 2.5 kg at reduced ambient pressure. A large double access door at the rear side of the chamber allows transportation of heavy (up to 5 tons) and large targets in and out of the chamber.

The range is a completely closed system connected to efficient vacuum and exhaustor installations.

Figure 6 shows a schematic drawing of the range. The launcher system itself is a hybrid-type launcher for different launch tube calibers (25 - 100 mm) and three different energy storages for a wide range of masses and velocities. For the low and ordnance velocity regimes single stage gas and powder gun propulsion are applied. Velocities higher than 2000 m/s are obtained with a two-stage light gas gun.

The bombs and the HTPs were launched from a 100 mm cal. and a 50 mm cal. resp. smooth bore gun with sabots made from hard styrofoam, polyethylene and hard plastics. The sabot segments which encase the projectile during the acceleration in the launch tube are aerodynamically separated from the projectile in the first blast tank and they are stopped by a steel catcher plate with a central hole.

Two supplementary velocity measurement systems are installed. The first system is located in the first blast tank and consists of three 150 kV X-ray channels, one orientated vertically, two horizontally. All X-ray film cassettes are well protected inside the tank, whereas the X-ray tubes are outside. The X-ray system is installed near the muzzle, and in addition to the velocity measurement, it permits the observation of the sabot separation process.

The second velocity measurement, the flow field around the projectile and its orientation after sabot orientation are obtained in the second blast tank by means of two shadowgraph stations with point light sources.

The penetrator hits the target in the impact chamber, which has five windows with 0.2 m diameter at opposite sides at the level of the flight axis, so that the above mentioned measurement techniques for the penetration process can be used.

Test Results and Interpretation

The first series of the test program were designed to provide data of the target protection function under strictly controlled test conditions. Inert PD 500 model bombs impacted normally to the target surface. The velocity and the projectile orientation (yaw angle) at the moment of the impact were measured.

The penetration behaviour of a bomb depends largely upon its yaw angle (angle between the trajectory and the penetrator axis). Figure 7 gives a schematical drawing of the craters, caused by bomb penetration in two tests (nos 751 and 752) with impact velocities of 400 m/s and yaw angles of $+2^\circ$ and $+6^\circ$, resp. The penetration depths of 20 cm and 18 cm, resp. (approximately 2 calibers), into the grouted rock rubble layer are relatively small. During the penetration process the bomb deformed. The casing underwent Euler buckling. Figure 8 shows the model bombs after penetration.

In test No 796, the bomb impacted without yaw and caused a deeper crater in the target - figure 9. The rock rubble layer was completely perforated and the bomb nose penetrated 10 cm into the concrete burster slab. The impacting bomb caused a wide crater hole with a zone of additional crushing of the rock material. The resulting amount of fragmented fine material was measured to be 17 litres. Figure 9 shows the actual impact crater dimensions and, in a broken line, the crater after removal of the 17 litres fragmented crush. The bomb penetrated without noticeable deformation - see figure 10.

In order to investigate the interaction between the PD 500 bomb and the hardened target structure at higher impact velocity, the thickness of the quartzit layer was doubled to 60 cm. The bomb hit the target at right angle to the surface at a velocity of 500 m/s and with a yaw angle of -5° . This resulted in a penetration depth of 40 cm - see figure 11, test 800. The figure shows the crater dimensions before and after removal of additional 55 liters crushed materials. On the right hand side of figure 10 the bomb deformation is shown.

In all bomb tests the backing slab was largely undamaged; and only small cracks could be observed. From these results it can be concluded that the grouted rock boulder layer offers a high level of protection against the effects of Armour Piercing bombs of this caliber.

The objective of the second test series was to study the penetration behaviour of HTP manufactured from tungsten sinter alloy on the specified protective structure. In earlier test series penetrator models had achieved very high penetration into low reinforced concrete blocks - more than 1.5 m at 720 m/s and more than 3 m at 900 m/s impact velocity. From the protection point of view the provision of grouted rock rubble layers as shielding material causes the attacker to reduce the impact velocity considerably, otherwise the penetrator will be destroyed.

The introduction of grout rock rubble layers as shielding causes the need to reduce impact velocities to prevent penetrating weapons being destroyed.

Two tests with the HTP design shown in figure 4 were carried out at 740 m/s impact velocity, the rock rubble layer thickness being, as already stated, increased to 0.90 m. As shown in figures 12 and 13 the maximum penetration depth achieved was 37 cm. The rear layers were undamaged, the penetrators had low horizontal yaw of 1° and 2° , resp. However, the HTP were broken into more than 10 pieces due to strong interaction effects between the penetrator and the matrix of high strength rock and concrete forming the shield. It is thought that if the HTP had been made of higher strength tungsten sinter alloys, the interaction of impact velocity and strength of shield would not have been critical and the weapon would not have disintegrated.

We intend to continue these studies with higher strength tungsten sinter alloys and high quality steel alloys.

Summary and Conclusions

With the development of more effective conventional weapons important point targets require a higher level of protection. The ERNST MACH Institut has performed scale tests to demonstrate the effectiveness of using a grouted rock boulder layer matrix as a shield.

The grouted rock rubble layers indeed offer a high protection level against AP bombs which strike the target with supersonic velocities. Hard target penetrators impacting at velocities of 740 m/s were destroyed by the grouted rock boulder matrix.

In conclusions, the current database for the design of hardened structures against such new threat weapons is inadequate and requires further study. The ERNST-MACH-Institut intends to carry out an advanced research project with wide parameter variations of modern threat weapons and new protective design concepts.

References

- (1) Higgins, C.J., Bates, A., Flory, R.A.:
A Technology Forecast of Potential Conventional Weapons Threats to Fixed Land-based Facilities in the Year 2030
Workshop NDCS (Norway), DNA (Washington), 16.-18.July 1990
- (2) Stilp, A.J., Langheim, Helga, Schilling, H.:
Eindringverhalten von KE-Penetratoren in Betonziele
Proc. 3rd Int. Symp. INMS, Mannheim Mz. 1987

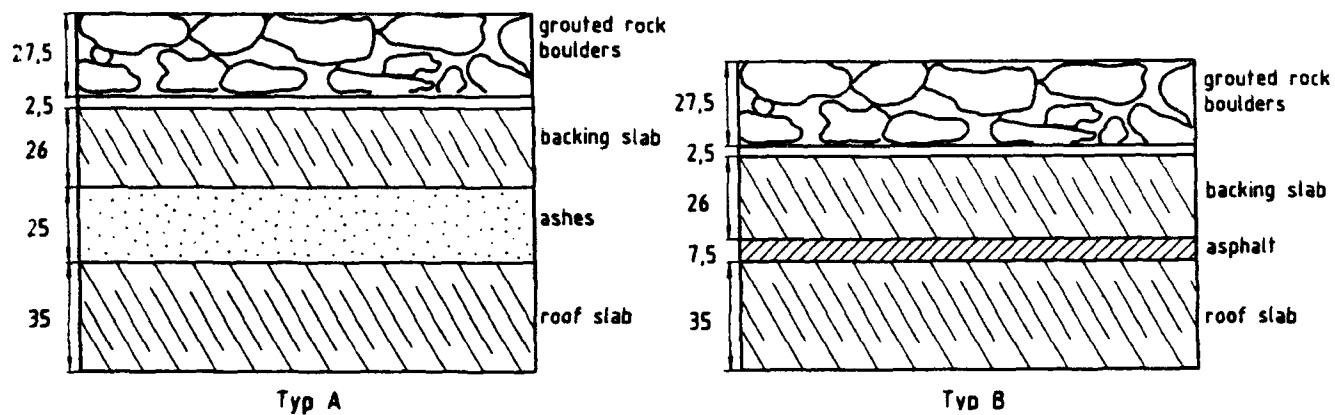


Figure 1: Model Target

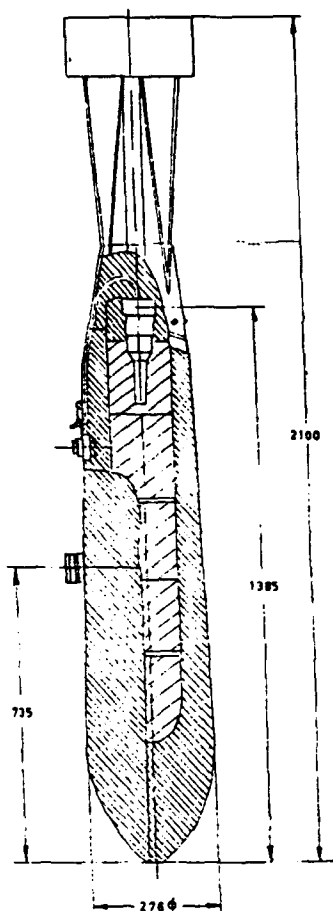


Figure 2: Prototype Bomb PD 500

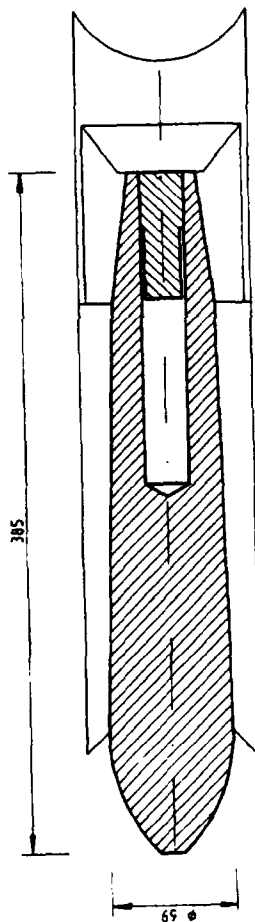


Figure 3: 1:4 Model Bomb with Sabot

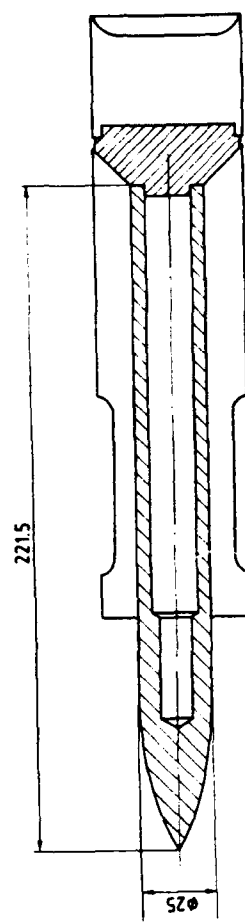


Figure 4: Model Hard Target Penetrator with Sabot

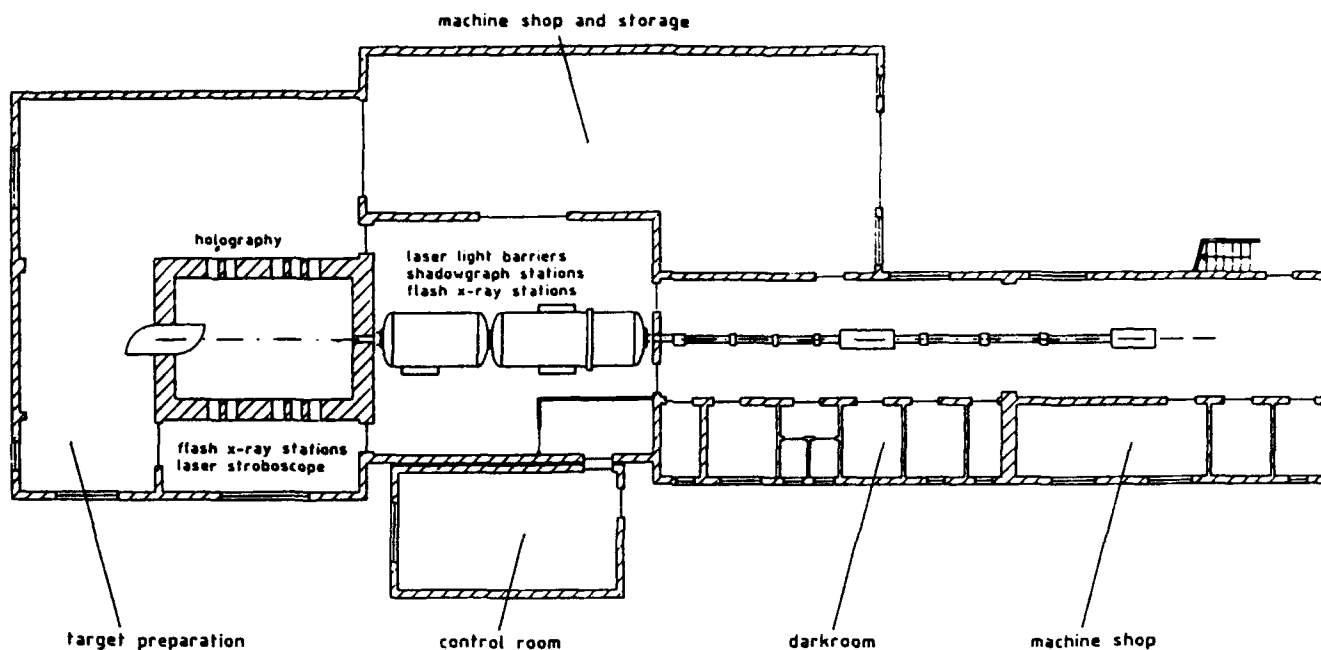


Figure 5: Floor Plane of the EMI Test Facility

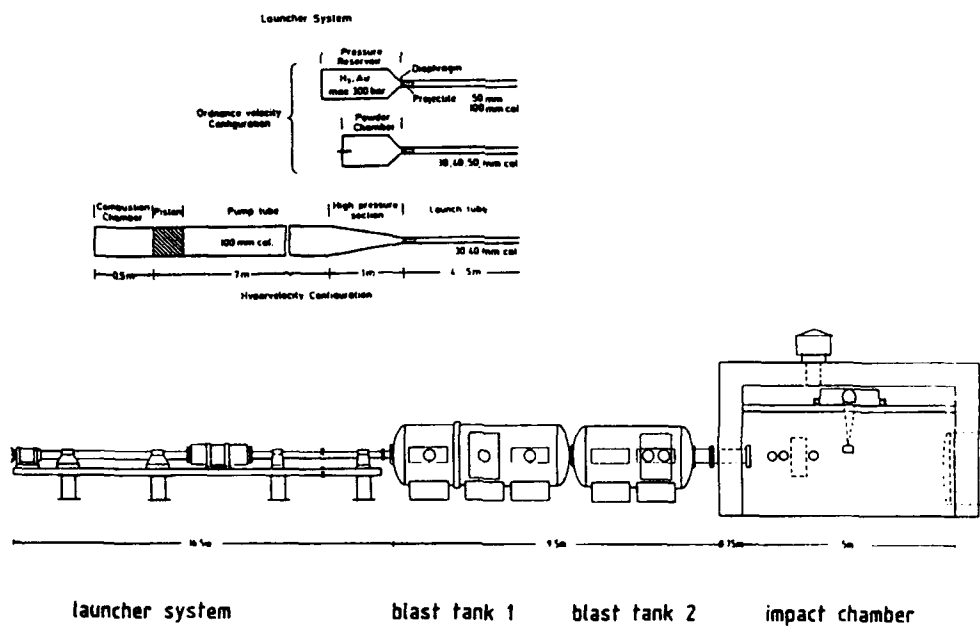
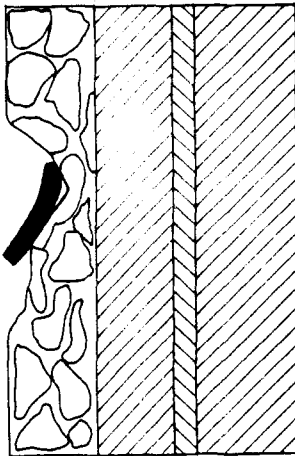
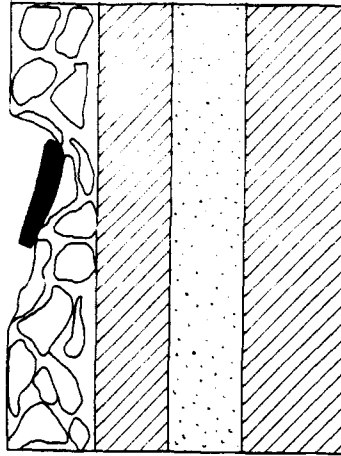


Figure 6: Schematic Drawing of the Range



751



752

Fig.7: Side View of the Bomb Crater
Test 751, v: 398 m/s, $\alpha: +20^\circ$,
Test 752, v: 405 m/s, $\alpha: +60^\circ$



751

752

Fig.8: Model Bombs after Penetration
Test 751, v: 398 m/s, $\alpha: +20^\circ$,
Test 752, v: 405 m/s, $\alpha: +60^\circ$

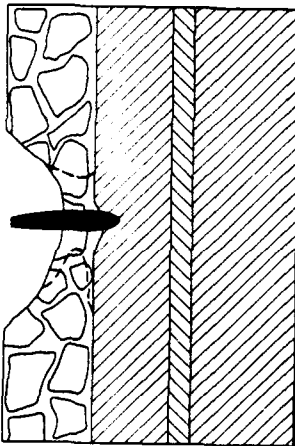


Fig.9: Side View of the Bomb Crater
Test 796, v: 393 m/s, $\alpha: 0^\circ$

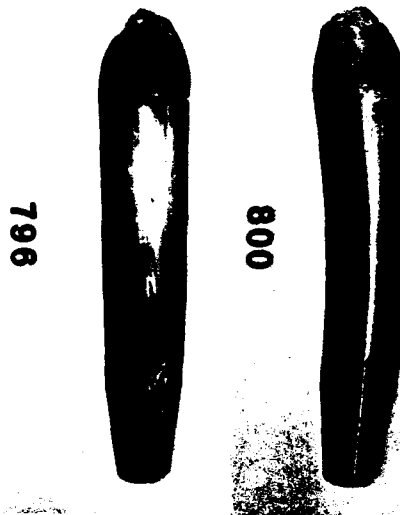


Figure 10:
Model Bombs after Penetration
Test 796, v: 393 m/s, $\alpha: 0^\circ$
Test 800, v: 504 m/s, $\alpha: -5^\circ$

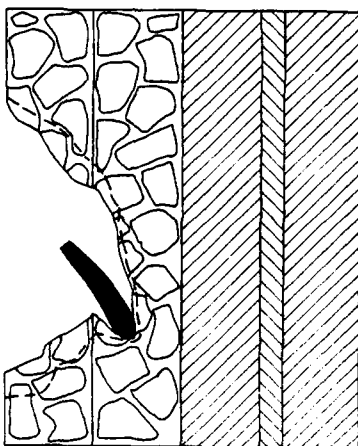


Figure 11:
Side View of the Bomb Crater
Test 800, v: 504 m/s, $\alpha: -5^\circ$

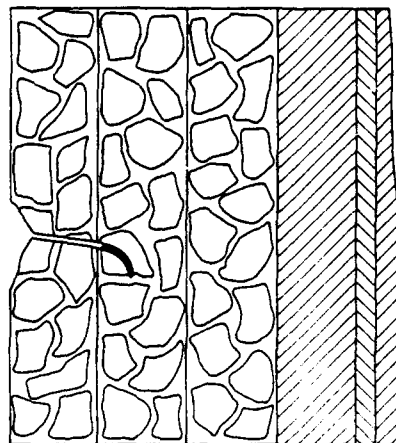


Figure 12:
Side View of the Bomb Crater
Test 797, v: 741 m/s, $\alpha: 0^\circ$

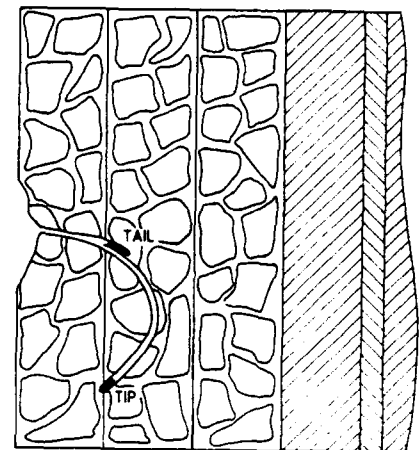


Figure 13:
Side View of the Bomb Crater
Test 801, v: 745 m/s, $\alpha: 0^\circ$

IMPACT OF PROJECTILES ON HARD LAYERS

T. Fries
D. Favarger

Defence Technology and Procurement
Agency (DTPA)
Ballistics, Weapons and Ammunition
CH-3602 Thun, Switzerland

M. Koller

Résonance SA
Consulting Engineers
CH-1227 Genève, Switzerland

A physical model simulating the impact behaviour of projectiles on hard layers will be presented. It is based on the Bernard theory [1]. The corresponding computer code accounts for the 3D geometry of a cylindrical projectile with ogival or blunt nose.

In the operational range of 200-300 m/s impact velocity, projectiles with ogival nose can penetrate into a burster slab for angles of incidence less than 45 to 55°. A greater obliquity leads to ricochet. Blunt noses enable more reliable penetration up to about 75° obliquity. For higher values of the obliquity, blunt projectiles rebound on hard layers.

Results of parametric studies on the impact behaviour -ricochet, tumbling motion or penetration- of projectiles with blunt and ogival noses will be presented.

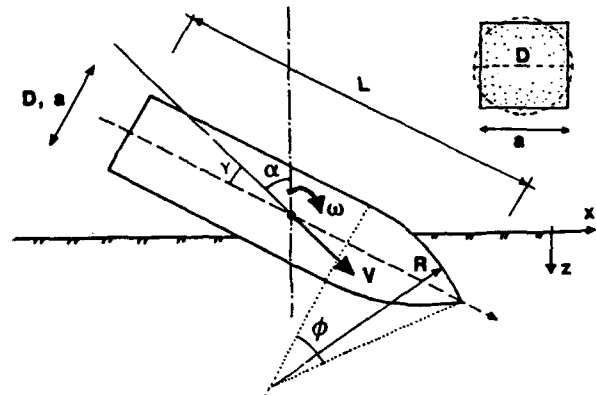


Fig. 1. Symbols and parameters.

1. Introduction

During the field tests in Val Nalps (Switzerland) in 1987 and 1988, 22 GP and SAP, inert and live Swiss bombs were dropped on rock rubble layers as well as 4 Mark 82 and 84 bombs. These full scale experiments have not answered all questions asked [2, 3]. It was assumed that Mark bombs with ogival nose would penetrate more into the protective layer than blunt Swiss bombs. Although this assumption was most likely right for targets of lower hardness than a burster slab, the effects of the four different Mark bombs dropped did not lead to clear conclusions. In previous field tests, bombs with ogival nose had showed strong path deflection in the target material and a poor penetration ability [4]. Since the publication of the last reports [2, 3] on the above mentioned tests, an attempt has been made to study these topics by using a physical model.

For this purpose, a previous 2D model simulating the impact behaviour of blunt bombs on hard layers [5, 6] has been extended for rigid bombs with ogival nose as well.

A further question has been how the number of dimensions influences the model results; Therefore, the model has been extended to 3 dimensions.

List of abbreviations, symbols and parameters

a	"calibre" of 2D projectiles
CRH	calibre radius head = R / D
D	calibre
F	penetration force
L	projectile length
L/D	projectile slenderness
R	curvature of the ogival bow
V	impact velocity
x, y, z	rectangular coordinates
xz-plane	plane of incidence ($y = 0$)
Y	target strength
2D	2 dimensional
3D	3 dimensional
GP	general purpose
SAP	semi armor piercing
α	obliquity or angle of incidence
lim(α)	limit of α
γ	angle of attack
ϕ	bow angle of the ogive
ω	angular velocity of the projectile in the xz-plane

Experiments in White Sands Missile Range (N.M) with I-2000 bombs [7, 2], have raised a few more questions as well. One of them will be to determine as well as possible the actual protection offered by existing shelters and their burster slab.

2. Development and description of the model

The penetration force due to material inertia and strength is calculated with the Bernard theory [1], discarding strain hardening, compressibility effects and friction. The influence of the reduced strength due to the free surface is taken into consideration [5, 6]. Such semi-empirical penetration theories often do not give accurate values of the penetration depth. In the code used, they are adjusted by one global factor to match the mean depth reached by the bombs dropped in the full scale tests. This model is not a penetration theory; it allows investigations only on the case of shallow penetration. Hence, the typical errors made by modelling roughly the mechanical properties of the target material do not play an essential role.

The equations of motion are solved numerically. The conservation of energy is checked throughout the time integration to get an estimate of the errors.

In an earlier study, excellent agreement between experimental results and the model was obtained for impacting spheres [1]. Another model for 2D projectiles described in [1] has been extended to account the observed bending of GP bombs at impact [6]: in [6], the projectiles are made of two rigid parts held by a hinge. This hinge has a rigid ideal plastic characteristic corresponding respectively to the yield bending strengthes of the GP and SAP bombs. The bending angles of the GP bombs established during the tests and the angles given by this simple model of projectile deformation correspond qualitatively.

The sphere referred to in fig. 2 has the same weight and the same cross section as the SAP bombs used in the tests. The motion of 2D projectiles remains in the xz-plane or plane of incidence (fig. 1). In a 3D space, such 2D projectiles would have a constant vertical shape in the y-direction. In the code, they have a square cross section of equal area to that of 3D cylinders. Their side a is given by:

$$a = \sqrt{\pi D^2/4} = 0.89 D$$

This useful assumption simplifies the comparison with 3D projectiles. The 2D projectiles have the shape of blunt or pointed beams depending on the type, "beam" or "2D ogive". The 3D projectiles have a circular cross section of diameter D and a blunt ("cylinder") or ogival nose ("3D ogive"). For 2D and 3D ogives, the CRH set is 4.

Actually, the model reported here in is not fully 3-dimensional: the angle between the c.g. velocity vector and the projectile axis (fig. 1) remains in the plane of incidence. It implies that the pitch angle is zero throughout the impact event. This limitation is of minor importance in this study. In most of the computations, the initial angle of attack set is zero.

3. Comparison between the 2D and 3D model

The curves of fig. 2 below show the limit of the obliquity α in function of the impact velocity V for several types of projectiles: for values of α below this limit, the projectile type considered penetrates into the target. For values of α above the curves, it rebounds after its impact on the burster slab or performs only shallow penetration. In the last case, defined by a penetration depth less than one calibre D , the damages caused by an unconfined explosion would be light; this case may occur if a projectile began to rebound throughout nose burial, but would come to rest before losing the contact with the target.

Currently, air-delivered bombs achieve an impact velocity between 200 and 300 m/s.

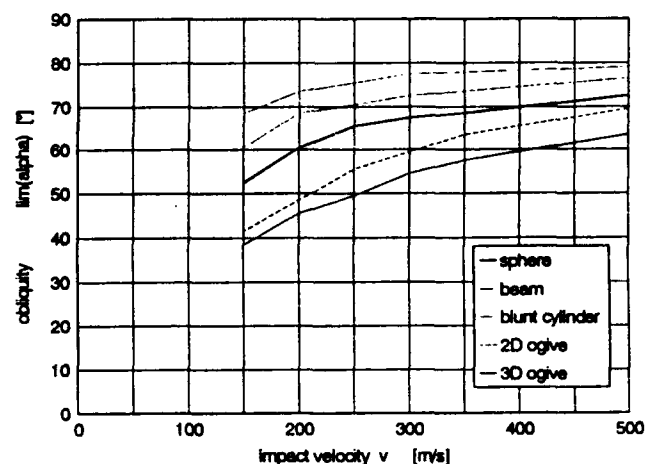


Fig. 2. Limit of the obliquity α in function of V for several types of projectiles.

A 2D beam rebounds on a hard layer for smaller angle of incidence than a 3D cylinder (fig. 3). The explanation is obvious: the penetration force F is proportional to the buried part of the front. The corresponding area and the force F are greater in the case of a 2D quadratic cylinder as long as less than half of the front is embedded. The resulting force acts farther from the projectile axis than in the case of a 3D cylinder. The resulting torque, inducing a forward rotation, is greater as well. The corresponding explanations for projectiles with ogival nose will be given below.

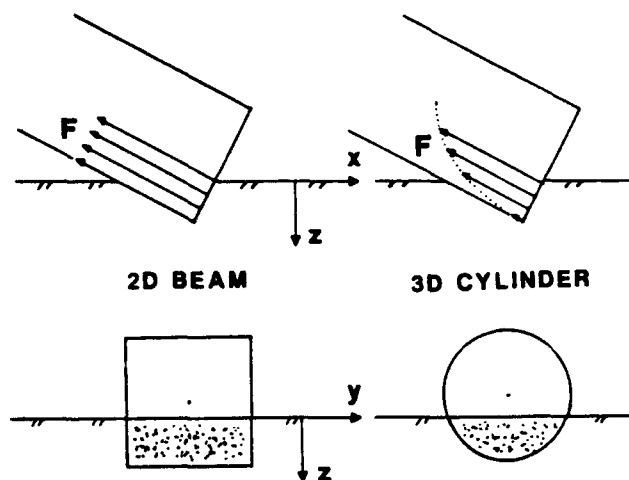


Fig. 3. Distribution of the penetration force F for 2D and 3D blunt projectiles.

Generally, the angle of attack γ increases throughout the impact event or shallow penetration of projectiles with ogival nose. If it becomes greater than the bow angle ϕ of the ogive (fig. 4), the pressure distribution on the tip depends essentially on the number of dimensions: in the case of the 2D model, no force can act on the underside of the ogive and the projectile penetrates into the target. In the case of 3 dimensions, because of the twofold curvature (fig. 4), vertical sections (parallel to the xz -plane) of the tip change with the distance to the plane of incidence. Therefore, the slab material can exert some pressure on the underside of the nose. If γ becomes greater than ϕ , 3D projectiles with ogival nose would ricochet more easily than 2D ones (fig. 5).

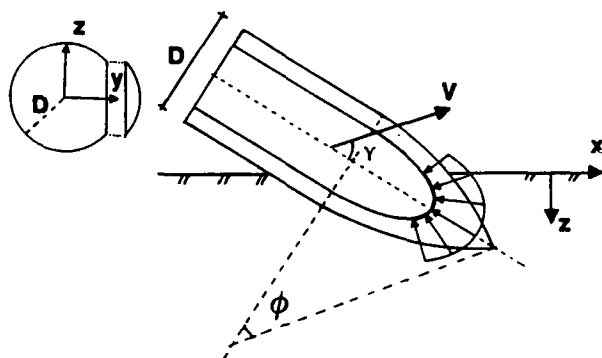


Fig. 4. Distribution of the penetration force F on the tip of a 3D ogive.

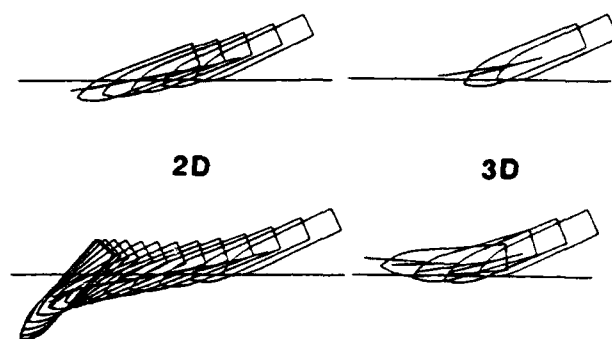


Fig. 5. The different impact behaviour of 2D and 3D ogives. The dash at the c.g. represents the velocity vector.

As we see, analysis of impact phenomena with 2D or 3D models may lead to opposite conclusions.

4. Different impact behaviour of 3D ogives and cylinders

The resulting force F acting on the front of a blunt projectile has a direction close to the velocity vector and primarily slows the projectile down. Its lever arm and torque are small. The forward rotation of the projectile in the xz -plane begins slowly (fig. 3 and 6). It has a tendency to raise the projectile and to enhance the penetration ability. Hence, the torque and the impact behaviour of blunt projectiles depend essentially on the angle of attack and much less on the impact velocity.

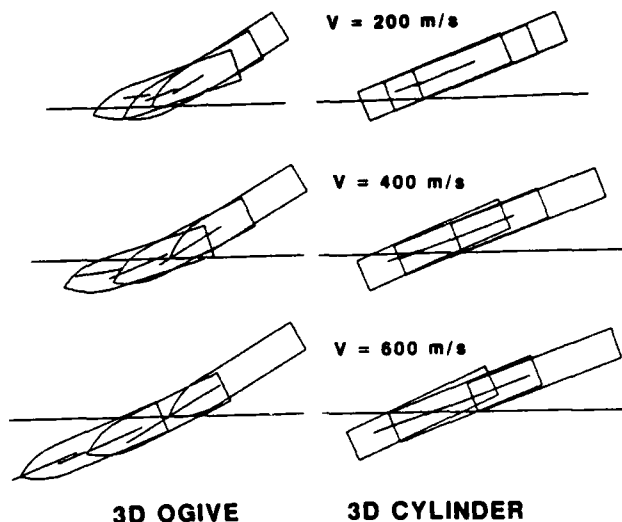


Fig. 6. The different impact behaviours of 3D ogives and cylinders. The dash at the c.g. represents the velocity vector.

In the case of an ogival nose, the angle between F and the velocity vector V is greater than in the case mentioned above. The torque of F , too. The projectile rotation backward is faster,

leading to a considerable deflection of its initial trajectory and to a ricochet tendency. Hence, projectiles with ogival nose rebound for clearly lower obliquity than blunt ones. But, as soon as the tip of an ogive is embedded, the pressure exerted by the target material on its upper side reduces the ricochet tendency. This effect increases with the impact velocity as will be discussed in section 5. Therefore, the impact behaviour of 3D ogives and the corresponding limit of α depend primarily on impact velocity. For such projectiles, it is almost independent of the angle of attack γ because a variation of γ induces only a small change of the angle between F and V mentioned above.

5. Influence of the impact velocity V

For all types of projectiles considered, the limit of α increases with velocity (fig. 2). The initial angular velocity is assumed to be zero; hence, it increases slowly throughout the impact event until it becomes noticeable. During this process, the projectile penetrates more or less into the target, depending on its initial velocity. The embedding process prevents further projectile rotation: in fig. 6 above, we can see the shape of cylinders and 3D ogives at equally spaced times of the impact event. The projectile deflection throughout nose burial decreases clearly with increasing impact velocity. The deceleration is greater for blunt projectiles than for the 3D ogives.

At lower impact velocities, say less than 200 m/s, the projectiles achieve only shallow penetration. In this case, it becomes difficult to distinguish between actual penetration or rebound with forward or backward rotation. The same problem occurs with very hard targets (cf. section 8).

6. Influence of the angle of attack γ

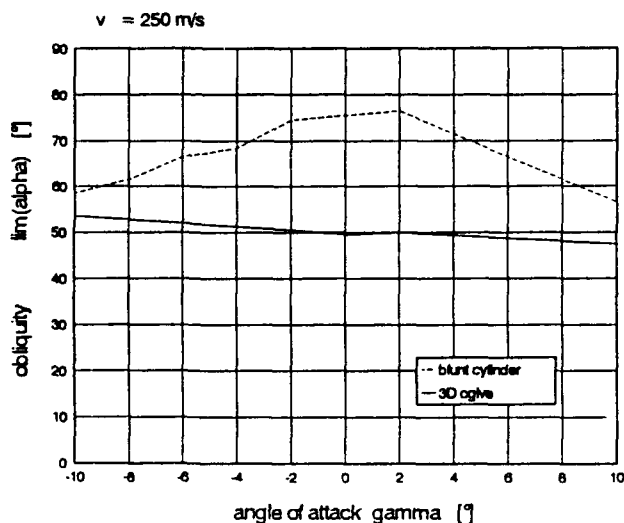


Fig. 7. Relation between the limit of α and the angle of attack.

Fig. 7 shows clearly that the impact behaviour of cylinders depends strongly on the angle of attack γ contrarily to the impact behaviour of 3D ogives. Nevertheless, they are able to penetrate into the target more reliably than projectiles with ogival nose.

7. Influence of the slenderness L/D

The slenderness ratios chosen correspond partly to existing bombs (Swiss bombs: L/D = ca. 4.8, I-2000: L/D = 7). In the model, weight and volume of explosive and case material remain equal for all L/D values. It implies that the calibre D decreases if the projectile length increases. The limit of α and the penetration ability increase with growing L/D ratio (fig. 8). The projectile cross section and, hence, the penetration force F decreases with increasing slenderness. The impact behaviour depends on the L/D ratio and on the impact velocity in a similar way for similar reasons (cf. section 5): the moment of inertia increases with the projectile slenderness, reducing the projectile rotation and the tendency to rebound.

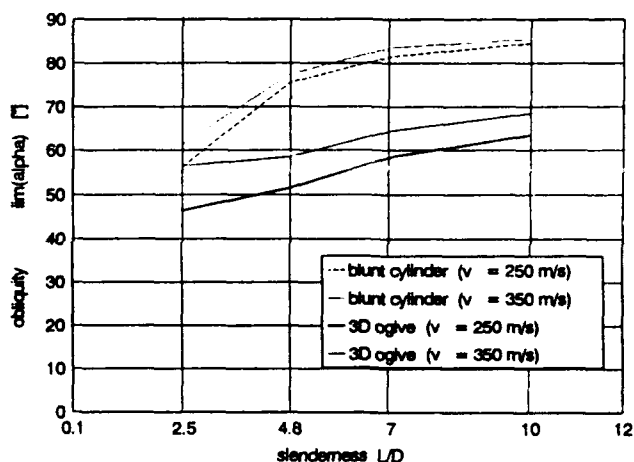


Fig. 8. Influence of the slenderness ratio on the limit of α .

The increase of the limit of α with growing slenderness is less pronounced above L/D = 7 than below this value. The opposite trend between L/D = 2.5 to 4.8 for 3D ogives can be explained by the chosen geometrical assumption: for such projectiles, the L/D ratio is changed by holding constant not their nose curvature, but their CRH. This assumption makes the nose sharper - R increases with decreasing slenderness. It leads to a higher penetration ability and compensates partly the effect of the decreasing slenderness on the limit of α . For 3D ogives, the slope of the line in that slenderness range would be steeper if the L/D ratio were changed by holding constant the nose curvature.

8. Influence of the target strength

The impact behaviour depends considerably on the target strength (fig. 9). On hard rocks reaching more than 150 MPa yield strength, the projectiles achieve only shallow penetration. Their impact behaviour is similar to that of slow projectiles - say $V < 200$ m/s - hitting a reinforced concrete slab of 35 MPa yield strength. Because the weapons effects would be minor in both cases mentioned, it is not important to know whether the projectiles would rather rebound or not.

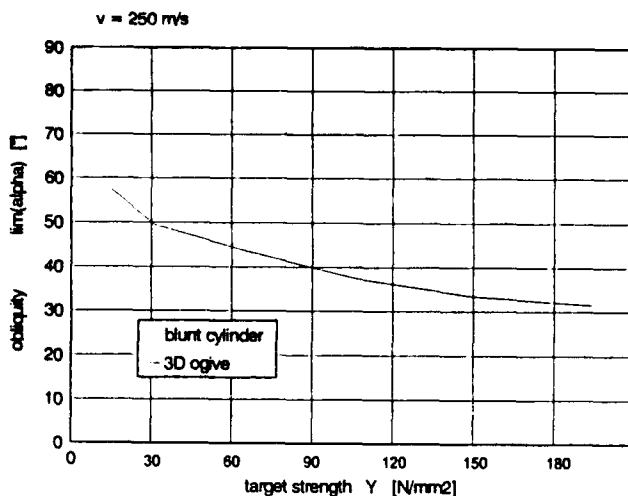


Fig. 9. Influence of the target strength on the limit of α .

9. Influence of the c.g. position

For aerodynamical reasons, the ballistic stability of projectiles requires the c.g. to be enough forward. The limit of α - i.e. the penetration ability - increases slowly for more forward c.g. positions. But, even if we replace explosive by steel in front of the projectile, the practicable improvement is very limited.

10. Final remarks

The study presented herein is only of interest if it leads to some link with the actual interaction of bombs with burster slabs. Blunt SAP ("rigid") bombs achieve penetration into a hard target for a greater obliquity than bombs with an ogival nose. But, this advantage may disappear if they are guided because their impact behaviour depends strongly on their angle of attack (fig. 7): a guidance system like Paveway II imparts considerable changes of this angle to the bombs throughout their trajectory. This is even visible with naked eye. Hence, the advantages of blunt bombs may be limited to unguided ones, falling with small angle of attack, dropped on bumpy ground, where the angle of incidence depends strongly on the impact location.

Bombs with ogival nose falling on a flat area penetrate better into a target than blunt ones if the angle of incidence is within the limit. Moreover, their impact behaviour is almost independent of the angle of attack. It cannot be made worse by a guidance system like Paveway II.

The full scale tests and the model have showed that burster slabs of about 3 calibres thickness offer a very good protection against 450 kg bombs independently of their impact behaviour - penetration or rebound. The level of protection can be expressed by a number of hits per unit area without significant damages. However, we cannot expect that burster slabs of the tested thickness achieve a sufficient protection against bombs like I-2000: investigations on the impact behaviour of such bombs with the model presented herein lead to the conclusion that guided I-2000, dropped under operational conditions, would not rebound. Such bombs can be defeated only by thick rock rubble layers imparting strong deviations to the penetrating bombs and limiting the penetration depth in this way. The costs for the corresponding level of protection are only justified for the most important installations. Of course, camouflage and deception is another important topic for the protection of all underground structures as well.

References

- [1] Bernard R. S. Development of a Projectile Penetration Theory. US Army Engineer. WES, Vicksburg, Mississippi. June 1975.
- [2] Favarger D. Bätzberg and Val Nalps Tests: Final Report. P. 109-118. of [7].
- [3] Favarger D. Wirkungen von konventionellen Waffen auf Schutzschichten und unterirdischen Anlagen. Bericht B 946. GRD FA 27. CH-3602 Thun 3. August 1992. VERTRAULICH.
- [4] Janser O. Bombenabwürfe in Kloten. Versuchsbericht Nr. 1191. GRD S 4.8. Flugversuche Emmen. 17. Mai 1976.
- [5] Favarger D., Eyer P. and Koller M. Ricochet and Shallow Penetration of Bombs Impacting on Hard Layers. Proceedings of the Fourth International Symposium on the Interaction of Non-nuclear Munitions with Structures. P. 86-92. Panama City Beach, Florida. April 17-21, 1989.
- [6] Eyer P., Koller M., Favarger D. Aufprallverhalten von Bomben auf Zerschellerschichten. Bericht FA27-SIG B 900511 910. GRD FA27, CH-3602 Thun. 11. Mai 1990.
- [7] Proceedings of the TELL 91 Symposium. Conventional Weapons. Penetration, Protection and Prediction Techniques to include Results from TELL 91 Test series. NC-Laboratory, CH-3700 Spiez. April 22-23, 1992.

RESISTANCE OF CONCRETE AND REINFORCED CONCRETE STRUCTURES IMPACTED BY CU AND TA PROJECTILES

Vladimir M. Gold, James C. Pearson, and Joseph P. Turci

US Army ARDEC, Energetics and Warheads Division
Picatinny Arsenal, N.J. 07806-5000

ABSTRACT

Spherical-nose Cu and Ta rods were gun launched with the velocities ranging from $0.15\text{cm}/\mu\text{s}$ to $0.19\text{cm}/\mu\text{s}$ against concrete and simulant reinforced concrete targets. Target hole profiles and projectile residual masses were measured and reported. Penetration performance $P/L\rho_p$ for both the Cu and the Ta projectiles against plain concrete targets was computed within the framework of the Tate's theory of penetration, and the calculations are compared with the experimental data for various velocities. Based on the results of these calculations, a comparison is made for the penetration efficiencies of the Cu and the Ta projectile materials. A rationale for treating a semi-infinite reinforced concrete structure as a composite comprised of layers of concrete proper and reinforcing steel was adopted, and the results of the analysis are compared with the experimental data for the simulant reinforced concrete targets. The effects of varying thicknesses of the surface layer of the concrete as well as the thicknesses of the steel reinforcement on the penetration resistance of a concrete/steel/concrete composite were investigated via this theory, and the results are discussed.

EXPERIMENTS WITH THE SIMULANT TARGETS

The experimental part of this study included terminal ballistic experiments which established the data on resistance of semi-infinite concrete and reinforced concrete structures attacked by high velocity projectiles. Spherical nose Cu and Ta projectiles with 1.3cm and 2.0cm diameters and varying L/D were gun launched against simulant concrete and reinforced concrete targets with the velocities ranging from $0.15\text{cm}/\mu\text{s}$ to $0.19\text{cm}/\mu\text{s}$. Most of the structures were instrumented with evenly spaced break gages, and the recorded trigger times provided the data of the flow field of the concrete as the projectile was traversing the target.

The simulant targets were 91cm diameter and 91cm long right circular cylinders, and were constructed from a concrete with maximum aggregate size of 1.9cm and unconfined compressive strength of 0.374Kbar. In order to minimize the influence of the lateral boundary of these moderately sized targets, to prevent their shattering, and to achieve accurate hole profiles, the lateral surface was constrained by a spiral reinforcing bar and tack welded to the enclosing corrugated steel shell. The rear and front ends of the skeleton of this structure were also fortified by a grid of transverse reinforcing bars, and the rear end grid was tack welded to a thin steel end plate. Since the diameter of the structure exceeded the projectile diameters by 50 to 70 times, and the lateral and rear boundaries were heavily

constrained, the flow field of the concrete was expected to be localized compared to the size of the target. Although the resulting penetration depths were of the order of one third to one half of the lengths of the targets, no visible traces of deformation were found in the rear of the structures. The examination of the condition of concrete near the edge of the front surface indicated that this portion of the material was subjected to a relatively low strain field, which further supported our initial assumption that the size of the targets would be adequate to approximate the impact response of a semi-infinite configuration. The targets that were intended to simulate the response of a semi-infinite reinforced concrete structure to a ballistic impact, included a 1.6cm thick and 30.5cm square steel plate imitating a reinforcing rebar, which was embedded 3.8cm away from the front face of the target and welded to the front grid of transverse reinforcing bars. The probability of hitting 1.6cm rebar by a gun launched projectile is very low, and this was the reason for simulating the reinforcing rebar with a steel plate of an equivalent thickness and strength. Steel grades with similar strength characteristics were used for both the plates and the reinforcing bars, which according to the manufacturer's specifications had an yield strength of 4.1Kbar. For the velocities above $0.15\text{cm}/\mu\text{s}$, the penetration depth is expected to be affected mostly by the thickness of the rebar rather than by its geometric form, therefore such an approach of substituting the equivalent plate for the rebar is acceptable for a meaningful study of penetration resistance of reinforced concrete structures.

The schematic of the test set up is shown in Fig. 1. The projectiles were positioned in a plastic sabot, placed in a 83mm diameter and 10.9m long launching tube, and fired. To ensure the structural integrity of the projectile-sabot assembly during the rapid acceleration in the launching tube, the rear end of the sabot was reinforced with an aluminum pusher plate. At the downstream end of the launching tube, past the gas expansion chamber, the accelerated projectile followed by the separating sabot proceeded along the drift tube, where their motion was photographed at two orthogonal viewing station with a streak camera. The stations were 75cm apart from each other, and comparing the two photographs taken at the set exposure times provided reliable measurement of the projectile's velocity. The targets were housed in a massive steel tank, and the access for the two X-ray shadowgraph systems was provided through the horizontal and vertical window ports located at the sidewall. The X-rays were focused to cover the area in front of the target, so that the yaw and the condition of the projectile just prior to the impact was confidently established from the shadowgraphs. The targets were positioned approximately 1m away from the muzzle of the gun, however, this distance was insufficient for complete aerodynamic separation of the sabot. In order to minimize

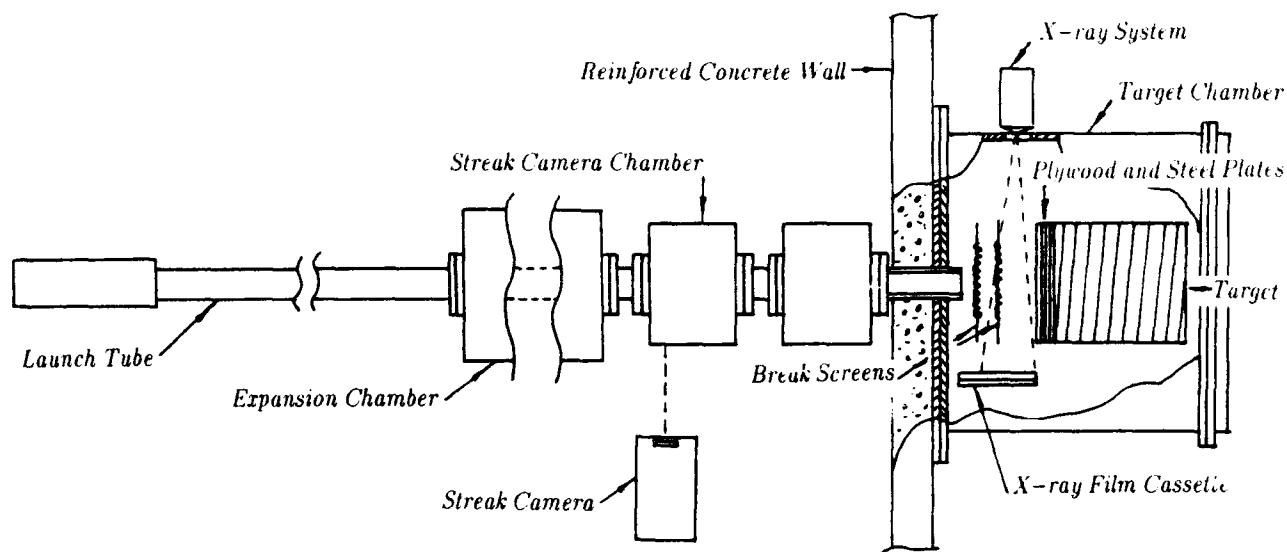


Fig. 1. Schematic of the experimental set up. The steel tank containing the target is located behind the reinforced concrete wall.

the damage to the front of the target by the debris of the sabot assembly, a sandwich of plywood and steel plates with a circular opening along the path of the projectile, was placed directly onto the target's surface. The diameter of the hole and the thickness of this buffer were chosen to allow the projectile to freely pass through, but to stop the aluminum pusher plate and the sabot parts from reaching the target. Two break screens placed 30.5cm apart from each other were employed to trigger the *X-ray* system as well as to provide an auxiliary measurement of the projectile velocity. The impact velocities were also verified from the *X-rays*, which correlated fairly well with streak camera records.

The performance of the launched projectiles against the targets is summarized in Table 1. In all the tests, the crater profiles were very similar for both the *Cu* and the *Ta*

projectiles with like diameters. A typical configuration of a crater for a plain concrete target is shown in Fig. 2. For the 1.3cm diameter projectiles the entrance of a crater measured typically 25cm in diameter and rapidly narrowed down to a diameter of 5cm, 10.5cm away from the level of the original surface of the target. The deeper portion of the crater exhibited a distinct form of a well rounded and slightly tapered tunnel. For the simulant reinforced concrete targets, the form of the entrance of the crater was significantly perturbed, since the front layer of the concrete was shaken off by the motion of the steel plate excited by the projectile piercing the plate. Behind the plate, the hole was very well preserved, and, similar to the plain concrete targets, resembled a well rounded and slightly tapered tunnel. The profiles of the tunnel portions of the craters are given in Table 2.

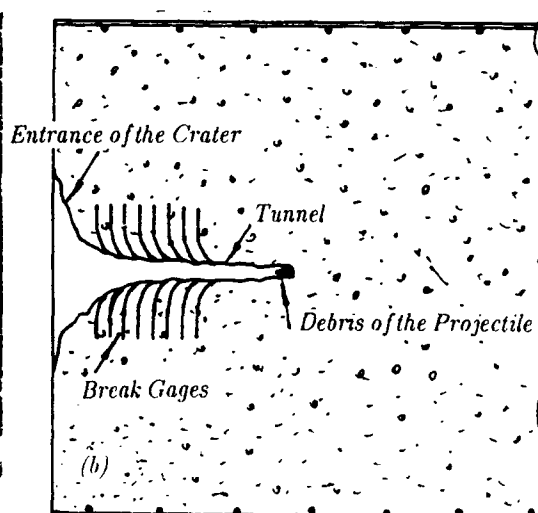
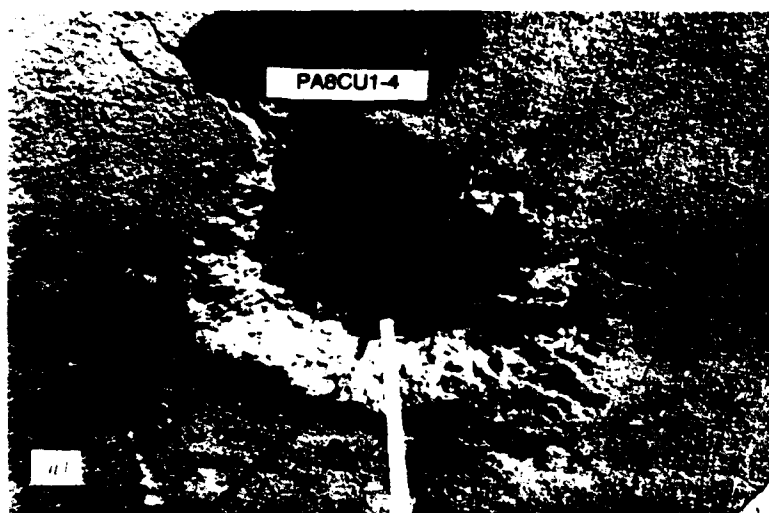


Fig. 2. Crater produced in a target by a projectile impact. (a) A close-up photograph of a crater caused by a projectile impact with velocity 0.1836cm/ μ s. The tunnel which starts approximately 10.5cm from the surface is visible in the center of the crater. (b) Schematic drawing of a typical crater profile.

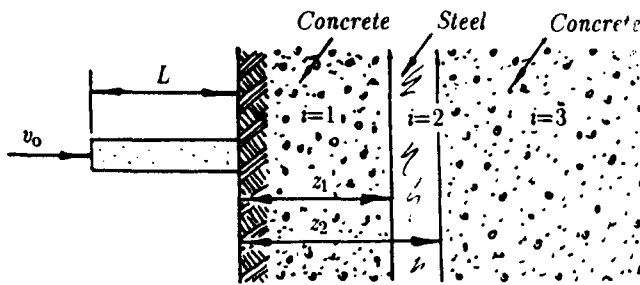


Fig. 3. A composite semi-infinite target is impacted by a rod projectile. The conditions of continuity of the projectile's length and the velocity of the rear end are imposed at the interfaces between the layers.

ANALYSIS OF THE IMPACT RESISTANCE OF CONCRETE AND REINFORCED CONCRETE TARGETS

We applied the one-dimensional theory of penetration of Tate (1-2) and extended it to the analysis of motion of projectiles penetrating semi-infinite concrete and reinforced concrete targets. Within the framework of this theory, the essence of the mechanics of penetration of a solid projectile into a solid target is represented through erosion of the penetrator's material which is combined with its rigid body motion. Although, the Tate's theory neglects the three dimensional nature of the flow field of the interacting projectile and target, it demonstrates good qualitative and quantitative agreement for the impact velocities in the ballistic range. In our experiments, all the targets were sectioned in search of the residual parts of the projectiles. The results of the sectioning of the targets are given in Table 1, which show that for the tested velocities the penetration was accompanied by almost complete erosion of the projectiles.

Referring to Fig. 3, we adopted a rationale for treating the reinforced concrete targets as comprised of layers of concrete proper and reinforcing steel. The Tate's theory was extended to include the analysis of composite targets so that the increased resistance of the reinforced concrete was primarily attributed to the strength and the thickness of the reinforcing steel, while the intricate effects of interactions between the motion of the penetrator with the reinforcing steel and the concrete were neglected. Thus, according to Tate's model, the motion of a projectile penetrating the composite target is governed by the following set of equations, which were applied to each of the layers

$$\begin{aligned} Y &= -\rho_p l \frac{dv}{dt} \\ \frac{dl}{dt} &= -(v-u) \\ \frac{1}{2}\rho_p(v-u)^2 + Y &= \frac{1}{2}\rho_{ti}u^2 + R_{ti} \end{aligned} \quad (1)$$

Here, l is the length of the projectile, ρ_p and ρ_{ti} are the densities of the projectile and the i th layer of the target (for the plain concrete $i=1$, and $i=1,2,3$ for the reinforced concrete), u and v are the velocities of the front and the rear ends of the projectile, and Y and R_{ti} are the strength factors of the projectile and the i th layer of the target, respectively.

The system of Eqs. (1) was integrated numerically, and the penetration depth per unit mass of the penetrator $P/L\rho_p$ was computed as a function of the initial impact velocity v_0 for both the Cu and the Ta projectiles, and plotted in Fig. 4. Normalizing the penetration depth by the areal mass of the penetrator, the penetration capabilities were collated for the projectiles of different materials with the same kinetic energy, and, thereby, comparative penetration efficiencies were inferred for the projectile materials. The set of values $R=4.26\text{Kbar}$ for the concrete, $Y=6.86\text{Kbar}$ for the Cu, and $Y=13.44\text{Kbar}$ for the Ta seems to provide the best agreement with the low velocity data for the steel from

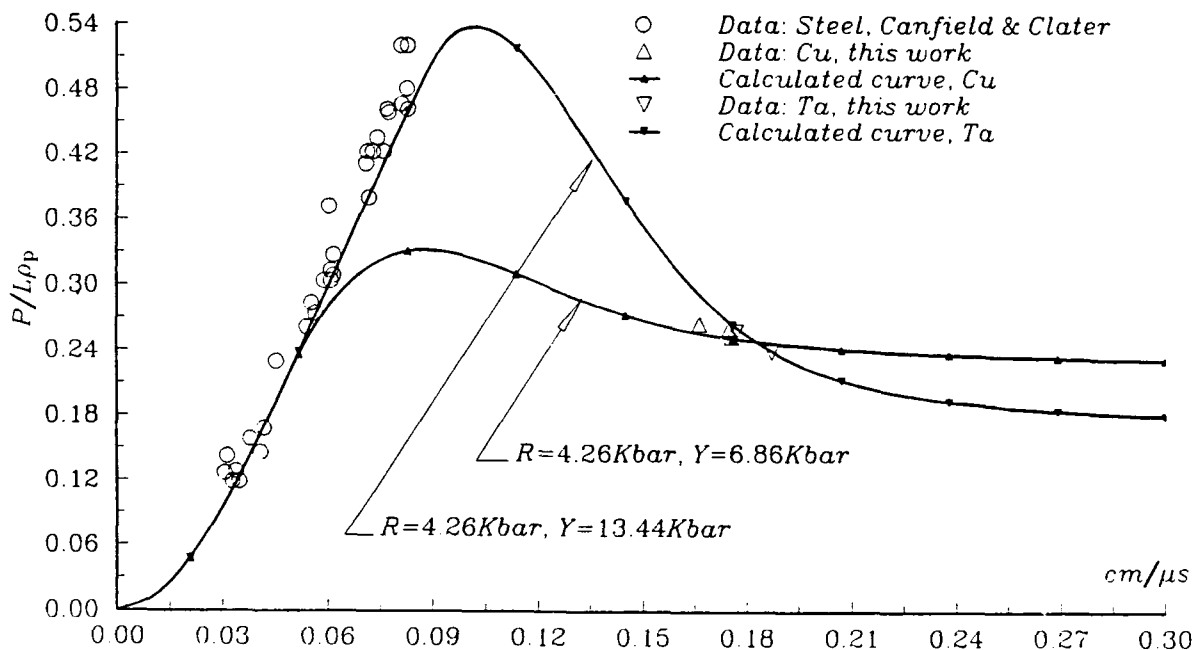


Fig. 4. Calculated penetration performance of the Cu and the Ta projectiles against plain concrete targets for varying impact velocities compared with experimental data.

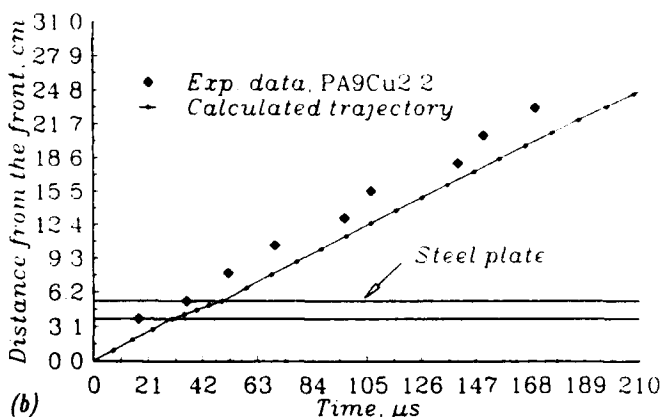
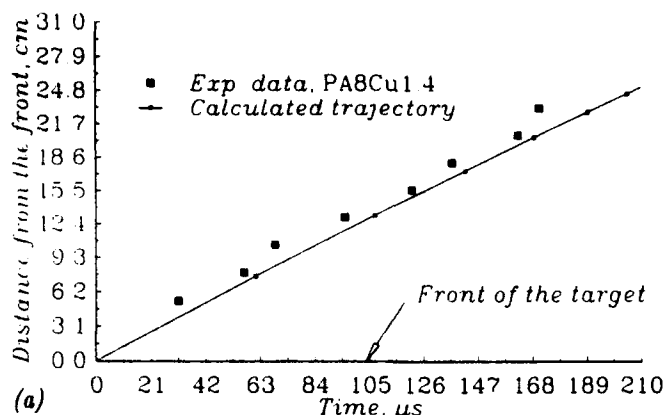


Fig. 5. The calculated trajectories of the front end of the projectile compared with the experimental records from the break gages. Parameters used: $\rho_p=8.9\text{g/cm}^3$, $Y=6.86\text{Kbar}$ for the projectile and $\rho_{t1}=\rho_{t3}=2.24\text{g/cm}^3$, $R_{t1}=R_{t3}=4.26\text{Kbar}$ for the concrete. (a) Plain concrete target, $v_0=0.1836\text{cm}/\mu\text{s}$. (b) Simulant reinforced concrete, $v_0=0.1875\text{cm}/\mu\text{s}$, $\rho_{t2}=7.9\text{g/cm}^3$, $R_{t2}=26.7\text{Kbar}$, $z_1=3.81\text{cm}$, $z_2=5.4\text{cm}$ for the steel.

Canfield (5), as well as with the Cu and the Ta data from this work. The values of $Y=6.86\text{Kbar}$ and $Y=13.44\text{Kbar}$ compare with the respective values for the Cu and the Ta of $Y=3.8\text{Kbar}$ and $Y=11.0\text{Kbar}$ found by Wilkins (6) at much lower velocities. The difference in the values for the Cu is 75%, while for the Ta is 22%, and these variations may be attributed to rate effects as well as to the initial conditions of the stock material. Comparing the calculated curves for the Cu and the Ta projectiles, the Ta is estimated to be a more efficient penetrator material than the Cu for the lower velocities, while the reverse is true for the higher velocities. Also, as illustrated in the Fig. 4, the penetration performance of a Ta projectile against plain concrete calculated within the framework of the Tate's theory, is evaluated to be almost 3 times higher for the velocities circa $0.11\text{cm}/\mu\text{s}$ than for the velocities above $0.18\text{cm}/\mu\text{s}$.

The penetration $P=P(v)$ and the time $t=t(v)$ were computed by solving the system of Eqs. (1). These two functions represent a trajectory of the front end of a projectile, where the parameter v is the velocity of the rear end of the projectile, $0 \leq v \leq v_0$. In Fig. 5 we compared the results of

these calculations with the experimental trigger time data from the break gages. For the plain concrete, Fig. 5(a), the experimental data agree very well with the slope of the calculated trajectory of the projectile. The offset of the experimental data from the calculated trajectory was attributed to the early trigger times of the break gages ahead of the projectile, apparently at the elastic-plastic boundary, where the strains were sufficient to cause an interruption in the applied voltage. For the simulant reinforced concrete, Fig. 5(b), the calculated trajectory exhibits a distinct change of slope as the projectile traverses different material layers of the target, and a similar trend is indicated in the experimental data.

In Fig. 6 we presented the results of penetration calculations for a composite concrete/steel/concrete target for varying the thickness of the first layer of concrete and the same thickness of the steel. The analysis indicated virtually identical penetrations for almost the entire range of the calculations. Since the computational model completely ignores the details of the flow field of the penetrator and the target materials, these calculations might not be realistic for small thickness of the first layer and more complicated projectile geometries.

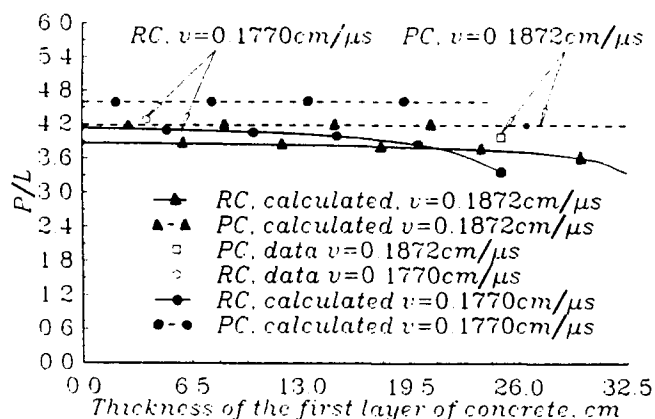


Fig. 6. Resistance of a concrete/steel/concrete composite for varying thicknesses of the surface layer of the concrete. $\rho_p=16.6\text{g/cm}^3$, $Y=13.44\text{Kbar}$ for the projectile, $\rho_{t2}=7.9\text{g/cm}^3$, $R_{t2}=26.7\text{Kbar}$, $t=z_2-z_1=1.59\text{cm}$ for the steel, and $\rho_{t1}=\rho_{t3}=2.24\text{g/cm}^3$, $R_{t1}=R_{t3}=4.26\text{Kbar}$ for the concrete.

Engineering analysis for a concrete/steel/concrete composite is presented in Fig. 7. The calculations indicated virtually linear decrease in the penetration P with varying the thickness of the steel layer $t=z_2-z_1$, while the areal weight of the structure $w=\rho_{t1}z_1+\rho_{t2}t+\rho_{t3}(P-z_2)$ required to defeat the projectile is almost the same. Areal cost of this structure was calculated as $\Omega=\Omega_c(P-t)+\Omega_r t$, where $\Omega_c=0.76\$/\text{m}^2\text{cm}$ and $\Omega_r=17.44\$/\text{m}^2\text{cm}$ are the areal costs per unit depth of the structure for the concrete and the reinforcing steel, respectively. The cost of the concrete was taken from the reference (3), and the Ω_r was estimated for the grade 60 #4 reinforcing bar from the reference (4).

The results of the penetration calculations for a concrete/steel/concrete composite for different thicknesses of the steel layer and varying impact velocities are presented in Fig. 8. These calculations are compared with the similar analysis for the plain concrete and the plain steel targets. The curves for the composite exhibit gradual transition from the plain concrete to the plain steel with increase of the thickness of the steel layer. Also, the analysis indicates that the penetration performance against a composite target is

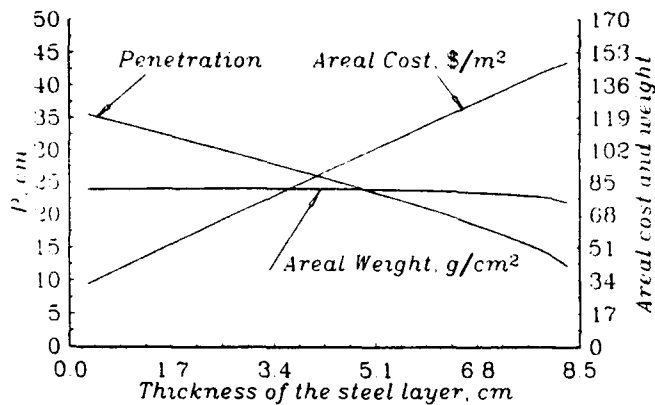


Fig. 7. Penetration resistance, areal weight, and areal cost of a concrete/steel/concrete composite structure for varying thickness of the steel layer. The structure is attacked by a 7.9cm long *Ta* projectile with the velocity 0.177cm/ μ s.

maximized for the velocities in the range from 0.1cm/ μ s to 0.14cm/ μ s with the varying thickness of the steel layer. The portions of the curves represented by dotted lines correspond to the low impact velocities where the application of this model is not valid. The unrealistic results obtained for this region are attributed to the qualitatively different mechanism of penetration at the low velocities, when a projectile is able to penetrate the composite target not only by erosion combined with the rigid body motion, but, in

addition, by shear plugging the steel layer of a moderate thickness. If these corrections are introduced in the computational model, the calculated curves should exhibit gradual transition from the plain concrete to the plain steel for the entire range of the impact velocities.

ACKNOWLEDGEMENTS

We acknowledge Mr. James Ray of WES for designing the targets and supervising their fabrication and Mr. John Ehr Gott, also of WES, for test direction. All the aspects of the break gages were the responsibility of Mr. George Hodges, Mr. William Finny and Mr. Allen McClendon of RTTC.

REFERENCES

- (1) Tate A., 1967, A Theory for Deceleration of Long Rods After Impact, *J. Mech. Phys. Solids*, Vol. 15, pp.387-399.
- (2) Tate A., 1969, Further Results in the Theory of Long Rod Penetration, *J. Mech. Phys. Solids*, Vol. 17, pp.141-150.
- (3) Material Prices, *Engineering News Record*, p.41, June 1, 1992.
- (4) Material Prices, *Engineering News Record*, p.159, June 22, 1992.
- (5) Canfield J. A., Clater I. G., 1966, Development of a Scaling Law and Techniques to Investigate Penetration in Concrete, *NWL Report No. 2057*.
- (6) Wilkins M. L., Guinan M. W., 1973, Impact of Cylinders on a Rigid Boundary, *J. Appl. Phys.*, Vol. 44, No. 3, pp.1200-1206.

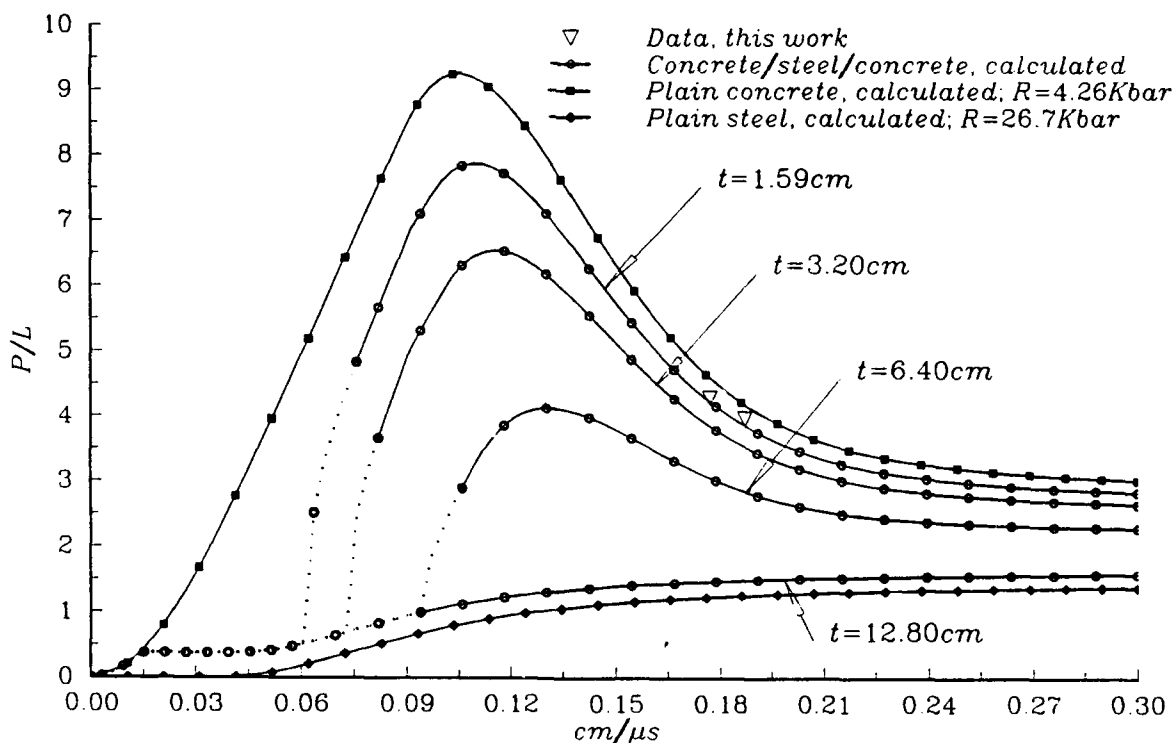


Fig. 8. Penetration performance of a *Ta* projectile against a concrete/steel/concrete composite with different thicknesses of the steel layer for the varying impact velocities. The curves for the composite are bound between the similar curves for the plain concrete and the plain steel. Parameters used: $\rho_p=16.6g/cm^3$, $Y=13.44Kbar$ for the projectile, $\rho_{t2}=7.9g/cm^3$, $R_{t2}=26.7Kbar$ for the steel, and $\rho_{t1}=\rho_{t3}=2.24g/cm^3$, $R_{t1}=R_{t3}=4.26Kbar$ for the concrete.

Table 1. Performance of *Cu* and *Ta* projectiles against plain concrete targets (PC) and simulant reinforced concrete targets (RC). The targets (i) were instrumented with the break gages. For the tests marked ⊗ no projectile debris were reported to be found from the sectioning of the targets.

Test	Target	Projectile mat.	diam., <i>cm</i>	length, <i>cm</i>	Impact Velocity <i>cm/μs</i>	Depth of penetration, <i>cm</i>	Projectile mass debris/initial, <i>g</i>
PA9Cu1.1	RCi	<i>Cu</i>	1.30	19.00	0.1626	32.5	⊗/224
PA9Cu2.2	RCi	<i>Cu</i>	1.30	14.00	0.1875	25.0	55/164
PA9Ta1.3	RCi	<i>Ta</i>	1.27	10.32	0.1717	35.4	8/216
PA8Cu1.4	PCi	<i>Cu</i>	1.30	19.00	0.1836	36.3	124/224
PA9Cu3.5	RCi	<i>Cu</i>	2.00	14.00	0.1663	33.5	160/381
PA9Ta2.6	RCi	<i>Ta</i>	1.30	7.66	0.1475	25.0	⊗/158
PA9Ta3.7	RCi	<i>Ta</i>	2.00	7.90	0.1770	33.8	⊗/397
PA8Ta1.8	PCi	<i>Ta</i>	1.27	10.32	0.1872	40.9	⊗/215
PA0Cu2.RS9	RC	<i>Cu</i>	1.30	14.00	0.1756	31.5	25/164
PA0Cu2.RL10	RC	<i>Cu</i>	1.30	14.00	0.1750	32.5	⊗/164

Table 2. Hole profiles of the tunnel portions of the craters. The measurements were obtained by inserting cylindrical gage probes into the hole and measuring the depth from the level of the original surface.

Probe Diameter, <i>cm</i>	Depth of the probe, <i>cm</i>						
	PA9Cu1.1	PA9Cu2.2	PA9Ta1.3	PA8Cu1.4	PA9Cu3.5	PA9Ta2.6	PA8Ta1.8
2.0	32.3	23.6	34.5	32.0	26.7	25.0	40.4
2.5	32.1	23.0	32.0	31.5	26.9	25.0	40.4
3.0	32.0	22.2	30.2	31.3	26.5	24.5	39.7
3.5	19.8	17.1	26.2	29.6	26.5	22.9	32.8
4.0	16.6	11.7	18.5	15.2	25.3	19.0	27.9
4.5	15.5	10.0	16.0	12.7	25.2	16.4	26.4
5.0	14.5	9.1	15.0	10.5	25.2	14.8	23.5

PENETRATION COUNTERMEASURES

James M. Underwood and LT Michael K. Westmoreland USN

Applied Research Associates, Inc., Tyndall AFB, FL
HQ AFCEA Tyndall AFB, FL

Abstract

If yaw is induced into a projectile prior to impacting a hard target, the projectile can be caused to break up or significantly reduce its penetration capability. Forty-four subscale tests were conducted to investigate the use of a cemetitious deflection grid to induce yaw during the free flight of the weapon. The tests investigated geometry and material composition to determine their effect on the amount of rotation induced into the projectile. To increase the contact time between the deflection grid and the penetrator, nylon fibers were added to the concrete which resulted in a material capable of absorbing higher amounts of energy. Through the use of higher unit weight concretes and the nylon fibers, the volume of material needed to deflect the weapon was significantly decreased.

Background

Current protective construction practice in the USAF and PACAF areas consists of heavily reinforced concrete, which requires massive amounts of materials and labor. This type of construction is designed to prevent breaching, and to reduce spall on the inside of exterior walls. Various combinations of soil layers, burster slabs, and rock rubble overlays have been used to trap penetrating weapons. Semihardened and hardened facilities are protected from aerial bombardment by a burster slab, designed for a particular threat. Weapon shape, weight, case material properties, charge-to-weight ratio, velocity, and fusing are the principal variables considered in the design of a burster slab. Its purpose is to break up or detonate the weapon at a sufficient distance to prevent serious damage to the target. With the increased accuracy of today's weapons, existing construction techniques do not provide guaranteed protection against weapon penetration, and the cost to do so could be prohibitive due to the sheer mass required to defeat a deep penetrating weapon. In tests conducted by the Waterways Experiment Station (WES), it was found that yaw, the angle between the penetrator's center of gravity translational velocity vector and its geometric centerline, induced into the projectile prior to striking the burster slab, greatly affects its penetration capability (1). Stress levels generated in the weapon case during impact can trigger a variety of failure mechanisms.

Various antipenetration systems have been tested, using rock rubble as an overlay against various types of weapons (2), but rock rubble is not practical if the rock is not readily available. Oblique impacts showed a tendency of the weapon to rotate in the boulder layer, revealing the importance of local impact conditions (3).

A yaw-inducing concept tested by WES using steel bars showed how effective a simple design could be in defeating low length to diameter, armor-piercing projectiles (4). The bars provided an unsymmetrical load on the projectile nose, which in turn caused a rotation of the projectile around its center of gravity.

Previous AFCEA tests at the Tyndall AFB Sky X Test Area had been conducted with deflection type devices constructed of cemetitious materials. A basic deflection grid geometry was tested to observe the reaction between the deflection grid and the projectile. Data reduced from these exploratory tests showed a variance in induced projectile rotational rate as the physical properties of the concrete changed. The magnitude of the effect of each material variable, such as compressive strength, density, and toughness, was not determined, nor was the effect of impact point. Due to the irregular design of the deflection grid, projectile rotation was induced, at least in part, by unsymmetrical loading. The findings of this earlier work indicated the material properties of the concrete provide a significant contribution to projectile tumble rate. For a system to be effective, it must have an overall weight advantage over existing construction techniques, and provide the structural integrity to resist multiple strikes and maintain consistent performance.

Approach

Many variables affect the behavior of dynamically loaded concrete. In the case of a deflection grid, the interaction of the projectile and the grid is very complex due to the grid's nonhomogeneous nature. Data from previous tests on concrete deflection grids made of normal steel-reinforced concrete showed a wide variation in induced projectile rotation rate. Figure 1 shows the projectile rotation in relation to body lengths of travel. The slope of the line is the projectile rotation rate. Figure 2 shows similar data for tests performed on grids constructed with a nylon fiber content of 10 pounds per cubic yard, and reduced conventional reinforcing steel. This tends to

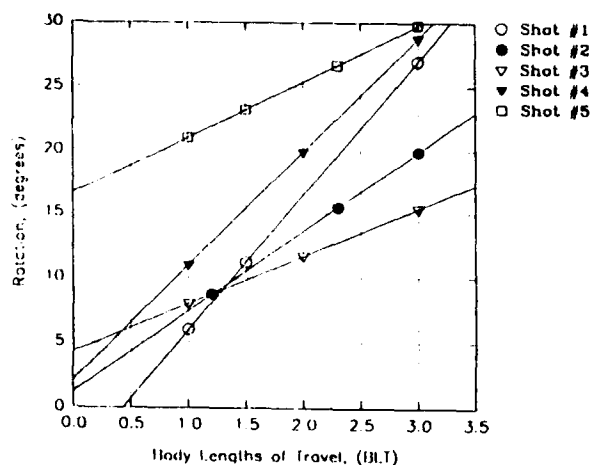


Figure 1. Projectile Rotation versus Body Lengths of Travel

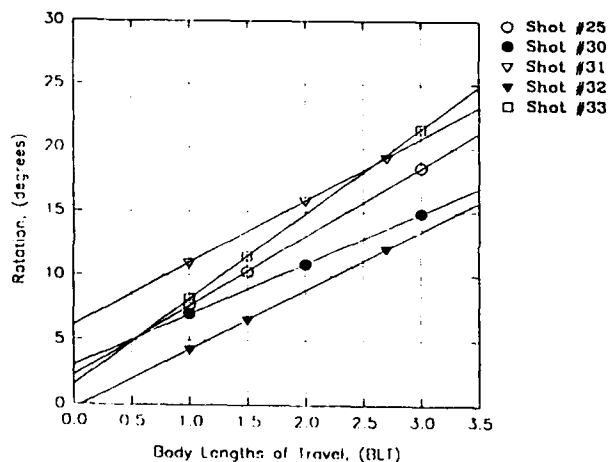


Figure 2. Projectile Rotation versus Body Lengths of Travel

support the theory that the fibers create a more homogeneous structure and thereby produce more consistent turning rates.

If the fibers add to the structural integrity of the concrete and delay the time to failure, an increased contact time between the penetrator and the deflection grid is achieved. Since reaction impulse is the key in determining the resultant projectile rotation rate, it might be beneficial to maximize the toughness of the grid material. By so doing, contact time for force application would be extended.

Contact time between the penetrator and the deflection grid is directly related to the time to failure of the material. Since toughness is a measure of the energy-absorption capability of the material, it seems reasonable to assume, that by maximizing the material toughness, contact time is increased,

thereby increasing the rotational energy in the system and maximizing the yaw induced into the projectile. The test plan was developed to find the system that would provide maximum deflection, consistent performance, survivability from multiple strikes and still provide a suitable cost trade off.

Laboratory Test Setup

The antipenetration tests were conducted at the SKY X Structures and Pavements Test Area located at Tyndall AFB Florida. The gun facility consists of a Third-Generation Aircraft Shelter for housing the targets and data acquisition equipment, with a smooth bore 155 mm howitzer located at the entrance to the shelter to launch the projectiles. The weapon being modeled is a generic design. It is 23.6 inches long and 3.35 inches in diameter, with a body cavity to house an instrument package for in-flight telemetry, or an inert material to simulate the explosive charge. The case is forged from a single piece of 4130 steel. The projectile is propelled by an explosive charge placed in the breech of the howitzer. A sabot constructed of poly-isofoam holds the projectile centered in the barrel. A nylon pusher plug seals explosive gases generated for launching the projectile. Velocities can be varied by altering the weight of the propellant charge. Various recording devices are used to collect data; such as high-speed Photec 16 mm cameras, capable of 10,000 frames per second and a four-tube 300 KV Flash X-Ray unit, which provides orthogonal imagery. As the projectile passes through the last velocity screen attached to the face of the deflection grid, a signal is sent to the flash X-ray trigger unit, which incorporates a delay to fire the first set of X-ray tube heads as the projectile just exits the grid. The second set of tube heads fire 3.28 milliseconds later, x-raying the projectile prior to impacting the burster slab.

Materials Testing

All material tests were conducted in the AFCESA Structural Materials Laboratory in the 9700 Area at Tyndall AFB Florida. Data on static compressive strength, flexural strength, and toughness were obtained with a Forney Static Compression Test Apparatus and a Forney System 2000 controller capable of a maximum load of 400,000 lbs. Information on load, deflection, and time are recorded for static compressive strength tests for cylinders and flexural tests for beams. Flexural tests were conducted using third point loading, with a 12 inch support span. Due to the presence of the nylon fibers, deflections were expected to be extremely high. To ensure accurate measurements, deflections for the beams were kept to .5 inches, so as not to exceed the linear range of the LVDT. Toughness indices for the flexural tests were calculated in accordance with ASTM C1018 and the Japanese Standard JCI-SF4 (6). In the ASTM standard, toughness indices I-5 and I-10 are calculated using deflections at 3δ and 5.5δ , where δ is the deflection at the first crack. These toughness indices are dimensionless numbers that represent the ratio of two areas under the load deflection curve. Another method for describing the energy absorbed a material in flexure is the Japanese Standard JCI-SF4, which calculates the area under

the curve up to the deflection equal to 1/150 of the span. This yields a value in inch-pounds, and is a reliable indicator of absorbed energy. For the compressive strength tests, a Chinese standard test method was implemented, in which the critical load point of 85 percent of the ultimate load replaces the first flexural crack point in defining the compressive toughness index (7). This method was selected because ASTM has no method for determining the toughness index for a cylinder in static compression.

Test Program

The FY 91 test program was an exploratory experimental effort to determine the effect of perforated concrete slab sections on the stability of an advanced penetrating weapon. This effort, in its early stages, focused on the geometry of the concrete deflection grid, and the influence of compressive strength. Due to a wide variance in projectile rotational rates, and the catastrophic damage to the deflection grids at high compressive strengths, steel and nylon fibers were added to the mix designs. Burstier slabs were not incorporated into the tests until FY 92, since observation of the projectile's induced rotation was the objective of the FY 91 tests. The projectile was allowed to travel freely for 20 feet after striking the deflection grid, to obtain sufficient high speed photography of the event. Based on the FY 91 test results, the FY 92 test program systematically varied deflection grid and burstier slab configuration parameters to obtain response data from which to develop an antipenetration system design procedure.

FY 91 Tests

A test matrix was developed to determine the effects of geometry, compressive strength, impact angle, amount of steel reinforcement, and fibers. Table 1 shows the test schedule.

TEST NO	GRID TYPE	CONCRETE MIX DESIGN VALUES					IMPACT ANGLE, deg
		F _c , psi		REINFORCEMENT TYPE			
		4,000	8,000	STANDARD REBAR	FIBERS NYLON STEEL		
1	01	X		X			0
2	01	X		X			0
3	01	X		X			0
4	01	X		X			30
5	01	X		X			30
6	01	X		X			45
15	01	X		X			0
16	01	X		X			0
17	01	X		X			0
18	01	X		X			45
25	01		X			X	0
26	01		X			X	0
36	01		X			X	0
30	01		X		X	X	30
31	01		X		X	X	30
32	01		X		X	X	30
33	01		X		X	X	45
37	01		X		X	X	0
7	02		X	X	X		45
8	02		X	X	X		0
9	02		X	X	X		0
13	02		X	X	X		0
20	03		X	X	X	X	0
22	03		X	X	X	X	0
27	03		X	X		X	0
28	03		X	X		X	0

Molds for three geometric deflection grid patterns were constructed from marine grade plywood. Grid type 01 was a square hole perforation design as shown in Figure 3. Grid type 02 was a staggered circular hole configuration to accommodate a higher percentage of reinforcing steel. Grid type 03 was a waffle style design which eliminated the grid perforations.

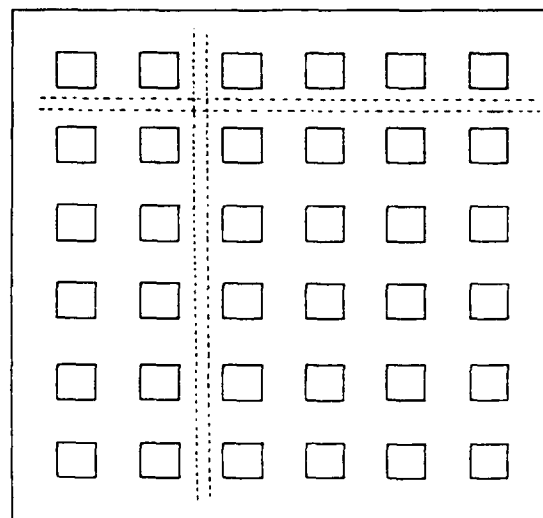
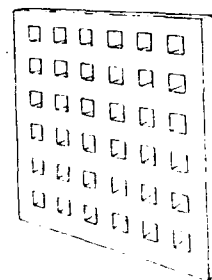


Figure 3. Deflection Grid Type 01

reduced the amount of steel reinforcement, and reduced the deflection grid thickness to four inches. Simplicity of construction was a major factor in these earlier designs, to minimize labor and construction costs for the full-scale systems. To achieve the target compressive strengths shown in the test matrix, four mix designs were developed. Low strength is classified as 4,000 psi and high strength as 8,000 psi. Table 2, contains results obtained in FY 91, including shot number, impact angle, exit angle out of the grid, rotation rate in degrees per body lengths of travel, and remarks on the material composition of the deflection grid.

FY 92 Tests

Based on observations during the FY91 program, a test matrix was developed to investigate the effects of geometry, density, and compressive strength for a series of eighteen experiments, as shown in Table 3. Four densities and two compressive strengths were selected, resulting in six concrete mix designs. Initially, strike points were selected at locations that would produce conservative rotation rates, with all shots conducted at normal impact. The test matrix shows three grid types tested for the FY 92 program. To conserve materials and reduce the test specimen weight, the grid dimensions were reduced to three foot square, with a thickness of four inches. Reinforcing steel was reduced to a single layer of #3 rebar. Figure 4 shows an isometric view of Grid Types 16, 20, and 25, named for the number of perforations. Grid Type 20 was designed with rectangular openings in an offset pattern to enhance irregular

TABLE 2. FY 91 DEFLECTION GRID TEST DATA

Shot No.	Impact Angle degrees	Exit Angle degrees	Yaw Rate DBL/F	Total Yaw degrees	Remarks
1	0	6.0	10.5	27	SI/DR/L/S
2	0	7.5	6.2	19.9	SI/DR/L/S
3	0	8.0	3.7	15.4	SI/DR/L/S
4	30	11.0	8.9	28.8	SI/DR/L/S
5	30	21.0	4.1	29.8	SI/DR/L/S
6	45	2	3.7	7.6	SI/DR/L/S
15	0	6.8	2.9	12.7	SI/DR/L/S
16	0	6.4	1.5	9.4	SI/DR/L/S
17	0	11.2	2.5	19.1	SI/DR/L/S
18	45	11.1	1.4	17.9	SI/DR/L/S
25	0	7.7	5.2	18.5	SI/NR/HIS/NF
26	0	6.2	7.4	21.0	SI/NR/HIS/NF
36	0	2.9	7	4.3	SI/NR/HIS/NF
30	30	7.0	3.9	14.9	SI/SR/HIS/NF
31	30	11.0	4.9	20.8	SI/SR/HIS/NF
32	30	4.3	3.6	13.6	SI/SR/HIS/NF
33	45	8.2	6.6	21.5	SI/SR/HIS/NF
37	0	2.5	1.8	6.2	SI/SR/HIS/NF
7	45	6.5	8.2	22.9	RI/DR/L/S
8	0	7.5	5.4	18.3	RI/DR/L/S
9	0	0	5.7	11.4	RI/DR/L/S
13	0	14.3	7.7	28.9	RI/DR/L/S
20	0	1.8	5	2.9	WT/SR/HIS/SF
22	0	3.5	1.5	6.6	WT/SR/HIS/SF
27	0	5.7	5.5	16.7	WT/NR/HIS/NF
28	0	5.7	5.3	16.3	WT/NR/HIS/NF

Remarks:

SI - Square hole grid design

RI - Round hole grid design

WT - Waffle style grid design

DR - Double layer of reinforcement steel

SR - Single layer of reinforcement steel

NR - No steel reinforcement

LS - Low compressive strength mix design (3500psi to 4500psi)

HS - High compressive strength mix design (7500psi to 8500psi)

NF - Nylon fibers

SF - Steel fibers

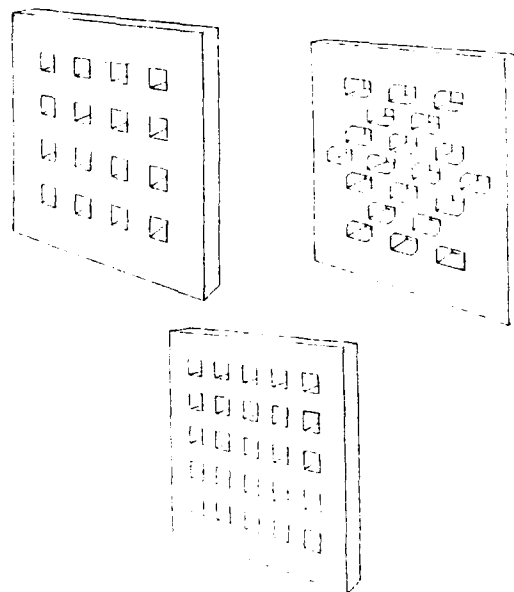


Figure 4. Isometric View of Grid Types 16, 20, and 25.

Eighteen deflection grid tests were performed on the three basic geometries. With the exception of four targets, impact points were generally confined to the center of a web where theoretical modeling had shown the resulting weapon rotation would be least. Table 4 provides data by shot number,

TABLE 3. FY92 ANTIPENETRATION DEFLECTION GRID TEST MATRIX							
TEST NO.	GRID TYPE	CONCRETE MIX DESIGN VALUES					
		UNIT WEIGHT, pcf				f _c , psi	
		110	190	210	325	4,000	8,000
47	16	X				X	
42	16	X					X
53	16		X				X
49	16		X				X
54	16			X			X
40	16				X		X
45	20	X				X	
41	20	X					X
52	20		X			X	
50	20		X				X
55	20			X			X
39	20				X		X
46	25	X				X	
43	25	X					X
51	25		X			X	
48	25		X				X
44	25			X			X
38	25				X		X

fracture lines upon impact. This design had the least volume of all six geometries. Grid Type 25 still maintains the same size hole perforation but has a reduction in spacing. The purpose was to retain the symmetry but decrease the mass in the web areas. Six concrete mixes were designed to achieve the target values in the test matrix. To maintain precise control during construction of the deflection grids, a single rubber mold was cast for each geometry type, and concrete mixes were poured in batches of three. The two light weight mixes were designed for a unit weight of 110 pcf and a static compressive strength of 4,000 and 8,000 psi, designated LW4000 and LW8000, respectively.

TABLE 4. FY 92 DEFLECTION GRID TEST DATA

Shot No.	p pcf	f _c psi	Exit Angle degrees	Yaw Rate DBL/F	Total Yaw degrees	Vel _{in} fps	Vel _{out} fps	Impact Point
47	116	3348	2.9	3.5	9.9	1136	1118	1
42	121	5638	2	2.3	4.8	1081	1054	1
53	151	5351	3.9	1.9	7.7	1102	1041	1
49	153	9853	41.2	13.0	67.2	1134	660	1
54	207	6028	9.3	5.8	20.9	1045	863	1
40	305	8615	7.6	5.4	18.4	1150	1067	1
45	116	3348	1.4	7	2.8	1147	1143	1
41	121	5638	2.9	1.8	6.5	1130	1092	1
52	151	5351	5.4	3.5	12.4	1140	1092	1
50	153	9853	7.5	2.5	12.5	1132	1118	1
55	207	6028	6.6	3.8	14.2	1107	1016	1
39	305	8615	5.6	5.3	16.2	1152	1118	1
46	116	3348	5.2	4.4	14.0	1173	1143	4
43	121	5638	9.0	4.5	18.0	1127	1118	3
51	151	5351	3.1	2.7	8.5	1140	1118	1
48	153	9853	4.3	1.7	7.7	1165	1143	5
44	207	6028	10.6	8.0	26.6	1093	1054	1
38	305	8615	12.1	7.7	27.5	1111	1067	2

including grid type designation, target material unit weight in pounds per cubic foot, static compressive strength in pounds per square inch, exit angle in degrees, rotation rate in degrees per body lengths of travel (DBLT), total yaw in degrees at three body lengths of travel (the distance between the deflection grid and the burster slab), velocities before and after

impact in feet per second, and strike point. Early in the testing series, the impact point was chosen to align with the center of a web to achieve the most conservative amount of rotation. As the light weight mix designs were tested, rotations of the projectile were not as high as expected, and the impact point was changed so as not to waste the possibly useful data that could be obtained for off-center impacts.

All penetrators stopped by the burster slab had an angle of attack of at least 12.5 degrees. The light weight concretes showed increased fracturing as the compressive strength was increased, and did not perform as well as did the heavier concretes. This could be related to the contact time of the penetrator and the deflection grid and the associated angular impulse. Lightweight, high-strength concretes have a shorter time to failure, and do not provide the contact time required to overcome inertia forces in the shorter distances.

To determine if a deflection grid system is a viable alternative to present construction practices, an example is presented, comparing a stand-alone burster slab system over a buried hardened structure, to the use of a deflection grid system and a thinner burster slab.

Stand Alone Burster Slab

The approach taken in this example is to design the slab with a thickness to prevent penetration of the weapon. Concrete f_c will be established at 4,000 psi, since quality control for massive concrete pours is difficult to maintain. The weapon will have the same parameters as tested in the laboratory for both scenarios.

- x = Absolute penetration depth (in)
- t = Thickness required to prevent perforation (in)
- V = Velocity of the projectile (1000ft/sec)
- f_c = Compressive strength of concrete (psi)
- W = Weight of projectile (lb)
- d = Diameter of projectile (in)
- N = Factor for projectile nose shape
- n = Caliber radius head

Using the NDRC equation for penetration, (Reference 8)

$$N = 0.72 + 0.25\sqrt{n - 0.25} = 0.72 + 0.25\sqrt{8.75 - 0.25} = 1.4$$

$$x = \frac{180 NW(V/d)^{1.8}}{\sqrt{f_c}} + d = \frac{180(1.4)(28)(1.1/3.35)^{1.8}}{\sqrt{4000}} + 3.35 = 18.37 \text{ in}$$

$$t = 1.24(x) + 1.32(d) = 1.24(18.37) + 1.32(3.35) = 27.2 \text{ in}$$

Therefore, the thickness of a burster slab required to prevent perforation is equal to 27.2 inches of concrete having a unit weight of 150 pcf. Total weight of a 10-foot by 10-foot section of the slab would be 34,000 pounds.

Burster Slab with Deflection Grid

Since heavier concrete mixes performed 100% of the time in preventing perforation, an HDM Grid Type 20 is selected, resulting in a unit weight of 207 pcf. Using the design parameters in the FY 92 test program, the deflection grid requires a thickness of 4 inches, followed by a 72-inch air gap, terminating at an 18-inch burster slab. The overall depth of the combined system is 94 inches. The weight of the deflection grid is 5,520 pounds for 26.6 cf of concrete at 207 pcf. The weight of an 18 inch burster slab is 22,500 pounds, for a combined weight of 28,020 pounds. This results in a 17 percent weight reduction and a 22 percent volume reduction based on a sectional slice of the overall system.

A cost breakdown was performed on the six mix designs for a 1-yard volume. The following represents the amounts based on bulk quantity purchases and then ranking in performance.

Mix Design	Cost per Yard	Performance
LW4000	\$ 108.16	6
LW8000	\$ 178.13	5
NW4000	\$ 111.95	4
NW8000	\$ 121.44	3
HDM	\$ 206.10	2
VHDM	\$ 1,623.10	1

All the costs include a set price of \$50 per 10 pounds of nylon fibers, which is excessively high. This was a price established by the supplier for both small and large quantities. Alternate materials could be substituted at a much lower price, but were not tested because of lack of time. In the construction of a full-scale deflection system, there would be a reduction in weight and volume of materials over existing protective construction practices. This would translate into a decrease in total labor costs and a possible reduction in material construction costs for the facility being protected, due to the reduced overburden pressure of the deflection grid system.

Conclusion

In reviewing the laboratory data on the compression and flexural tests, a significant relationship was observed between unit weight and material toughness. An almost linear relationship exists when toughness is calculated using the JCI Method as shown in Figure 5. Total yaw was related to unit weight, compressive strength, and toughness, where again toughness exhibited excellent linearity based on the FY 92 data. For this particular penetrator, angles of attack greater than 12 degrees upon impact with the burster slab defeated the weapon. The advantages of such a protective system become more apparent every day. With rising costs in the construction industry, and the penetration capability of advanced weapons increasing, current construction practices do not yield effective protection for critical airbase resources. This effort has developed an innovative design, and has achieved its original objective. Based on the observations and deductions of the FY

91 and FY 92 programs, this concept has displayed: (1) consistency in performance, as shown by the 20-hole geometry design; (2) limited damage to the deflection grid

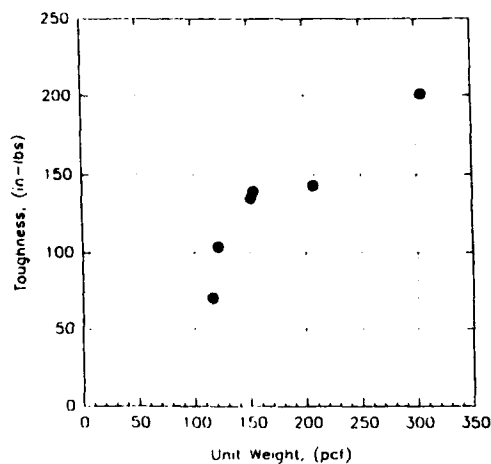


Figure 5. Unit Weight versus Toughness with JCI Test Method

with increased penetrator contact time, as a result of the nylon fibers; and (3) overall 17 percent weight and 22 percent volume reductions as compared to standard protective construction practices. The nylon fibers performed better than did the steel fibers in this particular application. At very high strain rates, the steel fibers failed from pullout, while the nylon fibers stretched to absorb the mechanical energy. These findings dictate a continued effort to exploit this extremely promising technology.

References

1. Rohani, B., "Shielding Methodology for Conventional Kinetic Energy Weapons," Technical Report SL-87-8, U.S. Army Engineer Waterways Experiment Station, Vicksburg, MS, 1987, Secret.
2. Austim, C.F., Halsey, C.C., Clodt, R.L., and Berry, S.L., "Protective Antipenetration Systems Development," Technical Report ESL-TR-83-39, Engineering and Services Laboratory, Air Force Engineering and Services Center, Tyndall Air Force Base, FL, 1982.
3. Gelman, M.D., Nelson, R.B., and Ito, Y.M., "Non-Normal Impact of AP Projectile into Array of Large-Ca' Boulders," Technical Report SL-91-2, U.S. Army Engineer Waterways Experiment Station, Vicksburg, MS, September 1991.
4. Cargile, J.D., and Cummins, T.K., "Effectiveness of Yaw-Inducing Bar Screens for Defeating Low Length-to-Diameter Armor-Piercing Projectiles," Technical Report SL-92-10, U.S. Army Engineer Waterways Experiment Station, Vicksburg, MS, March 1992.

5. Creighton, D.C., "Non-Normal Projectile Penetration in Soil and Rock: User's Guide for Computer Code PENCO2D," Technical Report SL-82-7, U.S. Army Engineer Waterways Experiment Station, Vicksburg, MS, September 1982.
6. Nemegeer, D., "An Identity Chart for Steel Fibres," Fiber Reinforced Cements and Concretes Recent Developments, Elsevier Applied Science, 1989, pp.401-410.
7. Zhao, J., Xu, P., and Fan, C., "An Investigation of the Toughness and Compressive Toughness Index of Steel Fiber Reinforced Concrete," International Symposium on Recent Developments in Concrete Fiber Composites, Transportation Research Record No. 1226, 1989, pp.88-93.

LEAKAGE PRESSURES BEHIND BLAST WALLS

T.A. Rose, P.D. Smith and G.C. Mays

Civil Engineering Group, Royal Military College of Science [Cranfield],
Shrivenham, Swindon, Wiltshire, SN6 8LA, United Kingdom

Abstract

This paper describes a programme of research in which detailed measurements of the blast environment were made behind a $1/10^{\text{th}}$ scale vertical blast wall when scaled realistic threats were detonated at appropriate distances from the wall. A grid for measurement was established out to six wall heights behind the wall and up to three wall heights above the ground. From the pressure-time histories thus obtained, contour plots of overpressure and impulse were developed. These were compared with histories obtained with the wall absent so that the regions of maximum benefit from the wall's presence could be identified.

Introduction

Car and other vehicle bombs have proved to be a major terrorist threat in many parts of the world. They can have devastating effects not only on the occupants of buildings but also on the building structure itself. Although a significant degree of hardening may be incorporated into new buildings at relatively low cost (Elliott, Smith and Mays [1]), the hardening of an existing building to minimise the damage sustained from every conceivable form of attack is a very expensive procedure. Furthermore, the resulting appearance of the hardened structure is likely to be extremely austere. An alternative method of protection is to construct a perimeter wall which increases the stand-off from any bomb and so reduces the blast resultants (overpressure, impulse and fragments) to an acceptable level from the point of view of the building and its occupants. Such a wall is designed to stop not only the vehicle but also to prevent any breaching by the bomb.

Procedures exist to enable solid and composite reinforced concrete walls to be designed to resist these threats provided there is some separation between the wall and the point of detonation of the explosive device [2]. Also, criteria exist for assessing the damage to buildings, given the blast environment at the building [3]. However, there is little published information on methods for predicting the blast environment in the region

between the wall and the building.

Whitham [4] describes an analytical method of calculating the shape of shock fronts which have diffracted around external corners. It is an approximate theory and if applied to a blast wall assumes firstly, that the shock wave incident at the top of the wall would be vertical and plane and, secondly, reflections from the ground do not occur. This method may be useful for examining waves which have progressed only a short distance from the wall.

Beyer [5] presents blast wall design criteria derived from a series of high explosive trials. These criteria are based on peak blast overpressure, total blast impulse and effective duration. The objective was to express these quantities in terms of the important problem parameters. These are net explosive weight, distance of point of interest behind the wall, elevation of the point of interest behind the wall, elevation of the charge above the ground, distance of the charge from the wall and the mass of the canopy attached to the wall. The experimental programme was performed at $1/6^{\text{th}}$ scale, and the results from one of the ten trials is comparable with the work undertaken in the study reported here.

Further experimental data is contained in Jones et al [6] which describes a series of blast wall tests which were carried out as part of the U.S. Department of State "Design of Structures to Resist Terrorist Attack" programme. There were two objectives to the tests. The first was to determine the benefit derived from a perimeter wall in terms of the airblast pressure reaching a building situated behind the wall. The second objective was to investigate various designs of perimeter wall. This data was employed in the formulation of exponential equations for both pressure and impulse contained in the U.S. Department of Transportation (DOT) Technical Manual [7].

A method is suggested by Philip [8] for estimating the blast pressure and impulse on one side of a wall resulting from the explosion of a charge on the other side of the wall. This method is based on empirical reduction factors linked to the sum of the charge/wall, wall/target angles. These are applied to blast parameters calculated from the charge to wall plus wall top to target path length.

This paper describes an experimental programme of research, the objective of which is to define accurately the blast environment behind vertical cantilever blast walls.

Experimental Method and Programme

The experimental layout and design of the apparatus was governed by the desire to make pressure measurements in an area which extended six wall heights beyond the blast wall and three wall heights above the ground. This was considered to be the most important area of interest given a typical operational wall height of about 3m. With this figure in mind it was also decided at the outset that $1/10^{\text{th}}$ scale experiments should be performed as this scale provided the best compromise in terms of ease of construction and measurement, and the charge weight limitations of the Explosives Research and Demonstration Area (ERDA) at the Royal Military College of Science (RMCS). The use of small-scale models to obtain useful blast loading data is discussed by Smith et al [9].

The test structure was a vertical cantilever wall 2100mm long and 350mm high with a base 600mm wide. It was constructed from 20mm thick steel plate in three 700mm long sections which were subsequently bolted together to form the test wall.

An area of ground at the ERDA was cleared and a bed of sand was laid and made flat. The wall was positioned and 600mm \times 600mm concrete slabs 50mm thick were laid over the base of the wall making the effective wall height $H=300\text{mm}$. The slabs extended away to a distance of 2400mm ($8H$) behind the wall and formed a flat reflecting surface above which measurements could be made. On the near side of the wall concrete slabs were also laid, but in the central region where the charges were to be detonated, thick steel plates were positioned and made level with the top of the slabs.

This layout proved to be fairly robust and although small adjustments had to be made to the wall and slabs throughout the experimental programme, no major alterations to the system were necessary during the trials. A diagram showing the layout of the concrete slabs and the blast wall is given in Figure 1.

The design of the measuring system was again linked to the aim of measuring in a $6H \times 3H$ space behind the wall. It was decided to make measurements of side-on overpressure using Kistler type 603B and 6031 piezo-electric pressure transducers in a "mushroom mount" arrangement. The action of this arrangement is effectively to separate the incident wave from any pulses which have reflected from the measuring equipment. Clearly, such reflected waves cannot be completely avoided, but the aim was to delay the reflections for a length of time sufficient to prevent them overlaying the incident wave.

The mounts themselves were attached at right angles to the end of long square section steel tubes. The transducer cables ran inside the tubes and were completely shielded from the blast.

A large wooden box was constructed around a steel angle frame, with a series of square holes at $H/2$ intervals in which the tubes and transducer mounts could be located and secured by clamps. This box also contained the amplifiers and an intercom system used to facilitate communication between the test area and the instrumentation laboratory. Generally, three pressure measurements were possible at one time by positioning the gauges at intervals above the ground. The box was moved forwards and backwards to complete the spacial grid for each series of tests. The box and mounts can be seen in Figure 1.

The two rows of concrete slabs behind the wall had a gap of about 80mm between them. In this gap an inverted steel

channel with pressure transducers located at $H/2$ intervals was placed to complete the spacial grid at $h=0$. For the experiments which involved the wooden box alone or when the channel section was located some distance from the wall, blanking plates (which were weighted on the underside to improve stability) were used to fill the gap between the slabs and ensure the uniformity of blast wave reflections.

In the main series of trials a charge equivalent to 75g of TNT was employed. The charge was spherical and supported on a polystyrene block so that its centre was located at $r=138\text{mm}$ from the wall and $z=109\text{mm}$ above the ground.

A summary of the experimental programme is contained in Table 1 below. In this table the column summarising the geometry contains three entries: the first states whether or not the blast wall was present, the second describes the vertical and horizontal intervals on which measurements were made, and the third describes whether measurements were made on or above the ground.

Results

In this section examples of the results of the pressure measurements and scaled impulse calculations are given. Figure 2 shows the logarithm of peak pressures measured with and without the wall along the horizontal gauge line $h = 0.5H$ (150mm), ie in the shadow of the wall half a wall height above the ground. Figure 3 is the graph of the logarithm of scaled impulse for the same gauge line. Both sets of data are plotted against scaled distance behind the wall ($R/W^{1/3}$). The benefit of the presence of the wall is clear in both graphs.

Contour plots of the natural logarithm of peak pressure and actual scaled impulse are shown in Figures 4 and 5 for the trials when the wall was not present, and in Figures 6 and 7 when the wall was present. Both sets of data are shown on spacial axes which are marked in intervals of the wall height H . In Figures 6 and 7 the wall occupies the region from (0,0) to (0, H).

Comparison with Other Methods

No Wall

The primary means of validating the data captured during the blast wall experiments was to perform the same series of experiments without the blast wall and compare the results with published data. Two sources were available for comparison with the data measured at the ground surface ($h=0$): the first was the program DNA BLAST [10] and the other was the program BLASTINW [11]. The second of these also provided a means of comparison for points above the ground ($h > 0$). In this section graphs are presented which show the comparison of peak pressure and scaled impulse data for the horizontal gauge line at $h=0$.

Figure 8 demonstrates good agreement between the surface pressure measurements and the data from the other two sources. The calculation of blast resultants by the program DNA BLAST was performed using appropriate scaling and a nuclear device twice the weight of the equivalent TNT charge. This is in accordance with the range of TNT equivalences for nuclear explosions given in Baker et al [12]. Figure 9 shows good agreement between experimentally determined scaled impulse values and

those obtained from the program DNA BLAST. However, all of the impulses calculated from the no wall records showed the experimental results to be approximately 50% higher than those calculated using BLASTINW.

Wall

The comparison of blast wall data with other sources is more difficult because of the scarcity of other data and predictive methods. In this section the data of Beyer [5] and the equations contained in Mayor and Flanders [7] are used for comparison. Because the data of Beyer were measured along only two gauge lines (at $h=0$ and $h=H$) there are only two sets of comparable data. Strictly, none of the Beyer data is directly comparable because different values of $H/W^{1/3}$ and r and z were employed. The Beyer data presented here is taken from the experiments which most closely matched those conducted for this project. The parameters are summarised in Table 2.

The graphs comparing peak pressure and scaled impulse with data from the above sources are given in Figures 10 and 11.

It should be mentioned that the equations of Reference [7] from the U.S. Department of Transport (DOT) were not intended to describe the process of blast wave diffraction around a wall but to provide a guide for designers based only on the distance behind the wall. As a consequence they predict the same pressures and impulses for the comparisons at both $h=0$ and $h=H$ and their correlation with the experimental data is poor.

Comparison of Wall with No Wall

In this section the benefit of a blast wall will be demonstrated by comparing the pressure and impulse data from the two sets of experiments, with and without the blast wall.

Intuition tells us that we might expect a region extending a short distance above and beyond the top of the wall where the pressures will be greater than expected in the absence of a wall because of the "focussing" effect caused by reflected waves travelling up the front face of the wall.

However, everywhere else, particularly in the region shadowed by the wall, the blast resultants should be greatly reduced. It is the extent to which these effects take place which is of most interest to a designer and it is this subject which is addressed here.

Figures 12 and 13 are "benefit plots", ie they show the pressures and impulses which occur in the region behind the wall in terms of the percentage of the quantity measured when the wall was not present. For example:

$$\text{Pressure benefit} = \frac{P_{\text{wall}}}{P_{\text{no wall}}} \times 100\%$$

Referring to the pressure plot (Figure 12) it can be seen that the area above 100% which is where the pressures are higher than if there was no wall present, extends upwards to over $3H$ and backwards to $\approx 0.75H$. The most benefit is seen directly behind the wall in the shadow region where the pressures are less than 10% of those experienced without a wall. From a designers point of view the most important generalisations which can be drawn from the plot are that in the area up to a distance of $3H$ behind the wall the pressures are less than 50% and up to $4H$ they are 30% - 40% of those without the wall. Beyond $4H$, although the pressures are obviously less, the benefit is reduced.

The benefit plot for impulse (Figure 13) shows a very similar pattern, except the reduction is less pronounced than for the pressure. The area above the wall and for a distance of H behind it shows a small disadvantage and the shadow region immediately behind the wall shows a reduction to 40% of the no wall value. Generally, for the area extending beyond $3H$ (the area most likely to be of interest) the impulses are between 60% and 80% of those measured without the wall.

It should be recognised that the generalisations mentioned above are for the one particular set of parameters and the shape of the benefit plots will vary with these parameters.

The summary of Reference [6] concludes that the pressure on a structure behind a blast wall is $\approx 54\%$ of that expected without a wall. Similarly, the impulse is 72% of the value without a wall. These are essentially the same results that have been found in the present study.

Conclusions

It has been demonstrated that blast experiments can be performed successfully at $1/10^{\text{th}}$ scale and that data obtained from experiments with blast walls are self-consistent.

The benefit of a blast wall has been quantified in terms of a so-called "shadow" region behind the wall where overpressure and overpressure impulse levels undergo substantial attenuation.

The experiments described here are a starting point for a more comprehensive investigation in which the parameters $H/W^{1/3}$, $r/W^{1/3}$ and $z/W^{1/3}$ will be varied with the aim of developing a series of charts that will be of assistance to designers in providing blast walls for optimum reduction of blast resultants.

Acknowledgements

This work has been carried out with the support of the Defence Research Agency, Christchurch, an executive agency of the Ministry of Defence, under Agreement No 2004/121/RARDE.

References

- [1] Elliott, C.L.; Mays, G.C.; Smith, P.D. "The Protection of Buildings Against Terrorism and Disorder." Proceedings of the Institution of Civil Engineers, Structures and Buildings. 1992. Volume 94, August. pages 287 - 297. Paper 9930.
- [2] "Structures to Resist the Effects of Accidental Explosions, Volume II. Blast, Fragment, and Shock Loads." TM5-1300 Candidate Upgrade, AD - A176 673 Armament Research, Development and Engineering Center, New Jersey, 1986.
- [3] "Military Engineering Volume IX: Assessment, Strengthening, Hardening, Repair and Demolition of Existing Structures. Army Code No 71523 D/HQDT/18/27/7, Ministry of Defence, April 1992.
- [4] Whitham, G.B. (1957) "A New Approach to Problems of Shock Dynamics. Part I. Two Dimensional Problems." Journal of Fluid Mechanics, 2, pp 146-171.
- [5] Beyer, M.E. (1986). "Blast Loads Behind Vertical Walls." 22nd Explosives Safety Seminar, Department of Defence Explosives Safety Board, Anaheim, California.

- [6] Jones, P.S.; Vitaya-Udom, K.P.; Watt, J.M., Jr. "Design of Structures to Resist Terrorist Attack, Report 1, 1/10th Scale Model Perimeter Wall Tests", Technical Report SL-87-13. Structures Laboratory, Waterways Experimental Station, U.S. Army Corps of Engineers, Vicksburg, Mississippi, October 1987.
- [7] Mayor, R.P.; Flanders, R. (1990) "Technical Manual, Simplified Computer Model of Air Blast Effects on Building Walls." U.S. Department of Transportation, Research and Special Programs Administration, Transportation Systems Center, Vehicle Crashworthiness Division, Safety and Security Systems Division. Kendall Square, Cambridge.
- [8] Philip, E.B. "The Passage of Blast Over a Wall." Ministry of Home Security, 1942.
- [9] Smith, P.D.; Mays, G.C.; Rose, T.A.; Teo, K.G.; Roberts, B.J. "Small Scale Models of Complex Geometry for Blast Overpressure Assessment." Int. J. Impact Engineering Vol. 12, No. 3, pp. 345-360, 1992.
- [10] "Blast Effects. Version 2.1" Defence Nuclear Agency, Washington, DC 20305. Horizons Technology, Inc, 7830 Clairemont Mesa Blvd. San Diego, CA 92111. 21st December 1984.
- [11] Britt, J.R.; Drake, J.L.; Cobb, M.B; Mobley, J.P. "Blastinw User's Manual." Applied Research Associates, Inc. U.S. Army Engineer Waterways Experiment Station, 3900 Halls Ferry Road, Vicksburg, Mississippi 39180-0631.
- [12] Baker, W.E.; Cox, P.A.; Westine, P.S.; Kulesz, J.J.; Strehlow, R.A. "Explosion Hazards and Evaluation" Elsevier Scientific Publishing Company, 1983.

List of Symbols

- H = Wall height, (mm)
 R = Distance to point of interest behind wall, (mm)
 h = Elevation of point of interest behind wall, (mm)
 W = Charge weight (kg TNT equivalent)
 r = Distance of charge to wall, (mm)
 z = Elevation of charge above ground, (mm)

Table 1: Experimental Programme

Series No	Experimental geometry	No of records	No of charges
1	with wall $H/2$ intervals ($h=0$ and $h>0$)	85	34
2	with wall $H/2$ & $H/4$ intervals ($h>0$)	77	32
3	with wall $H/4$ intervals ($h=0$)	31	8
4	no wall $H/2$ intervals ($h=0$)	24	6
5	no wall $H/2$ intervals ($h>0$)	90	27

Table 2: Comparison of experimental parameters

Parameter ($m/kg^{1/3}$)	RMCS	Beyer (ref [5])
$H/W^{1/3}$	0.711	0.654
$r/W^{1/3}$	0.327	0.291
$z/W^{1/3}$	0.258	0.291

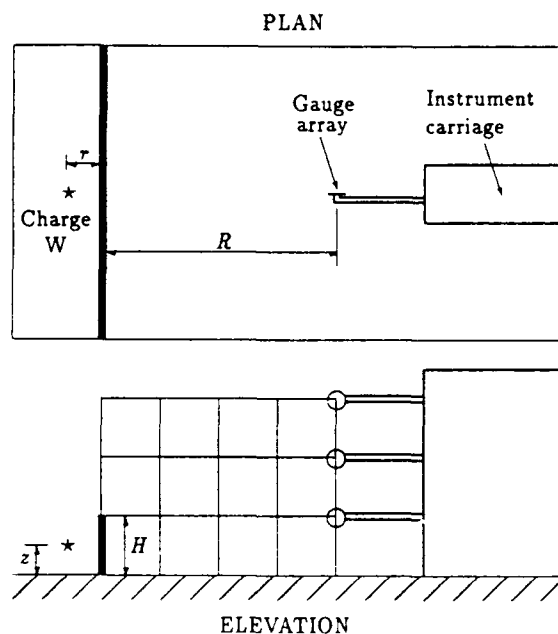


Figure 1: Experimental layout at ERDA

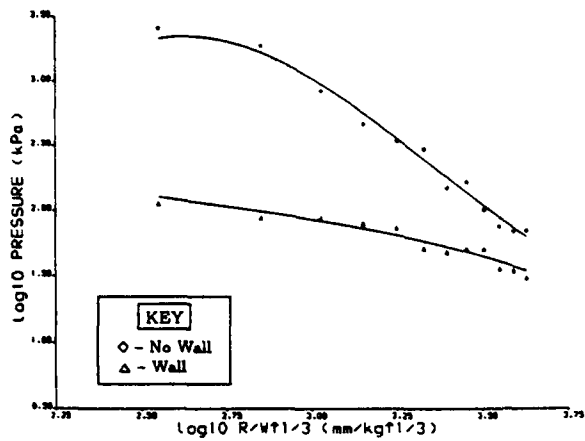


Figure 2: Comparison of peak pressure, $h=0.5H$

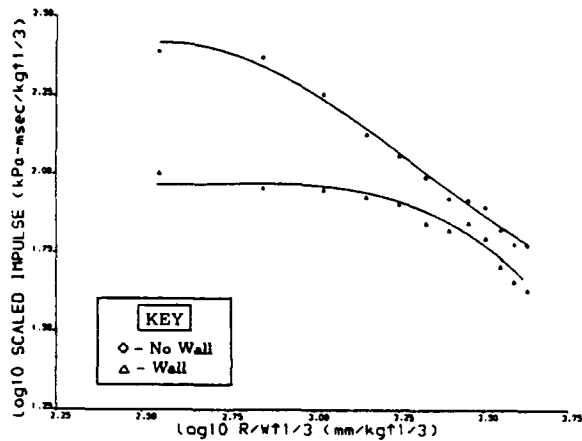


Figure 3: Comparison of scaled impulse, $h=0.5H$

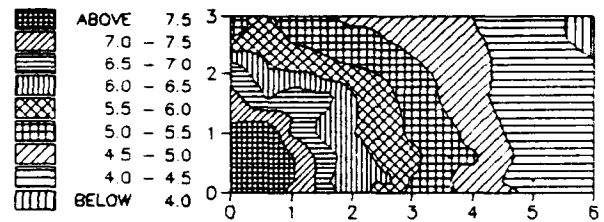


Figure 4: \log_{10} peak pressure (kPa) contour plot for experiment without blast wall

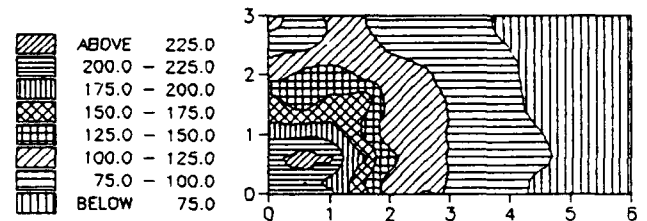


Figure 5: Scaled impulse (kPa-msec/kg $^{1/3}$) contour plot for experiment without blast wall

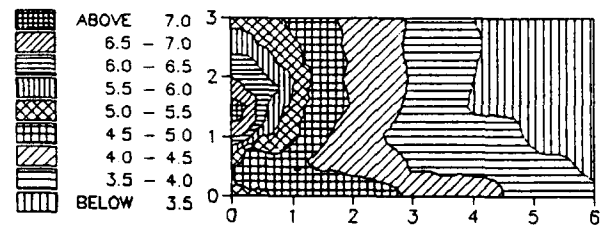


Figure 6: \log_{10} peak pressure (kPa) contour plot for experiment with blast wall

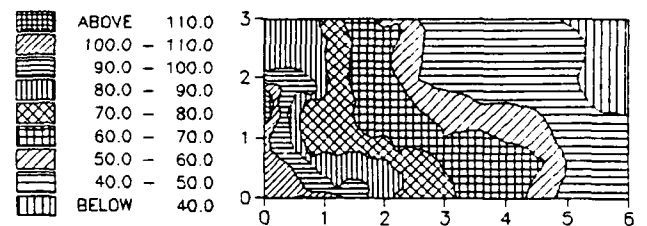


Figure 7: Scaled impulse (kPa-msec/kg $^{1/3}$) contour plot for experiment with blast wall

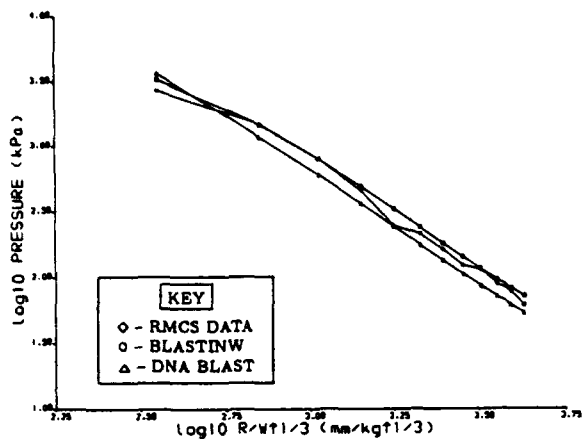


Figure 8: Comparison of peak pressure data with other methods (no wall, $h=0$)

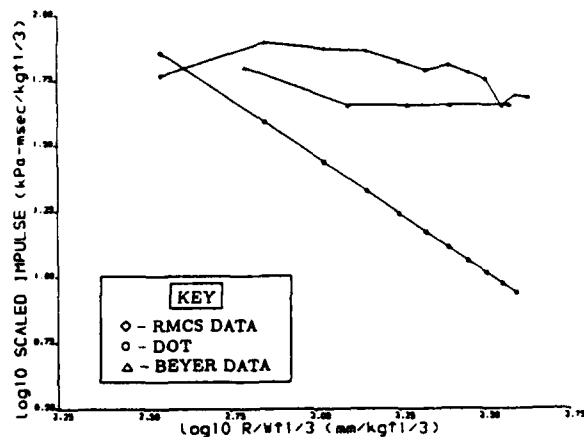


Figure 11: Comparison of scaled impulse data with other methods (with wall, $h=H$)

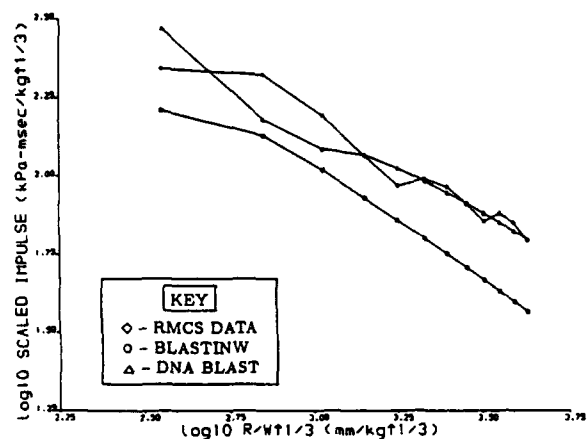


Figure 9: Comparison of scaled impulse data with other methods (no wall, $h=0$)

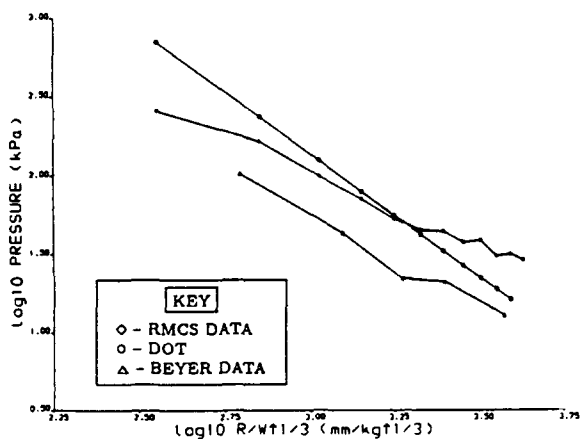


Figure 10: Comparison of peak pressure data with other methods (with wall, $h=H$)

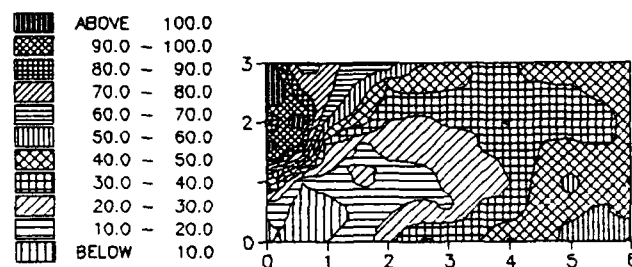


Figure 12: Percentage peak pressure contour plot - wall/no wall

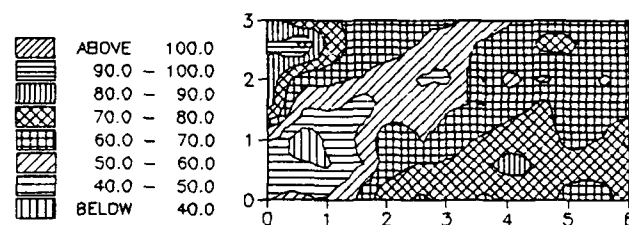


Figure 13: Percentage impulse contour plot - wall/no wall

ENVIRONMENTS FROM INTERNAL DETONATION OF WARHEADS

James A. Keller

Engineering Sciences Laboratory
Denver Research Institute
University of Denver
Denver, CO 80208

ABSTRACT

When a weapon or warhead detonates within the confines of a room or structure, a complex transient environment is produced. This environment includes hot gas flow, air shock, fragmentation from the weapon case, and elevated temperature. The relative magnitude and time of arrival of each effect will vary with size of the room, size of the weapon, type of explosive, and location within the room. In this paper, we use a single idealized explosion to show how the transient effects environment varies in time and space, to illustrate the implications for defining loading functions for the structure, and to indicate areas where caution must be exercised when weapon effects are idealized or simplified for model analyses.

INTRODUCTION

Consider a weapon which has successfully penetrated to the interior of a structure. Further, assume that the fuzing system of the weapon has survived, and will function at the desired time, detonating the weapon within a room or compartment of the structure. Explosion of the main charge produces large volumes of product gases, compressed to an exceedingly high pressure, within the confines of the weapon case. The internal pressure expands the case until the strain reaches the point of failure, at which time the case ruptures. The hot product gases, which had been contained within the expanding but unruptured case now jet through the interstices opened by the case fragmentation. Since these jets are exiting the case at supersonic speed, an air shock is formed at the forward edge of the

expanding product cloud. This shock propagates outward and initially is followed closely by the expanding products cloud. The fragments, which form when the case ruptures, are propelled outward, with an initial velocity equal to the radial velocity of expansion of the case at the moment of rupture. The gases are moving outward at a higher velocity than the case fragments, and hence cause these fragments to be accelerated, during the early phase of their flight.

The velocity and strength of the shock wave decrease with increasing distance outward from the weapon point of detonation. The velocity of the hot gas cloud decreases even faster, since it is experiencing cooling, as well as simple diffusion effects. The fragment velocity falls off still more slowly with increasing distance, since the principal velocity degradation for the fragments is aerodynamic drag. Note that, as indicated earlier, the fragments are actually accelerated during the early part of their flight, up to the point where their instantaneous velocity equals the velocity of the expanding products cloud.

This occurrence of multiple temporally and spatially varying effects produces the complex environment associated with internal detonation of a weapon. In fact, exactly these same effects are produced when a weapon detonates in free air. The internal explosion environment is further complicated by the stoichiometry of the situation. Only a certain amount of oxygen is present in the air within the enclosure. Dependent on the type of explosive in the weapon and its oxygen balance, the combustion process may be incomplete, may occur over a longer period of time than the same process in free air, or may require the breach of the initial compartment bounding planes, thus

allowing the reacting products to propagate into surrounding space, where more oxygen is available. The thermal environment within the initial space, or the expanded space, will be of more concern than for the same detonation in free air, since the reacting products cloud will expand throughout the structure until a volume of space has been enclosed sufficient to provide the requisite oxygen for combustion. Addition of admixtures such as powdered aluminum to the explosive fill simply compound the problem even further, due to the longer reaction times involved.

To an analyst or engineer attempting to assess effectiveness, vulnerability, or structure survival, it will be necessary to have modeling capability to treat this multicomponent, time- and space-dependent environment.

ENVIRONMENT ILLUSTRATION

Consider an idealized spherical, cased charge, as illustrated in Figure 1. Let us consider the detonation of this item in detail.

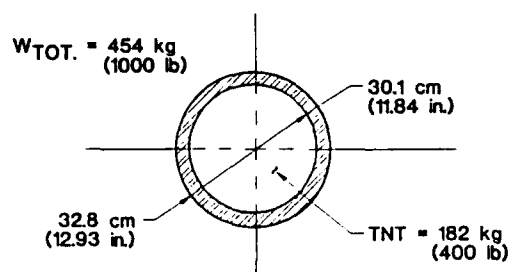


Figure 1

Initially, consider the charge of Figure 1 to detonate in free air. As discussed above, the case will initially expand to a radius of about 22 inches, before rupture. At that point, the gas escape and initial shock formation will begin. Initially, and out to a distance of some 2 charge radii, the contact surface, or interface between outer edge of products cloud and shocked air, will nearly coincide - the contact surface will be just over one shock front thickness behind the front of the shock

wave. As the radial distance is increased to about 5 charge radii, the contact surface will lag the front of the shock by about 0.4 charge radii. Figure 2 shows the approximate geometry at 5

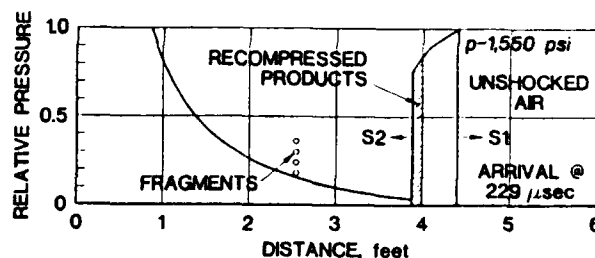


Figure 2

charge radii [after Kinney, 1968 and Brode, 1957]. In Figure 2, we show the relative overpressure. The position of the fragments from the weapon case is also indicated. As the expansion continues, let us take another "snapshot" at a distance equal to 11 charge radii, as indicated in Figure 3. Note

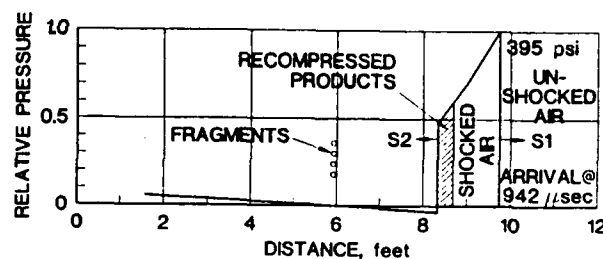


Figure 3

the second shock, inward directed, at this time. Note also the pressure rarefaction behind or inside the region of recompressed products.

In an idealized sense, assuming a sufficient supply of oxygen, the products cloud will reach a maximum dimension of about 16 charge radii. Within that distance from the weapon, the environment will be one of complex blast, as opposed to pure air blast, and any structural element within this region will first see the air

shock, followed closely by the products recompression flow, and finally the fragments. Note the relative position of the fragment mass at this 16 charge radius point, as indicated in Figure 4. The fragments are just within the

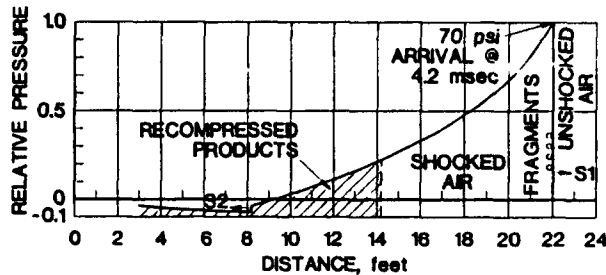


Figure 4

region through which the shock front has passed. Beyond this distance, the shock arrives first, followed by the fragments - the products cloud has ceased to enter into the environment (in the free air case). Figure 5 illustrates an interesting range - the fragmentation and shock front arrive simultaneously. In terms of momentum delivered to a structural target element within some critical time, this point represents the maximum threat intensity. Beyond the point indicated in Figure 5, the fragments will arrive first, followed by the air shock. This is the traditional "far field" regime,

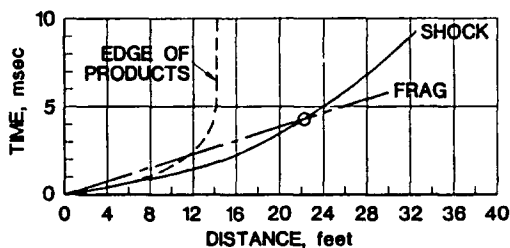


Figure 5

which is treated in most free field analyses of combined loading on structural elements. At some distance, dependent on the dynamic properties of the structural element being considered, the

fragments and blast will arrive with adequate time separation to allow the effects of each to be considered independently - i.e., by simple superposition analysis. Inside such a range, the combination of loading effects must be considered together - whichever effect arrives first will produce strain or section modification in an element, which then will be in some deformed state upon arrival of the second effect.

Let us consider some examples of the additional complexity resulting from detonation of this ideal weapon within a structural compartment. Unless the mean dimensions of the compartment are larger than about 30 charge radii, the entire bounding surface of the compartment will see composite blast, not simple air blast. This combined loading is difficult to model by any method short of a fairly rigorous hydrodynamic code, allowing for the "burn" of the explosive. Further, for most surfaces in compartments of that or smaller dimensions, the initial loading of the complex blast will be followed quite shortly by the arrival of the case fragments. Now such fragments are frequently considered only as perforation damage vectors, and often not included in momentum or energy analyses. However, particularly in the case of heavy construction, these fragments may produce both impulsive loading of structural elements, and reduction of sectional area, especially in cases in which the fragments do not perforate the structural element. Thus, ignoring fragments in structural loading calculations or analyses may give erroneous results.

The internal explosion environment is further compounded by the venting condition of the compartment. If the compartment is not vented, or only slightly vented (vent area \leq about 5% of the total surface area), the pressure-time history in the compartment is totally different than for the free air case. In such an unvented condition, the overpressure will not fall rapidly from the peak to ambient, and continue downward into a negative phase. Rather, the overpressure will decay from the peak shock value to a point of maximum quasistatic pressure. The overpressure will then decay very slowly from that point back to ambient, as the products cool adiabatically. For our TNT ideal charge, the maximum quasistatic

overpressure may be estimated from Equation 1, due to Weibull [1968].

(1)

$$P = 22.5 \left(\frac{Q}{V} \right)^{0.72}$$

Where: P = pressure, bars
Q = weight of TNT, kg
V = compartment volume, m³

This quasistatic pressure phase can be important for structural loading. A heavy element could survive the impulsive loading of the initial blast, only to fail under the effective static loading of this phase, at a lower pressure, but over a longer time.

Finally, one needs to consider the thermal environment produced by such an internal explosion. As indicated above, this effect is usually ignored in most free field weapon effects studies, since the high thermal excursions occur only in the fireball region, and within this region most targets of interest are damaged by the blast and/or fragmentation effects. Within a structure however, the fireball is likely to fill an "average" sized compartment, as indicated above. Two mechanisms lead to temperature reduction from peak fireball temperatures. First, the original walls or surfaces of the compartment may be breached, allowing expansion of the products cloud (or fireball) into adjacent spaces, and consequent cooling. Second, if the products are contained in an unbreached or unvented enclosure, only heat transfer to the surrounding surfaces will cool the fireball. In either case, the temperature will remain elevated for an appreciable period of time.

Peak (or fireball) temperatures may be estimated for our ideal TNT weapon, using published results [Kinney, Sewell, and Graham, 1979]. As can be seen from Figure 6, the peak temperature within a space is controlled largely by the ratio of explosive

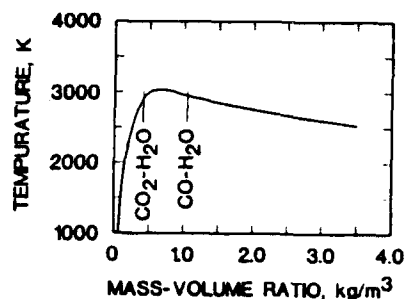


Figure 6

mass to air volume. Bear in mind that for an explosive with an oxygen balance that is different from TNT, a different thermal peak should be expected. Figure 7 shows an actual record of temperature obtained within a partially vented

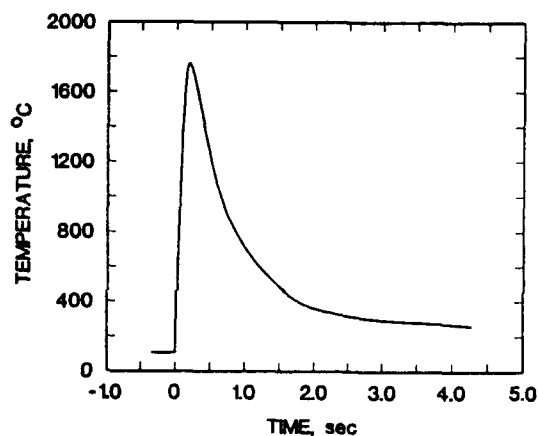


Figure 7

chamber during experiments at our laboratory. Note that, while the temperature reaches a high initial value, the longterm or residual temperature is much below this peak. The peak fireball temperatures, as inferred from data such as Figure 6, will last only a very short time - of the order of milliseconds to tens of milliseconds, while the elevated residual temperature will typically decay over durations of seconds to minutes.

AN INTERNAL EXPLOSION

Let us consider the detonation of our idealized warhead at the exact geometric center of a room, 32 feet square in plan, with 10 foot height, floor to

ceiling. Further assume that the structure is of very heavy reinforced concrete design. Let the structure be of single floor design, buried with a light earth cover, and with the floor slab bearing on compacted soil and subgrade. Consider that the 32 foot square room is only one of several rooms in the structure.

At about 280 microseconds after the detonation, the underside of the roof and the floor will see the arrival of the initial air shock. The peak reflected pressure from this shock will be approximately 11,300 psi, and will load the area of full normal reflection for approximately 4.9 milliseconds. This strong initial shock will give rise to strongly reflected shocks, which will reverberate over the floor to ceiling space several times, and will perturb the lateral shock and gas flow toward the walls. Approximately 55 square feet of the floor and roof will be subjected to the full normal reflected shock pressure. It is probable that such loading will cause a breach of the roof structure. The breach area will be only some 5% of the total surface area of this room, however, so that the situation will still fall within the limits of the Weibull relation discussed above.

The fragments from the warhead case will impact the floor and roof at about 1 msec after detonation, or during the time that those elements are still experiencing very high reflected pressure loadings.

Outside the region of full normal reflection on the roof and floor, the remaining area will be subjected to Mach pressures, of the order of 2,000 psi. This loading will propagate over the floor and ceiling over some period of time.

The walls of the room will see an initial reflected shock pressure of the order of 900 psi, arriving some 2.3 msec after the detonation. By this time, interactions of the strong reflected shocks from the roof and floor will complicate the post-peak behavior of the reflected pressure load on the walls to a high degree. Fragments from the warhead will impact the walls at about 3.3 msec, again while these elements are under significant blast load.

If we assume the only shock failure to be breach of the roof slab, the structure will still be only slightly vented. The maximum quasistatic pressure, from applying Equation 1, can be estimated as about 235 psi. The loading on each structural surface will decay from the peak resulting from the interacting shocks to this value, which will be effective over tens of msec.

The volume of this room is smaller than the volume required to allow full development and mixing of the gaseous products cloud with the internal air. Hence, the products cloud or fireball will completely fill the room, and the burn reaction will not proceed to the completed carbon dioxide end point, until the breach occurs, allowing products to exit the structure in a plume. Continued burn of the partially reacted products will occur in the initial phases of the plume exiting the breach. The internal temperature, following the form of Figure 6, will reach some 3,000 degK, and will drop from that peak to a value of perhaps 300 degK which will persist for several seconds to minutes.

As can be seen from this cursory actual case study, which is highly idealized, the time-dependent loading functions for structural elements are very complex. We point out that we have not considered realistic warhead geometries, which lead to loss of the simple spherical symmetry we have used to advantage in this illustration. Further, if the detonation occurs at a point other than the geometric center of the room, the time-dependent shock interactions become much more complex. Finally, we have used a "pure" explosive, without additives such as aluminum, which would have further compounded the problem. A final simplification, which we must point out, is that we have considered only the roof breach to represent failure reaction of the structural boundaries of this room. If the other surfaces - floor or walls - are treated as responding, the dynamic properties of these elements, and their failure times, will add further complication to the problem. Also, if the structural elements are considered as truly responding, the arrival of the impulsive loading from the fragments, during the time when the element is undergoing strain from the shock load,

will add complexity to the loading function, and the calculation of response of the element.

SUMMARY

We have discussed, in a cursory form, the processes leading to the formation of the complex environment created by an internal explosion, and presented some points of concern which should be addressed in attempts to model such an environment. We have not treated the complexities of even pure air blast in bounded spaces - corner reflections, constructive or destructive shock interferences, etc. We assume that these are recognized, and that appropriate hydrodynamic modeling approaches will consider these. Our main points are:

- the blast environment will be complex, consisting of both air shock and products components;
- fragmentation effects, as a source of momentum transfer as well as perforations, cannot be ignored;
- fireball dynamics and particularly thermal transients are a strong function of the oxygen balance of the explosive, and are complicated by additives such as aluminum.

All of these points must be considered when defining the internal environment, and establishing loading functions on structural elements.

ACKNOWLEDGEMENT

The author was supported in this and related research by Internal Research funds from the Denver Research Institute, University of Denver. The support of the Institute, the University, and the numerous colleagues who contributed ideas, suggestions, and stimulating technical discussion is most gratefully acknowledged.

REFERENCES

Kinney, G.F., *Engineering Elements of Explosions*, NWC TP 4654, Naval Weapons Center, China Lake, 1968

Brode, H.L., *Calculation of the Blast Wave from a Spherical Charge of TNT*, RM-1965, Rand Corporation, 1957

Weibull, H.R.W., "Pressures Recorded in Partially Closed Chambers at Explosion of TNT Charges," in *Prevention of and Protection Against Accidental Explosion of Munitions, Fuels, and Other Hazardous Mixtures*, Annals of the New York Academy of Sciences, Vol. 152, Art. 1, 357-361, NYAS, New York, 1968

Kinney, G.F., R.G.S. Sewell, and K. Graham, *Peak Overpressures for Internal Blast*, NWC TP 6089, Naval Weapons Center, China Lake, 1979

BLAST IN TUNNELS AND ROOMS FROM CYLINDRICAL HE-CHARGES OUTSIDE THE TUNNEL ENTRANCE

G. Scheklinski-Glück

Fraunhofer-Institut für Kurzzeitdynamik
Ernst-Mach-Institut
Freiburg, Germany

ABSTRACT

To protect an underground structure, the exact knowledge of the blast loading on blast doors and ventilation systems is needed at each location in a given configuration of tunnels and rooms. Using model tests, a data base for detonations of cylindrical charges outside the tunnel in a wide range of validity is generated. Empirical formulas for the blast parameters are developed, focussing on short analytical expressions. All information is bound in the reconstruction of the pressure time histories in form of Friedlander functions by means of a computer program. Comparison of measured and computed $p(t)$ curves delivers a quality check on the approximation model. Parameter influence studies are possible for numerous configurations of tunnels and rooms.

INTRODUCTION

This study is one step in a sequence of investigations concerning the propagation of blast waves from conventional weapons. In the case of a direct hit, if the charge detonates inside the tunnel entrance, empirical formulas for the blast in tunnels and rooms are reported in Reference 1. As a generalization for any chamber volume independent of the tunnel cross section, formulas are given in Reference 2. In this part, the results from surface detonation of standing cylindrical HE-charges in different distances and directions outside the tunnel entrance are elaborated.

EXPERIMENTAL SET-UP

The cylindrical RDX-charges have a length/diameter ratio of 5 and are standing upright outside the tunnel entrance in distances of 1 to 5 tunnel diameters D in steps of D . The direction is graduated from 0° (tunnel axis) to 90° in steps of 30° , additionally the 45° -direction. For 90° , the charge touches the wall (Fig. 1).

In full scale, the tunnel diameter is 3.56 m, the tunnel cross section 10 m², and the charge size 4000 kg, 2000 kg, or 1000 kg. In accordance with the cube-root scaling law, in model scale for a tunnel diameter of 9 cm, the charge size is 64 g, 32g and 16 g.

TRANSFORMATION TO AN INSIDE DETONATION

Shadow-schlieren photography is used to investigate the shock structure. Fig. 2 shows the oblique inflow of a shock wave in a tunnel entrance. The most significant feature are



Fig. 1 Experimental set-up. Cylindrical HE-charges with $L/D = 5$ in vertical position outside the tunnel entrance. The distance varies from 1 to 5 tunnel diameters, the angle from 0° (tunnel axis) to 90° (charge touching the wall).

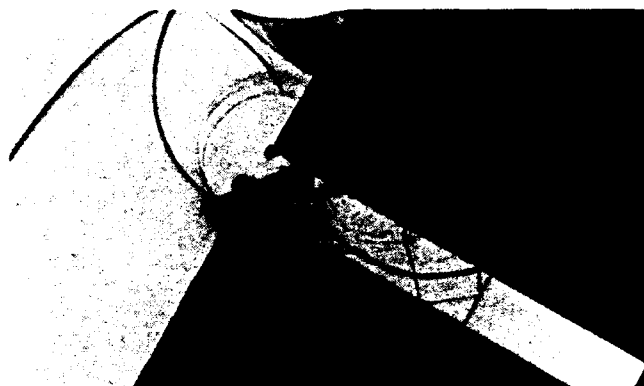


Fig. 2 Shadow-schlieren photography: oblique penetration of a shock wave in a tunnel entrance. Vortices at the entrance reduce the afterflow behind the passing shock front.

the vortices at the entrance. The speed of the afterflow behind the passing shock front is reduced by these vortices. This indicates a separation between inside and outside wave propagation.

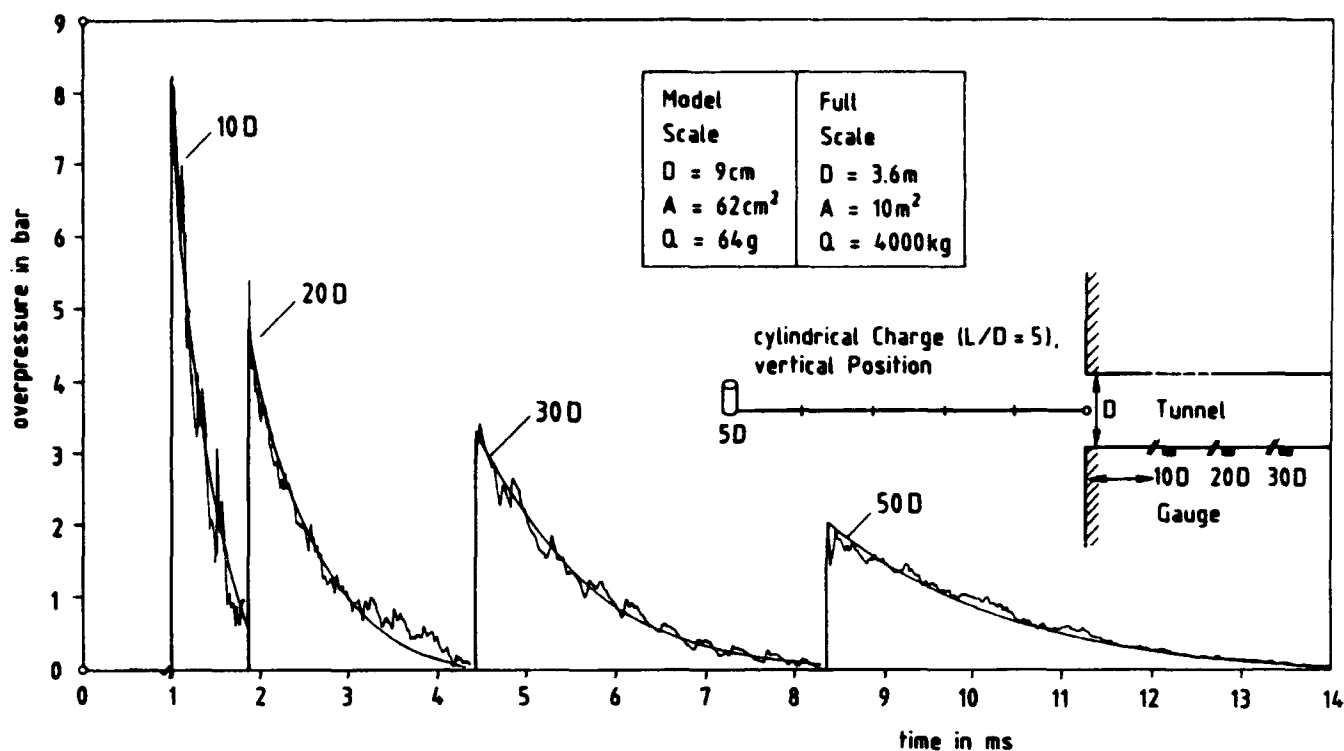


Fig. 3 Transformation to an inside detonation: measured $p(t)$ curves in the tunnel from an outside detonation smooth $p(t)$ curves: a reduced charge in the tunnel entrance generates the identical blast propagation

On this condition, we try to describe the blast inside by any smaller "reduced charge" detonating in the tunnel entrance by means of the equations in Reference 1 mentioned above. This procedure was successfully conducted for all measured distances and angles. Fig. 3 shows an example. The correspondence is evident.

DEVELOPMENT OF EMPIRICAL FORMULA: INFLUENCE OF THE DISTANCE

After transforming the problem from outside to inside detonation, the new task is to develop a mathematical algorithm for the reduced charge in dependence of the charge size, the distance and the angle outside the tunnel entrance.

The development of empirical formulas by means of the Hopkinson-Cranz law of similarity requires the invention of appropriate scaled parameters. For instance, the scaled charge $Z = Q/D^3$ is independent of the tunnel diameter D .

In this case, building the dimensionless parameter $p(\text{out})/p(\text{in})$ {peak pressure for charge outside/inside the tunnel entrance} is the key for solving the problem. In Fig. 4, $p(\text{out})/p(\text{in})$ is plotted versus the distance outside in D for the 0° - direction (tunnel axis).

For all charge sizes the same ratios are measured. It is important for the success in data reduction that the chosen parameter is independent of the charge size.

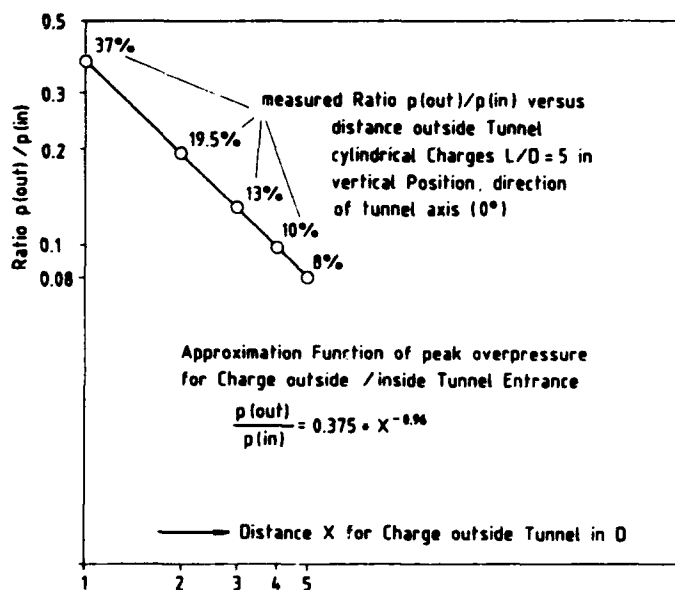


Fig. 4 Comparison between peak overpressure for charge outside/inside the tunnel entrance

The resulting equation is:

$$p(\text{out})/p(\text{in}) = 0.375 \cdot X^{-0.96} \quad (1)$$

X = distance in D outside the tunnel

for $D \leq X \leq 5 D$

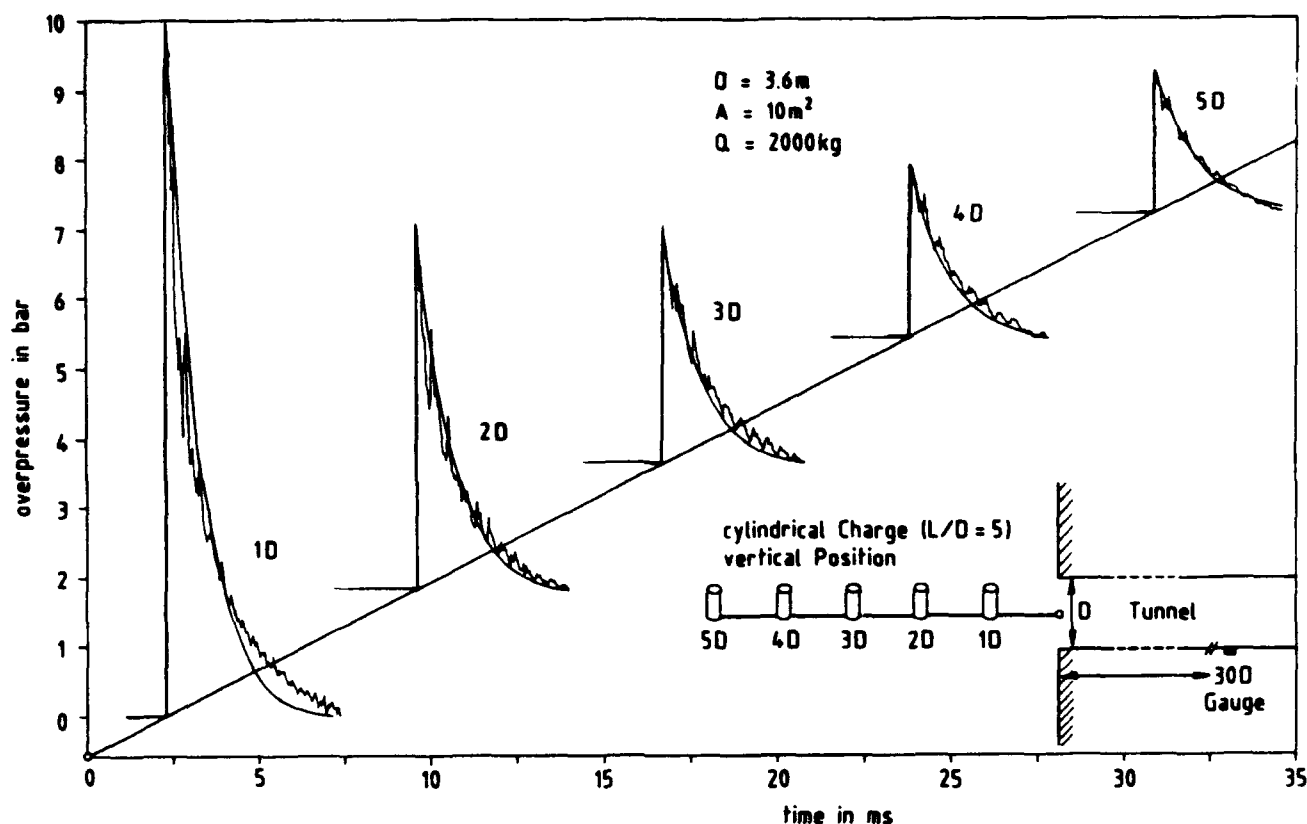


Fig. 5 Variation of the distance:
measured $p(t)$ curves in the tunnel from different outside detonations
smooth curves calculated for inside detonations according to equation (1).

The calculation of the reduced charge is possible by means of the formulas for inside detonation (Reference 1):

$$p_s = 53.1 \cdot Y^{-1.124} \cdot Z^{0.83}$$

$Y = L/D$ scaled distance of the gauge

$Z = Q/D^3$ scaled charge

The reduced charge Z' in the tunnel entrance

$$Z' = Z \cdot [p(\text{out})/p(\text{in})]^{1/0.83}$$

generates the same peak pressure p_s at the same location Y in the tunnel as the charge Z detonating outside. For the calculation, the distance X outside must be added to Y . Fig. 5 gives a piece of evidence for several distances from 1 D to 5 D outside the tunnel.

DEVELOPMENT OF EMPIRICAL FORMULA: INFLUENCE OF THE ANGLE

Fig. 6 shows the results for the whole test program.

It is a breakthrough in data reduction, to join together these results for the different distances and directions in one resulting equation, except the 90° -direction. There only diffracted waves can enter the tunnel. For $\alpha = 0^\circ$ to 60° , parallel lines in double log scale result. Their slope -0.96 is

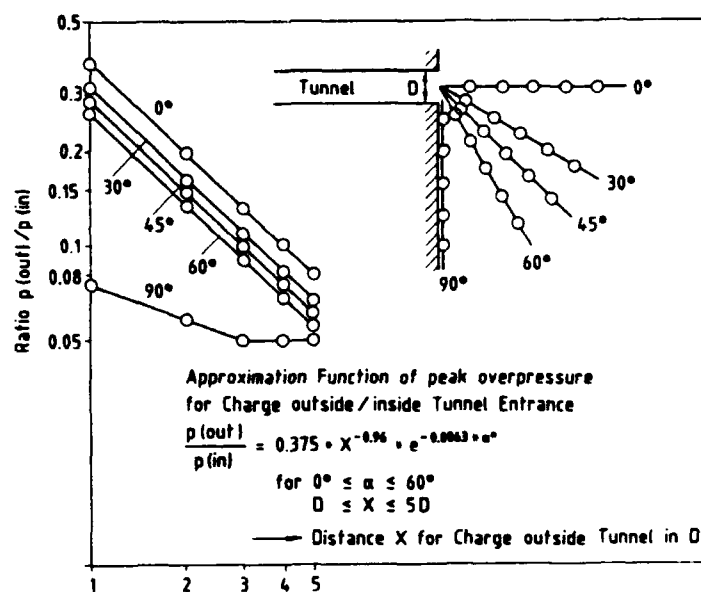


Fig. 6 Ratio of peak pressure for charge outside/inside the tunnel entrance for different distances and angles against the tunnel axis.

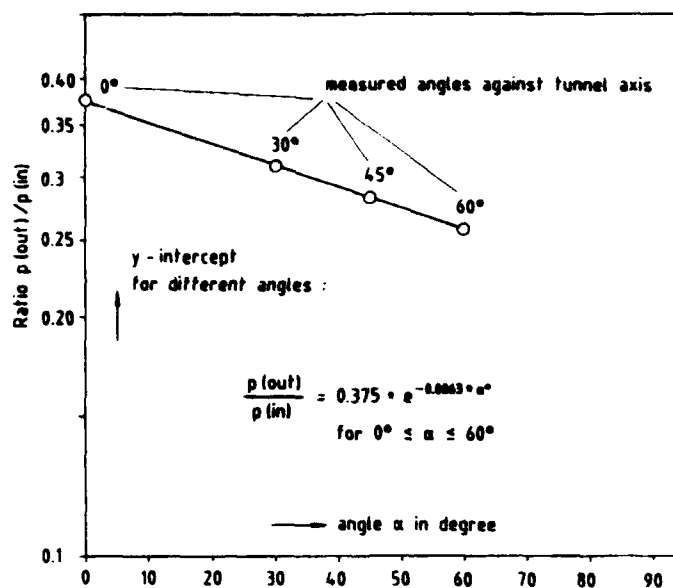


Fig. 7 Influence of the angle: y-intercepts versus angle α .

the exponent of the given power function for the distance X . The Y-intercept contains the influence of the angle α . In Fig. 7 half log scale is chosen to produce a straight line versus α . Their slope -0.0063 leads to the exponential function for α given in equation (2).

The resulting equation

$$p(out)/p(in) = 0.375 \cdot X^{-0.96} \cdot e^{-0.0063 \cdot \alpha} \quad (2)$$

range of validity: $D \leq X \leq 5 D$

$$0^\circ \leq \alpha \leq 60^\circ$$

masters the behaviour of the blast parameters for any distances and any angles in the given range of validity. Fig. 8 proves this for different angles by the evident correspondence of measured and calculated $p(t)$ curves.

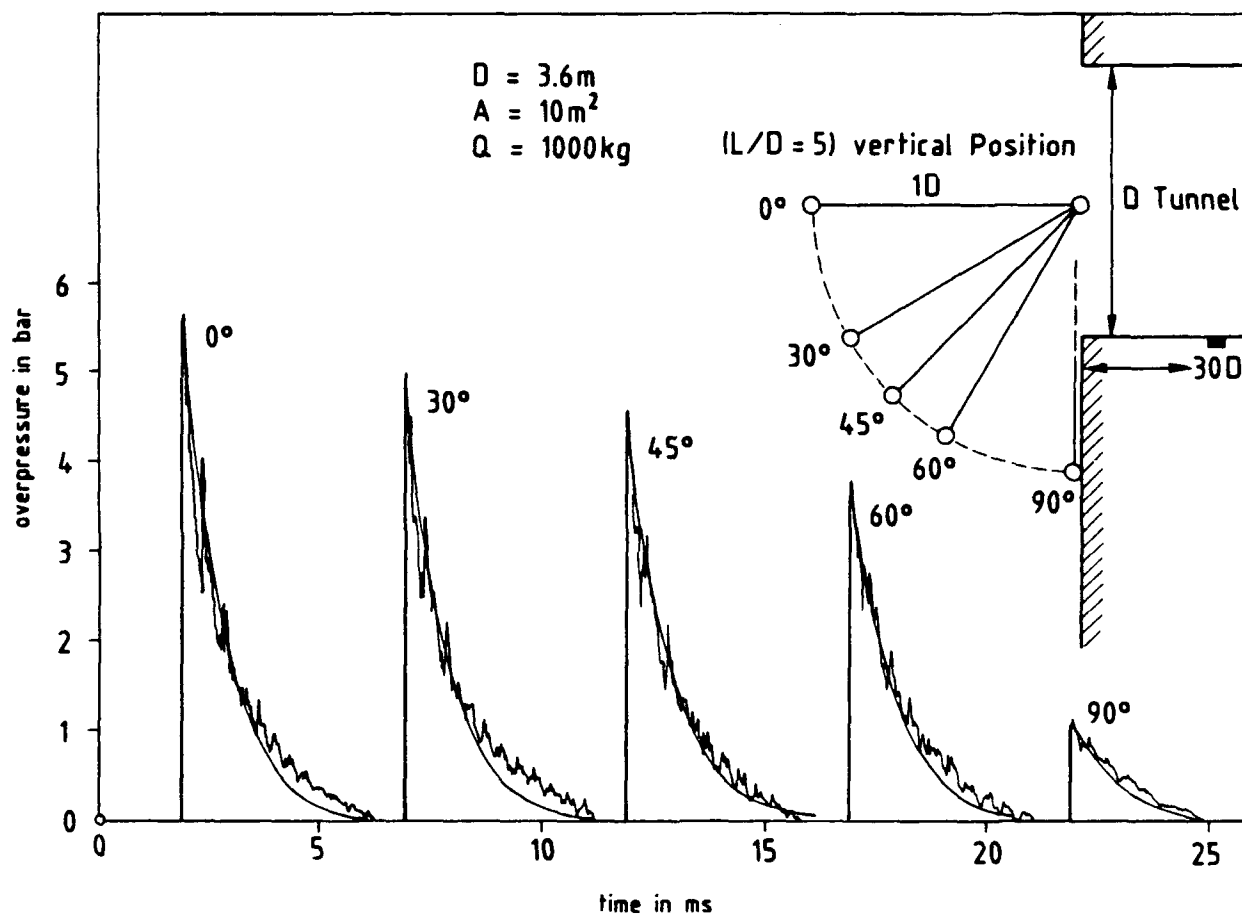


Fig. 8 Variation of the angle: measured $p(t)$ curves from outside detonations of different directions smooth curves calculated for inside detonations according to equation (2)

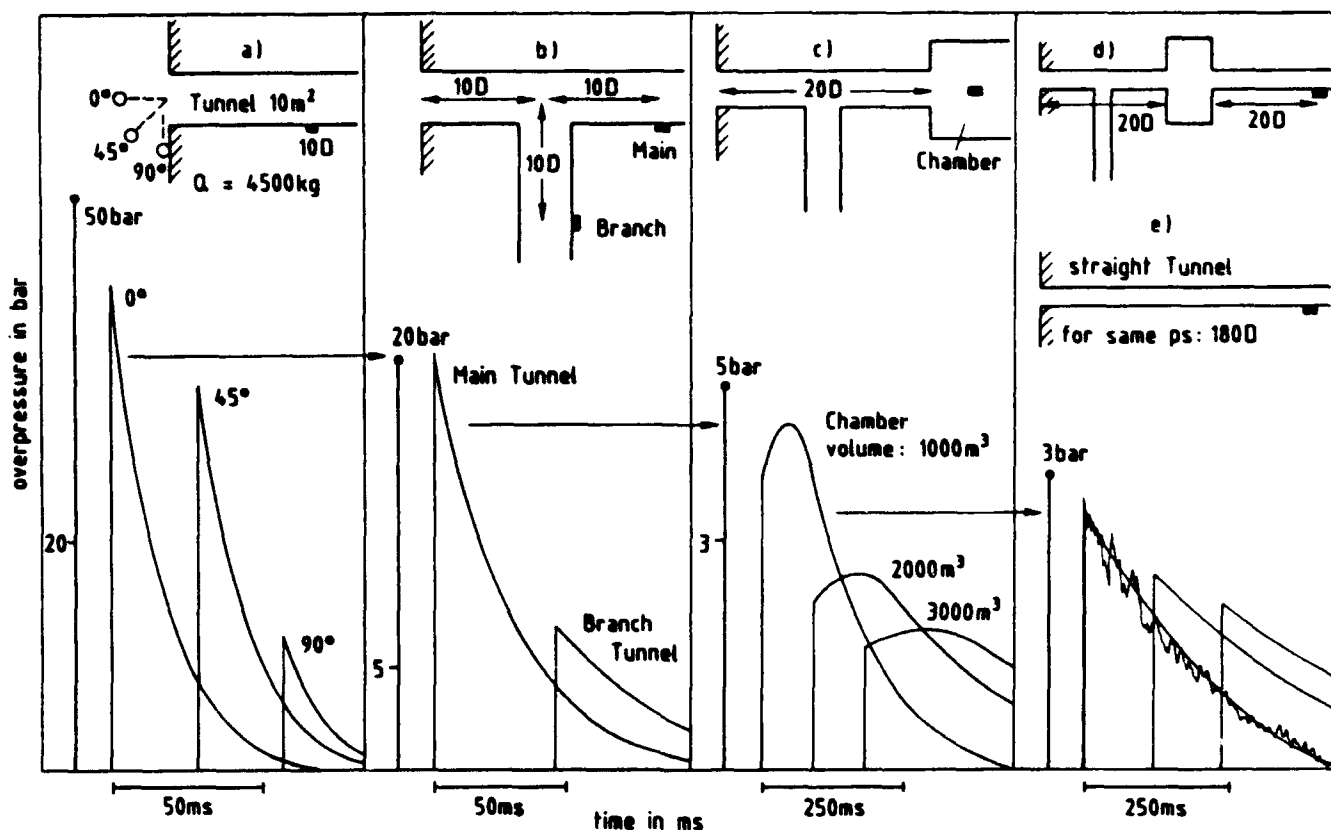


Fig. 9 Parameter study: Blast propagation through tunnels and rooms.
a) Variation of the direction for an outside detonation
b) Influence of a tunnel branching
c) Variation of the chamber volume
d) Blast in the tunnel behind the chamber
e) Comparison with a straight tunnel

APPLICATIONS AND PARAMETER STUDIES

Using this tool, we have the ability to carry out studies for several different parameter scenarios with a high degree of flexibility. We can examine the influence of each singular component of the configuration (tunnel length, tunnel cross section, charge mass, tunnel branches, chambers with different shapes and different volumes, tunnels behind the chambers etc.) at any location in the shelter.

For the planning of underground tunnel/chamber systems in which blast loading effects are to be predicted a program of this type will be economically advantageous in the engineering stages of development.

An example is shown in Fig. 9:

Part a) shows the blast inflow from the detonation of a standing cylindrical charge of 4500 kg with $L/D = 5$ from different directions outside the tunnel entrance, measured at a location $10 D$ in the tunnel. The peak pressure is 42/34/12 bar for $\alpha = 0^\circ/45^\circ/90^\circ$. We follow the 0° -direction. In part b), we are behind a tunnel branching $10 D$ in the main tunnel ($p_s = 20$ bar) and in the branch tunnel ($p_s = 7$ bar), respectively (see Reference 3). We follow the main tunnel. With 20 bar, the blastwave enters a chamber of 1000/2000/3000 m^3 volume. The $p(t)$ curve is here approximated by a parabola and annexed Friedlander function (see References 4, 5). In the chamber

we measure caused by the expansion effect of the blast wave a maximum pressure of 4.5/2.6/1.8 bar. On the way, the positive duration is increased to the fivefold. Section d) shows the blastwave in a tunnel $20 D$ behind the chambers (see References 6, 7). The peak pressure is decreased behind the 1000 m^3 -chamber to 2.6 bar after a total distance of ca. $40 D$ in the structure. At this location, we compare with a measured curve in order to prove as well this result as the whole sequence of calculations.

For comparison: in part e), leading to the same $p_s = 2.6$ bar, a straight tunnel (formulas see Ref.1) without junction and without chamber, needs a length of $180 D$.

COMPARISON WITH THE U.S.-HANDBOOK TM 5-855

Calculations by means of the TM 5-855 "Fundamentals of Protective Design" (Reference 8) are possible for hemispherical surface burst from end-on and side-on direction. For 0° (end-on), the TM 5 leads in part a) of Fig.9 ($Q = 4500$ kg RDX, $1 D = 3.57m$ outside the tunnel) to $p_s = 34$ bar, instead of 42 bar for the standing Cylinder with $L/D = 5$. For understanding see Reference 9. In the 90° - direction (side-on), the TM 5 calculates 19 bar for hemispheres, instead of 12 bar for the standing Cylinder touching the wall. The key for understanding this inverse behaviour is the different geometry, and the different touching area on the wall.

CONCLUSIONS

Empirical formulas are developed for detonations of cylindrical charges outside the tunnel entrance in a broad range of validity. The problem is transformed to calculations of reduced charges detonating in the tunnel entrance. Measured and calculated curves are compared. An analysis tool is created which can be used to predict conventional weapons effectiveness for numerous configurations of tunnels and rooms.

ACKNOWLEDGEMENTS

The support of this work by Mr. BOR M. Kropatscheck, Ministry of Defense, Rü T V 5, is greatly appreciated. The author expresses his thanks for thorough planning and suggestions to the Engineer Officers in the German Armed Forces Office, Division V, Infrastructure.

REFERENCES

1. Scheklinski-Glück, G.:
Scale model tests to determine blast parameters in tunnels and expansion rooms from HE-charges in the tunnel entrance.
Proceedings of the Fourth International Symposium on the Interaction of Non-nuclear Munitions with Structures, Panama City Beach, FL, April 1989
2. Scheklinski-Glück, G.:
Programm and Parameterstudien zum Luftstoß in unterirdischen Stollen-/Kammersystemen.
Proceedings of: 5. Internationales Symposium zur Interaktion konventioneller Munition mit Schutzbauten, BRD, Mannheim, April 1991
3. Gürke, G.; Scheklinski-Glück, G.; Mehlin, H. P.:
Luftstoß in geraden und rechtwinklig verzweigten Stollen bei Detonation im Stolleneingang
Report No. E 6/86, of the Ernst-Mach-Institut, Freiburg, Germany
4. Scheklinski-Glück, G.; Mehlin, H. P.:
Luftstoßparameter in Stollen mit Expansionskammern bei der Detonation von Explosivstoffladungen im Stolleneingang.
Report No. E 19/89 of the Ernst-Mach-Institut, Freiburg, Germany
5. Scheklinski-Glück, G.; Hülsewig M.; Mehlin, H. P.:
Luftstoßausbreitung in Expansionskammern mit variablem Volumen bei Detonation im Stolleneingang
Report No. E 10/91 of the Ernst-Mach-Institut, Freiburg, Germany
6. Hülsewig, M.; Scheklinski-Glück, G.; Mehlin, H. P.:
Luftstoßausbreitung in weiterführenden Stollen hinter Expansionskammern
Report No. E 13/91 of the Ernst-Mach-Institut, Freiburg, Germany
7. Hülsewig, M.; Scheklinski-Glück, G.; Mehlin, H. P.:
Blast in Stollen hinter Expansionskammern mit variablem Volumen.
Report No. E 16/92 of the Ernst-Mach-Institut, Freiburg, Germany
8. Hyde, D. W.:
Conventional Weapons Effects. collection of TM5-855-1, "Fundamentals of Protective Design for Conventional Weapons"
U.S. Army Engineer Waterways Experiment Station, USAEWES / SS-R, 13 Dec 1991
9. Gürke, G.; Scheklinski-Glück, G.:
Blastparameter bei der Oberflächendetonation senkrecht stehender Explosivstoffzylinder mit den Streckungen $L = 1 D$ bis $L = 6 D$
Report No. E 16/85 of the Ernst-Mach-Institut, Freiburg, Germany

BLAST VALVES - A SUPERFLUOUS INVESTMENT?

J. Hasler
Divisional Manager

LUWA Ltd., Shelter & Security Technology,
Kanalstrasse 5, 8152 Glattbrugg - SWITZERLAND

Abstract

Blast valves are often considered as an expensive surplus, developed for the benefit of a few manufacturers only. Therefore they are substituted, merely by openings, grilles and louvres or expansion chambers made in concrete as part of the building structure. But are such "blast protection elements" honestly capable of giving the required protection in the case of real events or is it just a gamble with the fact that if they do fail nobody will survive to complain?

The following paper, based on research and practical tests carried-out in the laboratories of the Swiss Defence Technology and Procurement Agency (GRD) and completed by field tests in USA, deals with this subject.

Comparisons are made between open holes, louvres, attenuators and blast valves, their possibilities and limits of application all depending on the blast pressure and duration.

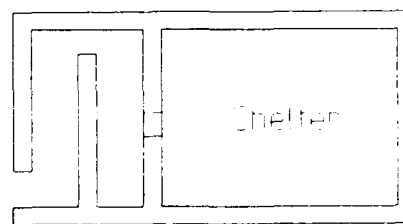
Background

Bunkers were already built in the I World War 1914-1918. During this period, breathing air was no real problem because the bunkers were not overcrowded and small openings to the outside insured the necessary supply of fresh air. The pressure waves, created from bombs available at that time, were not very harmful inside the shelter, after penetrating through the small ventilation openings.

The situation dramatically changed in World War II, 1939-1944. New, very powerful bombs had been developed and these were dropped in very large numbers. Not only the military but also the civil population sought protection in bunkers. The civil shelters were mainly overcrowded and therefore required the increased amount of fresh air to breathe and to provide acceptable survival conditions in respect of smells and humidity. With the increase of blast pressures, air inlets and outlets became a real problem. The openings became relatively large and mechanical ventilation had to be installed. This was then the moment when "blast protection" for air intakes had to be developed.

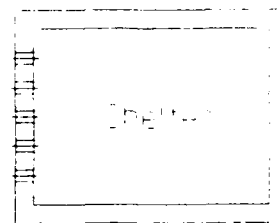
At the beginning it was quite understandable, that mechanical devices had not been considered, as there was no available knowledge about duration of positive and negative pressure phase or magnitude of impulses. Solutions were then studied and very pragmatic methods found.

Labyrinths



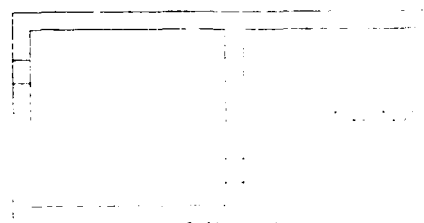
The oncoming pressure waves were reduced by several deviations

Pipe bundles



Oncoming blast wave to be split up and reduced in combination of pipes

Expansion chambers



The oncoming pressure wave is reduced by expansion within the antechamber.

Stone beds



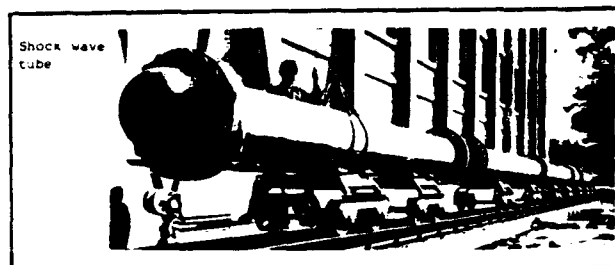
The labyrinths across the gravel reduces the oncoming pressure wave. Sand was also used with the idea to absorb war gases.

At the end of the fifties, beginning of the sixties, it became known that the new atomic bombs were creating a long lasting pressure wave of more than 100 milliseconds. This made it absolutely clear that systems unable to close off the openings were completely inadequate.

In the USA, but mainly in Europe, Government and private companies started to develop mechanical blast valves. Civil protection programmes, aimed at "a fully equipped shelter place for each inhabitant", created a large potential. It was also evident that standards and test facilities had to be established. We built the first blast wave test tube here in Switzerland, which today after some upgrading, still fulfils its duty in the Swiss Government test laboratory.

During this period, many different types of blast valves were developed. However, most of them have since disappeared as being unsatisfactory, although a small number are still on the market as historical monuments. Only a very few companies have permanently invested in research and new development to cope with today's modern weapon technology. After many years of more or less unlimited funds for protection buildings, nowadays the pressure increases to reduce costs. Quite a contradictory situation has developed: Old threats have vanished and led, under pressure from the people, to very reduced defence budgets. On the other side, the actual situation shows that political storm-centres have immensely increased in comparison to the last decade. Many of them concealing various unforeseeable dangers.

It is obvious, with restricted defence budgets, that the most economic solutions have also to be achieved in the construction of shelters. But are solutions, which were considered as obsolete twenty years ago, really what is required? Or are self declared experts trying to redevelop the wheel, due to the lack of real understanding of blasts? Is the application of blast valves really a waste of money?



Objective

No prejudices, but only an open mind can help to answer all these questions. As the weapons have changed menaces have altered too. The Gulf War has added supplementary experience and knowledge, plus research on the damaged shelters.

Therefore, the question of protection for air inlet and outlet openings requires careful consideration. Even though this is just a small problem within the entire shelter design, an incorrectly protected opening can weaken the whole shelter or even lead to its destruction.

The aim of this paper is to present different solutions with their specific performances.

Blast protection systems

Systems	Expectations	Production
Labyrinths in concrete or steel	Reduction of pressure, due to deviations	Simple design, to be built on site in concrete or by the local black-smith.
Pipe bundles	Splits up the blast wave front into smaller parts and reduced by friction in several pipes.	Simple and understandable principle. To be built by the local plumber.
Expansion chambers	Reduction of pressure expected through small opening with following expansion	Simple, to be built on site
Stone bed	Reduction of pressure wave expected through friction, deviation, contraction and expansion	Corresponding room to be filled with gravel on site
Blast louvres	Reduction of blast pressure expected by passing the fins of louvre	Local blacksmith
Blast attenuators	Compact unit. Reduction of pressure due to reflection, contraction, expansion and deviation	Standardised units, developed and practically tested, in volume production
Blast valves	Compact units. Closing under positive and negative pressure, therefore preventing blasts penetrating into the structure	Standardised units, developed and practically tested, in volume production

How far will the expectations be fulfilled? Let us try to evaluate the effectiveness of the different systems. A practical example will give us some useful hints without being perfect. The design of most of the checked systems can be altered with direct influence on blast attenuation, space requirement and price.

Example:

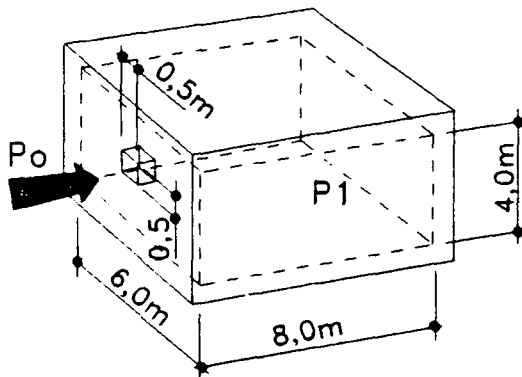
- Shelter size: W6 x L8 x H4m
- Airflow required for normal ventilation 10'000m³/h (5880cfm)
- Max. permitted pressure drop of blast protection system during normal ventilation mode 200 Pa (0,8"WG)
- Max. expected reflected blast pressure in front of blast protection system 11 bar (150 PSI)
- Blast duration (approx. effects of a 2000lbs GP bomb, exploding on ground at a distance of 15 meters) 10milliseconds
- Max. permitted pressure behind blast protection system, preventing harm to people and equipment 0,5 bar-1,0 bar (7-14 PSI)

Results

The following blast reduction systems have been calculated, based on literature and our own test results.

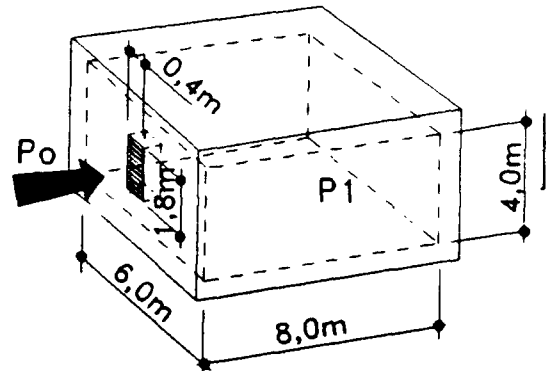
Open hole, pipe bundles

One open hole, several open holes or pipe bundles give very similar results.



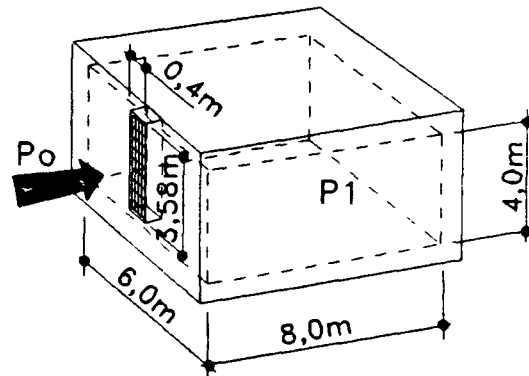
Peak pressure P1 (0,5m) 5,2 bar
Peak overpressure in room 2000 Pa

Blast louvre



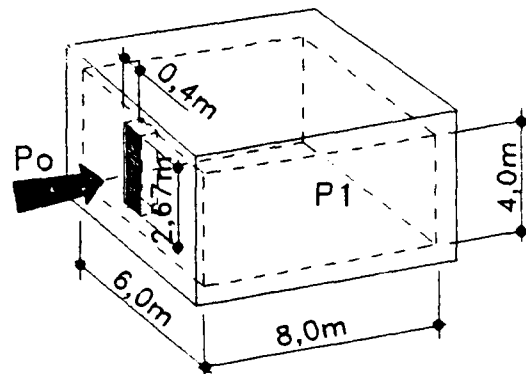
Peak pressure P1 (0,5m) 2,0 bar
Peak overpressure in room 820 Pa

Attenuator type AA



Peak pressure P1 (0,5m) 1,1 bar
Peak overpressure in room 400 Pa

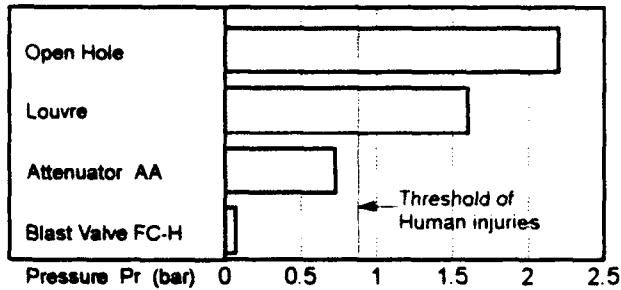
Blast valves type FC



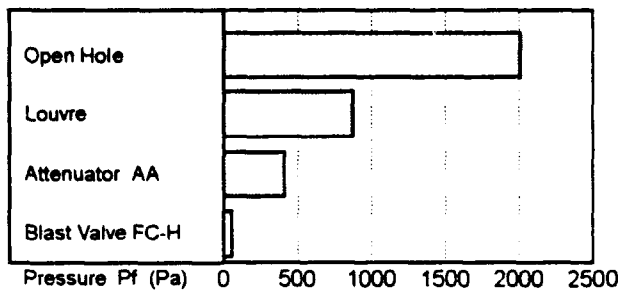
Peak pressure P1 (0,5m) 0,55 bar
Peak overpressure in room 40 Pa

These results can be compared diagrammatically.

Peak pressure behind blast reduction device



Peak overpressure inside shelter



The analysis of the results show that the shelter occupants would not survive a design with open holes or louvres. A well designed blast attenuator can be tolerated, given an optimal relation between hole and room section. Only the quick closing blast valve would stop the arriving blast wave, so that hardly any effects would be noticed in the shelter.

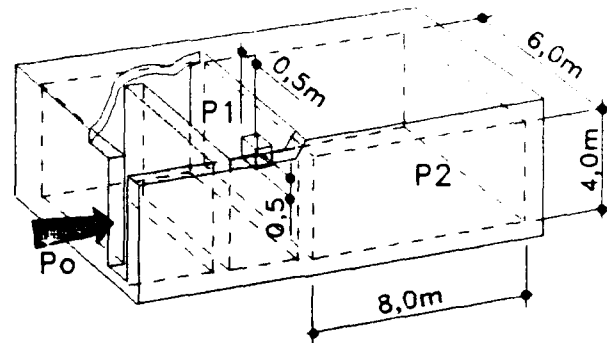
Construction measures

For purely civil engineering measures to give results comparable to those of a blast valve, considerable efforts must be taken.

We will take a look at some possibilities to reduce the blast pressure with such construction measures, always maintaining approximately 200 Pa maximal pressure drop under normal ventilation mode:

Chicanes

Chicanes in concrete with a small inlet slot and an open hole into the shelter



P_0 11 bar Blast pressure

P_1 6,5 bar

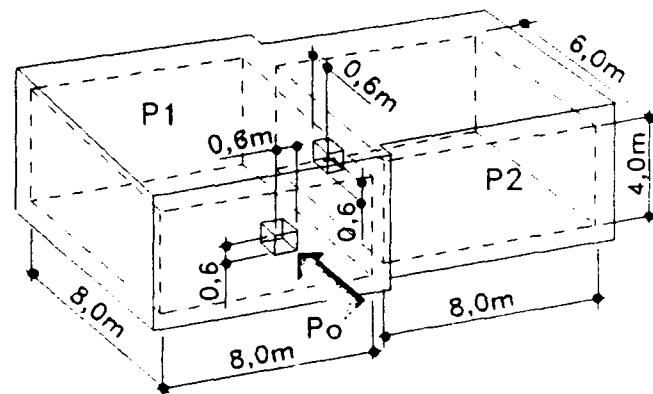
P_2 1,34 bar Shelter

Additional construction volume 95m³

Chicanes have only little efficiency and can not reduce the pressure to a safe level.

Single expansion chamber

A large expansion chamber with an open hole from outside and into the shelter.



P_0 11 bar Blast pressure

P_1 2,7 bar Expansion chamber

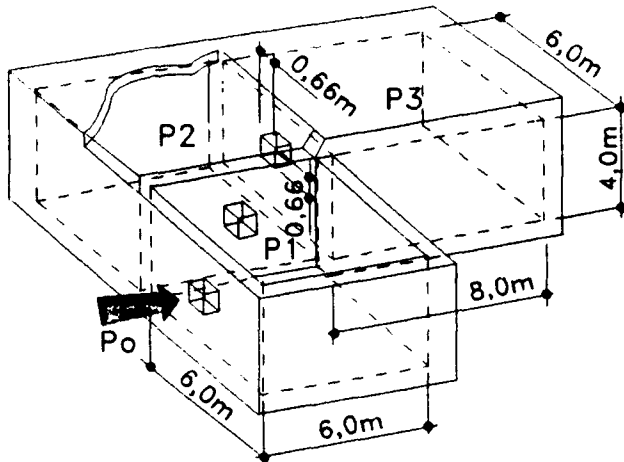
P_2 0,8 bar Shelter

Additional construction volume 256m³

With a large expansion chamber, the required pressure reduction can be attained.

Double expansion chamber

Two expansion chambers with open holes from outside into the first chamber, an open hole from chamber one into chamber two and into the shelter.



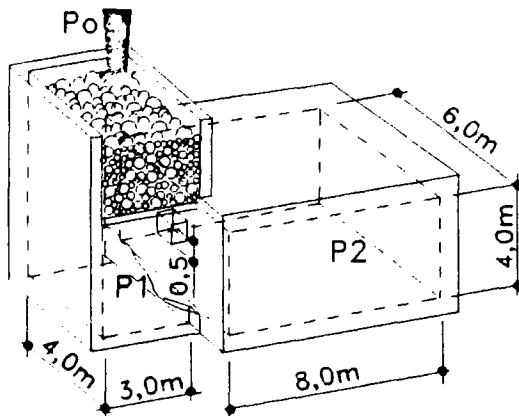
P0	11 bar	Blast pressure
P1	4,8 bar	Expansion chamber one
P2	1,7 bar	Expansion chamber two
P3	0,6 bar	Shelter

Additional construction volume 288m³

With this expanded construction, the necessary pressure reduction will be obtained.

Stone Bed

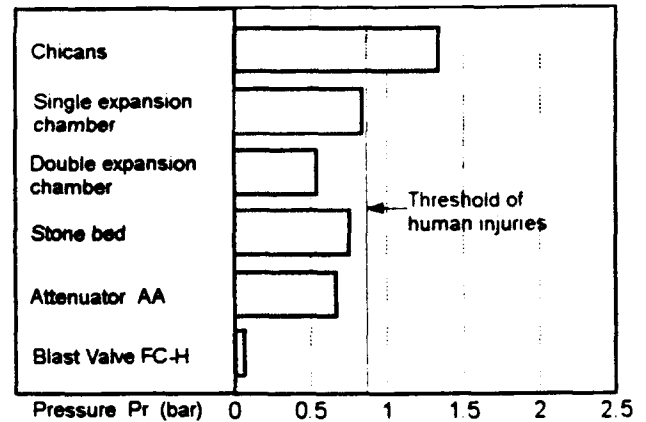
A 1m layer of gravel placed in the air inlet shaft and an open hole.



P0	11 bar	Blast pressure
P1	2,5 bar	
P2	0,7 bar	Shelter

Additional construction volume 105m³

The following diagram shows the final pressure in the shelter, obtained with structural measures. Also for comparison the blast attenuator and blast valve are listed.



The diagram shows clearly that the solution with chicanes is not acceptable, the others are marginally acceptable. The blast valves give the highest level of safety.

Cost comparisons

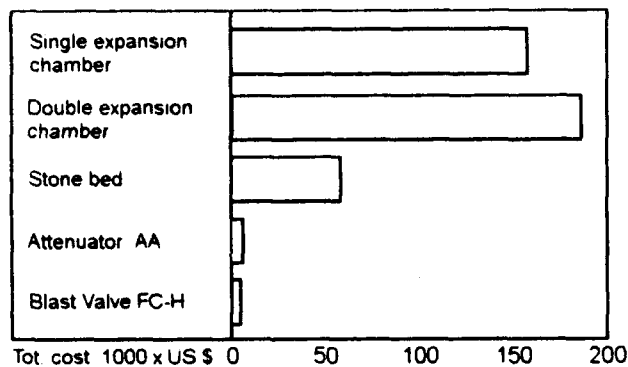
After finding technically feasible solutions, the next concern is the resulting costs. Since chicanes do not fulfil the requirements, they are no longer considered.

Attenuation measure	Additional required volume m ³	Cost of add. volume US\$ 1)	Cost of blast reduction device US\$ 2)	Total cost US\$
- Single expansion chamber	405	162'000	—	162'000
- Double expansion chamber	455	182'000	—	182'000
- Stone bed	105	42'000	18'000	60'000
- Blast attenuator	—	—	8'000	8'000
- Blast valve	—	—	7'000	7'000

1) Basing on US\$ 400 per m³ concrete construction, additional costs for land not included.

2) 60mm gravel and support, attenuator or blast valve

The following diagram shows the cost relation of the previously listed table in a graphic.



Conclusion

The comparison of the various possible solutions for blast reduction in a specific case, impressively reveals the high costs of the building measures, in obtaining the low pressure required for survival in the shelter. Also arguing about the cost per m³ concrete work or other values, will not make that much difference to the total amount.

Blast valves offer the most economical solution. They are standard products, which have been tested and manufactured under very high quality assurance standards. Technical leaflets are available giving all the information required, so that customer, consultants and contractors know exactly what they are going to get as well as the performance of the product. The effectiveness of blast reduction construction measures can not be physically demonstrated. The available formula for calculations are only approximations and estimations.

High quality blast valves are shown to be the best solution available today.

Summary

Are blast valves for the protection of air inlets and outlets really a waste of money? Can they be substituted by constructional measures?

The different possible technical solutions were studied based on realistic examples. Unsuccessful measures were dropped and only those reducing the pressure level inside the shelter to values allowing the survival of human beings, were included in the cost analysis.

The comparisons clearly showed that blast valves are the best technical and financial solution. Compared with construction measures, they only cost about 5% of the total sum.

Therefore it can be stated that the application of blast valves is not a waste of money - on the contrary - they help to keep the costs of effective shelters to a reasonable level.

- References:
- FMB 73-11, Weapon effects and shelter design, Swiss Research Institute for Military Construction.
 - Test Report: Louvres, Luwa FST-VS 9108, tested at Swiss Defence Technology Laboratories, Spiez.
 - Passive Blast Attenuators - A Possible Alternative to Active Blast Valves, (Luwa Ltd., J. Hasler) 5th Int. Seminar of Interaction of Non-Nuclear Munitions with Structures, April 1991 Mannheim, Germany.

PREDICTION OF IN-STRUCTURE SHOCK

Ph. van Dongen and J. Weerheijm

TNO Prins Maurits Laboratory
P.O. Box 45 - 2280 AA Rijswijk - The Netherlands

ABSTRACT

The in-structure shock in underground structures can cause considerable damage to the equipment installed inside, even if the structure itself resists the explosion load. For economic design of special shock isolators it is essential that the internal shock environment is well defined. The Military Technical Manual TM5-855-1 provides directives to quantify free-field soil motions and in-structure motions of an underground structure due to a non-nuclear underground explosion. The procedures described in the Technical Manual TM5-855-1 to obtain free-field and in-structure shock data are discussed in this paper. Predictions are compared with the results of scaled experiments.

INTRODUCTION

Economic protection of sophisticated military equipment against high amplitude accelerations and shocks in underground structures due to an external underground explosion is desirable. Sophisticated equipment can be protected against high accelerations and shocks with special shock isolators. For economic design of these shock isolators it is essential that the internal shock environment is well defined. If an acceleration-time histogram of the in-structure can be predicted a shock spectrum can be determined. This spectrum presents maximum response values of One-Mass-Spring Systems caused by this load as function of their natural frequencies. Together with damage criteria of the internal equipment, adequate shock isolators can be developed.

The Technical Manual TM5-855-1 is one of the literature references that provides directives to quantify in-structure motions of an underground structure due to an external non-nuclear underground explosion. The empirical formulas to estimate in-structure motions are derived from free-field ground shock empirical relationships. In this paper this procedure is evaluated and compared with the results of experiments.

PREDICTIONS TECHNICAL MANUAL TM5-855-1

The manual TM5-855-1 presents directives for predicting free-field ground shock parameters like peak-pressure, peak impulse, soil particle peak acceleration, velocity and displacement. These ground shock parameters are depending on charge weight, the distance to the point of explosion, the acoustic impedance of the soil and the attenuation coefficient of the soil.

The peak values of free-field stress and motion from bombs detonating in soil are given with equations 1 and 2.

$$P_0 = f \cdot (\rho \cdot c) \cdot 48.8 \cdot (2.52 \cdot R/W^{1/3})^{-n} \quad (\text{eq 1})$$

where	P_0	=	peak pressure	(Pa)
	W	=	charge weight	(kg)
	R	=	distance to the explosion	(m)
	ρ	=	mass density of soil	(kg/m ³)
	c	=	seismic velocity in soil	(m/s)
	$(\rho \cdot c)$	=	acoustic impedance of soil	(kg/s·m ²)
	n	=	attenuation coefficient	(-)
	f	=	coupling factor	(-)

$$A_0 = 1235.6 \cdot W^{-1/3} \cdot f \cdot c \cdot (2.52 \cdot R/W^{1/3})^{-(n-1)} \quad (\text{eq 2})$$

where A_0 = peak soil particle acceleration (m/s²)

For preliminary design considerations a table is presented in which the seismic velocity, c , the acoustic impedance, $(\rho \cdot c)$, and the attenuation coefficient, n , are given as function of soil descriptions. Disadvantage of the TM5-855-1 is that it presents only a limited group of soil characteristics.

Field experiments in dry, loose, backfilled sand have shown that the predicted free-field peak pressure as well as the free-field peak soil particle accelerations were underpredicted by about 5 to 100%, depending on the scaled distance [2, 3]. It was concluded that the attenuation coefficient of the shockwave must be chosen carefully since it influences the result largely. A 10% lower value of the coefficient means almost doubling of the peak values.

The in-structure motions are presented as the average peak pressure of a volume of free-field soil particles with the same dimensions as the structure. Therefore, the average acceleration of the soil particles, A_{avg} , across a rectangular structure (see Figure 1) is calculated by integrating the acceleration-range function (eq 2) over the span of the structure divided by the span ($R_2 - R_1$). To adjust the average one-dimensional acceleration, A_{avg} , to a volume unit a reduction factor, RF, is introduced which depends on the dimensions of the structure and the distance to the point of explosion (see Figure 2).

Test data have shown this method to be conservative for rectangular buried structures [1]. The estimated peak values for in-structure acceleration, velocity and displacement can be used to develop an approximate shock spectrum of the in-structure environment.

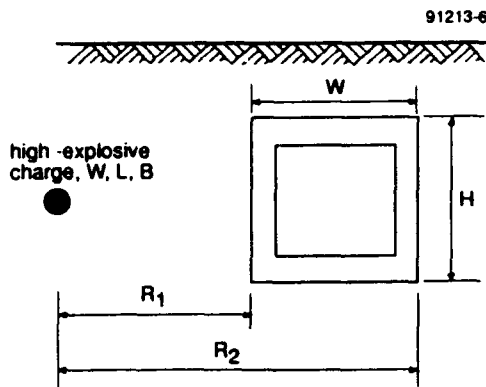


Figure 1 Side burst load case of a buried rectangular structure. [1]

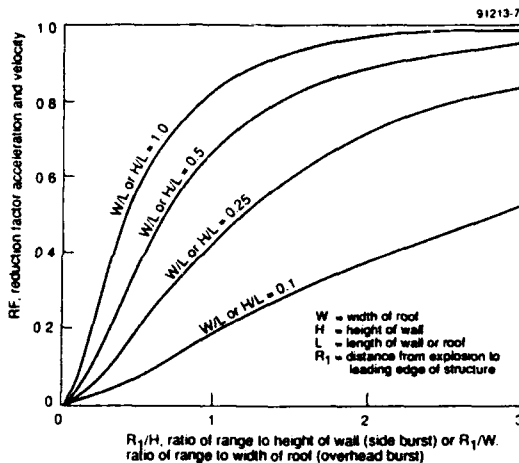


Figure 2 Reduction factor, RF, for in-structure acceleration. [1]

In this approach it is assumed that the average motion of a volume unit of soil particles responds in the same way as any given structure with the same dimensions. However the actual interaction process taking place is a function of shockwave, structure and surrounding soil characteristics. Because of the acoustic impedance difference between surrounding soil and structure, reflection of the shock wave will occur. Therefore the actual peak load on the structure can be significantly higher than the free-field stress. The decay of the load in time is determined by rarefaction waves which are developed at the edges of the structure. These wave properties depend on the free-field shockwave velocity and duration and the structure dimensions. One method to quantify the dynamic response of a structure loaded with an interaction pressure, $P_i(t)$, is modelling with a One-Mass-Spring System. In such a model the structure is characterized as a lumped mass and the surrounding soil that offers resistance against the motion of the structure is characterized with a spring and damper. A schematic view of this system is presented in Figure 3. Also presented in this

Figure is a schematic view of the interaction pressure, $P_i(t)$. The dotted line in this load diagram represents the free-field stress.

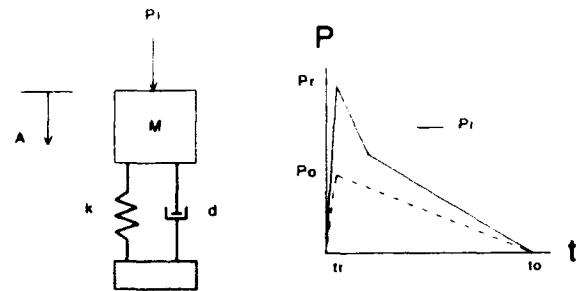


Figure 3 One-Mass-Spring System with damping and interaction load diagram, $P_i(t)$.

In the next section, the in-structure accelerations predicted with the TM5-855-1 are compared with response results of the Mass-Spring System loaded with predicted interaction pressures and with measured interaction pressures. These results are compared with measured in-structure accelerations.

COMPARISON PREDICTIONS WITH EXPERIMENTAL RESULTS

Set-up conditions

Experiments were performed in dry, loose, backfilled sand. The free-field ground shock pressure was measured with special soil pressure transducers. These transducers record the interaction pressure between soil particles and transducer adapter. A built-in accelerometer records the motion of the adapter which is used to adjust the measured interaction pressure to the actual free-field pressure the soil particles experiences. This measurement technique is discussed in [3] and appeared to be valid. The adjustment appeared to be essential. As mentioned earlier, references [2] and [3] concluded that the free-field ground shock parameters were underpredicted when compared to measured values.

A fully instrumented cubic concrete structure (volume = 1 m^3 , mass = 1000 kg) was buried at a depth of 2 metres. The measured in-structure accelerations are used to verify the TM5-855-1 predictions and the Mass-Spring System results.

Table 1 shows the scaled distances of the structure and the free-field pressure transducers to the point of explosion.

Table 1 View of performed experiments [2]

Experiment Number	Charge Weight (kg)	R_s^* Structure (m/kg ^{1/3})	R_s^* Transducer 1 (m/kg ^{1/3})	R_s^* Transducer 2 (m/kg ^{1/3})
1, 2, 3	0.125	6.0	6.3	4.0
4, 5, 6	0.250	4.8	5.0	3.2
7, 8, 9	0.375	4.2	4.4	2.8
10, 11, 12	0.500	3.8	4.0	2.5

$R_s^* = \text{Scaled Distance } R/W^{1/3}$

Prediction TM5-855-1

The manual [1] suggests for dry, loose sand an attenuation coefficient, n , of 3.00 to 3.25. A worst case value of 3.00 is chosen for the predictions. The acoustic impedance ($\rho \cdot c$) is suggested to be $2.7 \cdot 10^5 \text{ kg/m}^2 \cdot \text{s}$ [1]. The coupling factor, f , is for this set-up condition 1.0.

According to the Technical Manual [1] the duration of the free-field shock wave, t_0 , is twice the predicted time of arrival which is defined as the distance to the point of explosion (3 m) divided by the seismic velocity of the shock wave (183 m/s) and is therefore 32 ms for all charge weights. The risetime, t_r , is defined as 10% of the time of arrival, i.e. 1.6 ms [1].

In Table 2 the prediction of free-field shock wave parameters in front of the structure and the in-structure acceleration for this experimental set-up are presented.

Table 2 Prediction of free-field and in-structure parameters [1]

$R/W^{1/3}$ ($\text{m/kg}^{1/3}$)	P_0 (kPa)	t_0 (ms)	t_r (ms)	A_{TM}^* (m/s^2)
6.0	3.8	32	1.6	4.8
4.8	7.7	32	1.6	9.7
4.2	11.5	32	1.6	14.5
3.8	5.3	32	1.6	19.4

$A_{TM}^* = \text{In-structure acceleration } (= RF \cdot A_{avg})$

One-Mass-Spring System calculations

As explained earlier, the Technical Manual procedures ignore the interaction process taking place between the ground shock and structure. To quantify this miscalculation towards in-structure motions, One-Mass-Spring System calculations are performed with the predicted and the measured interaction load. One of the major difficulties to determine the dynamic response of a structure in soil is quantifying the volume of soil that offers resistance against the motion of the structure and therefore the spring constant. Richart [4] defines the spring constant, k , for a One-Mass-Spring System as function of the shear modulus, a normalized radius of the surface that experiences the resistance, the length of the structure and Poisson's ratio of the soil. According to reference [4] the spring constant for this set-up has a value of $9.6 \cdot 10^7 \text{ N/m}$.

The damping of the system is characterized with the acoustic impedance [5] and measures $2.7 \cdot 10^5 \text{ kg/m}^2 \cdot \text{s}$ [1].

The response of the Mass-Spring System is calculated with the predicted and measured interaction load. In the case of the predicted load its shape is simplified to a triangular shape with a certain risetime, peak load and duration. The risetime as well as the duration of the load function is the same as for free-field shock wave. The amplitude is amplified with a factor two to include the reflection process. This is the case in which the structure does not move during impact and is therefore the worst case. Calculations have shown that the influence of the rarefaction process, i.e. the influence of the kink in the decay of the load (see Figure 3) on the peak response is negligible. Therefore the decrease of the load is taken to be linear.

Figure 4 shows the response of the lumped mass loaded with a pressure-time diagram as predicted with the TM5-855-1 (scaled distance $3.8 \text{ m/kg}^{1/3}$), i.e. peak pressure is $30.6 (2 \times 15.3) \text{ kPa}$, duration is 32 ms and risetime is 1.6 ms.

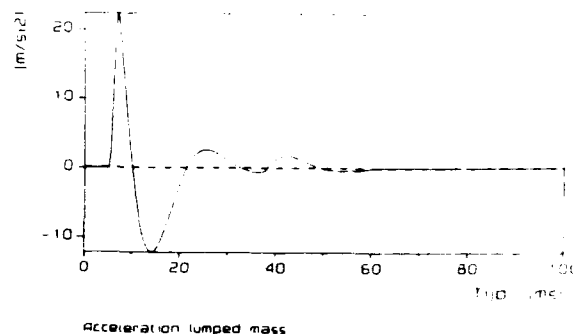


Figure 4 Acceleration of lumped mass (scaled distance $3.8 \text{ m/kg}^{1/3}$) to TM5-855-1 load.

The response of the Mass-Spring System on the measured load, i.e. peak pressure is 43.6 kPa, duration is 17 ms and risetime is 3 ms [2], is shown in Figure 5.

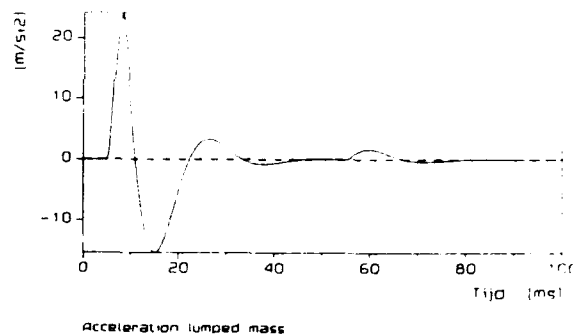


Figure 5 Acceleration of lumped mass (scaled distance $3.8 \text{ m/kg}^{1/3}$) to measured load.

This response simulations are also performed for the remaining scaled distances of 4.2, 4.8 and $6.0 \text{ m/kg}^{1/3}$. The results are presented in Table 2.

Experimental results

On each scaled distance three experiments are performed. Figure 6 shows an example of a measured in-structure acceleration in the case of a scaled distance of $3.8 \text{ m/kg}^{1/3}$.

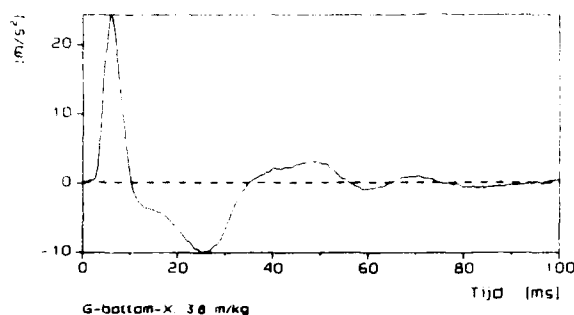


Figure 6 Example of measured in-structure acceleration (scaled distance $3.8 \text{ m/kg}^{1/3}$).

The mean measured peak accelerations of three experiments per scaled distance are presented in Table 3. In this table the predicted and Mass-Spring System results are also included.

Table 3 In-structure peak in-structure acceleration data

R/W ^{1/3} (m/kg ^{1/3})	ATM (m/s ²)	ATM-SDOF (m/s ²)	AME-SDOF (m/s ²)	AMEAS (m/s ²)
6.0	4.8	5.2	7.9	10.2
4.8	9.7	10.6	12.9	14.7
4.2	14.5	15.8	7.3	19.9
3.8	9.4	22.4	24.2	25.1

ATM = Prediction of TM5-855-1

ATM-SDOF = Response One-Mass-Spring System on twice TM free-field load

AME-SDOF = Response One-Mass-Spring System on measured interaction load

AMEAS = Mean measured value

Table 3 shows that the TM5-855-1 predictions, which are assumed to be on the conservative side, underpredict the in-structure acceleration.

The calculations of the response of the Mass-Spring System on the predicted free-field loads are executed with a reflection factor 2 (ATM-SDOF). The peak acceleration of the lumped mass is about 10% higher than the predictions (ATM). With this result it is concluded that in this particular test case the structures' peak response is almost the same as the soil particles so the TM5-855-1 procedure is in this particular case accurate. To quantify the effect of another mass weight on the dynamic response the same calculation is performed with a mass of 5000 kg and 500 kg in stead of 1000 kg on a scaled distance of $3.8 \text{ m/kg}^{1/3}$. The results are respectively a peak acceleration of 5.9 and 34.3 m/s² and are considerable different than the TM5-855-1 prediction of 19.4 m/s² (see Table 3). In this example only the mass is varied but it is obvious that also the other Mass-Spring parameters have effect on the response result. So it depends on the structure and surrounding soil characteristics if the prediction of the manual is acceptable or not.

In [2] and [3] it was stated that the measured free-field ground shock parameters were about 5 to 100% higher than the predictions depending on scaled distance. For useful comparison of the Mass-Spring System results with measured in-structure accelerations (AMEAS) the response calculations were also performed with the measured interaction pressure as load on the lumped mass. These Mass-Spring results (AME-SDOF) are almost similar with measured values (AMEAS).

The measured in-structure accelerations (AMEAS) are about 30 to 100% higher than predicted values (ATM). This means for this particular test program that the TM5-855-1 is not as conservative as it is presented. Nevertheless the TM5-855-1 procedures are presented only for preliminary design purposes and in that context they are useful.

CONCLUSIONS

The Technical Manual TM5-855-1 presents a procedure to determine in-structure shock data for preliminary design purposes. However, the manual ignores the aspects of the interaction process between ground shock and structure. The paper examined the introduced errors by comparison with experimental and theoretical results.

In the particular test set-up the approach of the TM5-855-1 to ignore the interaction process and the dynamic response of the structure, gives reasonable good results (within 10%). In general, it depends on the structure and surrounding soil characteristics in what extent the ignored interaction process influences the result.

The dynamic response determined with the proposed procedure agreed well with measured in-structure accelerations.

The applied procedure enables us to predict the in-structure shock, due to the measured load, within 30%.

The applicability of the TM5-855-1 to predict the in-structure shock is limited by the accuracy of the free-field ground shock. Under the applied test conditions the shock was underestimated up to 100%.

REFERENCES

1. TM5-855-1, 'Fundamentals of protective design for conventional weapons'. US Army Corps of Engineers, Huntsville Division, November, 1985.
2. Van Dongen, Ph., 'Verification of experimental determined ground shock parameters with TM5-855-1 and the response of a buried concrete structure' (in Dutch). PML 1991-69.
3. Van Dongen, Ph. and Weerheijm, J. 'Interaction of Ground Shock with Soil Pressure Transducers'. Structures Under Shock and Impact II: Proceedings of the Second International Conference, held in Portsmouth, U.K., 16th-18th June, 1992.
4. Richart, F.E. and Woods, R.D., 'Vibrations of soils and foundations', Prentice-Hall, Inc., Englewood Cliffs, New Jersey, 1970.
5. Hinman, E.E. and Weidlinger, P., 'Single-Degree-of-Freedom solution of structure-medium interaction. Internationales symposium 'Interaktion konventioneller munition mit schutzbauten', band 1. BRD, Mannheim, 09-13 März 1987.

STOCHASTIC SIMULATION OF IN-STRUCTURE SHOCK DUE TO CONVENTIONAL WEAPON EFFECTS

Erwin Kessler, Consultant of Laboratory Spiez
Bernard Anet

Defence Technology and Procurement Agency
Laboratory Spiez, CH-3700 Spiez, Switzerland

ABSTRACT

SHOCK is a computer program able to stochastically simulate in-structure shock effects within shelters due to conventional weapons effects. The simulation model combines three different shock components: the rigid body motion of the shelter, the inelastic deformation of the reinforced concrete structure and the elastic vibrations of the structure. The program provides stochastic default values, e.g. in term of probability distributions for many model parameters or the user has the option to define his own specific values for particular site conditions.

INTRODUCTION

Under contract with the Laboratory Spiez, a computer program has been developed to stochastically simulate in-structure shock effects within shelters. The name of the program is SHOCK. Some years ago, the nuclear shock simulation part of the program was completed and has been successfully applied since for various practical purposes such as shock testing of shelter equipment [1,2,3,4,5]. Conventional weapons effects are now implemented too and we are working on further improvements.

INSTRUCTURE SHOCK MODELING

The application range of the program SHOCK includes shallow buried reinforced concrete box-type shelters with

and without burster slabs (fig. 1). The simulation code combines three different shock components: (a) Rigid body motion of the shelter, (b) inelastic deformations and (c) elastic vibrations in the reinforced concrete structure.

(a) Rigid body motion

To calculate the motion of the center of gravity of the shelter, the structure is modelled by a rigid body embedded in the soil [2]. So far only a one-dimensional wave model is implemented, suited for superseismic nuclear loadings but less adapted to the case of conventional weapons loading because the plane wave assumption is rather inexact in this loading case. We are presently working towards a better solution.

(b) Inelastic deformations of the shelter

Dynamic inelastic deformations of the shelter are a main loading effect for equipment attached to the inside of the shelter. The ceiling, walls and floors of the shelter are modelled by Equivalent Simple Oscillators (one-degree of freedom) - a classical procedure - assuming that the main inelastic deformations are governed by the fundamental mode of the system. The soil-structure interaction is based on the interaction of one-dimensional ground shock waves with the moving and deforming shelter wall [2,5]. Meanwhile, this model has been developed and published independently by other authors [6,7,8]. The basic principle of the model is the physical fact that the dynamic soil pressure on a wall due to the reflection of a plane pressure wave becomes weaker, if the wall moves away due to rigid body motion and/or deformation.

(c) Elastic vibrations

The amplitudes of the elastic vibrations are limited by the ultimate strength of the shelter construction materials

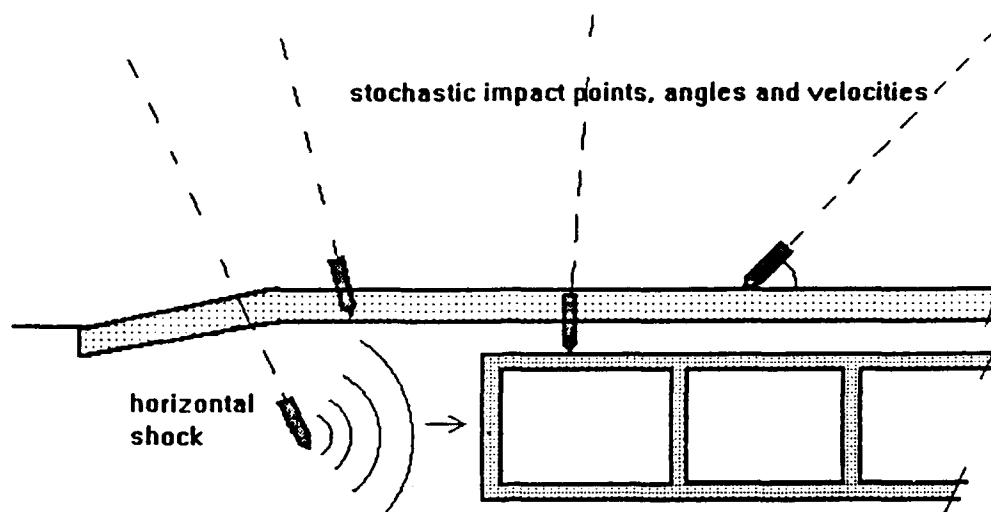


Fig. 1: Shelter concept underlying the program SHOCK

(steel, concrete). Although these elastic vibrations are mainly responsible for the peak acceleration level of the total shelter response, their contribution to the velocity and displacement of the shelter are small. They are therefore only critical for brittle equipment staying in direct contact with the shelter walls. Usual fixing elements are able to absorb the very small displacements related to high frequencies above 300 Hz. Thus the frequency range of the elastic vibration model for typical Swiss shelter has been chosen from about 50 Hz (the fundamental frequency) to 300 Hz. In this frequency range, nevertheless about 100 different vibrational modes can be identified for a three dimensional shelter construction. These modes cannot be calculated or measured exactly, as they are very sensitive to small variations in dimensions, stiffness, cracks etc that may occur under practical conditions. To overcome this inherent difficulty, a stochastic vibration model has been

developed with the the theoretical frequencies as mean values. Then 100 damped harmonic vibrations with stochastically changed frequency, phase and amplitude were superposed. This allows to determine the elastic vibration loading at each point of the shelter where equipments are attached. Although sophisticated analysis of the problem have been performed [4], the model is rather hypothetical and needs to be verified by large scale tests. The vibrations are damped by the soil contact as the vibration energy radiate into the soil. That means that the loading due to the elastic vibrations is less intense in small shelters than in larger ones with many partitioning walls which are not in contact with the soil. Such partitioning walls can vibrate quite freely in certain modes and induce resonance effects in attached equipment. The elastic vibrations of the shelter dominate the peak acceleration values of the total shelter response, but their contributions

to velocity and displacement are negligible.
The pressure time functions of the detonating weapons are taken from standard literature [10,11].

STOCHASTIC SHOCK SIMULATION AND EQUIPMENT TESTING

The not precisely known location of the many vibration modes of the shelter mentioned above is not the only aspect of the shock simulation problem requiring a stochastic modelling. The penetration of projectiles into soil and concrete is another one: to determine if a bomb perforates a shelter or if it causes spalling effects at the inside, a stochastic model has been implemented based on a paper presented by Lawrence Twisdale and others at the 5th International Symposium in Mannheim, Germany, in 1991. In this paper [9] probability distributions are given for the penetration depth of projectile and for the occurrence of spalling. For many other model parameters, our program provides "stochastic default values", that means probability distribution functions. Among these are: the actual impact point on the target taking into account the Circular Error Probability (CEP); the impact angle, velocity and the

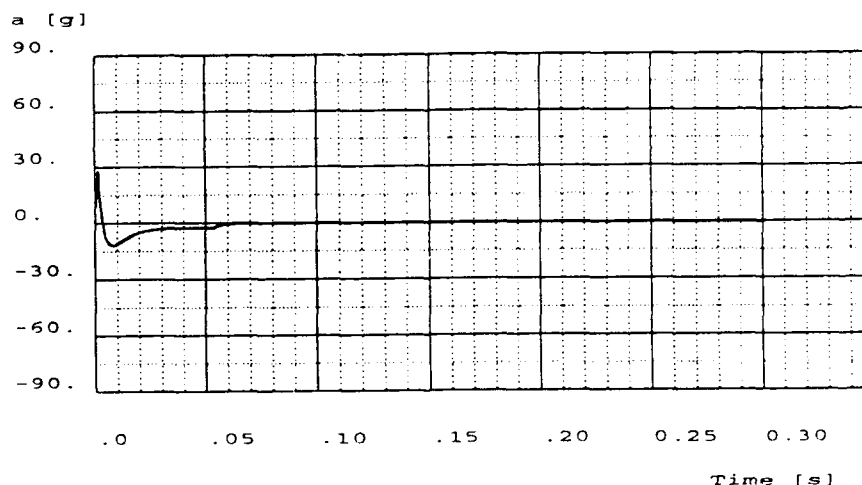
penetration characteristics of the bomb; the dynamic structural parameters of the shelter as well as the soil properties which are in our case representative of Swiss shelters. For each parameter the user has the option of applying either the pre-defined random variables or his own specific values for particular site conditions.

The results of a large number of purely stochastic simulations provide statistical information for certain shelter classes, enabling the user to define maximum instructure shock effects on the desired confidence level. This again is a basis for balanced shelter and equipment design. Furthermore, the stochastic shock-time-functions provided by the program can be used to drive servo-hydraulic facilities for shock testing of equipment and to gather information about survivability of a particular equipment.

EXAMPLE

A bomb with 250 kg TNT penetrates deep into the soil by the side of a small shelter and detonates 6 m away from the shelter wall. The shock time functions, here in terms of acceleration histories, are calculated for the following cases:

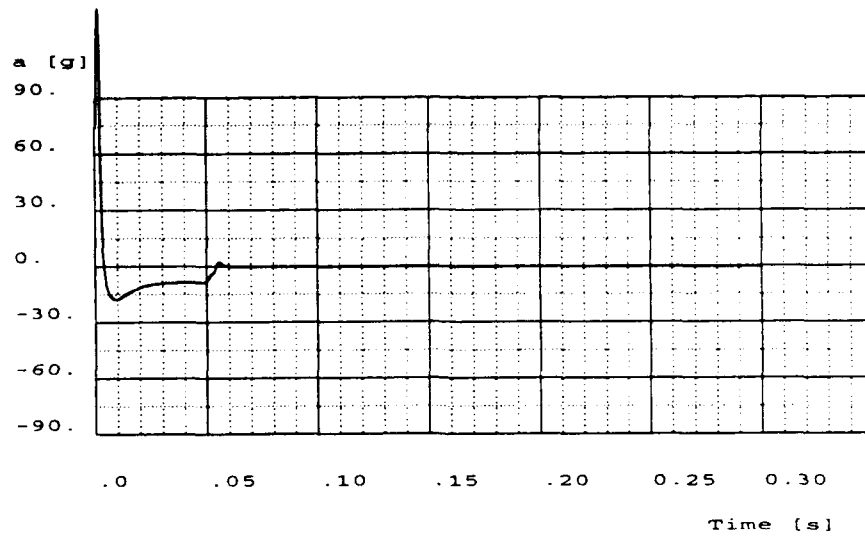
- a) **horizontal rigid body motion** of the the shelter (acceleration in units $g = 9.81 \text{ m/s}^2$):
- | | |
|----------------------|-----------|
| maximum acceleration | = 28.7 g |
| maximum velocity | = 2.0 m/s |



- b) **horizontal motion** at the center of the front wall due to rigid body motion
+ **inelastic deformation**:

maximum acceleration = 198.9 g

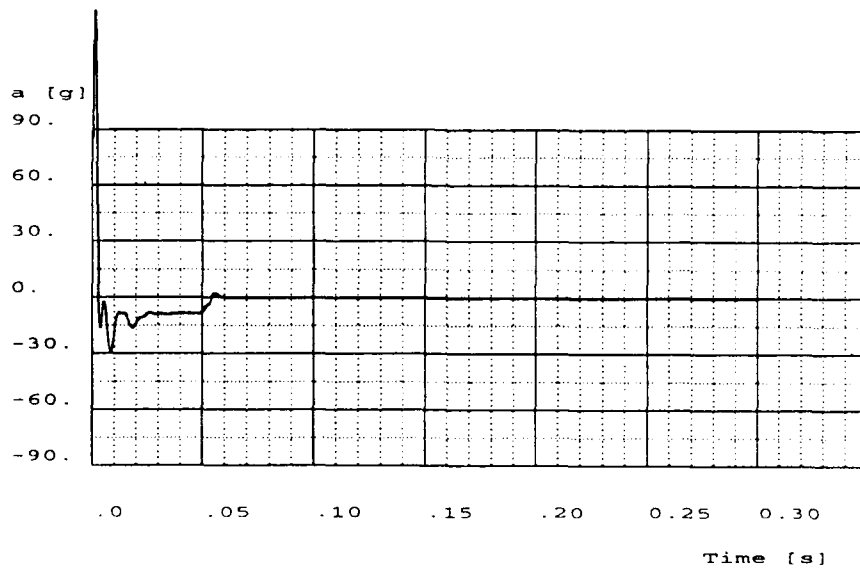
maximum velocity = 2.99 m/s



- c) **horizontal rigid body motion + inelastic deformation + elastic vibrations**
at the center of the wall:

maximum acceleration = 211 g

maximum velocity = 3.1 m/s



REFERENCES

1. **Kessler, E.**, "Stochastic Simulation of Shelter Equipment Vibrations due to Nuclear Explosions". Proceedings of the 8th International Symposium on Military Application of Blast Simulation MABS 8, 1983.
2. **Kessler, E.**, "Stochastische Simulation von Schutzraumerschütterungen infolge Nuklearexplosionen am Beispiel von 3-bar Zivilschutzbauten", Laboratory Spiez, 1985.
3. **Anet, B., Hunziker, P., Kessler, E.**, "Statistics of Stochastic Shelter Shock Motions Induced by Nuclear Explosions", MABS 9, 1985.
4. **Kessler/Brauchli**, "Step Load Response Analysis by Generalized Functions", Journal of Engineering Mechanics ASCE, No 112/3, March 1986.
5. **Kessler, E.**, "Loading of Shelter Walls due to Reflexion on Nuclear Air Blast Induced Ground Waves", Report Laboratory Spiez, No 8546, March 1987.
6. **Hinmann/Weidlinger**, "Single Degree of Freedom Solution of Structure-Medium Interaction", International Symposium on the Interaction of Conventional Munition with Shelters, Mannheim, Germany, 1987.
7. **Drake/Frank/Rochefort**, "A Simplified Method for the Prediction of the Ground Shock Loads on Buried Structures", International Symposium on the Interaction of Conventional Munition with Shelters, Mannheim Germany, 1987.
8. **Weidlinger/Hinmann**, "Analysis of Underground Protective Structures", ASCE Journal of Structural Engineering, July 1988.
9. **Sues/Hwang/Twisdale/Lavelle**, "Reliability-Based Design of R/C Structures for Protection Against Projectiles and Fragments", 5th International Symposium on the Interaction of Conventional Munition with Protective Structures, Mannheim, 1991.
10. **Drake/Twisdale et al.**, "Protective Construction Design Manual", ESL-TR-87-57, Air Force Engineering & Services Center, Tyndall Air Force Base, Florida, 1989.
11. "Fundamentals of Protective Design for Conventional Weapons", TM-5-855-1, Headquarters Department of the Army, Washington, 1986.

...

SUB SURFACE BARRIERS FOR GROUND SHOCK ATTENUATION: NUMERICAL TECHNIQUES TO MODEL EXPERIMENTAL RESULTS

Leslie J. Kennedy¹, Major Frederick G. Hulton RE² and Michael C.R. Davies³

¹Royal Military College of Science (Cranfield) Shrivenham UK

²Defence Research Agency, Christchurch UK

³University of Wales, Cardiff UK

ABSTRACT

The paper charts the development of a numerical model, using the AUTODYN finite difference computer code, designed to replicate centrifuge experiments carried out to examine the effects of sub surface barriers on ground shock attenuation. The experimental results have been used to validate the model performance but the material models used have derived from other sources. In this way the model is independent of the experimental parameters. The numerical modelling has not included the model structures used in the original experimentation but has concentrated upon free field pressures in front of and behind the various barrier options tried viz polystyrene foam, concrete and composite. The modelling results show an encouraging agreement with experimental measurements. Some limitation in the soil model has been identified due to the unknown effects of pore water pressures but, at a reasonable working range for structures, the model produces very acceptable results.

INTRODUCTION

Sub surface barriers have been considered for screening the effects of ground shock against underground structures. Such barriers might be installed during the building of these structures or else be added later to enhance protection. Barriers could screen out the ground transmitted shock altogether or just attenuate the shock and loading effects. The traditional approach to ground shock prediction has been to carry out instrumented tests at full scale and use the results to derive the likely effects in similar situations. Full scale tests are very expensive and considerable effort has been devoted to making use of scale modelling techniques and numerical analysis. Such techniques require validation. It has been shown that model testing in a centrifuge gives good results, because the self weight of the soil is increased to prototype values [Reference 1].

However, even centrifuge tests are considerable undertakings and this makes computer modelling an

attractive option as well. The benefits of computer modelling are: the accurate prediction of results by computer reduces the need for experiment, with savings in both time and money; also, because a computer can readily produce far more results than an experiment, the computer model can be used to select the most fruitful areas for experimental investigation and, finally, if the mathematical model is a good idealisation, it may aid understanding of physical behaviour.

With the rapid evolution of computer capabilities, the prime need is to validate the numerical models being developed. The paucity of data from explosive tests make the dynamic effects of explosive events and material response at high rates of strain difficult to model. A number of researchers are working to develop better material models and techniques [eg References 2,3 and 4].

Centrifuge model tests provide an excellent means of validating numerical methods by comparing results obtained. In a scale model, the boundary conditions are exactly specified; removing the necessity for making approximations of boundary locations in the analysis. Materials which have well defined properties may be chosen for the model and the repeatability of model tests permits the applied loading and system response to be closely monitored.

Studies of the attenuation of ground shock using protective barriers have been conducted using centrifuge model testing [References 1 and 5] and these have provided the opportunity to make use of the recent advances in numerical modelling to develop a method which can be validated using the results from the centrifuge experiments.

It is important to distinguish between models which rely on input data obtainable only from experiments involving the situations to be modelled and models that can predict results using input data obtained from other sources. The former type of model should, within its range of

applicability, produce good predictive results but it will be of limited value in increasing understanding of the physics of the problem. The latter type of model is more difficult to construct but is potentially more valuable; for once suitable idealisations have been developed, the predictive power of the model should not be restricted to the field for which it was developed. This latter approach has been followed in the modelling to be described.

This paper reports the development of a model using the AUTODYN finite difference computer code and compares the results obtained with those from the centrifuge experiments with barriers.

THE EXPERIMENTAL BACKGROUND

The experiments were carried out using the geotechnical centrifuge at the University of Manchester. This has a diameter of 6.4 m. A field of 20 gravities was applied to cylindrical steel experimental containers of 75cm diameter and 46cm depth. The containers were lined with 12mm polystyrene foam to reduce internal stress wave reflections and were filled with Mersey River sand, drained from saturation to equilibrium. A charge equivalent to 2g C4 was buried centrally and model structures were buried at a range of 20cm; some unprotected and some protected by subsurface barriers. Experiments were comprehensively instrumented. A typical experimental arrangement is shown in figure 1. Three types of barrier were used on chords 15cm from the axis. They were 12 mm polystyrene foam, 15 mm concrete and a combination of the two.

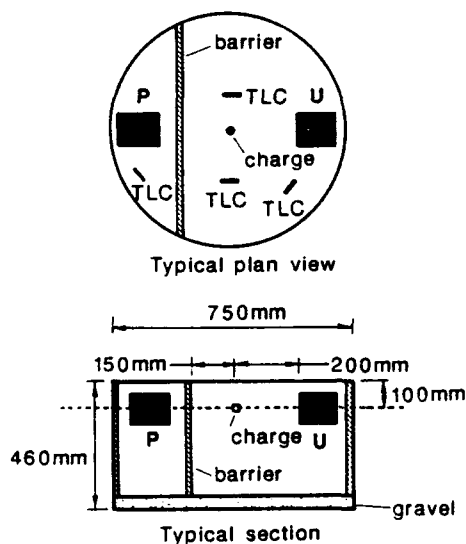


Figure 1. Details of experimental test bed (P: Protected structure, U: Unprotected structure, TLC: Total pressure cell)

NUMERICAL MODEL

The modelling was carried out using AUTODYN-2D Version 2.52. This is a two dimensional non-linear hydrodynamic finite difference computer code. In this code the conservation of mass, momentum and energy are expressed through differential equations which are solved with an explicit, centred difference time integration method. Materials are described through an equation of state and a failure model. Both Eulerian and Lagrangian processors are available. An axial symmetry option is provided.

Since the experiments took place in cylindrical containers the axial symmetry model was appropriate. Because of the large deformations involved in crater formation, it was decided to use a single Eulerian grid for the whole model. The grid chosen was rectangular, with a graduated mesh in both radial and axial directions. The mesh was finest in the area of the explosive and at radius 15cm (the barrier position). For preliminary studies a mesh of 30(radial) x 70(axial) was used. This was progressively refined to 140x60.

Various boundary conditions were used in developing the model and the final choice was a Foam-Transmit boundary in which the boundary behaved towards pressure waves as a polystyrene foam boundary. This option was chosen as the closest approximation to the experimental set-up.

An axial gravitational field was incorporated into the model. Time limitations prevented the development of an equilibrium stress distribution in the soil before the explosion, but a later computer simulation (over a two week period) showed that this deviation from physical reality is not important.

MATERIALS AND THEIR MODELLING

The materials to be modelled were explosive, air, sand and the barrier materials of polystyrene foam and concrete. AUTODYN contains a library of material models, including ones for explosives. Explosive C4 was chosen. For air, an ideal gas model was selected. The other material selections are discussed below.

Sand

The experimental material was a Mersey River sand. The grading curve for the sand is given in figure 2 and the relationship between its porosity and angle of friction in figure 3 [Reference 6]. The sand was modelled using the Porous equation of state and the Mohr-Coulomb Failure Model. Data on the static high pressure of West Freugh sand of the same mineral content and similar grading

(see figure 2) was provided [Reference 7]. This information was obtained from the database maintained by Imperial College, London and was generated using the GREAC cell technique [see Reference 4]. The data was modified by the incorporation of the experimental value of density and sound speed for the Mersey River sand. For the failure model, an angle of friction of 44 degrees was chosen, as appropriate to a dense condition or low porosity, the expected state at high pressures (see figure 3). The idealisation chosen was the simplest that could take into account the main physical characteristics of the sand. But, it does not model the effects of partial saturation on stiffness at high loading rates and does not take into account the varying relationship between porosity and angle of friction.

Foam

In comparison with the mass of sand, the mass of foam was very small and so thus was its comparative capacity for the irreversible absorption of energy through plastic action. It therefore seemed reasonable to model the foam as a linear elastic fluid; this being the most simple model in which a low acoustic impedance can be given.

Concrete

This was modelled using the Porous equation of state and the Mohr-Coulomb failure model. Input was based on data for a similar concrete [Reference 7].

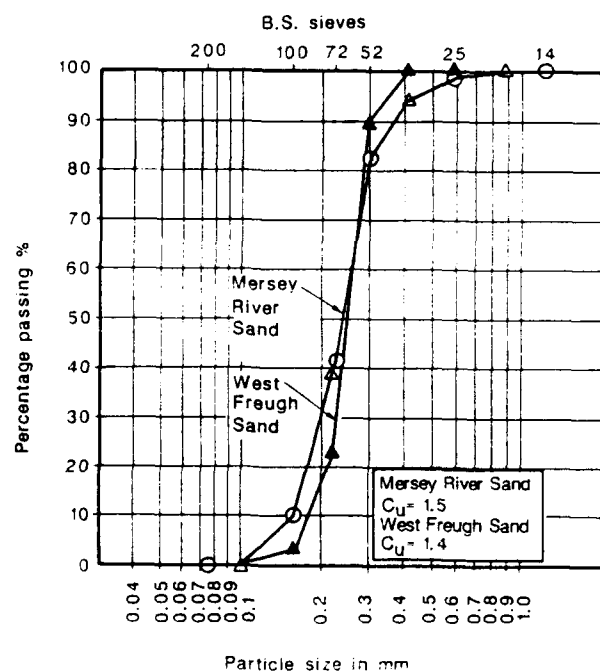


Figure 2. Grading curves for Mersey River sand (Reference 6) and West Freugh sand.

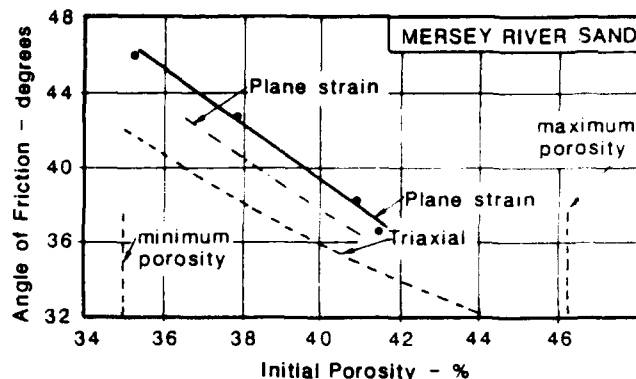


Figure 3. Mersey River sand: Angle of friction vs porosity (Reference 6).

MODEL DEVELOPMENT

Preliminary runs were made using a grid of 30(radial) x 70(axial) cells and forming a cylinder 75cm x 100cm, as in the experimental work. The objectives of the preliminary runs were to confirm that the model gave satisfactory qualitative behaviour, to investigate boundary models and to gain experience in the use and characteristics of the model. Several runs were extended until craters were fully developed; a process too time consuming to repeat using finer grids. Having confirmed the general suitability of the model and the selection of boundary conditions, the grid was refined to 50 x 70, with closely meshed areas containing the explosive and at the 15cm radius area, where foam barriers could be inserted. Runs were made both with and without a 12mm thick foam barrier at 15cm. At 20cm radius there was good agreement with experimental results. However, at low ranges the computer model gave lower values than the experiment and there were indications that some results were significantly affected by the discretisation chosen. The radial meshing was therefore refined to produce a final mesh of 140 x 60. The developments had the combined benefits of increasing the precision of the model and allowing the effects of varying the discretisation to be studied.

CRATERING

The modelling of crater development was most useful in confirming the qualitative behaviour of the model. Convincing results were achieved during the examination of crater development and a final result is illustrated at figure 4. The model crater shown is larger than a typical experimental one and conical in shape when compared with the bowl shape of experimentally produced craters.

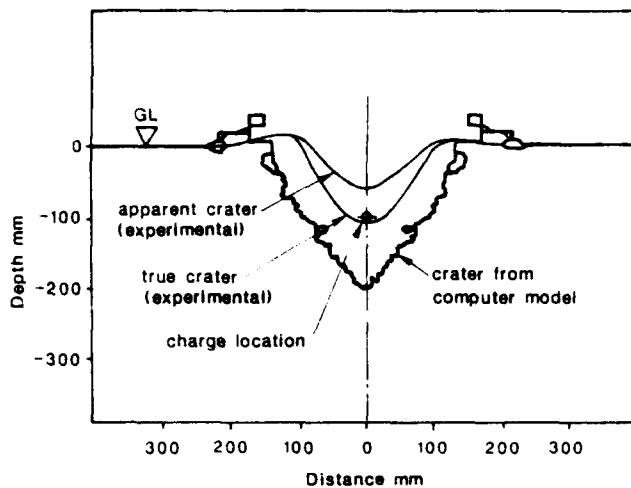


Figure 4. Typical crater outlines from modelling and experiment.

FREE FIELD PRESSURES

The pressure-time output from the model showed typical results with steep rise times to peak values that diminished with range (figure 5). Comparisons with experimental values are illustrated in figure 6, which shows peak pressures against distance from the charge centre. At shorter ranges the model appears to underpredict pressure values but at ranges of 20 cm and beyond the agreement is much better. In the experimental tests, 20 cm was taken as the target range.

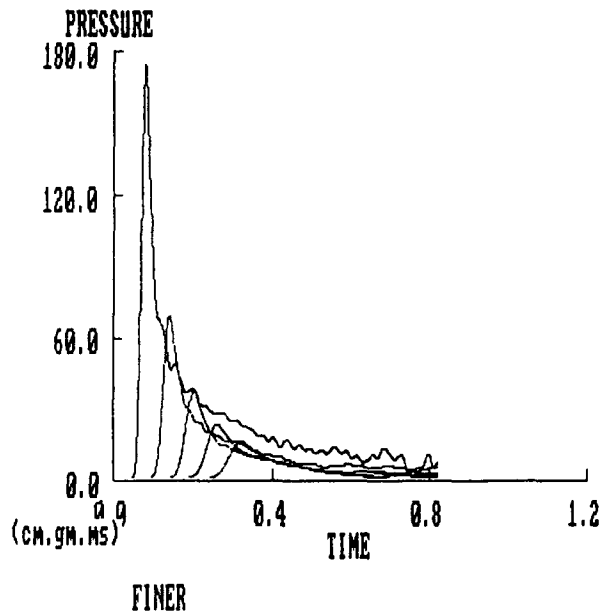


Figure 5. Free field pressure outputs at 5 to 17 cm from charge centre.

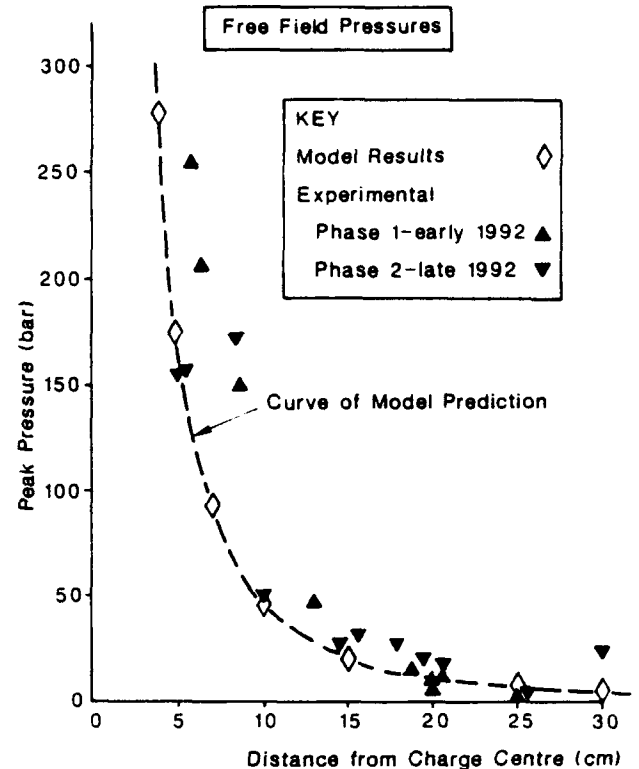


Figure 6. Free field pressure vs distance from charge centre

BARRIER EFFECTS

The modelling work included runs with barriers included at 15 cm range. The barriers were 12 mm polystyrene, 15 mm concrete and a composite of the two. The results are illustrated in figure 7. A typical set of pressure-time plots at ranges behind a foam barrier are shown at figure 8. Figure 7 shows the model free field peak pressures for comparison and the model and experimental values behind the various barriers. Table 1 shows the attenuation efficiency of the barriers as the percentage reduction in peak pressure values in comparison with the free field results. The target range of 20 cm has been selected to coincide with the experimental structure positions.

Table 1: Pressure reductions behind barriers at 20 cm range

Barrier Type	Model	Experiment
Foam	75%	92%
Concrete	30%	78%
Composite	69%	93%

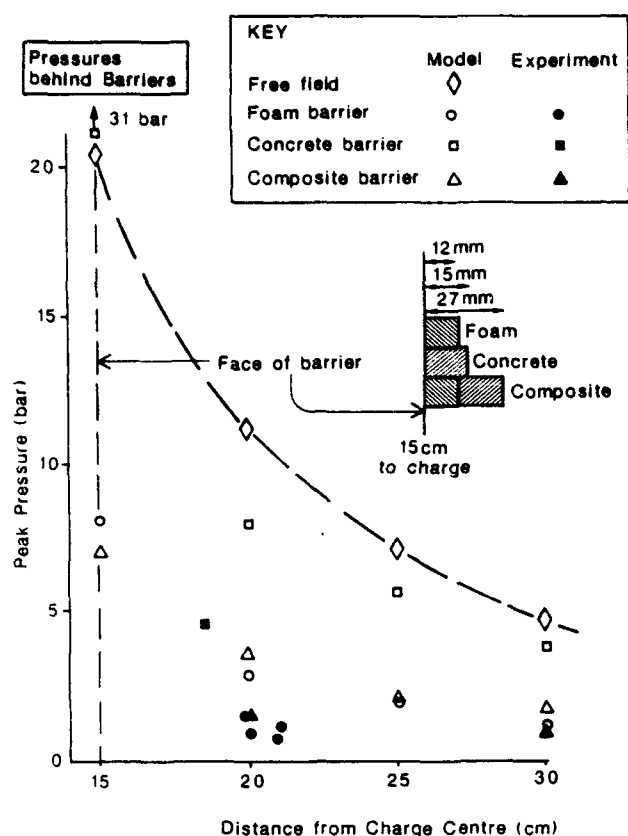


Figure 7. Pressure reductions behind barriers.

The figures in the table show a significant underestimate by the model of the experimental attenuations achieved. However, the general trend of variations between barrier types is modelled. Also, the model predictions are on the safe side. Because the experimental pressure gauges were not always at exactly 20 cm from the charge centre, some judgement has been necessary in calculating the figures. Figure 7 clearly shows the relationships too. In addition, it should be noted that the experimental barrier was planar, whereas the model barrier is cylindrical. Off the normal, the distance to the experimental barrier is increased and the barrier thickness is also increased. Refraction effects may occur.

DISCUSSION OF RESULTS

The preliminary work produced model craters of realistic form though incorrectly proportioned. The lesser scale of the experimental craters, when compared with the model version (figure 4), was probably due to the influence of pore water. The initial experimental set up had relied upon suction pressures in the pore water to achieve stability (to hold the model intact on its side prior to centrifuge spin up). During soil failure under explosive pressures, dilatancy effects would have enhanced negative pore

pressures and increased the effective soil strength. This would reduce the crater volume. The numerical model, of course, made no allowance for the presence of pore water.

The numerical model did not reproduce the standard bowl shape. The true angle of friction is a function of porosity, thus at the sides of the crater, where the sand has been compressed by the shock wave, the angle of friction is comparatively steep but elsewhere, particularly in fallen ejecta, the angle is lower. This produces the characteristic bowl shape. The linear Mohr-Coulomb model must inevitably produce a cone-shaped crater. To provide a more exact result, it is likely that a material model including the influence of pore water would be needed. However, crater prediction is not a particular area of uncertainty because there is plentiful empirical data available with reasonable predictive relationships [Reference 8].

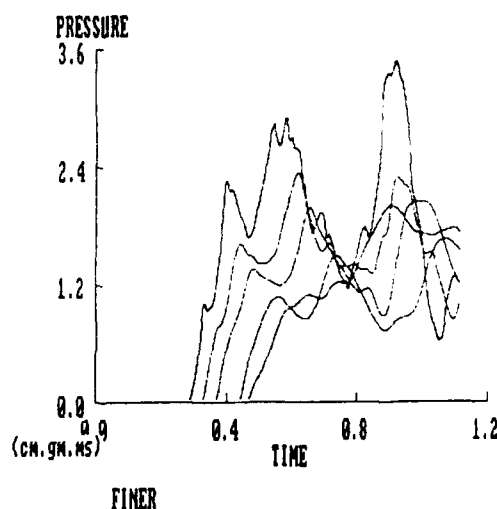


Figure 8. Pressure plots behind composite barrier at "targets" spaced from 20 to 28 cm from charge centre.

The free field pressure predictions, best summarised in figure 6, show reasonable agreement with experimental results, particularly at the range of interest for structures being considered for barrier protection ie 20 cm in the model. The higher experimental values at short range may be due to the means of recording pressures. Experimentally, free field pressures are measured using load cells of finite mass, so there is inevitably some soil-structure interaction which is likely to enhance the pressures recorded [Reference 9]. This effect is likely to be most marked in areas of high rate loading near the explosion and less significant when loading is slower. On the other hand, since the mathematical model chosen does not take account of stiffness enhancement on initial loading at high rates in partially saturated soil, the computer model might underpredict free field pressures close to the explosion.

The behind barrier effects, which are best summarised in figure 7, have been over-predicted by the model. This provides a safe solution. There is closer agreement with the foam barrier results and this also applies to the foam-concrete composite. These barriers are shown, by both modelling techniques, to be effective in reducing ground shock. This is, however, not the complete situation. Underground explosions can produce two forms of pressure loading on buried structures: "shock loading" and "inertial loading" [Reference 1]. Shock loading is essentially the loading produced by free field pressure waves, which may be enhanced on reflection at the soil-structure boundary. Shock loading may be mitigated by the insertion of low acoustic impedance barriers in the path of the shock wave. Inertial loading is the effect of the momentum of the soil mass set in motion by the explosion. Since momentum cannot be reflected, a foam barrier will have minimal effect on inertial loading but a rigid barrier may provide some protection.

The experimental programme was designed to study barriers protecting against both forms of loading. However, while free field pressures give a good indication of shock loading pressures, inertial loading does not become apparent until the motion of the soil mass is obstructed by a structure. Unlike the experimental set-up, the computer model does not contain structures and so is restricted for the time being to the investigation of free field pressures, the determinants of shock loading

CONCLUSIONS

There is very good qualitative agreement between the experimental results and the output of the mathematical model developed. For the region of predominant interest (range 20cm) there is good quantitative agreement for free-field stresses in the absence of a barrier and adequate agreement for the attenuation effects with various types of barrier.

A satisfactory mathematical model of the soil was constructed using data obtained from non-explosive experiments. However, the model could usefully be developed further to take account of the effects of partial saturation, though this would be difficult, and thereby improve the prediction of free-field pressures. Also, the variation of angle of friction with porosity could be incorporated to improve crater shape.

The shock attenuation effect, when using barriers, shown by the model was in line with the experimental results though less in scale. The numerical model developed gives sufficient confidence in the method and the material models to carry on with the work. It is intended to develop the model further: by the introduction of buried structures

to allow the study of soil-structure interaction, in particular the phenomenon of inertial loading and by the use of a 3-D model program.

ACKNOWLEDGEMENT

The experimental results were produced with the support of the Procurement Executive, Ministry of Defence and on behalf of the Defence Research Agency, Christchurch.

REFERENCES

1. Davies MCR and Williams AJ "Centrifuge Modelling the Protection of Buried Structures subjected to Blast Loading" Structures under Shock and Impact II Bulson PS Ed., Thomas Telford London, pp 663-674, 1992
2. Stevens DJ and Krauthammer T "A Finite Difference/Finite Element Approach to Dynamic Soil-Structure Interaction Modelling", Comp and Str 29 (2), pp 199-205, 1988
3. Pullen AD, Ianucci L, Newman JB and Perry SH, "Experimental Investigation of the Dynamic Loading of Soil and the use of Finite Element Simulation for Analysis", Structures under Shock and Impact Bulson PS Ed, Elsevier Amsterdam, pp 443-454, 1989
4. Sheridan AJ, Pullen AD and Newman JB, "The Search for a General Geologic Material Model for Application to Finite Element Methods and Hydrocodes", Structures under Shock and Impact II, Bulson PS Ed, Thomas Telford London, pp 199-210, 1992
5. Davies MCR, Williams AJ and Claber KJ, "Centrifuge Model Testing to investigate the use of Barriers to mitigate Blast Effects on Buried Structures", Proc 6th International Symposium on Interaction of Nonnuclear Munitions with Structures, Panama City Beach Florida, May 1993
6. Private Communication from University of Manchester Engineering Department, 1992
7. Private Communication from the Defence Research Agency Farnborough, 1992
8. TM5-855-1 Fundamentals of Protective Design for Conventional Weapons, HQ Dept of the Army, Nov 1986
9. Dongen Ph van and Weerheijm J, "Interaction of Ground Shock with Soil Pressure Transducers", Structures under Shock and Impact II, Bulson PS Ed, Thomas Telford London, pp 625-635, 1992

MATERIALS FOR EXTERNAL SHOCK MITIGATION

Larry C. Muszynski
Michael L. Rochefort

Applied Research Associates, Inc.
Gulf Coast Division, Tyndall AFB, FL

Abstract

Shock mitigating materials can be used to enhance the survivability of any buried structure subjected to ground shock. Two shock mitigating material systems were developed and tested. Both materials significantly reduced both peak pressure and the impulse transmitted to a buried structure. Both systems use large volumes of entrapped air to isolate a structure from the impinging shock wave. In explosive tests at Tyndall AFB, a conventional weapon was detonated near a below-grade wall of a typical hardened protective structure. Two sections of the wall were protected by candidate shock mitigation systems. Pressure gauges were used to record the actual ground shock attenuation. One section of the shelter wall was protected by a material system consisting of various size plastic bottles cemented together with a low density cementitious mortar. The second section of the wall was protected by a system of epoxied hollow ceramic beads. Pressure gauges showed that both material systems attenuated 90 percent of the peak ground shock stress, and the plastic bottle composite system attenuated 95 percent of the ground shock impulse.

Background

The structural design of buried protective structures to resist the effects of blast loading can be simplified if the structure can be designed to attenuate the stress wave when shock-loaded. Conservative designs of buried structures to resist blast loadings can result in costly solutions.

The use of external, shock-mitigating "backpack" materials surrounding a structure is one method of protecting a buried structure from the effects of blast loading. This method holds promise for retrofitting existing buried structures to provide additional protection from ground shock. By "backpacking" a buried structure, stress can be attenuated when a shock wave is transmitted through the backpacking material to the structure.

A suitable shock-absorbing backpacking material should be crushable and should possess a low compressive strength and a high degree of compressibility, thereby reducing the magnitude of peak stress reaching the structure, and should accommodate

the peak deformation of the backfill material without a sharp increase in stress above the compressive strength.

The majority of compressible materials that fit these criteria fall into two categories: materials having no distinct yield point; and materials having a distinct yield point. These materials are referred to as plasto-elastic and elasto-plastic, respectively, as shown in Figures 1 and 2.

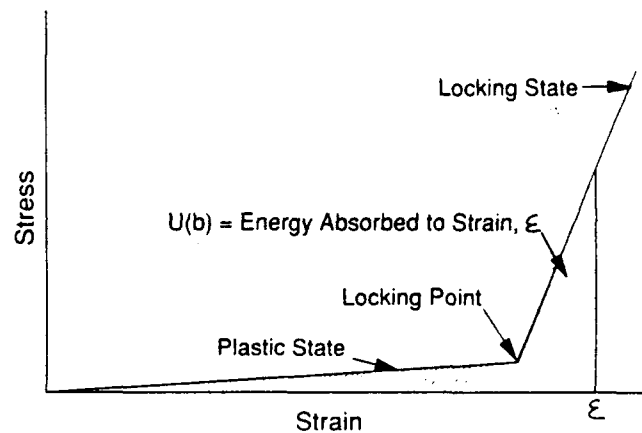


Figure 1. Stress-Strain Curve for Ideal Plasto-Elastic Material

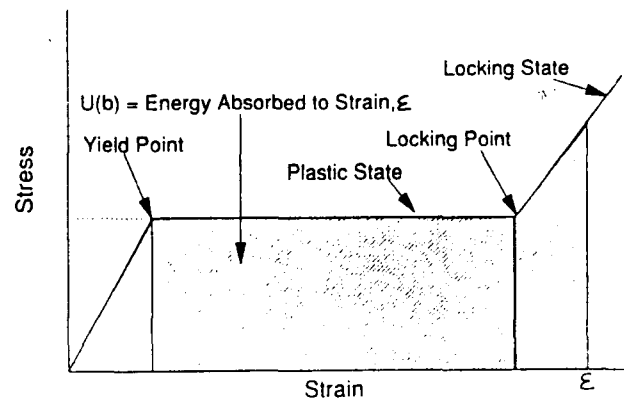


Figure 2. Stress-Strain Curve for Ideal Elasto-Plastic Material

The amount of energy absorbed by the backpacking material can be determined by calculating the area under the stress-strain curves. Typically, elasto-plastic materials are more efficient energy absorbers than plasto-elastic materials, but are also more costly.

Experimental

Materials that may mitigate the ground shock effects of close-in detonations of general purpose aerial munitions were evaluated. Assuming the detonation occurs at a sufficient scaled depth of burial for full energy coupling, that is, approximately $1.4 \text{ ft/lb}^{1/3}$ or greater; and at a scaled standoff of $2 \text{ ft/lb}^{1/3}$, the peak incident free-field stress may range from 200 to 10,000 psi, depending on the soil type and condition. For this type of scenario, the peak scaled free-field displacement may exceed $2 \text{ in/lb}^{1/3}$.

A. Selection Criteria

The basic requirement for external shock-mitigating (ESM) materials is that they possess certain characteristics associated with dynamic structure-medium interaction. The ESM material should dissipate incoming ground shock energy, reduce the input stress reaching the structure, and accommodate the deformation of the backfill surrounding the structure. Dynamic structure-medium interaction, due to ground shock resulting from detonating a conventional weapon below the ground surface, can be illustrated by three springs in series, the first representing the backfill, the second representing the ESM material, and the third representing the wall of a buried structure. Simply stated, the resistance of the ESM needs to be less than that of the wall, to accommodate the displacement of the backfill and reduce the deflection of the wall.

B. Materials

Materials that appear to perform satisfactorily as external shock mitigators are referred to as plasto-elastic and elasto-plastic. Examples of elasto-plastic materials include:

- Rigid Polyurethane foam
- Rigid Polystyrene foam
- Syntactic foam
- Cellular concrete
- Inorganic foam

Examples of plasto-elastic materials include:

- Expanded clay, shale, and slag
- Perlite & Vermiculite
- Flexible Organic foam
- Foamed Rubber
- Organic and Inorganic microballoons
- Expanded Polystyrene beads

Lab Evaluation of Candidate ESM Materials

Two candidate materials were thoroughly investigated. Hollow ceramic spheres, which are manufactured and distributed by 3M Corporation under the tradename Macrolite^R Ceramic Spheres, were utilized as a syntactic inorganic foam. These hollow,

ceramic spheres are made by a proprietary process that enables them to be very durable and lightweight.

A new and unique system was also proposed and tested. This system makes use of a novel method of incorporating large volumes of confined and entrapped air in a cementitious matrix. Empty polyester terephthalate (PET) bottles sealed with the caps in place were packed into a mold and infiltrated with a cellular cementitious material using a process similar to that used with preplaced aggregate concrete. The matrix was prepared using portland cement, water, and a chemical surfactant, to produce a lightweight cellular matrix having a dry unit weight of approximately 67 lbs/cubic foot.

1. Bonded Hollow Ceramic Spheres

The Macrolite^R (ML 535) hollow ceramic spheres used in this part of the laboratory effort had a size range of 5.7mm to 12.7mm, and a unit weight of 19 lbs/cubic foot. The spheres were bonded using an ordinary epoxy resin, at a concentration of 2 parts per hundred resin (phr), and having a viscosity of 500 centipoise at 25°C. The syntactic foam composite was ambient cured for 24 hours.

Figures 3 and 4 show static unconfined and confined compressive stress stress-strain curves for the bonded hollow ceramic spheres. In the unconfined state, the material was crushed, failing at a very small strain and producing a stress-strain curve similar to that of an ideal plasto-elastic material. In the confined condition, the material behaved like an ideal elasto-plastic material, and experienced lockup at about 20 percent strain.

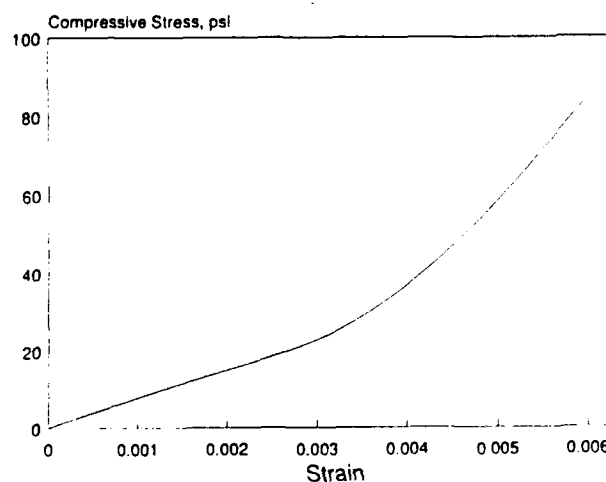


Figure 3. Unconfined Static Compressive Stress-Strain Curve of Bonded Hollow Ceramic Spheres

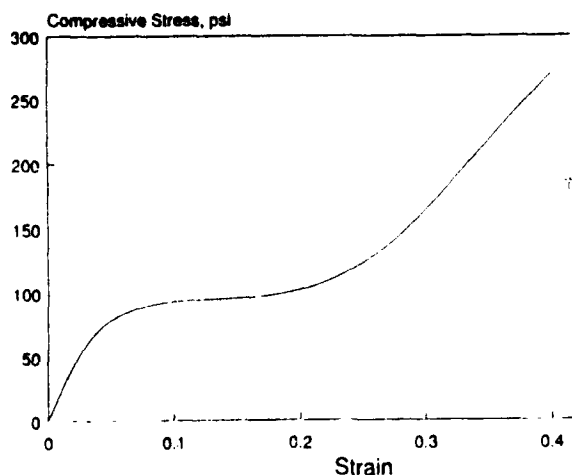


Figure 4. Confined Static Compressive Stress-Strain Curve of Bonded Hollow Ceramic Spheres

2. Cellular Grouted PET System

The cellular grout binder for the PET ESM material system was also tested, and the unconfined static compressive stress-strain curve is shown in Figure 5. The material appears to behave like an ideal plasto-elastic material. The static confined compressive stress-strain curve could not be generated in the lab because of load cell capacity restrictions.

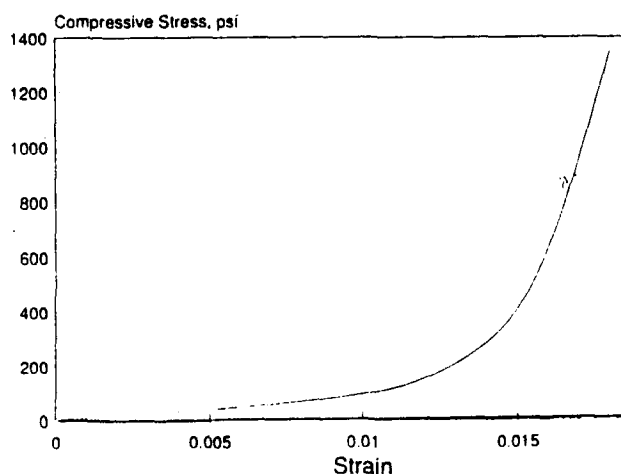


Figure 5. Unconfined Static Compression Stress-Strain Curve of the PET-ESM Cellular Grout Binder

Field Demonstration

A full-scale field demonstration was performed, incorporating a 1000 pound, general-purpose bomb, detonated against a buried basement wall of the NATO structure at the Tyndall AFB Sky-10 test site. The demonstration was performed to evaluate a current, state-of-the-art syntactic foam ESM material system, as

well as an entirely new system, consisting of grouted PET bottles

A Test Plan

Figure 6 illustrates the test site layout proposed for the two candidate ESM materials. Figure 7 shows the expected crater profile, from the denotation located on the north side of the NATO structure.

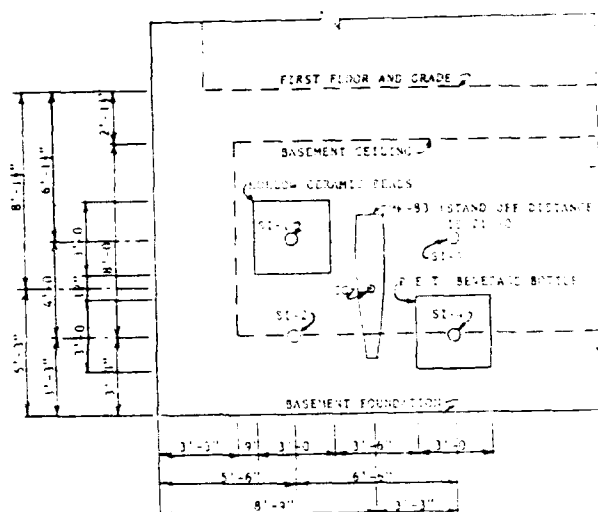


Figure 6. External Shock-Mitigation Field Test Site Layout

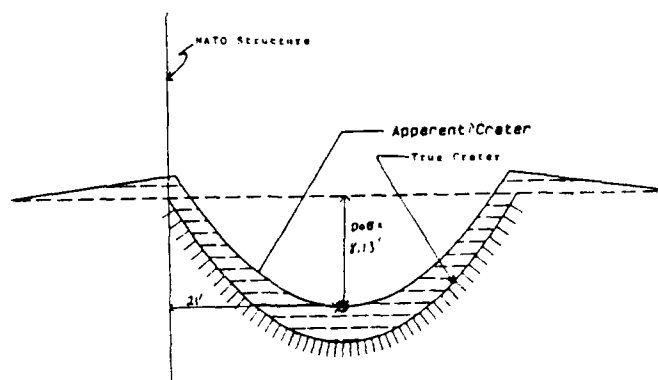


Figure 7. Crater Profile for 21 Foot Standoff

1. Test Description

The ESM systems were mounted against the basement wall of the NATO structure, equidistant from the center of gravity of the 1000-pound bomb, which was located 8.13 feet below the ground surface. Four pressure gauges were also placed equidistant from the bomb center of gravity. Gauges SI-2 and SI-3 were embedded in the bare concrete basement wall. Gauge SI-1 was centered and located directly behind the ESM material consisting of bonded hollow ceramic spheres (BHCS). Gauge SI-4 was centered and located directly behind the ESM material consisting of grouted PET (GPET) bottles.

The standoff distance for the bomb was 21 feet from the NATO structure (19.5 feet from the ESM outer surface). The standoff distance was calculated to give a soil displacement of approximately 0.75 feet, which corresponds to 50 percent strain in the 18 inch thick ESM material systems. The following equation was used for scaled peak free-field soil displacement:

$$d_0/W^{1/3} = f(500)(1/c)(R/W^{1/3})^{-n+1}$$

where $c = 600$ fps

$$n = 3.25$$

$$W = 526 \text{ lbs}$$

Seismic velocity, $c = 600$ fps, for loose, dry, poorly graded sand. This yields the following result for the standoff distance, R (ft):

$$R = (1.0)(500)(526)^{1/3} / 1.25 (526)^{1/3} = 21.4 \text{ feet}$$

2 Materials

The mold used to preplace the PET bottles measured 3 by 3-foot by 18-inch in depth. The cellular grout was poured into the sealed mold, and infiltrated the interspaces between the sealed PET bottles. The finished mold weighed 434 pounds, and based on the unit weight of the cellular concrete, 67 lbs/cubic foot, the void volume (percent volume of air) was calculated to be 52 percent.

The hollow ceramic spheres, ranging in diameter from 5.7mm to 12.7mm and having a bulk density of 19 lbs/cubic foot, were used to produce another potential ESM system. An epoxy binder was used to "glue" the beads together, and the composite material was cast into a mold of the same dimensions described above. The hollow spheres were premixed with 2 percent epoxy by weight prior to being introduced into the mold and cured overnight at room temperature. Based on the unit weight of the hollow spheres, and the weight of the finished ESM material, 305 lbs, the void volume (percent volume of air) was calculated to be 38 percent.

B. Explosive Test

The north basement wall of a typical hardened shelter at Tyndall AFB, was excavated, and pressure gauges were attached to the wall at the appropriate locations relative to the center of gravity of the 1000 pound bomb. The ESM material systems were then buried, and the soil compacted, prior to placement of the bomb guide tube at the 21 foot standoff distance, and at a depth such that the bomb c.g. would be 8.13 feet below the ground surface. The 1000 pound bomb was armed, and subsequently lowered into place.

1 Results

The detonation created a crater approximately 45 feet in diameter and 15 feet deep. The BHCS and the GPET ESM systems were excavated and examined. The BHCS ESM system sustained a permanent deformation of 9 to 10 inches, measured

with a rule. The GPET ESM system sustained a permanent deformation of only 1 to 2 inches, measured with a rule. It appeared from the excavated samples that the GPET ESM system experienced about the same peak deformation as did the BHCS system, but decompressed and returned to almost its original size.

The pressure gauges located on the bare concrete basement wall, SI-2 and SI-3, recorded peak interface stresses of 1,150 psi and 548 psi, respectively. The theoretical interface pressure predicted by Conwep was about 490-500 psi. From the shape of the measured stress-time curve, it appears that gauge SI-2 malfunctioned, due to being contacted by a rock or bomb fragment. The transmitted stress recorded by gauge SI-1, centered behind the BHCS ESM system, recorded a peak stress of 52.3 psi, as shown in Figure 8. Gauge SI-4, centered behind the grouted PET ESM system, recorded a peak stress of 59.9 psi, as shown in Figure 9.

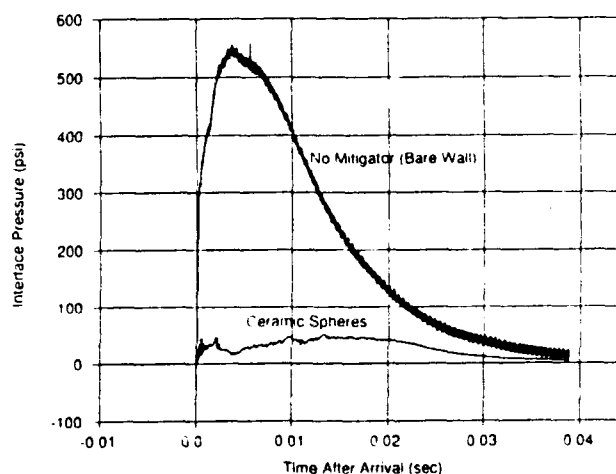


Figure 8. Interface Pressure for BHCS-ESM Material System versus that for Bare Concrete Wall

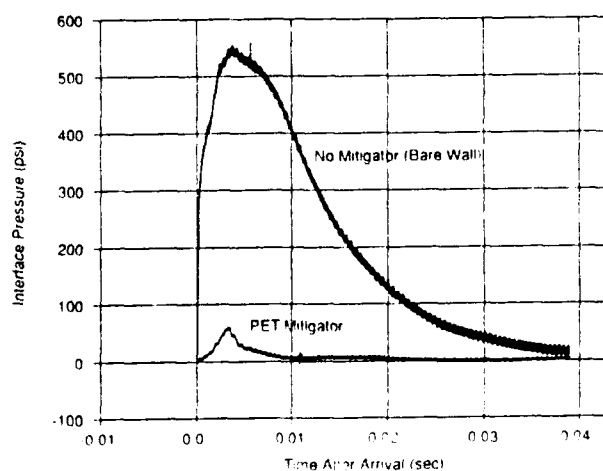


Figure 9. Interface Pressure for PET-ESM Material System versus that for Bare Concrete Wall

2. Conclusions

The primary conclusions that can be reached from the field test are the following:

- a Both ESM systems appeared to have accommodated the backfill deformation without lockup, and transmitted only about 10 percent of the peak free field stress to the concrete basement wall.
- b The grouted PET ESM system (GPET) appears to be able to function as desired under multiple ground shock loadings. This is a first for ESM materials, which in the past have all deformed or crushed irreversibly.
- c The GPET ESM system attenuated 96.1 percent of the ground shock impulse as shown in Figure 10, calculated from the area under the P-T curves.

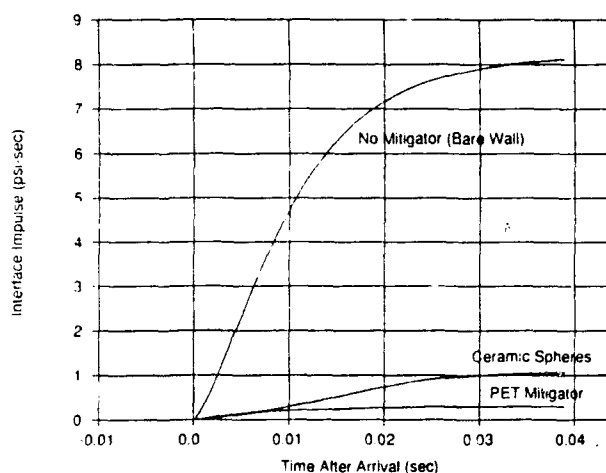


Figure 10. Comparison of Interface Impulse for Bare Concrete, the BHCS-ESM System, and the Grouted PET-ESM System

Summary

This work produced a very efficient ESM material system, composed of virgin or possibly recycled plastic PET containers, in a matrix consisting of a low-density foam system. Field testing demonstrated the utility of this ESM system, which transmitted only 10 percent of the peak ground shock stress, and attenuated 96.1 percent of the ground shock impulse.

Acknowledgements

The authors express gratitude to the Air Force Civil Engineering Support Agency (HQ AFCEA/RD), Tyndall Air Force Base for supporting this program.

References

- Sevin, Eugene, Ground Shock Isolation of Buried Structures, Armour Research Foundation of Illinois Institute of Technology, Report No. AFSWC-TR-59-47, Contract No. AF-29(601)-1134 for Air Force Special Weapons Center, Kirtland Air Force Base, New Mexico, August 1959.
- Sevin, E., Shenkman, S. and Welch, E., Ground Shock Isolation of Buried Structures, Armour Research Foundation of Illinois Institute of Technology, Report No. AFSWC-TR-61-51 Final Report, Contract No. AF-29(601)-2586 for Air Force Special Weapons Center, Kirtland Air Force Base, New Mexico, July 1961.
- Fowles, G.R., and Curran D.R., Experimental Testing of Shock Attenuating Materials, Final Report, AFSWC-TDR-62-22, Poulter Laboratories, Stanford Research Institute, Menlo Park, California, March 1962.
- Smith, E.F., and Thompson, J.N., A Study of Vermiculite Concrete as a Shock-Isolating Material, Structural Mechanics Research Laboratory, The University of Texas, Contract Report No. 6-83 for U.S. Army Engineer Waterways Experiment Station, Vicksburg, Mississippi, under Contract No. DA-22-079-ENG-342, October 1963.
- Hoff, George C., "Shock-Isolating Backpacking Materials. A Review of the State of the Art," Proceedings of the Soil-Structure Interaction Symposium, University of Arizona, Tucson, Arizona, June 1964.
- Hoff, George C., "Energy Dissipating Characteristics of Lightweight Cellular Concrete," Journal of the Mississippi State University, State College, Mississippi, 1963, pp. 195-196.
- Denson, R.H., Ledbetter, W.B., and Saylak, D., Six Candidate Shock Attenuating Material Systems for the Alternate National Military Command Center Improvement Project-Omaha District, Final Report SL-82-17 Prepared for the U.S. Army Engineer District, Omaha, Nebraska, September 1982.
- Drake, J.L., et.al., Protective Construction Design Manual: "Groundshock and Cratering" (Section V), Final Report, ESL-TR-87-57, Air Force Civil Engineering Support Agency, Tyndall Air Force Base, November 1989.

Shock Test Facilities for High Shock Tests

LTC Ronald Kaufmann
Armed Forces Office - Division V Infrastructure
PO Box 20 50 03, D 5300 Bonn 2, Germany

Dr. Fritz Rischbieter
Battelle Motor and Vehicle Technology
PO Box 90 01 60, D 6000 Frankfurt 90, Germany

Abstract

After close-in detonations from conventional weapons, the outer walls and adjacent floors of hardened structures are loaded by shocks in the high shock region with peak accelerations in the range of 200 g to 5000 g or even higher, and with pulse durations from 2 ms to 0.2 ms, respectively.

To meet these requirements, two types of test stands had to be designed, and are now in use for shock testing of shelter equipment.

The shock table was developed using loadings by water-tamped explosions for producing shocks with positive pulse durations of 1 to 2 ms and peak accelerations in the range of 200 g to 1000 g.

The shock slab is loaded by explosions in air for shocks with positive pulse durations of about 0.2 ms and peak accelerations of about 1000 g to 5000 g.

Introduction

Shock testing of shelter equipment for shocks from nuclear weapons is established in Germany with maximum values of 40 g acceleration, 4 m/s velocity, and 10 ms pulse duration of positive acceleration in the highest test category. This also covers some shock effects in the interior of hardened structures under the loading of detonating conventional weapons.

The effects are different after a close-in detonation of a conventional weapon against equipment and installation if connection to the exterior construction elements is necessary. The survivability of the entire structure may depend on the resistance of a single auxiliary element.

Test methods had to be developed for shock loads with the parameters as follows:

pos. duration	about	0.2 ms	to	2 ms
maximum accel.	about	5000 g	to	500 g
maximum displ.	about	10 mm	to	100 mm
maximum veloc.			to	4 m/s.

The two test stands were developed and tested in 4 phases by Battelle Motor and Vehicle Technology and Proving Ground 91 at Meppen. A total of 100 tests without and with equipment were conducted. Construction, function, and test results will be shown in the paper.

Principles of Shock Generation and Layout of Test Stands

On both test stands, shock generation is made by explosives. For producing shocks with pulse durations in the range of 1 ms to 2 ms, loading by water-tamped explosions (Fig. 1), for shocks with pulse durations of approx. 0.2 ms explosions in air are used.

A sectional view of the test stand with water-tamped explosions ("shock table") is shown in Fig. 2. It consists of a U-shaped reinforced concrete box open on top and rear side with a bolt-connected front slab, which moves like a sledge on lubricated steel rails. The movement is bounded by rubber buffers as stops on the rear and front side. The open top is covered by a light steel plate during the test to protect the inside installed equipment against the water. The air blast is relatively small because of the water stemming, the overpressure is about 5 kPa inside of the table.

The test objects can be mounted on the front and on the base plate. They can be fixed either with screws in steel profiles flush mounted in the concrete which are fastened to the reinforcement, or individually with dowels which have to be set according to the dimensions of the test object.

With the mass of the sledge of approximately 12 metric tons, equipment up to approximately 3 tons can be tested without reducing notably the performance data of the test stand. In practice, the most important restrictions are imposed by the space available inside the box. Inside dimensions are 1.5 m in length, 1.8 m in width, and 1.8 m in height.

Two charges in shape of columns are centered each in a plastic pipe of 1.2 m length and of 100 mm diameter which are dipped in the watertank in a defined arrangement. The total charge weight is in the range of 1200 g to 2400 g.

Fig. 3 shows a side view of the test stand with loading by air blast ("shock plate") from a free explosion. The test objects are mounted to a suspended concrete slab being the movable front plate of a chamber for blast protection of the test objects. The slab is guided in horizontal direction by steel rods, and hits against rubber buffers serving as stops when the slab is accelerated. The middle of the outside face of the slab is additionally reinforced by a 10 mm thick steel plate and covered by a soft material damping layer. Test objects can be fixed, as in the other test stand, either on flush mounted steel profiles or by dowels. The total weight of the slab is 5 metric tons. The amount of HE ranges from 1 kg to 20 kg.

Instrumentation is provided to measure accelerations on the rear of the front plates, on the bottom slab of the table, and on the equipment. In addition, the displacement of the table, and the blast pressures inside and outside of the shock stands are determined.

Representative Shock Data

On both stands, the shock strength varies with the driving charge applied. As far as the accelerations are concerned, the maximum values also depend on the filtering chosen in signal processing. Reasonable filtering frequencies for low-pass filtering adapted to the respective pulse length are 1 kHz for the shock table and 10 kHz for the shock plate.

Fig. 4 shows the charge dependend peak accelerations of the slabs acting as base drivers for the mounted equipment. The accelerations of the shock table indicate typical different amplitudes of the front slab and the bottom slab of the complete device. Also, the peaks vary with the thickness of the front slab.

Phase 4 of the project covered the main test series and also served as verification and last adjustment of the developed test standard. This phase included almost all equipment which is needed for the operation of a hardened structure. All tested equipment was mounted like normally installed during construction, e.g. hard mounted or mounted by means of dampers or springs using the usual fasteners.

The measured peak acceleration at the equipment is much lower than the driving acceleration depending e.g. on the type of the fasteners, the reaction of the fasteners during the test, and/or on the gage location inside of the equipment. Table 1 represents a selection of some test results indicating the tremendous drop of the peak accelerations. However, shock-spectrum-analyses indicate much smaller differences between base and equipment in velocities and in displacements (Fig. 5). Curve 1 is

the spectrum of the field data measured in the center of the shock plate, while curve 2 represents the equipment field data measured at an inside frame of the upper left corner of the switch cabinet.

Conclusions

The two new developed test stands are excellent means for testing of equipment, of spring systems, and of fasteners possibly exposed to an upper or high shock environment.

The now existing test standard with directions for the operation of the test facilities allows implementation of shock tests with well defined support motions on reasonable costs. The reproductions of shocks of the same quality are a good base for further studies about the resistance of equipment as well as about the behaviour and the effectiveness of different types of e.g. fasteners, dowels, dampers, and springs. The two test stands are ready for use at Meppen Proving Ground.

References

1. K.-E. Meier-Dörnberg. An Overview of Shock Analysis and Testing in the Federal Republic of Germany, The Shock and Vibration Bulletin, 1990
2. Fundamentals of Protective Design for Conventional Weapons, Department of the Army, WES, Nov. 1986
3. Preliminary Procedures for Assessing Equipment Survivability and Shock Isolation Requirements, NMERI-WA8-XX, AFWL, Kirtland AFB, Aug. 1987
4. Untersuchungen zur Schockverträglichkeit von Betriebseinrichtungen in Schutzbauten gem. MF 177, Bericht R-66.818-1 der Battelle Motor- und Fahrzeugtechnik GmbH, März 1988
5. Untersuchungen zur Schockverträglichkeit von Betriebseinrichtungen in militärischen Schutzbauten gem. MF 177, Phase II: Untersuchungen zur sprengtechnischen Schockerzeugung, Bericht R-67.231-1 der Battelle Motor- und Fahrzeugtechnik GmbH, Nov. 1989
6. Untersuchungen zur Schockverträglichkeit von Betriebseinrichtungen in militärischen Schutzbauten gem. MF 177, Phase III: Bau und Erprobung von Prüfständen, Band 1 u. 2, Bericht R-67.476-1 der Battelle Motor- und Fahrzeugtechnik GmbH, März 1991
7. F. Rischbieter, Entwicklung von Schockprüfständen zur Simulation konventioneller Waffenwirkungen im Hochschockbereich, 5. Int. Symposium Interaktion konventioneller Munition mit Schutzbauten, Mannheim, April 1991
8. Vorläufige Ergebnisse der Untersuchungen zur Schockverträglichkeit von Betriebseinrichtungen in milit. Schutzbauten, Phase IV, Jan. 1993

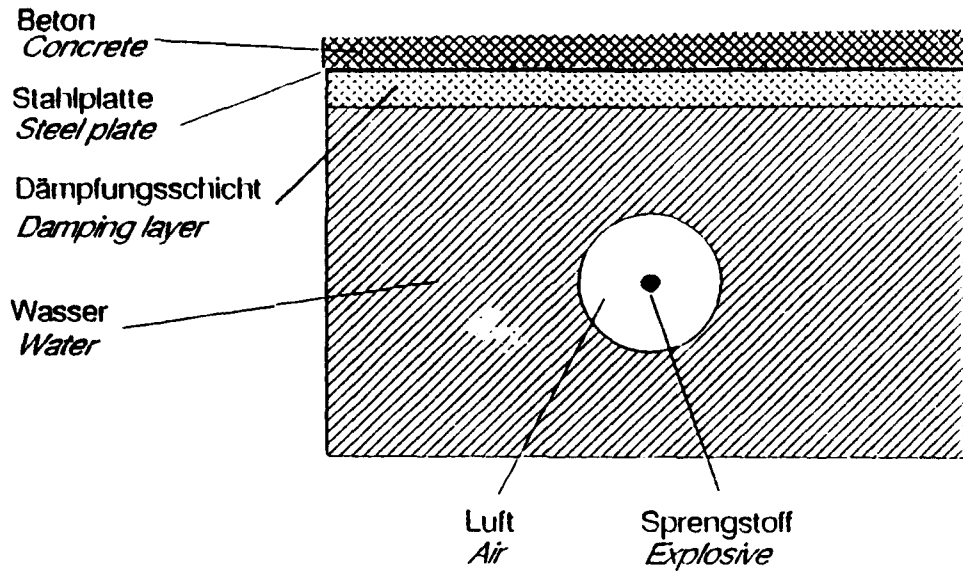


Bild 1: Prinzipieller Aufbau der wasserverdämmten Sprengung

Fig. 1: Scheme of the water-tamped explosion

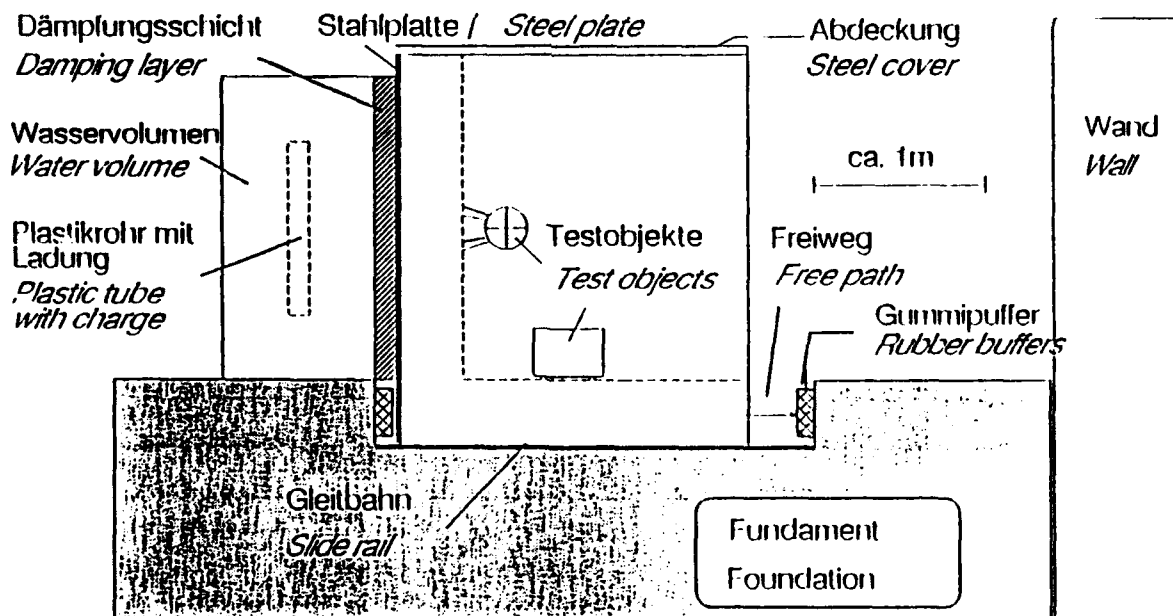


Bild 2: Schocktisch mit Antrieb durch wasserverdämmte Sprengung (Halbschematisch)

Fig. 2: Shock table with loading by water-tamped blasts (half schematic)

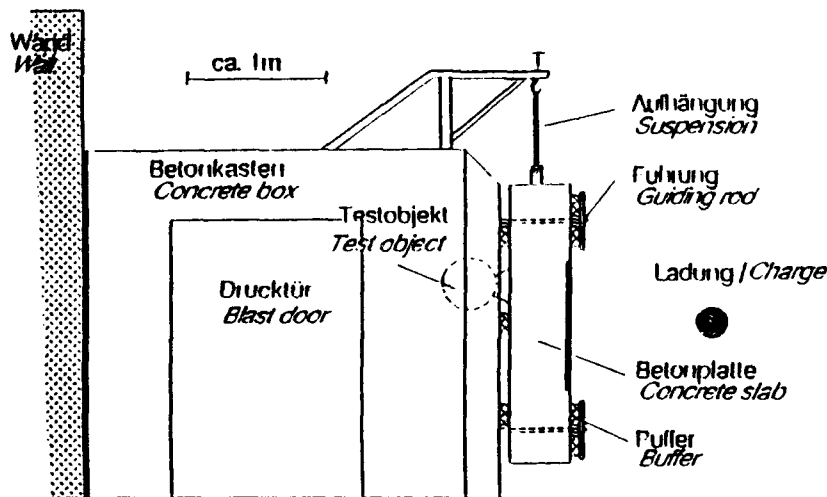


Bild 3: Prüfstand mit Betonplatte und Antrieb durch Sprengung in Luft

Fig. 3: Test stand with concrete slab and loading by air blast

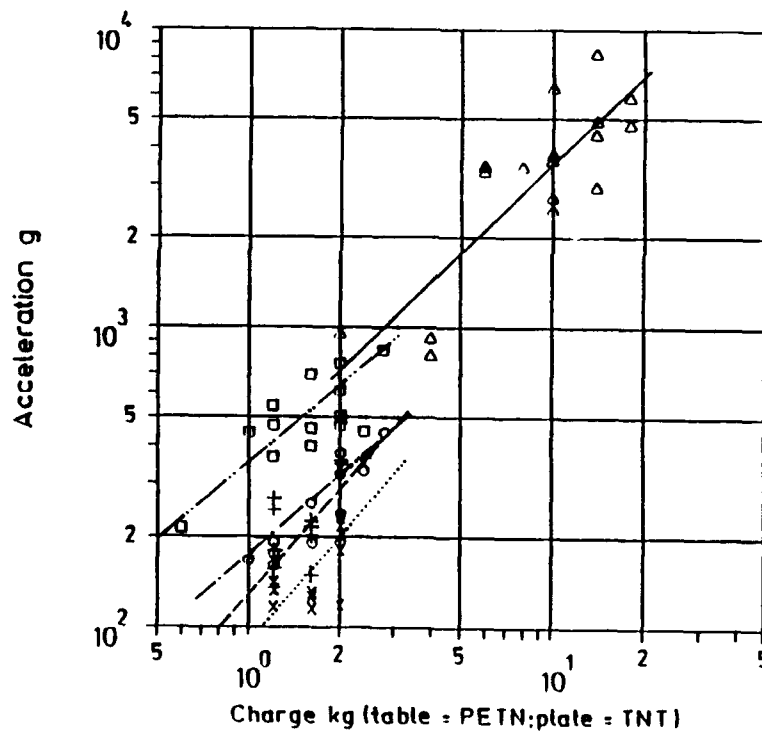
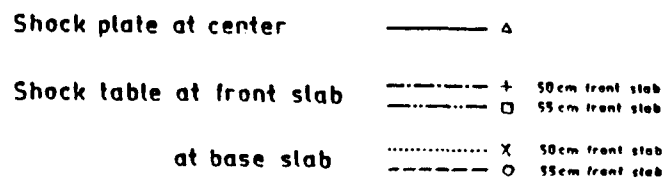
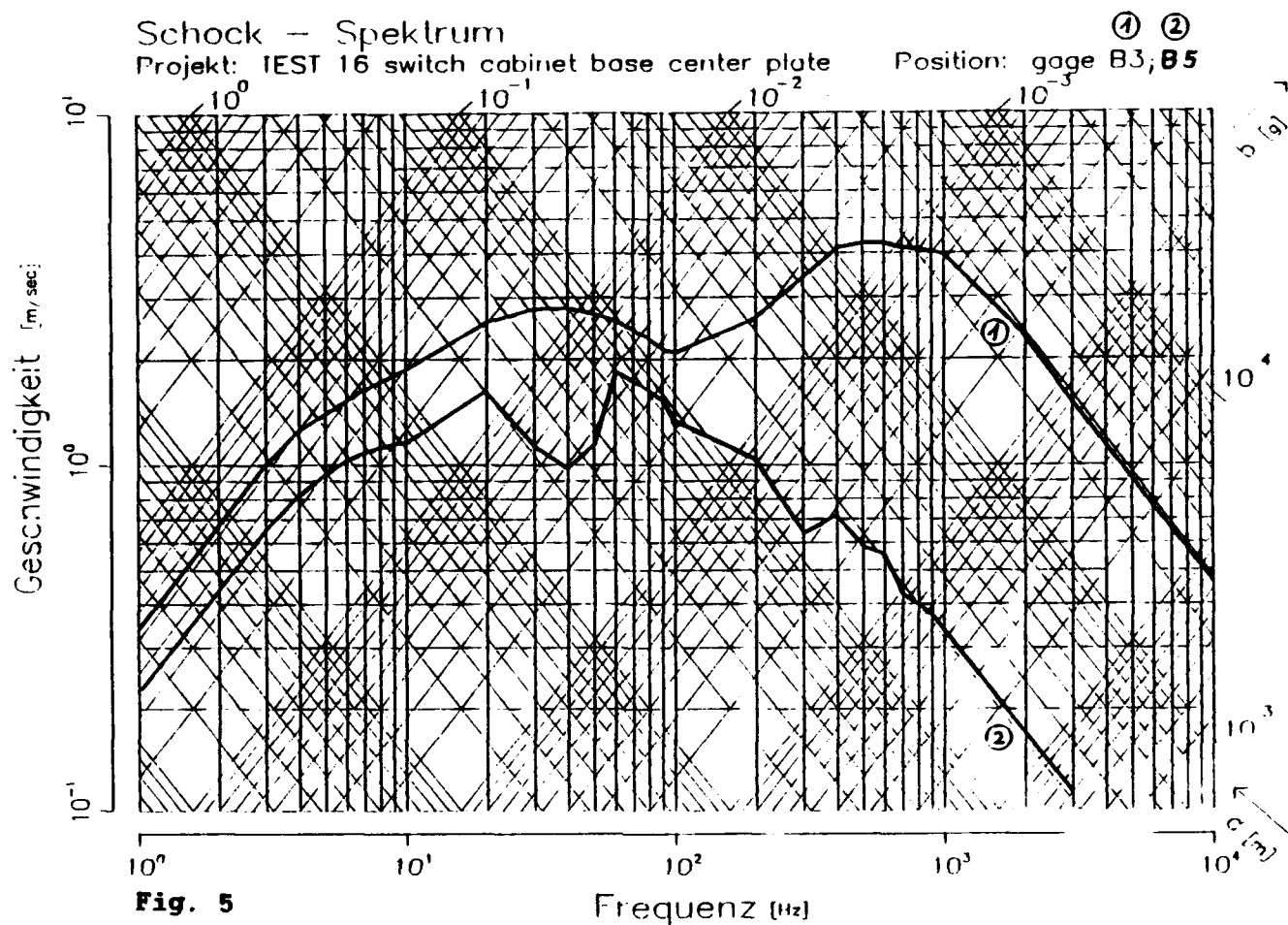


Fig. 4 Test results peak acceleration





Test No.	Specimen	Stand	Isolation (additional)	Charge (g)	Accel. base (g)	Accel. equip. (g)	Damage
5	fan	table	none	2x 800	347	11	none
6	fan	table	none	2x1000	510	54	none
15	switch cabinet	plate	Scherw. B200	10 000	2733	143	1 fuse base torn
16	switch cabinet	plate	Scherw. B200	14 000	2945	205	6 fuses switched
25	el. generator	table	none	2x 600	379	95	none
27	el. generator	table	none	2x1000	622	101	1 hinge broken
40	air filter	plate	none	14 000	4386	1735	none
41	air filter	plate	none	18 000	5870	1794	none

Table 1. Selected results of the main test series
 peak acceleration: base versus equipment

PRACTICAL STRENGTHENING MEASURES FOR EXISTING STRUCTURES
TO INCREASE THEIR BLAST RESISTANCE - WALLS AND CEILINGS

Reuben Eytan

Eytan Building Design Ltd. Tel Aviv, Israel

and

Arkadi Kolodkin

Hardening Consultant, Tel Aviv, Israel

ABSTRACT

The paper includes the description of practical strengthening measures for existing structures, developed in Israel, to increase the blast resistance of non-hardened structures. In the last years numerous non-hardened structures were subjected to real weapons and terrorist attacks in Israel (during the Gulf War) and in other countries. The observed damages were relatively high compared to the small explosive charges and the practical conclusion was that strengthening measures should be implemented. New strengthening methods for brick/blocks external walls as well as light ceilings and roofs were developed, following extensive full-scale test and research/development efforts. The wall strengthening methods include the addition of internal or external layers made of different materials and using new technologies. The light ceilings strengthening consists of the addition of an internal protective barrier beneath the ceiling, made of different materials and using new technologies.

INTRODUCTION

During the Gulf War, numerous structures were damaged in Israel by the explosive effects of Iraqi Scud missiles (see figure 1). Extensive practical experience was gathered on the levels of damage of masonry walls and light ceilings, which was complemented by the findings from full-scale tests on wall and ceiling test specimens, performed in Israel in 1991-1992. We have found that the damage threshold of normal masonry walls is at scaled distances of about $3.2 \text{ m/kg}^{0.33}$, at which range light ceilings/roofs are also damaged.



Figure 1 - Structures damaged by missile attack

The worldwide practice of strengthening existing walls and ceilings is mainly applied in key installations for withstanding the effects of explosive charges in terrorist attacks (vehicle bombs, etc). The recent large scale missile attacks on populated areas lead to the need of providing protection from blast effects to civilian population in normal unprotected structures. We have developed several types of strengthening measures for existing walls and ceilings, taking into consideration the types of buildings mostly found in Israel:

- Reinforced concrete framed structures with masonry infill walls.
- Structures with reinforced concrete external wall elements (mostly prefabricated units).
- Light wood/metal structures.

At scaled distances of more than $3.2 \text{ m/kg}^{0.33}$, no substantial damage occurs for normal masonry walls. At smaller scaled distances, the masonry walls are damaged, while the main structural elements remain functional. At these

ranges it is effective to strengthen the existing walls, taking into consideration the integration of the strengthening measures with the existing structural elements. Light ceilings/roofs normally used in residential homes can also be strengthened efficiently at these ranges. Obviously, the strengthening of existing walls and ceilings must be implemented together with adequate strengthening of the windows and doors.

STRENGTHENING MEASURES FOR EXISTING WALLS

Normal masonry walls have a low resistance to withstand lateral loads and therefore are damaged by relatively low blast pressures, starting at scaled distances of about $3.2 \text{ m/kg}^{0.33}$. Complete failure of the wall occurs at scaled distances of about $2.2 \text{ m/kg}^{0.33}$. The above figures are representative for masonry walls about 2.7 meter high and 3.0 meters long. Higher and/or longer walls may be damaged at larger scaled distances than those mentioned above. For comparison, the scaled distance at which a 25/25 cm. reinforced concrete column, 2.7 meters high, is severely damaged, has been found to be about $1.1 \text{ m/kg}^{0.33}$.

This shows that for scaled distances of $3.2-1.1 \text{ m/kg}^{0.33}$ it is effective to implement strengthening measures for the walls only, as the main structural elements are not in the damage range. It should be mentioned that careful design of the wall strengthening measures is required to ensure that the additional lateral loads are adequately transferred to the stronger structural elements (such as the horizontal ceiling slabs) and not to columns. Light existing walls - wood, metal, etc. cannot be used as a basis for the new strengthening measures which therefore, must be designed as independent elements.

DESCRIPTION OF WALL STRENGTHENING MEASURES

Three types of wall strengthening measures have been developed:

- Strengthening the existing wall by using its inherent resistance.
- Adding an internal barrier designed to stop the masonry wall debris.
- Adding an external barrier designed to absorb the blast loadings before reaching the existing wall.

Improving the blast resistance of the existing wall can be achieved by internal cover materials connected to the inner face of the wall. Cover materials such as thin steel plates (see figure 2) or ballistic material (see figure 3) have been used in full scale tests and adequate solutions have



Figure 2 - Steel plates cover

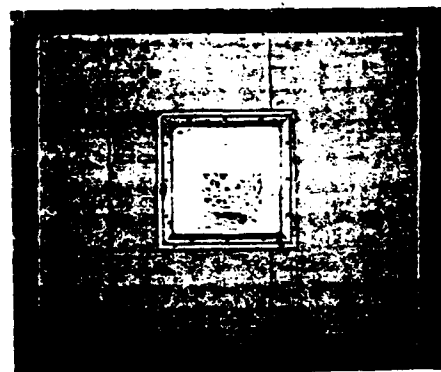


Figure 3 - Ballistic material cover

been defined for scaled distances of about $2.1 \text{ m/kg}^{0.33}$ where no injuries of people will be induced. When covering the internal face of the existing wall by a 5 cm sprayed concrete layer with an adequate steel mesh connected to the wall (see figure 4), injuries can be prevented at lower scaled distances of about $1.6 \text{ m/kg}^{0.33}$. Another type of wall

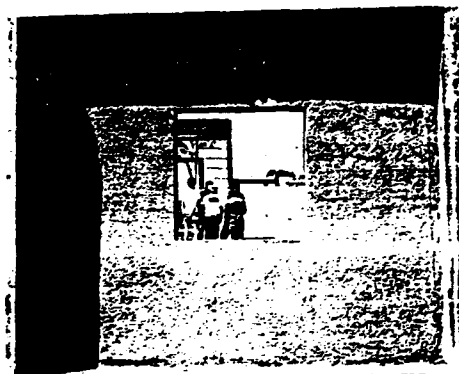


Figure 4 - Sprayed concrete layer

strengthening measures consists of the addition of an inner barrier behind the wall, strong enough to stop the masonry debris from inducing injuries. The use of such barriers made of silicate blocks with acrylic glue between them (see figure 5) or independent steel plate construction (see figure 6) prevents injuries at scaled distances of about $2.1 \text{ m/kg}^{0.33}$. Stronger barriers have been developed using wood - cement blocks filled with concrete, which proved efficient at scaled distances of $1.6 \text{ m/kg}^{0.33}$.

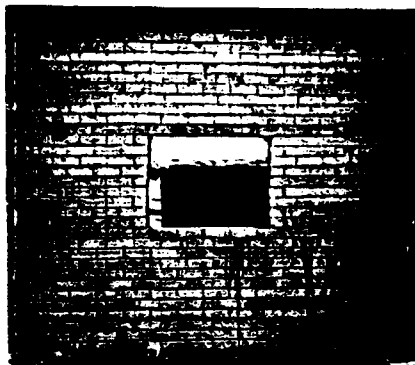


Figure 5 - Silicate blocks barrier

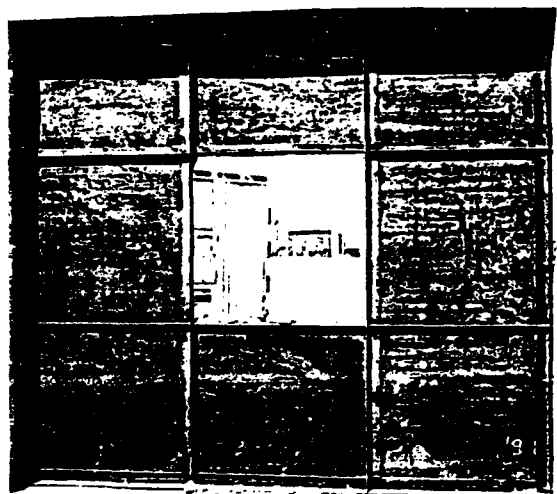


Figure 6 - Steel plate barrier

Finally, the use of sandwich metal plates with different fill materials, installed externally at a certain distance from the wall (see figure 7), proved effective in absorbing the blast energy and preventing injuries at scaled distances of about $2.1 \text{ m/kg}^{0.33}$. Weak walls can be replaced by adequately designed blast resistant walls such as reinforced concrete prefabricated

panels, double concrete walls with internal air gaps or wood-cement blocks filled with concrete. These new walls prevent injuries at scaled distances of $1.6 \text{ m/kg}^{0.33}$.

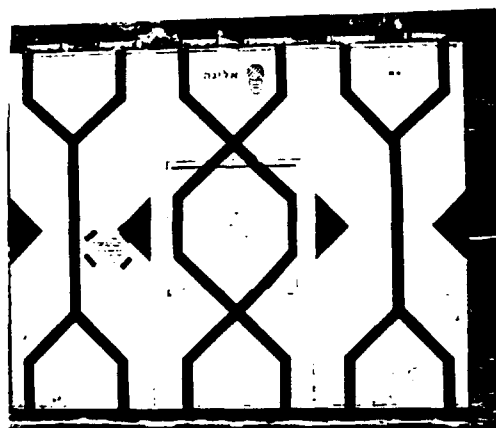


Figure 7 - External sandwich metal plates

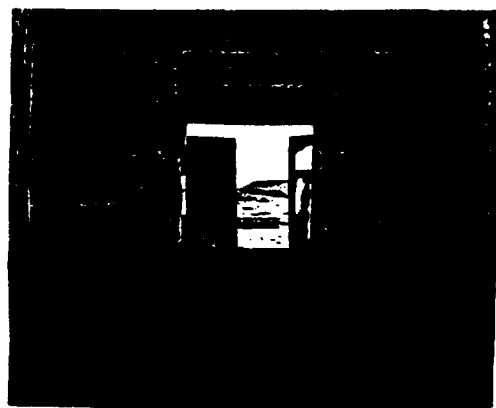


Figure 8 - Wood-cement blocks filled with concrete

STRENGTHENING MEASURES FOR EX-STING CEILINGS

Light ceilings and roofs are expected to fail and induce injuries to people at scaled distances of $5 \text{ m/kg}^{0.33}$. Two new types of innovative strengthening measures have been developed and tested:

- An additional barrier made of metal panels, installed beneath the ceiling (permanent solution), as shown in figure 9.
- An inner "tent" made of ballistic material (temporary solution), as shown in figure 10.

The above strengthening measures proved effective at scaled distances of $2.7 \text{ m/kg}^{0.33}$. Further permanent strengthening measures for existing ceilings, using different materials, are presently in development stage.

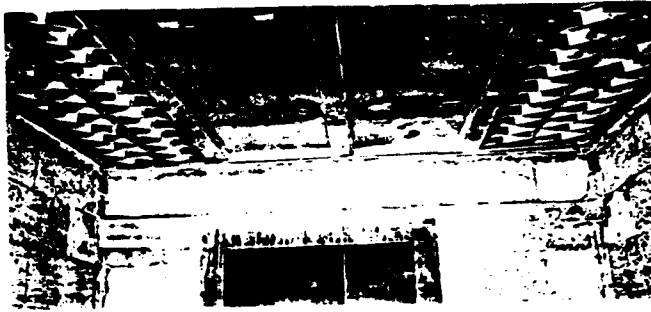


Figure 9 - Metal panels barrier beneath ceiling



Figure 10 - Ballistic material "tent"

SUMMARY

In the last two years, numerous strengthening measures for walls and ceilings have been developed and tested in Israel. These solutions are aimed to be applied in existing structures, to reduce considerably the rate of injuries in case of future attacks. Special care should be given to the adequate integration of the strengthening measures with the existing structural elements ensuring appropriate lateral and vertical loads transfer. Functional as well as cost considerations should be added to the protection aspects when choosing the optimal solutions. The research and development of further innovative strengthening measures for walls and ceilings is presently continuing in Israel.

PRACTICAL STRENGTHENING MEASURES FOR EXISTING STRUCTURES
TO INCREASE THEIR BLAST RESISTANCE - WINDOWS AND DOORS

Arkadi Kolodkin

Hardening Consultant, Tel Aviv, Israel

and

Reuben Eytan

Eytan Building Design Ltd. Tel Aviv, Israel

ABSTRACT

The paper includes the description of practical strengthening measures for existing structures, developed in Israel, to increase the blast resistance of non-hardened structures. In the last years numerous non-hardened structures were subjected to real weapons and terrorist attacks in Israel (during the Gulf War) and in other countries. The observed damages were relatively high compared to the small explosive charges and the practical conclusion was that strengthening measures should be implemented. The most vulnerable elements for blast effects were found to be windows (glazing and frames) and wooden doors. Following extensive full-scale tests and research/development efforts, two main types of strengthening measures for windows were finalized:

- a. Strengthening the existing window glazing by different films and using additional shielding elements.
- b. New blast-resistant windows including protective glazing materials and adequate aluminium/steel frames.

The same R/D effort included the development of new light blast resistant metal doors, fitting optimally in the existing structure.

INTRODUCTION

Literature references include the following information about the percentage of broken window glass as a function of the scaled distance:

- 100% broken glass at scaled distances of 8-10 m/kg^{0.33}.
- 50% broken glass at scaled distances of 13-17 m/kg^{0.33}.
- 10% broken glass at scaled distances of 40-60 m/kg^{0.33}.

Our experience from observing damaged windows in real attacks and in full-scale tests is that severe injuries to people are likely to occur at scaled distances of 15-18 m/kg^{0.33} from the glass fragments thrown inward by the explosion blast loadings. If we compare the above range with the scaled distance of 3.2 m/kg^{0.33}, which we found to be the damage threshold of external masonry walls, it is clear that the windows are much more sensitive to the blast effects and therefore should be strengthened. We have developed two types of strengthening measures for windows:

- a. Strengthening the existing window glazing by different films and using additional shielding elements - which can be done in emergency periods by unskilled people.
- b. Replacing the existing window by a new blast-resistant window - which requires skilled labor; this can be done anytime as a permanent solution.

Normal internal wooden doors were found to be severely damaged in real attacks at scaled distances of about 8 m/kg^{0.33}, putting the people behind them at risk from the doors debris. We have developed two types of strengthening measures for doors:

- a. Strengthening the existing wooden door by different cover materials and mechanical devices.
- b. Replacing the existing door by a new security door.

EMERGENCY STRENGTHENING MEASURES FOR EXISTING WINDOWS

Normal windows in Israel have a single 3-4 mm glass pane of about 1.2 square meters with wood or aluminum frame. Emergency strengthening measures should prevent injuries from flying glass debris and can consist of internal films on the existing glass, films on both

sides of the glass, or of an additional internal shield which will prevent the glass fragments from injuring people behind the window. Security or safety films to cover existing glass panes are commercially available, with thicknesses of 100 to 300 microns. We have found in our tests that the optimal films are 100 micron polyester films, which when properly glued to the internal face of the glass are effective in preventing injuries from the debris at scaled distances of about $8 \text{ m/kg}^{0.33}$. At this range the strengthened glass pane fails as a whole and falls near the wall, without endangering the people (see figure 1). Equivalent strengthening measures involve the use of 50 mm wide polypropylene bands, glued horizontally and vertically on both sides of the window glass or the use of 60 micron polypropylene films.

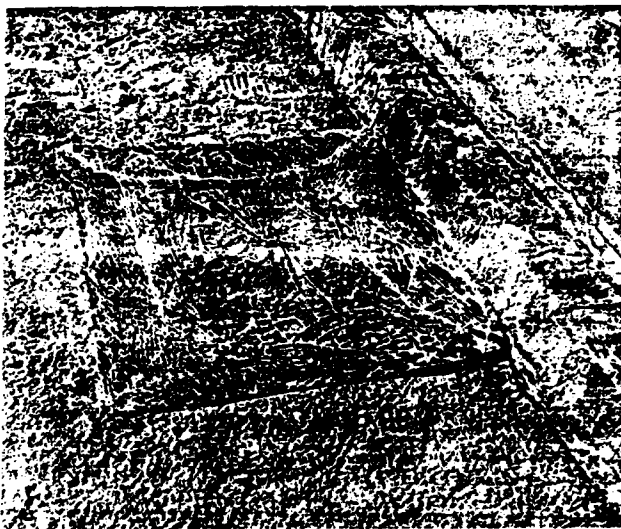


Figure 1 - Normal glass strengthened by safety film

It should be mentioned that although the above emergency measures are relatively simple and cheap, their effectiveness is limited to low blast pressure ranges: already at scaled distances of $6 \text{ m/kg}^{0.33}$ the strengthened glass panes are thrown inward and induce large fragments, endangering the people. Preventing glass fragments from injuring people can be achieved by adding an adequate barrier behind the window. In emergency times, different materials, such as wooden planks, can be used to seal off the window. An 8mm wood barrier will provide adequate protection against glass fragments at scaled distances of about $6 \text{ m/kg}^{0.33}$. However, at lower scaled distances the above strengthening barrier becomes itself a hazard. A preferred solution, found by us in full-scale tests, is the use of a "flexible" barrier such as a blast

curtain. A curtain made of two layers of kevlar or four layers of ballistic nylon proved effective in preventing injuries from glass fragments at scaled distances of about $4 \text{ m/kg}^{0.33}$ (see figure 2).

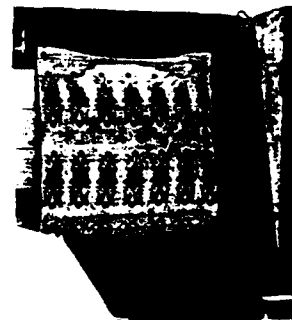


Figure 2 - Blast curtain

It should be ensured that the curtain is properly connected to the wall and that it has enough height to allow its deflection while catching the glass fragments. We also found that the curtain material must be continuous, without any holes. The main inadequacy of the above emergency measures is that blast leakage into the structure is not prevented. Protection against chemical agents is also not provided.

THE USE OF BLAST RESISTANT WINDOWS

A much more effective solution is the replacement of the weak glass window by a new blast resistant window, including polycarbonate or laminated glass glazing and adequate strong frame. Several innovative blast resistant windows were recently developed in Israel, providing adequate protection for scaled distances of $4\text{-}11 \text{ m/kg}^{0.33}$ (see figures 3 and 4):

- Windows with 6 mm polycarbonate or 7 mm laminated glass, providing protection at scaled distances of about $11 \text{ m/kg}^{0.33}$.
- Windows with 8 mm polycarbonate or 9 mm laminated glass, providing protection for scaled distances of about $8 \text{ m/kg}^{0.33}$.
- Windows with 10 mm polycarbonate or 10.5-11 mm laminated glass, providing protection for scaled distances of about $6 \text{ m/kg}^{0.33}$.
- Windows with 12 mm polycarbonate or 13.5 mm laminated glass, providing protection for scaled distances of about $4 \text{ m/kg}^{0.33}$.

When using laminated glass, the internal face of the glazing must be covered by an additional film, preventing spalling. Blast resistant aluminium and steel

window frames were also developed and proved effective after considerable R/D efforts. It should be mentioned that the blast resistant windows are permanent and are in daily use. Therefore functional requirements such as preventing U.V. radiation penetration, ensuring the transparency of the glazing, easy maintenance, etc. should obviously be considered when choosing the type of blast resistant window.

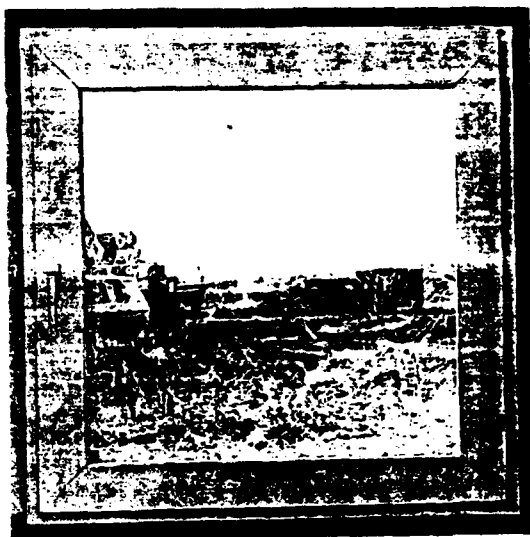


Figure 3 - Blast resistant window with polycarbonate glazing and steel frame

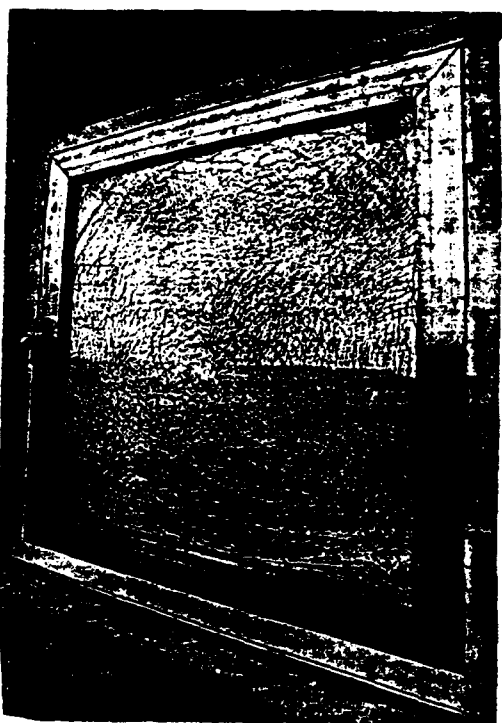


Figure 4 - Blast resistant window with laminated glass and aluminium frame

STRENGTHENING MEASURES FOR EXISTING DOORS

Strengthening measures for existing wooden doors included the door frame strengthening, provision of additional horizontal steel bars on the internal face of the door, as well as covering the door leaf by a ballistic material. These measures prevent the door from being dislocated or door debris to be induced, at scaled distances of about $8 \text{ m/kg}^{0.33}$. Blast leakage is still expected to occur although less than for an unstrengthened door (see figure 5).

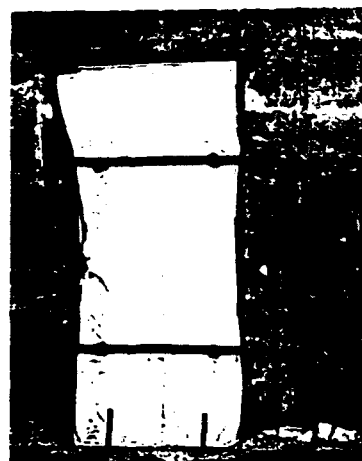


Figure 5 - Strengthening of existing wooden door

Commercially available metal security doors could be used to replace the existing weak doors (see figure 6).

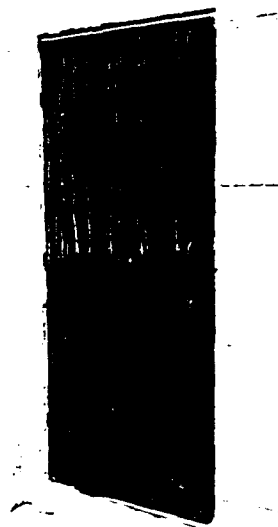


Figure 6 - Commercially available security door

Their protection effectiveness is at scaled distances of $6 \text{ m/kg}^{0.33}$. New innovative blast resistant doors have been developed in Israel and proven effective in full scale tests for scaled distances of about $4 \text{ m/kg}^{0.33}$. These doors can also provide protection against chemical agents, if required (see figure 7). It should be mentioned that the new blast resistant doors always open outwards.



Figure 7 - Blast resistant door

SUMMARY

In the last two years numerous strengthening measures for windows and doors have been developed and tested in Israel. These solutions are aimed to be applied in existing structures, to reduce considerably the rate of injuries in case of future attacks. In addition to their blast resistance, the improved windows and doors could also be designed to protect people against chemical agents. Functional as well as cost considerationss should be added to the protection aspects when choosing the optimal solutions. The research and development of further innovative strengthening measures for windows and doors is presently continuing in Israel.

FULL SCALE TESTS ON STRENGTHENING MEASURES FOR EXISTING STRUCTURES

Col. Yitzhak Fouks

Home Front Command
Israeli Defense Forces

ABSTRACT

The paper includes the description of extensive full-scale tests performed in Israel in 1991-1992 by the Home Front Command. The tests goals were to check the effectiveness of different strengthening measures for existing structures to increase their blast resistance. Explosive charges of several weights were activated in front of building elements such as walls, windows, doors and ceilings at different distances, in full-scale configurations. More than 140 targets were tested and considerable valuable information was recorded, enabling the definition of the blast damage threshold of the various building elements, in normal configuration and including different strengthening measures. Following the tests results analysis, cost-effective solutions, including innovative technologies, were summarized.

INTRODUCTION

It was repeatedly found that normal buildings are severely damaged by blast loadings from nearby explosions. At larger distances, the most sensitive building components are the normal glass windows which fail under low blast overpressures. At closer ranges, the doors in the building start failing, followed by light roofs and ceilings. As the blast level increases, normal brick and masonry walls fail and at close ranges the structural elements: columns, beams, etc. begin to "feel" the blast loadings. As the weaker building components: windows, doors, ceilings and brick/masonry walls are damaged by blast at relatively large distances and much earlier than the structural elements, the Home Front Command has started a five-year research and development program (1991-1995) to test and define

strengthening measures for existing building components, to increase their blast resistance.

TEST PROGRAM

In 1991-1992 the test program included three test series performed in October 1991, April 1992 and May 1992. The first tests in October 1991 included 24 explosive charges detonations affecting 89 targets: 49 windows, 16 doors, 23 walls and one complete single storey building. The following tests in April 1992 included 10 explosive charges detonations affecting 51 targets: 27 windows, 9 doors, 12 walls and 3 ceilings. In May 1992, 4 windows and one ceiling were tested. The tests goal of defining suitable strengthening measures for existing buildings was fully achieved and, based on the tests results analysis, the Home Front Command has issued technical regulations for practical application. In 1993-1995, additional innovative technologies will be tested.

EXPERIMENTAL PROCEDURES

The test configuration was a central explosive charge around which several targets were placed at different distances, in an "arena" layout. The targets location was such that no interference from adjacent targets occurred. The scaled distances - $R/W^{0.33}$ - for which the different tests were performed varied from 1.06 to 32.26 m/Kg^{0.33}. The "windows target" consisted of a 5.00m long, 2.50m high, 0.2 m thick concrete wall with two 1.0mx1.0m openings; in each explosive test two window specimens were installed in the target and replaced with other two in the following test. The "doors target" consisted of a 5.00m long, 2.50m high, 0.2m thick concrete wall with two 0.9mx2.05m openings in which two door

specimens were installed in each explosive test and replaced with two others in the following test. Each type of wall to be tested was built as a "wall target" - 3.50m long and 2.70m high with the wall material built within a concrete frame. The "ceiling target" was emplaced on a prefabricated room, 3.0m x 3.0m in plan and 3.0m high. The complete single storey building was a prefabricated building unit (two-rooms) 7.9 meters long, 3.5 meters wide and 2.7 meters high. "Bikini" gages indicating the blast level were placed near all targets.

In several tests, free field blast pressures were recorded by using KISTLER 6103 blast measuring devices. To estimate the damage from window glass fragments, wooden planks were placed behind the windows and the number and size of fragments was recorded for each windows test.

WINDOWS TEST RESULTS

The test results showed that normal 1.0m x 1.0m glass windows - 3+4 mm. thick - failed under blast loadings at scaled distances of $30+33 \text{ m/Kg}^{0.33}$. Severe injuries to people from glass fragments would occur at scaled distances smaller than $15-18 \text{ m/Kg}^{0.33}$. Temporary expedient strengthening measures such as:

- additional "security film", 100 microns thick, on the inner side of the glazing, or
 - additional "safety adhesive bands" on both sides of the glazing,
- prevent injuries to people behind the window from the glass fragments at scaled distances of $13 \text{ m/Kg}^{0.33}$. Providing an inner barrier behind the window, consisting of two layers of ballistic material, increases the injuries threshold to scaled distances of $6 \text{ m/Kg}^{0.33}$, while the use of 4-5 layers of ballistic material brings the threshold to $4 \text{ m/Kg}^{0.33}$. However, the above temporary strengthening measures do not prevent blast pressures from reaching the internal areas and affecting the people. Therefore, blast-resistant glazing materials were tested and the results were as follows:

- to prevent injuries to people at scaled distances of $11 \text{ m/Kg}^{0.33}$, glazings such as 7 mm polycarbonate or 7mm layered glass proved efficient.
- to prevent injuries to people at scaled distances of $8 \text{ m/Kg}^{0.33}$, glazings such as 8 mm polycarbonate or 9 mm layered glass proved efficient.
- to prevent injuries to people at scaled distances of $6 \text{ m/Kg}^{0.33}$, glazings such as 10 mm

polycarbonate or 11 mm layered glass proved efficient.

- to prevent injuries to people at scaled distances of $4 \text{ m/Kg}^{0.33}$, glazings such as 12mm polycarbonate or 14 mm layered glass or polycarbonate proved efficient.

The tests showed that changing the existing glass with stronger glazings is only efficient, without strengthening the window frame, down to scaled distances of $11 \text{ m/Kg}^{0.33}$. For lower values, the stronger glazings must be emplaced in strengthened window frames made of aluminum or steel. Using the tests results from October 1991 and April 1992, innovative blast resistant windows with adequate strengthened frames, locking devices and glazings were finally tested and proved adequate in May 1992.

DOORS TEST RESULTS

The tests results showed that normal wooden doors failed under blast loadings at scaled distances of $8 \text{ m/Kg}^{0.33}$. Strengthening existing wooden doors, opening inwards - in the direction of the external blast pressures - by additional steel bars and locking devices - proved adequate (with acceptable level damages) only for scaled distances of no less than $8 \text{ m/Kg}^{0.33}$. For lower values, the wooden doors should be replaced by metal doors. Different security metal doors tested in our tests proved to be effective at scaled distances of $6 \text{ m/Kg}^{0.33}$, preventing blast leakage, although exhibiting acceptable damages to the locking devices. The major "change" in the door design was the change in the opening direction - outwards. Innovative metal doors proved efficient for scaled distances of $4 \text{ m/Kg}^{0.33}$.

TEST RESULTS FOR LIGHT CEILINGS AND ROOFS

Light ceilings and roofs are expected to fail and induce injuries to people at scaled distances of $5 \text{ m/Kg}^{0.33}$. In our tests, two types of innovative strengthening measures proved efficient in preventing the debris of severely damaged light roofs and ceilings from injuring people:

- a. An additional barrier made of metal panels, installed beneath the ceiling.
- b. An inner "tent" made of ballistic material sheets installed on a metal structure.

The above strengthening measures proved effective at scaled distances of $2.7 \text{ m/Kg}^{0.33}$.

WALLS TEST RESULTS

The tests results showed that the damage threshold of various "normal" brick and masonry walls is at scaled distances of $3.2 \text{ m/kg}^{0.33}$.

Three types of strengthening measures were developed and tested:

- a. Additional strengthening measures on the inner face of the existing wall.
- b. Additional strengthening measures on the outer face of the existing wall.
- c. Replacing the weak existing wall by a new wall.

The following wall strengthening measures were found to be effective in preventing injuries to people at scaled distances of $2.1 \text{ m/kg}^{0.33}$:

- Additional ballistic material cover on the inner face of the wall.
- Additional internal 8 cm thick silicate blocks on the inner face of the wall.
- Additional metal panels on the inner face of the wall.
- Additional concrete layer on the inner face of the wall.
- Additional external metal panels at a small distance from the outer face of the wall.

The most effective wall strengthening measures which would prevent injuries to people at scaled distances of $1.6 \text{ m/kg}^{0.33}$ are:

- Additional concrete layer on the inner face of the wall.
- Additional wood-cement bricks filled with concrete built on the inner side of the wall.

The following "new" walls could be used to replace the weak existing walls:

- Reinforced concrete panels - prefabricated - with adequate connections.
- Double concrete wall with internal air gap.
- Wood - cement bricks filled with concrete.

CONCLUSIONS

Following the first two years of the research and development program including extensive full-scale tests, strengthening measures were defined as follows:

- Strengthening the glazing of existing glass windows from the blast threshold at scaled distances of $33 \text{ m/kg}^{0.33}$ to preventing injuries at scaled distances of $13 \text{ m/kg}^{0.33}$.
- Changing the existing glass with stronger glazing materials, preventing injuries at scaled distances of $11 \text{ m/kg}^{0.33}$.
- Replacing existing windows with innovative blast resistant windows, preventing injuries at scaled distances of $4 \text{ m/kg}^{0.33}$.

- Replacing existing wooden doors with new metal doors opening outwards, reducing the scaled distance from a blast threshold of $8 \text{ m/kg}^{0.33}$ to prevention of injuries at $4 \text{ m/kg}^{0.33}$.
- Adding an internal barrier beneath light ceilings/roofs, reducing the scaled distance from a blast threshold of $5 \text{ m/kg}^{0.33}$ to prevention of injuries at $2.7 \text{ m/kg}^{0.33}$.
- Strengthening existing walls by different internal or external measures, reducing the scaled distance from a blast threshold of $3.2 \text{ m/kg}^{0.33}$ to prevention of injuries at $2.1 \text{ m/kg}^{0.33}$.
- Replacing existing walls by new innovative walls, reducing the scaled distance from a blast threshold of $3.2 \text{ m/kg}^{0.33}$ to prevention of injuries at $1.6 \text{ m/kg}^{0.33}$.

SUMMARY

Various cost-effective strengthening measures for existing building components were defined following extensive full-scale tests. The research and development program is proceeding in the years 1993-1995 involving the definition of additional innovative strengthening methods.

Conventional Explosive Airblast Effects Within Compartmented Structures

M. Rosenblatt, D.W. Hatfield, & H.D. Zimmerman

California Research & Technology Div., Titan Corporation, Chatsworth, CA

ABSTRACT

California Research & Technology (CRT) has supported the Defense Nuclear Agency (DNA) in development and evaluation of numerical simulation techniques for predicting airblast effects due to bursts within compartmented structures, including the critical effects of severe local damage to walls and consequent ejection of debris and airblast into adjacent spaces.

Effects on structures from confined conventional explosives detonated in underground or aboveground facilities are increasingly important for targeting applications. Robust techniques are required to predict airblast propagation through / between rooms in compartmentalized structures (including passage through doors / openings and connecting tunnels), and to predict interactions with structural components. A unique calculational approach for predicting airblast within compartmented structures, wall loading, subsequent fracture/breakup, and multiphase airblast-debris-structure interaction will be presented.

BACKGROUND

The simplest airblast effects calculations involve treating the structural elements as rigid. Numerical techniques with rigid boundaries representing the structure/tunnel walls are able to model the airblast flowing through openings (like doors), reflecting off walls and ceilings, and interacting with defined geometric features (like internal equipment). As a second, decoupled step, the predicted airblast loads on the structural elements are then used in finite element structural codes to deform walls and doors, etc. This decoupled approach works as long as the airblast loading does not change due to structural deformation or failure.

In many realistic problems, however, the conditions which would justify decoupling are not satisfied, and a fully coupled approach is needed to correctly treat the airblast interactions with a structure. This is particularly true as the quantity of explosive increases in relation to the room volume, or when the explosion occurs close to a wall. In these situations,

large non-linear distortions and failure can occur during loading. Localized failure can alter the properties of the structure in important ways, and massive amounts of debris can be swept into the airblast flow, altering that flow and creating another agency for damage, i.e., debris impact. Thus, as the airblast loading forces increase, the structure and airblast can dynamically interact such that both the airblast and structure must be calculated simultaneously.

In order to predict the damage in the neighboring compartments, it is necessary to calculate:

- Munition detonation and case fragmentation
- Airblast and detonation product dynamics in the compartment containing the explosion
- Loading of the structural components (walls & ceiling) by airblast and fragments
- Wall response including the large distortion and fracture of material, and the breaching of the wall permitting airblast and wall debris to flow into the second compartment.
- Interaction of the airblast and detonation products with the dynamically fracturing wall and with the debris fragments of varying sizes and velocities (i.e. a multiphase highly interactive flow)
- Airblast and impact loading of walls in the second compartment
- Depending on the static and dynamic pressures remaining in the airblast, and depending on the momentum/energy in the debris fragments, additional rooms may be breached.

Numerical Analysis Tool - MAZ code

The primary numerical tool for calculating the coupled airblast/structure effects is the MAZ (Multiphase/multimaterial Addaptive Zoning) finite difference code. The key features of this code which make it uniquely suited for fully coupled multiphase airblast-debris-structure interaction:

- Air, concrete, soil/rock and other solid materials can be treated simultaneously to calculate the response of the structure. Material interfaces are treated in a pure Lagrangian fashion, permitting detailed elastic-plastic-failure material properties to be employed. MAZ uses an Arbitrary Lagrangian Eulerian scheme (ALE) so that the Lagrangian surfaces can be smoothly coupled with the Eulerian cells needed for the detonation products and air.
- Multiphase physics is treated with mature models that have been validated in dusty airblast and cloud calculations (Rosenblatt, et. al., 1979) (Hassig et. al., 1991, 1992). These models include the drag and thermal interactions of solid debris with hot combustion products as well as air. This feature is essential if the effects of the solid debris from a ruptured wall is to be calculated properly.
- A Second Order Closure Turbulence Model (SOCTM) is standard. This model is superior to $k-\epsilon$ models. For example, $k-\epsilon$ models solve only two differential equations while SOCTM solves all 6 differential equations for the Reynolds Stresses. Thus there are significantly less assumptions which must be made to achieve closure. SOCTM also treats the dispersion of dust/debris based on particle size and turbulent intensities. This feature is important for properly dispersing particulates debris and for calculating the airblast wave dissipation due to turbulence.

The MAZ (Multiphase/Multimaterial Adaptive Zoning) code is based on the mature physics and chemistry models from the DICE (Rosenblatt & Eggum, "1973), (Hassig et. al., 1991), and CRALE (Schuster et. al., 1984) codes. The aerodynamic and atmospheric multiphase physics models in DICE include drag/thermal interactions for particles, a second order closure turbulence model and finite rate chemistry. Both the MAZ and DICE codes have been validated with instrumented experiments (HE airblast, HE Nuclear simulators, Shock Tube and other events/experiments) (Hatfield, Hookham, & Rosenblatt, 1991), (Rosenblatt, et. al., 1979), and (Hookham, et. al., 1990). The solid mechanics models in CRALE include sophisticated hydro-elastic-plastic-fracture material models and an Arbitrary Lagrangian Eulerian (ALE) zoning methodology. Similarly, this code has also been extensively validated for cratering and ground shock against both HE and underground nuclear test (Rosenblatt, et. al., 1979), (Koik & Schuster, 1985), (Koik & Schuster, 1987), (Schuster, Cooper & Katz, 1991)

ALE (Arbitrary Lagrangian Eulerian) and Adaptive Zoning

MAZ uses a flexible adaptive zoning technique which includes an ALE feature; i.e., the ability to move the outer mesh points in a Lagrangian, Eulerian or user-specified mode. Figure 1 shows an early-time calculation of the airblast interaction with a 6 inch thick concrete wall and limestone floor in an underground bunker. The geometry considered, adaptive mesh, and the pressure field 0.25 msec after detonation of a 1000 lb conventional explosive (modeled in 2-D plane-strain) is presented. A real gas EOS was used for the air (Doan & Nickel, 1963) and HE products, a nonlinear Elastic Plastic constitutive model was employed, for the concrete and limestone. At the time shown, the stress wave is moving faster in the limestone than in the air, but negligible deformation at the air/floor interface is seen.

This calculation was run to 10 msec and compared to Case 2, described in the following section, which modeled the floor as a rigid boundary. The results were essentially identical which indicates that, at least for this yield and geometry, the rigid boundary approximation is adequate. This example illustrates the capability of MAZ to model complex multi-material geometries which is necessary in order to investigate more severe loading scenarios. Accurate modeling of the air/he/ground/structure interfaces and proper use of the hysteretic limestone/concrete material properties required the material interfaces to be treated in a Lagrangian fashion while the rest of the grid was smoothly moved between the interfaces. This ALE feature is essential if structural elements which deform and fail are to be accurately modeled.

The conditions for activating finer zoning or for dezoning are based on a user-specified subroutine involving gradients in any physical parameter and/or specific values and/or physical regions in space/time. Thus, very fine zoning can be placed in the airblast/structure regions of primary interest. The adaptive zoning captured the shock and contact discontinuities quite well.

Coupling Severe Local Distortion/Failure to Overall Structural Response and In-Structure Environment

The approach of treating airblast loading and response as two separate, decoupled processes is acceptable so long as the response does not affect the loading. However, there is a broad and important class of problems where this is not true, where the airblast loading is so massive that response is

immediate, or where the burst occurs close to a wall, where it produces severe local damage, breaching the wall and providing an early-time path for airblast and detonation products to flow into the adjacent room. This situation requires a fully coupled loading/response analysis.

For efficiency, we performed the following calculation in the 2-D plane-strain mode: The explosive was initialized as a uniform energy density source in a cylinder with radius 2 ft and length 10 ft (i.e., depth of room in z-direction). More realistic initial conditions, i.e. 1-D HE burn calculations overlaid into a 2-D or 3-D mesh, are of course also possible in MAZ.

The calculation, described in the previous section, indicated that modeling the floor boundary as a rigid surface is adequate in order to simulate to airblast interaction with the concrete wall.) Also, this second calculation involved airblast/debris interactions with two walls separating three bunker chambers.

Wall material was modeled with a 15 ksi unconfined compressive strength (f_c) concrete. For these calculations, two simplifications were made with respect to wall failure and break-up:

- Failure occurs when the tensile pressure in the concrete exceeds 100 bars ($\sigma_t = 1.5 \text{ ksi} = 0.1x f_c$) and directional shear fracture effects are ignored.
- Fracture occurs in regions defined by the outermost MAZ computational cell; that is, a majority of embedded cells in a outer mesh cell (6 inch by 6 inch) must fail in order that ALL cell material in that region be converted to a mixture of dense wall debris and air.

Figure 2a shows pressure fields at 1 msec. At this time, the first wall has just begun to break-up at the lower junction with the floor. Peak loading of 1 kbar on the wall at the centerline. The wall has been displaced by about 6 inches at this location and time. In order to show the location of the wall in the figures, a uniform gray-scale is used to tag the intact (non-fractured) wall material. Nevertheless, the full elastic-plastic stress tensor is calculated in the intact wall.

At the time of fracture, the wall material and momentum in a cell are converted to a mixture of air (10% volume fraction) and three debris size groups (0.01, 0.1, and 1.0 cm particles). Subsequently, the DICE multiphase logic is utilized to transport the gas and solids with size-dependent drag interactions.

By 8 msec (Figure 2b), the first wall has completely fractured. Note the relatively high debris density and pressure along the 10-20 ft height at the initial range of the first wall, indicating the airblast

has not had time to disperse through the wall debris. (The debris is shown by line contours superimposed on the pressure contour field). Also note the curved shape of these debris contours and the larger downstream displacement along the roof. Here the increased pressure due to the reflected wave off the roof serves to enhance the wall loading in this region. At lower heights, a relatively weak airblast (~10 bar) has penetrated through the dispersing wall debris. The start of deformation and the development of a reflected pressure wave is also apparent at the base of the second wall. The second wall is experiencing airblast pressures of 10 to 30 bars. A portion of the first wall debris is just beginning to impact the second wall. In this calculation, however, we did not explicitly impart debris momentum to the second wall. Failure of the second wall results from airblast only.

Figure 2c shows the pressure field and wall debris at 14 msec. Note, that at this time, the second wall has fractured from the floor to 11 feet, and that over 10 bar pressures exist in the third room. Figure 3 shows a blowup of the complex air velocity and debris concentration fields in the 2nd/3rd rooms. The low velocity motion field along the roof, to the right of the wall, is induced by the wall motion, prior to failure. This calculation was also run out to 20 msec indicating that the second wall completely shatters by 18 msec.

CONCLUSION

A calculational capability that allows for airblast interaction with dynamically deforming structure surfaces has been presented. This unique first principal calculational approach for predicting airblast within compartmented structures, wall loading, subsequent fracture/breakup, and fully coupled multiphase airblast-debris-structure interaction can now be used to address many realistic problems.

ACKNOWLEDGMENT

The work reported herein was conducted for the Defense Nuclear Agency under Contract No DNA001-92-C-0164. The permission from DNA to publish this paper is gratefully acknowledged.

References

- Doan, L. J. and Nickel, "A Subroutine for the Equation of State of Air," Air Force Weapons Laboratory, TM-63-2, May 1963.
- Hassig, P.J., Schlamp, R.J., McArdle, J.C., and Rosenblatt, M., "Numerical Simulation of Dust/Ice Clouds from Nuclear Bursts," DNA-TR-90-91, Defense Nuclear Agency, January 1991

Hassig, P.J., Hatfield, D.W., Hookham, P.A., Schlamp, R.J., C.T. Nguyen, and Rosenblatt, M., "Advances in Nuclear Cloud Modeling," DNA-TR-92-93, Defense Nuclear Agency, November 1992

Hookham, P.A., Lee, H.S., Hatfield, D.W., "Non-Ideal Airblast and Vehical Loads Predicions in Support of Rail Garrison", CRT3264f, 1990.

Koik, V.E., and Schuster, S.H., "MP2 Post-Shot Evaluation", DNA-TR-87-64, Defense Nuclear Agency, Feburary 1987

Koik, V.E., and Schuster, S.H., "Minor Scale Cratering & Ejecta Predictions", DNA-TR-87-64, Defense Nuclear Agency, Feburary 1987

Schuster, S., Macales, J., Koik, V., and Stokes, E., (1984), "CRALE users manual (revision 1)." Air Force Weapons Laboratory, AFWL-TR-83-48

Schuster, S., Cooper, A., Katz, S., "Prediction Calculation and Comparison with Misty Echo Ground Motions", DNA-TR-91-96, Defense Nuclear Agency, May 1991.

Rosenblatt, M. and G. E. Eggum, "DICE-A Two-Dimensional Implicit Code for Treating Compressible Flow in a Fluid-Particle Mixture", DNA 2976F, Defense Nuclear Agency, March 1973.

Rosenblatt M., K.N. Kreyenhagen, S.H. Schuster, R.J. Schlamp, P.J. Hassig, A.S. Porton, "Investigation of a High Explosive Technique for Simulation of Local Fallout From Shallow Buried Burst", DNA 5149F, Defense Nuclear Agency, November 1979.

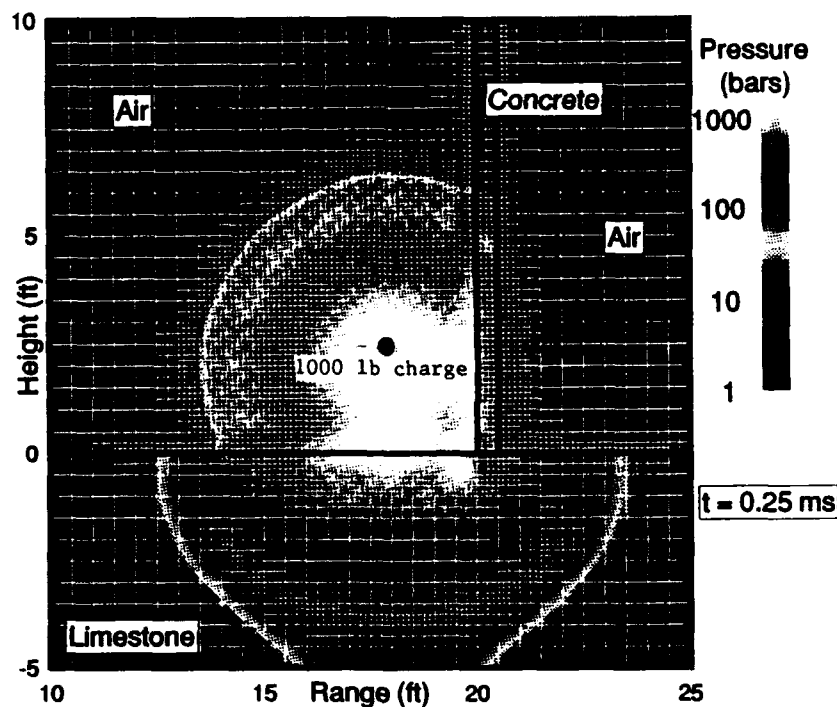


Figure 1. Air/Solid Blast Interactions In Vicinity of Air, Concrete Wall, And Limestone Floor.

CASE 2: 1000 lb Burst Close to Wall/Floor
Corner; Dual Concrete Walls.

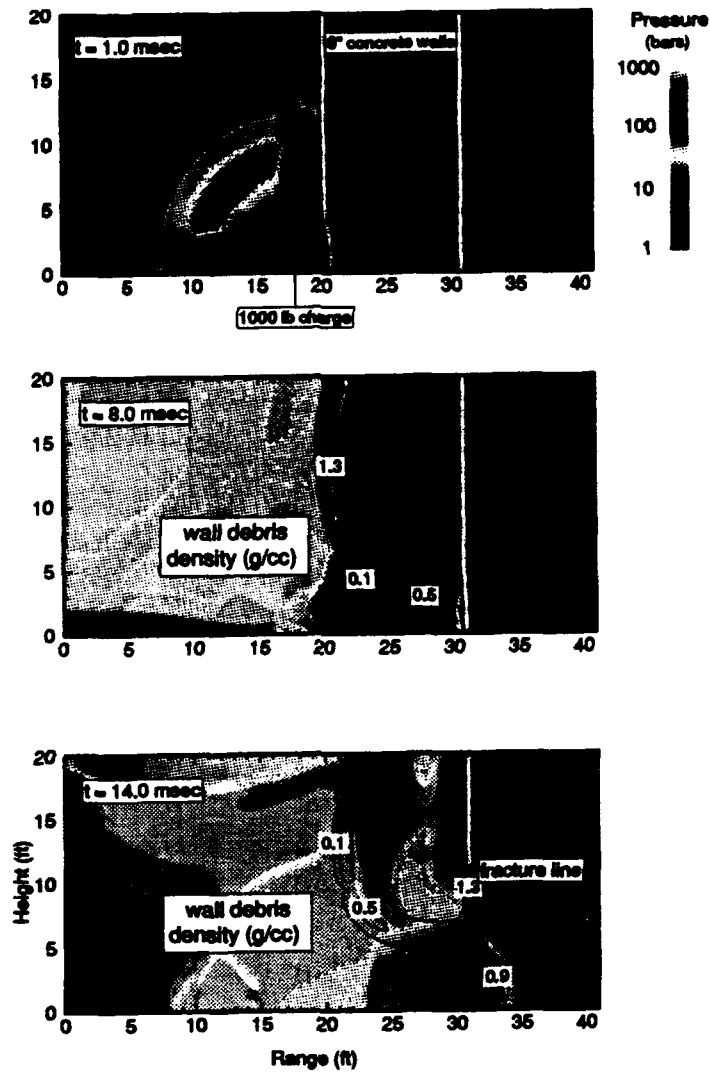


Figure 2. Pressure and debris density fields at 1.0, 8.0, and 14. msec.

CASE 2: 1000 lb Burst Close to Wall/Floor Corner; Dual Concrete Walls.

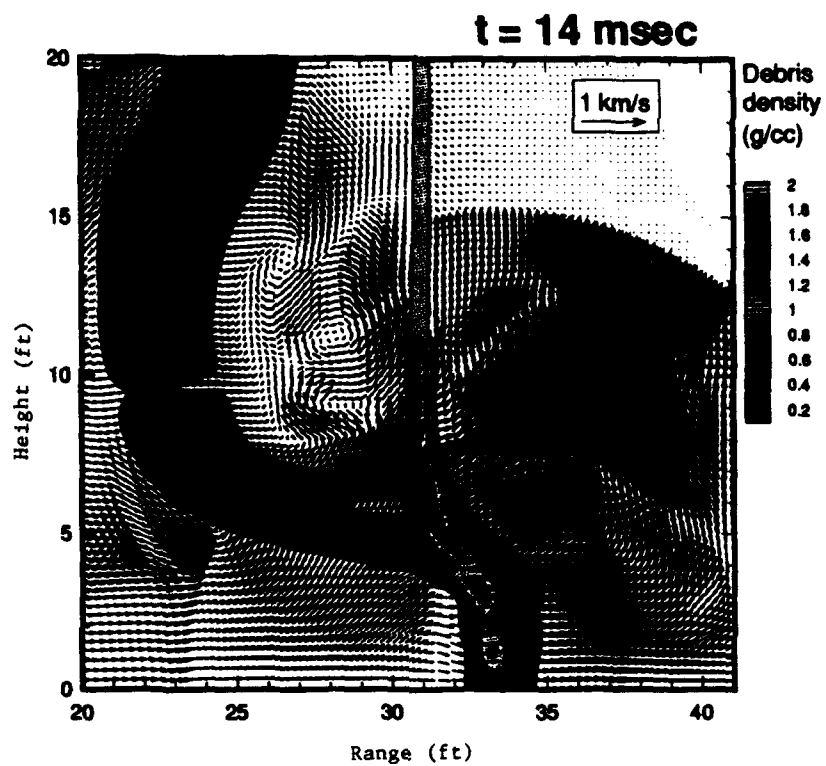


Figure 3. Air velocity vector field and debris concentration field near 2nd concrete wall.

Structural Response to Multiple Pulse Blast Loading

Mark G. Whitney
Darrell D. Barker
Johnny H. Wacławczyk, Jr.

Wilfred Baker Engineering, Inc.
8700 Crownhill, Suite 310
San Antonio, Texas 78209

Abstract

Blast resistant structures must often be designed to resist load histories made of several individual shock peaks which reach the structure in a very close time frame. Structural response to a multiple pulse shock load is often predicted by simplifying the load history as a single pulse. While this approximation is reasonable for structures in the impulsive and pressure response realms, it may not be appropriate for multi-pulse loading in the dynamic realm. This paper explores this area of loading, the dynamic realm, for a multiple pulse blast load, applied to both elastic and elastic-plastic responding systems. The paper principally references confined explosions but is general to the topic of multi-pulse loading.

Introduction

Structures subjected to a confined explosion experience distributed, time-varying blast loads on internal surfaces. These loading functions are most often approximated in design and analysis as a temporally well behaved, uniform load based on the average pressure and impulse values over a structural element. Analysis of blast loaded elements as equivalent Single Degree Of Freedom (SDOF) systems is widely accepted (Ref. 1, 2 and 3) for both elastic and elastic-plastic responding systems. Often the shock load is idealized as a triangular-pulse with an instantaneous rise to a peak overpressure followed by a linear decay to either ambient pressure or to a lower amplitude, longer term gas phase loading. A triangular shock pulse is chosen because of the availability of closed form solutions and design charts for response of elastic-plastic SDOF systems to such loads.

Methods predict loading in confined structures have improved in recent years. Programs such as SHOCK (Ref. 4) and BLASTX (Ref. 5) are available which predict blast loading inside concrete cubicles while accounting for reflections off surfaces both near the charge and adjoining the structural element under consideration. Hydrocodes have been used to predict loading on the structural shell of steel containment vessels such as test fire chambers (Ref. 6). Shock

history predictions representative of all methods are typified by multiple pulses which arrive close together in time, either separated or partially merged. These loads do not resemble the idealized single triangular-pulse often selected for input to SDOF analysis. They are likely to be non-uniform and characterized by random time variations in the arrival and duration's of individual pulses.

Figure 1, taken from Ref. 3 is typical of the shock loading measured inside a partially vented enclosure. Illustrated are multiple spikes which occur in close succession, with the first having the greatest magnitude and succeeding pulses reaching lower peaks until the shocks blend with the gas loading. Although Figure 1 is typical, it is possible for a blast environment to result in secondary shocks with greater amplitude than the first. The amplitude and phasing of individual shock pulses depends on the proximity of the charge to the point of measurement, the size and geometry of the enclosure, and proximity of other reflecting surfaces to both the charge and the surface where the measurement is made.

Figure 2 is output from BLASTX for shock loading inside a cubicle with four walls and roof that are non-responding. Predicted is multi-pulse loading similar to that in Figure 1. The SHOCK program does not provide a plotted output, however a summary of shock impulses and pressures are given (Figure 3) indicating the contribution from the incident wave and from adjoining surfaces. In addition, an "equivalent triangular pulse" is provided which has a peak pressure equal to the largest pulse pressure and a duration which is adjusted such that the impulse is equal to that provided by the total of all shock pulses. This equivalent pulse is recommended for use in design by Ref. 3. A similar methodology is offered by Ref. 2 which indicates that multiple pulses can be combined into a single triangular pulse; however, the initial pulse duration is maintained and the peak pressure is adjusted to conserve the total impulse.

In this paper we study structural response to time variations in the applied load similar to those

encountered in situations involving confined explosions. The results are compared with response to simple triangular approximations. The analysis is conducted using a one-dimensional elastic-plastic spring mass system which is a true SDOF system. This is appropriate since this study evaluates only time variations in the shock load and because SDOF equivalent systems are typically used in blast analysis and design. Variations in load distribution over an element are not considered here and are left to future studies. Also, consideration of a total load history, shock plus a longer term gas load, typical of confined explosions is not made here. Response to shock load alone is investigated and response to confined load are left to future investigation.

In Ref. 2 we have evaluated the response of an elastic spring mass system to a time varying load. The load is comprised of the three pulses shown in the inset in Figure 4 which are deemed representative of a shock history in a confined environment. The first pulse is the largest with the second having half the amplitude ($P/2$) and the same duration of the first. The third pulse has half again the peak of the first ($P/4$) while keeping its duration the same. The arrival of later pulses are spread in proportion to the arrival time of the lead shock, which Reference 2 indicates is related to the time for shocks to reverberate within a structure. The response of the spring-mass system to this triple pulse was compared to that under two separate triangular pulse load cases, also shown in Figure 4. One is a triangle with the duration of the first pulse of the triple-pulse, and a peak pressure adjusted to match the impulse of the triple pulse, we call the "combined pulse". The second is the first pulse of the triple-pulse, or referred to simply as the "first pulse".

The system can be solved for a maximum scaled elastic response

$$\bar{X}_{\max} = Xk/P$$

as a function of scaled pulse duration

$$\bar{t}_d = t_d \omega_n = t_d \sqrt{k/m}$$

Definitions of terms are provided in the nomenclature. The solution is shown graphically in Figure 4 for a particular scaled shock pulse duration and arrival time combination. The scaled maximum response for the triple-pulse tends to lie between the response of the first pulse and the combined pulse. This study indicated that the triple-pulse can cause maximum deflections in resonance as great as the combined pulse which serves as a conservative upper limit over a wide range of scaled frequency for elastic systems.

It was desired to expand this evaluation for the following conditions:

- Elastic-Plastic Response
- A Combined Pulse as Defined in SHOCK
- Variations of duration and Shock Arrival

Analysis

For the current study, a similar approach was taken to that in the analysis described above. Nondimensional terms now include scaled pulse duration, ultimate resistance, and deflection. These are defined as follows:

$$\bar{t}_d = t_d/T_n$$

$$\bar{X}_m = X_m/X_e$$

$$\bar{r}_u = r_u/P$$

where:

$$T_n = 2\pi \sqrt{m/k}$$

$$X_e = r_u/k$$

The responding system is described by a bilinear, elastic-perfectly plastic resistance-deflection curve. A program which solves the SDOF equation of motion for an undamped, elastic-plastic system through numerical integration was used to make numerous calculations of response under the varied load conditions. The results are provided in a series of plots which compare maximum scaled deflection to scaled duration (Figures 5-10 for several different scaled ultimate resistance values. In each plot four cases are evaluated as follows:

- **Case 1:** First Pulse Only
- **Case 2:** Combined Pressure Pulse; Duration equal to incident pulse with pressure increased to conserve impulse; i.e. Peak pressure = $1.75P$ and duration unchanged.
- **Case 3:** Combined Duration Pulse: Similar to that provided by SHOCK, pressure matching incident pulse with duration increased to preserve impulse, i.e. Duration = $1.75t_d$ and peak pressure unchanged.
- **Case 4:** Triple-Pulse: Second peak half the first, third peak half the second and all durations the same, t_d .

These four cases are depicted in figure 11. Note that the scaled pulse spacing for case 4 has not been specified in Figures 5-10 as was provided in Figure 4.

where a specific combination of pulse duration and pulse spacing was evaluated resulting in resonance peaks at several scaled time values in the dynamic range (remember that pulse spacing is tied to duration). In Figures 5-10 the reported scaled deflection for Case 4 at each scaled duration value are maximums determined by varying the pulse arrival times while keeping duration constant. For example, at a scaled duration of 1.0, the pulse arrival time was varied over a range starting with no separation between pulses out to at least one natural period past the maximum displacement; then, the largest scaled displacement over this range was plotted. Thus, the reported information considers an upper limit of response for a triple-pulse load (Case 4) regardless of their spacing. The pulse spacing which results in resonance at each scaled duration is thereby selected. Figure 12 is a summary of the triple-pulse solutions (case 4), presented in figures 5-10.

Discussion

A review of Figures 5-10 indicate that maximum displacements resulting from the triple-pulse load often agree closely with one or more of the single triangular pulse approximations and at times it deviates from all. To no surprise, triple-pulse displacements at small t_d/T_n are nearly identical to displacements for either of the single triangular pulses where the total impulse is conserved (Cases 2 and 3). Similar alignment is observed for large values of t_d/T_n when compared to results for single triangular pulses where the peak pressure is conserved (Cases 1 and 3). These are impulse and pressure sensitive load-response regimes, respectively.

In the range of about $0.3 < t_d/T_n < 2$ the triple-pulse deviates from the various single triangular approximations. For r_u/P between 1.0 and 2.0, it tends to stay with the $1.75P$ curve (Case 2) at smaller values of t_d/T_n and then transitions to the $1.75t_d$ curve (Case 3) as t_d/T_n increases. Response is underpredicted by the $1.75T_d$ approximation in this transition region and at these scaled resistances. The largest difference we encountered is an approximately 50% greater scaled displacement predicted for the triple-pulse condition than for Case 3. As ru/P decreases below 1.0, Case 3 tends to either approximate or overpredict (as r_u/p becomes smaller) deflections for the triple-pulse over the entire range of t_d/T_n . Demonstrated at $ru/P = 0.7$ is close agreement out to about $t_d/T_n = 1.0$. As ru/P decreases, the $1.75t_d$ curve generally predicts greater displacements than the triple-pulse results. Note that $1.75P$ (Case 2) always is an upperbound for displacements, although significant response overpredictions can occur, particularly in the pressure sensitive realm.

The following suggestions are made for determination of design loads in protective structure design:

1. A reasonable estimate of the time-varying load function could be made using methods such as BLASTX or others which distinguish between individual shock pulses. This allows definition of the pulse shapes (amplitudes and durations). Then, an adjustment of the pulse spacing is made to ensure resonance conditions. Thus, inaccuracies in predictions of system period and shock pulse phasing are accommodated.
2. After prediction of the shock load history, a design load can be defined as a single triangular pulse which has a duration equal to that of the principal shock pulse and a pressure adjusted to conserve total impulse. Such an approximation should always result in conservative response predictions.
3. The SHOCK program is often used to predict design loading. It provides an equivalent triangular pulse which adjusts the duration to conserve impulse as in Case 3 above. Application of this load can result in underprediction of response as noted. For $0.3 < t_d/T_n < 2$ and $0.7 < r_u/P < 2.0$ we suggest that response predictions using the SHOCK output be increased by 50%. This represents the largest expected difference compared to a multi-pulse load at resonance. Outside of these limits, no change in predicted deflections are necessary.
4. Figure 12 can be used to estimate response if the load under evaluation is characterized by a significant lead pulse and smaller training pulses such that the load history resembles the pattern in Case 4. If the first pulse is significantly larger than the trailing shocks, then we suggest the approach taken in Case 2. Maintain the lead shock duration and adjust the peak pressure to conserve impulse.

Nomenclature

r_u = ultimate unit resistance

k = unit stiffness

t_d = load duration

m = unit mass

ω_n = frequency

P = peak shock pressure

X = deflection

X_e = elastic deflection

T_n = natural period

X_m = max deflection of an elastic-plastic SDOF system

X_{max} = maximum deflection of an elastic SDOF system

References

1. Biggs, John M, "Introduction to Structural Dynamics", McGraw-Hill Book Company, New York, 1964.
2. "The Prediction of Blast and Fragment Loadings on Structures", prepared for United States Department of Energy, by Southwest Research Institute and Wilfred Baker Engineering, Inc., under contract with Mason & Hanger, and Battelle Pantex, Report No. DOE/TIC 11268, July 1992.
3. Department of the Army, the Navy and the Air Force, "Structures to Resist the Effects of Accidental Explosions," Department of the Army Technical Manual TM51300, Department of the Navy Publication NAVFAC P397, Department of the Air Force Manual AFM 8822, November 1990.
4. Anon., "SHOCK Users Manual", Version 1.0, Naval Civil Engineering Laboratory, Port Hueneme, CA, January 1988.
5. Britt, J. R. and Eubanks, R. J., "Modifications of the BLASTX Code to Treat Shock Wave Propagation Through Passive Blast Attenuating Structures," Contract Report SAIC Report 405915, March 1992 (Draft).
6. White, R.E., "Component Test Facility Test Cell Qualification Test Program," SwRi Project 06-1452 Final Report, September 1987.

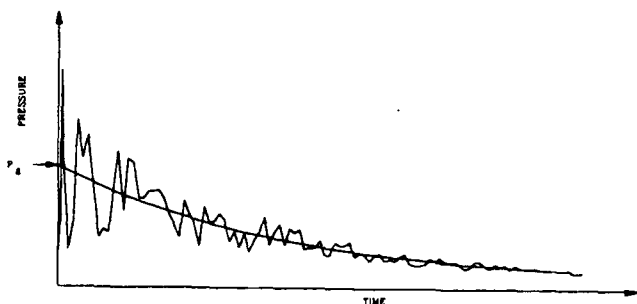


Figure 1: Typical Pressure-Time History for a Confined Explosion

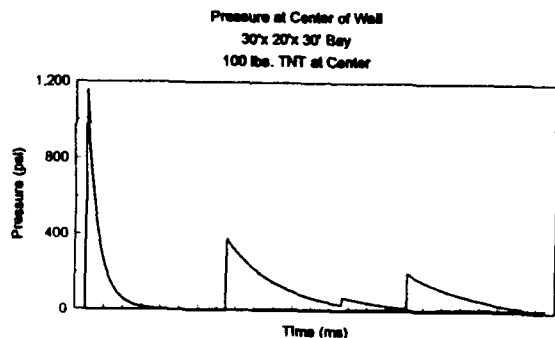


Figure 2: Typical BLASTX Output

PROGRAM SHOCK VERSION 1.0

PROGRAM FOR CALCULATION OF AVERAGE BARRIER REFLECTED
SHOCK PRESSURES AND IMPULSES DUE TO AN INCIDENT WAVE AND
REFLECTED WAVES FROM ONE TO FOUR REFLECTION SURFACES.
ORIGINAL PROGRAM "PAINPRES" DEVELOPED BY AMMANN AND WHITNEY
MODIFIED INPUT AND OUTPUT BY NAVAL CIVIL ENGINEERING LAB

INPUT DATA

DATA SET TITLE:

SHOCK INPUT 1

A. CHARGE WEIGHT, LBS.....	10.00
B. DISTANCE TO BLAST SURFACE, FT.....	13.50
C. WIDTH OF BLAST SURFACE, FT.....	30.00
D. HEIGHT OF BLAST SURFACE, FT.....	30.00
E. HORIZONTAL (X) DISTANCE TO CHARGE FROM REFLECTING SURFACE NO. 2, FT.....	15.00
F. VERTICAL (Y) DISTANCE TO CHARGE FROM REFLECTING SURFACE NO. 1, FT.....	15.00
G. REFLECTING SURFACES	
"1" FOR FULL REFLECTION, "0" FOR NONE	
SURFACE 1 (FLOOR).....	1
SURFACE 2 (LEFT SIDEWALL).....	1
SURFACE 3 (CEILING).....	1
SURFACE 4 (RIGHT SIDEWALL).....	1
H. REDUCED SURFACE CALCULATION.....	NO

ANALYSIS RESULTS

	AVERAGE SHOCK PRESSURE AND SCALED SHOCK IMPULSE ON BLAST SURFACE DUE TO WAVES OFF REFLECTING SURFACES				DUE TO INCIDENT WAVE
SURFACE	1	2	3	4	
IMPULSE	7.7	7.7	7.7	7.7	12.8
PRESSURE	14.5	14.5	14.5	14.5	28.9

MAXIMUM AVERAGE SHOCK PRESSURE AND TOTAL AVERAGE SHOCK IMPULSE ON BLAST SURFACE	
SCALED IMPULSE	43.8 PSI-MS/LB**(1/3)
IMPULSE	94.3 PSI-MS
PRESSURE	28.9 PSI
DURATION	6.52 MS

SCALED IMPULSES HAVE BEEN DIVIDED BY $W^{1/3} = 2.15$

Figure 3. TYPICAL SHOCK OUTPUT

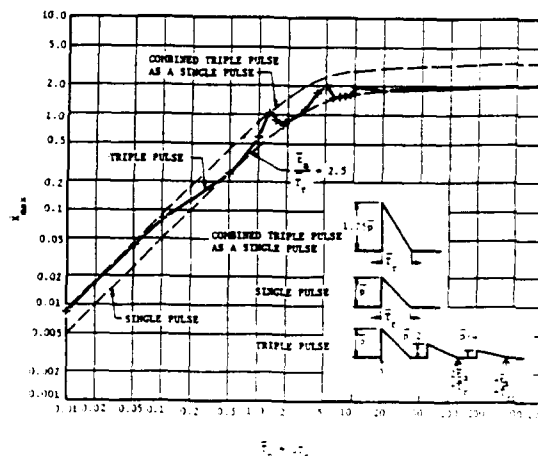
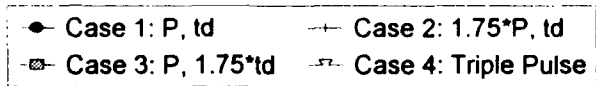
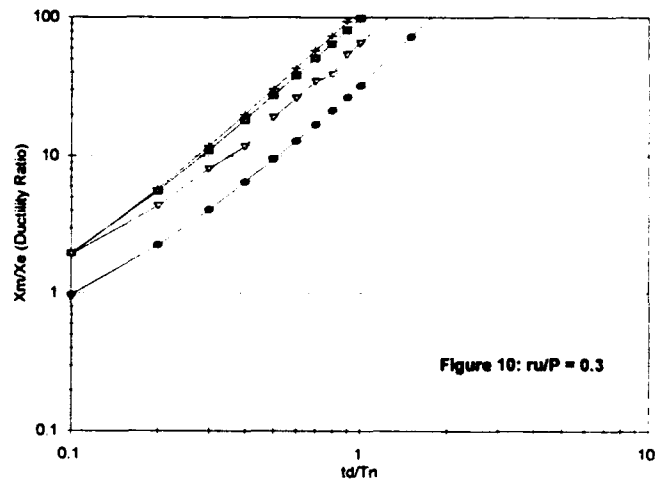
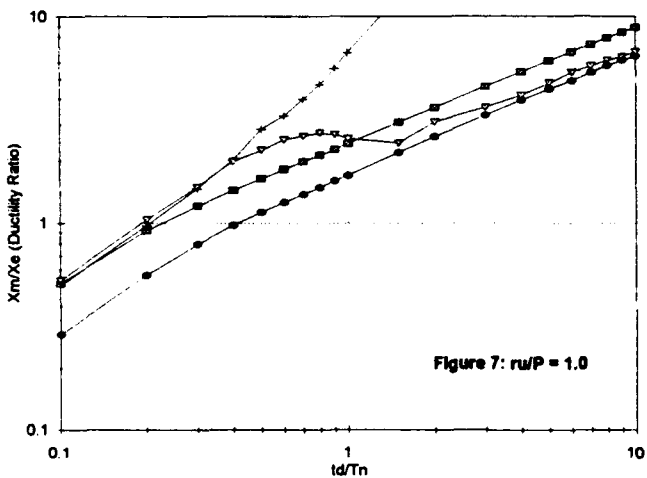
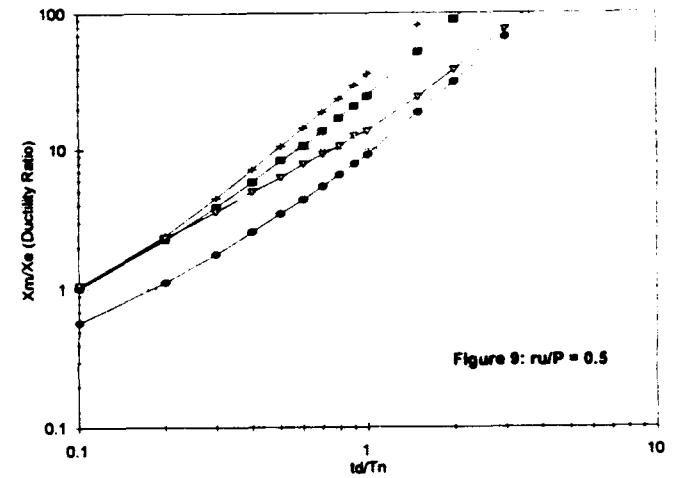
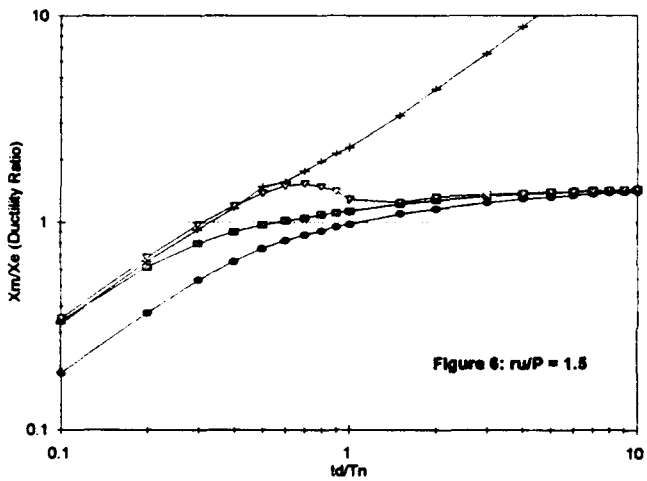
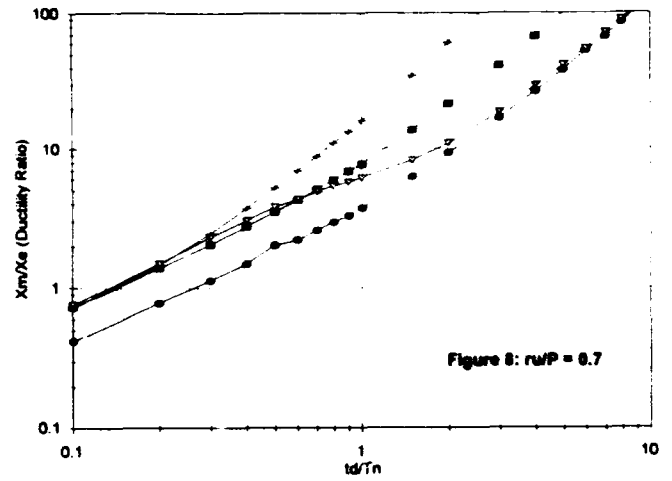
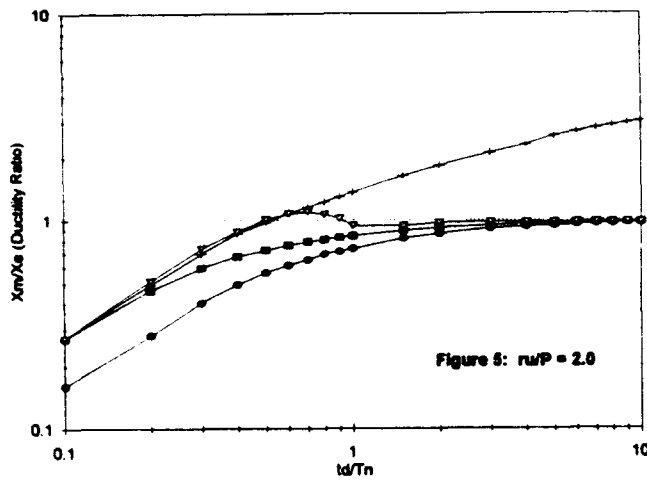


Figure 4. ENVELOPE OF SOLUTIONS FOR MAXIMUM DISPLACEMENT FOR TRIPLE PULSE BLAST LOADING



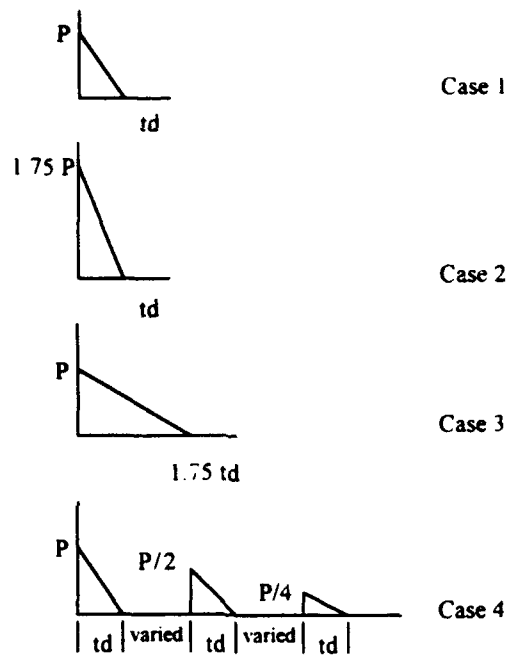
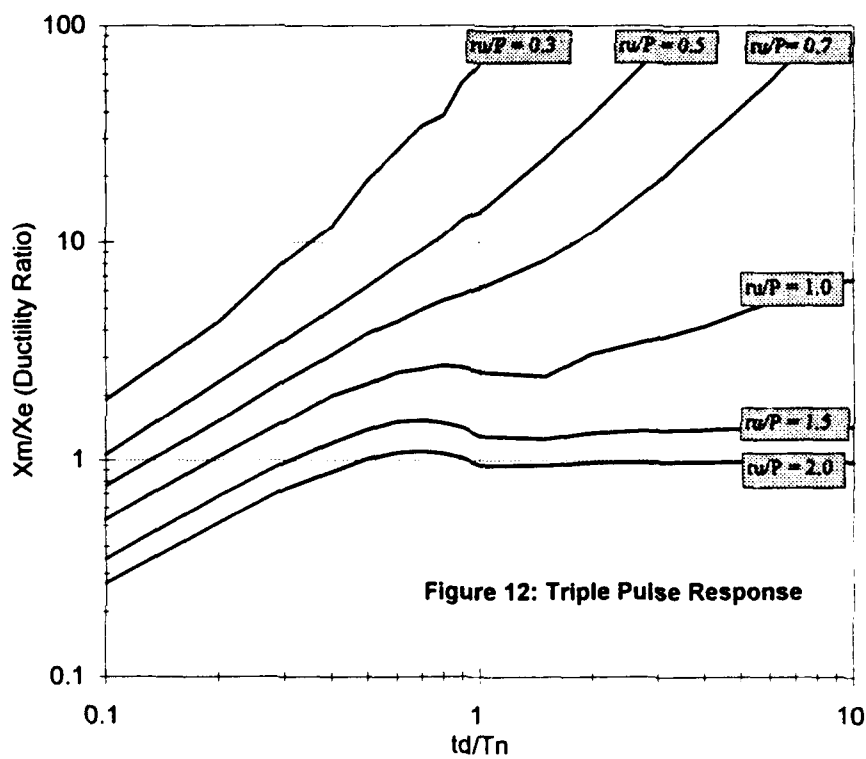


Figure 11: Blast Loads Functions used in Analysis



TEST OF CIVILDEFENCE CONTROL CENTRE, RC 90

Tommy Wirén

Swedish Rescue Services Board
Karlstad, Sweden

ABSTRACT

At White Sands Missile Range, NM, a series of tests with conventional weapons were performed against a civil defence rescue centre Rc 90. The purpose of the test was to validate the design and to perform a full scale test of all technical systems. There were systems for power-generation, ventilation, airpurification, cooling, radio and telephone. Also blast valves, doors, shutters and cable inlets were tested.

The test programme included MK 82 GP bombs, 31 Kg TNT charges and a 1000 Kg FAE charge.

The test results show the importance of regarding the fragment effect on doors and walls. The installation systems functioned satisfactory, but the effect of small charges at close range have to be considered when choosing blast valves and other light mechanical components.

INTRODUCTION

Rescue centres Rc 90 are operation centres for the peace time rescueservices and also for the civildefence. They are designed as two storey buildings with a total area of 300 - 420 m². They are built as a part of a firestation and used in the everyday command and control work. The underground storey contains all the technical installations. When used in war, all the windows are closed with shutters and the centre is then entered through the basement via a blast lock. See fig 1.

The rescue centre is designed to withstand the effects from 250 Kg GP bombs at 1.5 - 3.5 m from the walls depending on the size of the centre.

The test object was a shelter 5 x 6 m. See fig 2, fig 3 and fig 4.

The shelter components were:

- two types of doors (concrete/steel design), (one standard, one reinforced)
- steel shutter (40 mm outside and 10 mm inside plates)
- blast valves (2 round, with disc and springs), (1 rectangular with tubes and springs)
- over pressure valves

TEST PROGRAMME

The test object had been used during the DNA DISTANT IMAGE test before the conventional weapons test with minor damages, that was repaired.

The location of the charges can be seen on figure 5. In all 11 accelerometers and 11 pressure gages were used.

All installations were run during the tests.

TEST RESULTS

.1 Test C1, a 31 Kg TNT charge

The charge was placed 2.0 m in front of the shutter on the ground.

The maximum pressure at ground level was 26 MPa. The prototype rectangular blast valve was destroyed. The disc valves got 10 mm radial deformations and shortened springs.

.2 Test C2, a MK 82 bomb

The bomb was placed 3.5 m in front of the door.

The pressure pattern can be seen in figure 6. The maximum acceleration at the side wall and floor was 500 G.

The fragments made up to 170 mm deep holes round the door, which was penetrated. See fig 7. Extensive spalling occurred around the door frame. The front wall got a 5 mm permanent deflection. The valves were hit by 50 fragments, some penetrating the 40 mm steelplate.

The discs got an uneven load distribution causing deformations up to 14 mm on half of the discs. The flanges of the cooling radiator were bent, due to the let through impulse.

The tubes in the tubevalve got stuck in outer position, due to deformations.

.3 Test C4, a buried 31 TNT charge

The charge was placed 3,5 m from the backwall at a level of the half wall height. There were no significant damage on the test object.

.4 Test C5, a MK 82 bomb

The backfill was removed before the test. The bomb was placed 6 m from the right side wall. The pressure pattern on the wall can be seen in figure 8. The acceleration in the wall was about 1000 G. Extensive damages over the whole wall were caused by fragments. Specially in a band at 1,6 - 2, 2 m height. The depth of the band was 50-150 mm.

There was a hole $0,2 \times 0,2 \text{ m}^2$ which easily could be enlarged to $0,7 \times 1,4 \text{ m}^2$ by a small hammer. On the inside of the wall there was spalling from an area of about 2 m^2 and also diagonal cracks. See figure 9 and 10. The overpressure valves were pressed through their seats. The airpurification unit was torn from the wall, but otherwise working.

.5 Test C3A, a MK 82 bomb

The bomb was placed 6,9 m from the wall. Before the test all the installations were taken out.

The fragments gave also this time a band of damage about 1,9 m above ground. The damage was less severe than after test C5, with craters in the concrete with a depth of 50 - 150 mm. See figure 11. On the inside there were small areas ($4\text{-}5 \text{ cm}^2$) of spalling, and the wall was covered by cracks. The concentration of cracks was in the upper half of the wall. Also the largest deformation was at the same level, indicating that the fragments caused the biggest damage.

The permanent deflection was 8 mm and the maximum deflection was 24 mm.

.6 FAE test

The large hole in the right side wall was repaired with concrete before the test. The overpressure valves were covered with a steel plate.

The FAE charge was placed at 19,8 m distance from the front wall on a 3 m high structure. The charge consisted of a container with 1000 litre fluid. The fluid was blown into the air by an explosive charge in the container. The FAE cloud should get 47 m diameter and 8,5 m height. The cloud could thus cover half of the object. The cloud was ignited as far from the object as possible.

The reflected pressure on the front wall differed in the four gages from 3,5 - 12 MPa. On the left side wall was recorded 4 MPa and on right side wall 1,5 MPa. See fig 12. These pressures were of short duration only a few milliseconds. Inside the object 10 KPa was recorded.

The acceleration of the front wall was 3000 G. 5000 G was recorded on the door leaf and 1400 G on the shutter frame. Vertical acceleration in the floor and roof was 50 G and in the side walls 200 G and 300 G were recorded.

No new damages on the framework could be seen. It seems as the old cracks had been enlarged and extended in general. No enlarged permanent deflection of the walls could be found.

The valve discs got radial deformations from 5 - 11 mm. The upper valve disc got an asymmetric deformation. No damage on the tube valve, but the dustfilter behind the valve was destroyed. One of the cable transits was pushed inwards.

.7 Test C3

The test was performed as test C2 with the intention to test a reinforced door leaf. The door leaf consisted of a steel frame covered with 8 mm steelplates. Additionally the door had another two 8 mm steelplates inside. The interior of the door was filled with concrete. The door thickness was 120 mm.

The door got severely damaged by fragments, but no fragments penetrated the door leaf. It was not possible to open the door. The hinges had to be cut so the door could be pulled out of the frame. The fragments caused a large hole in the front wall. See figure 14.

CONCLUSIONS

The sidewalls of the test object was 0,35 m thick. That is the wallthicknes of Swedish standard shelters. These walls will give protection against MK 82 bombs from about 7 m distance. The fragments are the decisive factor. The same type of bomb will penetrate the Rc 90, 0,5 m wall after the second shot from 3,5 m distance.

The fragments do not likely penetrate the reinforced door, but the door need a redesign to function after a test.

The blast valves with discs worked well, but the let through impulse was a bit too high for the chosen type of cooling radiator.

Smaller charges at close distance can destroy light mechanical components in valves.

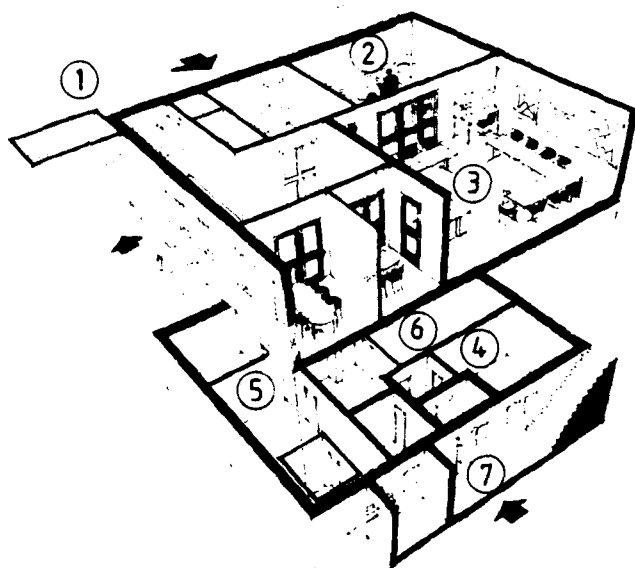
When designing protective structures great care should be used to shield off fragments from door, valves etc.

The powergeneration system worked well, although it had no protection against blast waves in the exhaust pipe

The radio and telecomsystems functioned well, but some modifications are needed in the fixation of the equipment.

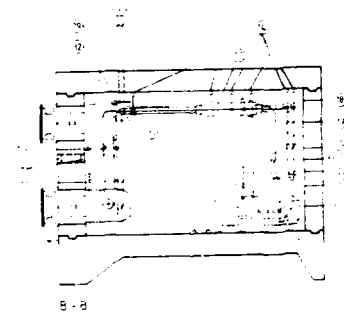
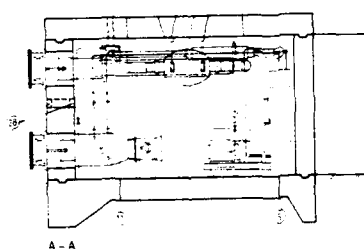
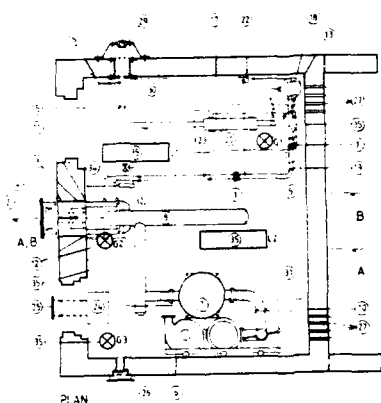
The air purificationssystem could withstand the blast without special attuniation volume other than the inlet pipe behind the valve.

The chosen types of fixation for the installations proved to be satisfactory.



1. Firestation
2. Radio communication room
3. Operation room
4. Power generation room
5. Air condition room
6. Staff accomodation
7. Entrance at war

Figure 1 RC 90



- | | | | |
|----|---|----|-----------------------------------|
| 1 | = Cramp with pendulum fixed to attachment beam at ceiling | 17 | Silencer |
| | = Cramp with pendulum fixed to wall | 18 | Expansion vessel |
| 2 | Rapid closing valve components and protection plates | 19 | Cooling pipe system |
| 3 | Valve disks and support plates | 20 | Power unit |
| 4 | Air Inlet | 21 | Cooling hoses |
| 5 | Electric Installation box | 22 | Feeder pump |
| 6 | Air purification unit | 23 | Power unit controle box |
| 7 | Prefilter | 24 | Rapid closing valve and filter |
| 8 | Air intake tubes | 25 | Protection plate |
| 9 | Pendulum suspension | 26 | Over pressure valves |
| 10 | Tube for the air purification unit | 27 | Cable Inlets "KGHS" |
| 11 | Cooling condensor and fan | 28 | Cable Inlets "RGB" |
| 12 | EMP transient supressor | 29 | External part of the exhaust pipe |
| 13 | Oiltank | 30 | Radiocommunication box |
| 14 | Attachment beams | 31 | Telecommunication box |
| 15 | Exhaust pipe | 32 | Air dome |
| 16 | Watertrap | 33 | Flexible exhaust hose |
| | | 34 | Safety pressure relief valve |

Figure 2 TEST OBJECT



Figure 3 VENTILATIONSSYSTEM



Figure 4 POWER GENERATION

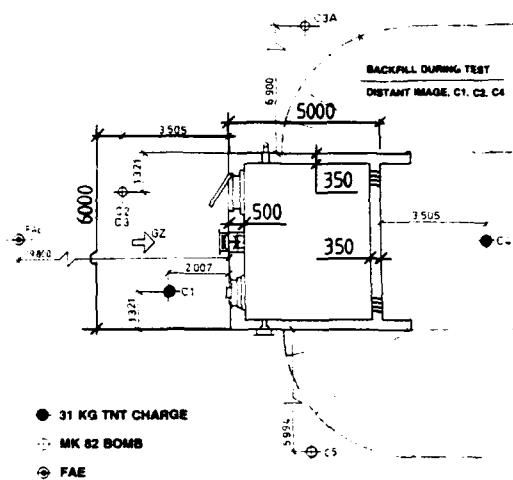


Figure 5 LOCATION OF CHARGES

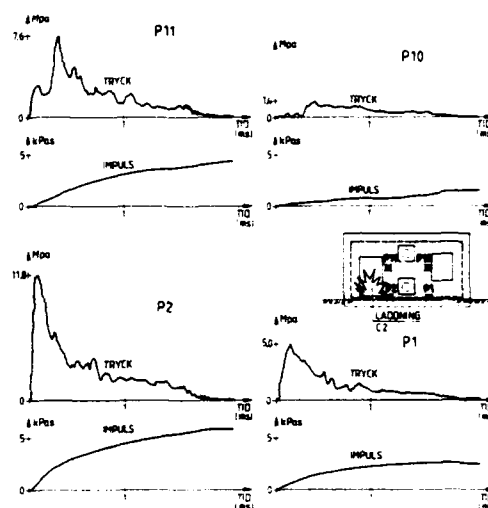


Figure 6 TEST C2



Figure 7 FRONTWALL AFTER C2

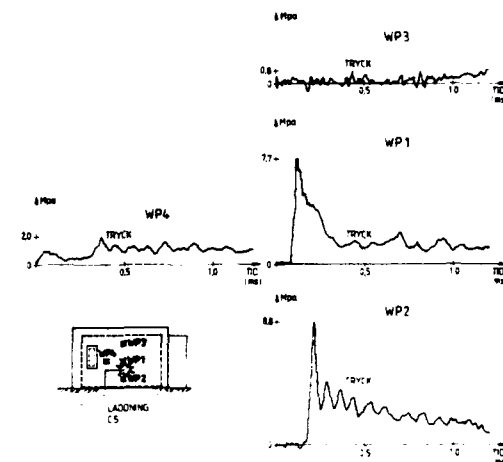


Figure 8 TEST C5



Figure 9 FRAGMENT EFFECT TEST C5



Figure 10 WALL INSIDE TEST C5

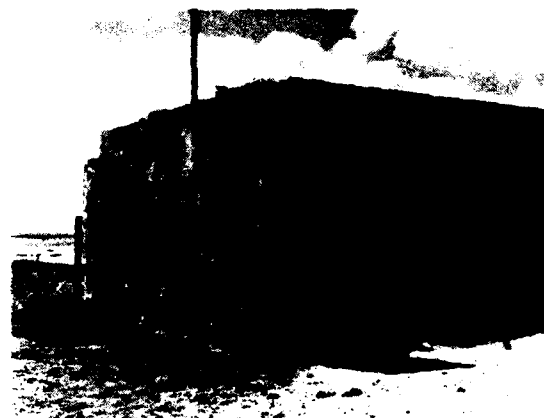


Figure 11 FRAGMENT EFFECT TEST C3A

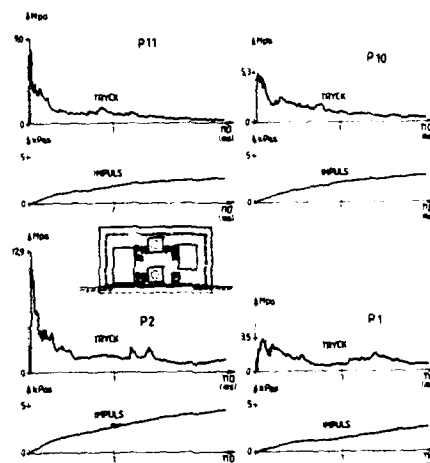


Figure 12 FAE

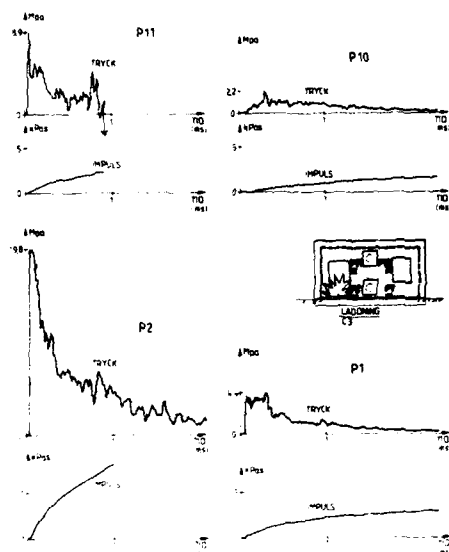


Figure 13 TEST C3



Figure 14 FRONTWALL AFTER C3

COUNTER TERRORIST FORTIFICATIONS IN NORTHERN IRELAND

by

Lieutenant Colonel R WATT RE
Commanding Officer 62 CRE (Works) Royal Engineers

and

Major MG RICHARDSON RE
Second In Command 523 Specialist Team Royal Engineers (Works)

INTRODUCTION

Fortification is the science and art of strengthening defensive works. It is a science because structures must be designed to be effective and durable. Equally it is an art because it requires ingenuity on the part of the engineer to outwit the aggressor. Within the British Army the Royal Engineers are responsible for fortifications and defensive works. The aim of this paper is to review the defensive and protective systems used by the Royal Engineers to defeat terrorist attacks in Northern Ireland.

BACKGROUND

In August 1969 the British Army deployed to Northern Ireland, in support of the Royal Ulster Constabulary (RUC), to control civil disobedience. The deployment was to be only temporary to allow the police time to reorganise in the face of the unrest. Initial structures were constructed using temporary engineering expedients such as sandbags for sangars and corrugated iron sheeting to provide Cover From View (CFV) screens. The structures could cope with the minor threat from small arms and could easily and quickly be removed as the political situation dictated. Designs and techniques evolved daily.

During the 1970's terrorist attacks became better organised and more sophisticated in the use of weapons. The threat spectrum widened to include grenades, rockets, mortars and car bombs. In response new building systems were developed. Sangars were constructed using specially configured high density blocks capable of providing protection against most small arms fire. They were surrounded by wire mesh anti-rocket and anti-grenade screens. Buttressed block work blast walls were constructed around vulnerable accommodation buildings and along exposed base perimeters. Bases were surrounded by more robust CFV screens and concrete bollards were positioned at key locations to create a greater stand-off against car bombs. During the 1980's the terrorist devices increased again in range, size and effective power. Current layouts and designs of military installations have been developed to counter the increased threat. By necessity some structures have become massive and consequently semi-permanent.

CURRENT THREATS

The aim in designing fortifications is to provide an engineering solution to a tactical problem. Specific forms of attack must not be examined in isolation because each mode of attack demands distinctive defensive measures and conflict may occur. The overall threat must be carefully assessed to determine the weapons likely to be used, the likely firing points, the chance of an attack and the acceptable level of damage.

Small Arms. Modes of attack, using small arms, include the opportunist hit and run, ambush/sniper shoots and conventional attacks with up to 30 terrorists mounting an assault. The weapons used include; 9 mm Pistol, Soviet AK 47, Armalite and Ruger 14, 0.5 inch Browning and 20 mm Recoilless M42. Technical data on the weapons and their effects are shown in Table 1.

Grenades. The latest (fifteenth model) PIRA grenade is contained in a large coffee jar and contains between 0.5 lb and 1.1 lb of SEMTEX high explosive and ball bearings as shrapnel. It is detonated via a pressure release switch which is triggered when the glass breaks on impact.

Rockets. The most popular rocket used by the terrorists is the Soviet RPG 7. The weapon weighs 5 lbs and has an effective static range of 500 m. It has a 0.9 lb shaped charge which is detonated either by piezo electric fuse triggered on impact or by a time delay fuse. On detonation it projects a jet of molten metal capable of penetrating 400 mm of mild steel. Neglecting the effects of the jet, the rocket body can strike a target with a kinetic energy of 1,035 Joules.

Mortars. There are a variety of improvised mortars used by the terrorist organisations. Technical data on those most commonly used is shown in Table 2. The devices are becoming more sophisticated with initiation methods including the use of; timers, light sensitive command, command wire and radio control. The terrorist is very creative in the use of readily available materials. Modern home made explosives now have the same power as an equivalent weight of TNT.

Ser	Weapon and Ammunition	Calibre (mm)	Weight of Round (gms)	KE (Joules) and Velocity (m/s)			
				Muzzle		200 m Range	
				KE	Vel	KE	Vel
(a)	(b)	(c)	(d)	(e)	(f)	(g)	(h)
1	9 mm Pistol 19 Ball	9.00	7.45	584	396	320	293
2	39 Soviet AK 47	5.45	3.45	1397	900	930	734
3	Armalite and Ruger 14 ball	5.56	3.56	1798	1005	1009	753
4	.30 M1 Carbine	7.62	7.13	1298	603	475	365
5	SLR/M60 Ball	7.62	9.33	3275	838	2225	690
6	7.62 x 39 Ball	7.62	7.90	1993	710	1071	520
7	0.5 inch Browning API	12.70	42.10	16583	888	12599	774
8	20 mm Recoilless M42 APT	20.00	136.00	45167	815	29263	656

Table 1. Small Arms - Kinetic Energy.

Ser	Type	Total Weight (kg)	Weight of Explosive (kg)	Dia (mm)	Max Velocity (m/s)	Eff Range (m)	Remarks
(a)	(b)	(c)	(d)	(e)	(f)	(g)	(h)
1	MK 6	1.8 (4 lbs)	0.3 (0.7 lb)	60	100	1000	Contents in all Mortars may be either Home Made or commercial explosive.
2	MK 10	64 (141 lbs)	20 (44 lbs)	150	45	300	Launch tubes are made from industrial gas cylinders and bombs from 1.4 m rolled steel pipe. The firing angle is 45 degrees. Variants with initiation systems are: MK 10/1: Time fused, flash bulb and safety fuse MK 10/2: Time fused, rimfire cap and safety fuse MK 10/3: Omni directional impact fuse.
3	MK 11	-	10 (22 lbs)	150	-	500	Omni directional impact fused. Uses same launch tube as MK 10, but has greater range.
4	MK 12	-	2 (4.4 lbs)	145	-	-	Shaped charge warhead with head-on impact fuse. Uses same launch tube as MK 10.

Table 2. Improvised Mortars.

Vehicle Bombs. Most vehicle bombs range between 100 lbs to 600 lbs equivalent weight of TNT. However some recent bombs have been found to contain up to 2000 lbs equivalent weight of TNT. The effects from a 1000 lb bomb can be seen in Figure 1.



Figure 1. 1000 lb Bomb - Coleraine, November 1992.

COMMON PROTECTIVE MEASURES

Design considerations must cover all means of providing protection to a location and not only the purely physical protection provided by building fortifications. Use should be made of camouflage and concealment techniques both to help disguise vulnerable buildings and to deceive the terrorist. A good choice of layout and of siting an installation can maximise natural protection and minimise the need for physical protection without detracting it from its primary function. Numerous protective measures have been developed over the years to combat terrorist attacks.

Firing Point Denial. Likely firing points can be denied to the terrorist either by physically changing the nature of the ground, by the use of obstacles and remote sensors, or by aggressive patrolling.

Access Denial. Wire obstacles, fences and vehicle ditches are used to delay or deny access. These are improved by the addition of modern electronic surveillance equipment such as ground sensors, motion detectors and remote Closed Circuit Television (CCTV) cameras.

Observation Denial. The terrorist is denied observation of military sites by the use of CFV screens. There are two systems currently being used in Northern Ireland. Temporary CFV screens utilize Corrugated Galvanised Iron (CGI) sheets supported by lattice braced scaffold frames which are set in 1½ ton precast concrete blocks placed directly on the ground. Permanent CFV screens are constructed using steel profile sheets supported by steel universal columns bolted onto concrete pads. The pads weigh over 6 tons and unlike those for the temporary screen are set into the ground. The system is known as Button On Fence (BOF) and after the bases have been positioned it is quick to erect and modify.

Blast Walls. There are 2 blast wall systems in general use. Temporary protection is provided by The Rapid Assembly Protective Wall (RAPW), a modular reusable system. It is constructed from 3 major components; a concrete pad, a steel 'A' frame and a reinforced concrete facing slab. The wall is 4 m high and is bolted together in multiples of 2 m bay lengths. RAPW gives protection against small arms rounds up to 0.30 inch AP. With the inside of the frame packed with sandbags the wall has been shown to withstand a 300 lb charge at 12 m stand off. Permanent blast walls are constructed using precast reinforced concrete panels supported between the flanges of universal columns set in large concrete foundations. The walls are expensive to construct and are only built either in areas exposed to car bombs or to protect "soft" important installations from mortar attacks. In extremely vulnerable locations 2 walls are built in parallel and the gap in the middle infilled with compacted sand.

Rocket Protection. Weld mesh 'Dudding' screens are built at a stand off from the defended structure to provide protection against rockets. Ideally they are provided at right angles to the likely line of flight of the rocket. In passing through the mesh, which can be of a number of types and sizes, the piezo electric fuse within the rocket may be disturbed and rendered inert. The rocket will go on to strike the target without detonating but may detonate a few seconds later due to the time delay fuse. The screens also fill a secondary role by protecting the structure from other projectiles such as grenades and some of the smaller mortars.

Mortar Protection. The provision of full protection against the kinetic energy effects of the larger mortars is very difficult, expensive and therefore seldom attempted. Key buildings are protected through the use of sacrificial roofs and by attaching anti-scabbing plates to the underside of the concrete roofing slabs. General protection is provided by wire mesh screens and glissades in an attempt to deflect the mortar onto the ground where the blast fragmentation effect can be minimised. Vulnerable buildings have in-situ reinforced concrete blast walls surrounding their footings. The walls have been shown to be capable of withstanding the in-contact detonation of a Mk 10 mortar.

Sangars. There are a great variety of sangars in use in Northern Ireland. High density concrete block sangars are still in use on the older sites. These were custom designed to meet the requirements of the particular location and most have now been upgraded with anti-scabbing plates and rocket screens. Mobile sangars are constructed from 20 mm mild steel plate and are for temporary use only. The latest sangars are of steel plate and reinforced concrete composite construction and include laminated glass windows with anti-shatter film. Additionally, Sangars positioned beside roads are upgraded with bolt on armour plating. An example of the new sangar, which costs approximately US\$100,000, is shown in Figure 2.

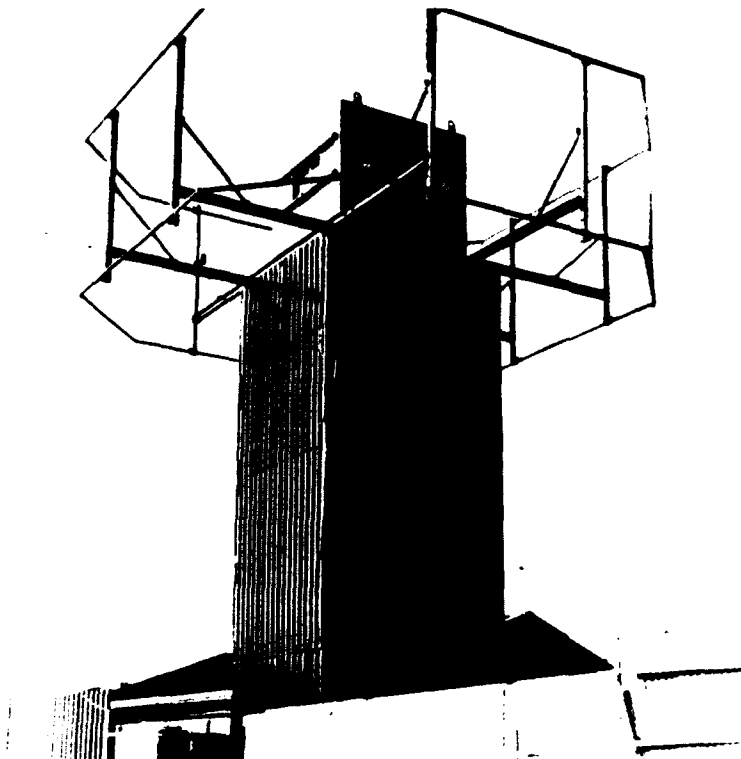


Figure 2. Raised Sangar with covered access and weld mesh rocket screens.

Hardened Accommodation. There are 3 types of hardened structure available for use in Northern Ireland and they are all of similar design. The basic structure consists of steel frames supporting precast composite steel and reinforced concrete panels. There are no windows and entry to the building is through 'Blast Lock' porches. Power and water supplies are run underground and enter the building through the floor. All services have been designed to withstand blast loadings. All 3 types of hardened structures have been proven against the Mk 10 mortar in direct contact. An example which costs approximately US\$ 1,000,000 can be seen in Figure 3.



Figure 3. Hardened Accommodation under construction.

CURRENT SITES

Hill Top Sites. Hill Top sites are located in remote areas overlooking the border and major roads. They house up to 20 men and are only accessible by helicopter or on foot. The major threats are from intruders and long-range opportunist shoots using heavy machine guns (HMG). Accommodation units are made from commercially prefabricated units. Maximum use is made of the natural ground and camouflage to conceal the units. Small arms protection is provided by steel plates welded to the faces exposed to the threat. Protection against infiltration is provided by wire obstacles, observation posts, modern surveillance equipment and patrols. Sandbags are positioned on the roof to provide some protection against grenades thrown by a successful intruder.

Border Sites. Border sites are located in rural areas along the border and house up to 20 men. Access is by helicopter and 4-wheel drive vehicles. The main threats are from intruders, tractor bombs, and from HMG, mortar and rocket attacks fired at long range from across the border. To gain maximum protection from the natural conditions the structures are buried below ground level. Only the heavily armoured command sangar and defensive sangar show above ground. Accommodation consists of commercial 'portacabins' positioned inside reinforced concrete bunkers. Sacrificial concrete slabs provide additional blast protection for the roof against mortar attack and vehicle bombs. Sangars are of armoured composite construction.

Permanent Vehicle Check Points (PVCs). There are 299 known border crossing points. PVCs are located on the major routes and can be manned by up to 45 personnel depending on the military requirement. These sites are vulnerable to the full threat spectrum. By necessity they are heavily fortified and are constantly upgraded with the latest

protective measures. Because of the increased threat from vehicle bombs the new designs for PVCs have the accommodation and main control centres located in 'Forts' positioned well away from the roads. (In the need to gain optimum stand off the Army has to purchase land. This is politically sensitive especially when compulsory orders have to be issued). The Forts are triangular in plan and are surrounded by BOF. The shape offers good all round defence using the minimum of manpower. Raised hardened sangars are positioned in 2 corners of the Fort and can view all sides. An example can be seen in Figure 4. Improvements include hardened accommodation and an array of sophisticated surveillance devices. The raised sangars also control the traffic on the roads which is the primary function of the PVC. The new PVC designs include the use of alternative routes for the traffic so that a suspect vehicle can be isolated. Traffic control measures include the use of; collision barriers to channel the traffic, speed humps to slow the traffic, traffic lights and drop arm barriers to stop the traffic, CCTV cameras and intercoms to check on drivers and passengers, and dragons teeth and rising steel bollards to prevent vehicles crashing through the check point. In addition, all the measures are covered by fire from sentries.



Figure 4. Modern Triangular Fort In Support of a PVC

RUC Stations. Police stations are generally located within the local community and will remain in place after the Army has been withdrawn. They often lack space to gain optimum stand off from a perimeter however because the buildings are permanent they can afford to be of more robust construction. Typical features include; perimeter blast walls to protect against vehicle and package bombs, a profile sheet topping to the wall to provide CFV and to defeat grenades, 'Barbican' entrances (screened search bays) for vehicle access which are guarded by a heavily armoured front sangar equipped with modern surveillance devices. The main station building is remote from other buildings to minimise the effect of a bomb being carried in. Protection from mortars is provided by a sacrificial top floor to the building.

CONCLUSION

The size and effectiveness of terrorist mortars and bombs have increased dramatically over the past few years. To contain the threat, the Army has been forced to enhance their fortifications. Where possible the stand off distance has been increased. Physical protection measures have been improved by the construction of more permanent, hardened structures. Further measures include the use of more sophisticated surveillance equipment. It is expected that fortifications and defensive works will continue to evolve to contain any developments in the threat.

RESPONSE OF PILE FOUNDATIONS IN SATURATED SOIL

Barry L. Bingham
Robert E. Walker
Scott E. Blouin

Applied Research Associates, Inc.
4300 San Mateo Blvd NE, Suite A220
Albuquerque, New Mexico 87110

ABSTRACT

This paper discusses the results of a 3-D finite element calculation of reinforced concrete piles in a saturated soil subjected to ground shock from a buried conventional weapon detonation (12.5 m standoff). The problem configuration models pile test structures from the Pile Cal Test conducted at UTTR, Utah in September, 1992. The calculation would have been a pretest prediction had it not been for technical difficulties that did not allow completion of the calculation before the event. Once the technical difficulties were detected and solved, a single calculation was performed within a week of the event with all model parameters identical to what would have been a pretest prediction. Digitized versions of the measured data were obtained several weeks later to allow the comparisons shown in this paper. The agreement between the calculation and measured test data (both free field and pile response) is excellent. Due to the limit of finite boundaries, the calculation was only run to 25.2 ms after detonation. Analysis of the test results and 25.2 ms of calculation results suggest that there may be significant aspects of pile response during the late time flow of the saturated free field. Future calculations will investigate late time behavior through the use of motion boundary conditions and simpler models of the reinforced concrete piles.

INTRODUCTION

The United States Air Force has numerous critical facilities supported on pile foundations at bases located atop weak saturated soils. Structures such as aircraft shelters and command and control facilities supported on pile foundations in these geologies are likely to be subjected to enhanced blast and shock effects from conventional weapons which were not considered in the design of these structures. Of particular interest are the TAB VEE aircraft shelters supported on a pile foundation in weak saturated soils found at Kunsan AFB, Korea.

Six piles were tested at a representative saturated site at the Utah Test and Training Range (UTTR) in September 1992. The Pile Cal Test (Blouin, et al. 1992) subjected piles to the ground shock environment of a buried MK83 bomb detonation. Baseline test piles were placed at four ranges, i.e., sure kill, sure safe, and two ranges bracketing moderate damage. Estimates for these ranges were 5, 7.5, 12.5 and 20 m from a MK83 conventional bomb, detonated at 5 m depth in the baseline geology. The piles had varying foundation support and tip bearing conditions. The soil strata consists of fine silty sand, clayey silt, and sandy,

silty clays. The depth to bedrock averages about 14 m below the testbed surface. The water table at the time of the event was about 2.1 m below the testbed surface.

Piles 3 and 6 from the Pile Cal Test were modeled using the finite element method in three dimensions. Piles 3 and 6 were both located 12.5 m from the center of a buried MK83 bomb detonation. Pile 3 supported 21,800 kg of lead weight above the ground surface to simulate the weight of an aircraft shelter. Pile 6 did not support lead weights, but it did have a reinforced concrete deadman to restrict the outward radial motion of the foundation to simulate the stiffness of the aircraft shelter arch.

FINITE ELEMENT MODEL DESCRIPTION

The finite element model discussed in this paper more closely resembles pile 3 in that it did not have the deadman restraint and it did model the 21,800 kg of supported lead weight. The modeling approach used a condensed version of the DYNA-3D code (Hallquist 1991). The condensed version of DYNA-3D is a non-vectorized version, with generic Fortran. It will compile and execute on a wide variety of machines including PC's. The foreseen uses and adaptation of the DYNA-3D code (insertion of material models, adaptation of structure-media-interaction interface models, concerns of memory allocation on in-house computers, etc.) necessitated the use of a much smaller and concise version of DYNA-3D.

The finite element model consists of a soil wedge covering 19.4 degrees of arc around the explosive center (see Figure 1). A vertical plane of symmetry exists that runs radially from the center of the explosive to the center of the pile such that a full arc of 38.8 degrees is represented in the finite element simulation.

The soil was modeled all the way to the explosive boundary interface. The MK83 conventional weapon used in the Pile Cal Test contains 189 kg of H-6 explosive. The density of H-6 explosive is 1760 kg/m^3 which results in an initial explosive volume of 0.1072 m^3 . The explosive volume was simplified into a spherical shape (0.2947 m radius) for ease of finite element meshing. The steel casing of the MK83 weapon was not included in the finite element model since the weapon detonates at a depth where the explosive energy is completely coupled with the surrounding media. According to Gurney equations (Gurney 1943), the work of expansion of the steel casing is less than 1% of the total explosive energy, which is a negligible amount compared to the other uncertainties of the problem.

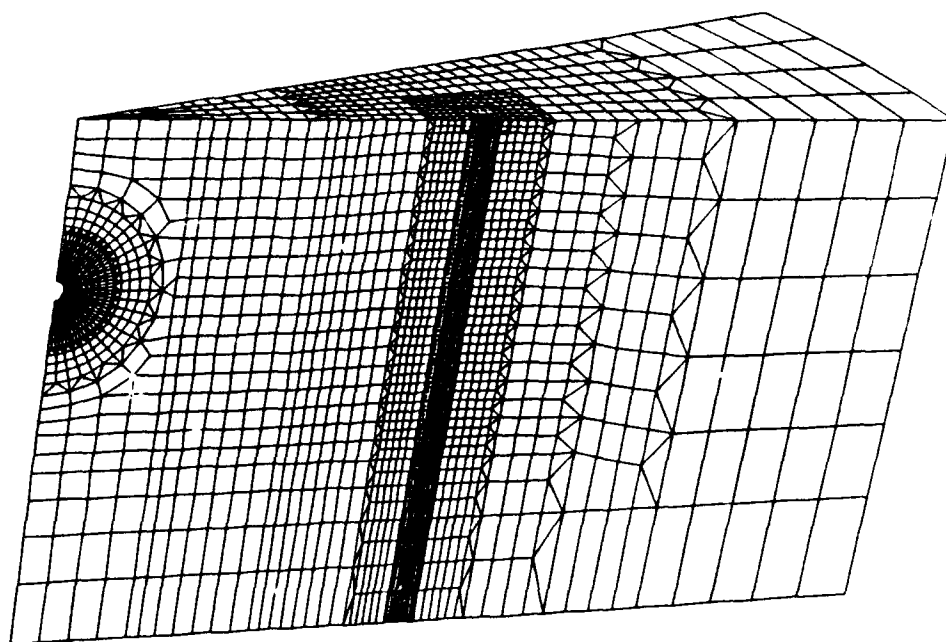


Figure 1. Three dimensional finite element mesh for the 12.5 m pile and soil wedge.

The inside surface of the explosive sphere is a large displacement/rotation pressure boundary with the pressure magnitude determined from the following JWL equation (Dobratz 1981):

$$P(V) = Ae^{-R_1 V} + Be^{-R_2} + \frac{C}{V^{\omega+1}}$$

where:

$P(V)$ = pressure magnitude in Mbar
 V = ratio of current explosive cavity volume to the original volume of the explosive material
 $A, B, C, R_1, R_2, \omega$ = Equation of state parameters dependent upon explosive type

The solid continuum elements used to represent the soil and concrete in the mesh use a constant stress formulation (Flanagan and Belytschko 1981) with exact volume integration. The exact volume integration is extremely important especially for the soil elements in close proximity to the explosive source due to the amount of distortion the grid experiences and the need to calculate exact volumetric strain for proper pressure-volume behavior of the host material.

The grid is partitioned into eight different regions of time step integration. Soil elements immediately adjacent to the explosive run at the finest time step, while the large soil elements at the more distant ranges run at the largest time step. The different regions are interfaced with tied or sliding/separating surfaces to permit common multiple integration across the interface. This capability, termed subcycling, allows very efficient calculation times for complicated geometry and material combinations.

Nodes on the two side boundaries and bottom boundary can only move within the planes of those boundaries. Nodes on the vertical axis above and below the explosive

sphere can only move along this axis. Nodes on the most distant curved surface are only free to move in the vertical direction. The bottom and back boundary locations were selected so that significant reflections would not influence pile response for a period of about 20 ms after shock arrival at the pile. The duration of the major transient ground shock was anticipated to be significantly less than 20 ms based on preliminary free-field calculations. The back boundary is 29 m from the explosive center, while the vertical height of the finite element grid is 16.41 m. Only 16.41 m of vertical height was modeled due to the uncertainty of soil stratification and bedrock location below 12.5 m. The first calculation was geared towards investigating pile response to the initial passage of the ground shock for a total run simulation of approximately 25 ms. Future calculations of longer duration will use prescribed motion boundary conditions for the bottom and back boundaries obtained from a 2-D free field calculation of the same soil stratification.

The analysis approach modeled the nonlinear response of the individual soil components; that is, the drained or effective stress-strain response of the porous skeleton and the pressure-volume relationships of the solid grains, pore water, and pore air. The behavior of these constituents were combined using fully coupled two-phase theory (Kim, et al. 1988 and Simons 1989). The fully coupled effective stress model considers the strain in the skeleton resulting from the compression of individual grains by pore pressure, and the volume change in the solid-fluid mixture due to effective stresses acting on the solid grains. This sophisticated formulation provides an accurate means of predicting undrained material response for any porous material up to very high pressures.

In the finite element simulation, the water table is 1.5 m below the testbed surface (the 2.1 m depth measured on the day of the event was not known by the analyst when the calculation was run). The Bingham Three-Invariant

(B-3I) material model (Bingham 1992) was used to model the soil skeleton and pile concrete. The B-3I model was selected due to its computational efficiency, versatility, and capability to model both tensile fracture and compressive strength loss under continued loading (strain softening). The material model fits to available laboratory test data on the different soil layers are presented in (Blouin, et al. 1992).

For the saturated layers, the pressure-volume behavior is strongly dependent upon the initial porosity. Higher initial porosity results in softer pressure-volume behavior, approaching the bulk stiffness of water. The porosities of the different soil layers in the baseline site model ranged from 25% to 67%. The pressure-volume behavior of the soil above the water table is based on drained laboratory test data of saturated soil samples. This resulted in a pressure-volume behavior that seemed excessively soft compared to the other layers. Assumptions used to represent the soil above the water table should be reviewed for reasonableness at some future date.

Gravity forces existed in the calculation and originally it was planned to initialize the soil strata to geostatic load conditions prior to detonation of the explosive. The particular technique developed at Applied Research Associates had been used successfully in the past for non-layered, single material geologies and had not been correctly adopted for layered geologies at the time of this calculation. Time constraints did not allow the modifications and testing of a corrected technique.

The finite element mesh for the reinforced-concrete pile is 9.754 m long from the bottom to the base of the foundation and the half foundation is 1.524 m by 1.068 m by 0.406 m in the X, Y, Z directions, respectively. A schematic showing the reinforcing details is shown in Figure 2. The grid for the pile/foundation combination has 2,115 nodes, 1,024 8-noded solid continuum elements to represent the concrete in the pile, 576 bar elements to represent the longitudinal prestressing steel, 256 bar elements to represent the longitudinal mild steel, 512 bar elements to represent the spiral reinforcement, 32 membrane elements to represent the steel plating on the end of the pile, and 280 solid continuum elements to represent the concrete in the foundation block. All reinforcing steel (except in the foundation) was modeled explicitly in the calculation with a permanent bond between steel bars and concrete continuum elements. The mass density of the foundation elements was artificially set to a very large number in order to account for the 21,800 kg of lead weights placed on top of the foundation.

The pile is initialized to prestress conditions determined from a prestressing finite element calculation of the pile structure without the surrounding soil. Prestressing is a condition of static equilibrium between the concrete and tensioned steel. Since DYNA-3D is an explicit integration code, static solutions are obtained through a technique known as dynamic relaxation. A type of mass damping is applied to the solution scheme such that when a step load is applied (such as the prestress in the longitudinal prestressing steel), the calculation approaches the static solution without dynamic overshoot.

The pile structure and the surrounding soil are interfaced with a sliding/separating (with re-impact capability) surface that transfers both normal and shear stresses. The

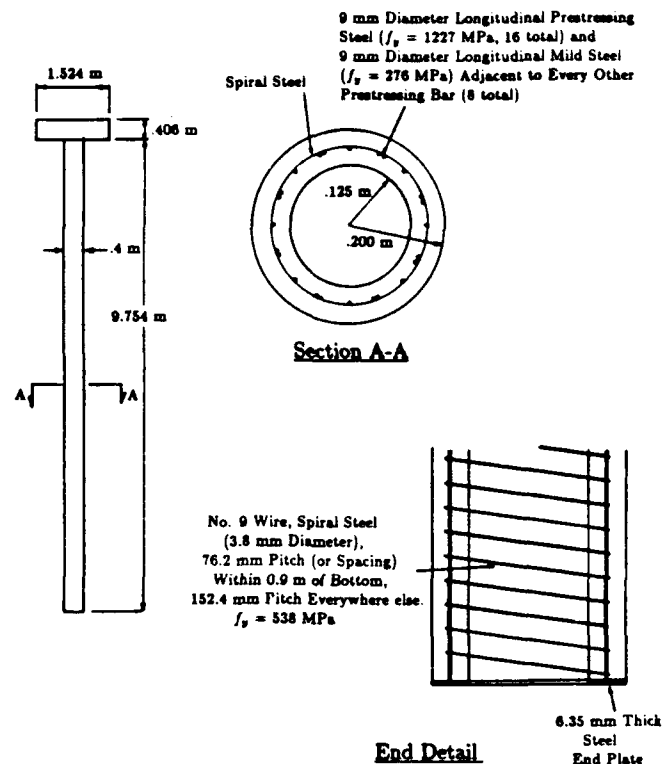


Figure 2. Design details of the piles in the Pile Cal Test.

sliding/separating surface has the added capability of allowing the pile structure to run at a fine time step, while the immediate surrounding soil runs at a larger time step. The normal stress that is developed at the interface does not allow nodes on the opposite side of the interface to pass through each other. The shear transfer is based on a $\rho C \Delta V$ model which has been shown in prior studies to adequately reproduce measured structure-soil interface data in a transient ground shock environment (Frank 1982 and Frank and Cole 1984). The value of the shear stress is a function of the relative tangential velocity between the soil and structure (ΔV) times the density of the soil (ρ) times the shear wave speed of the soil (C). The value of this shear stress is then limited by a bilinear envelope which is a function of the normal stress at the interface.

The combined soil and structure mesh for the entire wedge included 18,868 nodes, 19,052 elements, 8 interface surfaces (7 of which were tied), and 1 pressure surface. The calculation took 350 minutes of CPU time on a CRAY YMP for a 25.2 ms simulation.

RESULTS AND COMPARISON TO TEST DATA

During the 25.2 ms simulation, the concrete in the pile did not experience any strain softening which suggests that the piles at the 12.5 m range will not experience any compressive failure damage. Tensile strains reached a maximum of 0.02% strain over most of the length of the pile and 0.07% strain at the top of the pile at the junction with the foundation (upstream side). These suggest only minor, barely visible hairline cracks due to tensile fracture occurring at the top of the pile.

Figure 3 shows comparisons of calculation results to measured test data for horizontal motion at several ranges from the bomb at the depth of the bomb (5 m) in the saturated clay layer. The test data are integrated acceleration measurements. Positive motion is out, away from the bomb. All time history plots shown have zero time coincident with bomb detonation.

Both the calculation and the test data show an initial, high-frequency pulse of 1 to 2 ms duration, followed by a lower, yet steady, outward flow of the free field. In general the agreement between the peak velocities and late time outward flow is excellent. Close-in to the bomb at ranges of 1.8 m and 2.5 m where the finite element mesh is very fine, the wave shape of the initial pulse matches the measured data very well. But at greater ranges from the bomb, the increasing coarseness of the finite element mesh tends to spread out the width of the initial pulse compared to the measured data even though the peaks are closely matched.

The significant, late-time, outward flow in the calculation (and most probably the actual testbed) is due to the very low shear strength of the shocked, saturated, host material. In the calculation, the soil does not develop any shear strength due to the presence of water and the algorithms in the effective stress formulation. The lack of shear strength (liquefaction) allows the free field to flow with little resistance to shear deformation.

Figure 4 shows comparisons of horizontal (radial) stress time histories at several different ranges from the bomb center at the depth of the bomb in the saturated clay layer. Again, the agreement is excellent both in peak and waveform. The excellent agreement both in velocities and stresses, suggests that the effective stress model does a very good job in characterizing the response of the saturated soil media. Both the calculation and the test data show a stress pulse of 1 to 2 ms duration upon initial passage of the ground shock, followed by a nearly stress free environment during the late-time, outward flow of the free field.

Figure 5 shows comparisons of measured horizontal/radial motions on the piles with corresponding results from the finite element calculation. The radial motion of the foundation from the finite element calculation showed very little outward motion for two main reasons; (1) the foundation elements are very massive to represent the presence of the supported lead weights and (2) the relatively soft character of the upper dry layer does not put significant load on the foundation and upper portion of the pile. The motion measured on the pile foundation is low compared to the motion measured in the rest of the pile, but it is greater than as indicated by the calculation. It is possible that some slippage may have occurred between the foundation and supported lead weights and it is also possible that the soil layer next to the foundation is more substantial than that modeled in the finite element calculation. It is also possible that the differing locations of the center of mass of the lead weights/foundation combination played a role. A future calculation should probably include a separate block of material representing the supported lead weights, separated by a sliding/separating surface.

It is clear to see from Figure 5 that the middle section of the pile at bomb depth is the first to see outward radial motion. Quickly after this, the bottom tip of the pile sees

radial outward motion since it is in a higher bulk stiffness, saturated media. The top of the pile sees a significantly reduced outward pulse, since it is in an unsaturated soil media and connected to a large amount of lead weights. This story is spelled out very clearly in what appears to be an excellent set of measured data in conjunction with well-thought-out placement of these gages.

Post-test inspection (internal video probes, internal still photographs and visual inspection of the piles after excavation) revealed the following damage to piles 3 and 6. Pile 3 had barely visible hairline cracks on the upstream side at the top of the pile near the foundation. Pile 3 also had localized bending failure at 1.54 m depth below the ground surface. No corresponding bending failure was observed in pile 6. However, the tensile hairline cracks on the upstream side at the top of pile 6 were much more noticeable than on pile 3.

The orientation of the bending failure in pile 3 suggests a rotation of the lower part of the pile out away from the bomb while the upper part remained relatively still. Inspection of the measured test data shows that the greatest amount of differential motion on the pile occurred between 40 and 300 ms, which suggests that the damage may have been a late time phenomenon. But why did this failure not occur in pile 6 where the foundation seems to be even more restricted against outward radial motion due to the presence of the deadman? It is most likely not due to any variance in the ground shock seen by the piles, because the measured data suggests an extremely uniform distribution around the bomb. The answer probably lies in the very heavy mass supported by pile 3. The extra compressive stress placed in the pile due to the supported weight in combination with the late time bending stresses caused the compressive failure. Apparently the bending stresses alone in pile 6 were not enough to cause failure.

CONCLUSIONS

The DYNA-3D finite element calculation closely matched the free-field data and pile response data measured from the Pile Cal Test. The effective stress modeling technique was very successful in reproducing the measure free-field environment.

The finite element calculation did not result in any significant compressive damage to the concrete in the pile. The calculation suggests only minor, barely visible hairline cracks due to tensile fracture near the top of the pile near the foundation junction. This damage description is an accurate description of the post test condition of pile 6, while pile 3 sustained more damage as discussed above. A review of the calculational results and measured test data suggests that the failure occurred late time (after 25 ms) and was due to the combined loading of induced bending from the late time flow of the free field and axial compression from the supported lead weights.

Future calculations will include free-field velocity driven boundary conditions, which will allow the calculation to be run to much greater simulation times. A simpler structural model, possibly using beam elements with damage capability, is needed for the pile in order to make longer simulation times feasible. Longer simulation times will allow investigation of late time interaction with free-field expansion. It is possible that the 25.2 ms simulation time of the calcu-

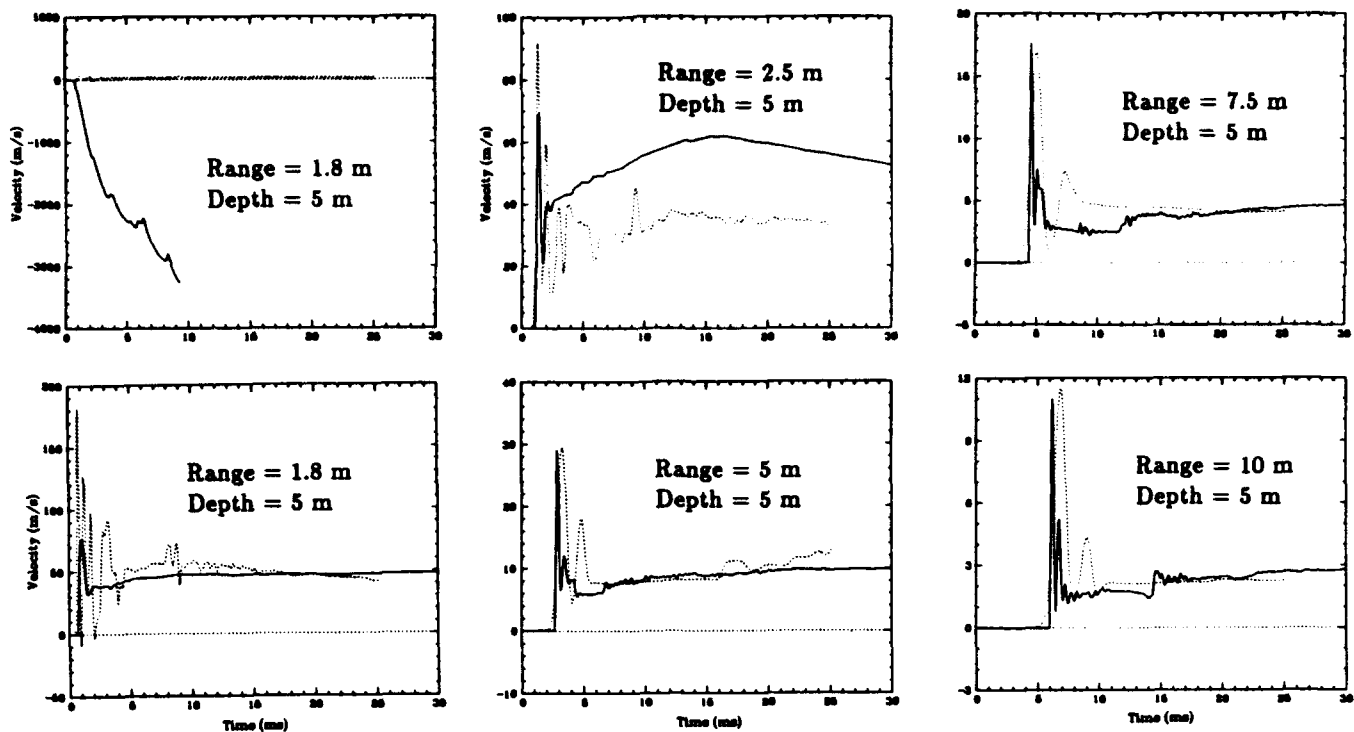


Figure 3. Free-field horizontal/radial velocities.

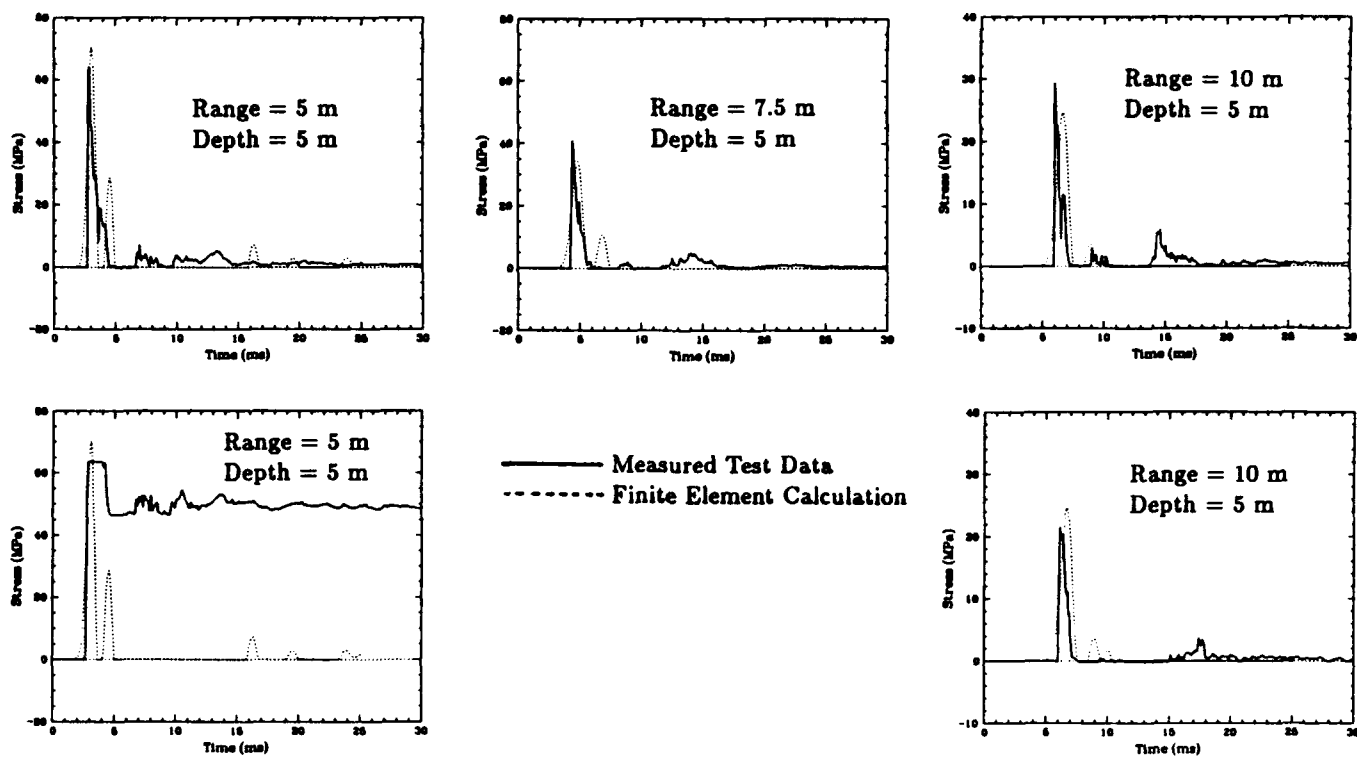


Figure 4. Free-field horizontal/radial stresses.

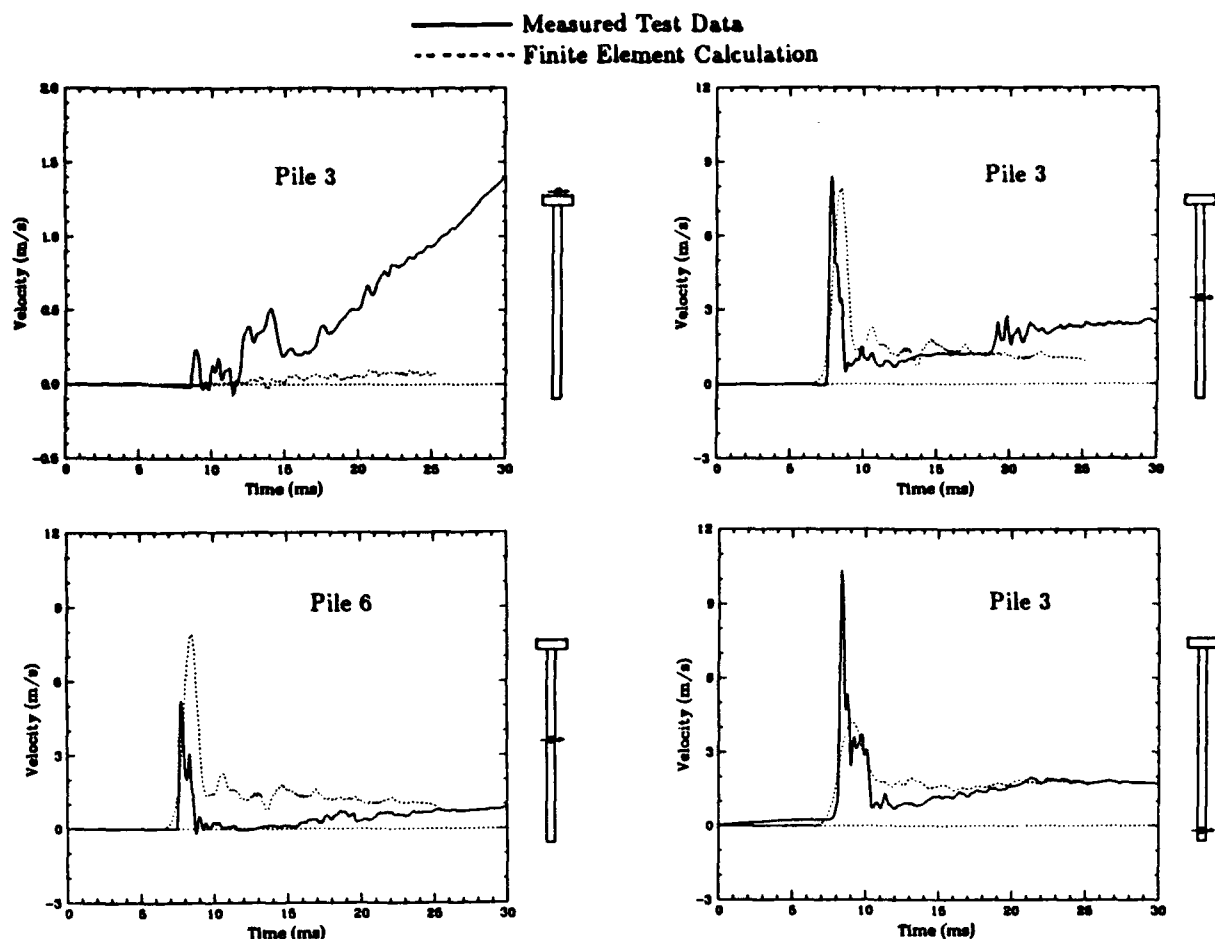


Figure 5. Piles 3 and 6 horizontal/radial velocities.

lation presented in this paper, did not capture the peak flexural/axial response of the pile.

REFERENCES

1. Bingham, B.L., "Bingham Three Invariant Material Model," Internal Letter Report, Applied Research Associates, Inc., Albuquerque, New Mexico, November 1992.
2. Blouin, S.E., et al., "Response of Structures on Pile Foundations in Saturated Soils to Loadings from Conventional Explosives," Final Report for Scientific and Engineering Technical Assistance (SETA) Contract Number F08635-88-C-0067, Applied Research Associates, Inc., Albuquerque, New Mexico, 30 November 1992.
3. Dobratz, B.M., "LLNL Explosives Handbook, Properties of Chemical Explosives and Explosive Simulants," UCRL-52997, Section 8.3.1, Lawrence Livermore Laboratory, Livermore, California, 16 March 1981.
4. Flanagan, D.P. and T. Belytschko, "A Uniform Strain Hexahedron and Quadrilateral and Orthogonal Hourglass Control," Int. J. Numer. Meths. Eng., 17, pp. 679-706, 1981.
5. Frank, R.A., "Analysis of Structure-Media Interaction Data Measured in MX Horizontal Shelter Tests," AFWL-TR-82-105, Air Force Weapons Laboratory, Kirtland Air Force Base, New Mexico, August 1982.
6. Frank, R.A. and D.M. Cole, "Analysis of Soil-Structure Interaction Data Measured in High Explosive Tests on Buried Structures," Proceedings of the Eighth World Conference on Earthquake Engineering, San Francisco, California, 21-28 July 1984.
7. Gurney, R.W., "The Initial Velocities of Fragments from Bomb Shell and Grenades," Ballistic Research Laboratory Report Number 405, Aberdeen Proving Ground, Maryland, 14 September 1943.
8. Hallquist, J.O., "DYNA-3D, A Nonlinear, Explicit, 3-Dimensional Finite Element Code for Solid and Structural Mechanics, User Manual," UCRL-MA-107254, Lawrence Livermore National Laboratory, California, May 1991.
9. Kim, K.J., S.E. Blouin, D.E. Chitty, and D.H. Merkle, "Experimental and Theoretical Response of Multiphase Porous Media to Dynamic Loads," Final Report to U.S. Air Force Office of Scientific Research, Washington, D.C., September 1988.
10. Simons, D.A., "Comparison of Several Two-Phase Models for Saturated Porous Media," Report to Defense Nuclear Agency, March 1989.

RESPONSE OF SATURATED AND PARTIALLY SATURATED SOILS TO HIGH EXPLOSIVE LOADINGS

Numerical Analysis

R. E. Walker and S. E. Blouin

Applied Research Associates, Inc.
Vicksburg, MS and South Royalton, VT

ABSTRACT

Within the last two years ARA has participated in field tests to determine the response of saturated soils to surface and buried HE charges. The field tests and empirical analysis are described in Part I. This paper describes supporting numerical analysis used to gain a better understanding of the material response and to provide detailed pre-test predictions and post-test analysis. Numerical calculations were used to study basic phenomenology such as the influence of pore fluid motion relative to the porous skeleton on shock propagation and the influence of degree of saturations on the attenuation and loading waveforms. Test predictions and analysis include development of axisymmetric two dimensional source models for various bombs and two dimensional calculations of site response in layered saturated geologies with water tables. Calculations use ARA's Three Invariant effective stress model with soil skeleton parameters fit to laboratory drained test data for each individual soil stratum. Computational results are compared to the field test measurements.

INTRODUCTION

Two dimensional finite element free-field calculations have been performed for the UTTR layered site using an ARA modified HONDO code (References 1-3). The computed ground shock from these calculations was used to apply ground shock stresses and motions to an SMI loading of an approximation of the piles to be tested. An energy pill was developed and calibrated and used as the source definition of the HE detonation. The energy pill was calibrated using the recommended properties of the second layer, Layer-B, a saturated clay. The computation was carried out to a time of 70 msec with snapshots of the field variables being stored at 2.5-msec intervals. For these computations, material properties for the layers as discussed in PART I were used for the ARA Three Invariant skeletal model for the effective stress formulation of the constitutive model for the test site.

ENERGY SOURCE

The term "energy pill" is used to denote a modified material for the immediate source region. The basic premise is that the material very close to the detonation (about a meter from a spherical representation of the HE) is moving with the particle velocity at the shock front at that range, i.e., a meter. The source is then represented with an initial velocity boundary condition applied to the nodes at that range. To conserve momentum, the mass of

the boundary nodes is adjusted to equal the mass of the material from the shock front to the origin of the source. A pressure time history is also applied to this same boundary. The pressure time history is estimated from the time history that was calculated in the close-in source region. This pressure time boundary condition can be interpreted as the recoverable inner energy as the material relaxes as well as the residual pressure signature from the detonation. The initial velocity and the pressure time history are determined from first principle calculations of the explosive detonation and early time flow field.

The above procedure has been applied to the current site configuration of interest. First, a detailed first principle 1-D calculation with burn was performed using a spherical source of 190 Kg of HE and the Layer-B at 100% saturation. The close-in computed data at the range of 0.9 meter were used to construct a cylindrical energy pill of 0.9-meter radius and 1.8-meter high. This energy pill was used in the 2-D HONDO ground shock calculation.

FREE-FIELD GROUND SHOCK

The axisymmetric two dimensional grid is shown in Figure 1. Shown on the figure are the location of the recommended layers, the source region, and the location of the output points from the computations. A cylindrical energy pill was constructed with the center of the pill located near mid-depth (5.18 m) of the 2-D grid with an ideal reflector at the bottom and a free surface at the top. The layers are replicated as outlined in the recommended site profile of PART I. The site is assumed 100% saturated except for the top 1.5 m of dry sand.

The calculations are summarized in Figure 2 which presents the peak radial stress and the peak radial particle velocity with range along the horizontal. For each free-field borehole range, vertical and horizontal velocity time histories and stress time histories were computed. Complete field snapshots were saved for pressures, velocity and volumetric strain.

The horizontal velocity time histories are characterized by a rapid rise to their peak, a double peak, and then a decay as the pressure wave passes by the zone. The decay reaches an almost steady state "flow" velocity with a very gradual decay toward

zero velocity. A linear extrapolation of this decay results in a zero velocity in approximately 250 to 500 msec. Vertical spill was obvious at the Z coordinate of 12.5 m (top of grid) for each range. There was also an upward peak in the vertical time histories corresponding to the arrival of bottom reflected pressure pulse.

Snapshots of the field variables, pressure and velocity are presented in Figure 3. This snapshot portrays the development of the shock propagation and the momentum field of the media behind the shock front. In Figure 3, the very dark or black zones represent the compressive shock front while the light zones represent decreases in pressure with white being the unloaded state. As seen from an inspection of the pressure snapshot, there is a primary compression wave almost spherical at the 2.5-msec snapshot. Note that this wave has already interacted with the dry sand layer and the pressure front has started to unload in the region above the detonation. By 5.0 msec the primary shock has reached the bottom and reflected. Also the unloading from the free surface has begun to relieve the pressures behind the primary shock. At 7.5 to 10 msec the bottom reflected shock has interacted with bomb cavity and the unloaded region behind the primary shock. Note the formation of a pressure field that closely resembles the "mach stem" pressure field that occurs in airblast propagation. The bottom reflected shock is almost dissipated by 20.0 msec and only a horizontally moving primary wave remains. This wave continues to propagate to the right while decreasing in amplitude and broadening in space until impingement with the left boundary between 40.0 and 50.0 msec.

The velocity vector field snapshots assist in the understanding of the developing flow field. Many of the features of the pressure field are replicated in these snapshots and a discussion of these will not be repeated here. By 5.0 msec the primary wave in the clay layer (Layer-B), has outrun the loading wave in the dry sand causing the sand to move up almost in plane loading. There is a complex horizontal scouring motion developing along the cobble layer at 5.0 msec that interacts with the bottom reflection by 10.0 msec. This interaction turns the particle velocity field upward. Beneath the sand layer the motions in the primary shock front are horizontal followed by an upward rotation. The upward rotation is dominated by the unloading and the bottom reflection.

The analysis of the volumetric strain contours display the dilated zones. A net volumetric dilation zone is produced by the late time motions (those after the passage of the shock fronts) of the flow field. A color presentation of these contours reveals that most of the test site is in some state of dilation and hence the soils in the crater region will appear "dry" for some time after the transients die out. The fallback and dynamic crater have settled by approximately 8 seconds. The soils in the crater region are no longer at a degree of saturation of 100%. The crater and the soil zones of less than 100% saturation will provide a place for the water to migrate during the long time consolidation phase of the settlement.

COMPARISONS

Shown in Figures 4 and 5 are overlays of selected velocity and stress time histories from the experiment with the calculated results. There is excellent agreement between the calculations and the data with all of the predominate features of the experimental histories being reproduced in the calculations. Even the long duration flow field is reproduced in the numerical simulation. Figure 5 is a display of the comparison of the peak stress and particle velocity verses range along the horizontal center line of the detonation. The computations are presented as the solid lines and the experimental data as the symbols. Shown also for comparison is the empirical 1-D estimates. Note that the velocity is slightly high and the stress are much closer. This is due in part to the use of the energy pill with the pressure-time loading of the equivalent cavity being set equal to the pressure-time in the element at the range of the equivalent cavity. This pressure function is high by at least by the dynamic flow pressures that are contained in this pressure function.

CONCLUSIONS

The following conclusions may be drawn from this study. The peak free field stresses and motions in a saturated layered soil site can be reliably calculated using the effective stress formulation of the global constitutive law. There are large late time motions due to the lack of shear strength and the peak stresses and motions decay very slowly with range. These late time motions are evident in the calculated response as in the experimental data and manifest themselves as a very slowly decaying velocity time history. Damage that can be attributed to peak stress or peak velocity will occur at much greater ranges than would be expected in a completely dry site.

ACKNOWLEDGEMENT

This project was funded through the Engineering Service Center, Tyndall AFB, Florida. The Defense Nuclear Agency was a primary supporter of the field test which was conducted by the Waterways Experiment Station, Vicksburg, MS.

REFERENCES

1. Key, S.W., HONDO--A Finite Element Computer Program for the Large Deformation Dynamic Response of Axisymmetric Solids, SLA-74-0039, Sandia Laboratories, Albuquerque, NM, April 1974.
2. Key, S.W., Z. E. Beisinger, and R.D. Krieg, HONDO II--A Finite Element Computer Program for the Large Deformation Dynamic Response of Axisymmetric Solids, SLA-78-0042, Sandia Laboratories, Albuquerque, NM, October 1978.
3. Hallquist, J.O., A Procedure for the Solution of Finite-Deformation Contact-Impact Problems by the Finite Element Method, UCRL-52066, Lawrence Livermore Laboratory, Livermore, California, April 1976.

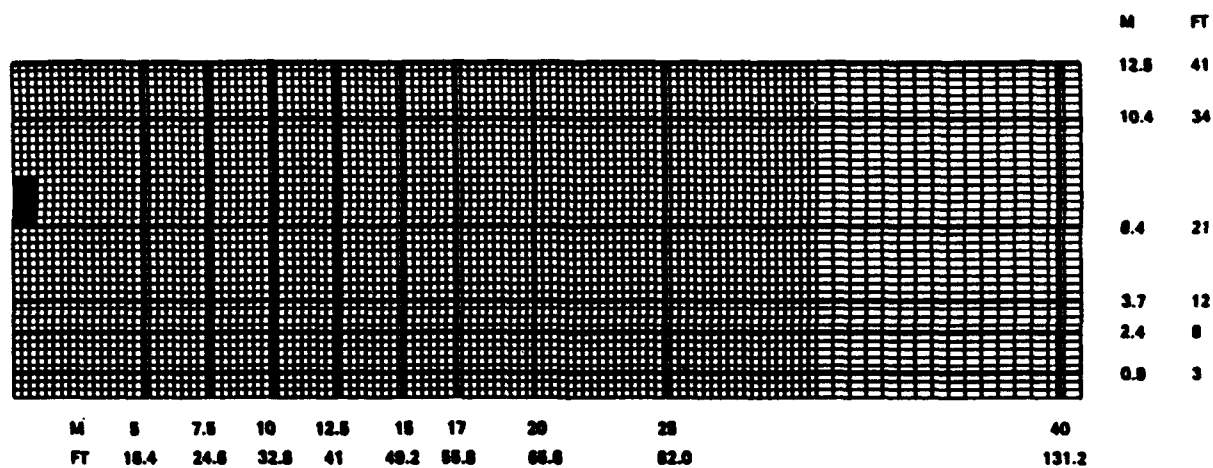


Figure 1. Initial grid, site layering and ranges for output data.

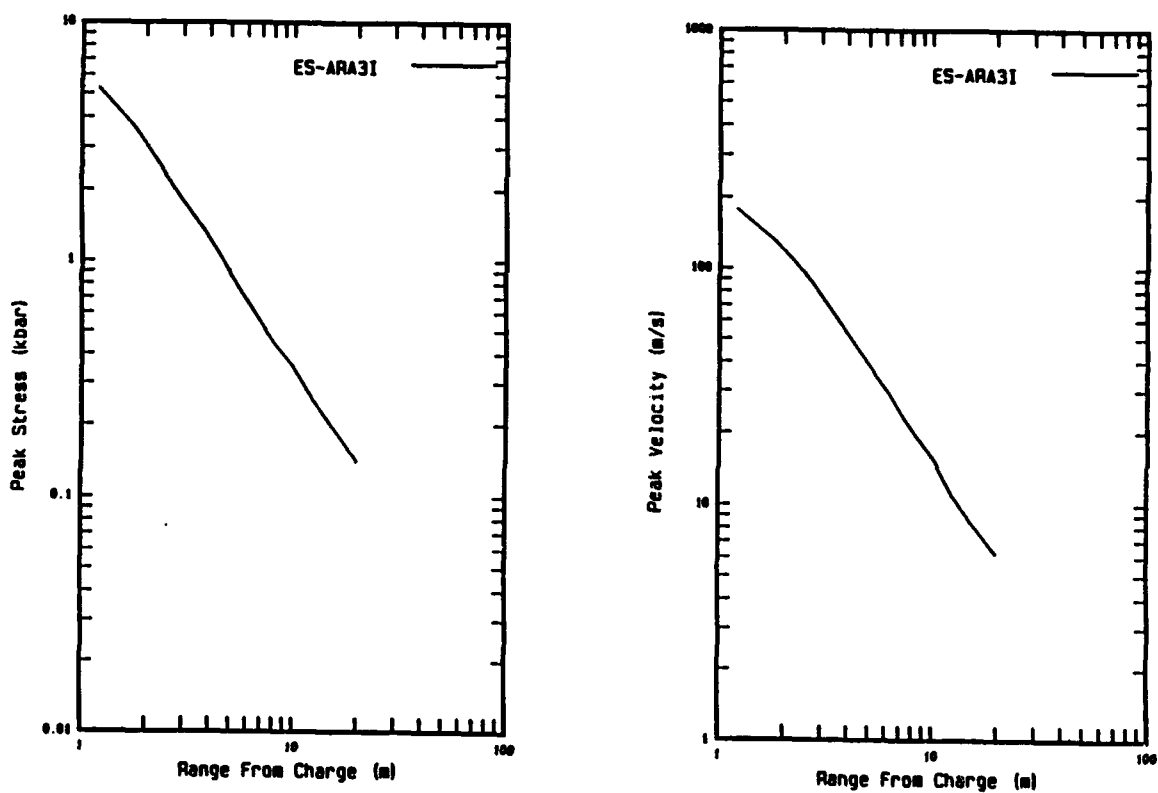
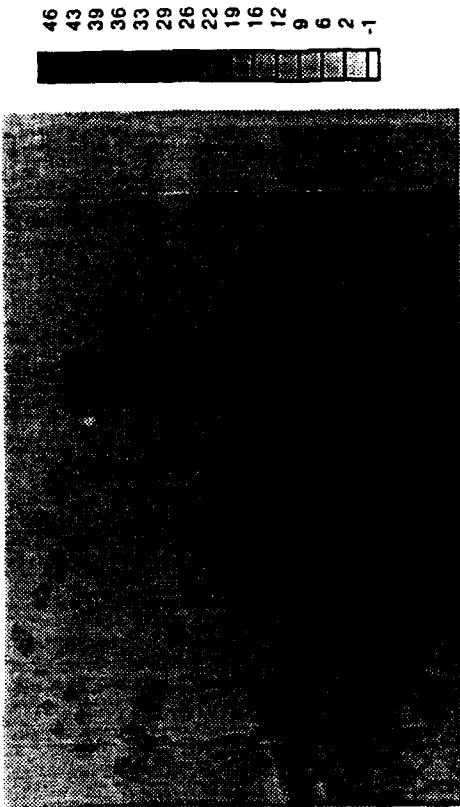


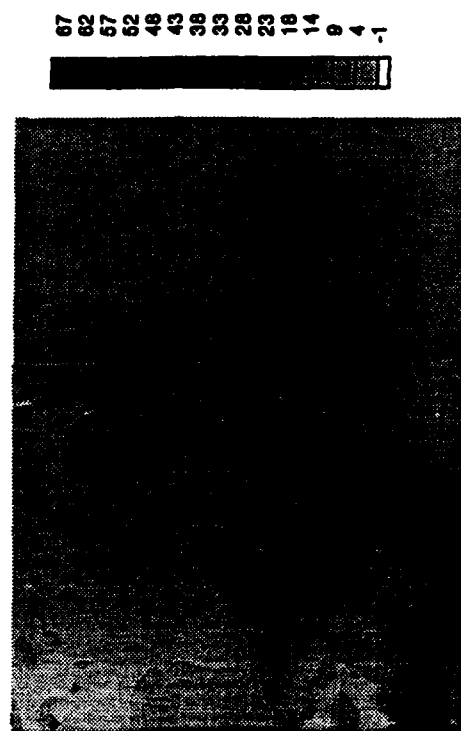
Figure 2. Pile free-field prediction.



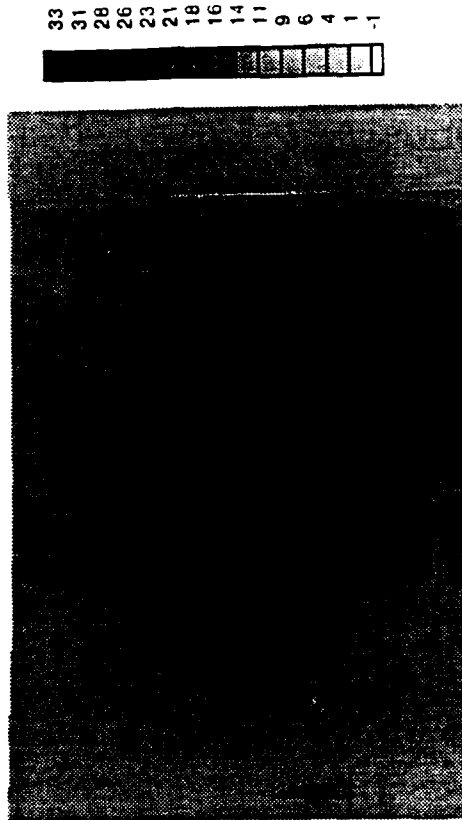
a) time = 2.5 msec



c) time = 7.5 msec



b) time = 5.0 msec



d) time = 10.0 msec

Figure 3. Pressure contours at 2.5-msec intervals.

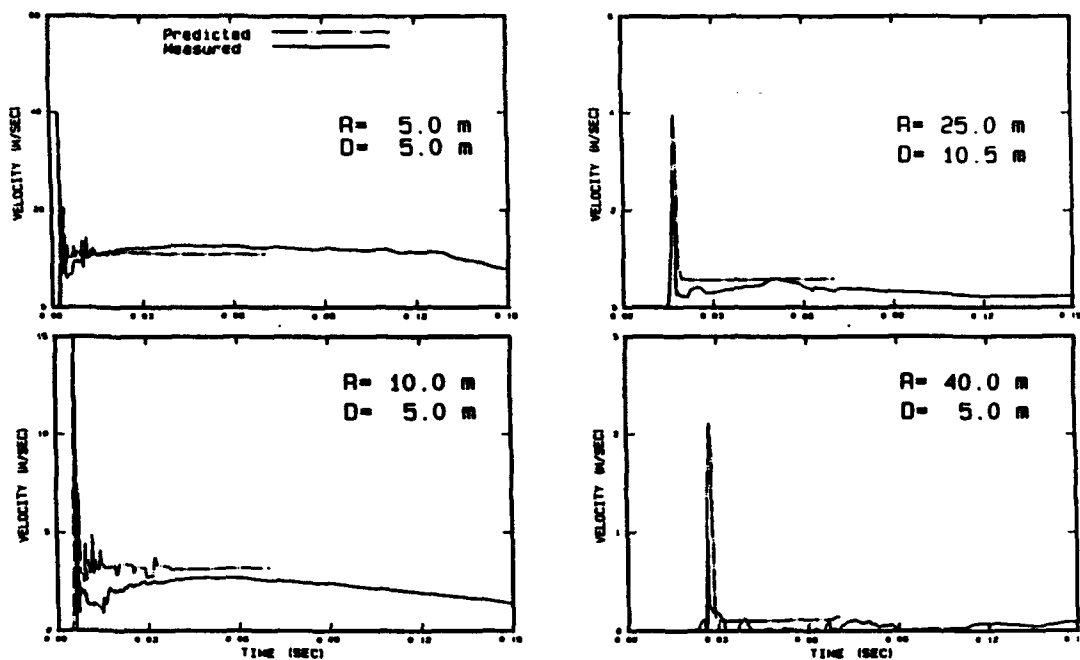


Figure 4. Comparison of predicted and computed free-field horizontal velocity.

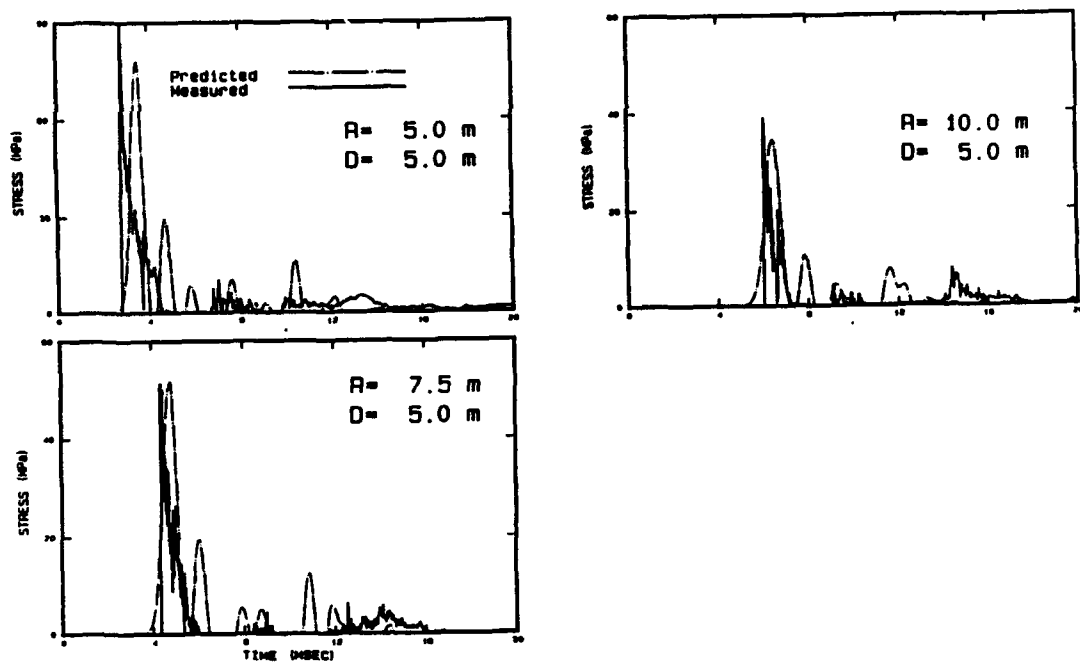


Figure 5. Comparison of predicted and computed free-field horizontal stress.

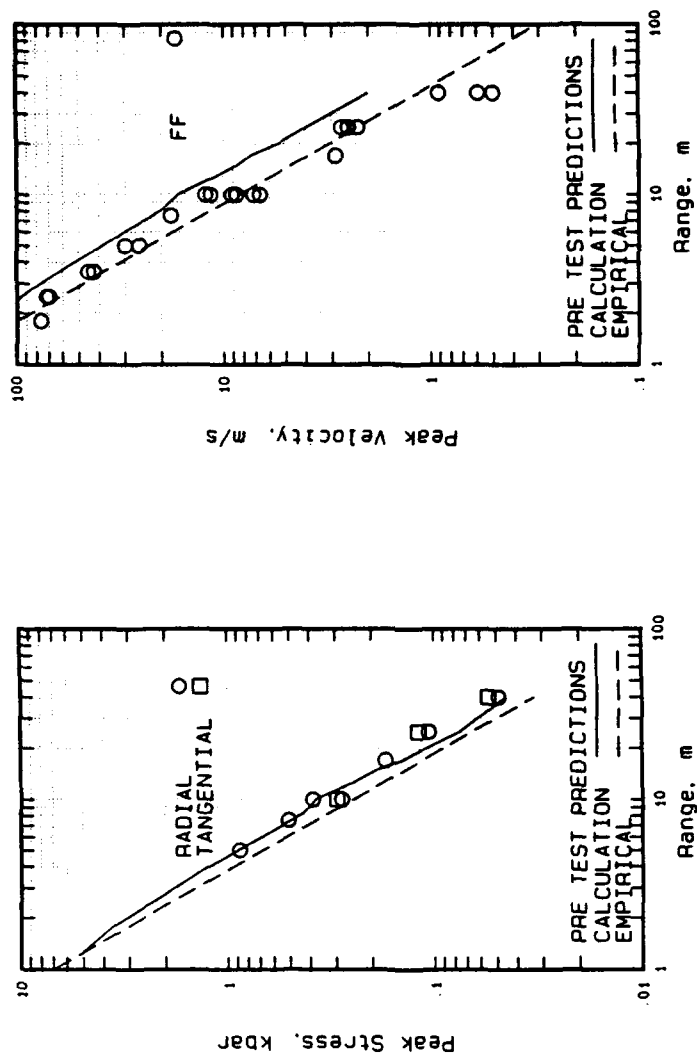


Figure 6. Comparison of field data with computations for peak shock stress and velocity with range at 5-meter depth.

FIBER-REINFORCED CONCRETE IN HARDENED SHELTER CONSTRUCTION

David L. Read and Larry C. Muszynski

Applied Research Associates, Inc., Tyndall AFB, FL

ABSTRACT

A test program was conducted to develop a fiber- and rebar-reinforced beam design(s) using lightweight, high-strength concrete. The goal of the testing program was to develop a beam design(s) that provides superior performance at a reduced cost and weight versus the symmetrically rebar reinforced beam design using normal-weight, standard-strength concrete currently used by the U.S. Air Force in hardened structure construction. Beams of various designs, including a baseline symmetrically reinforced beam designed using current hardened structure criteria, were fabricated and tested on a load-frame under deflection control and flexural third-point loading to generate load-deflection curves. From these curves, the ductility, energy absorption characteristics, and overall material toughness of each beam design were determined.

TEST PROGRAM STRUCTURE

The test program consisted of two phases. In the first phase, the performance of fiber-only reinforced beams was compared to the performance of symmetrically reinforced beams designed using current hardened structure criteria. Performance comparisons were based on the area under load-deflection curves for each beam type. In the second test phase, the best fiber and rebar reinforcement combination to enhance a beam's performance was investigated. Load-deflection curves were generated for each beam type. Then using these curves, ductility indices, energy ratios, and energy absorption as a function of beam weight were calculated for each beam type. Using these material ductility and energy absorption characteristics, comparisons were made between beam types.

TEST SPECIMENS

Beams and Cylinders

The beams used in the test program are summarized in Table 1 (all tables follow at the end of this paper). Three beams of each type were poured. All beams were 40 inches long, 8 inches deep, and 4 inches wide. Beam types F1, F2, and SR1 were used in the first phase of the test program. All remaining beam types were used in the second test phase. Compression strengths and maximum concrete compressive strains given in Table 1 come from compression tests of 6-inch diameter, 12-inch long concrete cylinders. Average unit weight is based on the average weight of all three beam specimens for a particular type, including fibers and rebar as applicable.

Fiber Types

Six different types of fibers were used during the fabrication of beam specimens. Four of the fiber types consist of individual steel fibers of differing lengths and shapes. Another fiber type is composed of individual nylon fibers. The remaining fiber type is composed of steel, but in an interwoven mat matrix 4 inches wide and 1 inch thick. Table 2 summarizes the fiber types used in the test program.

Beam Standard Reinforcing Parameters

Number 3, 60 Grade steel rebar was used in SR and M2 beam types. The Number 3 rebar stock was tested, and the rebar's actual yield strength was 54.5 ksi. In beam types FR1 and FR2, FibeRGlass (FRG) rebar was used instead of steel. The FRG rebar was 3/8-inch in diameter, with a 100 ksi yield strength and a modulus of elasticity of 7,000,000 psi.

Six beam cross-sections were used during the test program. Beam cross-sections are shown in Figure 1. Due to the limited cross-sectional area of each beam no stirrups were used. The locations of steel or FRG rebar reinforcement in the beams are shown in Figure 1.

No rebar reinforcement was used in beam types F1, F2, and M1. For the singly reinforced beam types (SR2, SR5 to SR11, FR1, and M2), the balanced reinforcing ratio (ρ_b) was determined using the American Concrete Institute (ACI) equation given below:

$$\rho_b = \frac{\alpha \epsilon_c}{(f_y / E_s) + \epsilon_c} \frac{f_c'}{f_y} \quad (\text{eq-1})$$

Where: ϵ_c = Maximum concrete compressive strain from compression cylinder tests

f_y = Steel or FRG rebar tensile yield strength

E_s = Steel or FRG rebar modulus of elasticity

f_c' = Concrete compressive strength

$\alpha = 0.72$ for $f_c' \leq 4,000$ psi, $0.72 - .00004(f_c' - 4000)$ for $4,000$ psi $< f_c' < 8,000$ psi, and 0.56 for $f_c' \geq 8,000$ psi

The values for α were developed by the ACI for concrete without fiber reinforcement. However, use of these α values in

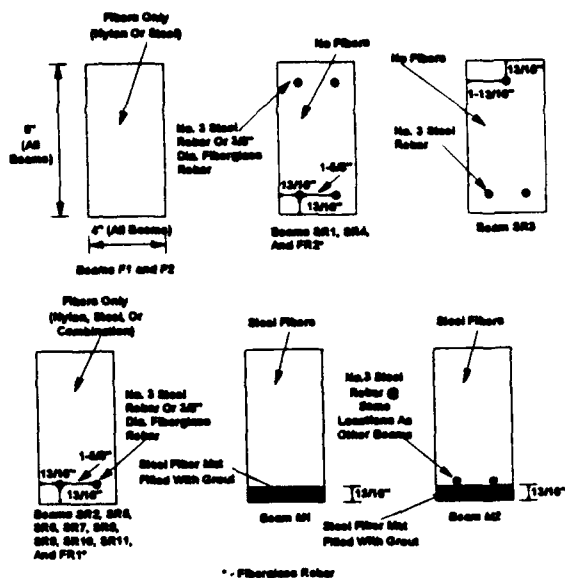


Figure 1. Test Beam Cross-Sections, Test Phases I and II.

the design of fiber-reinforced concrete members provides sufficient accuracy according to References 1, 2, and 3. Next the maximum allowable ACI reinforcing ratio was determined using $\rho_{max} = 0.75\rho_b$. Finally, the actual reinforcing ratio for each beam was determined using $\rho = A_s/bd$, where A_s is the reinforcing steel area, b = beam width, and d = depth to the centroid of tension reinforcement. Average reinforcing parameters for all singly reinforced beam types are summarized in Table 3. All beam types except one were under reinforced by 4.5 to 5.75 times and exhibited good ductility characteristics during the test program. Beam type FR1 is over reinforced because of the high tensile yield strength (100 ksi) and relatively low elastic modulus (7,000,000 psi) of its FRG rebar. The FR1 beam type exhibited poor ductility characteristics during the test program

For the doubly reinforced beam types (SR1, SR3, SR4, and FR2), ρ_b was determined using Equation-1. Then, as before, ρ_{max} and ρ were determined for each beam type. According to the ACI, if ρ is equal to or less than ρ_{max} a doubly reinforced beam may be designed with acceptable accuracy by ignoring the compression reinforcement and designing the beam as a singly reinforced beam. As seen in Table 4, ρ_{max} was greater than ρ for all SR doubly reinforced beam types. These beam types exhibited good ductility characteristics during the test program. However, ρ_{max} was less than ρ for the FR2 beam once again because of the FRG rebar. As a result, FR2 beam reinforcing parameters must be calculated using the ACI equations given below.

$$\rho' = \frac{A'_s}{bd} \quad (\text{eq-2})$$

$$\bar{\rho}_{max} = 0.75\rho_b + \rho' \quad (\text{eq-3})$$

$$\bar{\rho}_{lim} = 0.85\beta_1 \frac{f'_c d'}{f_y d \epsilon_u - \epsilon_y} + \rho' \quad (\text{eq-4})$$

Where: A'_s = Compression steel area
 $\beta_1 = 0.65$ for $f'_c \geq 8,000$ psi

d' = depth to centroid of comp. reinforcing steel

$\epsilon_u = 0.00253$ (see Table 1)

$\epsilon_y = 0.0143$ (f_y/E_s , i.e., 100 ksi / 7,000 ksi)

$\bar{\rho}_{max}$ = Max. allowable reinforcing ratio

$\bar{\rho}_{lim}$ = Min. tensile steel reinforcing ratio

Using Equations-2, -3, and -4 with $A'_s = 0.22$ in² and $d' = 1.0$ inch, the following reinforcing ratio values were determined: $\rho = 0.0079$, $\rho_{max} = 0.0138$, and $\rho_{lim} = 0.0063$. Since the actual ρ of 0.0079 is between these limits, failure should be initiated by tensile yielding and the compression rebar will have yielded at failure. This assumes FRG rebar exhibits behavior similar to steel rebar. However, FR2 beams exhibited explosive failures during testing, indicating the FRG rebar is more brittle, i.e., less ductile, than steel rebar.

Beam Fabrication and Mixture Properties

A portable, rotary, finned mixer was used to mix the concrete. Fibers, if used, were added toward the end of the mixing process. The concrete was mixed for approximately 10 minutes, and then poured into the forms. A pencil, internal vibrator was used to consolidate the concrete in the forms. The exposed concrete surface was finished with trowels. The forms were then covered with wet burlap for approximately 24 hours. Then the beams were removed from the forms and cured under water for 28 days. As beams were being poured, some concrete was poured into 6-inch diameter, 12-inch long cylinder forms. The cylinders were also water cured for 28 days. Mix designs for the different concretes are given in Table 5. A Type-1 cement was used in all mixes.

A slurry mixture consisting of 23.7 pounds of Type-3 cement, 5.9 pounds of fly-ash class "C", 10.4 pounds of water, and 105 grams of Cormix Super 2000-C plasticizer was used in beam types M1 and M2. The slurry was used to infiltrate the steel fiber mat matrix preplaced in the bottom of the concrete forms. After slurry infiltration, concrete was poured over the infiltrated steel mat to complete the beams.

Test Equipment

A 50,000-pound capacity Material Testing System (MTS) load-frame and data acquisition system were used to test beams under deflection control to failure or a maximum mid-span deflection of 2 inches, which ever occurred first. In general, test procedures from ASTM C 78-84 and ASTM C 1018-89 were used to conduct the tests and obtain load-deflection curves for each beam. The beam loading configuration used on the MTS machine is shown in Figure 2.

Compression tests of 6-inch diameter, 12-inch long concrete cylinders poured at the same time individual beams were poured were done using a 500,000-pound capacity Forney load-frame under load control. Test procedures from ASTM C 39 were used to conduct the compression cylinder tests.

TEST PHASE I RESULTS

In Test Phase I, beam types F1 (nylon fibers only), F2 (steel fibers only), and SR1 (symmetrically reinforced with Number 3 rebar) were tested on the MTS machine. Typical generated total load versus mid-span deflection curves of each beam type are shown in Figure 3. As seen, the symmetrically reinforced SR1 beam without fibers is clearly superior, with the area under its curve much greater than the F1 or F2 beams.

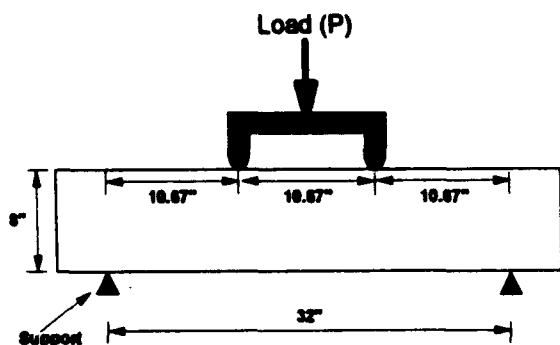


Figure 2. Test Beam Configuration.

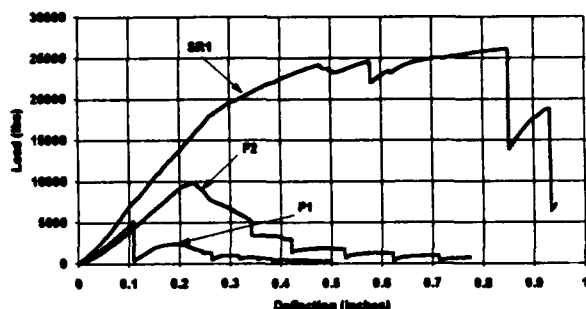


Figure 3. Load-Deflection Curves, Test Phase I.

The clear superiority of beam type SR1 over beam types F1 and F2 is further shown by the results presented in Table 6. For each beam type in this table, the maximum mid-span deflection, the average maximum mid-span deflection, the maximum total load, the average maximum total load, the Japanese area (see Reference 4), the average Japanese area, the total (ultimate) area under the load-deflection curve, and the average total area are presented. The Japanese Area Method calculates the area under a load-deflection curve up to a deflection equaling the beam's load span in inches divided by 150.

TEST PHASE II RESULTS

Load-Deflection Curves

A total of 14 beam types were tested (3 per type). SR2 to SR11 beams were reinforced with steel rebar and usually some type of fiber reinforcement. FR1 and FR2 beams were reinforced with FRG rebar, with FR1 beams also containing nylon fibers. M1 beams were reinforced at the bottom with the slurry infiltrated steel mat fiber matrix, with steel fiber-reinforced concrete above the mat. M2 beams were reinforced like M1 beams, but also had steel rebar in the tension zone.

Because rebar was used in all beam types except one in this test phase, with or without fiber reinforcement, the specified mid-span deflection rate for fiber-only reinforced beams in ASTM C 1018-89 of 0.002 to 0.004 inches per minute was changed to 0.1476 inches per minute as recommended in Reference 2. Typical generated total load versus mid-span deflection curves for each beam type are shown in Figures 4 through 7.

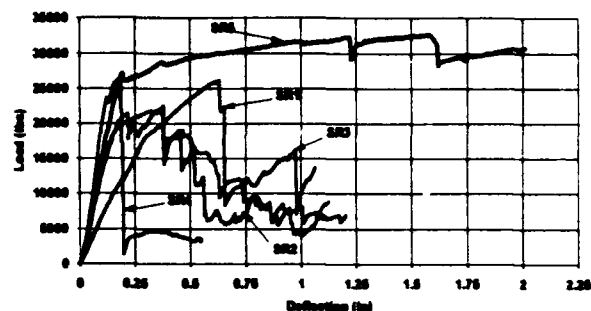


Figure 4. Load-Deflection Curves (Beam Types SR1 to SR5)

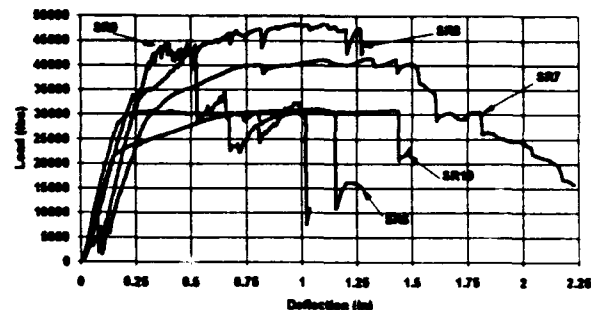


Figure 5. Load-Deflection Curves (Beam Types SR6 to SR10).

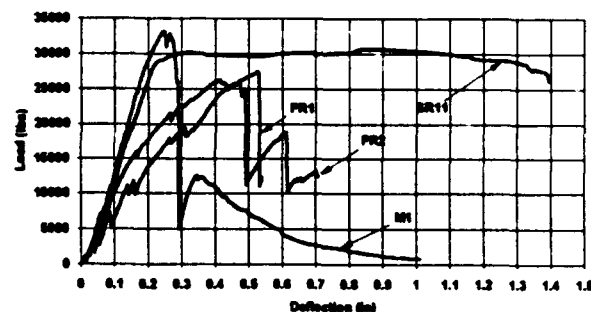


Figure 6. Load-Deflection Curves (Beam Types SR11, FR1, FR2, and M1).

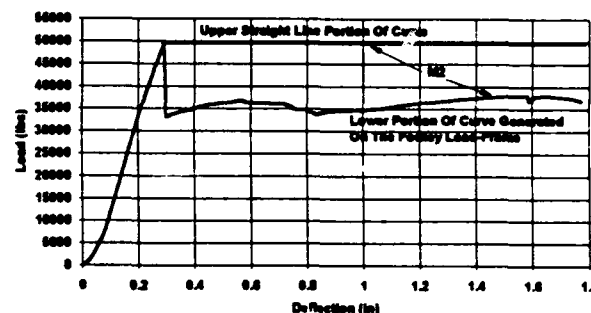


Figure 7. Load-Deflection Curve of Beam Type M2.

Beam type SR4 in Figure 4 is the baseline beam. In Figure 7, two different lines are shown for the curve M2 after the maximum load is reached. While testing the M2 beams on the MTS machine, the 50,000-pound capacity of the machine was reached before any significant cracking of the beams occurred and deflection was only 0.292 inches. One of the beams was tested

on the Forney load-frame to determine its ultimate capacity. However, the beam only supported a maximum load of approximately 34,000-pounds and failed at a maximum mid-span deflection of 1.769 inches. The portion of this Forney generated curve from a deflection of 0.299 inches (the closest matching deflection point to the MST curve) is superimposed in Figure 7 on the curve from the MTS machine. Also a straight line is drawn on Figure 7 from the maximum load point of 50,000 pounds to the maximum deflection point. Both portions of this load-deflection curve were used to calculate the ductility index and energy ratio for beam type M2.

Ductility Indices and Energy Ratios

The performance of the beam types was compared using ductility indices, energy ratios, and average total absorbed energy divided by beam weight. The method used to calculate ductility indices and energy ratios from load-deflection curves is shown in Figure 8. This method was obtained from Reference 2. The maximum load P_{max} is determined. Then, a straight line is drawn parallel to the deflection axis until it intersects the load axis. Next, a secant is drawn from the origin through the point corresponding to $0.75P_{max}$ on the load-deflection curve, and extended until it intersects the straight line running from P_{max} to the load axis. At this intersection point, a vertical line parallel to the load axis is drawn until it intersects the deflection axis. The point where this line intersects the deflection axis (Δ_y) is considered the yield deflection for the beam. The energy dissipated at yield (E_y) is the shaded area under the load-deflection curve up to the yield deflection as shown in Figure 8. Next, the ultimate deflection point of the curve (Δ_u) is determined and the total area under the load-deflection curve up to this point (E_u) calculated. The ductility index is defined as the ultimate deflection divided by the yield deflection (Δ_u / Δ_y), while the energy ratio is defined as the ultimate area divided by the yield area (E_u / E_y).

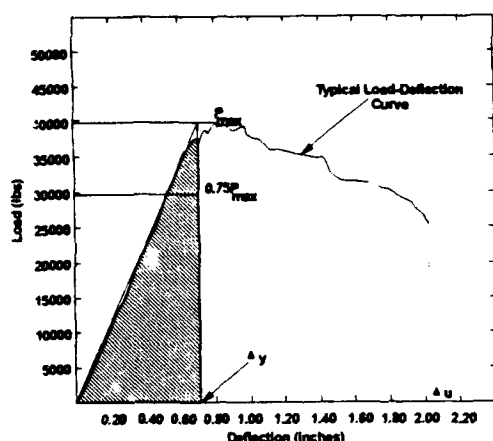


Figure 8. Calculation of Ductility Index and Energy Ratio From a Load-Deflection Curve.

Test Results

Ductility indices, energy ratios, and total absorbed energy per pound were calculated for each beam. A beam's span length, i.e., 32 inches, was used to calculate a beam's weight for absorbed energy per pound calculations. Results of all these calculations are given in Table 7. From the average results shown in Table 7, each beam type was ranked by average ductility index, energy ratio, maximum load, and energy absorption per pound. This information is presented in Table 8. Average ductility index, energy ratio, and energy absorption per pound were normalized with respect to the baseline beam type

SR4. This information is presented in Table 9.

As seen from Table 8, beam type SR5 appears in the top five in ductility index (1), energy ratio (1), and energy absorption (2). Beam type SR6 appears in ductility index (2), energy ratio (2), and energy absorption (5). Beam type SR7 appears in the top five in all four categories: ductility index (4), energy ratio (5), maximum load (4), and energy absorption (4). Beam type M2 appears in the top five in energy ratio (3), maximum load (1), and energy absorption (1). For the three beam types mentioned above that fall outside the top five in 1 of 4 categories, all but beam type SR6 are still above the average for that category. Beam type SR6 falls slightly below the average maximum load (32,063 lbs versus the 32,984 lbs average).

As seen from Table 9, only three beam types fail to provide ductility indices, energy ratios, or energy absorption per pound values superior to the baseline beam. This strongly suggests that the use of some type of fiber reinforcement in combination with standard reinforcement in the structural members used in hardened structures would, by increasing their ductility and energy absorption characteristics, greatly improve the members ability to sustain large deformations caused by blast and dynamic impact loading without catastrophic failure.

Fiber-reinforcement appears to eliminate the need for compression rebar reinforcement. Beam types tested with compression reinforcement and no fibers, i.e., beam types SR1, SR3, and SR4, did not perform as well as beam types with tension rebar and fiber reinforcement only. Minimization, or possibly elimination, of compression rebar by using fiber reinforcement would save weight and cost in hardened structure construction.

CONCLUSIONS

Based on all test results, the use of fiber reinforcement in combination with standard reinforcement in hardened structures would provide a significant performance enhancement over currently fielded hardened structures. The major benefits are threefold. First, the ductility and energy absorption characteristics of fiber- and rebar-reinforced structural members are clearly superior versus the symmetrically reinforced structural members currently used by the U.S. Air Force. Second, using fibers would minimize, or possibly eliminate, the need for compression reinforcement in concrete structural members without sacrificing performance. Third, inclusion of fibers would minimize, or possibly eliminate, spalling of the interior walls of hardened structures from blast loading or projectile impacts as stated in Reference 5.

FUTURE RESEARCH

The U.S. Air Force is continuing this research effort. A new testing program is investigating the toughness characteristics of large concrete beams that use various combinations of fiber- and rebar-reinforcement. The beams are 14 inches deep, 8 inches wide, and 10 feet long. The load span of the beams is 9 feet with a corresponding L/D ratio of 7.71. The performance of these fiber- and rebar-reinforced beams will be compared to a baseline, symmetrically rebar reinforced beam (including stirrups) to verify the results of the testing program documented in this paper.

ACKNOWLEDGMENTS

The authors express their gratitude to the Air Force Civil Engineering Support Agency's (AFCEA) Air Base Survivability Branch (RACS) and Air Base Operability and

Repair Branch (RACO), Tyndall AFB, Florida for supporting this research effort.

REFERENCES

- (1) Craig, R.J., "Flexural Behavior and Design of Reinforced Fiber Concrete Members," Fiber Reinforced Concrete Properties and Applications, ACI SP-105, American Concrete Institute Publication, P.O. Box 19150, Redford Station, Detroit, Michigan, 1987, pp. 517-563.
- (2) Naaman, A.E., Reinhardt, H.W., and Fritz, C., "Reinforced Concrete Beams with a SIFCON Matrix," American Concrete Institute Structural Journal, Vol. 89, No. 1, Jan-Feb 1992, pp. 79-88.
- (3) Craig, R.J., Editor, Design with Fiber Reinforced Concrete, ACI SCM-10(85), American Concrete Institute Publication, P.O. Box 19150, Redford Station, Detroit, Michigan, 1985.
- (4) Nemegeer, P.O., "Identity Chart for Steel Fibres," Fibre Reinforced Cements - Recent Developments, Elsevier Applied Science, 1989, pp. 401-410.
- (5) Kaushik, S.K., and Menon, V., "Behavior of Fibrous Composites Under Impact and Blast Loading," International Conference on Fiber Reinforced Cements and Concretes - Recent Developments, University of Wales College, U.K., 18-20 Sept., 1989, pp. 240-251.

TABLE 2. FIBER TYPES AND PROPERTIES.






Fiber ID	Description	Length (in)	Dia. (in)	Aspect Ratio (L/D)	Shape	Tensile Yield Strength (ksi)
Steel-1	Bekaert Steel Fibers Hooked Ends	1.2	0.02	60		170
Steel-2	Anchorloc Steel Fibers By Mitchell Fiberson, Inc. Twisted Shape	1.0	0.10 by 0.044	42		60
Steel-3	Short Steel Fibers By MeH-Tec	0.625	0.020	32.25		100
Steel-4	Long Steel Fibers By Bekaert	2.4	0.03	80		170
Nylon	Nylon 6 By NyCon, Inc.	1.0	0.0009	111.11		130
Mat	Steel Fiber Mat By Ribbon Technology	N/A	N/A	N/A	N/A	N/A

TABLE 3. REINFORCING PARAMETERS - SINGLY REINFORCED BEAM TYPES.

Beam ID	b (in)	d (in)	A _s (in ²)	P _b	P _{max}	ρ	P/P _b	P/P _{max}
SR2	4.0	7.0	0.22	0.0471	0.0353	0.0079	0.1668	0.2226
SR5	4.0	7.0	0.22	0.0522	0.0382	0.0079	0.1505	0.2015
SR6	4.0	7.0	0.22	0.0581	0.0435	0.0079	0.1360	0.1816
SR7	4.0	7.0	0.22	0.0369	0.0277	0.0079	0.2141	0.2852
SR8	4.0	7.0	0.22	0.0551	0.0413	0.0079	0.1434	0.1913
SR9	4.0	7.0	0.22	0.0539	0.0405	0.0079	0.1466	0.1953
SR10	4.0	7.0	0.22	0.0580	0.0435	0.0079	0.1362	0.1816
SR11	4.0	7.0	0.22	0.0587	0.0440	0.0079	0.1346	0.1794
FR1	4.0	7.0	0.22	0.0077	0.0058	0.0079	1.0260	1.3654
M2	4.0	7.0	0.22	0.0609	0.0457	0.0079	0.1297	0.1730

TABLE 1. TEST BEAMS DESCRIPTIONS AND PROPERTIES.

Beam ID	Binder Type (1)	Avg. Comp. Strength (psi)	Avg. Max. Strain (in/in)	Bars: Tension	Bars: Comp.	Fiber Type (2)	Fiber Vol. (%)	Avg. Unit Wt. (pcf)
F1	LW/HS	9,873	0.00251	None	None	Nylon	0.5	124.78
F2	LW/HS	9,648	0.00273	None	None	Steel-1	2.0	127.05
SR1	LW/HS	8,475	0.00221	2 No. 3 (3)	2 No. 3	None	N/A	128.46
SR2	LW/HS	8,475	0.00221	2 No. 3	None	None	N/A	124.76
SR3	LW/HS	9,494	0.00265	2 No. 3	1 No. 3	None	N/A	126.46
SR4	NW/MS	6,537	0.00186	2 No. 3	2 No. 3	None	N/A	152.85
SR5	LW/HS	8,983	0.00245	2 No. 3	None	Steel-2	2.0	130.78
SR6	LW/HS	9,499	0.00276	2 No. 3	None	Steel-1	2.0	128.61
						Nylon	0.15	
SR7	NW/MS	6,537	0.00186	2 No. 3	None	Steel-1	2.0	157.15
SR8	LW/HS	9,294	0.00259	2 No. 3	None	Steel-3	4.0	134.64
SR9	LW/HS	9,073	0.00258	2 No. 3	None	Steel-4	1.0	126.68
SR10	LW/HS	9,873	0.00231	2 No. 3	None	Nylon	0.5	125.49
SR11	LW/HS	9,648	0.00273	2 No. 3	None	Steel-1	2.0	130.28
FR1	LW/HS	8,976	0.00259	2 FRG(4)	None	Nylon	0.5	122.97
FR2	LW/HS	9,269	0.00253	2 FRG	2 FRG	None	N/A	123.86
M1	LW/HS	10,459	0.00277	None	None	Steel-1	2.0	132.26
						Mat	0.65	
M2	LW/HS	10,111	0.00266	2 No. 3	None	Steel-1	2.0	135.63
						Mat	0.65	

- Notes: (1) LW=Light Weight, NW=Normal Weight, HS=High Strength, And MS=Medium Strength
 (2) Fiber Types (see Table 2 for fiber details): Steel-1=Glued, Hooked Ends Or Loose, Hooked Ends, Steel-2=Anchorloc, Steel-3=Short And Straight, and Steel-4=Long And Hooked Ends
 (3) Standard No. 3 (3/8" Dia.) Steel Rebar, 60ksi (54.5ksi tested)
 (4) 3/8" Dia. Fiberglass Rebar, 100ksi

TABLE 4. REINFORCING PARAMETERS - DOUBLY REINFORCED BEAM TYPES.

Beam ID	b (in)	d (in)	d' (in)	A _s (in ²)	A _{s'} (in ²)	P _b	P _{max}	ρ	P/P _b	P/P _{max}
SR1	4.0	7.0	1.0	0.22	0.22	0.0471	0.0353	0.0079	0.1668	0.2226
SR3	4.0	7.0	1.0	0.22	0.11	0.0571	0.0428	0.0079	0.1376	0.1836
SR4	4.0	7.0	1.0	0.22	0.22	0.0369	0.0277	0.0079	0.2129	0.2837
FR2	4.0	7.0	1.0	0.22	0.22	0.0078	0.0059	0.0079	1.0073	1.3317

TABLE 5. CONCRETE MIXES FOR TEST BEAM SPECIMENS.

Beam ID	Fibers (1)	Cement (lbs)	Fine Agg. (lbs)	Coarse Agg. (lbs)	Solite (lbs)	F-10K (lbs)	Water (lbs)	WRDA -79 (oz)	WRDA -19 (oz)
F1	1.11 lbs (N)	104	135	N/A	94	24	23.5	5.64	6.35
F2	21 lbs (S1)	104	135	N/A	94	24	23.5	5.64	N/A
SR1	None	104	135	N/A	94	24	23.5	5.64	N/A
SR2	None	104	135	N/A	94	24	23.5	5.64	N/A
SR3	None	104	135	N/A	94	24	23.5	5.64	N/A
SR4	None	83.5	108	200	N/A	9.5	32	N/A	N/A
SR5	21 lbs (S2)	104	135	N/A	94	24	24	5.64	N/A
SR6	21 lbs (S1) 0.33 lbs (N)	104	135	N/A	94	N/A	24	5.64	N/A
SR7	29.4 lbs (S1)	83.5	108	200	N/A	9.5	32	N/A	N/A
SR8	42 lbs (S3)	104	135	N/A	94	24	23.5	5.64	N/A
SR9	10.5 lbs (S4)	104	135	N/A	94	24	23.5	5.64	N/A
SR10	1.11 lbs (N)	104	135	N/A	94	24	23.5	5.64	6.35
SR11	21 lbs (S1)	104	135	N/A	94	N/A	23.5	5.64	N/A
FR1	1.11 lbs (N)	104	135	N/A	94	24	23.5	5.64	6.35
FR2	1.11 lbs (N)	104	135	N/A	94	24	23.5	5.64	6.35
M1	21 (S1) Plus Mat	104	135	N/A	94	24	23.5	5.64	N/A
M2	21 (S1) Plus Mat	104	135	N/A	94	24	23.5	5.64	N/A

- Notes: (1) N=Nylon, S1=Steel-1, S2= Steel-2, S3= Steel-3, S4=Steel-4
 (2) Lightweight aggregate
 (3) Force-10K liquid silica fume by W. R. Grace, Co.
 (4) Water reducer by W. R. Grace, Co.
 (5) Super plasticizer by W. R. Grace, Co.

TABLE 6. COMPARISON BETWEEN BEAM TYPES F1, F2, & SR1.

ID	No.	Max. Deflec. (in)	Avg. Max. Deflec. (in)	Max. Load (lbs)	Avg. Max. Load (lbs)	Japanese Area (in.lbs)	Avg. Japanese Area (in.lbs)	Ultimate Area (in.lbs)	Avg. Ultimate Area (in.lbs)
F1	1	0.3337	0.3443	5,146	4,181	323.5	318.1	437.8	389.9
	2	0.4533		3,814		365.0		458.3	
	3	0.2460		3,582		265.8		273.5	
F2	1	0.5169	0.4388	9,784	9,985	1,184.1	1,207.3	1,709.7	1,683.0
	2	0.4600		9,742		1,202.4		1,768.0	
	3	0.3394		10,429		1,236.7		1,571.2	
SR	1	0.9439	1.0839	26,109	25,105	1,530.5	1,453.5	17,551.7	15,932.4
	2	1.0992		23,006		1,436.2		15,113.6	
	3	1.2087		26,199		1,393.8		15,131.9	

TABLE 8. BEAM TYPE RANKINGS.

Avg. Ductility Index	Avg. Energy Ratio	Avg. Max. Load (lbs)	Energy Absorp. Per Pound
SR5 - 8.92	SR5 - 16.96	M2 - >50,000	M2 - 876.9
SR6 - 7.54	SR6 - 13.71	SR8 - 49,708	SR5 - 749.7
SR10 - 6.94	M2 - 10.55	SR9 - 47,284	SR8 - 666.3
SR7 - 6.91	SR10 - 9.93	SR7 - 39,292	SR7 - 562.3
SR2 - 6.27	SR7 - 9.19	M1 - 33,128	SR6 - 538.2
SR3 - 6.02	SR11 - 8.80	SR5 - 32,713	SR9 - 524.4
M2 - 6.00	SR3 - 8.22	SR11 - 32,423	SR10 - 493.1
SR11 - 4.92	SR2 - 6.63	SR6 - 32,063	SR11 - 473.8
M1 - 4.59	SR8 - 6.54	SR4 - 29,006	SR3 - 210.4
SR8 - 3.96	SR9 - 5.63	SR10 - 28,473	SR1 - 209.3
SR9 - 3.85	SR4 - 4.23	FR1 - 27,076	SR2 - 170.0
SR4 - 3.66	SR1 - 3.23	SR1 - 25,078	FR2 - 140.8
SR1 - 2.66	M1 - 2.58	FR2 - 24,208	FR1 - 125.2
FR2 - 2.64	FR2 - 2.29	SR2 - 22,521	SR4 - 108.3
FR1 - 1.48	FR1 - 1.84	SR3 - 21,793	M1 - 104.0
Avg: 5.09	Avg: 7.36	Avg: 32,984	Avg: 396.8

TABLE 7. DUCTILITY INDICES, ENERGY RATIOS, AND ABSORBED ENERGY PER POUND FOR TESTED BEAMS.

Beam ID	Beam No.	Yield Deflec. (in)	Max. Deflec. (in)	Duct. Index	Avg. Duct. Index	Yield Area (in.lbs)	Ult. Area (in.lbs)	Energy Ratio	Avg. Energy Ratio	Max. Load (lbs)	Avg. Max. Load (lbs)	Energy (in.lbs) Per lb (1)
SR1	1	0.4033	0.9438	2.34	2.66	5,208	17,552	3.37	3.23	26,109	25,078	209.3
	2	0.3480	1.0991	3.16		3,769	15,114	4.01		23,006		
	3	0.4865	1.2087	2.48		6,326	15,132	2.32		26,119		
SR2	1(2)	—	—	—	6.27	—	—	—	6.63	—	22,521	170.0
	2	0.1797	1.1265	6.27		1,895	12,566	6.63		22,521		
	3(2)	—	—	—		—	—	—		—		
SR3	1(2)	—	—	—	6.02	—	—	—	8.22	—	21,793	210.4
	2(2)	—	—	—		—	—	—		—		
	3	0.1770	1.0650	6.02		1,919	15,768	8.22		21,793		
SR4	1	0.1737	0.4378	2.52	3.66	2,568	8,634	3.36	4.23	30,877	29,006	108.3
	2	0.1342	0.5509	4.11		1,650	4,569	2.77		26,500		
	3	0.1866	0.8117	4.35		2,470	16,227	6.57		29,641		
SR5	1	0.2258	2.0147	8.92	8.92	3,426	58,101	16.96	16.96	32,713	32,713	749.7
	2(2)	—	—	—		—	—	—		—		
	3(2)	—	—	—		—	—	—		—		
SR6	1	0.1903	1.1958	6.28	7.54	2,826	32,951	11.66	13.71	30,913	32,063	538.2
	2	0.1965	1.8181	9.25		3,298	55,921	16.96		34,171		
	3	0.1792	1.2713	7.09		2,732	34,176	12.51		31,104		
SR7	1	0.2395	1.9976	8.34	6.91	4,562	45,703	10.02	9.19	38,328	39,292	562.3
	2	0.2491	1.9977	8.02		4,584	46,731	10.19		38,125		
	3	0.4587	1.9999	4.36		8,780	64,665	7.37		41,423		
SR8	1	0.3079	1.5102	4.90	3.96	7,051	56,945	8.08	6.54	49,544	49,708	666.3
	2	0.4752	1.2791	2.69		12,52	49,743	3.97		49,743		
	3	0.2990	1.2791	4.28		6,982	52,797	7.56		49,838		
SR9	1	0.3052	1.5328	5.02	3.85	6,899	53,941	7.82	5.63	48,003	47,284	524.4
	2	0.3507	1.0378	2.96		7,040	28,781	4.09		44,573		
	3	0.3116	1.1141	3.58		7,088	35,374	4.99		49,275		
SR10	1	0.2101	1.8672	8.89	6.94	2,813	34,739	12.35	9.93	26,950	28,473	493.1
	2	0.2758	1.4935	5.42		4,529	39,720	8.77		30,847		
	3	0.2788	1.8131	6.50		4,097	35,547	8.68		27,622		
SR11	1	0.4677	1.6055	3.43	4.92	7,401	41,759	5.64	8.80	33,087	32,423	473.8
	2	0.2064	1.1188	5.42		3,245	30,198	9.31		33,442		
	3	0.2360	1.3946	5.91		3,297	37,774	11.46		30,740		
FR1	1	0.3647	0.5117	1.40	1.48	4,393	7,384	1.68	1.84	24,638	27,076	125.2
	2	0.3346	0.5409	1.62		4,748	9,942	2.09		27,486		
	3	0.3804	0.5410	1.42		5,760	10,055	1.75		29,105		
FR2	1	0.4066	0.7084	1.74	2.64	5,259	10,452	1.99	2.29	26,192	24,208	140.8
	2	0.3532	1.1310	3.20		4,532	15,778	3.48		25,768		
	3	0.3346	0.9975	2.98		3,429	4,768	1.39		20,663		
M1	1	0.2266	1.0109	4.46	4.59	3,480	8,947	2.57	2.58	33,140	33,128	104.0
	2	0.2098	0.8682	4.14		3,137	7,209	2.30		32,644		
	3	0.1767	0.9149	5.18		2,894	8,292	2.87		33,601		
M2	1	0.2948	1.7690	6.00	6.00	6,679	61,025	9.14	10.55	>50K	>50K	876.9
	(4)	—	—	—		—	79,938	11.97		(5)		

- Notes: (1) Average ultimate area (in.lbs) divided by beam weight in pounds
(2) Bad data due to equipment problems
(3) Baseline beam
(4) Ultimate area values were derived from the two curves shown in Figure 9 (lower values from the lower curve, higher values from the higher curve)
(5) Average of the two energy ratios for the two different curves (this value is probably very conservative)
(6) Determined from the average of the 2 ultimate areas (61,025 and 79,938) divided by average beam weight in pounds (this value is probably very conservative)

TABLE 9. NORMALIZED BEAM TYPE RANKINGS.

Beam ID	Avg. Ductility Index	Avg. Energy Ratio	Energy Absorp. Per Pound
SR1	0.73	0.76	1.93
SR2	1.71	1.57	1.57
SR3	1.64	1.94	1.94
SR4	1.00	1.00	1.00
SR5	2.44	4.01	6.92
SR6	2.06	3.24	4.97
SR7	1.89	2.17	5.19
SR8	1.08	1.55	6.15
SR9	1.05	1.33	4.84
SR10	1.90	2.35	4.55
SR11	1.34	2.08	4.37
FR1	0.40	0.43	1.16
FR2	0.72	0.54	1.30
M1	1.25	0.61	0.96
M2	1.64	2.49	8.10

A COMBINATION OF STEELFIBERS AND CONVENTIONAL REINFORCEMENT IN PROTECTIVE CONCRETE STRUCTURES SUBJECTED TO NEAR MISS EXPLOSIONS, CONTACT EXPLOSIONS, DIRECT HITS, AND EXPLOSIONS AFTER PENETRATION

LTC G. Naeyaert *, CE A. H. Verhagen **, B. Sc. Phys. T. Türker ***, M.Sc. Mec. Eng.

* Infrastructure Dep., MOD BELGIUM
 ** Royal Military Academy, THE NETHERLANDS
 *** President UNITEK Consult. Eng., TURKEY

OBJECTIVE.

Allmost all existing studies and calculation methods relating to the determination of the resistance of structures to nearby explosions have been carried out and adapted to the use of conventional reinforced concrete (CRC). The concrete matrix with a top and bottom reinforcement lends itself particularly well to determining the required calculation elements used in dimensioning, such as I (moment of inertia), M_{pl} (plastic moment of resistance), and others. Thus taking into consideration simple, rough calculations, a design calculation can be carried out without many aids. When using steel fibres (SF) and conventional reinforcement (CR) in the same concrete slab, the calculation elements are no longer as simple to establish. To remedy this in the first instance a comparative study was required between :

1. slabs with conventional reinforced concrete (CRC).

2. slabs with a combination of both CR and steelfibres (SF).

The main objective is therefore to determine empirically the differences in behaviour between the two slabs when subjected to equivalent explosion and impact loads. By comparing the damage phenomena such as deflections, cracks, plastic hinges, scabbing, spalling and perforation, a good dimensioning method can be established for the combination CRC + SFRC. The purpose of this article is simply to demonstrate the comparison of both types of reinforcement CR and CR + SF, and draw quantitative conclusions from this comparison.

CRC-SFRC TEST PROGRAMME.

These tests may be divided into two important areas.

1. Near-miss explosion tests on slabs (scale approximately 1/4). Here use was made of explosives without a metal encasement (uncased charges). Supplementary tests, to study the effects of the steel encasement, such as altered pressure build-up and fragmentation, followed by impact of splinters on the wall, will therefore have to be carried out at a later stade.

2. Firing tests on slabs (scale approximately 1/4.)

In this case use was made of inert projectiles for testing slabs for penetration resistance. The inert projectile was then replaced, at its place of rest in the slabs, by an HE explosive charge wich was finally caused to explode. The complex phenomenon of impact and explosion after penetration was therefore clearly unravelled here so that both factors could be studied independently. These tests were carried out in Turkey.

EXPLOSION TESTS ON SLABS.

1. WORKING METHOD.

Slabs with different reinforcement configurations - CRC only, combinations of CRC and SFRC, and all in varying dosages - were subjected to identical explosion loads. Different behaviour patterns were observed and compared. Table 1 gives a summary of the test slabs used, totalling some 50 slabs.






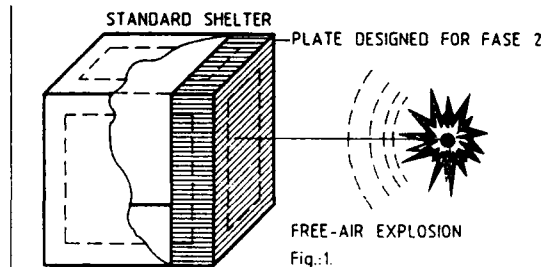
TEST	MODEL SHAPE	SLABS
1		9
2		8
3		5
4		20
5		20

TABLE I

2. STUDY OF THE MODEL. (Fig.no.1)

In terms of response the model was used to simulate as closely as possible the lateral wall of a standard shelter. A one-storey shelter already has a height of 5 m. The study of an area of approximately 5 m by 5 m was envisaged, with the explosion at a distance of about 3 m. Due to limitations in the test area, a scale of approximately 1 to 4 was selected. Finally, a model was accepted on the basis of symmetry considerations with the scaled dimensions : 120 x 120 x 16.26 cm (48 x 48 x 6.6 Inches). The load had to conform to that derived from a classic bomb. Standard military plastic HE explosive (3.75 kg) was used on each occasion.



3. TEST ARRANGEMENT. (Photo no.1)

In the first phase ten conventional square plates were inseried and tested when placed neatly on the four sides. Very soon it became apparent that in order to allow the influence of the solidity of the plate with the rest of the shelter to be exerted on the one hand, and to guarantee adequate reproducibility of the tests on the other, the plates for the next phase had to be provided with a reinforced edge (Fig.no.2). However, it was not intended to provide an absolutely perfect clamp. The entire arrangement rested on a heavy Stelcon plate. The surfaces of contact between the test slab and this Stelcon plate were provided with a Bentonite slurry to guarantee continuous contact between them. The explosive charge was suspended above the centre on the slab. The stand-off distance could be adjusted simply as required.

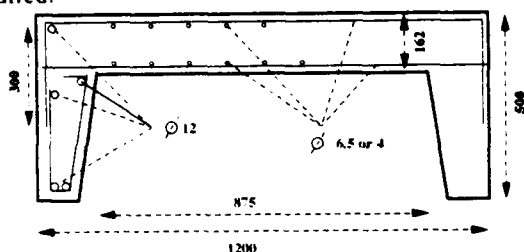


Fig 2. SLAB (FASE 2)
(all distances in millimetres)

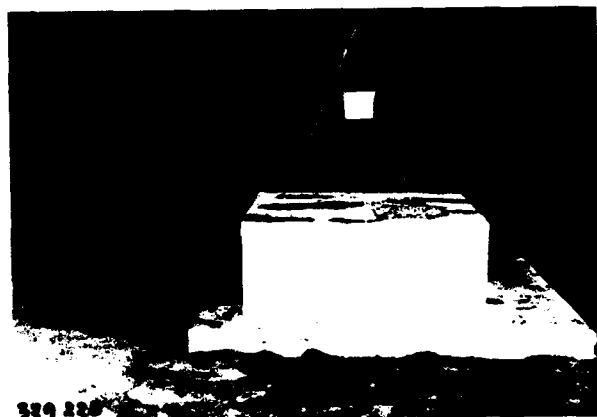


Photo no.1

4. FIRST PHASE: TESTS / RESULTS.

The first test series, carried out in 1988-89, clearly demonstrated the positive effect of the steel fibres. Because these slabs with a high reinforcement percentage (see Table no.2) offered very good resistance to the explosive load, the stand-off distance was decreased to 37.5 cm.

Slab no.1 (see Table no.2), with a reinforcement of 190 kg/m³, without fibres, showed a deflection of the same order as that displayed by some slabs with a combination of CRC + SFRC.

Slab no. 7 (see Table no.2), with a total reinforcement of only 150 kg/m³, in a combination of CRC + SFRC, clearly displayed the same deflection and no resultant scabbing. This is very important for the continued survivability in the shelter. A further comparison of the scabbing material thrown out from both slabs clearly demonstrated the superiority of slab no. 7.

By using a combination of CR + SF a saving in reinforcement of 40 kg/m³ was achieved. This means that out of a total of

190 kg/m³ a saving of well over 20% can be achieved on the entire steel reinforcement. It must be pointed out, however, that because this first test package (1988-89) was very limited - only 9 slabs were tested - this could not be accepted as an absolute conclusion.

It is important to know, however, that the idea of a reduction in reinforcement coupled with steel fibre addition conforms to a number of calculations carried out in this respect by MOD Belgium. As an example of this we give here the moments of resistance of a beam of constant dimensions, where we varied the reinforcement percentage as well as the combination of CR + SF (Fig.no.3). With the same total reinforcement percentage it was observed that the beam with both CR and SF had a slight advantage over the beam reinforced with CR only, an advantage which may result in a reinforcement saving of 15%. This advantage is lost if the total reinforcement percentage exceeds a certain value (point of intersection of the two curves in fig.no.3). In this specific case ($\pm 3\%$), the reinforcement content lies outside the normal reinforcement quantities.

Fig. no. 4 shows that a beam with single reinforcement - i.e. only provided for resistance to static loads - a combination of CR + SF, will always be inferior to CR.

ULTIMATE STRENGTH

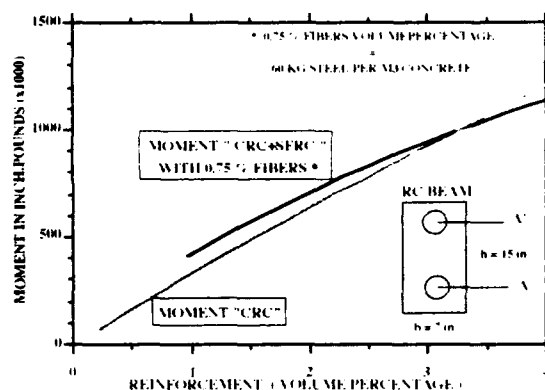


Fig 3 BEAM DESIGNED TO WITHSTAND DYNAMIC LOADS
(BARS A = A')

ULTIMATE STRENGTH

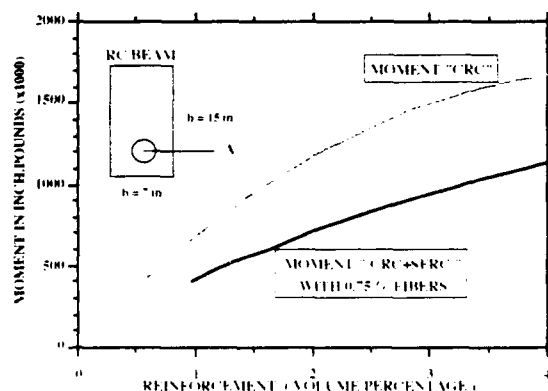


Fig 4 BEAM DESIGNED TO WITHSTAND STATIC LOADS
(BARS ONLY A)

5. SECOND PHASE : TESTS + RESULTS.

In this phase (1991-1992) all the slabs with a reinforced edge were treated. This test series covered around 50 slabs which clearly had much less reinforcement than the previous slabs. Two identical slabs were made from each reinforcement combination. Only 4 stirrups, required for structural purposes, were placed in all the slabs in order to study the influence of the steel fibres when the traditional stirrups were replaced. Four identical reference slabs were made with 88 kg/m^3 CR. These "reference slabs" were used, among other things, to examine the reproducibility of the tests. The reference slabs therefore had to display almost identical damage patterns under an identical load.

STAND - OFF 750 MM.

The first series of slabs produced a number of results which may be considered reliable in view of the good reproducibility of the test series. Fig.5 shows the results in connection with deflection as a function of the total reinforcement. It is important to point out that the slabs showed no visible damage or cracks. Cracks did not become visible until the slabs were moistened. However, the effect of the fibres was not so immediately visible here.

The deflections of a number of slabs with CR + SF were extremely low : slab no.5 (Photo 2) with a total reinforcement of 79 kg/m^3 CRC+SFRC (1 % by volume) had a deflection less than that of slab no.1 (Photo 3), with 88 kg/m^3 CR.

The general deflection pattern include the well-known plastic hinges, which varied from a fine crack to a series of parallel cracks bearing no direct relationship to the reinforcement percentage. No scabbing was observed.

Fig. no.7 shows that steel fibres contribute more to deflection limitations than the same weight of reinforcing bars. It represents the mean deflection at a constant bar reinforcement content and variable fibre content, with the total reinforcement content as abscis. Here it is clearly seen that with the same total reinforcement the slab with the lowest weight of reinforcement bars shows the least deflection (88 and 56 kg/m^3)

CONCLUSION : So an addition of fibers in the same total weight of reinforcement produces a higher resistance resulting in a reduced deflection. Despite the fact that the use of the steel fibres in this phase of the tests is not immediately visible, the latter observation is still very important in view of the deflection limiting property of the fibres, even in low dosages.

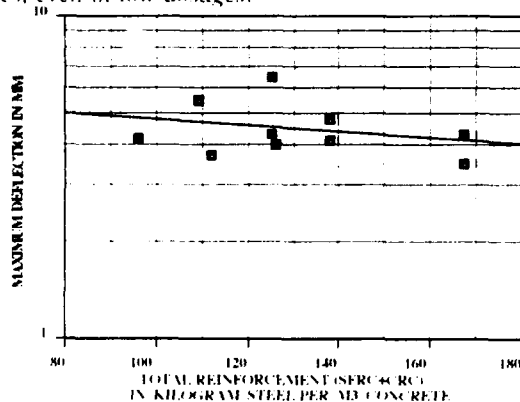


Fig 5. RESULTS OF SLAB 10 TO 22 WITH A STAND-OFF EQUAL TO 750 MM

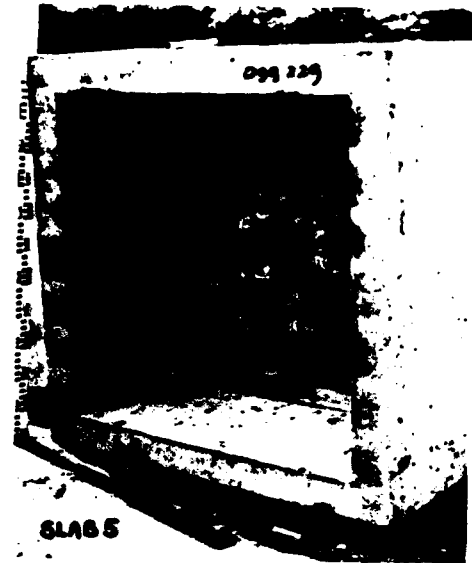


Photo no.2 SLAB 5



Photo no.3 SLAB 1

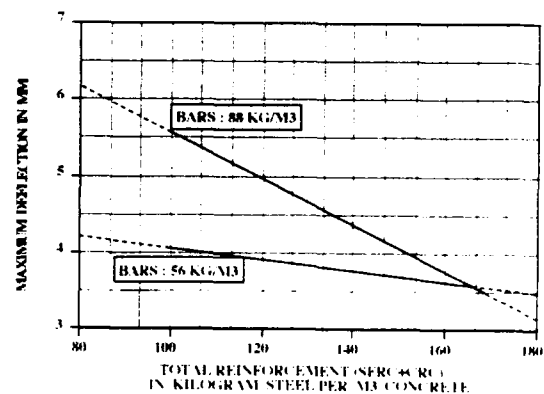


Fig 7. INFLUENCE OF THE FIBERS WITH A CONSTANT WEIGHT OF BARS

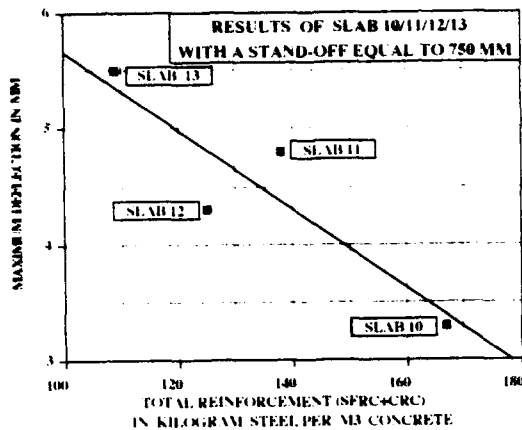


Fig 6 . SLABS WITH 88KG / M3 FIBERS AND A DIFFERENT QUANTITY OF BARS

STAND - OFF 550 MM.

Even in these tests good reproducibility was observed. In this series of tests the deflections were higher than in the previous series. Yet the deflection pattern is totally different: cracks along the edge, followed by a circular crack along about ten cm of the edge. The well known plastic hinges - as seen with a stand-off of 75 cm, had disappeared almost completely. Different slabs with a higher reinforcement content showed no scabbing, whilst slabs with a lower reinforcement content did show scabbing.

The slabs with CR only, however, displayed major scabbing without exception. Photo 4 (slab 1xx) and photo 5 (slab 5) show the slabs sawn through and clearly indicate the difference between the crumbled areas in a slab without fibres (slab 1xx) and with fibres (slab 5).

The deflections of both slabs are roughly identical. However, slab 5 had a reinforcement content of 78 kg/m³ CR+SFRC, whilst slab 1xx had a reinforcement of 88 kg/m³ CR. Absolutely no deflection or damage was observed on the front of the slabs.

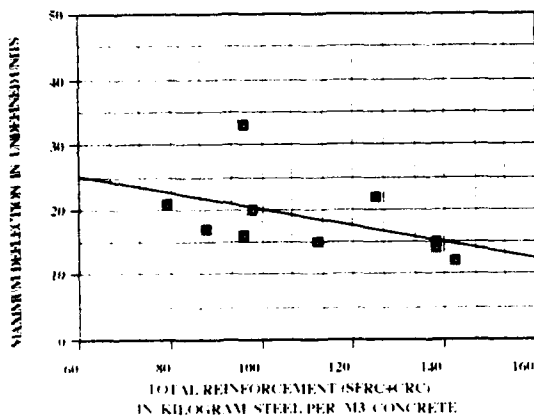


Fig 9 . RESULTS WITH A STAND-OFF EQUAL TO 550 MM



Photo no.4 SLAB 1xx

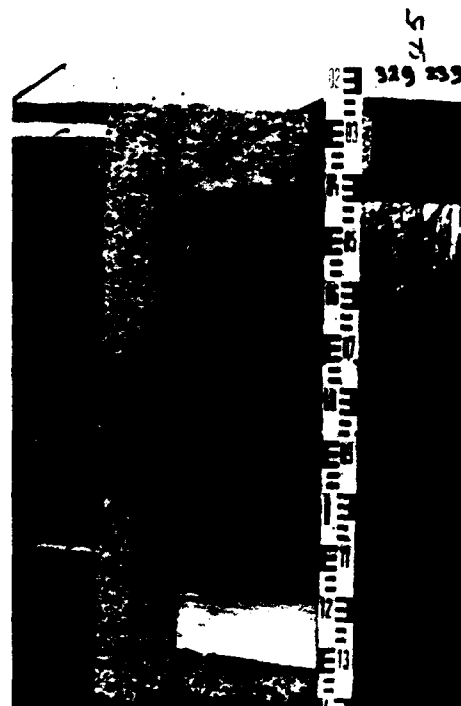


Photo no.5 SLAB 5

STAND - OFF 350 MM.

In the case of the slabs reinforced with CR only, the load resulted in complete breaching (see Photo no.6 - slab no.2). All the slabs provided with CR + SF offered resistance to breaching to the extent that a third to half the thickness of the slab remained intact. This positive effect of the fibres was already observed from a content of 21 kg/m^3 upwards (photo no 7 - slab 13). Good resistance was displayed by slab no.9 (photo no.9), which showed almost no scabbing, despite the very close explosion. This slab had 10 kg/m^3 more reinforcement than slab no. 1 and only 30 kg/m^3 less reinforcement than slab no.2. A comparison of the two slabs (photos 8 and 9) requires no further comment. In the slabs sawn through (photo no.8 - slab lxxx and photo no.9 - slab 9) it was very clear that the addition of steel fibres counteracted the disintegration of the slab. This conforms to other studies carried out in Belgium which confirm that steel fibres can partially replace stirrups. This conclusion only applies to the stand-offs of the tests carried out here.

CONCLUSION : The effect of the steel fibre is seen more clearly than in the previous tests. Specifically the breaching is impeded here and the crumbling area, the scabbing effect and the deflection are reduced.



Photo no.8 - SLAB 1^{xxx}

Photo no.9 - SLAB 9

CONCLUSIONS.

The addition of steel fibres (CR + SF) provides the following advantages :

- reduction in deflection
- prevention of breaching
- reduction in the crumbled area, thereby guaranteeing greater resistance to total collapse of the structure
- replacement of the stirrups, not apparent until a greater load is applied (or shorter stand-off distance).

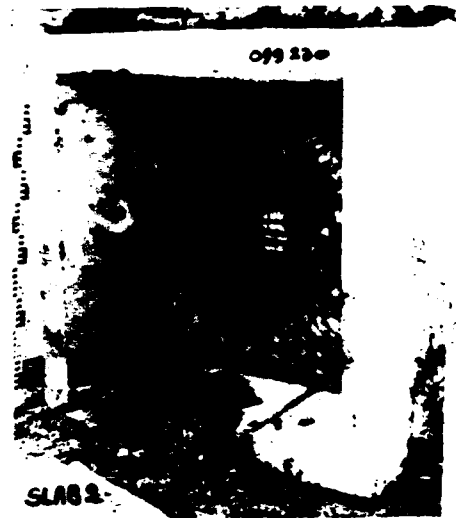


Photo no.6 SLAB 2



Photo no.7 SLAB 13

These characteristics are increasingly evident as the stand-off is reduced and the deflection becomes more pronounced. It is important to note that the fibres actually exert their influence from very low dosages (21 kg/m^3) upwards, but in the case of structures which are statically loaded the presence of fibres is only observed from a dosage of 35 kg/m^3 upwards.

Besides the specific positive contribution made by the fibres the following may also be stated. From testing experience it may be established that under the same explosion load the reinforcement content can be drastically reduced to approximately 1 per cent by volume, whether we are looking at CRC or the combination of CRC + SFRC. The order of magnitude of one per cent by volume had already been proposed by other bodies around the years 1989-1990, and is here confirmed once again.

Last but not least it must be stated that a shelter designed to resist a specific explosion load, will also resist the same explosion, at well below half the stand-off distance if a combination of CR + SF is used. This is certainly not the case when only CRC is used.

SLAB NO	STEELFIBERS KG M3	REBARS KG M3	TOTAL REINFORCEMENT KG M3
1	0	190	190
2	50	122	172
3	50	104	154
4	50	124	174
5	40	116	156
6	60	90	150
7	60	90	150
8	80	64	146
9	0	116	116

SLAB NO	SCABBING SURFACE	SCABBING THICKNESS cm	DEFLECTION cm	LACING Y (1 dir) Y (50%)
1	30 x 30 cm	2	1	Y (1 dir)
2	30 x 50 cm	5	2	Y (50%)
3	35 x 60 cm	10	5	N
4	20 x 50 cm	5	2	N
5	50 x 50 cm	5	2	N
6	20 x 35 cm	4	4	N
7	10 x 20 cm	2	1	N
8	50 x 65 cm	12	5	N
9	50 x 50 cm	1	1	Y (2 DIR)

TABEL NO. 2 SLABS (FASE 1)

SLAB NO	STEELFIBERS KG M3	REBARS KG M3	TOTAL REINFORCEMENT KG M3
1	0	88	88
2	0	126	126
3	81	44	125
4	44	44	88
5	35	44	79
6	79	63	142
7	63	63	126
8	50	63	113
9	35	63	98
10	79	88	167
11	50	88	138
12	37	88	125
13	21	88	109
14	70	56	126
15	56	56	112
16	40	56	96
20	79	88	167
21	50	88	138
22	37	88	125

TABEL NO. 3 SLABS (FASE 2)

FIRING TESTS

1. MODEL ELEMENTS.

A practical scale was used for the test walls, projectiles and explosives. Three reinforced concrete test walls 250 cm high, 250 cm long and 40 cm thick were constructed including foundation with appropriate dimensions. (Photo no. 10)



Photo no. 10

The walls no.1 and no.2 had steel fibres in addition to the reinforcing steel. The reinforcements were three layers and the ratio was 60 kg/m³ concrete. The ratio of steel fibres (Dramix ZP.30/.50, 30 mm long, 0.50 mm diameter) was 40 kg/m³ concrete. All three model walls had rock embedded concrete outer layer on the faces to which projectiles were fired. The rock used was of basaltic type with 2.7 specific gravity and 2000 kg/cm² strenght. The nominal sizes the rock pieces were 10 cm and they were placed in three layers to get 35 cm thickness. As simulation of the actual threat to the structure, 105 mm standard tank gun inert rounds, 6.56 kg TNT equivalent explosives enclosed in 400 mm long, 100 mm diameter cylindrical containers with proper fuses were used. The required nominal values for the tests were identified as :

Weight of projectiles : 12.00 kg

Weight of explosives: 6.56 kg

Striking velocity of projectiles: 300 m/s

Compressive strenght of the reinforced concrete :350 kgf/cm²

The objective was to have no scabbing at the back surfaces of the walls after impact and blast effects.

2. TEST SEQUENCE AND OBSERVATIONS.

The tank gun with inert round was fired to wall no.2 from approximately 290 meters distance. The projectile perforated the rock embedded concrete and penetrated 7 cm into reinforced concrete. Very few fine hair cracks were observed behind the wall (photos no. 11,12).



Photo no. 11

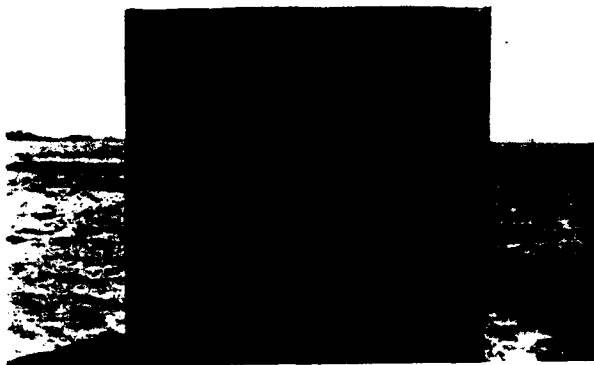


Photo no. 12

Similar round was fired to the wall no.3. The projectile perforated rock embedded concrete and penetrated 20 cm into the reinforced concrete. Severe cracks and scabbing were observed at the back surface of the wall (Photo no. 13).

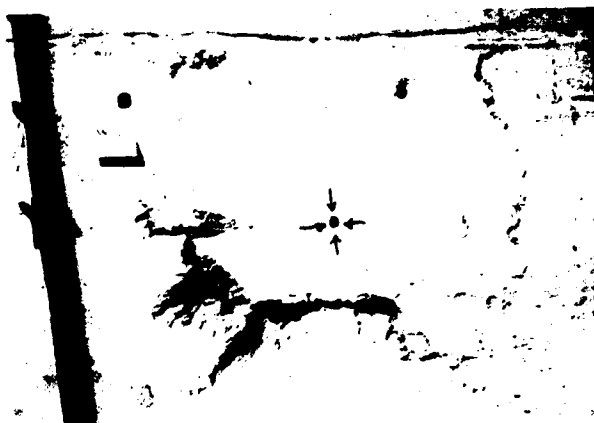


Photo no. 13

Same type inert round was fired to wall no.1 and complete perforation was observed (Photo no. 14).



Photo no. 14

Second round was fired to wall no.1 (Photo no. 15) and the same result, complete perforation, was observed again.



Photo no. 15

A second round was fired to the wall no.2. (Photo no.16) Similar results as stated before. 6 cm penetration into the reinforced concrete layer was observed.



Photo no. 16

The first projectile was removed from wall no.2. The explosive was placed in the same location. After blasting of the explosive, a crater of 80 cm diameter was observed in front of the rock embedded layers. On the back surface of the reinforced concrete layer some more fine cracks were noticed.

3. EVALUATION OF OBSERVATIONS.

Due to the circumstances beyond the control of the test design group, the following major deviations from test design parameters were occurred :

	Test design values	Actual model values
Projectile weight	12.0 kg	15.0 kg
Projectile impact velocity	300 m/s	360 m/s
Concrete strenght		350 kgf/cm ² < 175 kgf/cm ²
Grouting concrete strenght	350 kgf/cm ²	< 60 kgf/cm ² for wall no.1*

* Close to 110 kgf/cm² for walls no.2,3

The lower quality of grout in rock grouted wall might be the main factor for the explanation for the perforations occurred on wall no.1. Grouted rock layers adjacent to R/C walls were used to reduce residual velocity on R/C wall surface and to deviate the projectile path.

For a projectile, required velocity to fully perforate a rockfill (given by Rohani) is inversely proportional to a quality factor of the filler material between rock units. If the filler is fine sand then the factor is 0.6. If the filler is ideal grout then the factor is 0.185. As filler of the grouted rocks deviates from ideal grout to sand, the residual velocity increases. It has been calculated that a round weighing 15.0 kg with residual velocities greater than 152 m/s can perforate 40 cm reinforced concrete wall with 175 kgf/cm² strenght. Taking 360 m/s striking velocity, filler grouts with quality factors greater than 0.27 will lead perforation of the concrete walls. Comparison of observed deviation angles of trajectories and deflections of projectiles fired to wall no.1 and to other walls confirms the greater residual velocity hence the lower quality of the filler on wall no.1.

The input parameters; deviation angles and deflections for the penetrating process into reinforced concrete layers of walls no.2 and 3 were observed to be very similar but different penetrations and cracking/scabbing on them is due to presence/ absence of steel fibres. The presence of Dramix steel fibres has decreased the penetration depth yielding to less cracking and no scabbing at the back surface of the wall no.2.

4. CONCLUSIONS.

It seems reasonable to state that perforation of wall no.1 is mainly due to accidental lower quality of grout used in wall no.1 with respect to those used in other walls. Test results signified the adequacy of the formulas used in design, hence the validity of the projective measures applied to the real structure. Comparison of the results on wall no.2 and wall no.3 had indicated the positive effect of addition of steel fibres to concrete.

5. ACKNOWLEDGEMENTS.

The author expresses his thanks to NATO Infrastructure Dept. TURKEY for providing personnel, equipment and site for executing of the tests. He wishes also to thank TUBITAK (Turkish Scientific and Technical Research Institute) for their support on taking high speed camera pictures and projectile velocity calculations.

REFERENCE LIST.

- **B. Rohani**, "Penetration of kinetic energy projectiles into rock rubbles/boulder overlays" U.S. Army, 1987
- **Herman Pahl**, "Penetration of Projectiles into Finite Thick Reinforced Concrete Targets" . NATO Headquarters, Belgium. (4 th Intern. Symposium, Florida 1989)
- **G.C.G. Naeyaert**, "Criteria used for the partial substitution of laced and bar reinforcement by steelfibers in protective structures". Structures for enhanced safety and physical security ARLINGTON, VIRGINIA, March 1989
- **G.C.G. Naeyaert**, "Criteria used for the partial substitution of steelbars by steelfibers in protective concrete structures". Fourth International Symposium on the interaction of nonnuclear munitions with structures . PANAMA CITY BEACH, FLORIDA, April 1989

EXPEDIENT REPAIR OF MISSION-CRITICAL STRUCTURAL FACILITIES

David L. Read and Douglas H. Merkle

Applied Research Associates, Inc., Tyndall AFB, FL

ABSTRACT

To fulfill its mission after an attack, an airbase must be able to quickly generate sorties, and sustain them. To generate sorties, an airbase must have a usable and accessible runway surface. To sustain sorties, an airbase's mission-critical facilities must be operational. The U.S. Air Force has begun fielding systems to rapidly repair cratered runways and taxiways. However, the U.S. Air Force currently has no fielded systems to expediently repair mission-critical facilities at forward operating bases (FOBs) in a postattack environment. To address this problem, systems to expediently repair conventional weapon damage to mission-critical facilities at United States Air Forces in Europe (USAFE) and Pacific Air Forces (PACAF) FOBs in a postattack environment were developed and demonstrated in the field. Included in the development of each repair system was the identification of the personnel, equipment, materials, and procedures required to support it.

DEFINITION OF EXPEDIENT REPAIR

In this research effort, expedient repair of structural facilities (ERSF) was defined as simple, nonpermanent repairs to mission-critical facilities that can be accomplished within 4 hours. The 4-hour limit is the maximum time an individual repair can take to be accomplished. The purpose of such repairs is to allow the damaged facility to continue to accomplish its mission without undue hazard to personnel within the facility, or at a minimum allow critical resources to be safely removed from the facility.

ERSF is applicable to all mission-critical structural facilities on FOBs. This includes steel-framed, reinforced concrete, masonry block, and wood structures.

ERSF REPAIR SYSTEM DEVELOPMENT

The expedient repair system development process consisted of three phases. Each of these phases are discussed below. Mission-critical structural facilities at Bitburg Air Base (AB), Federal Republic of Germany (FRG) were used as the baseline facilities during the development process. For a detail description of the ERSF system development process see References 1 and 2.

Identification of Damaged Modes (Phase I)

In this phase, structural blueprints of mission-critical facilities at Bitburg AB were reviewed in detail. The purpose of the review was to determine likely damage modes to the facilities from conventional weapon effects. Based on this review, the following expediently repairable damage modes were determined.

- | | |
|------------------------|----------------------|
| 1) Damaged Steel Frame | 7) Floor/Roof Breach |
| 2) Destroyed Column | 8) Damaged |
| 3) Cracked Column | Overpressure Door |
| 4) Damaged Beam/Girder | 9) Stuck Blast Door |
| 5) Destroyed Wall | 10) Destroyed Window |
| 6) Wall Breach | 11) Fractured A/C |
| | Shelter Floor Slab |

System Development and Screening (Phase II)

ERSF systems to repair the damage modes to mission-critical facilities listed above were developed, and underwent a preliminary, subjective screening process. Systems were modified, if possible, to improve their viability. Based on this screening and refinement process, the most viable candidate ERSF systems to repair each damage mode were identified. These candidate ERSF systems were then evaluated in-depth for effectiveness, and ranked in order of merit using evaluation matrices.

Each ERSF system was evaluated in operational, structural, and logistical categories for criteria such as manpower, simplicity, strength, durability, storage life, and cost. Each system was assigned a score for each criterion. Scores ranged from one (poor) to five (excellent). A system's criterion scores in each category were summed, and the sum multiplied by a weight factor to obtain the system's category score. The three category scores were then summed to obtain the system's total evaluation score. Based on this score, the system was ranked against other repair systems for the same damage mode. The outcome of this process was recommended and backup ERSF systems to repair each anticipated damage mode. These repair systems are listed below. Recommended and backup ERSF systems are denoted by the letters (R) and (B), respectively.

- | <u>Damage Mode</u> | <u>Repair Method</u> |
|------------------------|-------------------------------|
| 1) Damaged Steel Frame | Cutting and Welding (R) |
| 2) Destroyed Column | Column Replacement |
| | 1 - Shoring Jack (R) |
| | 2 - Glued, Laminated Timber |
| | Column (R) |
| 3) Cracked Column | Steel Plate Column Splint (R) |

<u>Damage Mode</u>	<u>Repair Method</u>
4) Damaged Beam/Girder	Vertical Shoring (R) King Post Support (B)
5) Destroyed Wall	Plywood Backing (R) Shotcrete Repair (R) Earth Beam (B) Precast Slabs (B)
6) Wall Breach	Plywood Backing (R) Shotcrete Repair (R) Precast Slabs (B) Earth Berm (B)
7) Floor/Roof Breach	Plywood and Rolled Roofing (R) Rapid Set Concrete (R) Seal Stairs (B)
8) Damaged Overpressure Door	Canvas/Sheeting Covering (R) Third Door Insertion (B) Door Replacement (B)
9) Stuck Blast Door	Pry Open Door (R)
10) Destroyed Window	Plastic Sheeting Covering (R) Acrylic Panel Replacement (R)
11) Fractured A/C Shelter Floor Slab	AM2 Panel Ramp (R) Rapid Set Concrete Ramp (R) Shotcrete Ramp (B)

ERSF System Field Demonstrations (Phase III)

To validate the ERSF system development process three ERSF systems were field-demonstrated. The demonstrated systems were; 1) the column splint system, 2) the glued, laminated timber (Glulam) column replacement system, and 3) the shotcrete wall replacement and wall breach repair system. Beyond validating the system development process, the field demonstrations verified the concept of each individual ERSF system with respect to the equipment, materials, supplies, and procedures needed to accomplish the repairs. Brief summaries of each demonstration are given below. All tables and figures reference in the remainder of the text follow at the end of this paper.

Column Splint Demonstration. In this repair scenario, a reinforced concrete column is cracked, but still capable of carrying a load. However, because of the crack(s) it is necessary to laterally constrain the column at the location of the crack(s) to prevent slippage. Steel plates connected together with threaded rods are used to splint the column.

Demonstration results are summarized in Table 1. The splinting process took from 4 minutes and 27 seconds to 7 minutes and 38 seconds to complete. Figure 1 shows a nearly completed column splint repair. Overall the column splinting process was very fast and is a viable ERSF system. Some modifications were required to increase the splint's capacity and make its hardware easier to use. These modifications were done and the ERSF column splint system was demonstrated again during the FOAL EAGLE Air Base Operability (ABO) exercise at Osan AB, Korea (see below).

Glulam Column Replacement Demonstration. In this repair scenario, a reinforced concrete column is damaged by blast and/or fragments, to the extent that it can no longer support its design load and must be replaced. Consequently, a Glulam replacement column is inserted next to the destroyed column and braced laterally to carry part of the destroyed column's load.

Demonstration results are summarized in Table 2. The column replacement process took from 23 minutes and 52 seconds to complete during Test Iteration 1 and 11 minutes and 45 seconds to complete during Test Iteration 2. Reducing the

repair time by over half between Test Iterations 1 and 2 showed that a learning curve existed during the first iteration. Figure 2 shows a nearly completed column replacement repair. The column replacement process was fast, easy to accomplish and is a viable ERSF system. This ERSF system, but using a modular steel box section instead of a Glulam timber, was also demonstrated during the FOAL EAGLE Air Base Operability (ABO) exercise at Osan AB, Korea (see below).

Shotcrete Wall Replacement/Wall Breach Repair. In this repair scenario, a non-load bearing reinforced concrete or masonry block wall has been destroyed or breached. To repair the wall, a plywood backing is placed behind the damaged area. Then steel fiber-reinforced, rapid-setting, high-strength shotcrete is sprayed onto the backing to complete the repair.

The shotcrete ERSF system field demonstration was plagued by equipment problems. The shotcrete equipment used for the demonstration was too small for the job and broke down numerous times. Consequently, the repair process lasted two days with the actual repair time being 2 hours and 58 minutes. The completed shotcrete repair is shown in Figure 3.

Because of the equipment problems during this demonstration, an effort was undertaken to identify and evaluate a high-capacity, automated, remotely controlled piece of shotcrete equipment for use in the ERSF system. A piece of equipment sold by Surecrete, Inc in the United States was identified and evaluated. This piece of equipment is shown in Figure 4. The evaluation involved using the equipment to repair a 5-foot diameter wall breach in a 26-inch thick wall. The breach was approximately 15 feet above ground level. Using the automated shotcrete equipment, it took approximately 16 minutes to fill in the breach. Backing the breach prior to the placement of shotcrete added 35 minutes to the repair time. Figure 5 shows the wall breach repair in progress. Using the automated shotcrete equipment, the wall breach repair process was fast, easy to accomplish and is a viable ERSF system. This ERSF system, with the automated shotcrete equipment, was also demonstrated during the FOAL EAGLE Air Base Operability (ABO) exercise at Osan AB, Korea (see below).

FOAL EAGLE ABO EXERCISE, OSAN AB KOREA

As indicated above, the column splint, column replacement, and shotcrete wall breach repair ERSF systems were demonstrated during the FOAL EAGLE exercise in late October and early November 1991. In addition, an earth berm wall breach repair was conducted. The objective of the demonstrations was to convince MAJCOM civil engineers that ERSF systems were ready for Engineering and Manufacturing Development (EMD). The demonstration process consisted of two phases. In the first phase, Osan AB civil engineering personnel were trained to use the ERSF systems. In the second phase, repairs were conducted under timed conditions. Each of these phases is described below. For a detailed description of the ERSF system demonstrations during the FOAL EAGLE ABO exercise see Reference 3.

FOAL EAGLE Training (Phase I)

Column Splint Training. A 20-inch square concrete column located in a mechanical room in the basement of the base hospital was used to conduct column splint training. The repair team consisted of two Osan AB civil engineering personnel from the 51 CES. Two repairs were conducted. Results from each repair are summarized in Table 3. Both training repairs went well, with no significant problem

encountered during the process. The two repair team members felt comfortable with the process and associated hardware.

Column Replacement Training. A 25-inch diameter, 10-foot 9-inch tall circular column located in the emergency entrance to the base hospital was used to conduct column replacement training. The repair team consisted of four 51 CES personnel. Results from the repair are summarized in Table 4. The repair went very well. No significant problems were encountered during the process. The four repair team members felt comfortable with the process and associated hardware.

Earth Berm Wall Breach Repair Training. A burned-out, single-story, laundry building located behind the base civil engineering equipment yard was used to conduct the training session. A door opening in the structure was repaired by backing the opening with plywood, leaning a precast slab against the building to cover the opening from the outside, and then forming a earth berm against the slab using a front-end loader. The repair team consisted of five 51 CES personnel. One repair was conducted, with the results summarized in Table 5.

One problem arose during the repair process due to the weakened structural condition of the burned-out laundry building. The roof of the building was completely destroyed and the standing masonry block walls could not resist a significant lateral load. As a result, when the precast slab was leaned against the building's wall, a visible lateral deflection occurred. To prevent collapse of the wall, only a partial berm was formed against the slab. The berm covered approximately two-thirds of the slab. To alleviate this problem during the actual demonstration, the building's wall was braced from behind with lumber.

Except for the problem just described, earth berm repair training went very well and the five repair team members felt comfortable with the process and associated hardware.

Shotcrete Wall Breach Repair Training. The main purpose of shotcrete training was to familiarize 51 CES personnel with the use and maintenance of the shotcrete and support equipment. Additionally, one person was trained to use the remote, hand-held, control panel to operate the automated shotcrete equipment. Training consisted of lining a drainage ditch, which was experiencing erosion problems. The lining process took approximately 2.5 hours to complete. A view of the ditch lining process is shown in Figure 6.

Two problems were encountered during shotcrete training. First, it was difficult to control the water flow rate to the shotcrete nozzle. It took approximately 30 minutes to troubleshoot the water supply system and obtain the correct flow rate in a reliable manner. The second problem involved supplying shotcrete material to the shotcrete equipment's hopper. Great care had to be taken in securing the bag (Supersack) containing the shotcrete material and the attached lifting harness to the forks of a forklift. The forklift was used to lift the bag over the hopper of the shotcrete equipment. If the lifting harness was not properly secured, the bag could drop to the ground and burst open.

Except for the problems described above, shotcrete training went well. The five man repair team felt comfortable with the repair process and associated equipment and hardware.

FOAL EAGLE Demonstrations (Phase II)

Earth Berm Wall Breach Repair Demonstration. A wall of the burned-out laundry building behind the civil engineering

equipment yard was used to conduct this demonstration. As indicated above, this wall had been braced with lumber to increase its lateral strength. The plywood backing placed behind the door opening in the wall during training had not been removed and was used for the demonstration. One repair was conducted. Results from the earth berm repair are summarized in Table 6.

Even with bracing, the wall was still weak laterally. Consequently, only a partial berm was formed against the precast slab. Overall the repair went very well, with no significant problem encountered. The completed repair is shown in Figure 7.

Shotcrete Wall Breach Repair Demonstration. This demonstration took place immediately after the earth berm wall breach repair demonstration. Another door opening in the burned-out laundry building, previously backed with plywood, was used to conduct the demonstration. Repair thickness was 8 inches. No lateral bracing was attached to the wall. One repair was conducted. Results from the shotcrete repair demonstration are summarized in Table 7.

Overall the repair the demonstration went very well, with no significant problem encountered. A view of the shotcrete repair in progress is shown in Figure 8.

Column Splint Demonstration. Two column splint demonstrations took place during the FOAL EAGLE exercise. The first demonstration was conducted using a 20-inch square column located in a mechanical room in the basement of the base hospital. Results from this column splint demonstration are summarized in Table 8. The second column splint demonstration was conducted using a 14-inch square column located at the front entrance to the 7AF headquarters building. Results from this demonstration are also summarized in Table 8. Both demonstrations went very well. No problem was encountered during either demonstration.

Column Replacement Demonstration. A 10-foot 9-inch tall, 25-inch diameter circular concrete column located in the emergency entrance to the base hospital was used to conduct the demonstration. Results from the column replacement demonstration are summarized in Table 9. The repair went very well with no significant problem encountered. The nearly completed column replacement repair is shown in Figure 9.

CONCLUSIONS AND RECOMMENDATIONS

Viable ERSF systems were developed for a wide range of damage modes. All recommended and backup ERSF systems are relatively simple, fast, and easy to use. These system, if available to civil engineering personnel on a FOB after an attack, would significantly speed up the recovery process.

Engineering and Manufacturing Development (EMD) of the ERSF system should be undertaken immediately. To this end, it is recommended that Operational Requirements Documents (ORDs) for facility expedient repair be developed to initiate the facility recovery EMD process.

REFERENCES

- (1) Read, D.L. and Merkle, D.H., Expedient Repair of Structural Facilities (ERSF), Volume I: ERSF System Development, ESL-TR-91-13, Vol. I, Headquarters Air Force Civil Engineering Support Agency, Civil Engineering Support Agency Laboratory, Tyndall AFB, Florida, April 1991.

(2) Read, D.L. and Merkle, D.H., Expedient Repair of Structural Facilities (ERSF), Volume II: ERSF System Requirements and Users Guide, ESL-TR-91-13, Vol. II, Headquarters Air Force Civil Engineering Support Agency, Civil Engineering Support Agency Laboratory, Tyndall AFB, Florida, July 1991.

(3) Merkle, D.H., Read, D.L. Reid, R.A., Underwood, J.M., Karaszewski, N.F., and Purcell, N.M., Airbase Structural Facility Postattack Recovery - FOAL EAGLE Demonstration, CSL-TR-92-26, Headquarters Air Force Civil Engineering Support Agency, Civil Engineering Support Agency Laboratory, Tyndall AFB, Florida, March 1992.

TABLE 1. COLUMN SPLINT DEMONSTRATION RESULTS.

Activity Time (Min:Sec)

Test Iteration	Position Two-By-Fours	Position Plates	Attach Chains	Tighten Splint	Total Time
1*	0:12	0:18	1:50	4:17	6:37
2*	0:08	0:16	1:04	2:52	4:27
3**	0:27	0:38	0:57	5:36	7:38

* Splint placed at the bottom of the column.

** Splint placed 4 feet high on the column.

TABLE 2. GLULAM COLUMN REPLACEMENT DEMONSTRATION.

Clock Time (Min:Sec)

Test Activity	Test Iteration 1 Start	Test Iteration 1 Stop	Test Iteration 2 Start	Test Iteration 2 Stop
Position Jack	0:00	4:00	0:00	2:00
Raise Jack	4:00	4:30	2:00	3:07
Trim Column	4:30	5:00	2:00	4:20
Position Column	5:00	7:45	4:20	6:00
Wedge Column	7:45	11:10	6:00	7:30
Brace Column	11:10	22:30	7:30	11:00
Remove Jack	22:30	23:52	11:00	11:45

TABLE 3. FOAL EAGLE COLUMN SPLINT TRAINING.

Clock Time (Min:Sec)

Repair Task	Repair 1	Repair 2
Position Two-By-Fours	0:40	0:30
Position Plates	3:30	2:20
Tighten Splint	4:30	3:55
Remove Two-By-Fours	Not Done	4:25

TABLE 4. FOAL EAGLE COLUMN REPLACEMENT TRAINING.

Repair Task	Repair Clock Time
Access Damage To Column	0:15
Position Column Parts	0:45
Measure Column Height & Assemble Column	2:35
Position Column	2:50
Extend Jack Extender	3:45
Remove Ladder	4:16
Attach Bracing Members	Not Done

TABLE 5. FOAL EAGLE EARTH BERM WALL BREACH REPAIR TRAINING.

Repair Task	Repair Clock Time
Place Plywood Backing	9:50
Position Precast Slab	15:00
Form Berm With Soil	19:40

TABLE 6. FOAL EAGLE EARTH BERM WALL BREACH REPAIR DEMONSTRATION.

Repair Task	Repair Clock Time
Place Plywood Backing	Not Required
Position Precast Slab	2:30
Form Berm With Soil	5:42

TABLE 7. FOAL EAGLE SHOTCRETE WALL BREACH REPAIR DEMONSTRATION.

Repair Task	Repair Clock Time
Position Supersack Over Hopper	1:00
Charge Hopper With Material	1:47
Begin Water Spray From Nozzle Onto Plywood Backing	7:40
Delay Due To Low Water Flow	10:30
Begin Water Spray Again	11:00
Begin Spray Pattern Onto Backing	12:00
Begin Spraying Shotcrete	15:00
Delay Due To Low Water Flow	16:30
Complete Shotcrete Repair	20:55

TABLE 8. FOAL EAGLE COLUMN SPLINT DEMONSTRATIONS

Repair Task	Repair Clock Time Test 1	Repair Clock Time Test 2
Position Two-By-Fours	1:53	1:08
Position Plates	2:10	1:27
Tighten Splint	6:29	6:37
Remove Two-By-Fours	Not Done	

TABLE 9. FOAL EAGLE COLUMN REPLACEMENT DEMONSTRATION.

Repair Task	Repair Clock Time
Assess Damage To Column	0:15
Position Column Parts	0:45
Measure Column Height & Assemble Column	2:20
Position Column	2:50
Extend Jack Extender	3:38
Remove Ladder	3:50
Attach Bracing Members	Not Done



Figure 1. Nearly Completed Column Splint Repair.



Figure 2. Nearly Completed Column Replacement Repair.



Figure 3. Completed Shotcrete Wall Breach Repair.

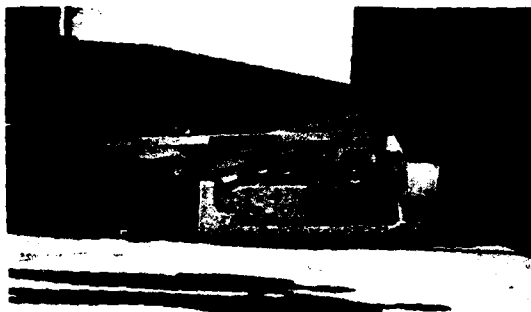


Figure 4. Surecrete, Inc. Automated Shotcrete Equipment.



Figure 5. Second Shotcrete Wall Breach Repair In Progress.



Figure 6. View of Shotcrete Equipment Lining Drainage Ditch.



Figure 7. FOAL EAGLE - Completed Earth Berm Wall Breach Repair.



Figure 8. FOAL EAGLE - Shotcrete Wall Breach Repair In Progress.



Figure 9. FOAL EAGLE - Nearly Completed Column Replacement Repair.

IMPACT COMPRESSION PROPERTIES OF CONCRETE

D. E. Grady

Experimental Impact Physics Division 1433
Sandia National Laboratories
Albuquerque New Mexico 87185

ABSTRACT

Controlled impact experiments have been performed on concrete to determine dynamic material properties. The properties assessed include the high-strain-rate yield strength (Hugoniot elastic limit), and details of the inelastic dynamic stress versus strain response of the concrete. The latter features entail the initial void-collapse modulus, the high-stress limiting void-collapse strain, and the stress amplitude dependence of the deformational wave which loads the concrete from the elastic limit to the maximum dynamic stress state. Dynamic stress-versus-strain data are reported over the stress range of the data, from the Hugoniot elastic limit to in excess of 2 GPa.

INTRODUCTION

The transient response of concrete to impact loading represents a complicated mix of thermodynamic compression and dynamic strength resistance. The development of computational models which adequately describe the behavior of this complex engineering material to such loads represents a challenge not afforded by most other materials.

In the present study, controlled impact experiments are performed which are intended to reveal the response of concrete to transient loading conditions, and to provide a base of dynamic compression and strength data for developing constitutive response models. Specifically, a smoothbore gas gun was used to perform planar impact experiments on concrete. A maximum velocity of 1.0 km/s constrained the range of impact test data to below approximately 2.5 GPa compressive stress. Within this stress range statistically significant data describing the dynamic strength, compressibility and deformational wave speed of aggregate concrete were obtained.

MATERIAL DESCRIPTION

Concrete tested in the present study was prepared and supplied

by the Army Waterways Experimental Station (WES) [Ergott, 1992]. A 15-cm by 30-cm core of concrete obtained from a larger body of material was machined to precise cylindrical dimensions. Density and ultrasonic measurements were performed on the cylinder before further machining to impact specimen dimensions was performed. A bulk density of 2263 kg/m³, and a longitudinal and shear elastic wave velocity of 4.45 km/s and 2.68 km/s, respectively, were determined. Ultrasonic measurements both along and across the cylindrical axis indicated isotropic elastic behavior. Density and ultrasonic properties are in good agreement with independent measurements at WES [Ergott, 1992]. A crystal density of about 2550-2680 kg/m³ and a free water content of 4.1-4.8% by weight are reported for this concrete [Ergott, 1992].

EXPERIMENTAL METHOD

Impact experiments were performed with a single-stage light-gas gun of 100 mm inner-bore diameter capable of achieving controlled velocities over a range of approximately 50 m/s to 1 km/s. A reverse ballistic configuration was used (Grady and Furnish, 1988) in which a disc-shaped specimen of the test concrete was mounted in the projectile and caused to undergo planar impact on a stationary diagnostic target. The principal component of the stationary target was a large polymethyl methacrylate (PMMA) disc with an interior reflecting interface (vapor-deposited aluminum). A diffused laser velocity interferometer (Barker and Hollenbach, 1972) was used to measure the time-resolved motion as shock waves caused by the planar impact traversed the recording interface. The impact experimental configuration is illustrated in Figure 1.

The reverse ballistic experimental configuration was used in the present study because the method effectively averages the measured dynamic compression state over a sensibly large volume of the test sample. This feature is attractive in heterogeneous

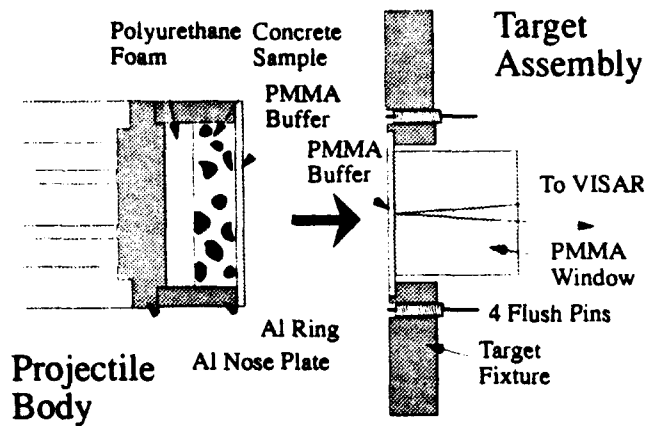


Figure 1. Experimental configuration for dynamic property studies on concrete.

samples such as the present aggregate concrete. A representative VISAR measurement of the interface velocity profile is illustrated in Figure 2. The initial velocity amplitude u_1 reflects only the impact of the projectile and target PMMA buffer plates. The second velocity amplitude u_2 is determined by the dynamic compression properties of the concrete. Useful velocity data is recorded until the shock wave transits the PMMA window. This transit occurs at about $17.5 \mu s$ in Figure 2. A low density polyurethane foam sample is placed behind the concrete in the projectile. However, release waves from this interface do not reach the recording interface before the VISAR recording time is exceeded. Pertinent experimental dimensions are provided in Table 1. The concrete discs are approximately 10 cm in diameter. The target buffer and window assembly is approximately 15 cm in diameter.

Table 1:
Dimensions of Impact Test Components

Test Number	Density (kg/m ³)	Concrete Thick. (mm)	Projectile PMMA Thick. (mm)	Target PMMA Thick. (mm)	Window PMMA Thick. (mm)
1	2234	15.23	4.80	4.76	35.7
2	2261	15.25	4.80	4.76	35.4
3	2216	15.20	4.82	4.76	36.0
4	2247	15.26	4.82	4.76	35.6
5	2225	15.23	4.82	4.78	35.5
6	2216	15.19	4.80	4.78	35.7
7	2225	15.25	4.80	4.77	36.3
8	2202	15.24	4.80	4.76	36.0
9	2209	15.20	4.80	4.77	35.3
10	2239	15.26	4.80	4.76	35.6

EXPERIMENTAL ANALYSIS

The initial amplitude of the velocity profile u_1 corresponds to a symmetric impact of the projectile and target PMMA buffer, and consequently the projectile velocity is exactly twice this measured velocity value ($V_p = 2u_1$). The relevant particle velocity interactions are indicated in Figure 3. The Hugoniot particle velocity (particle velocity jump) due to the impact-induced shock-wave propagation into the concrete is just the difference between the projectile velocity and the velocity amplitude u_2 . That is,

$$u_h = V_p - u_2 = 2u_1 - u_2. \quad (1)$$

Since the Hugoniot stress behind the compressive shock wave in the concrete is continuous across the PMMA interface, it is determined directly from the relation,

$$\sigma_h = \rho' C' u_2 + \rho' S' u_2^2. \quad (2)$$

In Equation 2 the set $\{\rho', C', S'\}$ are the initial density and linear shock-velocity versus particle-velocity parameters for PMMA (Barker and Hollenbach, 1970), while u_2 is the measured velocity amplitude indicated in Figures 2 and 3. Experimental results are provided in Table 2, and the stress versus particle-velocity Hugoniot for the aggregate concrete is shown in Figure 4. The amplitude of the second plateau in the experimental velocity profiles (see Figure 2) exhibits large fluctuations due to intrinsic heterogeneity of the aggregate concrete. Uncertainty in the amplitude of u_2 is the principal source of uncertainty indicated by the error bars in Figure 4.

The shock-wave conservation equations (Hugoniot relations) used to determine shock-velocity and compressive-strain properties of the concrete cannot be immediately applied to the pressure versus particle-velocity Hugoniot data. This complication

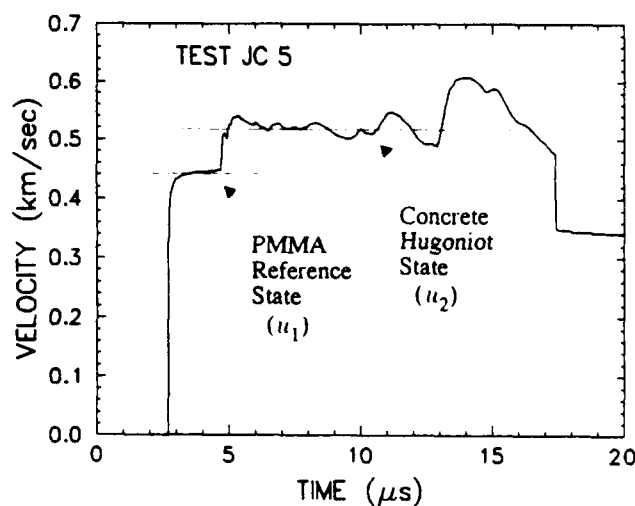


Figure 2. Representative interface velocity profile for concrete impact-property studies.

Table 2:
Interface Profile Data

Test number	u_1 m/s	u_2^* m/s	V_p m/s	u_h^* m/s	σ_h^* GPa
1	132	164(40)	264	103(40)	0.61(.16)
2	221	250(25)	442	192(25)	0.95(.10)
3	298	330(50)	596	266(50)	1.28(.21)
4	328	380(40)	656	276(40)	1.49(.17)
5	446	520(40)	892	372(40)	2.11(.18)
6	365	405(30)	730	325(30)	1.60(.13)
7	152	178(45)	304	126(45)	0.66(.18)
8	225	250(40)	450	200(40)	0.95(.16)
9	390	460(80)	780	320(80)	1.84(.34)
10	430	500(50)	860	360(50)	2.02(.23)

* Number in parentheses is error estimate from uncertainty in velocity amplitude.

occurs within the present range of shock amplitudes because of wave separation into an elastic and a deformation component in the concrete. The effective amplitude of the elastic wave (the Hugoniot elastic limit) can be determined, however, from the set of stress versus particle-velocity data. In Figure 4 a slope corresponding to the longitudinal elastic modulus is drawn from the origin. The intercept with a curve representing the best fit to the Hugoniot data is identified as the Hugoniot elastic limit and characterizes the effective amplitude of the elastic stress wave. The functional form of the curve fit to the stress versus particle-velocity data is established by assuming linear shock-velocity versus particle-velocity behavior of the deformation shock wave. That is,

$$U_s = C_\theta + Su = C_\theta \Delta u, \quad (3)$$

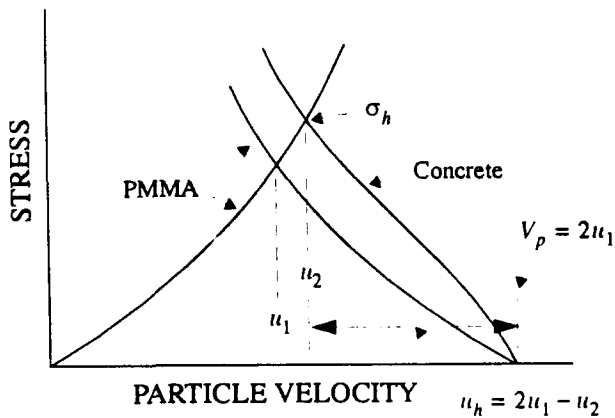


Figure 3. Stress versus particle-velocity plot illustrating interface wave interactions and Hugoniot state analysis.

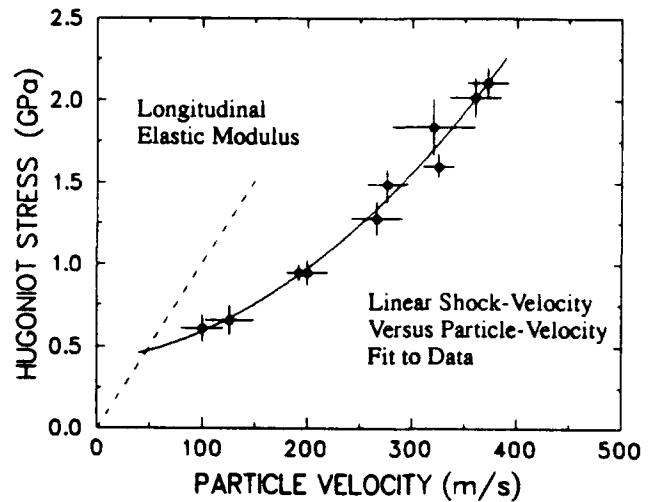


Figure 4. Hugoniot-stress versus particle-velocity states for concrete.

where $\Delta u = u - u_c$. Through the momentum Hugoniot conservation relation $\Delta \sigma = \rho_o U_s \Delta u$ we arrive at a quadratic expression for the stress versus particle-velocity Hugoniot,

$$\Delta\sigma = \rho_o C_o \Delta u + \rho_o S \Delta u^2. \quad (4)$$

Again, $\Delta\sigma = \sigma - \sigma_e$ where σ_e is the stress amplitude of the elastic wave.

A least squares fit of Equation 4 to the compression data in Figure 4 results in the properties $C_o = 551.0$ m/s, $S = 4.52$, $\sigma_e = 0.475$ GPa and $u_e = 47.2$ m/s.

A method has now been established to calculate the deformation shock velocities and compression strain from the experimental data. In particular the shock velocity is calculated from

$$U_s = \Delta\sigma/\rho_0\Delta u, \quad (5)$$

and the compression strain from,

$$\varepsilon_h = \varepsilon_e + \Delta u / U_s. \quad (6)$$

In Equation 6, $\epsilon_e = C_1/\mu_e$ is the compression strain at the elastic limit ($\epsilon_e = 0.0106$).

The shock-velocity versus particle-velocity data are plotted in Figure 5. The complete Hugoniot data are provided in Table 3. The data are found after the fact to be fully consistent with a linear shock-velocity versus particle-velocity behavior, justifying the assumption made earlier to establish the amplitude of the elastic limit. Deformation wave velocities within this range of shock amplitudes (less than 25 GPa) are observed to be quite slow in comparison with the elastic wave speed. The limiting wave speed for vanishingly small shock amplitude is $U_s = \bar{C}_0 = 764.3 \text{ m/s}$.

Table 3:
Concrete Hugoniot Data

Test No.	u_h^* m/s	σ_h^* m/s	U_h^* m/s	ϵ_h^*
1	100(40)	0.61(.16)	1130(430)	0.057(.057)
2	192(25)	0.95(.10)	1449(240)	0.110(.032)
3	266(50)	1.28(.21)	1626(400)	0.145(.061)
4	276(40)	1.49(.17)	1960(360)	0.127(.040)
5	372(40)	2.11(.18)	2224(300)	0.157(.037)
6	325(30)	1.60(.13)	1790(220)	0.166(.034)
7	126(45)	0.66(.18)	1037(460)	0.087(.067)
8	200(40)	0.95(.16)	1374(360)	0.122(.053)
9	320(80)	1.84(.34)	2211(680)	0.134(.071)
10	360(50)	2.02(.23)	2183(390)	0.154(.046)

* Number in parentheses is error estimate from uncertainty in velocity amplitude.

Compression strain data are plotted in Figure 6. The elastic modulus and limiting deformation-wave modulus are identified. The curve representing the best-fit linear shock-velocity versus particle-velocity behavior is compared with the experimental results. The functional form for this stress versus compression-strain curve is,

$$\Delta\sigma = \frac{\rho_0 C_0^2 \Delta\epsilon}{(1 - S\Delta\epsilon)^2} \quad (7)$$

A limiting compression is predicted from this relation at $\Delta\epsilon = 1/S$ or at a value of $\epsilon_l = 0.22$. Strains of order $\epsilon = 0.16$ are achieved in the present data at the highest stress

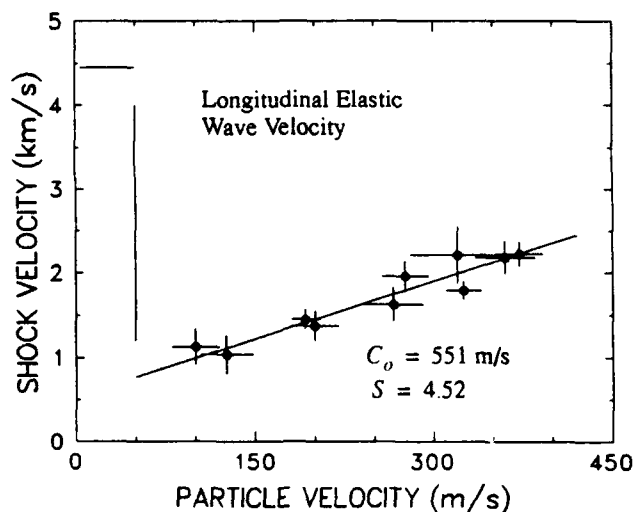


Figure 5. Shock-velocity versus particle-velocity data for concrete

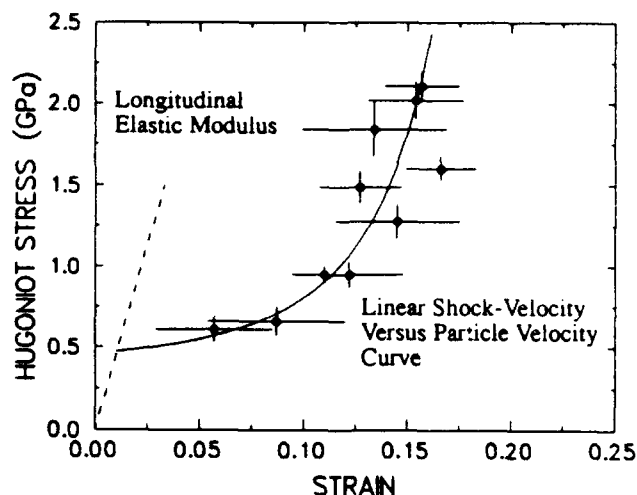


Figure 6. Dynamic compression stress versus strain data for concrete.

states of about 2.5 GPa. The slope of the compression curve at this amplitude is approaching the magnitude of the elastic modulus indicating that most of the void volume has been crushed out.

CONCLUSIONS

Through controlled impact methods dynamic strength and compression data for aggregate concrete has been obtained in the stress range of 0.5-2.5 GPa. A confined dynamic compression strength of approximately 0.5 GPa is inferred from the data. Compression wave splitting is also predicted from the experimental data with deformation wave velocities as low as 760 m/s at shock amplitudes just exceeding the elastic limit. Excessively low deformation wave velocities are a consequence of void volume collapse during the compression shock process. A strong amplitude dependence of the deformation wave velocity was determined from the data. Merging of elastic and deformation waves into a single shock wave at stresses in excess of 7.5 GPa is inferred from extrapolation of the linear shock-velocity versus particle-velocity behavior of the data to this amplitude.

Sponsored by the U.S. Department of Energy and conducted under the auspices of the U. S. Department of Energy under Contract DE-AC04-76DP00789

REFERENCES

1. Ergott, J., (private communication), December 1992.
2. Grady, D. E. and Furnish, M. D., Sandia National Laboratories Report, SAND88-1642, December 1988.
3. Barker, L. M. and Hollenbach, R. E., *J. Appl. Phys.*, 43, 4669, 1972.
4. Barker, L. M. and Hollenbach, R. E., *J. Appl. Phys.*, 41, 4208, 1970.

HIGH LOADING RATE EFFECTS ON STRUCTURAL CONCRETE RESPONSE UNDER IMPULSIVE LOADS

D. Chandra and T. Krauthammer

Department of Civil Engineering
Pennsylvania State University
University Park, PA 16802

ABSTRACT

There have been several attempts to explain strain rate effects in concrete, but they are either empirical models or based on hypothetical potential functions. The present approach shows how the fracture process of concrete with pre-existing cracks is affected by high loading rates and how that ultimately causes an apparent strength enhancement of concrete under dynamic loads. A self-consistent micromechanical damage model is presented, and is verified by comparison with experimental data.

INTRODUCTION

Concrete contains aggregates and cement gel with complex networks of voids, cracks and other flaws that are primary sources of weakness. Yet, concrete exhibits a puzzling phenomenon of increased resistance when loaded at a very high rate. Strength magnification factors as high as 2 in compression and about 4 in tension for strain rates in the range of 10^2 - 10^3 /sec have been reported (Weerheijm and Reinhardt, 1989). Existing models to explain this behavior are based on either empirical curve-fitting techniques or hypothetical potential functions. Chandra and Krauthammer (1992) proposed a different approach to explain this phenomenon, as further developed in this paper. Employing the principles of fracture mechanics, as discussed by Loeber and Sih (1972) and Parton and Boriskovsky (1989), Chandra and Krauthammer (1992) showed that an increase in strength should be expected based on the energy balance for an incremental crack growth. The presence of a kinetic energy growth rate (with respect to the crack size a), $\partial U_k / \partial a$, demands for increased energy release rate (denoted by J , as defined by Ewalds and Wanhill, 1989). Chandra and Krauthammer (1992) showed that:

$$J_{\text{eff}} = J - \frac{\partial U_k}{\partial a} \quad (1)$$

It is noticed from Eq. (1) that the presence of $\partial U_k / \partial a$ retards the crack development or the fracture process, and the role of inertia effects was demonstrated by the following expression:

$$\frac{\partial U_k}{\partial a} = \int \int \int_V (\dot{u} \cdot \frac{\partial \dot{u}}{\partial a}) \rho dx dy dz - \int \int \int_V (\ddot{u} \cdot \frac{\partial u}{\partial a}) \rho dx dy dz \quad (2)$$

where, V is a control volume of the body under consideration. It is quite obvious from Eq. (2) that the denser the material is, the more pronounced will be this retardation effect. For linearly elastic materials subjected to monotonically increasing loads, J is related to the stress intensity factor, K , as follows:

$$J = \frac{K^2}{E'} \quad (3)$$

where, E' equals to E for plane stress conditions, or to $E/(1 - \nu^2)$ for plane strain conditions, E and ν are the Young's modulus and Poisson's ratio, respectively. Thus, the increase or decrease of J is directly proportional to that of K^2 , and J in Eq. (1) can be replaced according to Eq. (3) to yield,

$$J_{\text{eff}} = \frac{K^2}{E'} - \frac{\partial U_k}{\partial a} \quad (4)$$

K can be expressed according to Loeber and Sih (1972) and Parton and Boriskovsky (1989), as:

$$K_j = c_j q \sqrt{\pi a} D_j(1) \exp(-i\omega \bar{t}) \quad (5)$$

where, K_j is the stress intensity factor for fracture mode j ($j = I, II$ and III); c_j is a constant for mode j ; q is the amplitude of remotely applied dynamic stress; D_j is a complex function of a complex variable, ξ , for mode j (ξ in this case reduces to the real number, 1); a is the radius of the penny-shaped crack under consideration; i is the imaginary number, $\sqrt{-1}$; ω is the frequency of applied dynamic stress (assumed harmonic); \bar{t} is a time variable.

It is evident from Eq. (5) that the magnitude of K is directly affected by the complex function, D_j , all other parameters remaining unaltered. (The complex term $\exp(-i\omega \bar{t})$ does not affect $|K|$ even when ω of the applied stress is changed). In general, $D_j(\xi)$ is given by a Fredholm integral equation, as discussed in detail by Chandra and Krauthammer (1992). It was shown that the kernel of $D_j(\xi)$ is a function of several variables that are dependent on the density of the material, ρ , frequency of applied stress, ω and some other material properties. Hence, it is quite logical to deduce that $D_j(\xi)$ would be affected by ρ and ω , keeping all other parameters unaltered. So, the

evaluation of K_j by the method outlined above takes into account the effects of both inertia (through ρ) and rate of applied loading (through ω). Generally, for very high value of ω , the ever decreasing magnitude of K_j along with the fracture process involved therein, reinforce the explanation for apparent strength enhancement of concrete under highly time-varying loads. Furthermore, when the effect of crack propagation through the concrete is included, there will be a further reduction of the stress intensity factors, K_j , as discussed by Achenbach and Brock (1972) and Freund (1972). This decrease of K_j under dynamic conditions leads to a corresponding decrease in J_{eff} . Thus, higher energy input would be required to produce the same level of damage, creating the effect of strength enhancement.

Chandra and Krauthammer (1992) explained the incorporation of this rate effect phenomenon within a stress-based constitutive model developed on the basis of previous works by Fanella and Krajcinovic (1988), Ju and Lee (1991) and Lee and Ju (1991). This type of micromechanical model was chosen as opposed to a continuum damage model because the latter type fails to correlate appropriately the microstructural microcrack kinetics with the overall constitutive behavior of concrete. Moreover, a continuum damage model often requires a good number of fictitious material constants that have to be predetermined by fitting experimental data. Also, a stress-based model is chosen as opposed to a strain-based model because the former type of model allows the additive split of the strain tensor, facilitating the consideration of anisotropic brittle behavior of concrete. The most important of all is the fact that the present model is able to simulate the rate sensitivity of concrete under the previously described framework of fracture mechanics principles.

The following mixed-mode failure criterion is applied to determine the unique set of conditions prevailing in different regions (subdomains) within the control volume:

$$\left(\frac{K_I'}{K_{Ic}^{wp}} \right)^2 + \left(\frac{K_{II}'}{K_{IIc}^{wp}} \right)^2 = 1 \quad (6)$$

where, K_I' , K_{II}' are the stress intensity factors at the crack tip under mode I and mode II fracture, respectively (prime refers to the coordinate system local to the crack); and K_{Ic}^{wp} , K_{IIc}^{wp} are the critical stress intensity factors for the concrete material at the weak plane under mode I and mode II fracture, respectively. The weak plane referred to above could be the interface plane between an aggregate facet and the cement paste when the crack size, a , is smaller than the aggregate facet, D , or it could be the plane through the cement paste along which the initial crack kinks into the cement paste. K_{Ic}^{wp} and K_{IIc}^{wp} are material constants that are not affected by the kinetic effects. On the other hand, K_I' and K_{II}' , as described previously, are crucially dependent on the rate of applied load, propagation speed of the crack tip during instability, etc. Hence, the fracture criterion employed here is made rate sensitive. The computational algorithm for this model is based on the approach by Ju and Lee (1991), as presented by Chandra and Krauthammer (1992).

STRENGTH ENHANCEMENT AT HIGH LOADING RATES

Strength enhancement of any material at very high loading rate (when existing flaws cease to grow because of low SIF, etc.) is a relative effect of its increased load-intake (or, equivalently, energy-intake) capacity before internal failure occurs. This will be illustrated by employing lumped mass models (devoid of any initial flaw), starting with a single degree of freedom system approximation (SDOF). Let us assume that a lumped mass, M , is connected to a linear spring of stiffness, K , and is subjected to a dynamic force, $P(t)$ with loading rate α , as follows:

$$P(t) = \alpha t \quad (7)$$

In the following analysis, α is always kept positive and constant to ensure the monotonically increasing load. The governing equation of motion for this undamped system is:

$$M \ddot{x} + Kx = P(t) \quad (8)$$

where, x is the displacement of the mass which is, in this case, equivalent to the elongation in the spring.

It has been found experimentally (Mlakar et al. 1985, Weerheijm 1992) that the deformation capacity of concrete does not change with increasing loading rates. This leads to the assumption that the internal failure of concrete can be reckoned by a characteristic value of strain which is *independent* of loading rates. Assuming this phenomenon is true for any system under dynamic load, it can be utilized for setting a failure criterion of the linear spring in the SDOF system: The spring is considered to attain failure if

$$|x| \geq x_f \quad (9)$$

where, x_f is the elongation at failure, a pre-set limit for x . The solution of Eq. (8) is,

$$x = \frac{\alpha}{K} \left[t - \frac{1}{\omega} \sin \omega t \right] \quad (10)$$

$$\omega = \sqrt{\frac{K}{M}}$$

and the internal force in the spring can be expressed as,

$$F_s = Kx = \alpha t - \frac{\alpha \sin \omega t}{\omega} = P(t) - \frac{\alpha \sin \omega t}{\omega} \quad (11)$$

Eq. (11) is plotted in Figure 1. Here, the straight line represents $P(t)$ and the nonlinear curve represents $(\alpha \sin \omega t)/\omega$. The difference in ordinates of these two curves yields the value of F_s as expressed in Eq. (11). The effect of the non-zero loading rate, α is very clear: The internal failure strength of the spring remains unchanged with loading rate or with time, and it has a constant value, F_{su} given by,

$$F_{su} = Kx_f \quad (12)$$

But externally, as an input to the system, the load at failure will be decided by the value of $P(t)$ at the time of failure. It is evident from Figure 1 that the value of $P(t)$ at failure is greater than F_{su} because of the presence of the term, $(\alpha \sin \omega t)/\omega$. Hence, although internally the failure in the spring occurs only when the force in it (i.e., the difference between $P(t)$ and

$(\alpha \sin \omega t)/\omega$ just exceeds a constant value, F_{su} , externally it appears to occur with a value of $P(t)$ greater than F_{su} . This produces an apparent strength enhancement for the spring.

If the value of $P(t)$ at failure (denoted as P_f) is plotted against the logarithm of α , a familiar looking curve will be generated (Figures 2a and 2b). The shape of the resulting curve resembles quite well the experimental curves obtained when strength of concrete specimens is plotted against the logarithm of loading rates or strain rates (Weerheijm 1992). Researchers tried to

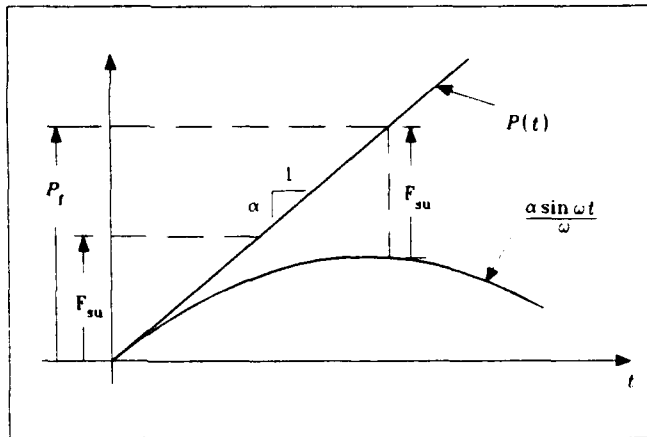


Figure 1: Effect of α on P_f

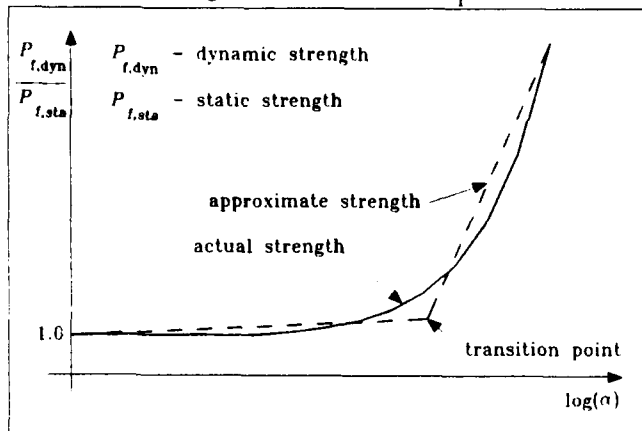


Figure 2a: Actual and Approximate Strengths as functions of α

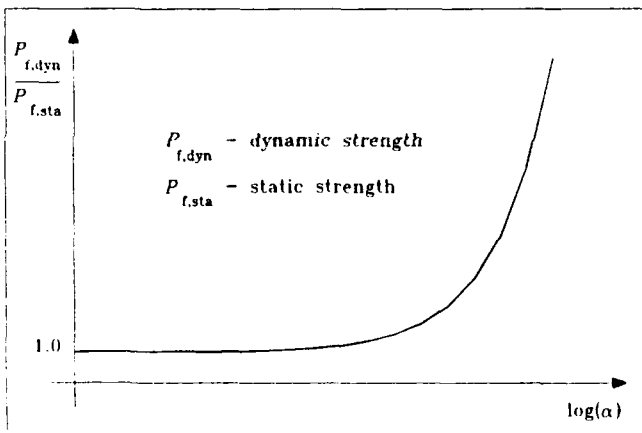


Figure 2b: Shape of Strength curve with many data points

explain the rate effect in light of the shape of strength curves similar to those shown in Figures 2a and 2b (Curbach 1987, Weerheijm 1992). They approximated the strength curve with the help of a bi-linear curve having an initial milder slope followed by a steeper slope (shown in dashed lines in Figure 2a). Thence, they ascribed two different strength enhancement mechanisms to these two different parts of the strength curve. And, they regarded the point where two slopes intersect (denoted in Figure 2a as *transition point*) as a point of demarcation between different kinetics involved in the two regimes of loading rates. But validity of this treatment can be questioned when quite a good number of data points obtained from the present analysis are used to generate the strength curve (Figure 2b). It is evident from Figure 2b that the overall shape of the strength curve is not changed; but the transition point is changed. If the transition point were dependent on the system parameters, it should have been a constant. Hence, it may not be a characteristic point for the system under consideration, but a result of the logarithmic scale used to generate the strength curve.

This issue can be visualized better when P_f is plotted against α both on linear scales as shown in Figure 3. This curve exposes a mode of linear variation of P_f with respect to α particularly for high values of α . However, this curve does not have a well-defined transition point as the curves in Figures 2a and 2b do.

In conclusion, it is possible to characterize this behavior in a SDOF system as follows: F_{su} , which is constant (the failure load, P_f , for high values of α), is: directly proportional to α , directly proportional to \sqrt{M} (inertia effect), and inversely proportional to \sqrt{K} . More simply put, for high values of α , P_f is directly proportional to α and inversely proportional to the natural frequency, ω of the system (where, $\omega = \sqrt{K/M}$). Another important outcome of this analysis is that as α is increased, the effective stiffness of the spring is also increased. The effective stiffness is defined here as.

$$K_{eff} = \frac{P_f}{x_f} \quad (13)$$

Substitution of P_f from equation (11) into Eq. (13) yields,

$$K_{eff} = K + K' \quad (14)$$

$$\max |K'| = \frac{\alpha \sqrt{M}}{x_f \sqrt{K}}$$

Thus, for an approximate analysis with a very high loading rate (high α), the effective stiffness of the spring can be increased by K' whose maximum possible value can be calculated very easily from equation (14) using all known quantities. And, subsequent analysis can be carried out as if a static load were applied to a spring having an effective stiffness equal to K_{eff} .

Since concrete is a combination of cement matrix and aggregates with marked difference in their densities and elastic moduli, it is not appropriate to idealize a concrete body as an SDOF system. Any idealizing model of this kind should entwine at least two different masses and two different stiffnesses. One set of mass and stiffness should represent the cement matrix and the other set should represent aggregates.

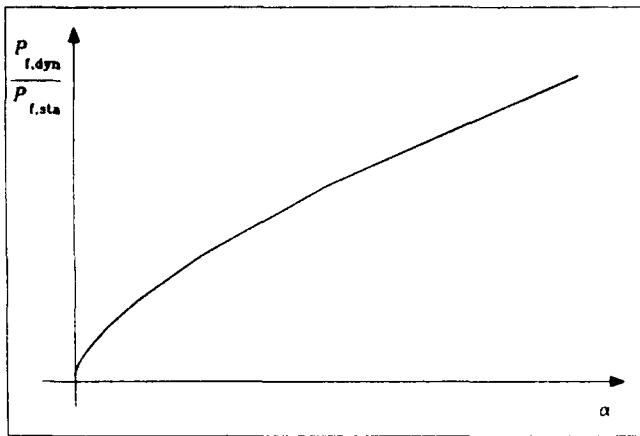


Figure 3: Shape of strength curve on linear scale

For this reason, a 2-DOF system under dynamic loading is studied and the behavior thereof is tried to correlate that of a concrete body.

Consider two sets of undamped mass-spring combinations, M_1 - K_1 and M_2 - K_2 connected in series to a fixed base, as shown in Figure 4. A concentrated force, $P(t)$, linearly varying with time is applied to M_1 . The relative values of these two masses and stiffnesses are changed by changing the two parameters of this system: Mass ratio, $r_M = M_1/M_2$, and the associated stiffness ratio, $r_K = K_1/K_2$. For this idealized model, it is assumed that the spring with stiffness, K_1 has a failure strength, F_{s1} and that with stiffness K_2 has a failure strength, F_{s2} . It is also assumed that F_{s1} is always greater than F_{s2} for any combination of r_M and r_K . The governing equations of motion for this 2-DOF system can be written as:

$$\begin{aligned} M_1 \ddot{x}_1 + K_1(x_1 - x_2) &= P(t) \\ M_2 \ddot{x}_2 + K_2 x_2 - K_1(x_1 - x_2) &= 0 \end{aligned} \quad (15)$$

where, x_1 and x_2 are defined in Figure 4.

As for the SDOF system, the value of load at failure, P_f is studied for different values of α . For this 2-DOF system, there are two values of P_f : The two different values of $P(t)$ at the onset of failures of the first spring and the second spring, denoted by P_{f1} and P_{f2} , respectively. The failure criterion is similar to that used for the SDOF system: Spring 1 fails if $|x_1 - x_2| \geq x_{f1}$ while spring 2 fails if $|x_2| \geq x_{f2}$. x_{f1} and x_{f2} are maximum elongations for springs 1 and 2, respectively, without causing failure in them. They are assumed to be independent of the loading rate, α , and can be derived from the given parameters of the system, as follows:

$$\begin{aligned} x_{f1} &= \frac{F_{s1}}{K_1} \\ x_{f2} &= \frac{F_{s2}}{K_2} \end{aligned} \quad (16)$$

Furthermore, the times required to cause failure in the two springs are also studied for different values of α . The times of failure (t_{f1} for spring 1 and t_{f2} for spring 2) are measured from the epoch, $t=0$. It should be noted here, however, that as soon as one of the springs fails (either spring 1 or spring 2), the

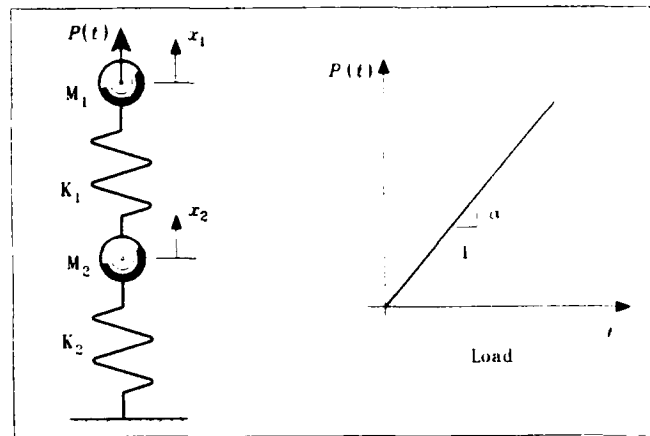


Figure 4: 2-DOF system and time-varying load

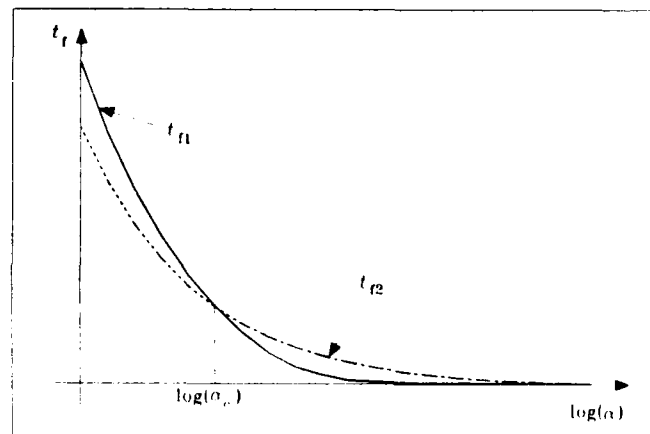


Figure 5: Effect of α on t_f

system as a whole should be considered to attain failure since the two springs are connected in series. But, after the first failure occurs, the response computation is still continued until the other spring also fails (with an assumption that the failed spring continues to resist load in a regular fashion). Hence, this routine yields, in general, distinct values for t_{f1} and t_{f2} . But, there is no physical significance for the higher one of these two time values which is calculated just for comparison.

t_{f1} and t_{f2} vary with α , r_M and r_K . These two time variables when plotted against $\log(\alpha)$, yield graphs as shown in Figure 5. It is interesting to note in Figure 5 that both t_{f1} and t_{f2} decrease with increasing α . Also, there is a particular value of α for which t_{f1} and t_{f2} are equal (at the intersection point). This value of α is, henceforth, referred to as the *critical rate*, α_c . This value of rate demarcates the occurrence of failure in one spring from that in the other. If, for example, failure occurs first in spring 2 for $\alpha < \alpha_c$, then failure will occur first in spring 1 for $\alpha > \alpha_c$. Observing the variation of t_{f1} , t_{f2} and α_c with r_M and r_K , it is found that:

If $\alpha < \alpha_c$, failure occurs first in weaker spring (i.e. spring 2 here), be it associated with lighter mass or with heavier mass. However, for $\alpha > \alpha_c$, failure occurs first in stronger spring (i.e. spring 1). α_c increases as the mass ratio, r_M increases. This means that as M_1 becomes heavier relative to M_2 , higher loading rates are required to cause failure first in spring 1

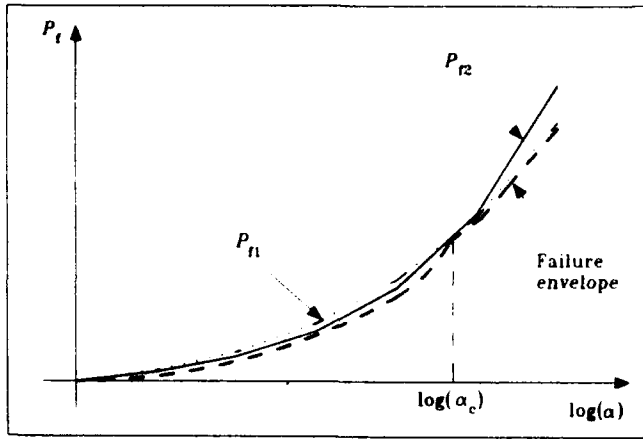


Figure 6: Failure envelope for 2-DOF system

(which is stronger). On the other hand, α_c decreases as the stiffness ratio, r_K increases. This means that as spring 1 becomes stiffer relative to spring 2, lower loading rates are required to cause failure first in spring 1.

The two strengths, P_{f1} and P_{f2} when plotted against $\log(\alpha)$, also intersect at α_c as shown in Figure 6. The overall strength curve for the system can be drawn by connecting the points of lower ordinates as shown in dashed line. And, when α_c is plotted against r_M and r_K , a 3D surface is generated as shown in Figure 7 which depicts very clearly its mode of variation with r_M and r_K as described earlier. For practical purposes, this 3D surface can be obtained by fitting an approximate spline surface through an analytical transfer function (refer to Eq. 18).

The main goal for applying 2-DOF analysis to a concrete body is to obtain equivalent moduli for concrete at high loading rates. Thereafter, these equivalent moduli are used to determine its fracture mechanics behavior governing the constitutive model described by Chandra and Krauthammer (1992). The concrete body is idealized as a combination of two different materials: Cement matrix and aggregates. Each of these entities is considered homogeneous within itself. Nevertheless, one must consider the effect of a continuum, and the following procedure is proposed:

Using the given moduli for cement matrix and aggregates (assuming each to be homogeneous within itself), find an overall modulus, E_{ovl} for the concrete body at a given loading rate as follows:

$$\begin{aligned} E_{ovl} &= (1 - \alpha/\alpha_c)E_m + (\alpha/\alpha_c)E_a, \quad \text{if } \alpha \leq \alpha_c \\ E_{ovl} &= E_a, \quad \text{if } \alpha > \alpha_c \end{aligned} \quad (17)$$

where, E_m and E_a are the elastic moduli for cement matrix and aggregates, respectively. The rate of loading, α , in this case, is considered to be the rate of applied stress. This algorithm requires the determination of a critical loading rate, α_c similar to that defined for a true 2-DOF system. The mass ratio, r_M as introduced for the 2-DOF system, is replaced by the ratio of mass densities of cement matrix and aggregates (denoted by r_ρ) and the stiffness ratio, r_K in 2-DOF system, is replaced by the ratio of moduli of cement matrix and aggregates (denoted by

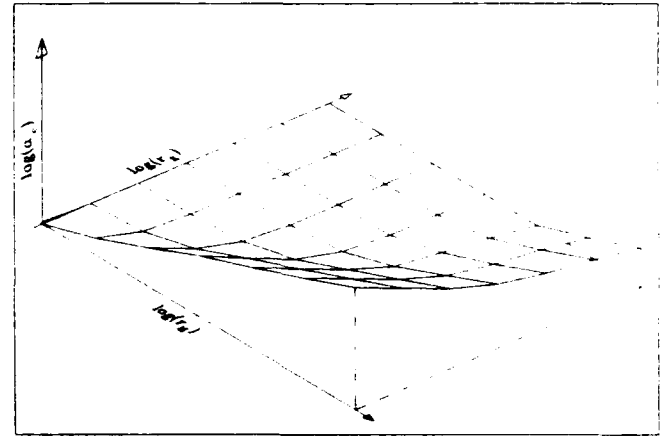


Figure 7: Variation of critical rate, α_c with r_M and r_K

r_μ). Evaluation of critical rate, in turn, requires consideration of the continuum to include all possible modes of wave propagation. To simplify this problem, longitudinal and transverse vibrations of the concrete body are considered separately. Thus, two critical rates, α_{c1} and α_{c2} are evaluated corresponding to longitudinal and transverse vibrations, respectively. Then, the overall elastic moduli corresponding to longitudinal and transverse deformations are determined from α_{c1} and α_{c2} , respectively. To calculate α_{c1} and α_{c2} , similar transfer functions as used for the 2-DOF system can be employed. Thus,

$$\log(\alpha_{c\beta}) = \sum_{i=1}^k c_{i\beta} [\log(r_\rho) + a_{i\beta}]^{m_{i\beta}} [\log(r_\mu) + b_{i\beta}]^{n_{i\beta}} \quad (18)$$

where, $a_{i\beta}$, $b_{i\beta}$, $c_{i\beta}$, $m_{i\beta}$, $n_{i\beta}$ and k are constants and $\beta=1,2$ stands for longitudinal (1) and transverse (2) waves. Numerical methods can be employed to evaluate these constants rigorously.

Thereafter, find the effective modulus, E_{eff} of concrete body to be used in the subsequent analysis by incrementing E_{ovl} as follows:

$$E_{eff} = E_{ovl} + \frac{8\alpha l}{\pi^2 \epsilon_f} \sqrt{\frac{\rho_{ovl}}{E_{ovl}}} \quad (19)$$

where, ϵ_f is the failure strain of concrete (either in longitudinal or in transverse mode); l is a characteristic linear quantity (equal to either mean aggregate diameter [if $\alpha > \alpha_c$] or mean inter-aggregate clear spacing within the concrete [if $\alpha \leq \alpha_c$]); ρ_{ovl} is an overall density of concrete that can be obtained by an interpolation function similar to Eq. (17). Eq. (19) was derived using the analogy with an SDOF system and the principles of elastodynamic wave propagation in an elastic solid.

The performance of the present model in comparison to other analytical and experimental results is illustrated in Figure 8. The solid bold line was obtained for a concrete body under pure uniaxial tension.

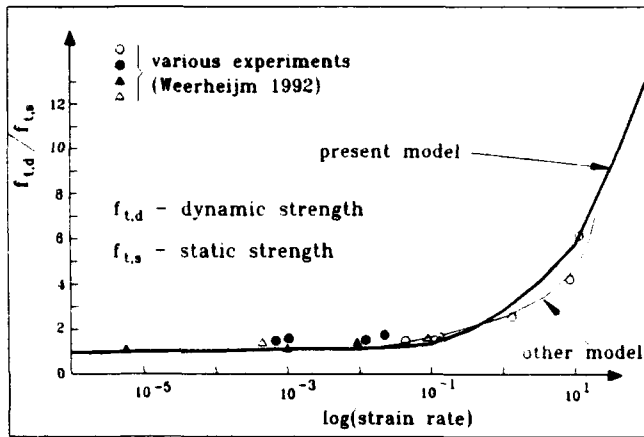


Figure 8: Tensile strength of concrete versus strain rates

REFERENCES

- Achenbach, J.D. and Brock, L.M. (1972), "On Quasistatic and Dynamic Fracture", in *Dynamic Crack Propagation '72* (Ed. Sih, G.C.), pp.513-528, *Proceedings of an International Conference on Dynamic Crack Propagation*, Lehigh University, Bethlehem, USA, Noordhoff International Publishing, Leyden.
- Chandra, D., and Krauthammer, T. (June 1992), "Fracture and High Loading Rate Effects on Concrete Response", *Proc. Structures Under Shock and Impact II, SUSI 92*, Portsmouth, England, 16-18 June 1992.
- Curbach, M. (1987), "Festigkeitssteigerung von Beton bei hohen Belastungsgeschwindigkeiten", Ph.D. dissertation (in German), Universität Fridericiana zu Karlsruhe, Karlsruhe.
- Ewalds, H.L. and Wanhill, R.J.H. (1989), *Fracture Mechanics*, Edward Arnold, Delftse Uitgevers Maatschappij, Delft, Netherlands.
- Fanella, D. and Krajcinovic, D. (1988) "A Micromechanical Model for Concrete in Compression", *Engineering Fracture Mechanics*, Vol.29, No.1, pp. 49-66.
- Freund, L.B. (1972), "Crack Propagation in an Elastic Solid Subjected to General Loading - I. Constant Rate of Extension", *Journal of Mechanics and Physics of Solids*, Vol.20, pp. 129-140.
- Freund, L.B. (1972), "Crack Propagation in an Elastic Solid Subjected to General Loading - II. Non-Uniform Rate of Extension", *Journal of Mechanics and Physics of Solids*, Vol.20, pp. 141-152.
- Ju, J.W. and Lee, X. (July 1991), "Micromechanical Damage Models for Brittle Solids I: Tensile Loadings", *Journal of Engineering Mechanics, ASCE*, Vol.117, No.7, pp. 1495-1514.
- Lee, X. and Ju, J.W. (July 1991), "Micromechanical Damage Models for Brittle Solids II: compressive Loadings", *Journal of Engineering Mechanics, ASCE*, Vol.117, No.7, pp. 1515-1536.
- Loeber, J.F. and Sih, G.C. (1972), "Torsional Wave Scattering about a Penny-shaped Crack Lying on a Bimaterial Interface", in *Dynamic Crack Propagation '72* (Ed. Sih, G.C.), pp. 513-528, *Proceedings of an International Conference on Dynamic Crack Propagation*, Lehigh University, Bethlehem, USA, 1972. Noordhoff International Publishing, Leyden.
- Mrakar, P.F., Vitaya-Udom, K.P. and Robert, A.C. (July-August 1985), "Dynamic Tensile-Compression Behavior of Concrete", *ACI Journal*, Vol. 82, No. 4, pp. 484-491.
- Parton, V.Z. and Boriskovsky, V.G. (1989), *Dynamic Fracture Mechanics*, Vols.1 and 2, Hemisphere Publishing Corporation, New York, USA.
- Weerheijm, J. and Reinhardt, H.W. (September 1989), "Modelling of Concrete Fracture Under Dynamic Tensile Loading", *Proceedings of the Symposium on Recent Developments in the Fracture of Concrete and Rock*, Cardiff, Wales.
- Weerheijm, J. (1992), "Concrete Under Tensile Impact and Lateral Compression", Ph.D. Dissertation, Delft University, The Netherlands.

DYNAMIC COMPRESSIVE BEHAVIOUR OF CONCRETE AT STRAIN RATES UP TO $10^3/\text{s}$ - COMPARISON OF PHYSICAL EXPERIMENTS WITH HYDROCODE SIMULATIONS.

A D Pullen¹, A J Sheridan², J B Newman¹

¹ Department of Civil Engineering, Imperial College, London, SW7 2BU, UK.

² Defence Research Agency, Farnborough, Hants, GU14 6TD, UK.

ABSTRACT

Experiments designed to determine dynamic material properties often indicate modification of those properties when compared with material properties determined statically. The hydrocode assisted analysis of a split-Hopkinson bar experiment is described, the aim of which was to determine how much of the apparent enhancement of the material strength often observed in such experiments is generated by inertial effects within the apparatus and the specimen. It was concluded that inertial effects within the specimen significantly modify the stress state and hence the results of such physical experiments.

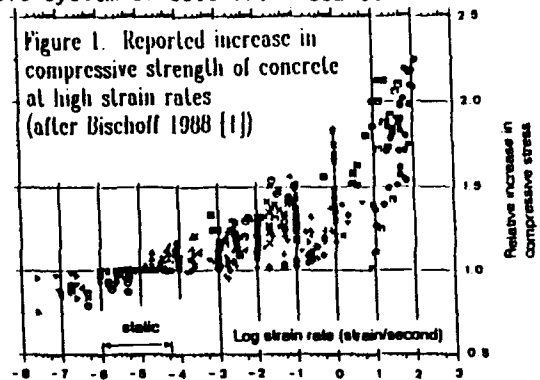
1 INTRODUCTION

The use of analysis techniques which involve computational simulations of the real world is now widespread across many disciplines. Hydrocodes or dynamic finite-element programs used by scientists and engineers to analyse the behaviour of structures subjected to dynamic loads are just one example of this. A realistic hydrocode simulation requires that the engineering properties of the materials from which the structure is built are accurately represented. These properties must be applicable at the appropriate strain rates for the real event. There is evidence that the engineering properties of many materials under dynamic loads (at strain rates greater than 10^{-5}) differ from those which are measured under static loads (at strain rates of less than 10^{-5}). For example, a concrete specimen loaded at a strain rate in the region of 10^2 may support twice the load than when loaded at a strain rate of 10^{-5} . Consequently, there is a need to quantify these differences in order to improve the accuracy of hydrocode simulations.

Bischoff [1] reviewed earlier experimental investigations into the properties of concrete loaded at strain rates from 10^{-8} to 10^2 . He found a wide variation in the reported increase in concrete strength at strain rates from 10^{-5} to 10^2 (Figure 1) and suggested that much of this variation may be due to differences between the testing techniques employed.

A typical experimental system designed to measure the engineering properties of concrete will

comprise of a specimen of the material and the apparatus used to load it. Such systems exhibit their own peculiar characteristics which may significantly influence the measured results. Systems which perform predictably at low strain rates may have dynamic characteristics which must be accounted for before the true dynamic properties of the material can be determined. Some of the investigations reviewed by Bischoff (eg., [2]) have involved attempts to calculate and remove system effects from results.



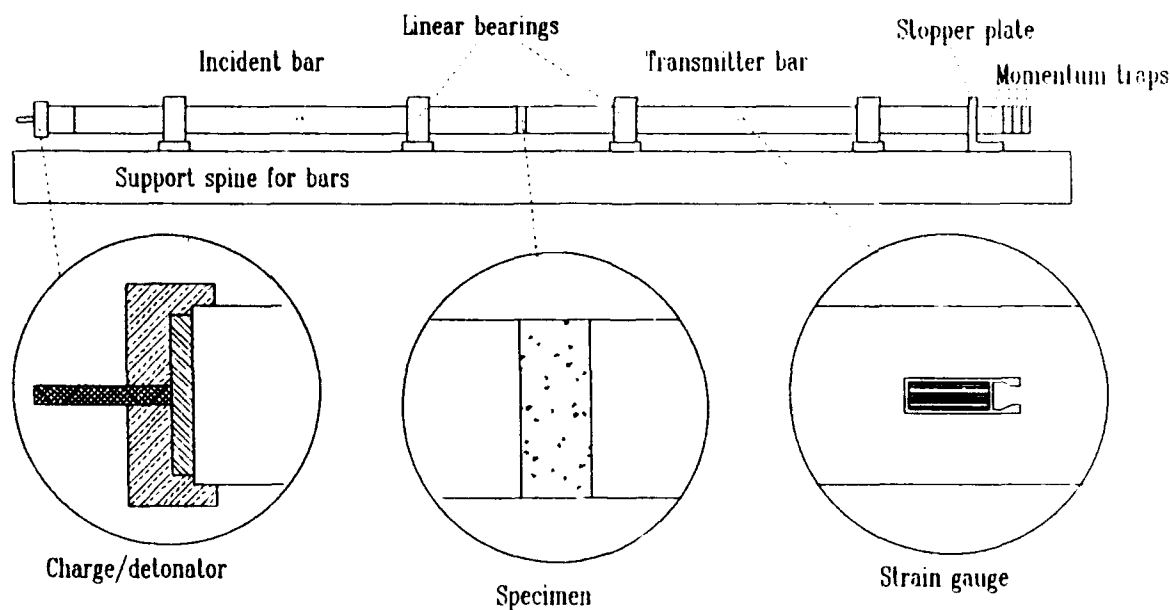
This paper describes the hydrocode assisted analysis of a split-Hopkinson bar (SHB) experiment. The aim was to determine how much of the apparent enhancement of the material strength often observed in such experiments is in fact generated by inertial effects within the system, that is, the apparatus and the specimen.

2 DESCRIPTION OF PHYSICAL EXPERIMENTS

2.1 76.2mm diameter split Hopkinson bar

A series of experiments have been carried out using a 76.2mm diameter split Hopkinson bar sited at DRA Farnborough (Figure 2). Each experiment involved the detonation of a PE4 explosive charge using an L2A1 detonator. The charge was generally a disc 70mm in diameter and 5mm thick with a mass of approximately 30g. This geometry was defined by the internal profile of a cylindrical perspex block which held the charge in contact with a steel anvil 76.2mm in diameter and 75mm long, itself in contact with the end of the incident bar. A concrete specimen, 76.2mm in diameter and typically 20 to 25mm thick was placed between the incident and transmitter bars (each 1780mm long). The transmitter bar butted against a 25mm thick stopper plate attached to the support "spine" of

Figure 2. DRA 76.2mm Split Hopkinson Bar



the apparatus. Cylindrical plates were placed in contact with the other side of this plate, to act as momentum traps. An acoustic coupling gel was used on the steel/concrete and anvil/incident-bar interfaces. This also reduces friction at these interfaces. A single 6mm long electrical resistance strain gauge was placed on each of the incident and transmitter bars, at mid-length and aligned axially.

The fourth trial after commissioning the apparatus (T4) was the first to successfully produce a full set of high-quality data suitable for comparison with hydrocode predictions. The 21.5mm thick concrete specimen was cut from a 76.2mm diameter by 150mm long cast cylinder produced from the same batch as similar specimens tested statically. The fifth trial (T5) also used this concrete.

2.2 Static testing of the concrete material

The concrete from which the SHB specimens were made (designated DRA92-3-5) was one of many concretes tested statically as part of the production of a large database of triaxial concrete, rock and soil properties. DRA92-3-5 was made with a crushed limestone coarse aggregate of nominal size 10mm, this aggregate composing 58% of the concrete by weight. The free water/cement ratio (by weight) was 0.50. For each concrete in the database, three 101.6mm cubes were crushed, one at 28 days and two at 42 days. Also at 42 days, a single 76.2mm diameter by 150mm long specimen was tested in indirect tension (the split-cylinder or Brazilian test) and two 76.2mm diameter by 148mm long specimens were tested in a "Gauged REActive Confinement" (GREAC) cell. The GREAC cell consists of a gauged cylindrical (steel) jacket around an axially loaded specimen. Using this apparatus, a complete set of axial and

lateral stress and strain curves can be evaluated for conditions of approximately uniaxial strain ([3] and [4]).

2.3 Age of concrete at testing

Although the primary static testing took place at 42 days, the timing of dynamic testing was controlled by the date of implementation of the SHB apparatus and the availability of range time. Consequently, the age of the concrete specimens used in T4 and T5 was 100 days and 148 days respectively. The concrete properties may have changed significantly in this period, thus complicating the analysis which follows. Further experiments are planned in which specimen age will be 42 days for all test techniques.

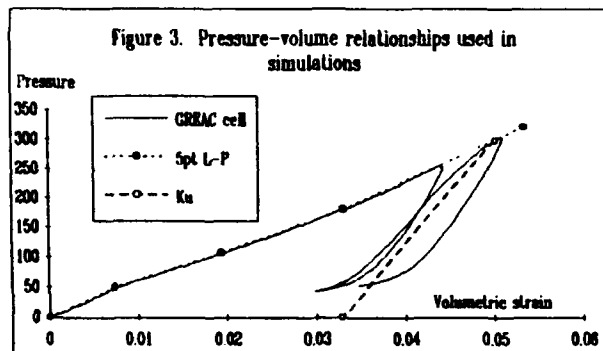
3 HYDROCODE SIMULATIONS OF THE SHB EXPERIMENT

T4 has been simulated using the hydrocodes DYNA2D and AUTODYN2D. The compressive material data used was generated from the GREAC cell tests carried out on the same concrete mix as described in section 2.2. A pressure/compaction relationship and yield stress/pressure relationship were extracted from the GREAC cell data and used as input data to the following hydrocode material models.

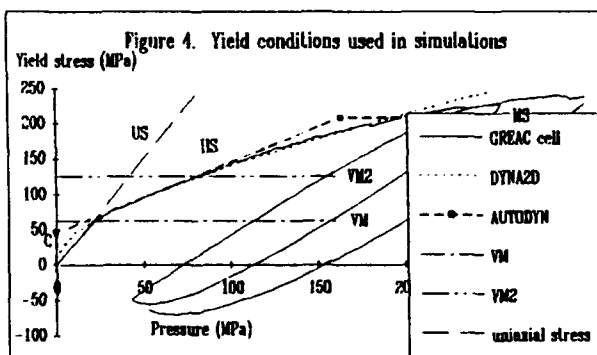
- (a) "Soil and crushable foam" (material 5) - DYNA2D/3D and NIKE2D/3D [5]
- (b) "Porous" Equation of State and "Mohr-Coulomb" strength models - AUTODYN2D/3D [6]

The pressure-volume relationship used is shown in Figure 3. Both models used a 5-point linear-piecewise (5pt L-P) relationship for the uncompacted material which is easily fitted to the GREAC cell data. For unloading and reloading partially compacted material, a constant bulk

modulus (Ku) was used (approximately constant for AUTODYN), though this does not fit the GREAC cell data particularly well. However, the unload/reload characteristics were less significant than the main load curve for the simulations considered here.



DYNA2D uses a polynomial yield-stress/pressure relationship and AUTODYN a linear Mohr-Coulomb type (Figure 4). In each case, the model was fitted to that part of the data thought most significant for these simulations; - that is, ignoring that data on or close to the uniaxial stress path (yield stress = 3 times pressure, US) and treating data above a pressure of 100MPa as less significant. A multi-point linear-piecewise model would fit the GREAC cell data better in both cases (and has subsequently become available for both hydrocodes). A point of particular interest is that at which the yield stress coincides with the uniaxial stress path, at yield stress = 57.8MPa and 71.4MPa for the DYNA2D and AUTODYN models respectively. This theoretically indicates the axial stress at which a (long) statically loaded specimen will fail, for example, if such a specimen were simulated using NIKE2D. These values can be compared with the stresses indicated in the transmitter bar to establish any apparent enhancement to the specimen strength. Yield behaviour to the left of the uniaxial stress path is probably not represented accurately by either of these models.



The indirect tensile test results were used to estimate the tensile pressure limit for both material models. For the DYNA2D model, that value had to be reduced (that is, made less tensile) in order to bring it within the yield envelope and thus prevent the simulation from failing/crashing as soon as any significant tensile pressure was

achieved. The cube crushing strengths were used to provide data for an alternative "Von-Mises" strength model (VM), ie., constant yield stress (no pressure hardening). The properties of the steel were calculated from the recorded wave velocities in the bars and from the measured density of an anvil.

The detonation was not modelled explicitly, but was instead represented by a triangular pressure pulse applied at the far end of the incident bar, the shape and magnitude of this pulse being calculated from the incident bar gauge record and then adjusted until the simulation incident pulse closely matched that from T4. T5 was not specifically simulated, that is, the incident bar pulse was not matched with a simulation, but comparison of the pulses from T4 and T5 shows no significant differences (figure 5). The incident pulse is not dependent on the specimen behaviour, either in the simulations or in the physical experiments. The simulations used 895 elements (179 x 5) in each bar and 100 elements (10 x 10) in the specimen. Slidelines at the interfaces between the specimen and the bars were either frictionless or frictional, both with voids permitted.

The initial analyses used the static triaxial properties of concrete and assumed no friction at the interfaces. Nearly identical simulations were carried out using AUTODYN (A) and DYNA2D (D0) to confirm that the two hydrocodes would produce similar results (see Figures 5 to 8). Subsequent DYNA2D simulations assumed a frictional coefficient of 0.1 at the interfaces (D1) or a Von-Mises yield condition (DV), as well as the latter enhanced by a factor of 2 (DV2).

4 COMPARISON OF EXPERIMENTS AND SIMULATIONS

Table 1 summarises the peak transmitter bar stresses indicated by the experiments and the simulations:

Table 1	(ref.)	(peak stress)	(/strength)
T4	144.7 MPa	/62.5=	2.32
T5	164.7 MPa	/62.5=	2.64
A	114.1 MPa	/71.4=	1.60
D0	117.6 MPa	/57.8=	2.03
D1	140.0 MPa	/57.8=	2.42
DV	86.9 MPa	/62.5=	1.39
DV2	152.6 MPa	/125.0=	1.22
CU	62.5 MPa	/62.5=	1.00

(where CU is the cube crushing strength, and strength for the simulations is the intersection of the yield envelope with the uniaxial stress path.)

Figures 5 to 8 show the incident pulse, the transmitted pulse, the reflected pulse and the specimen circumferential strain (respectively) for the trials and for the simulations.

The incident stress pulses for T4, T5, A and D0 only are plotted in figure 5 since the pulses for the remaining DYNA2D simulations were identical to that for D0. T4 and T5 show similar pulse shapes

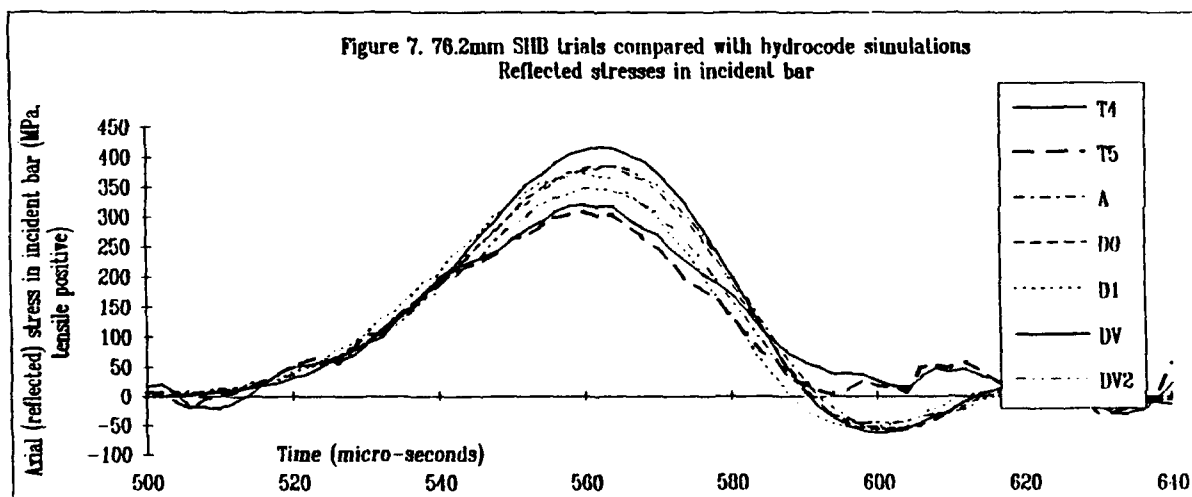
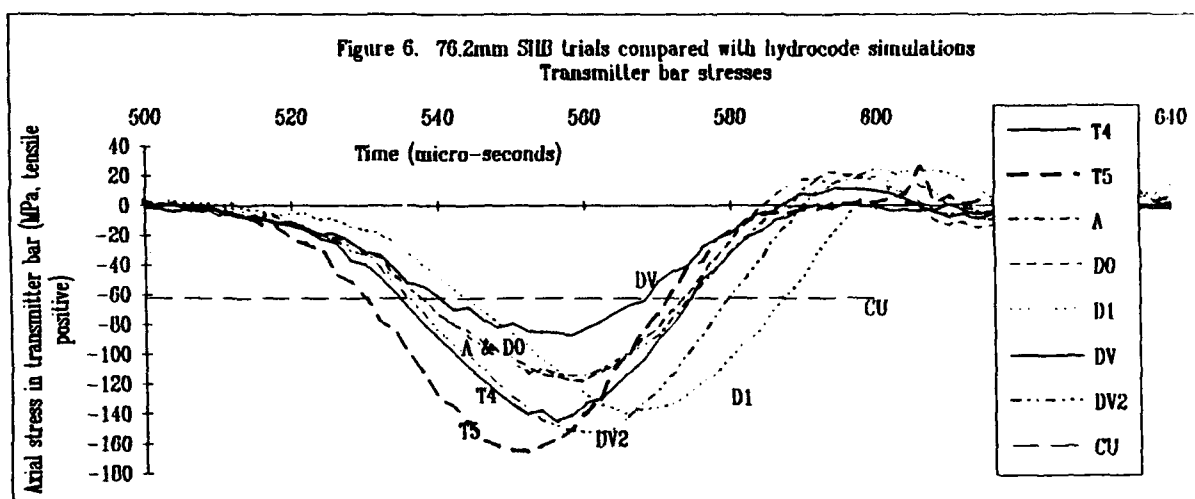
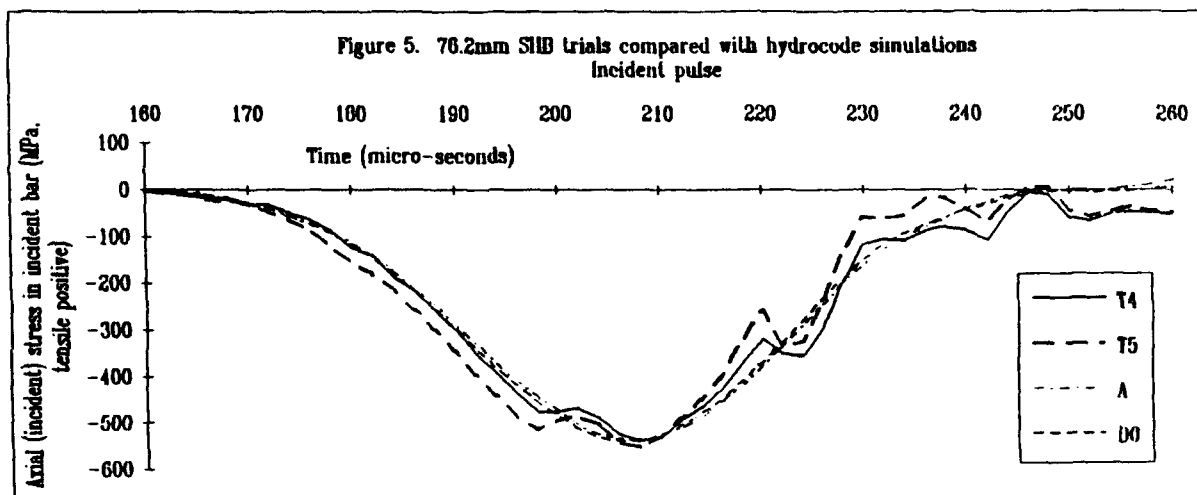
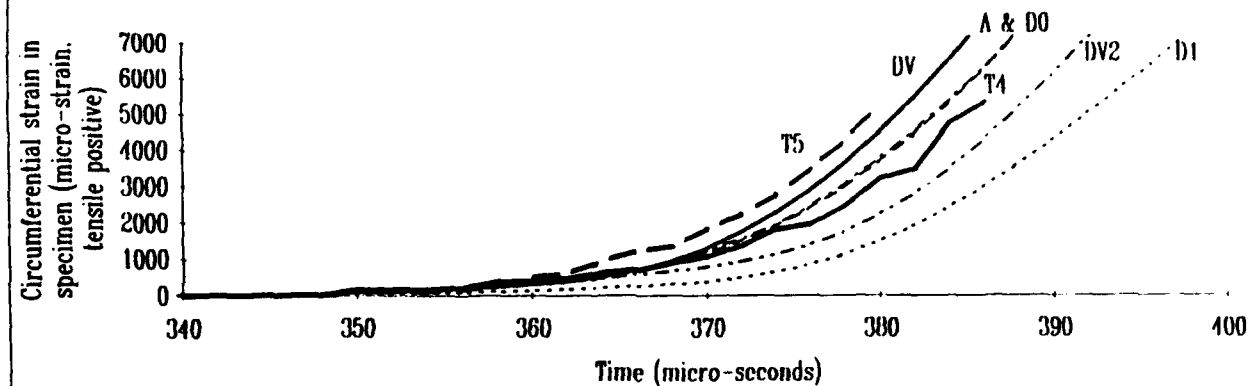


Figure 8. 76.2mm SHB trials compared with hydrocode simulations
Specimen lateral strain



with small variations in magnitude. An attempt was made to reproduce the detail within the real pulses by using a similarly detailed pressure pulse for DYNA2D. However, these details were smeared (presumably by the mesh size) and the resultant stress pulse was indistinguishable from that produced by a triangular pressure pulse input, hence the latter was used for all subsequent simulations. A much finer mesh might allow this detail to be retained, but this has not yet been investigated.

The stress pulses recorded in the transmitter bar (Figure 6) all achieved a higher peak stress than that indicated by either the cube crushing strength of the concrete or the point at which the simulation yield stress coincides with the uniaxial stress path. The lowest peak was that for simulation DV. The effect of using either triaxial strength properties, increased friction or enhanced constant yield strength was to increase the peak stress and hence improve agreement with T4 and T5. The variation in the age of the specimens may be significant here. The T5 pulse is significantly higher than T4 and could be due to increased strength with age, though alternatively, this could also be a statistical variation. Clearly there is a need to repeat these experiments with better control of concrete age.

The tensile stress pulse reflected from the specimen (Figure 7) compares well for all trials and simulations until the stress reaches a value of around 220MPa, at which point the pulse recorded in T4 and T5 markedly reduces in gradient, recovering slightly a few micro-seconds later. This may be due to the detail in the incident pulse, specifically to the first peak of a slightly lower stress than the maximum peak. This needs to be investigated by further hydrocode analysis.

During the onset of lateral strain in the specimen (up to about 360 micro-seconds; - see Figure 8), the trials and simulation data agree well, with the exception of D1 where the additional lateral

constraint provided by friction at the interfaces significantly reduces the magnitude of this strain. After 360 micro-seconds, T4 and T5 differ to the extent that it is not possible to draw many conclusions from the comparison with hydrocodes. Comparisons of the various simulations, however, indicate that increasing concrete strength reduces the magnitude of the lateral strain, as would be expected since shear deformation is the primary mechanism.

The use of hydrocode simulations in the analysis of physical events allows the assessment of aspects of such events which were not or cannot be physically recorded, for example, the state of stress at any point within the SHB specimen. For simulation D0, the pressure (or mean stress) in the centre of specimen achieved a value of approximately 83.5MPa, indicating a local increase of the yield stress to 126.5MPa and a consequent increase in the axial stress to 167.8MPa. This effect reduces with increasing radius, but when the axial stress is averaged through the radius to calculate the peak total load on any x-section through the specimen normal to its axis, this load will be far greater than that expected if a uniaxial stress state is assumed. The specimen axial strain rate for analysis D0 was determined to be of the order of 1000/sec during the first loading. The strain history calculated from the relative motions of the ends of the bars agreed well with that experienced by an element within the specimen, until voids formed at one or both interfaces.

It is appreciated that the specimens considered in this study have a length to diameter ratio (L/D) of 0.28 whereas many of the specimens used in the investigations reviewed by Bischoff have L/D greater than 1.0. Consequently, a D0 analysis was carried out with a 76.2mm long specimen substituted for the original specimen 21.5mm long. The peak transmitted stress pulse in this case was 83.4MPa, greater by a factor of 1.44 than that indicated by static analysis. During the first loading, the specimen axial strain rate for this simulation was of the order of 250/sec.

5 CONCLUSIONS

The hydrocode analyses described above, particularly A and D0, used realistic static compressive triaxial properties for the concrete material and had no rate dependent components. Nevertheless, an increase in the axial load supported by the specimen was noted. It can be concluded that at least some of the ability of such a specimen to support a higher axial load than its statically-loaded uniaxial-stress counterpart can be explained by the presence of a compressive triaxial stress state within the specimen, caused by the radial inertia of the specimen itself. This is often referred to as lateral inertial confinement [1]. It has been concluded by other workers [1,7] that significant lateral inertial confinement occurred only after the peak stress had passed through the specimen because lateral deformation increased rapidly at that time (at strain rates up to 100, an order of magnitude less than those considered in this study). Analysis D0 indicates that (at strain rates of the order of 1000) lateral inertial confinement increases immediately with increasing axial stress, though more rapidly once the yield envelope is achieved. Moreover, the peak lateral confinement coincides with the peak axial stress. At least at the strain rates considered here, the effect of lateral inertial confinement significantly modifies the otherwise uniaxial stress state throughout the period of interest.

Unfortunately it is not possible to determine how much of the observed increase in specimen strength in this study was due to lateral inertial confinement and how much was a true increase in material strength dependent on strain rate, because of differences in the ages of the dynamically and statically loaded specimens. However, the work described here demonstrates that care must be taken when determining rate-dependent effects on material properties if the dynamically generated triaxial stress state within the specimen is not fully accounted for.

6 FURTHER WORK

For the analysis described in this paper, hydrocode simulations were carried out using concrete material properties measured under conditions of approximately uniaxial strain. Although the SHB specimen is initially loaded under these conditions, it subsequently tends toward uniaxial stress as it deforms and unloads radially. This can be prevented by confining the circumference of the specimen using a cylindrical steel jacket similar to the GREAC cell. Measurement of the circumferential strain on the outside of this jacket facilitates determination of the lateral stress and strain in the specimen. AUTODYN2D and DYNA2D simulations of this proposed GREAC cell/split Hopkinson bar combination indicate that a reasonably consistent state of stress exists throughout such a confined specimen. A prototype trial has been carried out and is being analysed.

The material models used in this study are not particularly complex and do not allow for the yield stress increasing to a higher ultimate stress with volume dilation during the failure process, as has been observed in static triaxial testing of concrete [8]. More complex material models could be used in the hydrocode simulations provided that suitable static data can be measured, for example, material type 16 in DYNA2D [5].

7 ACKNOWLEDGEMENTS

This research was funded by the Procurement Executive of the Ministry of Defence and forms part of the programme of the Defence Research Agency to investigate the response of concrete structures to conventional weapons effects.

British Crown Copyright 1993 /DRA
Published with the permission of the
Controller of Her Britannic Stationary
Office

8 REFERENCES

- [1] Bischoff, P. H., "Compressive response of concrete to hard impact", PhD Thesis, University of London (Imperial College of Science, Technology and Medicine), 1988.
- [2] Hughes, B. P., and Watson, A. J., "Compressive strength and ultimate strain of concrete under impact loading", Magazine of Concrete Research, Vol. 30, No. 105, December 1978, pp189-199.
- [3] Sheridan, A. J., "Response of concrete to high explosive detonation", PhD Thesis, University of London (Imperial College of Science, Technology and Medicine), 1990.
- [4] Sheridan A. J., Pullen, A. D., Perry, S. H., "Material Modelling for Hydrocode Analysis of Concrete Response to Explosive Loading", 5th Internationales Symposium Interaktion Konventioneller Munition mit Schutzbauten, Mannheim, 22-26 April, 1991, pp301-308.
- [5] Whirley, R. G., Engelmann, B. E., and Hallquist, J. O., "DYNA2D - A nonlinear explicit two-dimensional finite element code for solid mechanics - user manual", Lawrence Livermore National Laboratory, UCRL-MA-110630 April 1992.
- [6] Century Dynamics Inc., "AUTODYN Users Manual Supplement version 2.2", 1989.
- [7] Malvern, L. E., Tang, T., Jenkins, D. A., and Ross, C. A., "Dynamic compressive testing of concrete", Proceedings of the Second Symposium on the Interaction of Non-Nuclear Munitions with Structures, Panama City Beach, Florida, April 1985, pp. 194-199.
- [8] Kinoshita, M., "Constitutive relations of concrete under passive confinement and their use in structural analysis", PhD Thesis, University of London (Imperial College of Science, Technology and Medicine), 1992.

'Use of Large Diameter Hopkinson Bar to Investigate the Stress Pulse Generated During High Velocity Projectile Penetration into Construction Materials'

by

Mr J Peters, Dr W F Anderson And Dr A J Watson

(Department of Civil and Structural Engineering,
University of Sheffield, UK)

Abstract

This paper documents the design and construction of a large diameter Hopkinson Bar to investigate the stress pulse generated during the penetration of 7.62 mm Armour Piercing Projectiles into construction materials. Details are given of a laser based alignment device along with typical results obtained from both confined and unconfined specimens and an initial analysis of the results.

1.0 Introduction

As part of an ongoing study into the fundamental mechanisms of projectile penetration into concrete and mortar, it became evident that during the penetration of 7.62 mm armour piercing projectiles a complicated time dependant stress regime is developed. In order to study this stress event, to better understand the penetration event as a whole, and to assist in the development of a realistic model for perforation and rear face tensile scabbing of the impacted target, a realistic stress pulse for the penetration of projectiles into construction materials would have to be determined.

To determine the effective stress pulse induced by a penetrating projectile, the Hopkinson bar technique has been used. The standard analysis of the Hopkinson bar is well documented and it is this that is frequently used for the experiment carried out at laboratories of Civil Engineering Dynamics at Sheffield University to measure impact and explosive events (1). To allow for some deviation in the bullet flight path it was decided to construct a 100 mm diameter bar for these tests and develop a precise method for aligning the bar with the flight path of the projectile. This paper describes the design instrumentation and construction of the bar, manufacture of test specimens and the test procedure.

2.0 Design of the Bar

2.1 Bar dimensions

The standard specimens used for other related tests in this study of projectile penetration, were 450 mm diameter and 125 mm thick and results are reported elsewhere, (2). The Hopkinson bar specimens have the same thickness, 125 mm, but the diameter could not be so large as 450 mm.

The factors considered in the choice of bar and specimen diameters were as follows:

- The length of a Hopkinson bar must be twenty times its diameter if a one dimensional analysis is to be reasonably accurate.
- The length of bar had to be sufficient to avoid signal overlap from the pulse reflected at the end.
- The design of the test facilities limited the length of the bar to around 3.15m (including support frame).
- The minimum dimension of a concrete specimen, considered representative, is often stated as four times the maximum aggregate dimension. For the specimens tested, which had a maximum aggregate size of 10 mm, this gave a minimum specimen diameter of 40 mm.
- The deviation in bullet flight path with standard 7.62 armour piercing projectiles and the firing system used gave a spread of impact lying within a circle of 15 mm diameter on a flight path of 20 m (3). To obtain relatively central impacts a large diameter specimen and hence bar would be required.
- The specimens were to be cored from a number of 450 mm diameter specimens cast for this purpose therefore the bar would have to be of a diameter of the available coring facilities, this limited the maximum diameter to 100 mm.

From the above considerations, the largest practical size of bar and specimen, chosen for these tests, was 100 mm diameter and 3.1m long.

2.2 Bar material

The material chosen for the construction of this Hopkinson bar was EN 24(T) (817M40), a heat treated high tensile steel with composition and properties suitable for this work. This steel has a low cost, compared to maraging steel for example.

2.3 Support frame

With the bars approaching 200 kg in mass a support system had to be provided and a support frame/trolley was fabricated as shown in Fig. 1.

The alignment of the bar can be achieved as shown in Fig. 2 by simply adjusting the supports to bring it into position with the aid of the laser device discussed later. The slings supporting the bar, at roughly quarter points, are of fabric to minimise any stress pulse modification due to the supports.

3.0 Construction of the bar

3.1 Ends of bar

The ends of the 3100 mm x 100 mm diameter bar of EN 24 (T) were surface ground and lapped to provide a flat surface perpendicular to the axis of the bar. A 50 mm long section of 100 mm diameter bar was used as an anvil and was butted against this end to protect the bar from damage by the bullet or specimen.

3.2 Strain gauging

A number of strain gauge stations were prepared on the bar, but only two were used during these tests. The gauges were Kyowa KFG-3-120-C1-11 and were applied

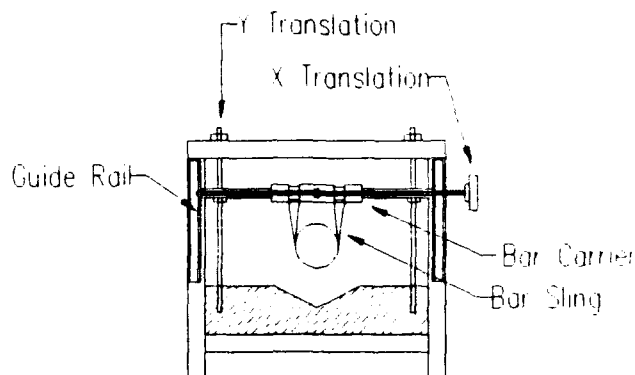


Fig. 2. Hopkinson Bar X-Y Translation Details

to the bar with CN glue after careful surface preparation of the bar. The cable used for connecting the gauges to the bridge and amplifiers was 4 core semiconductor shielded cable which gave excellent resistance to noise. The gauges had attached terminal wires so that the connections to the 4 core cable were separate from the gauge.

The gauges had a 3 mm length with gauge factor of 2.09 and a nominal resistance of 120Ω. Each station consisted of four gauges, at 90° intervals around the perimeter of the bar at 500 mm and 1000 mm from the end of the bar. The use of four gauges was in order to cancel out any bending induced in the bar due to any eccentric impact. The length of the gauge was chosen to be 3 mm as a compromise of the following constraints.

- The longer the gauge the easier it would be to place accurately.
- The shorter the gauge the more accurate will be the recording of the time varying signal.

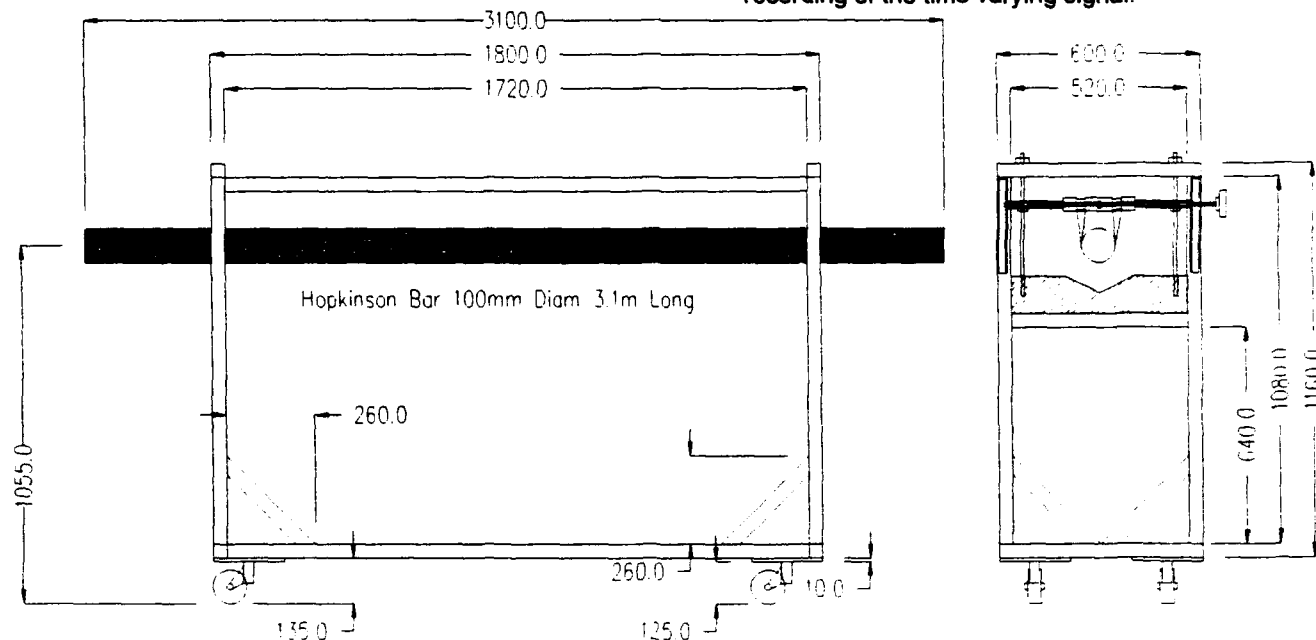


Fig. 1 100 mm Diameter Hopkinson Bar In Support Frame

With the rod velocity of sound in steel of the order of 5.2 mm/ μ sec and a data sampling frequency of 2 MHz, a gauge length of around 3 mm would be activated by a pulse of 520 mm length for about 100 μ sec during which 200 data points would be recorded at intervals of 0.5 μ sec. This would mean that each data point sampled represented 2.6 mm of the pulse in the bar, which gave some smoothing of the measured pulse.

4.0 The Specimens

4.1 Concrete specimen preparation

A number of 125 mm thick x 450 mm diameter specimens were cast and later cored to form the specimens for this series of Hopkinson bar tests. The pattern of coring is shown in Fig. 3 and allowed for nine 100 mm diameter cores to be taken out of each specimen. Exactly the same batch of concrete was used for these specimens as the related rear face scabbing tests, (2), thus ensuring comparability of results.

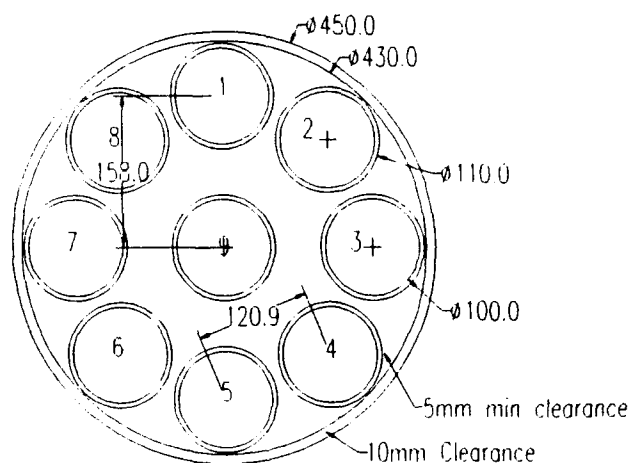


Fig. 3. Coring Pattern

Each of these 125 mm thick x 100 mm diameter specimens was mounted on the 50 mm thick x 100 mm diameter 817M40 steel anvil using plaster of Paris, approximately 0.3 mm thick, to provide acoustic coupling.

4.2 Confined concrete specimens

To investigate the effect of lateral confinement on the fracture of the concrete specimen and on the stress pulse, high tensile steel bands were placed around some of the concrete and mortar specimens. These bands were pre-tensioned to remove any slack, and produced a pre-test confinement in the order of 0.5 N/mm². Fig. 4 shows the arrangement of the 9 No 12.7 mm wide 0.5 mm thick straps and clips around the specimen. These specimens were mounted onto anvils in the same way as the unconfined specimens.

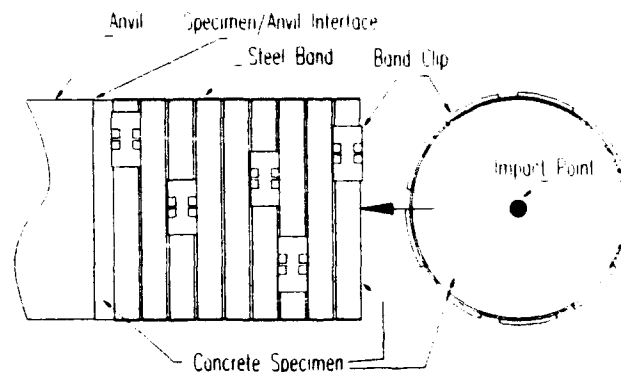


Fig. 4. Confined Concrete Specimen

The steel straps were not in contact with each other and so had little effect on the stress pulse travelling down the specimen and transmitted into the bar. Because the bands were only 0.5 mm thick it was probable that the level of confinement was not as efficient as the thicker solid steel jacket employed in other confined tests (4). However the nature of the straps facilitates them being strain gauged to obtain some measure of bursting pressure against time, for a number of distances from the impact face.

4.3 Steel specimens

To study the stress pulse generated during the penetration of 7.62 mm armour piercing projectiles into steel, 50 mm thick x 100 mm diameter machined and surface ground anvils were mounted onto the bar without a concrete or mortar specimen. The stress pulse from the impact of the projectiles was then compared with to that of impact into concrete / mortar specimens and is discussed in Section 7.0.

5.0 Instrumentation

5.1 Wheatstone bridge

As stated earlier each of the strain gauge stations on the bar consisted of 4 gauges. Dummy gauges, mounted on steel anvils, were used to complete the Wheatstone bridge. The gauges were powered at 5V DC using bridge amplifiers with the amplification factor set at 1,000 times. Even with this high amplification factor the noise levels were very low and during triggering tests, using an amplification factor of 10,000 times, the noise levels remained remarkable low. The use of semiconductor shielded cable in the wiring of the gauges is felt to have an influence on this although no comparative data was obtained during these tests.

5.2 Data storage

A Gould Biomation 2805 Digital Storage Oscilloscope (DSO) was connected to the Fylde bridge amplifiers and sampled the gauge output at intervals of 0.5 μ sec. This information, stored in the digital storage oscilloscope was

later transferred data to a PC using in-house developed software. The traces were processed and the graphs were plotted using commercial spreadsheet software.

6.0 Test method

6.1 Specimen mounting

The concrete specimen is held in place on the anvil by the plaster of Paris. Each of the combined concrete (or mortar) / steel anvil assemblies was suspended on two adjustable straps. This assembly was accurately aligned and mated to the Hopkinson bar using a very thin layer of Swarfega, a thin thixotropic jelly acting as an acoustic interface, by being wrung onto the bar to ensure minimum couplant between the anvil and the bar.

6.2 Bar alignment

In the tests a projectile is fired along the projected axis of the bar to impact the end of the bar. To obtain a central and normal impact on the bar, the bar is aligned such that it is coaxial with the projectile flight path. To achieve this, a laser line was established at a fixed distance (68.5 mm) directly above and in line with the gun barrel. (Fig. 5) This laser line was accurately targeted at a point at the far end of the range, the same fixed distance (68.5 mm) above the normal and central impact point. This offset ensured that with the bar in position there was still an unobstructed path for the laser beam between the bar and its supports.

Two 'Jockeys' were fabricated as shown in Fig. 6 and were placed one at each end of the bar so that by adjusting the bar the shadow of the cross hairs from the first jockey was cast by the laser beam onto the cross marked on the removable screen on the second jockey. The bar was then aligned and on axis. The screen on the second jockey could be removed to demonstrate that the laser was still in alignment, the shadow of the cross being cast on the far wall and the point established 68.5 mm above the central, theoretical impact point. The wire cross hairs needed to be no finer than 0.6 - 0.8 mm diameter in order that the Moiré fringes, produced by the coherent light source, have no detrimental effect on the shadow of the cross cast on the screen.

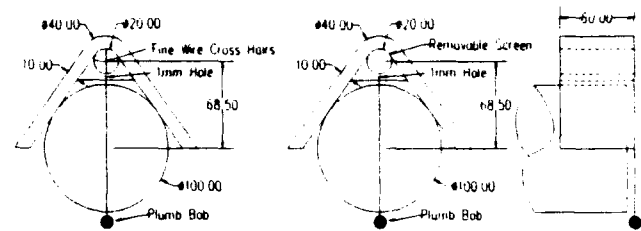


Fig. 6. Bar Alignment Jockeys

6.3 Firing system

All tests used a 7.62 mm pressure barrel attached to a pressure housing. The firing lever was connected by a mechanical linkage to a solenoid of stroke 18 mm and pullout force 11.8N. This solenoid was connected, through a full bridge rectifier for greater efficiency, to the 240 volt supply via an interlocked key operated firing box. (3)

7.0 Results.

Figure 7 show the load time histories for 7.62 armour piercing projectiles impacting mortar, concrete and steel. Figure 8 compares the load time histories for both confined and unconfined concrete. Figure 9 shows the pulse, measured at a gauge station 1000 mm from end of the bar, and its associated reflected the tensile wave, generated during penetration into a confined concrete specimen.

In order to compensate for the impedance miss-match between the specimen and the bar the Transmission Factor (θ_T) for the concrete / bar interface was calculated, from the equation below, and this factor applied to the test results.

$$\sigma_t = \left(\frac{2\rho_2 A_1 C_{o2}}{\rho_2 A_2 C_{o2} + \rho_1 A_1 C_{o1}} \right) \sigma_i = \theta_T \sigma_i$$

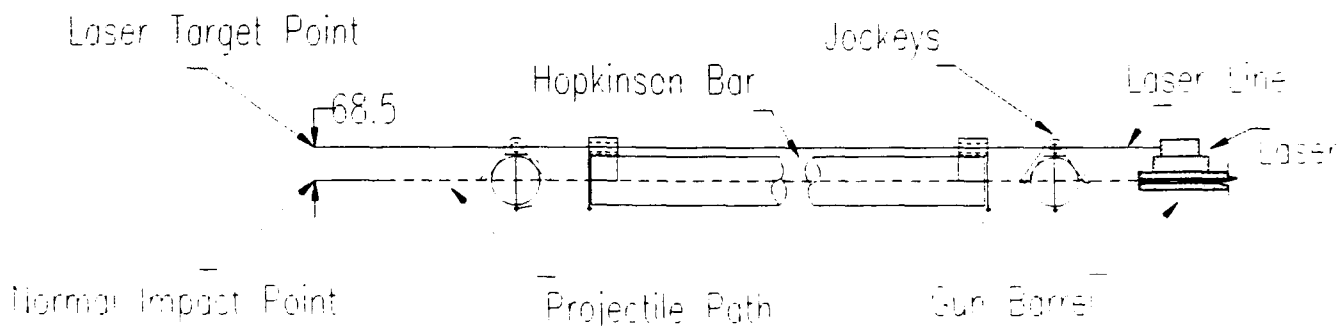


Fig. 5 Hopkinson Bar Alignment

where:-

ρ = density

A = Cross sectional area

C_o = Longitudinal wave velocity

subscripts indicate: concrete (1), steel (2)

The values used are given in Table 1 below and the Transmission Factor was calculated as $\theta_T = 1.649$

	Steel EN24(T)	Concrete / Mortar
ρ = density (kg/m^3)	7800	2400
A = Cross sectional area (mm^2)	7853	7853
C_o = Longitudinal wave velocity ($\text{mm}/\mu\text{sec.}$)	3.6	5.2

Table 1. Values for Transmission Factor Calculation

Table 2 gives peak loads, measured impulse, average strain rate (for the bar area as a whole) and implied strain rate at the bullet tip (assuming a forged nose diameter of 7.62 mm), for the penetration events detailed. As can be seen, the peak load for impact on the steel specimen is greater than the corrected loads on either the concrete or

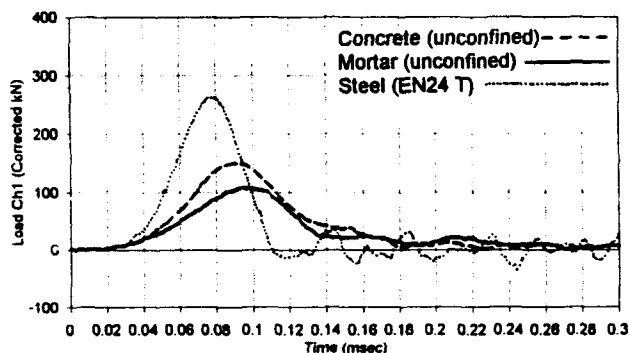


Fig 7 Stress Pulse (Concrete, Mortar and Steel).

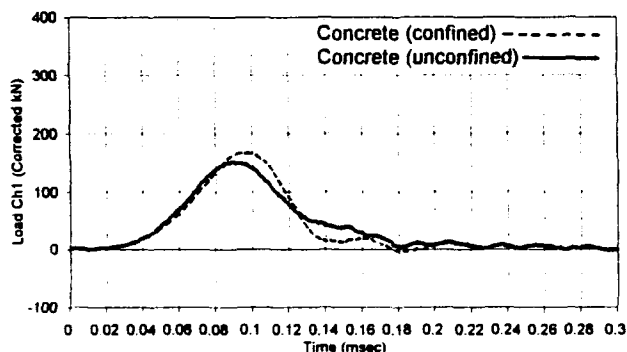


Fig 8 Stress Pulse (Confined and Unconfined Concrete).

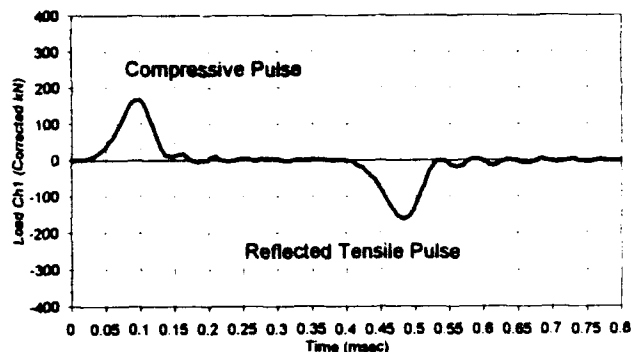


Fig 9 Stress Pulse Showing Reflection (Concrete).

mortar specimens, coupled with a correspondingly reduced duration for the event. In order to compare these values the impulse received by the bar was calculated and the results compared to the theoretical value for the projectile of 8084 $\text{N } \mu\text{sec}$ for a nominal impact velocity of 860 m/sec. This showed good correlation for the cementitious materials but an error of around 30 % for the steel specimens. The authors feel that this error may be due to assumptions made in measuring the area of the pulse from the graph along with some self compensating errors in the cementitious materials.

Specimen	Peak Load (kN)	Impulse ($\text{N } \mu\text{sec}$)	Average 'bar' Strain Rate (Strain/sec)	Implied (forged tip) Strain Rate (Strain/sec)
Mortar Unconfined*	108	7000	1.09	188
Mortar Confined*	120	7400	1.18	203
Concrete Unconfined*	151	8900	1.82	313
Concrete Confined*	167	9300	2.18	375
Steel EN24(T)	262	10650	4.49	773

*figures corrected for impedance mis-match.

Table 2. Values of Load, Impulse and Strain Rates.

If these values of peak load are used, and it is assumed that the forged nose of the projectile has a diameter of 7.62 mm, then the range of peak stresses, at the forged tip of the projectile during penetration, range from 2.37 kN/mm^2 for the unconfined mortar to 3.66 kN/mm^2 for the confined concrete up to 5.74 kN/mm^2 for the steel specimens. These figures must be viewed in the light of the actual penetration event in which the mass and diameter of the projectile reduce during the penetration event from 9.41g and 7.62 mm to 4.42 g and 5.73 mm due to the shedding of the soft copper jacket which surrounds the hardened steel core of NATO standard armour piercing rounds.

8.0 Discussion

The pulses measured in the bar are a result of a highly complex event generated by a moving source and by many reflections of the stress waves at both fixed and eroding boundaries. These include the specimen / bar interface, circular sides of the specimen and, most complex of all, the front face of the specimen which is subject to cratering and bursting as the bullet penetrates. These initial results have not taken into account these reflections, the moving source or the attenuation of the stress pulse in the either the concrete or steel but have proved the practicality of using this technique to record load time histories for penetration / impact events.

The confinement of the specimens in a hopkinson bar test is known to increase the stress wave velocity by up to 10% Ref. (1) these effect have not been taken into account for these results as the ultimate state of confinement due to the strapping system is not believed to be high and therefore any correction to the Transmission Factor for the specimen/bar interface would be small.

It can be seen from Table 2 along with figure 8 that confinement has the effect of increasing both the peak load and the measured impulse but has little effect on the initial part of the measured stress pulse.

The objective of these experiments was to measure the stress pulse generated during projectile penetration so that more accurate modelling of rear face tensile scabbing and of the penetration event as a whole could be developed. The results given in figs 7, 8 and 9 suggest that the stress pulse may be simplified to that of a triangle of duration and peak load shown.

9.0 Conclusions

The results show the viability of using a large diameter Hopkinson bar for the determination of load time histories for impact events.

The use of a laser to align the bar provides a simple yet effective method of what would otherwise be a difficult task.

There is a close correlation between the theoretical and experimental impulse values.

Confinement has little effect on the initial pulse but increases the peak load measured during penetration.

Acknowledgements

The authors would like to express their thanks to the Science and Engineering Research Council and the Ministry of Defence (DRA, Christchurch) who are jointly funding this work under Grant Number GR/F 20735.

References

1. Johnson, W. 1972 'Impact Strength of Materials'. Arnold, London, UK.
2. Peters J., Anderson W.F., Watson A.J. 'Development of Instrumentation Techniques to Investigate High Velocity Projectile Penetration into Construction Materials' Sixth International Symposium on Interaction of Nonnuclear Munitions with Structures, Florida, USA 1993.
3. Anderson W.F., Watson A.J., Peters J. (1991) 'High velocity projectile penetration into cementitious materials.' pp 381-387 The Interaction of Non Nuclear Munitions With Structures, Mannheim, Germany. 22-26 April 1991.
4. Sheridan A.J., Stephens W.H., Perry S.H. 'The Behaviour of Concrete Under Explosive Shock in relation to its Compaction under Uniaxial Strain Loading' pp87-96 Proc. 1st Int. Conf. of 'Structures Under Shock & Impact' Ed Bulson P.S., Cambridge Massachusetts USA July 1989.

LOAD RATE EFFECTS ON CONCRETE COMPRESSIVE STRENGTH

J.W. Tedesco

Dept. of Civil Engr., Auburn University, Auburn, AL 36849

C. Allen Ross

University of Florida, Eglin AFB, FL 32542

M.L. Hughes

WL/FIVCS, Tyndall AFB, FL 32403

ABSTRACT

Plain concrete cylindrical specimens, 51 mm in length and diameter, were tested in compression quasi-statically at strain-rates between 10^{-6} /sec and 1/sec in a standard MTS machine, and dynamically at strain rates between 1/sec and 300/sec in a Split-Hopkinson Pressure Bar. The results of these tests indicate a true strain rate sensitivity of the pertinent concrete material strength parameters such as compressive strength, strain at maximum compressive stress, and ultimate compressive strain. Complete stress-strain curves for various concrete strengths at a broad range of strain rates have been generated from the experiments which clearly illustrate the strain-rate sensitivity.

INTRODUCTION

Most all materials exhibit some load-rate or strain-rate sensitivity relative to strength. Strain-rate effects in materials, induced by high amplitude short duration impulse loads, are important in the design and analysis of structures to resist dynamic loads from conventional weapons explosions, accidental explosions and high speed impact. Analytical and numerical modelling of such events require knowledge of dynamic material properties, response mechanisms, fracture mechanics, and constitutive relations. Laboratory experiments and equipment required to investigate material properties at high load or strain-rates must simulate an environment very similar to that of the field. The split-Hopkinson pressure bar (SHPB) is capable of producing high strain-rate loading in the range of 10 to 10^4 /sec on small specimens, inducing uniform stress over the length of the specimen.

A range of strain-rates associated with testing of concrete may be obtained if one compares the time required to reach a strain of 0.003 in the very low load-rate of a standard concrete cylinder test to the loading pulse of close proximity conventional explosion. The loading time for the low load-rate cylinder test is approximately 30 minutes or 1.8×10^3 seconds, resulting in a strain-rate of 1.7×10^{-6} /sec ($3 \times 10^{-3}/1.8 \times 10^4$). The loading pulse of a conventional explosion is on the order of 1.0×10^{-4} seconds with a strain-rate of 30/sec ($3 \times 10^{-3}/1 \times 10^{-4}$).

The Split-Hopkinson pressure bar has been used extensively to investigate the dynamic response of solid materials [1,2,3]. Illustrations of the SHPB, which is maintained and operated by the Air Force Civil Engineering Support Agency (AFCEA), Tyndall AFB, Florida, are presented in Figures 1 and 2. The

direct compression experiment consists of a concrete specimen placed between, and in contact with, the two pressure bars. Each pressure bar is 51 mm in diameter and constructed of PH 13-8 MO stainless steel. The concrete specimen is 51 mm in diameter and 51 mm in length. The loading compressive stress wave is initiated by the impact of the striker bar (which is propelled by the gas gun) on the incident bar (Figure 1). The amplitude of the incident stress pulse is determined by the impact velocity and material properties of the striker bar, which the duration of the pulse is dependent on the length and the wave speed of the striker bar [4].

The incident stress wave (σ_i) generated in the incident bar travels down the bar and is recorded at strain gage A (Figure 2), is partially reflected at the incident bar/specimen interface, and partially reflected at the specimen/transmitter bar interface. Strain gage B (Figure 2) on the transmitter bar records the portion of the wave that has transmitted the specimen (σ_T), while strain gage A on the incident bar records that portion of the wave reflected at the incident bar/specimen interface (σ_R). From these strain gage measurements, the stress and strain in the specimen, which is sandwiched between the two pressure bars, can be computed as a function of time using simple wave mechanics [5].

In the present study five different concretes were examined for strain-rate sensitivity. The specimens for all five concretes were tested quasi-statically in a standard MTS machine at strain rates of 10^{-6} /sec and 10^{-5} /sec, and dynamically in the SHPB at strain rates ranging from 3/sec to 375/sec. The quasi-static material properties for the five concretes are presented in Table 1.

RESULTS OF SHPB EXPERIMENTS

An approximate dynamic stress-strain curve can be obtained using the raw data traces obtained from the SHPB experiments. A typical data trace, corrected for dispersion and phase change, is presented in Figure 3. By applying continuity of force and velocity between the two specimen/bar contacting faces, the average strain, ϵ_s , average stress, σ_s , average strain-rate, $\dot{\epsilon}_s$, and approximate stress-strain curve at any strain-rate can be determined.

Concrete strength as a function of strain rate for concrete mix A is presented in Figure 4. The secant modulus as a function of strain rate is presented in Figure 5 and the strain at maximum stress (ϵ_c) as a function of strain rate is presented in Figure 6. The dynamic stress-strain curves for concrete mix A at the five

TABLE 1. QUASI-STATIC CONCRETE MATERIAL PROPERTIES			
Concrete Mix	E, Young's Modulus (GPa)	f'_c , Compressive Stress (MPa)	f'_t , Tensile Stress (MPa)
A	29.2	27.8	2.8
B	28.4	38.6	2.4
C	25.1	39.3	2.4
D	31.7	54.5	3.1
E	52.3	56.8	3.7

different strain rates are presented in Figure 7.

DISCUSSION OF RESULTS

Figure 4 indicates that dramatic increases in concrete strength over the quasi-static strength are exhibited when specimens are subjected to loading at high strain-rates, both in tension and compression. The critical strain-rates at which these increases occur are notably different, however, for tension and compression, the former appearing at a strain rate of approximately 3/sec, and the latter at a strain rate of about 40/sec. Figure 5 shows that there is no significant variation in dynamic secant modulus values as compared to static values. As seen in Figure 6, the strain value corresponding to the maximum compressive stress increases sharply as the strain rate reaches the critical threshold value of 40/sec, which correlates well with the critical strain rate value observed in Figure 4. This same pattern is also exhibited in Figure 6 by the ultimate compressive strain. Several of these trends can also be distinguished in Figure 7, which shows that as the strain-rate increases, the maximum compressive stress increases, as does the strain value corresponding to the maximum stress, whereas no significant change is noted in the secant modulus values.

CONCLUSIONS

The results of the SHPB experiments conducted reveal that the compressive and tensile strengths of concrete are indeed strain-rate dependent properties. There appear to be distinctly different threshold strain rates at which this sensitivity begins to be manifested, however, for tension and compression. Also, it can be concluded that the strain at maximum compressive stress and the ultimate compressive strain are rate-sensitive parameters and exhibit the same approximate threshold value of strain-rate as the compressive strength itself. Conversely, the secant modulus is a relatively rate-insensitive property, showing only very slight deviation for tests conducted at high strain-rates over those conducted at quasi-static rates.

ACKNOWLEDGEMENT

This research was sponsored by a contract from Headquarters Air Force Civil Engineering Support Agency (AFCEA), Contract No. F08635-92-C-0031. All experiments were conducted at AFCEA, Tyndall AFB, FL.

REFERENCES

1. Tedesco, J.W., Ross, C.A., and Brunair, R.M. et al., "Numerical Analysis of Dynamic Split Cylinder Tests," *Computers & Structures*, vol. 32, no. 3/4, pp. 609-624, 1989.
2. Tedesco, J.W., Landis, D.W. and Hayes, J.R., "Dynamic Response of Layered Structures Subject to Blast Effects of Non-Nuclear Weaponry," *Computers & Structures*, vol. 26, no. 1/2, pp. 79-86, 1987.
3. Tedesco, J.W., Ross, C.A., McGill, P.B., and O'Neil, B.P., "Numerical Analysis of High Strain Rate Concrete Direct Tension Tests," *Computers & Structures*, vol. 40, no. 2, pp. 313-327, 1991.
4. Follansbee, P.S. and Franz, C., "Wave Propagation in the Split Hopkinson Pressure Bar," *Journal of Engineering Material Technology*, vol. 105, pp. 61-66, 1963.
5. Nicholas, T., "Material Behavior at High Strain Rates," Chapter 8 in *Impact Dynamics*, Zukas, J.R., Editor, John Wiley & Sons, New York, N.Y., pp. 277-332, 1982.

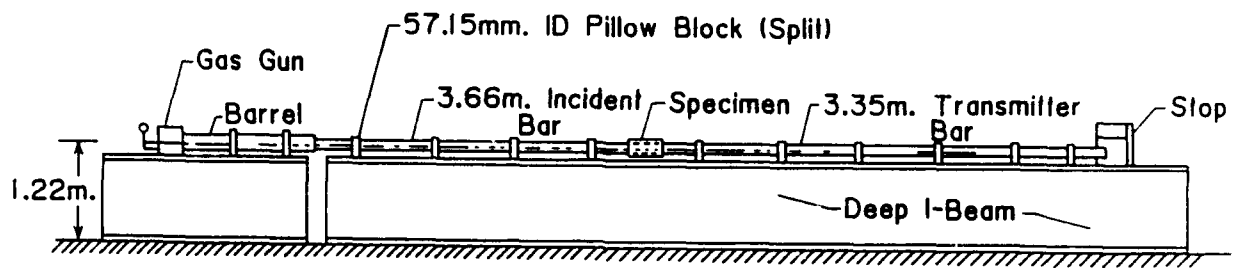


Figure 1. Illustration of the SHPB.

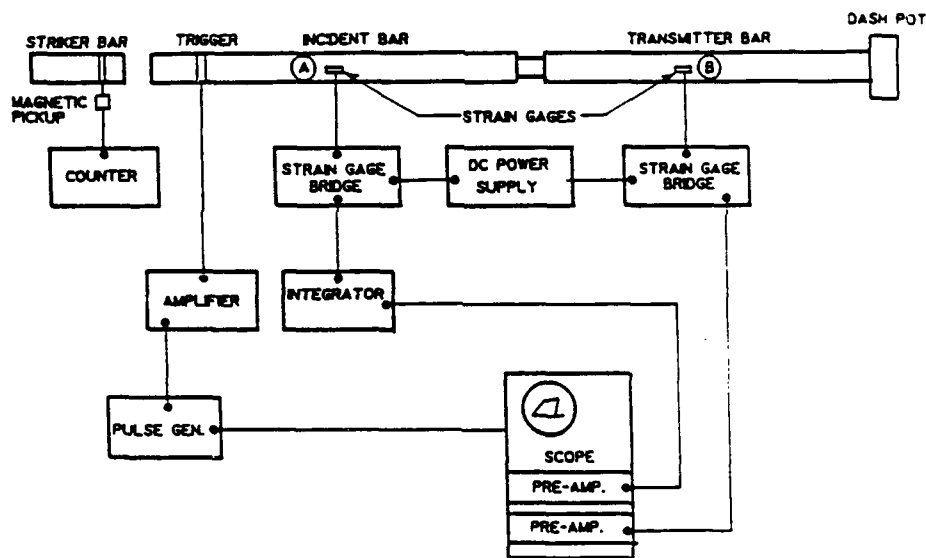


Figure 2. Operational schematic of the SHPB.

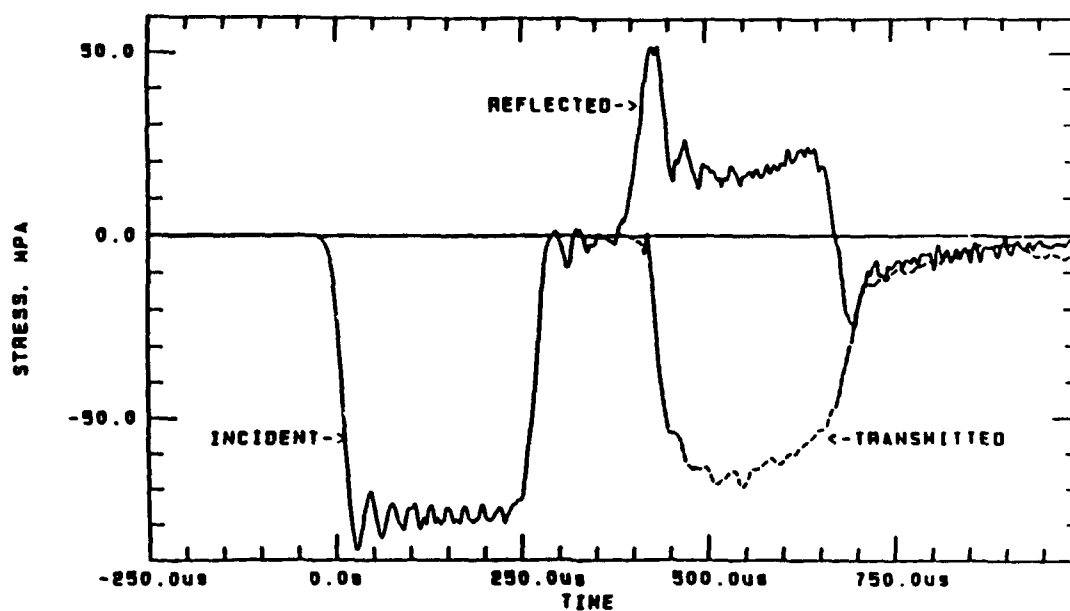


Figure 3. Typical data trace for SHPB experiment.

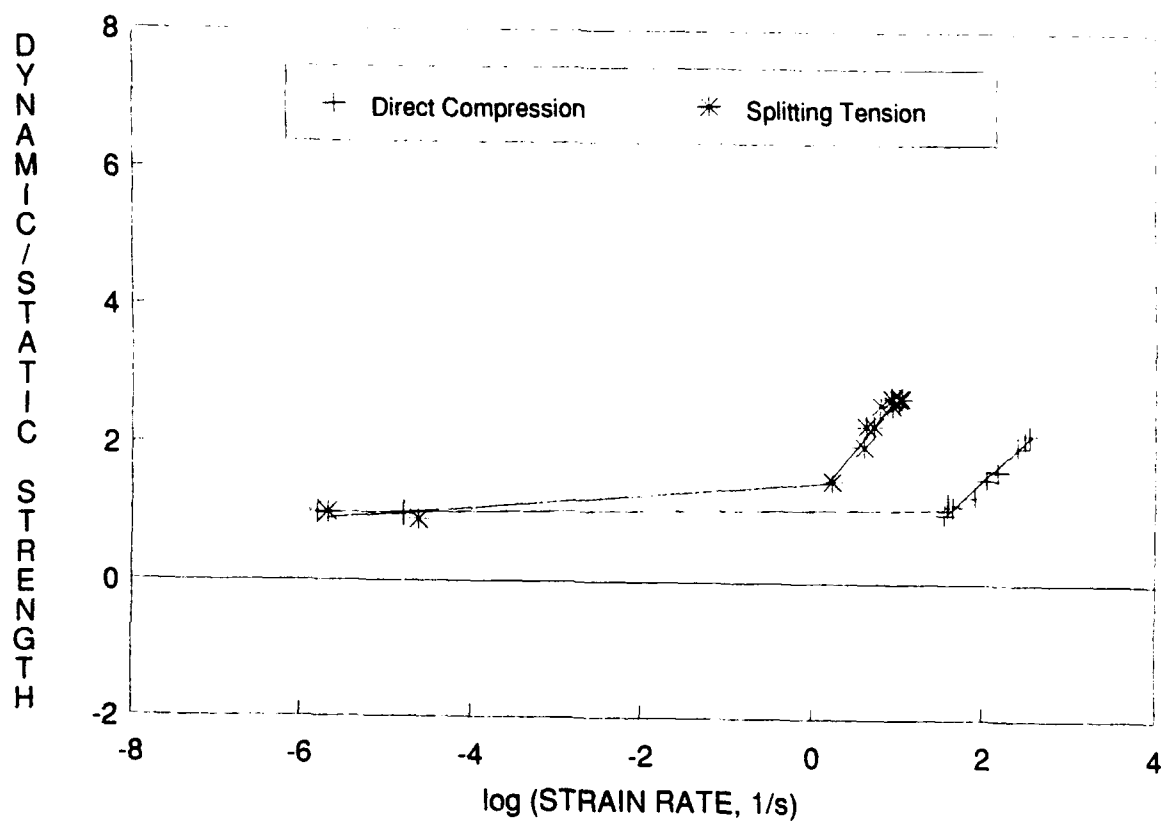


Figure 4. Concrete strength vs. strain-rate.

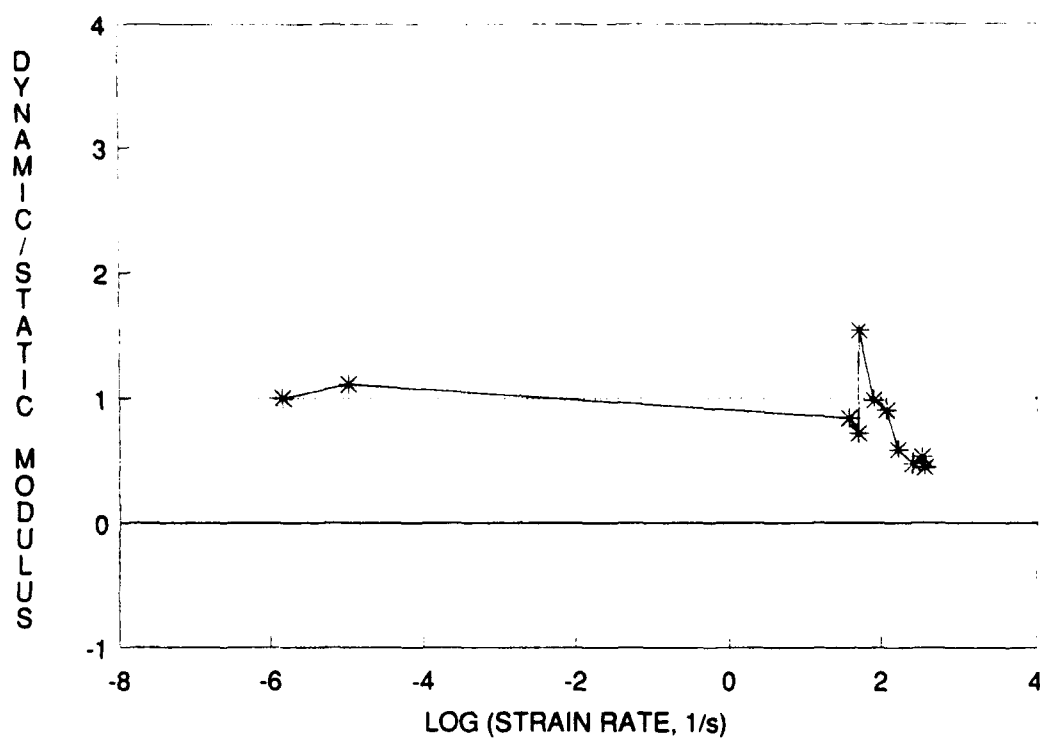


Figure 5. Secant modulus at $.5f'_c$ vs. strain-rate.

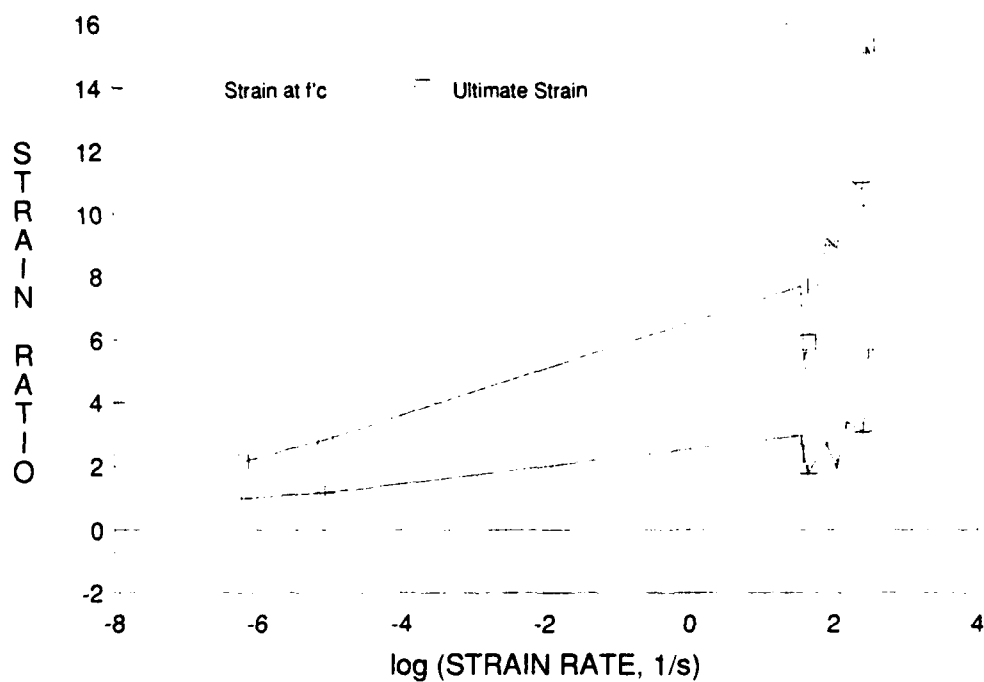


Figure 6. Strain at f'_c and ultimate strain vs. strain-rate.

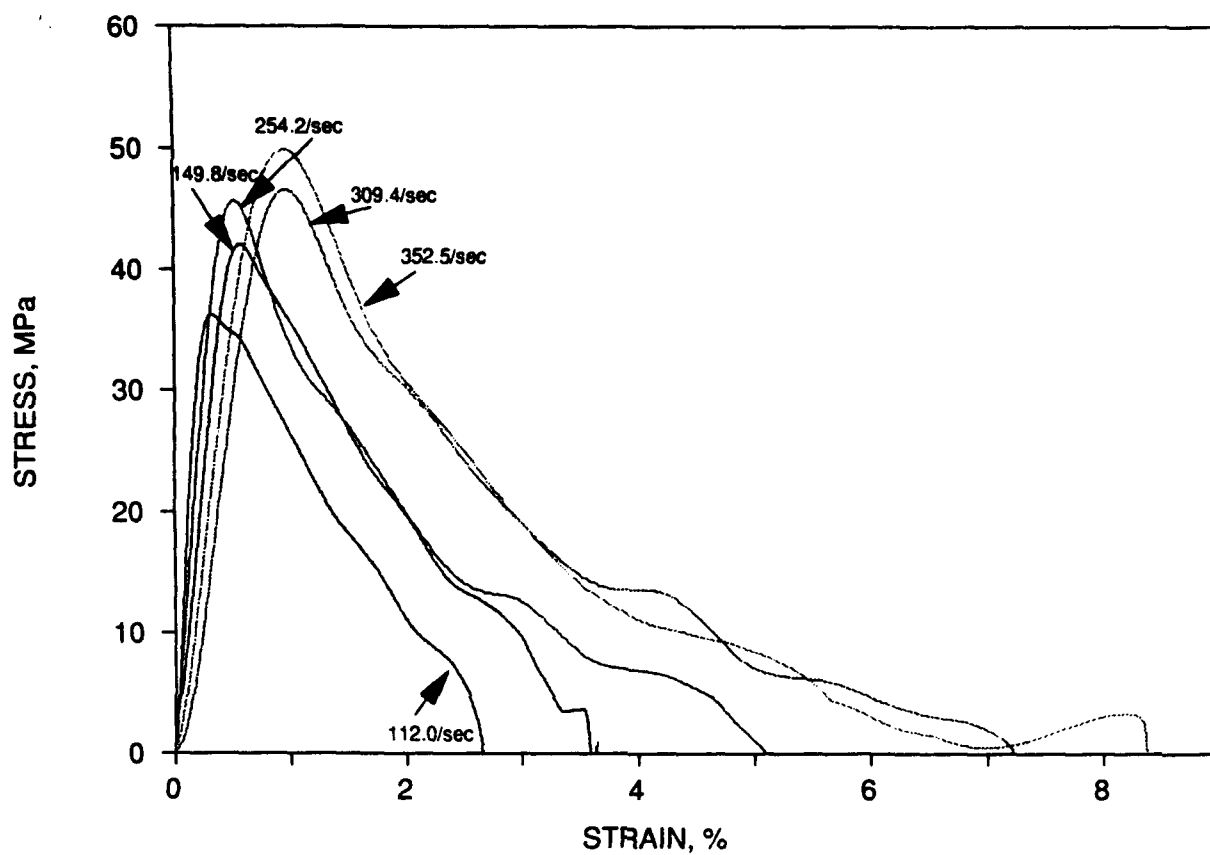


Figure 7. Stress-strain curves for various strain-rates.

FRACTURE ENERGY OF CONCRETE UNDER DYNAMIC TENSILE LOADING

J. Weerheijm^{*)}, J.C.A.M. van Doormaal^{*)} and L.J. Sluys^{**)}

^{*)} TNO Prins Maurits Laboratory, P.O.Box 45, 2280 AA Rijswijk, The Netherlands

^{**)} Delft University of Technology, Department of Civil Engineering,
P.O.Box 5048, 2600 GA Delft, The Netherlands

ABSTRACT

In an experimental programme, impact tensile tests were performed on notched and unnotched cylindrical specimens in a Split Hopkinson Bar apparatus to determine the dynamic fracture energy of concrete. The results have been compared to static deformation controlled tensile tests. Distinction must be made between material and structural response in order to obtain a correct material model. The combination of experiment and numerical calculations offers the possibility to analyse these contributions. It has been observed that the fracture energy just slightly increases with the loading rate.

INTRODUCTION

For the design of concrete structures, which must resist explosive and impact loadings, knowledge of the dynamic material behaviour is essential. Advanced computer codes offer the possibility to calculate the distribution of the load in complex loading situations. A necessary condition to obtain reliable results, is the implementation of a correct material model.

In this study, we focus on the dynamic deformation capacity and fracture energy. From many studies in preceding years ([1], [2], [3], [4]) it is well known that a higher loading rate results in a higher uniaxial strength, but the influence of the loading rate on the deformation capacity is more debatable. There is still little knowledge of the dynamic deformation capacity and fracture energy.

Uniaxial impact tensile tests have been performed by TNO-PML and DUT in a Split Hopkinson Bar apparatus on notched cylindrical specimens in order to determine the influence of the loading rate on the fracture energy. In former experiments [5] this testing technique in combination with numerical simulation appeared to offer good possibilities for the determination of correct material models.

The results of these tests concerning the deformation capacity will be discussed here. They will be compared with static experiments and a numerical simulation. The influences of the loading rate, geometrical aspects and inertia on the fracture energy will be of primary interest.

DEFORMATION UNDER DYNAMIC LOADING

The general opinion ([6] and [7]) is that the deformation capacity increases with the loading rate, in the same fashion as the strength is sensitive to the loading rate. Figure 1, determined by Körmeling [6] from impact tests with a Split Hopkinson Bar apparatus, illustrates this sensitivity for concrete under dynamic tensile loading. This figure shows that the strength increases, but that the maximum deformation is not affected by the strain energy that can be absorbed and which can be found by

integrating the load-deformation-curve, is proportional to the increase in strength. This can be described by:

$$G_{\text{frac,dyn}} = \frac{f_d}{f_{st}} \cdot G_{\text{frac,stat}} \quad (1)$$

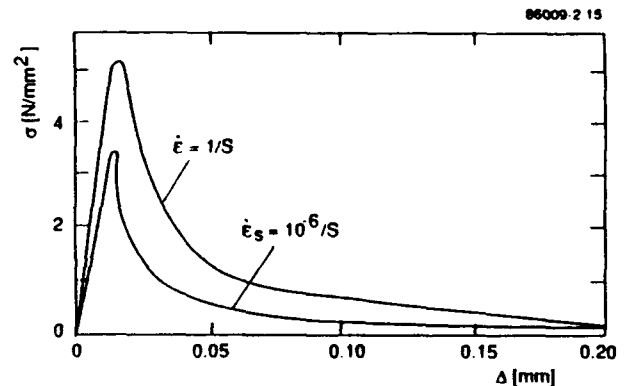


Figure 1 Rate effect on load-deformation curve for tension [6].

If this relation (1) is true, it implies that the rate dependence on the tensile strength in the pre-peak deformation process, where micro-cracking occurs, can be extended to the macro-cracking process. But the question arises whether the increase in absorbed energy during the post-peak deformation is not just caused by structural instead of material response. The fracture zone for instance is not fixed and multiple cracking occurs. The larger number of (micro) fracture planes increases the total fracture energy. But this does not mean that the fracture energy per fracture plane changes. Inertia effects can also influence the behaviour. These aspects were not considered in the past.

The possibility that deformation data could be influenced by these aspects of structural response was realised by the authors [5]. Therefore, we tested notched specimens in a Split Hopkinson Bar apparatus. Because of the notch, fracture was limited to a single zone.

As a result of these tests, after taking the influence of the notches into account, a tendency was found that concrete had a more brittle behaviour under a higher loading rate. The total deformation decreased with an increasing loading rate and the fracture energy remained approximately the same. Furthermore, it was shown by numerical simulation that these data still overestimated the real fracture energy because of inertia effects.

EXPERIMENTS

The conclusion of a more brittle behaviour under higher loading rates by Weerheijm [5] was based on a small set of experiments and the test conditions were not optimal. The experiments were carried out within the scope of a biaxial study, in which the primary interest was neither the deformation capacity nor the fracture energy under uniaxial load conditions. For the biaxial study it was necessary to use a prismatic geometry, which is not the best choice for uniaxial tests. Furthermore, the comparison with static behaviour was done on the basis of experimental data available in literature and not on the basis of static experiments on the same specimens.

For these reasons, it was decided to perform additional tests with improved conditions to verify the test method and the conclusion of the previous experiments with regard to the influence of the loading rate on the deformation capacity and fracture energy.

In the Split Hopkinson Bar apparatus impact tensile tests with a loading rate of approximately 20 GPa/s were performed on cylindrical notched specimens with a diameter of 74 mm and a height of 100 mm. The notches were 2 or 4 mm deep, which corresponds with a reduction in cross-section of 10% or 20%. These test series will further be indicated as D2 and D4 (D stands for dynamic and the number for the depth of the notch). Unnotched specimens (indicated as D0) were also tested.

Static, deformation controlled tests with a loading rate of approximately 0.03 GPa/s were performed on the same notched cylindrical specimens at the DUT (indicated as S2 and S4, where the S stands for static).

From the measurements the load-deformation curves of the total specimen and of the fracture zone could be derived. They are

depicted in Figures 2 and 3. These load-deformation-curves give information about the deformation and fracture energy of the specimens. These data are given in Table 1.

Table 1 Strength, deformation and fracture energy

		D0	D2	D4	S2	S4
dp/dt	[GPa/s]	24.0	22.8	19.7	0.03	0.03
f_t	[MPa]	5.1	4.6	3.9	2.5	2.4
df_{top}	[μ m]	-	6.0	9.5	4.5	7.7
df_{tot}	[μ m]	270	153	135	>200 [#]	>200 [#]
$G_{f,top}$	[N/m]	-	22	25	9.8	16.1
$G_{f,tot}$	[N/m]	270	163 [*]	170 ^{**}	108 [*]	114 ^{**}

[#] Tests were stopped at 200 μ m

^{*} Determined at a deformation of 153 μ m

^{**} Determined at a deformation of 135 μ m

Some observations can be made from the load-deformation-curves and from the deformation data.

The expectation that the strength increases with the loading rate has been confirmed. The specimen strength in the dynamic tests was higher than in the static tests. This increase can be attributed to the changing geometry of the fracture plane and inertia effects on crack propagation (see model as described by the author [5]).

The difference in strength between the D0, D2 and D4 specimens shows that another phenomenon also influenced the strength of the specimen. This phenomenon must be coherent to the application of notches since that is the only difference between the specimens. The most probable explanation is the

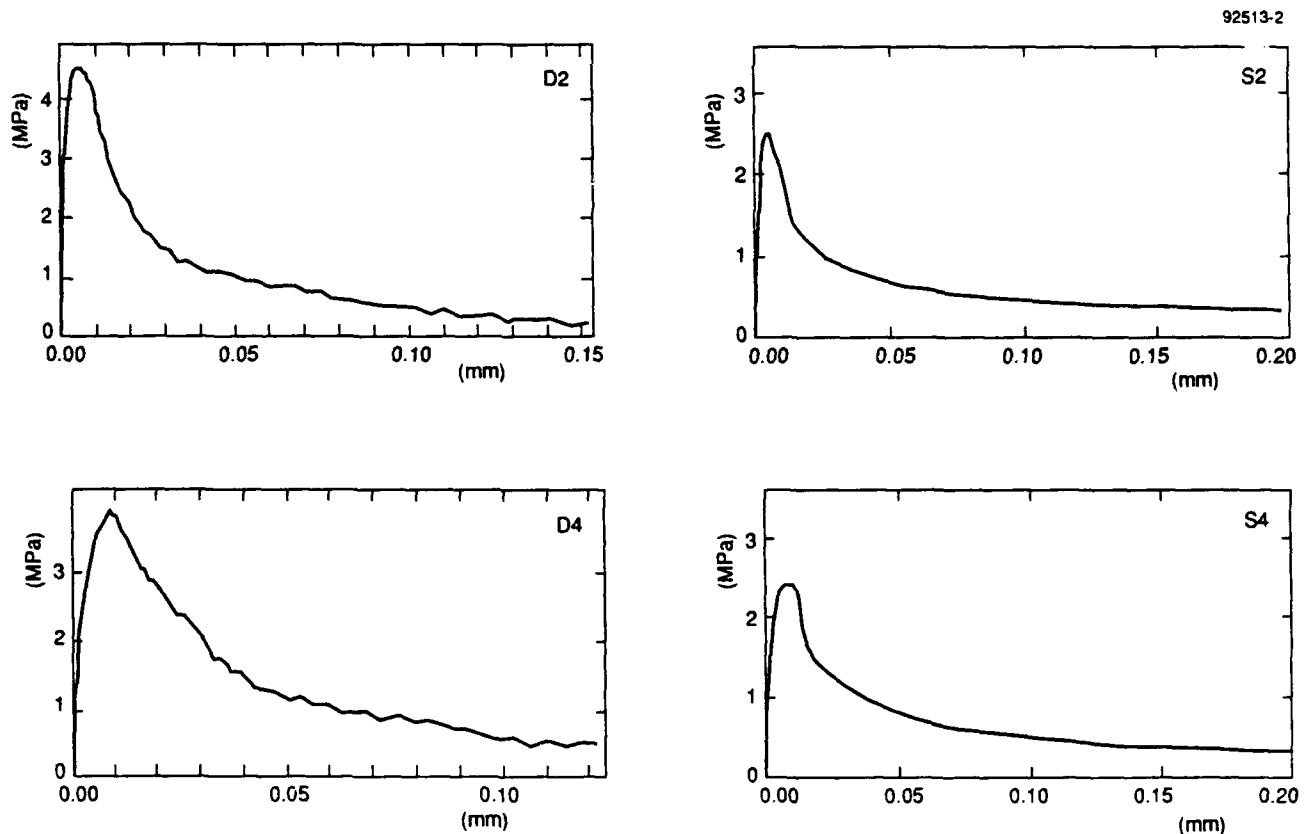


Figure 2 Average load-deformation-curves of the fracture zones.

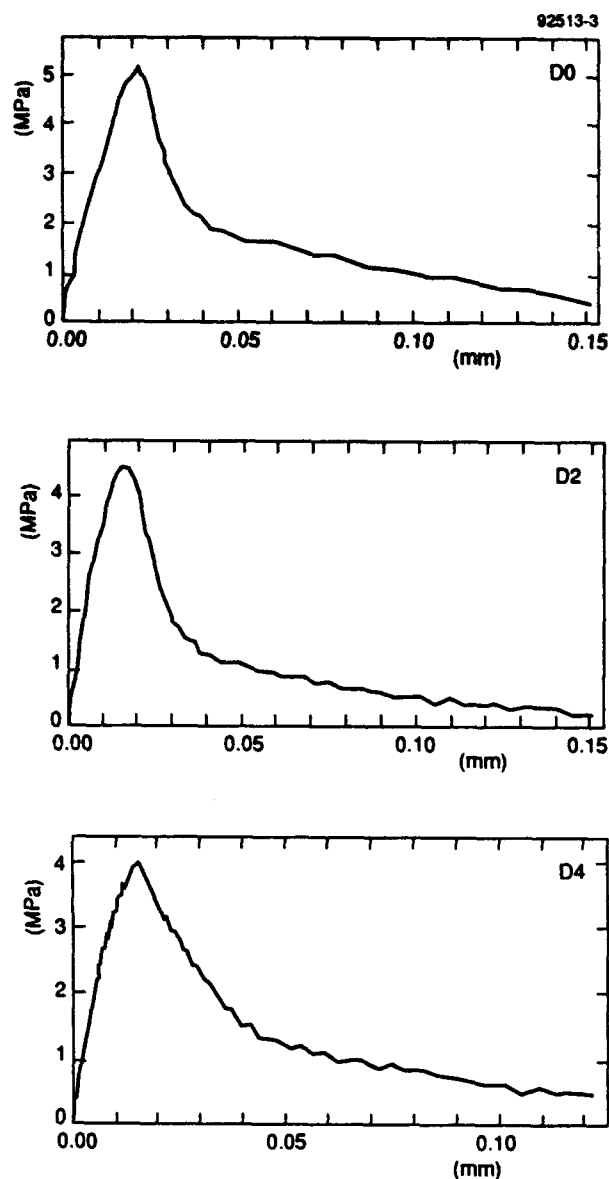


Figure 3 Average load-deformation-curves of the whole specimen.

sensitivity for stress concentrations, which occur due to the applied notches. This sensitivity is more pronounced for high loading rates, when time available for redistribution is limited.

In the dynamic tests the pre-peak deformation is larger than in the static tests. From comparison of the deformation-load-curves it emerges that for the dynamic curves the ascending branches become nonlinear sooner. In the D2-series the nonlinearity starts at approximately 60% of the maximum stress and in the D4-series the nonlinearity starts at approximately 30%. In the static tests nonlinearity starts at approximately 80% of maximum stress for the S4-series and at approximately 90% for the S2-series. Because of stress concentrations at the notch the strength is reached locally and the specimen becomes nonlinear. Micro-cracking increases and enables redistribution

of stress before maximum stress (see also [5]), thanks to which failure is delayed. Another reason why the resistance did not immediately drop is rotation. While the strength is reached on one side of the specimen, the other side has still some reserve. Rotation occurs because of the heterogeneity of concrete.

Comparison of the dynamic deformation data of unnotched specimens with those of notched specimens shows clearly the effect of the size of the fracture zone. In the unnotched specimen the location of the fracture zone was not fixed, which caused multiple cracking, a larger deformation and a higher fracture energy. This effect can also be observed from the form of the load-deformation-curve for the D0-series. The ascending branch of the curve showed a considerable pre-peak deformation. Since this non-linear response cannot be caused by notch-sensitivity as for the D2 and D4-series, it must be attributed to the larger fracture zone, where multiple micro-cracking occurs. The descending branch showed a similar feature. After an initially steep drop the descending branch becomes moderate sooner.

The dynamic fracture energy, found in the D0, D2 and D4 test series is larger than the fracture energy in the static experiments S2 and S4. This result is in contradiction with the results of the former experiments [5], in which it was seen that the dynamic fracture energy was approximately the same as static and showed the tendency to decrease with an increasing loading rate.

This contradiction can be explained by the difference in geometry of the specimens in both experimental programmes. In the former programme the specimens were prismatic (50 mm wide, 80 mm deep and 100 mm high). The cross-section was reduced by applying notches at two opposite sides. So, the cross-section was reduced in just one direction. Due to heterogeneity concrete behaves asymmetrically. This means that in one direction failure starts earlier than in the other direction. In the prism probably the weakest direction was reduced, resulting in a more brittle behaviour.

The asymmetrical behaviour of concrete is shown in Figure 4, which gives the load-deformation-curves, derived from measurements at different sides of the specimen. It is obvious from the differences in mainly the descending branches that the average of the left and right curves differs from the average of the front and rear curve: which also results in different fracture energies. And it is likely that again another result would be found if measurements were performed at two other opposite sides of the concrete specimen.

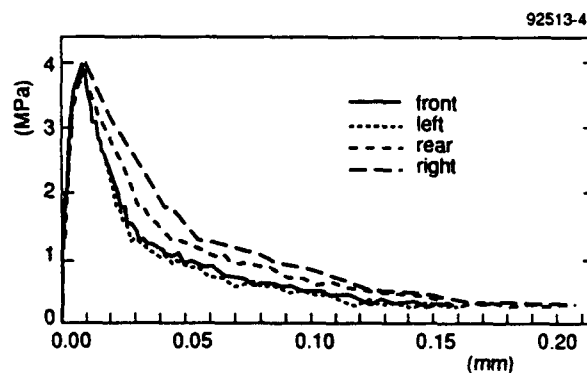


Figure 4 Load-deformation curve at different sides of the specimen for the D4-series.

Next, it will be shown with use of numerical results that inertia influences the energy data. These inertia effects are another reason why the fracture energy found from the current tests is higher. The higher loading rate increases the influence of inertia.

The fracture energy in the dynamic experiments is not as large as predicted by equation (1). This equation overestimates the dynamic fracture energy as is shown by the difference in the predicted and the measured dynamic fracture energy and by Figure 5.

Based on equation (1) a fracture energy of respectively 220 N/m and 233 N/m for the 2 and 4 mm test series is predicted, which is more than found in the dynamic test series D2 and D4.

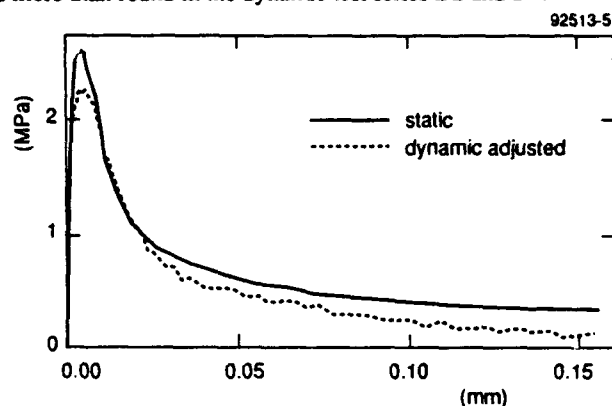


Figure 5 Comparison of the static load-deformation curve with the dynamic curve which has been divided by f_d/f_{st} for the D2-series.

In Figure 5 the static and dynamic load-deformation-curves for the 2 mm test series are compared. For that purpose, the dynamic curve is divided by f_d/f_{st} . The figure shows that the form of the moderate part of the descending tail is not the same in both curves. It is due to this part of the curve that the fracture energy is overestimated by equation (1). The ascending branch and the steep drop is the same for both curves except for the top of the curves because of the greater notch sensitivity in the dynamic experiments.

NUMERICAL SIMULATION

The response measured in the experiments is influenced by structural effects as the geometry, the inertia of the specimen and the stiffness of the experimental set-up. For this reason the material parameters which determine the post-peak response can not be derived directly from the test. A combination with a numerical analysis can overcome this problem.

The specimen with a 4 mm notch was modelled with eight-noded axis-symmetric elements, using a nine-point Gaussian integration scheme. By making use of the axial-symmetry of the specimen it suffices to analyse a plane section of the specimen along its axis of symmetry. The finite element modelling of the experimental set-up was done similarly to a previous study on prismatic specimens (see [8]). The elastic material properties have been taken as: Young's modulus $E_c = 40$ GPa, Poisson's ratio $\nu_c = 0.2$ and mass density $\rho_c = 2325$ kg/m³ for the concrete and $E_a = 68$ GPa, $\nu_a = 0.2$ and $\rho_a = 2400$ kg/m³ for the aluminium.

A smeared crack model [9] was used to model fracture in the notched zone. For the inelastic material parameter set we

followed a dual approach, namely, that for the tensile strength we included the dynamic effect and for the fracture energy we did not.

The increase of the tensile strength under dynamic loading conditions is measured in this programme and is commonly accepted (e.g. [4]). The measured value, $f_{ct} = 4.0$ MPa, in the D4-series is influenced by geometrical effects and is not a material parameter. It turned out that the value we had to put in the smeared crack model should be taken larger, namely $f_{ct} = 5.2$ MPa, to compute the same tensile strength as it has been measured in the test. Compare this value with the strength found in the D0-series.

One of the objectives of this study is to investigate the influence of the strain rate on the fracture energy. The fracture energy of the specimen is influenced by three effects, namely (i) the geometry of the specimen, (ii) the inertia of the specimen and (iii) a possible increase of the material parameter due to rate-effects. The first two effects have been covered by the numerical simulation. By taking the static value for the fracture energy $G_f = 125$ N/m the third effect has been analysed.

Next to the tensile strength and the fracture energy two parameters determine the smeared crack model, namely the shape of the strain-softening curve and the crack band width h .

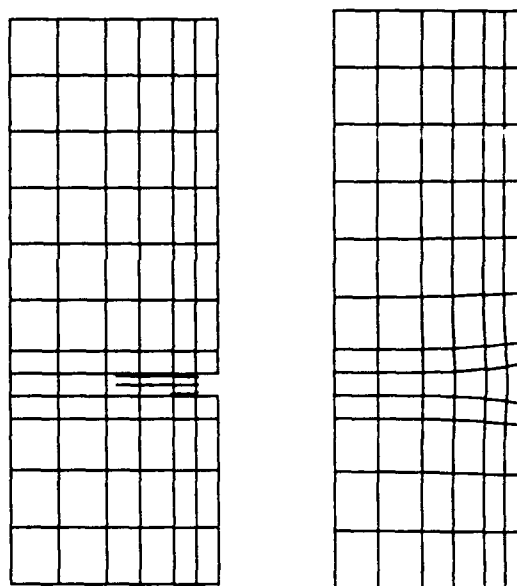


Figure 6 Crack patterns and displacements.

The power-law function of Moelands [10] has been taken to describe the nonlinear post-peak behaviour. The crack band width h is a parameter which controls the mesh sensitivity of the solution. A finite element representation of strain-softening materials results in a severe mesh dependence, because the crack will always propagate along one row of integration points [8]. But by introducing a parameter which is dependent on the size of the zone belonging to that row of integration points, the result can be kept objective with respect to the finite element size.

The results have been plotted in Figures 6 and 7. Cracks start to propagate in one row of elements from the notch to the centre of

the specimen. In Figure 6 the crack pattern and the total displacements show the development of the crack plane. When the crack reaches the axis of symmetry the deformation pattern changes into a symmetric failure mode. In Figure 7 the stress-deformation curve has been plotted, where σ represents the vertical stress at the top of the specimen and δ the deformation at the notch.

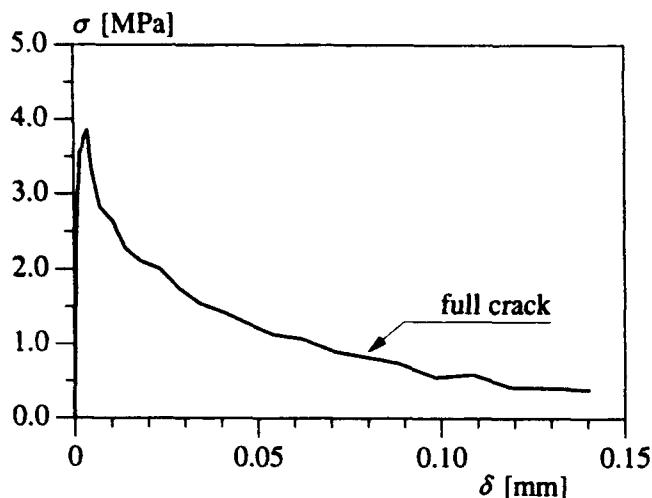


Figure 7 Calculated stress-deformation curve in fracture zone.

Two main conclusions can be drawn from the calculations. First, the inertia of the specimen contributes to the increase of G_f in comparison to the static case. This phenomenon is obvious from Figure 7 in which it is observed that at a certain stage a full crack situation occurs, without the ability to transmit a force. Despite of the full crack the stress contribution to inertia effects is still present.

Secondly, comparison of the calculated load-deformation curve and the measured curve shows that the long tails, in which inertia dominates the transmitted force, almost coincide. The main difference occur just beyond the peak. The applied softening model and the static G_f (125 N/m) results in a calculated curve just below the measured load-deformation curve. Because geometry and inertia effects have been taken into account, the difference is caused by a small increase of G_f due to the rate-dependent material response.

So far, only the first numerical simulations of the experiments have been carried out. A complete numerical study will be carried out including a variation of loading rate and geometry (notch-depth) to quantify the different contributions (geometry, inertia, material) to the fracture energy. By following the experimental-numerical approach for a variety of problems a proper material model should be derivable.

At this stage, it is still recommended to apply the static fracture energy value and the power-law function of Moelands [10] to present the softening branch for dynamic response calculations.

CONCLUSIONS

As a result of the research programme the following conclusions can be drawn:

- Deformation data in dynamic experiments are influenced by structural response. This has been demonstrated by the difference (40-50%) in total deformation and fracture energy between unnotched and notched specimens
- The observed dynamic fracture energy of a specimen is larger than the material fracture energy because of inertia effects. These effects are responsible for the observed and calculated long tailed load-deformation curves.
- The fracture energy slightly increases with the loading rate.
- In order to obtain the best results currently possible, it is recommended to apply the static fracture energy in dynamic calculations.

REFERENCES

- [1] Reinhardt H.W., Concrete under impact loading. Tensile strength and bond, Heron, Vol. 27, No. 3, 1982
- [2] Suaris W. and Shah S.P. Constitutive model for dynamic loading of concrete. Fracture Mechanics of Concrete, ed. F.H. Wittmann, Elsevier Science Publisher B.V., Amsterdam, 1983
- [3] Jensen J.J., Ductility of high strength concrete under special loading conditions, SINTEF Report, No STF65 A91011, Norway, December 1990
- [4] Zielinski A.J., Fracture of concrete and mortar under uniaxial impact tensile loading, Dissertation, Delft University of Technology, Delft, 1982
- [5] Weerheijm J., Concrete under impact tensile loading and lateral compression, Dissertation, Delft University of Technology, Delft, 1992
- [6] Körmeling H.A. and Reinhardt H.W., "Strain rate effects on steel fibre concrete in uniaxial tension", Int. Journal of Cement Composites and Lightweight Concrete, Vol. 9, No. 4, pp. 197-204, 1987
- [7] Oh B.H., Fracture behavior of concrete under high rates of loading, Int. J. Eng. Fract. Mech., Vol. 35, No. 1/2/3, 1990, pp 327-332
- [8] Sluys L.J., Wave propagation, localisation and dispersion in softening solids, Dissertation, Delft University of Technology, Delft, 1992
- [9] Borst R. de and NAUTA P., Non-orthogonal cracks in a smeared finite element model, Eng. Comp., B 2(1), pp. 35-46, 1985
- [10] Reinhardt H.W., Cornelissen H.A.W. and Hordijk D.A., Tensile tests and failure analysis of concrete, J. Struct. Engrg. ASCE, 112(11), pp. 2462-2477, 1986

A Numerical Simulation of Stress Wave Propagation in Concrete and its Effect on Spall and Breach in Scaled Tests

Charles J. Oswald
Kirk A. Marchand
Ben H. Thacker

Southwest Research Institute
6220 Culebra Road
San Antonio, TX 78228-0510

Abstract

Numerical simulation is used to analyze the stress wave induced in small scale and prototype reinforced concrete slabs by high pressure airblast loading from close-in detonations. The stress wave is of interest because localized concrete damage such as spall and breach, which is caused by the wave, does not scale in replica scaled tests. In this paper, through thickness stress histories calculated with the PRONTO2D code are shown to compare reasonably well with experimental results. It is also proposed that the use of reduced concrete strength in small scale models can be an effective way to produce subscale localized damage similar to that in the prototype.

Introduction

Reinforced concrete structures have been used for decades as protective structures for use in warfare, in hazardous material processing and storage applications, and as robust structures designed for secure storage of sensitive or valuable material. To more effectively design concrete structures for these applications it is important to gain a better understanding of concrete spall (rear face impact induced tensile failure) and localized breach or shear failure. These types of response can control the design in cases such as near miss bomb explosions in air or soil, storage facilities subjected to the accidental detonation of high densities of stacked munitions or explosives, or secure storage facilities attacked with terrorist tools or explosives.

In order to establish this understanding, a combined theoretical and experimental approach is necessary. Typically, experimental testing of structural response to blast loading relies heavily on the use of small scale testing. However, as the body of this paper discusses, significant problems have been encountered in applying this approach because localized spall and breach observed in scaled tests does not compare well with that in full-scale tests. This paper describes a computational simulation of the stress wave induced in concrete by close-in explosions and applies the computational approach to the problem of scaled testing of localized concrete response.

Use of Scale Modelling to Investigate Concrete Spall and Breach

In this section, scale modelling is briefly discussed since a primary goal of this paper is to apply the computational approach which is presented to available scaled data of localized concrete response. Principally, replica, or geometric scaling has been used for blast and impact loaded structures since this approach is more straightforward than other types of scaling and a number of complexities, such as large plastic responses and dramatic failures, often occur. Replica scaling laws require that all dimensions and

time scale with the scale factor, and all material properties, such as strength, stiffness (modulus), and density are scale independent. All dimensionless parameters are also scale independent (the same in both the prototype and scale model). Provided that replica scale modelling laws are correctly applied, the damage mode and relative amount of damage should be scale independent.

A potential problem with the application of replica scaling to cases with dynamic loading is that the strain rate, which can affect material parameters such as strength and stiffness, is not identical in the prototype and scale model. In almost all previous scale tests on reinforced concrete structures the effect of load or straining rate on material strength, stiffness or ductility has been ignored. This assumption is not a bad one in cases of blast and impact provided the primary response mode of concern is flexural motion where strain rates are below 0.1 sec^{-1} . In these cases scale model tests involving blast loading of structures have typically yielded results which compare well against those obtained from full scale experiments.[1][2][3]

However, in a number of recent cases where scale modelling has been used to investigate spall, breach, and concrete wall breakup under severe close-in loading, good correlation with full-scale results has not been observed. This is due in large part to the fact that strain rate has a significant effect on material properties in this response realm. The principal set of data that will be used throughout the remainder of this paper to consider the effect of strain rate on concrete strength is shown in Figure 1. This data was generated through the use of the Split Hopkinson Pressure Bar (SHPB).[4] Concrete tensile strength is of primary interest here because most spall and breach damage is caused by tensile stresses induced by close-in explosions which overcome the relatively low tensile strength of concrete.

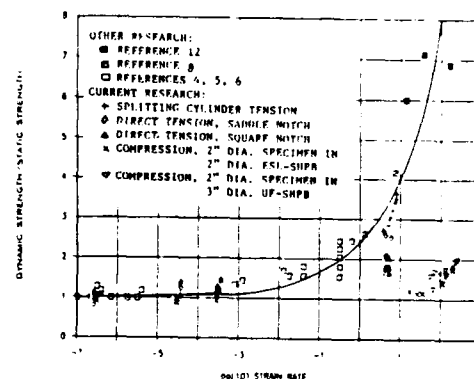


Figure 1. Tensile and Compressive Strength Ratios of Concrete versus \log_{10} of strain rate (from Reference 4)

Data from Recent Scaled Tests Investigating Concrete Spall and Breakup

An example of replica scaled tests where the observed localized damage did not follow replica scaling laws is shown in Table 1. This data is from a large test series performed recently by SwRI for the Department of Energy (DOE) which studied the breakup of reinforced concrete and masonry structures subjected to close-in explosive loading.[5] Replica scaling laws were used to construct the scaled walls in the test series and Hopkinson-Cranz scaling (which is based in replica scaling) was used to apply the scaled blast loads. The reinforcing steel size and placement and concrete aggregate size were scaled except as noted in the table and material strengths, and therefore stiffnesses, were scale independent within practical limits, except for Test 3.1. In this test the scale model strength was intentionally reduced in order to cause damage more similar to that measured in the prototype.

The test results in Table 1 clearly show that more severe modes of damage occurred in the larger scale tests in each pair of scaled tests. The debris velocities also were not scale independent as replica scaling predicts. Other wall breakup parameters, such as total number of debris and average debris weight, also did not follow replica scaling laws. If the response of the prototype had been predicted solely by "scaling up" the response measured in the scale model using replica scaling laws, it would be significantly underpredicted.

In addition to the test series summarized above, other researchers have also noted that local damage to concrete from close-in explosive loading in small scale studies is significantly less than that in the prototype.[6][7] It is emphasized here that this trend is observed within the limited loading realm of close-in airblast loading of concrete and masonry walls.

Stress Wave Propagation in Concrete

Most of the damage to the concrete walls in Table 1 was caused by the stress wave that propagated through the thickness of the wall near the explosive, reflected off the unloaded face as a tensile wave with a magnitude greater than the dynamic concrete tensile strength, and failed the concrete. As shown in Figure 1, the dynamic tensile strength differs from the static strength by a factor which depends on the strain rate of concrete response to the stress wave. An understanding of the stress wave propagation and the concrete response is therefore critical to an understanding of how a scaled test should be conducted so that it will accurately predict concrete spall and breakup observed in full-scale.

Figure 2 shows an idealized representation, based on results obtained with the computational approach explained below, of how the stress wave generated by an close-in explosion

propagates through the thickness of a twelve inch concrete slab. At time 1, the wave is shown prior to reflection off the back face of the slab. The wave shape is similar to that of the applied pressure history except that an elastic precursor, which has a stress slightly greater than the assumed unconfined concrete yield stress, travels ahead of the rest of the wave, where much higher stresses exist. The peak pressure and impulse in the high stress "plastic" region of the wave attenuate as the wave propagates so that in a very thick slab the wave shape becomes nearly square with a peak stress near the unconfined yield stress. The concrete is assumed to be an elastic, perfectly-plastic material where only the deviatoric stresses cause yielding. The equation for the von-Mises stress (σ_0), which is used in the computational approach to define the yield condition, is shown below in terms of the three principal stress differences.

$$\sigma_0 = \left[\frac{1}{2} [(\sigma_1 - \sigma_2)^2 + (\sigma_2 - \sigma_3)^2 + (\sigma_3 - \sigma_1)^2] \right]^{1/2}$$

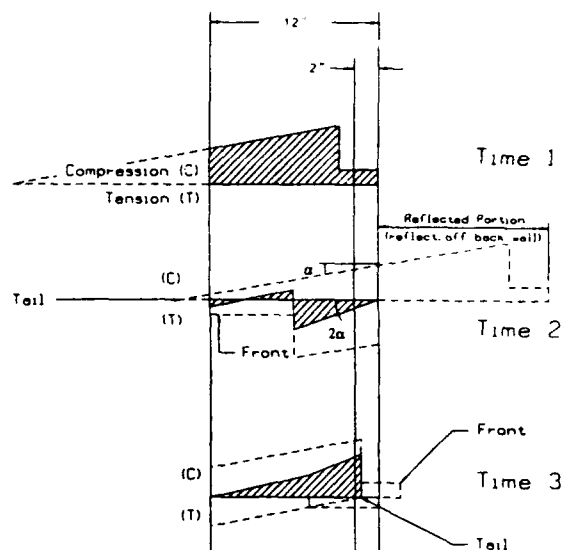


Figure 2. Simplified Illustration of Stress Wave Propagation in Concrete Slab

Table 1. Summary of Results from Tests of Reinforced Concrete Walls Investigation Effect of Scale Factor

Group	Test No.	Scale	Concrete Cylinder Strength (psi)	Wall Thickness (inches)	Typical Wall Dimension (ft)	Charge Weight (lbs)	Standoff (ft)	Wall Damage	Debris Velocity (ft/sec)	
									Maximum	Average
1*	1.1	1/2	6400	6	4.5	25	1.5	Total Collapse	92	62
1*	1.2	1/4	5800	3	2.25	3	0.75	Spall	54	25
1*	3.1	1/4	1600	3	2.25	3	0.75	Total Collapse	108	65
2	3.3	Full	4000	12	9	25	1.5	Single Crack	32	26
2	3.4	1/4	5000	3	2.25	0.4	0.375	Large Spall Area	17	15

* 1/4" aggregate used for all tests

Stress in the through thickness direction greater than the von-Mises yield stress exist because large stresses also develop in the other two directions. Plots of calculated stresses in these directions confirm that this is the case. The attenuation of the plastic portion of the wave is most probably due to the gradual conversion of the energy in this portion of the wave into strain energy. The large strains also cause significant lateral strains which are in turn restricted by the lateral confinement of the localized region of the slab. This lateral restraint is the cause of the large lateral stresses that permit the plastic portion of the wave to exist.

At time 2, the plastic portion of the wave has reflected and the stress at a point in Figure 2 two inches in from the back face is tensile. For the simplified case shown here, where the slope of the plastic portion of the stress wave is constant, the tensile stress at a given point remains constant until either the whole wave passes through the point or the front of the wave reflects off the loaded face and passes back through the point as a compressive wave. As the stress history shown at time 2 indicates, the tensile stress is heavily dependent on the slope of the receding portion of the stress wave (the "backslope") and distance from the back face. For a non-idealized case, this slope is not constant.

The stress history at time 3 shows the wave has reflected off the loaded face as a compressive wave and has passed through the point of interest two inches off the back face. Because of the high sound speed of concrete, the wavelength of the stress wave caused by blast loading is usually equal to several wall thicknesses and therefore "wraps around" on itself within the thickness. The duration of the tensile stress at any point through the thickness is dependent on time required for the stress wave to wrap around as a compressive wave, which is a function of the wall thickness and the concrete density and stiffness.

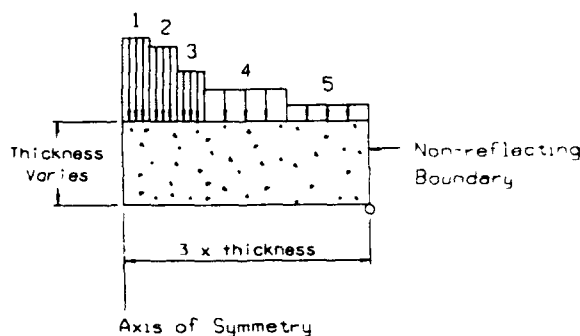
Description of Computational Study of Concrete Response to Close-in Blast Loading

The previous section described the propagation of a stress wave induced in the slab near the explosive for the blast loading realm of interest here in a general manner. In the following sections results from the numerical simulation of two experiments where close-in blast loading was applied to concrete slabs are presented and discussed.

PRONTO2D, which is used to perform the simulations, is a two-dimensional transient solid dynamics code for analyzing large deformations of highly nonlinear materials subjected to extremely high strain rates.[9] It is the latest in a series of transient dynamics finite element codes that has been developed at Sandia National Laboratories, beginning with HONDO.[10] As such, PRONTO2D contains a number of state-of-the-art numerical algorithms, including an adaptive timestep control algorithm, a robust hourglass control algorithm, an accurate incremental rotation algorithm, and a robust surface contact algorithm. Four-noded, uniform-strain, quadrilateral elements with single-point integration are used in the finite element formulation. Beyond its general capabilities, PRONTO2D was chosen for this study because of the extensive suite of existing constitutive models, and the fact that new models can be easily added. A three-dimensional derivative of the program is also available (PRONTO3D).

The equations of motion are integrated using a modified central difference scheme in PRONTO2D. The velocities are integrated with a forward difference and the displacements are integrated with a backward difference. Numerical damping is introduced in the solution by adding artificial viscosity. This prevents high velocity gradients from collapsing an element before it has a chance to respond, and to quiet truncation frequency ringing. The technique used in PRONTO2D is to add viscosity to the "bulk" response. This generates a viscous pressure in terms of the volume strain rate.

Figure 3 shows the model of the concrete slab used in the PRONTO2D simulation of both sets of experiments. The slabs and applied loading were modeled as axisymmetric with the axis of symmetry extending from the center of the charge through the thickness of the slab. Therefore, a circular portion of the slab was modeled centered below the explosive charge. The slab thickness in the model was equal to the actual thickness and the radius of the slab volume considered in the model was equal to at least three times the thickness. This radius was found to give the same results in a preliminary study as a model with a radius equal to six times the thickness. A non-reflecting boundary condition was used at the far boundary through the thickness so that no stress wave reflections would occur there. A very fine mesh (a minimum of 2200 elements) was used for all analyses.



Region in Figure 3	Test in Reference 13		Test 3.4 in Table 1	
1	33000	0.1	23000	0.2
2	15800	0.08	20000	0.2
3	15800	0.08	16000	0.2
4	15800	0.1	11000	0.2
5	5000	0.1	5000	0.25

Figure 3. Model Used in Numerical Simulations of Close-in Blast Loading Applied to Concrete Slabs

The blast pressures applied to the slab surface were calculated from the charge weight and standoff used in the experiments with the CONWEP computer program.[11] This code uses the methodology in the U.S. Army handbook TM5-855 [12] to calculate blast pressures. Separate pressure histories were applied at various distances from the axis of symmetry as drawn to scale in Figure 3 to model the spatial variation in the applied blast load. The pressure and impulse used within these areas were average values calculated from contours of reflected pressure and impulse calculated with the CONWEP code from a free air explosion. A simplified linearly decaying blast pressure history was used in all the analyses which preserved the calculated positive phase peak pressure and impulse. In the case of the test in Reference 13, the pressure distribution was simplified to cause the average pressure over locations in the slab where the stress was measured to be exactly equal to the pressure calculated over the gage locations.

An elastic, perfectly plastic material model was used in all the analyses. A von-Mises yield strength equal to 1.5 times the measured cylinder strength of the concrete in the experimental slabs was assumed. The factor of 1.5 approximately accounts for strength enhancement caused by the high strain rate of the concrete response to the compressive stress wave and enhanced strength due to lateral confinement provided by the concrete surrounding the region of

interest. A Young's modulus equal to $57,000(f'_c)^{1/2}$ was assumed, where f'_c is the measured unconfined concrete strength in the units of lb/in². Also, a Poisson's ratio of 0.18 was assumed.

There are several material models available in the PRONTO2D code including elastic, elastic-plastic with kinematic or isotropic hardening, and a model for soils and crushable foams. The elastic-plastic model used in this analysis allows unlimited volumetric stresses. The soils and crushable foams model allows separate yield criteria to be input for deviatoric and volumetric parts of the response. Several different equations of state are also available that can be used to control the volumetric material response. Some preliminary runs were made using the material model for soils and crushable foams where an elastic, perfectly-plastic criteria was used to model the deviatoric response and a hydrostatic pressure vs. volumetric strain curve based on some limited measurements was used to model the volumetric response. The primary effect of this model was to cause faster attenuation of the plastic portion of the stress wave. The use of this model did not cause an appreciably better fit between calculated and measured stress histories discussed in the next section.

Comparison of Calculated and Measured Stress Histories in a Concrete Slab

The first experiment modeled with the PRONTO2D code is shown in Figure 4. In this test, which was recently conducted at SwRI [13], a set of stress histories were measured in a concrete slab with very thin embedded carbon stress gages at two locations close to the explosive as shown in Figure 4. The measured concrete cylinder strength was 5500 psi. The blast load was applied with a spherical charge of 2.8 lbs of C4. The total slab dimensions were 4 ft by 4 ft by 4 inches thick. The calculated pressure history used in the analysis is summarized in Figure 3.

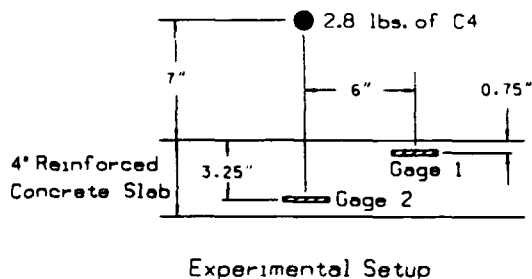


Figure 4. Experimental Setup for Test in Reference 13

Figures 5 and 6 show a comparison of the calculated and measured stress histories at the two gage locations. Compressive stress is positive. Figure 5 shows that the calculated stress history at gage 1 compares very well with the measured value. Figure 6 shows that, at a gage location where more compressive wave propagation occurred prior to the measurement, the calculated peak compressive stresses overestimate measured values. However, there is good correlation between the measured and calculated tensile stress histories and between the duration and shape of the calculated and measured stress histories. Based on the comparison in Figure 6, the material model is evidently not accounting for all the attenuation in the stress wave that occurs during propagation through the concrete above the gage location. It is also possible that the gage did not measure the peak stress in the stress wave. The accuracy of the measured stress histories in Figures 5 and 6 is not really known since this type of in-slab stress measurement has not been made except very recently and only for a limited number of cases.

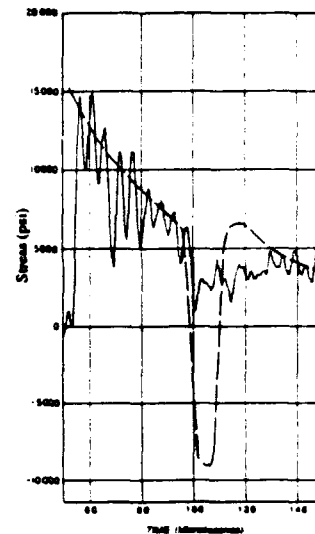


Figure 5. Calculated and Measured Stress Histories at Gage 1 in Figure 4

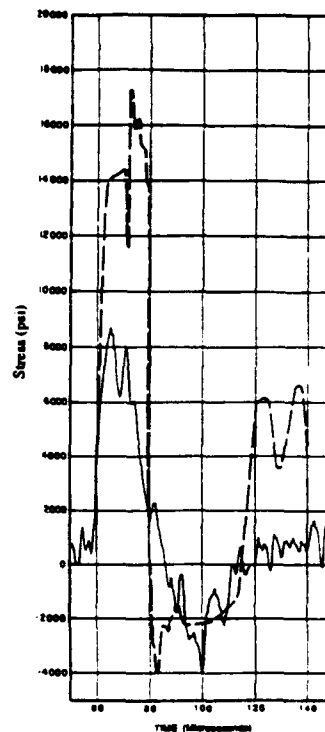


Figure 6. Calculated and Measured Stress Histories at Gage 2 in Figure 4

The second set of experimental tests modeled with the PRONTO2D code are Test 3.3 (full-scale) and Test 3.4 (quarter scale) described in Table 1. As Table 1 shows, scaled blast loads were applied. This means that the peak pressures in both tests were identical at similar locations (the geometry scales with the scale factor) and the duration of the blast load in the small scale test was one quarter that in the full-scale test. The pressure distribution used for the full-scale test (Test 3.3) is summarized in Figure 3. The pressure distribution used in the model of the quarter scale test was scaled from this distribution.

Figures 7 and 8 show the stress histories calculated at scaled locations near the back face of the models of Tests 3.3 and 3.4. One point is along the axis of symmetry and the other point is 1.5 ft in full scale (0.375 ft in quarter scale) off the axis of symmetry. The observed radius of the spall area in the full scale test was approximately 2 ft. Both locations are 2.5 inches away from the back (unloaded) slab surface in full scale, which is approximately equal to the observed spall depth. The stress history at the loaded face directly below the charge, which corresponds to the applied blast pressure history at this location, is also shown for reference.

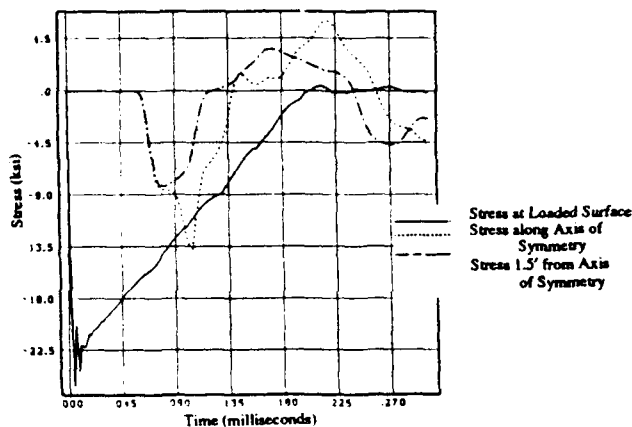


Figure 7. Calculated Stress Histories for Test 3.3 (Full Scale) in Table 1

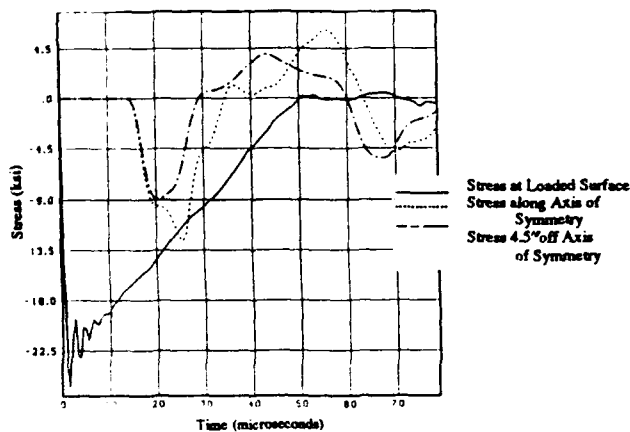


Figure 8. Calculated Stress Histories for Test 3.4 (Quarter Scale) in Table 1

The figures show that the calculated stress histories scale according to replica modelling laws where the stress is the same in both the prototype and scale model and time scales with the scale factor. Since the primary interest in these tests is the fact that the prototype had significant spall whereas the scale model had no spall, the calculated tensile stress histories (shown as positive stress in Figures 7 and 8) are important. The peak tensile stress is equal to between 4000 and 6000 psi, for an average of 5000 psi, at the two locations and the full-scale rise time at both locations is near 50 microseconds. This loading rate information, along with an assumed concrete modulus of 4.0×10^6 psi, can be used to calculate the strain rate. Then the measured relationship between strain rate and dynamic increase factor (DIF) in Figure 1 can be used to calculate the DIF which can be applied to the static concrete tensile strength to determine dynamic strength. The static tensile strength is assumed to be one tenth the measured cylinder compression strengths shown for each test in Table 1. This strength can be compared to the peak tensile stress in order to predict determine if spalling will occur. These calculations are summarized in Table 2.

Table 2. Analysis of Calculated Tensile Stress Histories for Tests 3.3 and 3.4

Test	Peak Tensile Stress (psi)	Rise Time (microseconds)	Strain Rate (sec ⁻¹)	Dynamic Increase Factor	Dynamic Strength (psi)	Ratio of Peak Stress/Strength
3.3	5000	35	35	5.7	2565	2
3.4	5000	9	140	9	4500	1.1
3.4*	3000	30	40	6	1200	2.5

* with reduced concrete strength of 2000 psi

The summary in Table 2 shows that the difference in observed damage in tests 3.3 and 3.4 can be predicted using a wave propagation simulation and the measured relationship between tensile strain rate and concrete tensile strength DIF. As a last numerical simulation, the input for Test 3.4 (the quarter scale test) was reanalyzed assuming the test was conducted using a reduced concrete strength of 2000 psi, one-third of the original strength. The von-Mises yield stress was assumed equal to 1.5 times this reduced value and the entire analysis was performed according to the method previously described. Figure 9 shows the calculated stress histories at the same locations shown in Figure 8 for the full strength results. Note the increased rise time to the peak tensile stress which causes a smaller strain rate and therefore smaller DIF. This fact, and the lower static tensile strength, both cause a smaller dynamic tensile strength. The intermediate calculations used to determine the strain rate and dynamic tensile strength for this case are shown in Table 2 where a reduced Youngs modulus has been used to calculate the strain rate. The calculated ratio of peak tensile stress to tensile strength for this last case with a reduced concrete strength, and the measured response for Test 3.1 shown in Table 1, both indicate that reduced concrete strength in small scale tests may be a good way to cause approximately equal local damage in tests which are otherwise scaled according to replica scaling laws.

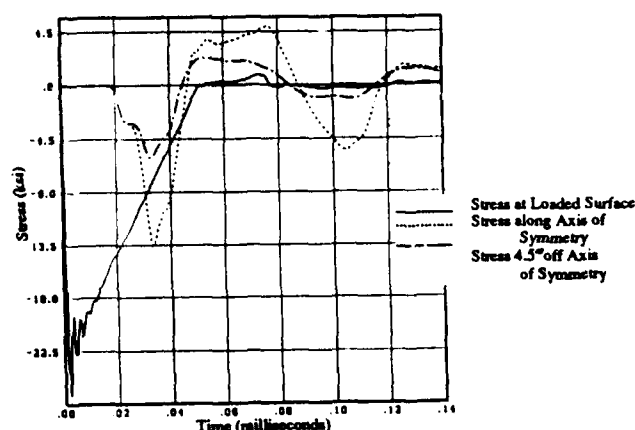


Figure 9. Calculated Stress Histories for Test 3.4 in Table 1 Assuming Reduced Concrete Strength

Conclusions and Recommendations

The results in Figures 5 through 9 and in Table 2 indicate that a computational approach, such as that described here using the PRONTO2D code, can be a very useful tool for gaining a better understanding of local concrete response. The results in this paper also indicate that a reduction in concrete strength in the scale model by approximately one-third can cause localized damage in the scale model which more closely models that which occurs in full-scale.

There are clearly a number of improvements in available material models which would greatly benefit this computational approach. These include incorporating a material model for concrete which models the effect of both strain rate and lateral confinement on the material stiffness and yield surfaces.

References

1. Baker, W.E., Cox, P.A., Westine, P.S., Kulesz, J.J., Strehlow, R.A., "Explosion Hazards and Evaluation", Elsevier Scientific Publishing Co., Amsterdam, 1983.
2. Baker, W.E., Westine, P.S., and Dodge, F.T., "Similarity Methods in Engineering Dynamics", Southwest Research Institute, San Antonio, TX.
3. Forsen, R., "Experiments Used for Comparison of Blast Damage to Full Scale and One Fourth Scale Reinforced Concrete Structures", paper presented at the Twenty-Fourth Department of Defense Explosives Safety Seminar, St. Louis, MO, Aug 28-30, 1990.
4. Ross, C.A., Thompson, P.Y., and Tedesco, J.W., "Split-Hopkinson Pressure-Bar Tests on Concrete and Mortar in Tension and Compression", *ACI Materials Journal*, V.86, No.5, (Sept-Oct 1989).
5. Bowles, P.M., Oswald, C.J., Vargas, L.M., and Baker, W.E., "Debris Hazard Evaluation, Task 3: Test Program and Predictive Model Refinement", Final Report, Southwest Research Institute Project 06-2945, prepared for Bernard Johnson Inc under Mason & Hanger - Silas Mason Co., Inc., Contract H0760103, U.S. Government Contract DE-AC04-76DP-00487, November 1990.
6. McVay, M.K., "Spall Damage of Concrete Structures", USAEWES Technical Report SL-88-22, prepared for U.S. Army Corps of Engineers, Jun 1988.
7. Wright, R.S., Coltharp, D.R., Vretblad, B., and Balazs, P., "Blast Response Tests of a Swedish-Norwegian Structure", Proceedings of Internationales Symposium Interaktion Konventioneller Munition Mit Schutzbauten, Mannheim, West Germany, Mar 1987.
8. Watson, A.J., Hobbs, B., and Wright, S.J., "Scaling Explosive Damage to Reinforced Concrete Beams and Slabs", *Proceedings of the First International Conference on Structures Under Shock and Impact*, Cambridge, MA, Jul 1989.
9. Taylor, L.M., and Flanagan, D.P., "PRONTO 2D: A Two-Dimensional Transient Solid Dynamics Program," SAND86-0594, Sandia National Laboratories, Albuquerque, NM., 1987.
10. Key, S.W., Beisinger, Z.E., and Krieg, R.D., "HONDO II: A Finite Element Computer Program for the Large Deformation Dynamic Response of Axisymmetric Solids," SAND78-0422, Sandia National Laboratories, Albuquerque, NM, 1978.
11. Hyde, David W., Instruction Report SL-88-1, "User's Guide for Microcomputer Programs CONWEP and FUNPRO, Applications of TM 5-855-1, Fundamentals of Protective Design for Conventional Weapons", Structures Laboratory, Department of the Army, Waterways Experiment Station, Corps of Engineers, Sep 1989.
12. "Fundamentals of Protective Design for Conventional Weapons - TM 5-855-1", prepared by the U.S. Army Waterways Experiment Station, Vicksburg, MS, 1982.
13. Marchand, K.A., Vargas, L.M., Nixon, J.D., "The Synergistic Effects of Combined Blast and Fragment Loadings", Interim Technical Report, Southwest Research Institute Project 06-2821 prepared for AFESC, Tyndall Air Force Base, FL, contract No. FO8635-89-0195, Munitions Systems Division, Eglin AFB, FL, Jun 1990.

CUMULATIVE DAMAGE ALGORITHMS DEVELOPMENT FOR REINFORCED CONCRETE

Mr. Robert W. Cilke, Applied Research Associates, Inc.
Albuquerque, New Mexico, U. S. A.

Dr. Frank A. Maestas, Applied Research Associates, Inc.
Albuquerque, New Mexico, U. S. A.

Mr. Marvis Adams, Aeronautical Systems Directorate
Eglin Air Force Base, Florida, U. S. A.

ABSTRACT

Applied Research Associates, Inc. (ARA) under contract to the USA, Department of the Air Force, Aeronautical Systems Directorate, at Eglin AFB was tasked to develop algorithms that address the cumulative damage to reinforced concrete resulting from multiple weapon attacks.

In many attack scenarios against an underground hard target, the penetrating weapon detonates in soil near a roof or wall. The concrete slab may be breached or damaged, providing less penetration resistance for a subsequent weapon passing through the slab. The objective of the effort presented in this paper is to quantify the damage that occurs in a concrete slab due to a nearby soil burst. Numerous finite element calculations were performed for various explosive weights, concrete thickness, reinforcing steel percentages and standoff distances. Presented in this paper are the results of calculations and a comparison to test data. The information was used to modify the resistance to penetration experienced by subsequent weapons impacting the slab. Based on the results of numerical effort, algorithms were developed to incorporate the reduced resistance into the Effectiveness/Vulnerability Assessment in Three Dimensions (EVA-3D) computer code. (Reference 1)

INTRODUCTION

Previous versions of the EVA-3D computer code did not address the reduced capacity in concrete due to detonation in soil. It was assumed the zone of damaged concrete was completely destroyed, and thus treated as air for subsequent weapons. In addition, the previous versions of EVA-3D used only two mechanisms for damaging concrete: panel collapse and punching shear. In panel collapse, the walls are assumed to be constructed of prefabricated concrete panels supported by beams and columns. The concrete panels between support columns could only be damaged by an edge shear failure mechanism. The second mechanism treated by EVA-3D is punching shear as manifested in breach. The breach holes were determined by comparing the free-field impulse on the slab to the shear capacity of a circular concrete plug within the slab. Figure 1 shows the breach curves used in the EVA-3D code for a soil detonation. The curves represent the largest circular plug that can withstand the impulse in a quarter of the slab's flexural period. The figure relates the breach radius to the soil detonation range for 1-foot, 2-foot, and 3-foot-thick slabs. The 1-foot and 2-foot curves compare well to test data. However, little test data exists for the 3-foot-thick slabs. It is the author's opinion that shear failure mechanism does not apply for slabs thicker than 3 feet for the spans commonly found in construction. Damage to thicker slabs is discussed in this paper. Computer simulations of thicker slabs were performed to build a more thorough concrete damage algorithm.

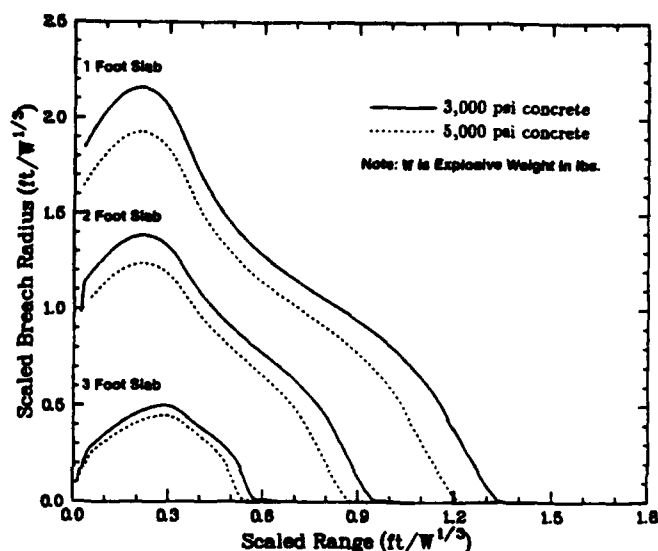


Figure 1. EVA-3D concrete breach curves due to detonations in soil.

Failure and reduced concrete capacity were determined by performing a series of two-dimensional, axisymmetric finite element calculations. In these calculations, a spherical, uncased charge was detonated in a soil medium at prescribed standoff distances from a supported concrete slab. The following calculational matrix was used.

Explosive weight: 100, 1,000 pounds
Scaled standoff distance: 0.50, 0.75, 1.0, 1.25, 1.5 ft/W^{1/3}
Amount of steel reinforcement: 0%, 0.5%, 1% Slab thickness: 39.4 in, 78.7 in, 118.1 in (1 m, 2 m, 3 m)

SAMSON2

The extent of concrete damage was based on axisymmetric SAMSON2 (Reference 2) calculations. SAMSON2 is a two-dimensional, nonlinear finite element computer code designed primarily for dynamic analysis of plane and axisymmetric solids. The program is commonly used to analyze buried protective structures subjected to blast and shock loading. SAMSON2's main features include nonlinear material modeling, explicit time integration, large displacement sliding/separating interfaces, and multiple time step integration.

Four material models were used in the SAMSON2 calculations: explosive, concrete, soil, and steel. The explosive was modeled by a spherical cavity with a pressure boundary at the soil-cavity interface. The pressure, P , at the interface was determined using the Jones Wilkens Lee (JWL) equation of state parameters. These parameters calculated the cavity interface pressure using the cavity's relative volume.

$$P = Ae^{-R_1 V} + Be^{-R_2 V} + C/V^{\omega+1} \quad (\text{psi}) \quad (1)$$

$$V = \frac{\text{(current explosive volume)}}{\text{original explosive volume}} \quad (\text{dimensionless}) \quad (2)$$

where $A, B, C, R_1, R_2, \omega$ = JWL parameters

The explosive type modeled in the calculations was H-6. H-6 is a composite high explosion (HE) with non-ideal behavior, and has the following JWL values:

$$A = 109.95 \times 10^6 \text{ psi} \quad R_1 = 4.9$$

$$B = 1.235 \times 10^6 \text{ psi} \quad R_2 = 1.1$$

$$C = 0.1658 \times 10^6 \text{ psi} \quad \omega = 0.20$$

The concrete and sand were modeled using ARA's 3 invariant, double radius CAP model (Reference 3). The concrete had an unconfined compressive strength of 5,000 psi and a density of 145 lb/ft³. The soil in the calculations used a Fort Polk sand model. This type of sand is stiff and dry, having a friction angle of 31 degrees, and density of 116 lb/ft³. The reinforcing steel was modeled as an elastic-plastic material with yielding occurring at 67,000 psi.

CALCULATION SET-UP

In the SAMSON2 calculations, an explosive cavity is placed in a soil medium centered above a concrete slab at a prescribed stand-off distance. Figure 2 shows the axisymmetric mesh for a typical SAMSON2 calculation. The explosive was modeled by a spherical cavity in a soil medium with a pressure boundary at the soil-cavity interface. The slab's horizontal bottom surface extended 116 inches from the centerline, and the slab was supported at the edge with a 40-inch-thick concrete wall. The wall extended at least 8 feet below the horizontal slab to minimize any wave reflection effects from the mesh's lower boundary. A large soil extended at least 8 feet below the horizontal slab to minimize boundary effects. Additionally, 20 feet of soil covered the slab, again to minimize boundary effects. Radial and circumferential bar elements were placed in the concrete mesh to model the steel reinforcing bars. These bar elements simulated reinforcing bars at 8-inch centers running each way on each face in the 39.4-inch-thick slab. Layers of similar reinforcing bar elements were placed horizontally in 39.4 inch increments in the 78.7 and 118.1-inch-thick slabs. Hence, the 39.4-inch-thick slab had four layers of reinforcement. The elements simulated No. 6 reinforcing bars (approximately 0.5 percent total reinforcement) or No. 10 reinforcing bars (approximately 1.0 percent total reinforcement). For the 1,000 pound calculations, elements simulating vertical shear stirrups were placed between the top and bottom reinforcing bar layers. These stirrups were half the cross sectional area of the other reinforcing bars, and they were spaced 16 inches apart (8 inches apart near the corner). The reinforced design is typical of what is found in most structures.

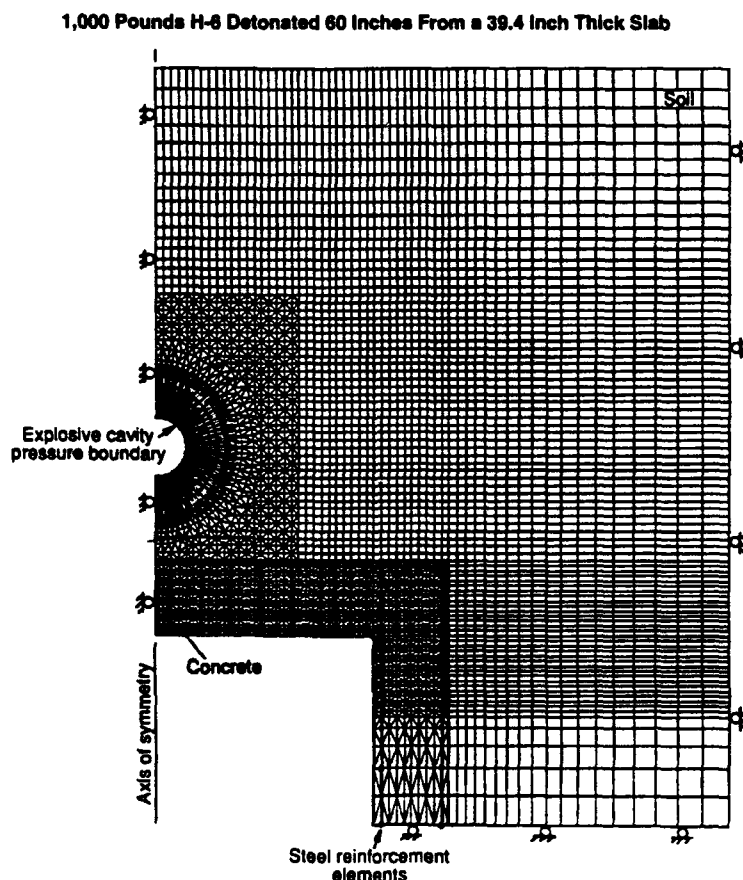


Figure 2. Typical SAMSON-2 axisymmetric calculation.

The calculations were run 15 to 18 milliseconds after detonation. Most of the damage to the concrete was expected to occur during this time frame. The slab was considered to have failed when large vertical displacement occurred in the slab. A large vertical displacement indicated that the slabs breached.

Modeling crack formulation in concrete is a complicated process. Concrete commonly cracks at tensile strains of 0.02 percent of unconfined compressive strength. If the concrete is compressively confined, the tensile strains can be orders of magnitude higher before the material cracks. However, if the material is in uniform tension the concrete is expected to crack with tensile strains of 0.02 percent. Cracks large enough to effect the penetrability of the concrete are assumed to occur when the material is in tension in all directions and the maximum principle strain is above 0.2 percent.

1,000 POUND CALCULATIONS

1,000 pounds of H-6 was detonated near 39.4, 78.7, and 118.1-inch-thick slabs at a variety of stand-off distances. The stand-off distances ranged from 60 inches to 18 inches.

For a 1,000 pounds of explosive standoff distances of 60, 90, 120, 150, and 180 inches corresponds to scaled ranges of 0.5, 0.75, 1.0, 1.25, and 1.5 lb ft/W^{1/3}. Results of several of these calculations are provided in Figure 3. The calculations indicate that in the zones where the concrete experiences only tensile strains, the maximum tensile strain is almost always above 0.2 percent.

The results of the 1,000 pound explosive calculations generally showed that if the slab failed, it failed near the corner where the wall and slab intersected. A failure near the corner indicates that the slab failed flexurally rather than from a punching shear. The following calculations showed a failure in the slab near the corner:

Concrete Thickness	Standoff Distance
39.4 inch	60 inch
"	90 inch
"	120 inch
"	150 inch
78.7 inch	60 inch

These calculations showed a significant vertical displacement at the slab's center.

Figure 1 indicates that 1,000 pounds of explosives detonated 60 inches away from a 39.4-inch-thick slab would cause the slab to breach. From Figure 3, the damage to the slab is so catastrophic that it is impossible to determine if it initially failed due to a punching shear or flexure.

The slabs which do not fail showed a few common traits. First, little damage (scabbing) is seen on the slab's top side. Since the concrete in this region generally experiences compressive strains only, minimal damage occurs. Second, the surviving slabs have spall zones where tensile strains extend far into the slab. These zones extend into the slab up to 75 percent of the slab thickness. The maximum principle strains are large in these zones, indicating that there is heavy cracking and spalling. Though the slab did not fail, zones of partially damaged concrete were created in the slab.

COMPARISON TO DATA.

The results of the finite element calculations were compared to test results for validation. Figure 4 compares the calculations to the National Defense Research Committee's (NDRC) soil burst curves (Reference 4).

The NDRC soil burst curves indicate breaching, heavy scabbing, moderate scabbing, and light scabbing (not shown in Figure 4) for a given stand-off distance, concrete thickness, and explosive weight. These curves, are based on tests of walls whose face dimensions (length to width) have a ratio of 3 to 5, and whose span to thickness ratio is between 5 to 1 and 15 to 1. The test concrete had approximately 1 percent steel reinforcement by volume. The explosive weights used in the tests ranged from 1/8 pound to 1,000 pounds. Note that the breach curve in Figure 4 includes all failure mechanisms for the slab (i.e., shear and flexure failure).

The calculations performed follow the NDRC breach curve reasonably well. All the SAMSON calculations which clearly indicate failure to the concrete slab fall within the NDRC breach curve. The two borderline calculations, 1,000 pounds explosives 60 inches from a 118.1-inch-thick slab and 1,000 pounds 180 inches from a 39.4-inch-thick slab, are plotted near the breach curve in Figure 4. Three of the five calculations which did not indicate slab failure are located outside the breach curve, the other two are found just on the inside of the breach curve.

The calculations which did not indicate slab failure showed signs of heavy cracking and scabbing. These calculations all fell within or on the heavy scabbing curve in Figure 4.

CONCLUSION

Previous versions of EVA-3D incorporated damaged concrete to effect the penetration of subsequent weapons. However, they modeled punching shear failure only. SAMSON2 calculations were run for various concrete thicknesses, reinforcing steel percentages, and standoff distances. These calculations were compared to the test results provided in the NDRC report. Not presented in this paper is the algorithms developed for incorporation into EVA-3D. The presented information was, however, the basis for the algorithm development.

REFERENCES

1. Maestas, F.A., and Galloway, J.C., Methodology of EVA-3D, Version 2.0, Applied Research Associates, Inc., for AFATL/SAA, F08635-85-C0220, May 1989.
2. Schreyer, H.L., et al., SAMSON2, A Nonlinear Two-Dimensional Structure-Media Interaction Computer Code: Users Manual, New Mexico Engineering Research Institute, University of New Mexico, AFWL-TN-82-018, September 1982.
3. Bingham, B.L., Bingham Three Invariant, Double-Radius Cap Model, Internal Report, Applied Research Associates, Inc., Albuquerque, New Mexico, November 1992.
4. Effects of Impact and Explosion, National Defense Research Committee, Division 2, Washington, D. C., 1946.

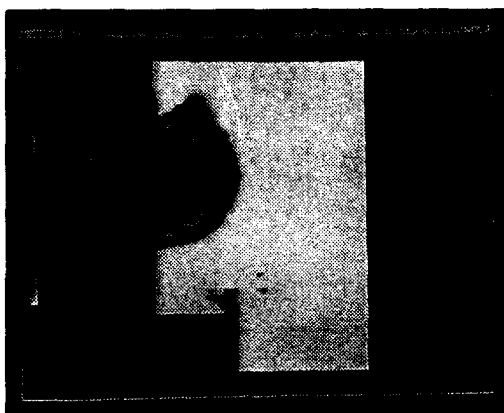


Percent strain softening, 18 ms

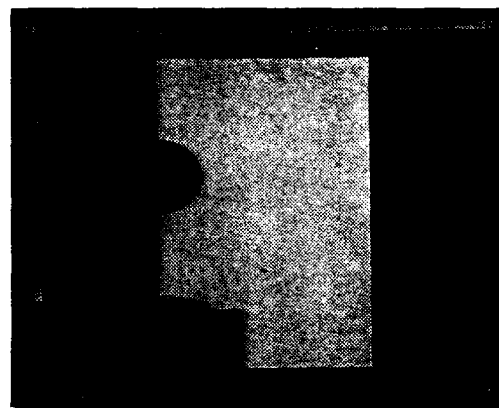


Minimum principle strain, 9 ms

a.) 39.4-inch-thick slab, 60-inch range.



Percent strain softening, 18 ms



Minimum principle strain, 12 ms

b.) 39.4-inch-thick slab, 180-inch range.

Figure 3. 1,000 pounds of explosives detonated in soil near a concrete slab, 1% reinforcement.

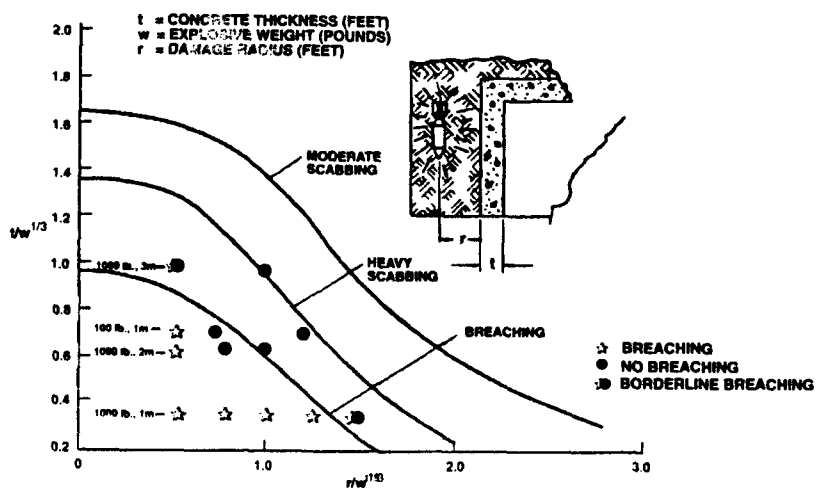


Figure 4. Comparison of SAMSON2 calculations to the NDRC curves.

EXPERIMENTAL/ANALYTICAL PROGRAM FOR CONSTRUCTING MODELS FOR THE DYNAMIC RESPONSE OF CONCRETE MATERIALS

Mr. John A. Collins, WL/MNMW
Eglin Air Force Base, Florida, U.S.A

Dr. Frank A. Maestas, Applied Research Associates, Inc.
Albuquerque, New Mexico, U.S.A.

Mr. Barry L. Bingham, Applied Research Associates, Inc.
Albuquerque, New Mexico, U.S.A.

Mr. James A. Keller, Denver Research Institute
University of Denver, Denver, Colorado, U.S.A.

Dr. W. Russ Seebaugh, Denver Research Institute
University of Denver, Denver, Colorado, U.S.A.

ABSTRACT

This paper describes an analytic and test effort conducted by Denver Research Institute (DRI) and Applied Research Associates, Inc. (ARA) for Wright Laboratory, Armored Directorate, (WL/MNMW) to define concrete material models to establish equations of state (EOS), constitutive behavior and failure. Specific applications of the concrete models are related to material behavior resulting from high pressures generated by projectile impact and/or detonation. Provided in this paper is an overview of the EOS and constitutive behavior for the ARA model and an application to an experimental program conducted for WL/MNMW. A comparison of the test results and analysis is also presented.

INTRODUCTION

The results obtained using a computational code for a given material and loading condition depend on the dynamic response of the material to the imposed loading and is governed by specific material properties. The volumetric response, or the resistance to compression, is described by the equation of state. The resistance to distortion is described by the constitutive relations. Finally, the reduction in the ability of the material to carry stress as damage accumulates is described by a damage model.

Modern codes for calculation of dynamic material response use the principles of continuum mechanics in the form of equations for mass, momentum, and energy balances to determine the time dependence of the distributions of density, velocity, and stress within the target material. If the stress depends only on the density and internal energy, no further relationships are needed. The material response in this simplified situation is called hydrostatic behavior. If the stress depends on additional dynamical variables, additional constitutive equations are required to describe the yield strength, shear modulus, tensile strength, and other properties of the material. These are termed deviatoric properties. If material damage, such as the formation of crater ejecta, is important in the problem, then additional relationships are required to describe these aspects of the material behavior.

For an impact into concrete or a contained explosion within a mass of concrete, the response of the concrete spans a wide range of material behavior as the high pressure generated by the impact or explosion attenuates as the shock propagate through the material and the release waves from the free surfaces overtake the shock. The highest pressures of interest in the test program to be discussed later are several hundred ksi (tens of kbar) for impacts and 100 ksi (7 kbar) for explosions (Reference 1). The lowest pressures of interest (or stresses), after attenuation by spherical shock expansion and the release waves are about 1 ksi (0.7 kbar).

ANALYSIS

The analysis of the test program was performed using SAMSON2 with an ARA concrete material model. Each of these are discussed in the sections that follow.

SAMSON2: The SAMSON2 computer program (Reference 2) is a two-dimensional finite element code designed primarily for dynamic analysis of plane and axisymmetric solids. The code contains the following capabilities:

- explicit time integration
- large deformation/rotation formulation
- static solutions through dynamic relaxation
- sliding/separating boundaries
- multiple time step integration or subcycling
- element library that includes:
 - solid continuum (4-noded quadrilaterals or 3-noded triangles)
 - beam elements
 - shell elements
 - membrane elements
 - 2-noded spring or truss elements
- material library that includes:
 - isotropic elastic
 - multi-linear elastic-plastic
 - ARA 3-Invariant model (ARA-3I, Reference 3)
 - Bingham 3-Invariant, Double-Radius Cap model (B-3I, Reference 4)
 - effective stress modeling
- a variety of boundary conditions to include:
 - large displacement/rotation pressure boundary
 - prescribed force time history
 - prescribed velocity time history in an optional, user-defined, local-coordinate system
 - initial velocity
- restart capability

SAMSON2 has sliding/separating boundary capabilities with the options of Mohr-Coulomb, relative velocity formulation or perfect slip shear transmission. The sliding/separating boundary formulation is very useful in modeling the large relative deformation that can occur between a rigid structure and its softer, surrounding support media. The sliding/separating boundary also permits the use of multiple time step integration (or subcycling). Subcycling has a significant effect upon the computational efficiency of a calculation that requires relatively small time steps in certain areas of a finite element mesh, but larger time steps in a substantial remainder. Regions that may require relatively small time steps include finely detailed portions of stiff structural components or fine material elements in the immediate vicinity of an explosive charge.

SAMSON2 has a variety of element types which make it highly versatile in analyzing a wide range of different problems with different degrees of complexity. Plane strain, plane stress, or axisymmetric continuum elements use velocity-strain, linear-displacement, single-point integration with optional hourglass damping for quadrilaterals (not applicable for 3-noded triangles). Rebar spring elements (uniaxial stress or uniaxial strain) have an optional bond/debond capability with adjacent continuum elements for modeling rebar pull-out. The element library also includes two-dimensional, plane beam elements and axisymmetric shell elements.

Detonation pressures of a large variety of explosive types are included in the SAMSON2 code through the use of JWL equations-of-state (Reference 3). The JWL equation-of-state can be implemented in either hydro-dynamic continuum elements or pressure boundary interaction with volume voids.

MATERIAL MODEL: Stress states which occur in concrete can be very complicated and diverse. A material model that can mathematically handle all of the stress states occurring in laboratory testing is well adapted to handle the more complicated stress states that occur in the field. Two such material models are the ARA Three-Invariant and the Bingham Three-Invariant (B-3I).

Both material models are very versatile in matching material response characteristics. The ARA-3I model is primarily used for soil, while the B-3I model can be used to represent soils, concrete, rock, ceramics and metals in Lagrangian finite element or finite difference computer codes. The ARA-3I model is more expensive to use in terms of run time, but it is more theoretically rigorous in calculating plastic strain vectors and a plastic stiffness matrix, which allows the material model to be used in both explicit and implicit finite element codes. The B-3I model is much more efficient in computational speed, but currently is only adapted to explicit finite element codes. Both material models have the capability to reproduce many behavior characteristics observed in laboratory testing to include:

- elastic response
- plastic response or irrecoverable strain
- strength dependence upon mean normal stress
- strength dependence on intermediate principal stresses
- strain hardening
- tensile fracture
- dilation
- shear compaction
- non-linear elastic bulk moduli

- elastic stiffness modification with plastic strain
- two phase capability (pore water pressure and effective stress formulation)
- solid-solid phase change

The B-3I model also has the additional capability to model:

- non-linear elastic shear moduli
- compressive failure or strength loss with continued loading

Some of these characteristics are associated with material subjected to very large strains, high pressures, and failure. Behavior modification based on strain rate is currently not a capability of either material model, but this capability can be indirectly implemented through material property definition based on anticipated strain rates and published data.

Both material models use a shear yield surface and a cap to obtain the plastic strain observed in material response. Both material models use non-associated flow models in the form of potential surfaces to define the direction of the plastic strain vector (or the direction of stress correction in the case of the B-3I model). The potential surface capability allows the user to control dilation behavior which typically cannot be controlled in associated flow models. Strain hardening parameters on the cap describe the volumetric compaction behavior of the material. In the B-3I model, the response of the shear yield surface and the cap are coupled providing a type of "unified" or "single" yield surface concept.

TEST PROGRAM

Since concrete exhibits complex behavioral features, improvement in constitutive modeling was needed. A set of experiments was designed to allow measurement of the distortional behavior of concrete under dynamic loading - in this case, explosive loading. The resulting data were intended to provide a point of review for researchers involved in developing equations of state for the material, to provide a controlled data set for evaluation of existing constitutive models, or the suggestion of new constitutive models and to indicate how various failure mechanisms should be treated.

The material model concrete test target is shown in Figure 1. The test series involved the detonation of a 1-lb sphere of Pentolite explosive inside an 8-ft diameter by 6-ft-thick concrete target. Table 1 presents the specifications for the concrete used in the tests.

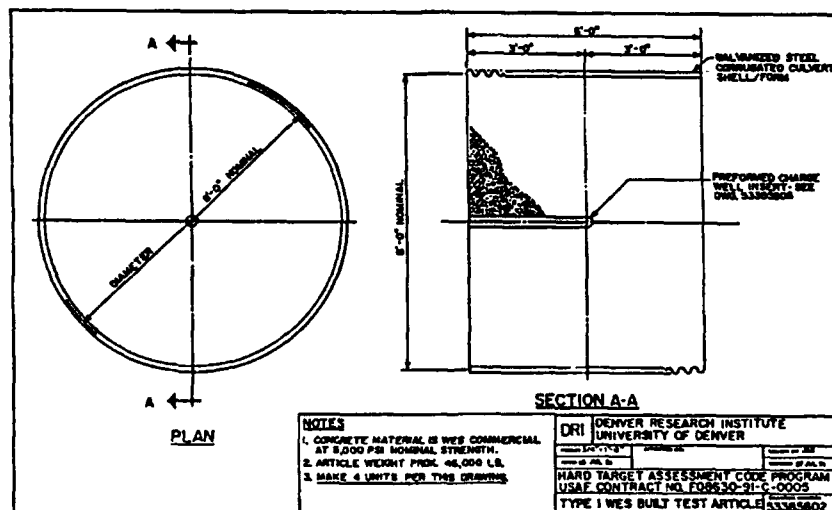


Figure 1. Design of material model data test article.

TABLE 1. CONCRETE SPECIFICATION.

COMPONENT MATERIAL	LBS/CU YD OF CONCRETE	SPECIFICATION
TYPE 1 PORTLAND CEMENT	445	ASTM C150-90
FLY ASH	94	ASTM C618-89a
COARSE AGGREGATE	1,749	ASTM C33-90
FINE AGGREGATE (SAND)	1,417	ASTM C33-90
WATER REDUCING AGENT (HR)	3.4	ASTM C494-85
WATER REDUCING AGENT	1.7	ASTM C494-85
WATER	247	Municipal Supply
TOTAL WEIGHT, CU YD	3,957	

In addition to the specifications shown in the table, requirements were levied on the particular components of the mix, such as the cement type, fine aggregate, coarse aggregate, water reducing agent, air detrainment agent, and fly ash. All materials were required to conform to the applicable ASTM specifications. It should be noted that this material has now, at the conclusion of this first year of research, become somewhat standardized within the experimental ballistics and structural response community. The material has been given the designation "SAC-5", denoting "Small Aggregate, Chert (a rock mineral type), 5,000 psi strength."

EXPLOSIVE: The explosive used was cast Pentolite spheres. The Pentolite formulation employed was a 50/50 mix - 50% TNT (Trinitrotoluene) and 50% PETN (Pentaerythritol Tetranitrate). This material exhibits a heat of explosion of 1,220 cal/gm, compared to TNT at 1,080 cal/gm and is thus a more energetic material. The design density for cast Pentolite charges in this research was chosen as the nominal or 1.65 gm/cc value.

INSTRUMENTATION: The data desired from these experiments included radial stress, radial acceleration/velocity, and hoop strain, as well as methods for confirming stress wavefront shape. An additional constraint placed on the choice of instrumentation was that all transducers used in this program must represent types which had been used in similar applications in other programs - i.e., the transducers must have been demonstrated in similar applications.

- The direct measurement of transient stress was accomplished using a Model LQ-080U soil stress gauge, with maximum capacity of 10,000 psi. The gauge has approximately 50% over-range capability with acceptable linearity.
- For measurements of radial acceleration, the Endevco Model 7270A accelerometer was used.
- Measurements of hoop strain was accomplished using a resistance strain gauge made by Ailtech Division of Eaton Industries. The gauge consists of a resistance element encapsulated within a tube which is attached to a perforated disc at each end. As the gauge is strained - either compressed or stretched - the length of the resistance wire changes, and hence the resistance.

- The wavefront shape was confirmed by the use of simple time-of-arrival gauges. A small, piezoelectric transducer from PCB Corporation, commonly referred to as the "Microgauge", was used.

The positioning of the gauges for the material model data collection tests is illustrated in Figure 2.

ANALYSIS

Pretest predictions using the SAMSON2 Finite Element computer code were made. Figure 3 provides the pretest prediction of the radial stress using SAMSON2. Also, time histories of radial velocity, radial stress and strain at four distances from the centerline of the concrete block; 10 in, 18 in, 30 in, and 42 in were provided prior to the test. Predicted peak accelerations at these four ranges are 139,000 g's, 19,600 g's, 11,000 g's, and 2,530 g's, respectively. The predicted peak radial stress was 25 ksi, 10 ksi, 5 ksi, and 1.4 ksi for 10 in, 18 in, 30 in, and 42 in ranges respectively. The peak stress from the tests were 11 ksi, 7 ksi, and 2 ksi for 18 in, 30 in and 42 in ranges respectively. The peak stress matches well. The duration of the pulse does not however. As seen in Figures 4, 5, and 6, the duration is much shorter for the test data than for the pre-test predictions. The figures present the test results for four tests and the associated pre-test predictions. The exact reason for the difference in duration is still being investigated, however at this point it appears that the presence of the sand stem and moisture in the concrete effected the pulse duration.

CONCLUSION

A test program was conducted where a 1-lb sphere of explosive was detonated inside a massive concrete slab. The slab was instrumented at various ranges. The objective of the test effort was to obtain sufficient test data to validate/improve/develop concrete material models.

Prior to the performance of the tests, pre-test predictions were made using SAMSON2 with the B-31 material model. The test results and predictions match very well with regard to peak values but differ in duration. Continued evaluation is underway.

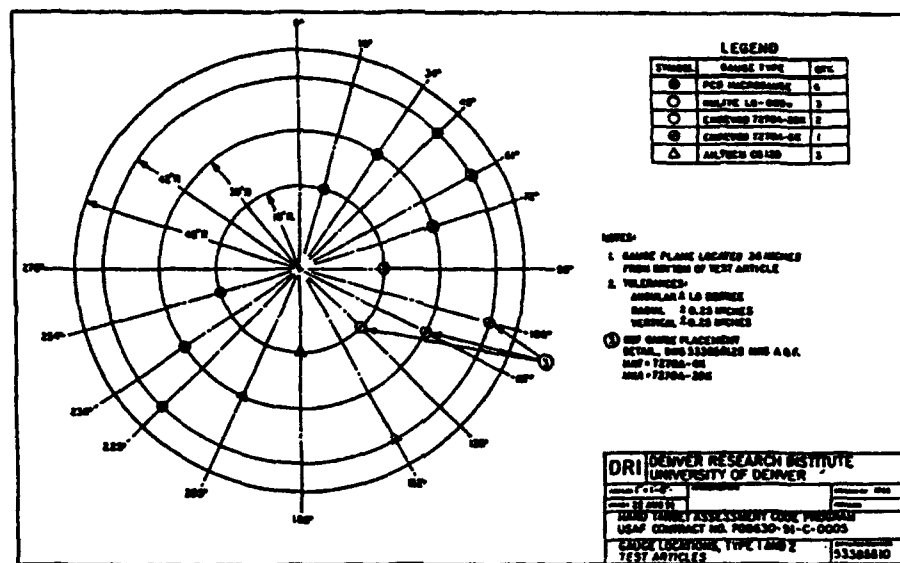


Figure 2. Gauge placement in material model data test article.

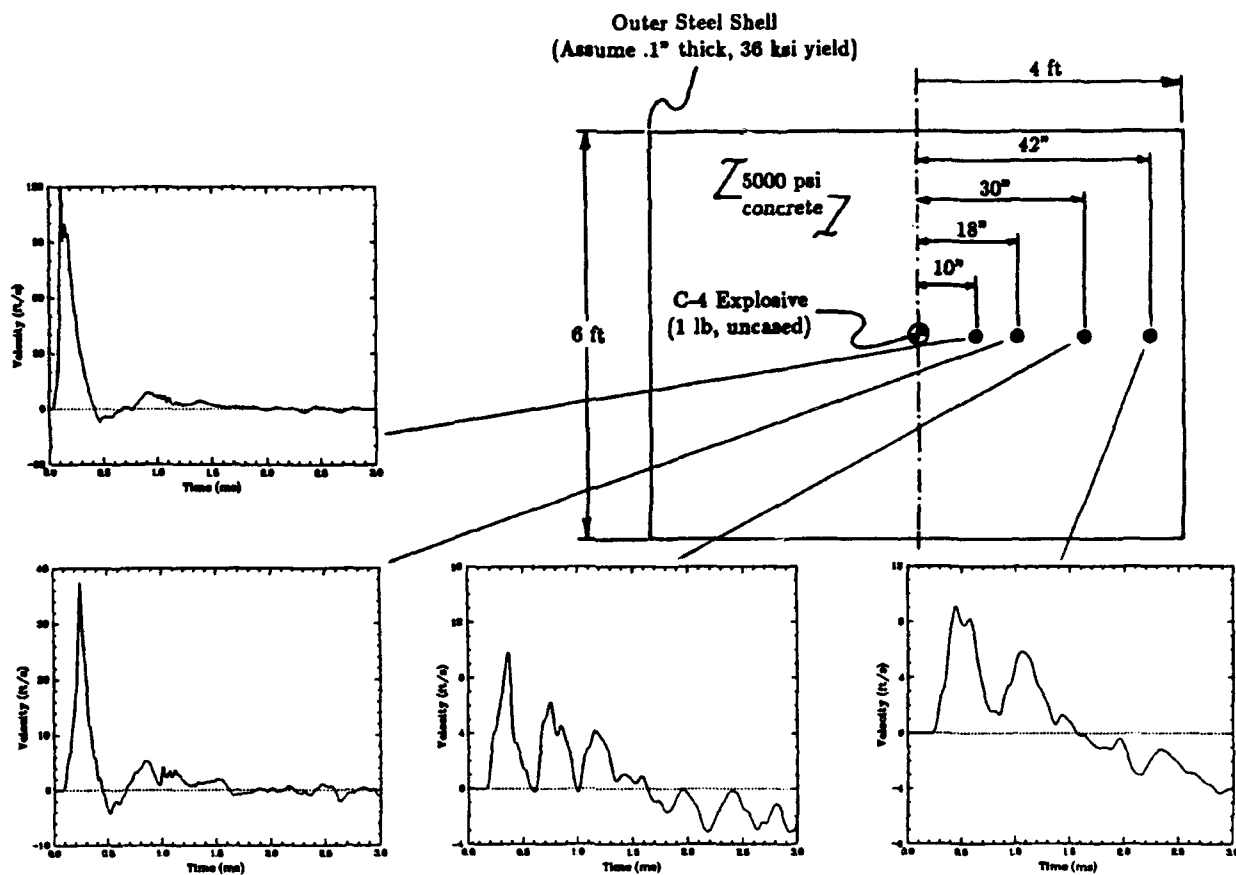


Figure 3. Predicted radial velocities.

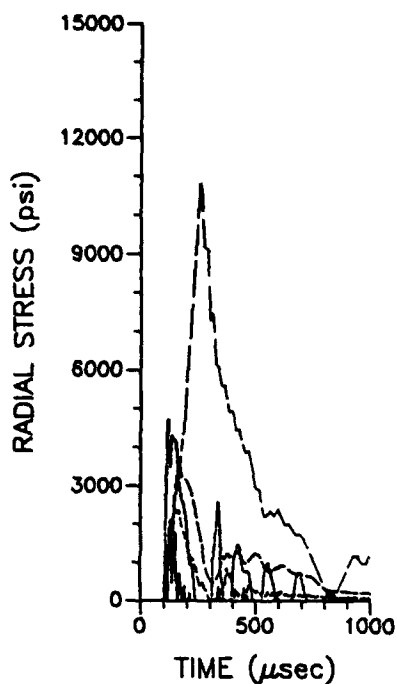


Figure 4. Radial stress at 18 inches.

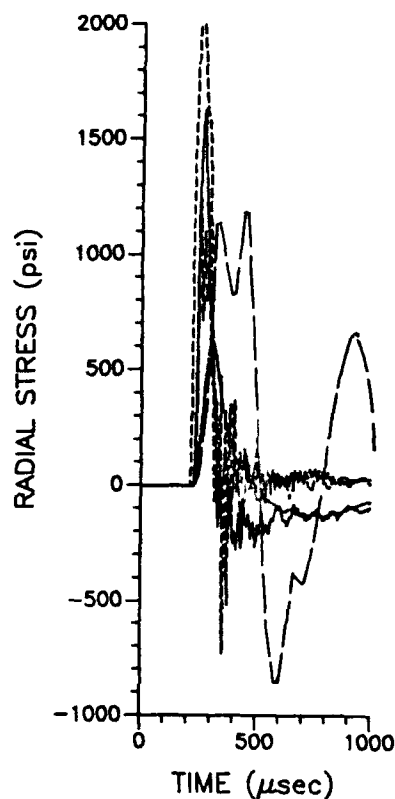


Figure 6. Radial stress at 42 inches.

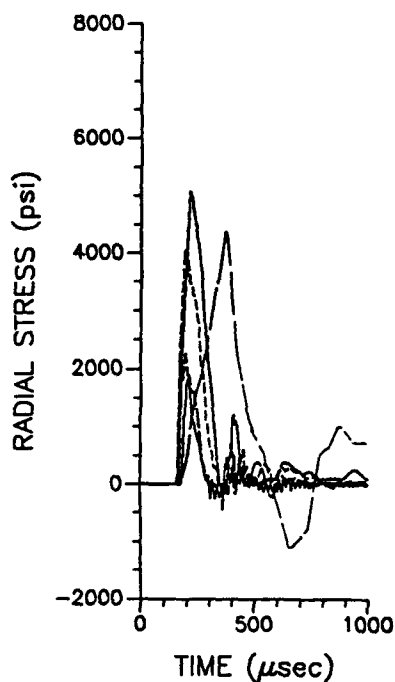


Figure 5. Radial stress at 30 inches.

REFERENCES

1. Dobratz, B.M., LLNL Explosives Handbook. Properties of Chemical Explosives and Explosive Simulants, UCRL-52997, Section 8.3.1, Lawrence Livermore Laboratory, Livermore, California, 16 March 1981.
2. Belytschko, T. and R.R. Robinson, SAMSON2: A Nonlinear Two-Dimensional Structure/Media Interaction Computer Code, AFWL-TR-81-109, Air Force Weapons Laboratory, Kirtland Air Force Base, New Mexico, January 1982.
3. Merkle, D.H., and W.C. Dass, Fundamental Properties of Soils for Complex Dynamic Loadings: Development of a Three Invariant Constitutive Model, AFOSR-TR-85-1232, Final Report on AFOSR Contract No. F49620-80-C-0088, Applied Research Associates, Inc., Albuquerque, New Mexico, April 1985.
4. Bingham, B.L., Bingham Three Invariant, Double-Radius Cap Model, Internal Report, Applied Research Associates, Inc., Albuquerque, New Mexico, November 1992.

JOINT SERVICES PROGRAM FOR THE DESIGN AND ANALYSIS OF HARDENED STRUCTURES TO CONVENTIONAL WEAPONS EFFECTS

J. E. Welter

Defense Nuclear Agency
Structural Dynamics Division
6801 Telegraph Road, Alexandria, VA 22310

ABSTRACT

Recent experiences during DESERT STORM brought to light the vulnerability of hardened structures to conventional weapons and their delivery systems. Existing Service manuals on protective construction are incomplete, out of date, and in part based on erroneous assumptions. Designers and analysts alike require clear concise, state of the art design and analysis tools for protective structures.

The Joint Services Program for the Design and Analysis of Hardened Structures to Conventional Weapons Effects (DAHS CWE Program) is a joint DoD effort sponsored by the Defense Nuclear Agency (DNA) to replace existing, out of date, redundant, and conflicting Service manuals with state of the art DAHS CWE methodology, criteria and automated "tools".

DISCUSSION

The Defense Nuclear Agency (DNA), in cooperation with the Services, is sponsoring a multi-year, Joint Service initiative to modernize the design and analysis methodology for hardened structures against the effects of conventional weapons. The products of this program, depicted in Figure 1, will comprise the Design and Analysis of Hardened Structures to Conventional Weapons Effects System (DAHS CWE System). The DAHS CWE System integrates new design and analysis methodology for hardened structures with PC-based codes and digitized references into a single automated system.

The basis of the DAHS CWE System is the Joint Services Manual for the Design and Analysis of Hardened Structures to Conventional Weapons Effects (DAHS CWE Manual) currently under development. The supporting components of the system, in addition to the Manual, include the DAHS CWE

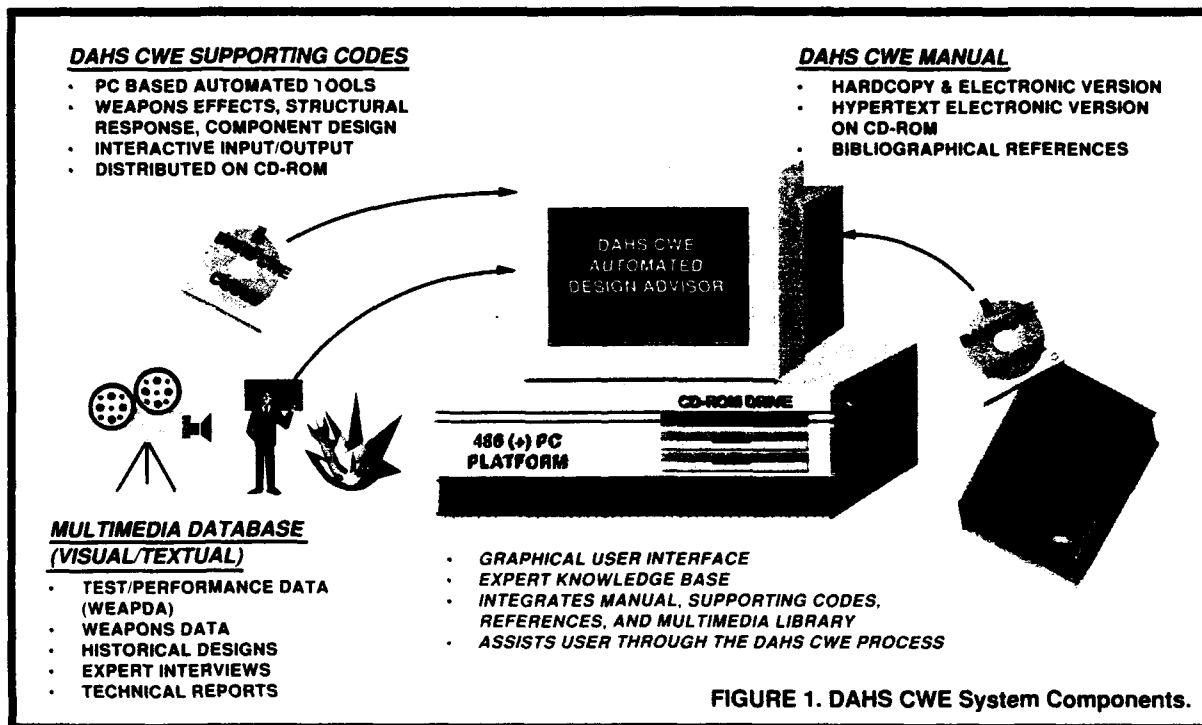


FIGURE 1. DAHS CWE System Components.

Supporting Codes, a digitized Bibliography, a Multimedia Reference Library, and an Automated Design Advisor which will integrate the Manual with the supporting components and guide the user through the DAHS CWE process. All DAHS CWE System software and codes will be produced and distributed on CD-ROM and will eventually operate on both DOS- and UNIX-based platforms.

As currently conceived, the DAHS CWE System will be developed in two multi-year phases as shown in Figure 2. In Phase I, the focus or centerpiece of the system will be an electronic hypermedia version of the DAHS CWE Manual. In concept, the Phase I user will be able to access applicable PC-based DAHS CWE Supporting Codes and digitized bibliographical references via a graphical user interface program directly from within the Manual text. Phase I will be developed in parallel with the first hard copy edition of the Manual. First editions of the hard copy and hypermedia versions of the Manual are planned for the end of calendar year 1994.

In Phase II, the Automated Design Advisor will be developed and become the centerpiece of the DAHS CWE System. Based on expert opinion, intelligent technologies, and detailed decision trees, the Phase II Automated Design Advisor will guide the designer or analyst through the DAHS CWE methodology providing quick, user friendly access to supporting automated tools, archived multimedia references, and the DAHS CWE Manual.

The primary purpose of the DAHS CWE Manual development program is to replace existing outdated, conflicting, and redundant Service manuals with a greatly improved, state of the art Joint Services Manual in both hard copy and electronic versions. The program objectives include improving the reliability of the DAHS process through a better understanding of the basic science and physics governing the response of hardened structures to CWE, developing a clear concise design and analysis methodology for hardened structures, and developing a comprehensive PC-based code "toolbox" that facilitates the automation of the DAHS process and reflects the new DAHS CWE methodology.

Figure 3 depicts the overall DAHS CWE Manual development process and lists the seventeen chapters which will make up the new Joint Services DAHS CWE Manual. Joint Service Technical Working Groups (WG) have been established to write and review the chapter drafts. The WGs are typically comprised of five to six government technical experts from each of the three Services. Where state of the art technical expertise does not reside within the government, contractors are providing the needed expertise. A senior level Joint Services CWE Advisory Group (AG) has also been established to review and approve the completed WG chapter drafts. DNA functions as the overall project integrator for the Manual. DNA coordinates and sponsors WG and AG activities, ensures the chapters are technically integrated, arbitrates differences between the Services, and publishes

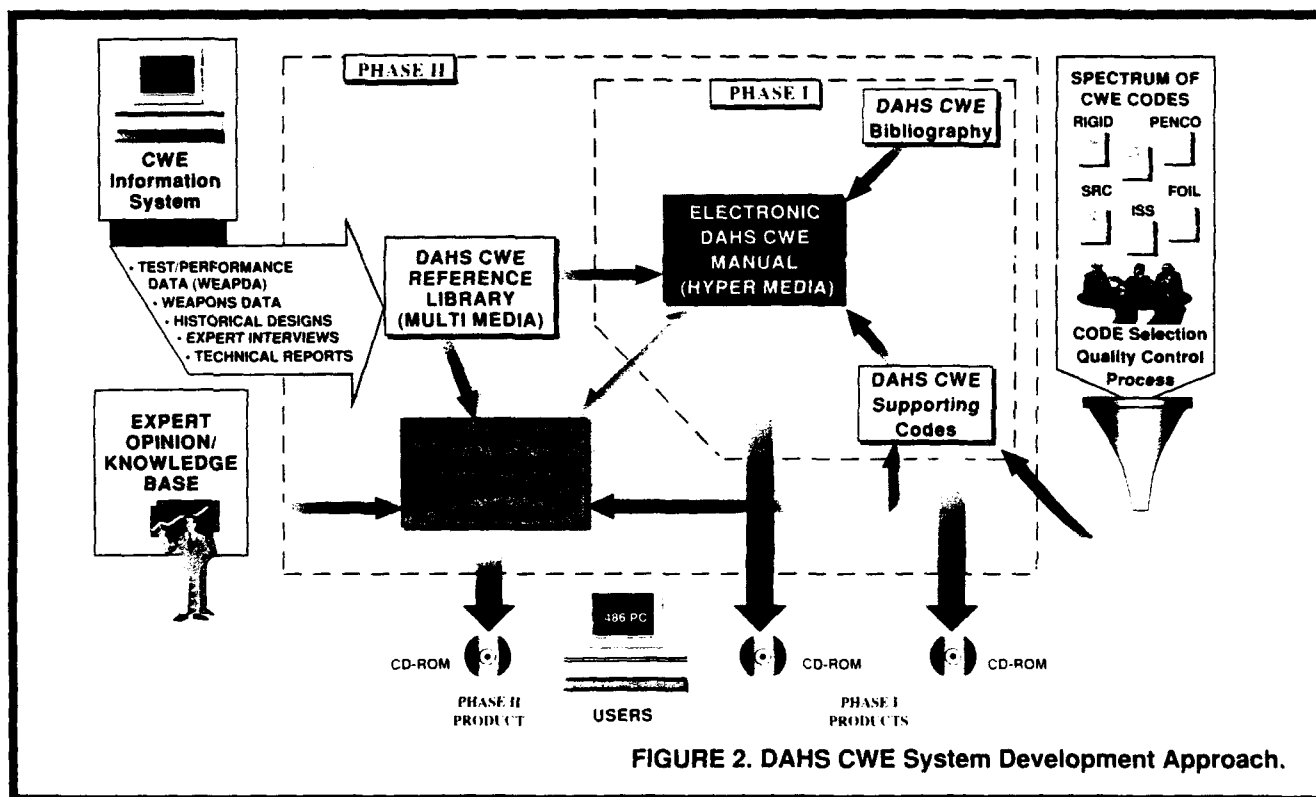


FIGURE 2. DAHS CWE System Development Approach.

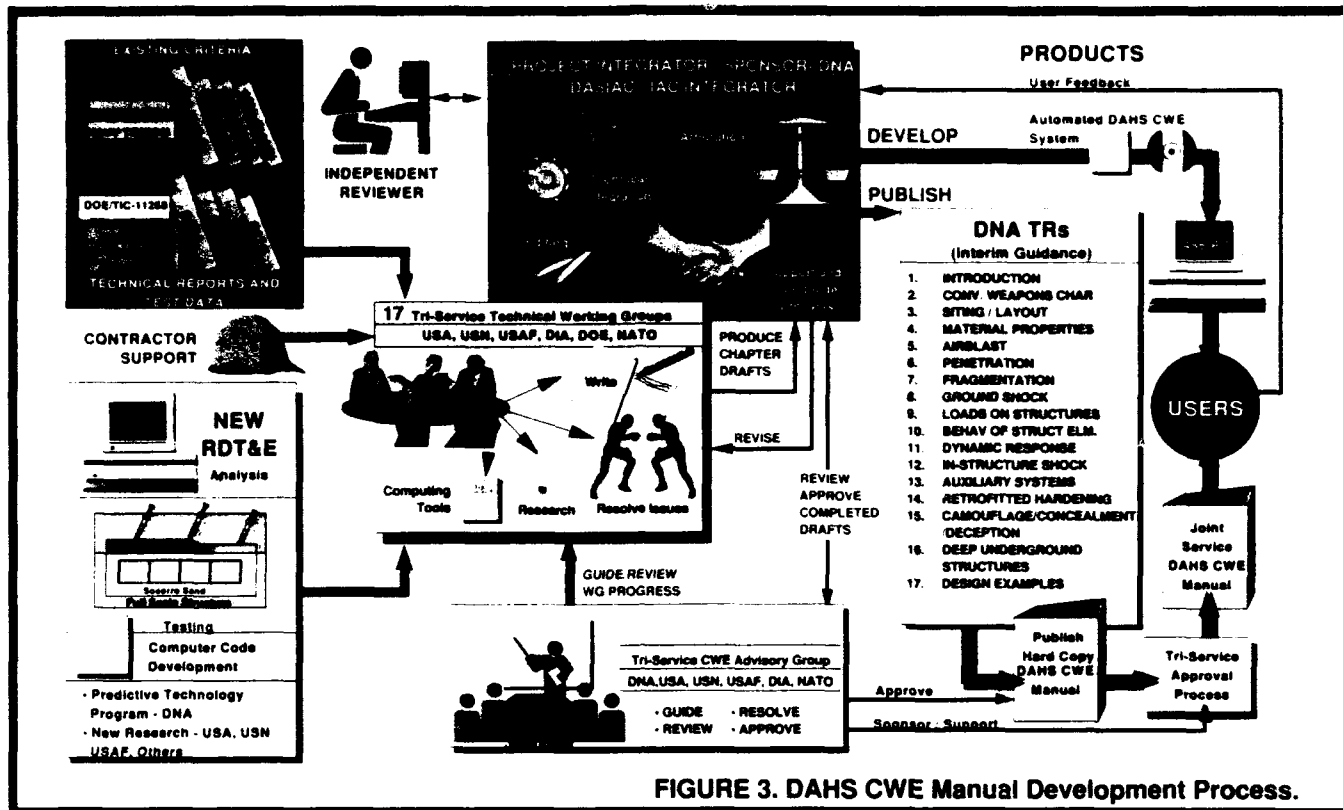


FIGURE 3. DAHS CWE Manual Development Process.

the Manual. The contractor operated, and DNA-sponsored, DoD Nuclear Information Analysis Center (DASIAC) assists DNA in its project integrator role.

The DAHS CWE Manual improves upon existing Service manuals in the protective structures area by incorporating relevant topics and material not currently covered in existing manuals, updating and revising existing weapons effects predictive techniques with the state of the art, and incorporating overarching design example problems that illustrate the new DAHS CWE methodology.

The new manual will incorporate six entirely new chapters. The focus of the new chapters is to fill in "gaps" in the existing design and analysis methodology and thus provide the user with a more complete DAHS CWE methodology. The first new chapter covers siting and facility layout considerations. Topics covered include factors which must be considered by the user when choosing initial siting and orientation of the facility (or facilities) to maximize survivability, and once sited, what factors must be considered in laying out the facility floor plan to minimize the vulnerability of the facility to single and multiple weapon attacks. There are also new chapters covering material properties, retrofit hardening of existing structures, camouflage/concealment/and deception (CCD), deep underground facilities, and design example problems.

The chapter on CCD may prove to be the most valuable addition to the new manual. CCD techniques are relatively inexpensive and highly effective in improving the survivability of protective structures. In these times of austere infrastructure budgets, CCD may be the first technique considered for improving the survivability of our existing facilities and become a viable alternative to traditional hardening approaches in new facilities.

The deep underground chapter will address an entirely different class of protective structure, those that are constructed in tunnels or mines deep beneath the surface or tunneled into the side of hard rock mountains. These types of protective construction have been in existence for literally thousands of years. We are, however, now seeing a resurgence in their popularity with the advent of modern tunneling techniques and the realization of lessons learned from DESERT STORM.

Finally, the new design example chapter will contain three overarching design problems illustrating the design methodology defined in the manual. The three examples covered include an above ground structure, a below ground cut and cover facility, and a generic aircraft shelter. The examples will showcase certain key aspects of the DAHS process from site layout to auxiliary system design. The examples will also demonstrate the use of many of the DAHS CWE supporting codes in the design and analysis process.

The remaining 11 chapters will be major rewrites of chapters in existing Service manuals. The Chapter 1 introduction will become the cornerstone chapter in the manual. Chapter 1 will contain general design methodology flow-charts for at least three major categories of hardened structures, above ground, below ground (shallow buried cut and fill, and deep underground) and aircraft shelters. The flowcharts in Chapter 1 will link major steps of the design and analysis process to the applicable chapter sections of the manual. In the hypermedia version of the Manual, these relationships will be heavily hyperlinked to the manual chapters, design problems, and supporting codes. In this way a less experienced user can maneuver quickly and easily to applicable sections of the manual by following the design process/methodology outlined in Chapter 1 or Chapter 17, containing the DAHS CWE Design Example Problems, for the type of problem he is interested in.

Chapter 2, the weapons characteristic chapter, will contain greatly expanded weapon parameter and characteristic data on a range of generic conventional weapons systems necessary for consideration in the design process. The chapters on airblast, penetration, fragmentation, and ground shock are being completely rewritten and updated with the latest weapons effects predictive techniques and methodologies. For example, the new ground shock prediction methodology will be based on analytical fits to a series of SABER code runs using the Cray supercomputer. Recent research has shown that the SABER code does a much better job of matching actual ground shock test data than existing ground shock equations found in current Army and Air Force manuals.

The chapters covering loads on structures, behavior of structural elements, dynamic response of structures, and in-struc-

ture shock mitigation will be reformatted and expanded to bring structural response analysis and shock isolation design in line with current standard practice and computational capabilities. Much more emphasis will be given to multi degree of freedom modeling and analysis techniques than in past manuals. This is a conscious acknowledgment of the greatly improved capability to perform these type of analyses on a PC. The equipment shock mounting methodology has been greatly expanded and is based on comparison of calculated shock response spectra to equipment fragility curves recently developed from navy ship shock data. The auxiliary systems chapter is also greatly expanded and includes important new guidance on active versus passive airblast valves and chemical and biological design considerations.

The chapters of the manual and the supporting codes are being developed roughly in parallel. Several of the chapters are scheduled for initial publication as DNA technical reports in FY 93. The remaining chapters will be published in FY 94 or early FY 95. Once all chapters have been completed, the complete manual will be sponsored through the tri-service approval process and published as a Joint Service Manual. The supporting codes will be available with the first edition of the hypermedia version of the Manual in early FY 95.

SUMMARY

DNA's DAHS CWE Program is an excellent example of how DoD and the Services must work together now and in the future to achieve common objectives. In the spirit of Joint Service cooperation, the DAHS CWE Program will develop common, consistent, and state of the art methods and automated "tools" for use by all the Services in the design and analysis of protective construction.

CENTRIFUGE MODELLING TESTING TO INVESTIGATE THE USE OF BARRIERS TO MITIGATE BLAST EFFECTS ON BURIED STRUCTURES

M.C.R. Davies and A.J. Williams¹ and Major K.J. Claber R.E.²

¹ School of Engineering, University of Wales College of Cardiff, PO Box 925, Cardiff CF2 1YF, UK

² DRA, (RARDE, Christchurch), UK

ABSTRACT

A study of the protection of buried structures against blast loading using barriers has been conducted using the technique of centrifuge modelling. Four concepts were appraised in the trials. Barriers were formed from polystyrene, reinforced concrete, a composite of polystyrene and reinforced concrete and an air void (an open trench). The effectiveness of each barrier concept was measured using the results of strain gauges and accelerometers to compare the response to loading of protected structures with similar unprotected structures. Methods recommended by TM-5-855 for predicting crater dimensions and stress wave attenuation were also assessed in the study.

INTRODUCTION

The stress strain behaviour of soil is highly non-linear. The response of soil to loading being dependant on both the in-situ stress and stress history. Hence, in order to extrapolate model tests to prototype situations these effects have to be modelled correctly. By placing a suitably prepared n^{th} scale model on a centrifuge in an elevated gravity field ($n \times g$) the correct stress state may be simulated in the model. A consequence of the scaling laws is that mass of explosive scales by n^3 thus very small quantities of charge may be used to model large explosives. For example, in the tests described herein which were conducted at 20 g a charge totalling 2 g of C-4 explosive was equivalent to a 16 kg charge at prototype scale; had the test been conducted at 100 g the equivalent charge size would have been 2,000 kg. When considering the effect of blast close to buried structures it is important that any influences of crater geometry on the soil/structure interaction are correctly modelled. This can satisfactorily be achieved at elevated gravity. Benefits of using centrifuge models to investigate blast phenomena in soils include a high standard of repeatability, control over variables, such as soil density, together with time and financial savings compared to full scale trials. The

techniques has been used by other workers to study blast effects on buried structures and the effect of blast loading on deep foundations [References 1].

The experiments described herein were conducted using the geotechnical centrifuge at the University of Manchester, UK. This has a diameter of 6.4 m and is capable of carrying a soil package 2 m x 1 m x 0.6 m. For the test programme described herein, the models were contained in a strong box 0.75 m diameter and 0.46 m deep. All tests were conducted at a centrifuge acceleration of 20g.

CENTRIFUGE MODEL TESTING

A general arrangement of the models may be seen in Fig. 1. Two structures were subjected to blast loading in each experiment. One, the "protected" structure, was located behind a low acoustic impedance (the product of mass density, \dot{E} , and wave velocity, c) protective barrier and the other, the "unprotected" structure, was placed at the same distance from the charge and acted as a control specimen. The sides and base of the strong box were lined with a 12 mm thick polystyrene sheet to reduce the reflection of stress waves as they reached the boundaries of the model. A 40 mm drainage layer of pea gravel was placed in the bottom of the box.

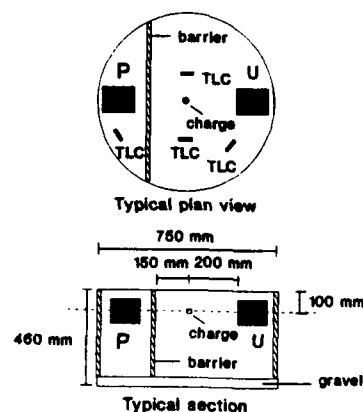


Fig. 1 Centrifuge model package

The soil used in the centrifuge tests was a fine Mersey River Sand ($D_{50} = 0.22$ mm, $C_U = 1.5$). Sand was placed in the box by pluviation; resulting in a density of 16.68 kN/m³. The model structures and instrumentation were installed at the required depth during formation of the soil model. Layers of dyed sand were placed at regular intervals during the pluviation process. The layers enabled discontinuities to be observed in the foundation layer when it was sectioned following the test. On completion of the model the soil was saturated and then allowed to drain thus producing a damp sand exhibiting negative pore pressures.

The structures used in the experiments consisted of a cubical steel box of internal dimensions 90 mm x 90 mm x 90 mm and side wall thickness 5.0 mm. Steel plates, either 0.5 mm or 2.0 mm thick were located on the front and back faces of the structure. These plates were fixed to the side walls only (i.e. spanning one way) and are considered as encastre for analysis purposes. The plate facing the charge was instrumented with strain gauges on both its outside and inside face. At prototype scale the face plates of the model structures represented a steel plate either 10 mm or 40 mm thick with a span of 1.8 m. The mid-height of the structures was located at a depth of 100 mm beneath the ground surface, i.e. 2 m at prototype scale.

Four barrier concepts were investigated in the model tests. These were:

- (i) a low acoustic impedance barrier - a 12 mm thick sheet of expanded polystyrene (equivalent to 0.24 m a prototype scale)
- (ii) a stiff barrier - a 15 mm thick reinforced concrete wall (equivalent to 0.3 m a prototype scale)
- (iii) a composite barrier - polystyrene and reinforced barriers (similar to concepts i and ii) placed together with the polystyrene facing the charge
- (iv) an air void - a 15 mm wide trench excavated to the inverse level of the structures and supported by cantilever sheet piled walls.

The barriers spanned the full width of the strong box and extended to the full depth of the box or the invert level of the structures as determined by the requirements of each experiment.

In all tests the charge consisted of 1.5 g of plastic explosive plus a detonator (equivalent to 0.5 g); giving a total charge weight of approximately 2 g. This corresponded to 16 kg at prototype scale. The charge was placed in a borehole with its centre of gravity at a depth of 100 mm, the same level as the mid-height of the structures. The borehole was backfilled following placement of the charge.

In addition to the strain gauges located on the structures, accelerometers were placed in each structure and earth pressure transducers located in both the free field and protected zones of the models. The signals were conditioned and stored digitally on the centrifuge arm, the amplified signals being passed through the slip rings for storage on disk and analysis following the test.

RESULTS

Crater Profile

Investigations into cratering phenomena in centrifuge models (e.g. Reference 3) have indicated that scaled crater volumes agree closely with those measured in full scale field tests. In both centrifuge and field studies empirical correlations between crater volume, V and charge mass, W indicate that

$$V \propto W^n \quad (1)$$

where $0.75 < n < 1.0$.

Typical crater profiles measured in the centrifuge tests are shown in Fig. 2. An advantage of these centrifuge models was that it is possible to section the model following the test to locate the outline of the true crater profile in addition to that of the apparent crater. The diameter of the craters in the experiments was typically 300 mm, the apparent depth 80 mm and the true depth 120 mm. This corresponding to 6 m, 1.6 m and 2.4 m at prototype scale, respectively. Measured dimensions are in excellent agreement with predictions using the method proposed in TM 5-855-1 (Reference 4) which are also shown in Fig. 2.

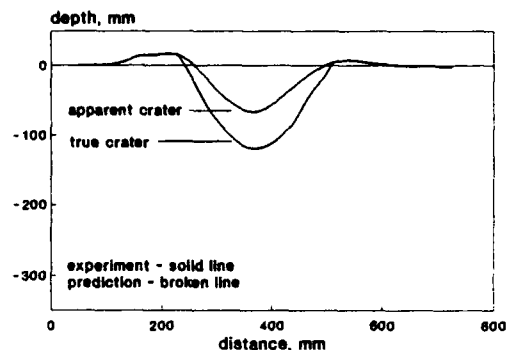


Fig. 2 True and apparent crater profiles - measured and predicted using TM-5-855

As Fig. 2 shows, the protective barrier and hence the structures were located outside the true crater. The soil/structure interaction therefore resulted from the effects of stress waves propagating through soil and not from ejecta interacting with the structure or barrier.

Stress Attenuation

Measurement of peak stress amplitude at varying

distances from the charge in the free-field (i.e. in the unprotected region of a model) are shown in Fig. 3. Also plotted is the predicted stress attenuation calculated using the attenuation formula suggested in TM 5-855-1 (Reference 4) with values of soil density and stress wave velocity measured in the experiments and the value of the attenuation coefficient, n , for sand with >4% air voids. Figure 3 shows very good agreement between measured and predicted values of peak stress amplitude.

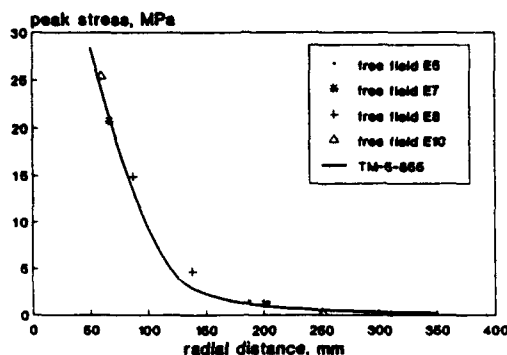


Fig. 3 Stress wave attenuation - measured and predicted using TM-5-855

The predominant cause of attenuation in the free-field is geometric damping. Protection of buried structures close to blast may be achieved by screening the wave using a barrier. The effect of screening the propagating stress wave by placing a polystyrene barrier in its path was a reduction in its peak amplitude. At a distance of approximately 200 mm from the blast (i.e. the location of the structure) the peak amplitude was reduced from 1.17 MPa to 0.08 MPa. Using the theory of wave propagation in an elastic medium the attenuation provided by a barrier may be quantified by the value of the "transmission coefficient" i.e. the ratio of the intensity of the incident wave on the barrier to the wave transmitted through the barrier, Reference 5. The average value of this coefficient was measured to be 0.027 in the centrifuge models which compares with a predicted value of 0.013. Thus measured and predicted values were in close agreement.

Soil-Structure Interaction

A comparison of strain gauges located at the mid-span of the front face in the protected and unprotected structures is shown for each of each barrier type in Figs. 4, 5, 6 and 7 (N.B. in these figures tensile strains are negative). The plots indicate that:

- (i) As the stress wave arrived at the two structures the mid-span gauges went into tension - indicating bending. The gauges on the unprotected structure and the structure protected by the reinforced concrete barrier initially recorded a compressive strain - indicating hogging - prior to tension. During this phase the protected structure displayed higher

values of tensile strains. The period of this loading phase, about 550 μ s, corresponded with the length of the compressive wave impulse at this distance from the blast.

- (ii) Following this first phase there is a continued increase in strain development in both structures. Both reach a peak some time after the propagating wave passed the structure.

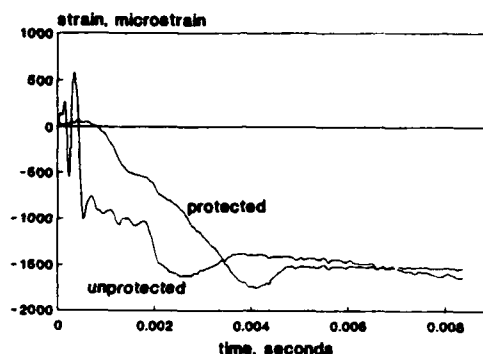


Fig. 4 Response of mid-span strain gauge on protected and unprotected structures - polystyrene barrier

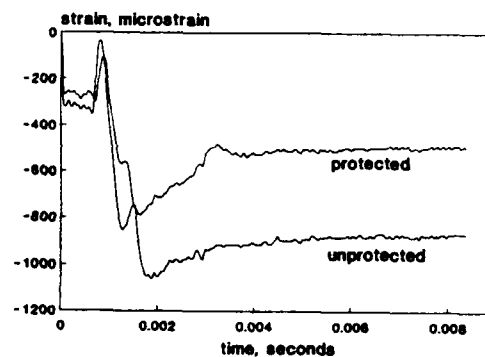


Fig. 5 Response of mid-span strain gauge on protected and unprotected structures - reinforced concrete barrier

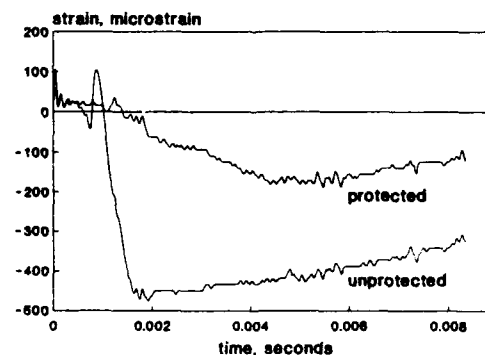


Fig. 6 Response of mid-span strain gauge on protected and unprotected structures - composite barrier

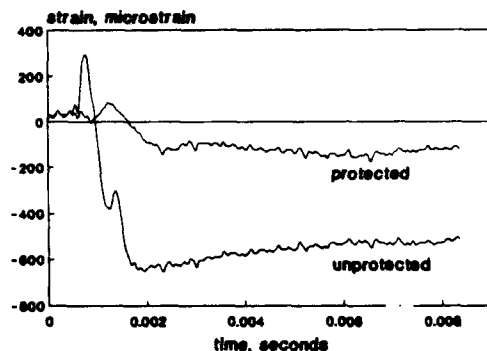


Fig. 7 Response of mid-span strain gauge on protected and unprotected structures - open trench

These observations indicate that there are two distinct loading mechanisms operating on the structures. In Phase 1 the dominant loading of the structures resulted from interaction with the propagating stress wave - "stress wave loading". This was highly attenuated by the low acoustic impedance materials in the polystyrene and composite barriers and by the open trench, Figs. 4, 6 and 7, but not by the high acoustic impedance reinforced concrete barrier, Fig. 5.

The increase in deformation with time after the wave front had passed the structure indicated a continued loading. This resulted from the acceleration of the soil located between the structure and the edge of the crater. The response of the structure develops over a relatively longer time because of the inertia of this mass of soil - loading in Phase 2 is thus referred to as "inertial loading". Similar behaviour has also been observed in other series of centrifuge tests References 1 and 6.

Although the polystyrene barrier was demonstrated to be highly effective in reducing the stress wave loading on the structure, the results show that it provided limited, if any, resistance to inertial loading. This is because the location of the barrier in relation to both the crater and the structure was such that significant inertial force could be developed by the acceleration of the soil between the crater and the barrier. Since the barrier was highly flexible this loading was not distributed over a large area, but was transferred to the soil in the zone immediately behind the barrier and hence to the structure.

In contrast, although there was only limited attenuation of the stress wave loading by the reinforced concrete barrier, Fig. 5, significantly less strains were developed in the protected structure than in the unprotected structure during the inertial loading phase. This was because the barrier had a significantly greater bending stiffness than the polystyrene barrier and thus acted to distribute the loading over a greater area. The most efficient barrier

concept was obtained by combining both polystyrene and reinforced concrete to optimise the favourable properties of both materials, i.e. the low acoustic impedance of the polystyrene and the stiffness of the reinforced concrete, Fig. 6.

The best protection was afforded by an open trench, as indicated by the lowest protected structure strains measured in the series of tests shown in Fig. 7. Loading of the protected structure resulted from distribution of stress due to inertial loading on the embedded portion of the cantilever sheet pile walls.

Although in the experiments the open trench resulted in the lowest structural response this concept may not be the best practical means of protection. Should the trench become inundated with water (which has a high acoustic impedance) this will facilitate the transmission of stress waves. Collapse of support, resulting in closure of the void, during a first strike will also reduce second strike protection. This later situation is particularly a problem with unsupported trenches excavated in cohesive soils and has been observed in centrifuge tests using a clay medium, Reference 7.

Structural Accelerations

The presence of the barrier reduced the frequency of vibration and magnitude of the acceleration experienced by the structure. Figure 8 shows typical acceleration history plots for a structure protected by a polystyrene barrier and the unprotected structure from the same test; the peak acceleration was reduced from 130 g to 25 g. This type of barrier would therefore be effective in reducing the magnitude of shock loading to buried structures and the foundations of surface structures.

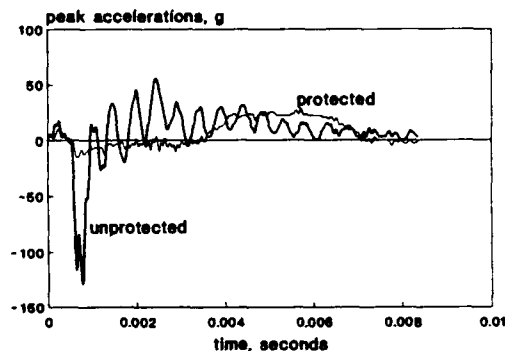


Fig. 8 Acceleration response - protected and unprotected structures

CONCLUSIONS

The following conclusions can be made from the results of the series of centrifuge tests:

1. Centrifuge experiments may be used for modelling the effects of blast on buried structures. Measured model crater dimensions corresponded well with predicted prototype values. Centrifuge modelling laws permit inertial loading effects to be correctly simulated at small scale.

2. The recorded values of peak stress amplitude reduced with distance from the source of the blast. Predictions of attenuation agreed very well with the experimental results.

3. Barriers containing low acoustic materials were highly effective in attenuating propagating stress waves and reducing the magnitude of shock loading on structures.

4. The soil structure interaction revealed that there were two distinct loading mechanisms. The first resulting directly from the propagating stress wave and the second due to inertial loading from the soil located between the crater and the structure. Although a low acoustic medium barrier was highly effective in reducing peak stresses and accelerations it only provided limited resistance to inertial loading. Stiff barriers distributed the inertial loading providing greater protection for the buried structures.

ACKNOWLEDGEMENTS

The study described herein has been carried out with the support of Procurement Executive, Ministry of Defence, on behalf of Defence Research Agency, RARDE (Christchurch). The authors wish to thank Dr W.H Craig, Mr M. Cruickshank and Dr C.M. Merrifield and their colleagues in the centrifuge modelling group at Manchester University for their help in conducting the experiments.

REFERENCES

1. Kutter, B.L., O'Leary, L.M. Thompson, P.Y. and Lather R. Gravity-scaled tests on blast-induced soil-structure interaction. *Journal of Geotechnical Engineering*, Vol 114, No. 4., pp 431-447, 1988.

2. Steedman, R.S., Felice, C.W. and Gaffney E.S. Dynamic response of deep foundations. *Proc. 4th Int. Conf. on the Interaction of Non-nuclear munitions with structures*, Panama City, U.S.A., 1989.

3. Serano, C.H. Dick, R.D., Goodings, D.J. and Fournay, W.F. Centrifuge modelling of explosion induced craters. *Centrifuge 88*, (Ed.) J-F Corte, *Proc. International Conference Centrifuge 1988*, Paris, Balkema, pp 445-450, 1988

4. U.S Army. Fundamentals of protective design for conventional weapons, TM 5-855-1, Engineering Waterways Experimentation Station, Vicksburg, Miss., 1986.

5. Davies, M.C.R. and Ismail, A.B. Retro-Fitting of Expedient Protection for Buried Structures. *Rapidly Assembled Structures*, (Ed.) P.S. Bulson, *Proc. Int. Conf on Mobile and Rapidly Assembled Structures*, Southampton, pp 163-174, 1991.

6. Davies M.C.R. Modelling of Dynamic Soil Structure Interaction resulting from impulsive surface loading. *Centrifuge 91*, (Eds.) H-Y Ko and F.G. McLean, *Proceedings International Conference Centrifuge 91*, Boulder, Colorado, Balkema, pp 487-493, 1991.

7. Davies M.C.R. and Williams A.J. Centrifuge Modelling of the protection of buried structures, Phase II contract report to DRA RARDE, University of Wales Cardiff, 1993.

FROUDE-SCALED TESTS OF EXPLOSIVELY LOADED BURIED STRUCTURES USING A SOIL SIMULANT

Maynard A. Plamondon (1)

Daniel E. Chitty (2)

Robert L. Guice (3)

Douglas H. Merkle (4)

Applied Research Associates, Inc.

(1) Albuquerque, NM

(2) South Royalton, VT

(3) Lakewood, CO

(4) P. O. Box 40128, Tyndall AFB, FL 32403

ABSTRACT

Operation Desert Storm conclusively demonstrated the vulnerability of aboveground structures to modern, precision-guided, air-to-ground munitions. It is now abundantly clear that earth berming or deeper burial of hardened military structures is required if they are to possess an acceptable survivable probability, unless they are protected by special armor.

The mechanism of cohesionless soil resistance to penetrating weapons involves shear strength derived from the weight of soil above. This means that gravity is a vital factor in determining the survivability of a bermed or buried structure.

Explosive tests of full-scale, buried, hardened structures are expensive. Since, in principle, all physical relationships relating weapon attack parameters to structural response can be rendered dimensionless, the prospect of using relatively less expensive reduced-scale models to develop design criteria and methods is very attractive. The problem is to satisfy important scaling relationships between model and prototype, so the model results can be extrapolated to yield accurate predictions of prototype behavior. In the project at hand, powdered coal was used to simulate the stress-strain-strength properties of dry sand, and lead shot was used to increase the average mass density of the soil simulant without significantly affecting its stress-strain-strength behavior. Froude scaling was then used to properly account for gravity without using a centrifuge.

INTRODUCTION

The following discussion describes the development of Froude scaling relationships between the important parameters for the general problems of both static and dynamic loadings on soil or buried structures affected by gravity. The results of laboratory tests on potential simulant materials are presented, and the rationale for selecting crushed coal, and a mixture of crushed coal and lead shot as sand simulants is presented.

Results of proof-of-principle static tests of cone penetrometers pushed into sand and the crushed coal and crushed coal/lead shot simulants are presented, and results of three field tests involving a buried explosive loading a buried cylinder are presented. The results are very encouraging for the use of coal and a coal/lead mixture as Froude-scaled sand simulants.

GENERAL THEORY

Determining the response of a protective structure to a

conventional weapon detonation can be reduced to the solution of a differential equation of the type indicated by Equation (1).

$$\frac{\partial \sigma}{\partial x} = \rho \frac{\partial^2 u}{\partial t^2} + C_1 \rho g \quad (1)$$

In this equation, σ is stress, x is distance, ρ is mass density, u is particle displacement, t is time, and g is the effective gravitational acceleration. The nondimensional constant, C_1 , relates the X direction to the direction of gravity. Using smaller than actual size test structures can result in different behavior for the model than for the prototype, if proper scaling is not used. To prescribe how model quantities should vary with respect to prototype quantities, scale factors can be introduced in Equation (1), resulting in the following expression for the model response, where each K is the ratio of the indicated model quantity to the corresponding prototype quantity:

$$\frac{K_\sigma \partial \sigma}{K_l \partial x} = K_\rho \rho \frac{K_l \partial^2 u}{K_t^2 \partial t^2} + C_1 K_\rho \rho K_g g \quad (2)$$

or, rearranging terms:

$$\frac{\partial \sigma}{\partial x} = \left(\frac{K_\rho K_l^2}{K_\sigma K_t^2} \right) \rho \frac{\partial^2 u}{\partial t^2} + \left(\frac{K_\rho K_g K_l}{K_\sigma} \right) C_1 \rho g \quad (3)$$

If the scale factors are chosen so that:

$$\frac{K_\rho K_l^2}{K_\sigma K_t^2} = 1 \quad (4)$$

and

$$\frac{K_\rho K_g K_l}{K_\sigma} = 1 \quad (5)$$

then Equations (1) and (3) will be identical, and the computed responses will be identical for model and prototype.

REPLICA SCALING AND ITS CONSEQUENCES

Replica scaling normally uses smaller versions of the larger prototype structure. The model structure is geometrically scaled by the length scale factor, K_L , and the same materials are used in the model as in the prototype. This results in the mass density scale factor, K_ρ , and the stiffness scale factor, K_G , being equal to one, which in turn leads to the other scale factor values shown in Table 1.

The replica scaling requirement that all accelerations scale as the reciprocal of the length scale factor results in the requirement that gravity be artificially simulated. This is often done by conducting small-scale centrifuge experiments, whereby the centrifugal forces simulate the increased gravity.

FROUDE SCALING AND ITS CONSEQUENCES

Froude scaling accepts the fact that the gravity scale factor, K_g , will be equal to one. Therefore, as shown in Table 1, the stress scale factor must equal the product of the mass density and length scale factors. The dimensional properties of the scaled material must then be different from those of the prototype material, but the dimensionless properties, such as Poisson's ratio, must be the same.

SIMULANT SELECTION FOR FROUDE SCALING

Selection Criteria: Soil simulant selection criteria were based on Froude scaling laws, which were enforced only at the macroscopic level. Thus, the materials were considered homogeneous, and no attempt was made to scale grain size. Further, attention was restricted to simulating a cohesionless sand. Within these restrictions, a cohesionless sand simulant was sought that would satisfy the Froude scaling relationships for mass density, nonlinear uniaxial stress-strain behavior (up to lock-up) in one-dimensional (constrained) compression, Poisson's ratio, and friction angle. The objective was to find materials having modulus and density properties yielding three length scale factors up to 1/50. Materials with porosity significantly higher than the prototype porosity were eliminated, because their deformation behavior did not scale properly at large strains. Like strain, Poisson's ratio is dimensionless, and its value should be equal in model and prototype. For a sand loaded in uniaxial strain, the incremental Poisson's ratio varies as a function of axial strain. In this simulant selection effort, only the initial value of Poisson's ratio was considered.

To a very good approximation, sand can be considered a cohesionless, frictional material. Therefore, the only strength property that need be considered is the friction angle, which is also dimensionless, implying that its value must be the same for the prototype and simulant materials.

Prototype Properties: The prototype material was a fine sand that had been extensively characterized by the U.S. Army Engineer Waterways Experiment Station. Properties of the prototype sand are summarized in Table 2, and its uniaxial stress-strain curve is presented in Figure 1.

Laboratory Testing for Material Selection: Strength and deformation properties of over 20 candidate materials were determined by triaxial testing. The tests were performed on reconstituted specimens that were carefully measured to

determine their initial density. The tests were fully instrumented to record both axial and radial components of load and deformation. Two different types of loading were employed: uniaxial strain, and conventional triaxial compression. Uniaxial strain was used to determine deformation properties, and triaxial compression to measure the friction angle. If axial stress is plotted as a function of axial strain in a constrained compression test, the slope of the initial linear portion of the curve is the initial constrained modulus, M .

Primary screening of candidate materials was done on the basis of the computed length scale factor, which is the ratio of the mass density and stress scale factors determined by laboratory tests. To assess a material's suitability in terms of nonlinear stress-strain behavior, plots were made of both the model and prototype stress strain curves. The model stress data was then scaled by the stress scale factor, K_σ , derived from the initial loading slopes of the model and prototype curves. If the two curves then matched over the entire strain range of interest, that aspect of the model material behavior was judged perfectly Froude-scaled to the prototype. For materials that passed initial screening based on constrained modulus and density, triaxial compression tests were performed to determine their friction angle, using standard soil testing procedures.

Sand Simulant: Two materials were eventually selected as Froude-scaled sand simulants, although it was necessary to compromise on the length scale factors initially desired. At a length scale factor of approximately 1/5, finely crushed bituminous coal was selected. To obtain a more extreme scaling, fine lead particles were added to the coal, resulting in a material about twice as dense, with approximately the same stiffness. A 60/40 mixture (lead/coal by weight) produces a length scale

factor of approximately 1/10. Due to the large difference in mass density between the two constituents (11.3 Mg/m³ for lead; 1.33 Mg/m³ for bituminous coal), this is equivalent to 85% coal and 15% lead by volume. Because of the high volume fraction of coal, the strength and deformation properties approximate those of plain coal. However, the high weight fraction of lead significantly increases the density.

Tests were performed on coal and coal/lead specimens with a variety of grain-size distributions, all in the range of natural sands. A very fine-grained lead shot was used, having 10% in the 0.22-0.41 mm range, and 90% in the 0.41-1.14 mm range.

Figure 1 shows the axial stress-strain curve from uniaxial strain tests on a coal/lead specimen compared with the criterion curve for WES Flume Sand. In the figure, the coal/lead data have been scaled by a factor of 10. Within the variation in laboratory test data for the various coal-based simulants, the data can also be considered representative of the mechanical response of pure coal. In Table 2, the properties of the crushed coal and the coal/lead mixture are compared with those of criterion sand. Both candidate simulants closely satisfy all density, strength, and deformation criteria for Froude-scaled sand simulants at length scale factors up to 1/10. This, combined with the reasonable cost of coal, and the dearth of other suitable simulant materials, led to the decision to compromise the requirement for three length scale factors up to 1/50, and to concentrate on coal-based simulants.

STATIC PROOF-OF-PRINCIPLE TESTS

Tests were conducted to demonstrate the application of Froude scaling under static conditions, in which the response is

sensitive to the influence of gravity. Electric cone penetrometer tests (ECPT) were conducted in specially prepared uniform test beds at three different scales. An existing set of data from full-scale (1.4 inch (36-mm) diameter) ECPT work at the Misty Port III field test site was used as the prototype. Two sets of Froude-scaled tests were performed in the laboratory, one with a length scale factor of 1/3.5 using crushed coal as the sand simulant, and the second in a coal/lead mixture at a length scale factor of 1/7.

Prototype Tests: The prototype penetrometer has a diameter of 35.7 mm, conforming to ASTM D3441. Care was taken in testbed construction to achieve as uniform a density as possible. Four cone penetrations were made through the nominally uniform testbed.

1/3.5 Scale Tests: The first laboratory tests in the static POP series were conducted using a specially constructed 10.2-mm diameter cone in a test chamber filled with bituminous coal. It was considered desirable to keep the coal grain size less than one tenth of the cone diameter. The resulting material had over 90% passing a U.S. Standard No. 16 (1.0 mm) sieve. On the fine end of the grain-size distribution, 10% passed a No. 140 sieve (0.11 mm). To be consistent with the laboratory material property tests, the target density for the test chamber material was 857 kg/m³. To control the density, the crushed coal was placed in 100 mm lifts. The final average density was 852 kg/m³.

Four cone penetrometer tests were conducted in the bituminous coal. The test holes were located so that each was well separated from the others, and from the chamber walls.

1/7 Scale Tests: The final static POP tests were conducted in a test chamber filled with a mixture of crushed bituminous coal and lead particles, using a 5.1 mm diameter electric cone penetrometer. Although the details differ, the penetrometer was conceptually the same as the 10.2 mm penetrometer used for the 1/3.5 scale tests.

The sand simulant for the 1/7 scale static POP tests consisted of a mixture of crushed bituminous coal and fine lead particles. The bituminous coal was first crushed, and only material that passed a U.S. Standard No. 20 (0.71 mm) sieve was used to prepare the simulant. The coal was then mixed with fine lead shot in a ratio of 40% coal to 60% lead, by weight. The target density for preparing the sand simulant in the test chamber was 1.81 Mg/m³. Based on this density, quantities of lead and coal sufficient to form 25-mm lifts were weighed out and mixed together. The actual density achieved was 1.845 Mg/m³.

Comparison of POP Test Results: If the laboratory penetrometer tests had been completely Froude-scaled, the results could be compared by simply scaling the depth and stress data by their respective scale factors. In these tests, the length scale factors of the cone penetrometers were somewhat different than the length scale factors suggested by the material properties. The cones in the two model tests scaled to the prototypes by factors of 1/3.5 and 1/7. The best estimate of the simulant scale factors, based on incomplete knowledge of the material properties as they existed in the actual testbeds, is 1/3.9 and 1/8.3. To compare the results of the three tests as accurately as possible, they were converted to nondimensional quantities, using the following expressions:

$$\text{Dimensionless Depth} = \frac{\rho g D}{M} \quad (6)$$

$$\text{Dimensionless Stress} = \frac{\sigma B \rho g}{M^2} \quad (7)$$

where: B is penetrometer diameter, D is depth, M is initial constrained modulus, g is gravitational acceleration, ρ is dry bulk mass density of sand or simulant, and σ is cone penetrometer tip stress.

Figure 2 compares the tests at the three different scales. The agreement is good. Comparison with the one-standard-deviation bounds showed that the variation among tests at different scales is of the same order as the scatter in nominally identical tests.

FIELD TESTS

Objective: The objective of the field tests was to obtain shock wave propagation data in sand simulants, using Froude scaling procedures, and to obtain data on the rigid-body motion response of a buried structure. To meet this objective, three field tests were conducted.

The full-scale prototype system is a simplified version of the French-designed Survivable Collective Protection System (SCPS) that has been tested under conventional weapon effects. The prototype threat is a penetrating weapon with 500 kilograms of TNT, detonated at a depth of 4.2 meters beneath the ground surface, and at a distance of 6.0 meters from the outer edge of the SCPS, as shown in Figure 3.

Of the three model field tests conducted, two were at different Froude scales, to provide results showing whether Froude scaling can be used with appropriate material simulants. The third was a replica-scaled test at the same scale as one of the Froude-scaled tests. This test provided results that could be compared directly to the Froude test results, as well as scaled to the prototype size.

Test Description: The simulant selection study showed that the smallest practical Froude scale sizes were 1/5 for coal as the sand simulant, and 1/10 for a mixture of coal and lead as the sand simulant. While it was desirable to also Froude-scale the reinforced concrete structures, that was not economically feasible. Therefore, the structures were scaled geometrically, which kept their mass generally correct, but they were stiffer than if Froude-scaled. However, this was acceptable, since rigid-body motion, not structural deformation, was of primary interest.

The test bed dimensions were chosen to reproduce results of a prototype system test out to a time of 40 milliseconds. This corresponds to 4 msec for the 1/10 replica-scaled, 12.6 msec for the 1/10 Froude-scaled, and 17.9 msec for the 1/5 Froude-scaled tests.

True Froude scaling of explosives requires that the explosive energy density vary by the same ratio as the stress scale factor. Such explosives are not available. C-4 was chosen as the explosive because it is moldable, does not require a container (a bomb case was not simulated), and is relatively safe. Since the prototype explosive was TNT, the energy equivalency of C-4 had to be accounted for. When this was done, the sizes of the C-4 charges for the 1/10 and 1/5 Froude-scaled tests and the 1/10 replica-scaled test were 310, 390 and 39 grams respectively.

The 1/10 replica-scaled testbed consisted of mortar sand, which approximated the grain-size distribution of flume sand. It was clean, fairly fine, and uniform. At least 90 percent passed a No. 20 sieve, and the coefficient of uniformity was less than 4. Because the testbed was small, compaction of 6-inch lifts was obtained by hand tamping, using a 1-foot square metal plate. The measured unit weight was 97 lb/ft³, which corresponds to a bulk mass density of 1550 kg/m³.

The 1/5 Froude-scaled testbed consisted of crushed, bituminous coal. Since the properties of coal vary, depending on its origin, the same coal used in the simulant selection process was used for the tests. The coal was crushed to obtain grain-size distributions similar to sand (90 percent passing a No. 16 sieve, and 10 percent passing a No. 140 sieve). The coal was compacted in 6-inch lifts, using a steel plate hand compactor and a water-filled roller. The measured unit weight was 53 lb/ft³, which corresponds to a bulk mass density of 850 kg/m³.

The 1/10 Froude-scaled testbed was a mixture of the same type and size coal used in the 1/5 Froude-scaled test, and lead shot. The ingredients were mixed together in a 60 percent lead to 40 percent coal ratio, resulting in an average bulk mass density of 1890 kg/m³ (measured unit weight 118 lb/ft³), and a porosity of 0.34. Again, because the testbed was small, compaction was obtained by hand tamping, using a metal plate.

Analysis of Test Results: The test data was scaled, nondimensionalized and plotted. The peak free-field particle velocity data is shown in Figure 4. If scaling has been adequate, the results from all tests should provide single estimates for such quantities as variation of scaled peak acceleration, peak velocity, peak stress, and time-of-arrival, as functions of scaled range. The scatter of the acceleration, velocity, and time-of-arrival data for all tests was about the same as that to be expected from a single test, thus validating both replica and Froude scaling for those measured free-field parameters, for the range of scales investigated. The stress data was less conclusive.

Table 3 presents nondimensional peak structural velocities from all three field tests. Comparison of the nondimensional radial velocities (relative to the burst location) shows an average nondimensional value of 0.0048, with a variation of 15 percent on either side of the average value.

CONCLUSIONS

Crushed coal can be used as a Froude-scaled sand simulant. The mass density scale factor of about 1/2 and stiffness scale factor of about 1/10 lead to a length scale factor of about 1/5. The initial porosity, Poisson's ratio, and angle of internal friction for appropriately prepared coal and sand are very similar.

A mixture of crushed coal and lead can also be used as a Froude-scaled sand simulant. A small amount of lead shot by volume does not appreciably change the stiffness or nondimensional values of the coal. The lead, however, does increase the mass density. Length scale factors of about 1/10 can be obtained.

The use of coal and a mixture of coal and lead as Froude-scaled sand simulants leads to the same nondimensional results for the variation of stress at the tip of a cone penetrometer as a function of depth as was obtained from a full scale test in sand.

Comparison of the nondimensional dynamic response of the

testbed and buried cylinder from scaled tests involving 1/10 replica-scaled, 1/5 Froude-scaled and 1/10 Froude-scaled parameters shows considerable agreement among all the tests. The largest difference existed in nondimensional peak free-field stress as a function of nondimensional range for the replica test, when compared with the two Froude tests. Peak scaled bending velocities of the buried structure in the transverse direction showed a wide variation. Both differences may be related to parameters that were not scaled or not scaled appropriately. Also, the measurement of stress is difficult in dynamic tests.

Both replica and Froude scaling of buried structures subjected to weapon effects offer cost-effective means for investigating the response of a prototype system. The choice of which scaling to use depends on the objectives of the test.

ACKNOWLEDGEMENT

This work was funded by two Small Business Innovation Research grants from the Air Force Civil Engineering Support Agency, whose sponsorship is gratefully acknowledged. Capt Richard A. Reid was the AFCEA Project Officer.

REFERENCES

1. Zahrah, T.F., Merkle, D.H., and Auld, H.E., Gravity Effects in Small-Scale Structural Modeling, Applied Research Associates, Inc. final report to the Air Force Engineering and Services Laboratory, ESL-TR-88-57, December 1988.
2. Plamondon, M.A., Chitty, D.E., and Guice, R.L., Froude Scaling of Buried Structures Using Coal and Coal/Lead as Simulants for Sand, Applied Research Associates, Inc. draft final report to the Air Force Civil Engineering Support Agency, 19 June 1991.

TABLE 1. SCALING FACTORS

Variable	Scale Factor Symbol	Froude Value	Replica Value
length	K_l	K_l	K_l
mass density	K_ρ	K_ρ	1
acceleration	K_g	1	K_l^{-1}
stress	K_σ	$K_\rho K_l$	1
time	K_t	$\sqrt{K_l}$	K_l
velocity	K_v	$\sqrt{K_l}$	1
force	K_f	$K_\rho K_l^3$	K_l^2
unit weight	K_γ	K_ρ	K_l^{-1}
impulse	K_I	$K_\rho \sqrt{K_l^7}$	K_l^3
energy	K_E	$K_\rho K_l^4$	K_l^3

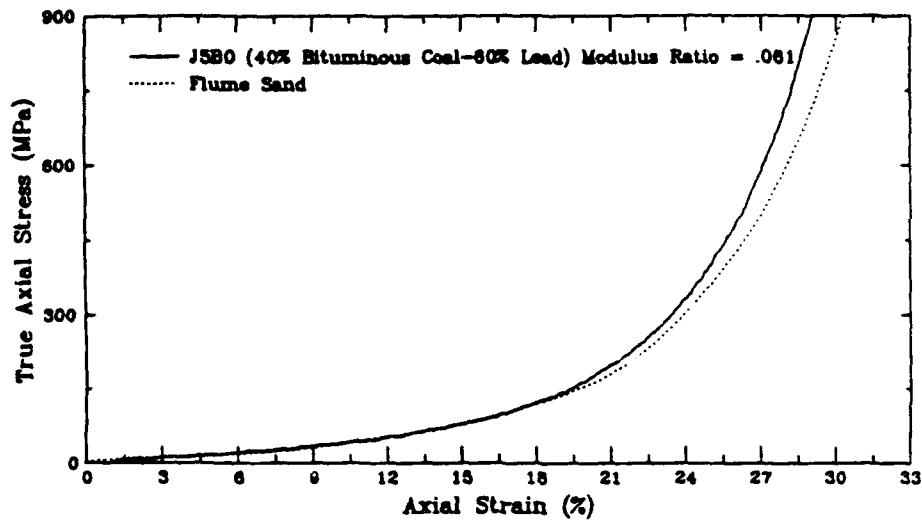


Figure 1. Comparison of Uniaxial Strain Behavior of WES Flume Sand with the Scaled Response of a Mixture of Crushed Bituminous Coal and Lead Shot.

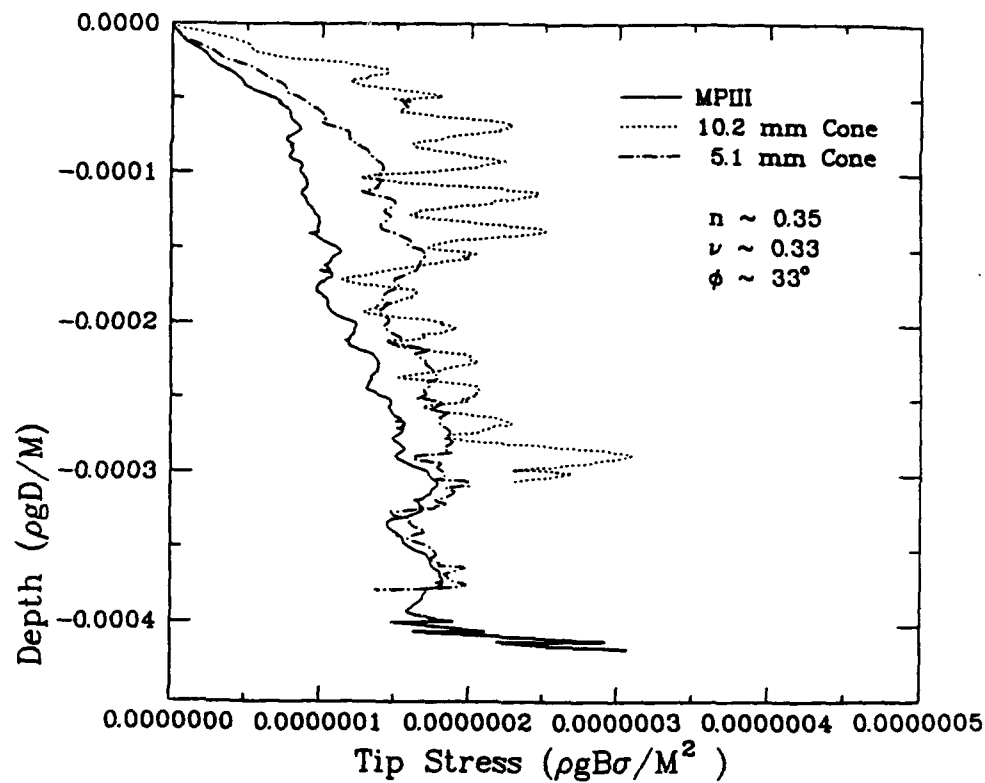


Figure 2. Comparison of Non-dimensional Tip Stress Data from Cone Penetrometer Tests at Prototype Scale and Two Reduced (Froude) Scales.

TABLE 2. SUMMARY OF SAND AND SELECTED SIMULANT PROPERTIES BASED ON LABORATORY TESTS

Property	WES Flume Sand	Coal	Lead/Coal 60/40 by Wt. 1330 (coal) 11300 (lead)
Grain Density, kg/m ³	2640	1330	
Porosity, dimensionless	0.39	0.4	0.4
Bulk Mass Density, kg/m ³	1610	850	1850
Initial Constrained Modulus, MPa	230 - 375	20 - 40	20 - 40
Poisson's Ratio, dimensionless	0.34	0.34	0.34
Angle of Internal Friction, Deg	30	31	31

TABLE 3. MODEL STRUCTURAL RADIAL RIGID BODY AND BENDING VELOCITY

Radial Velocity	Test		
	1/10 Replica	1/5 Froude*	1/10 Froude**
Actual Values (m/s)	1.8	0.7	0.31
	1.6	0.6	0.37
	1.4	0.6	0.31
	1.2	0.45	0.39
Nondimensionalized by Soil/Simulant	0.0064	0.0058	0.0037
Properties (v/c)	0.0057	0.0050	0.0044
	0.0050	0.0050	0.0037
	0.0043	0.0038	0.0046

*Mass and Bending stiffness approximately correct.

**Mass: 0.8X low and bending stiffness factor of 10X high for "exact" 1/10 Froude Scaling

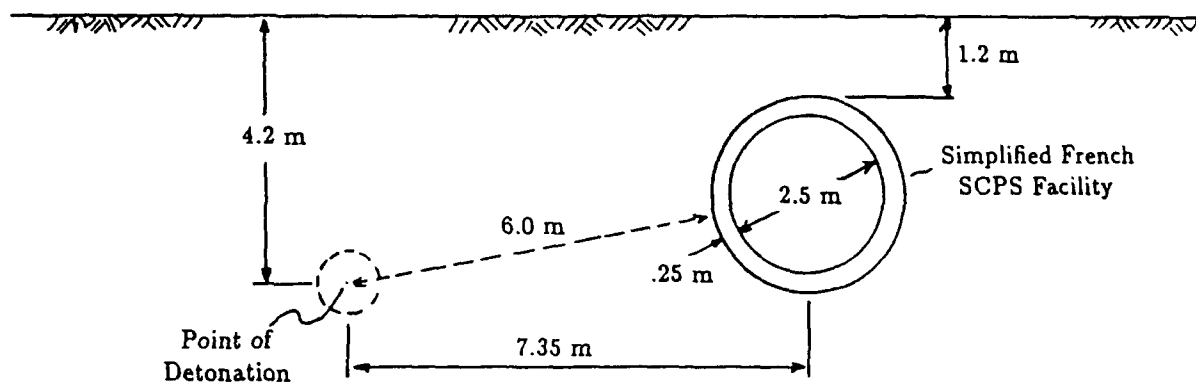


Figure 3. 500 Kg TNT Prototype System.

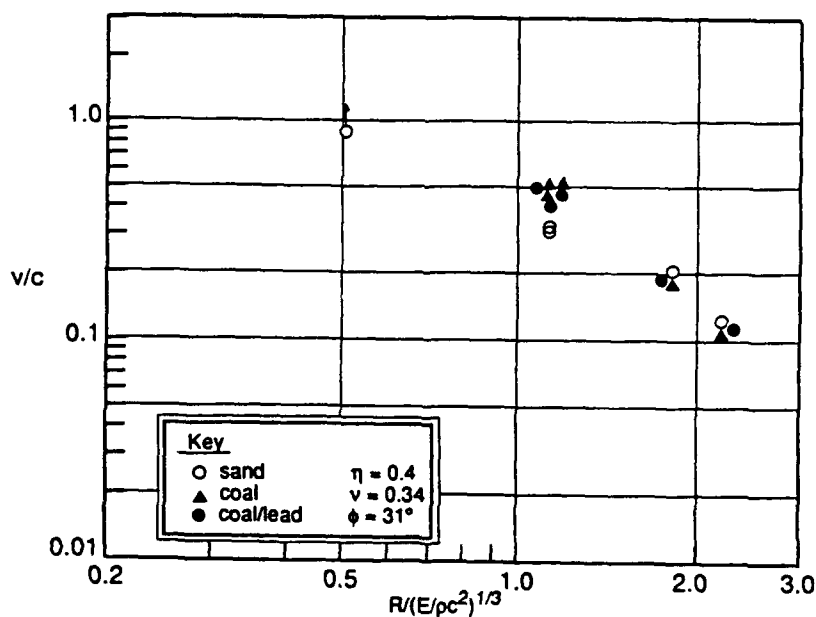


Figure 4. Non-dimensional Velocity vs. Non-dimensional Range.

IMPACT LOADING OF PLATES A COMPARISON BETWEEN NUMERICAL SIMULATIONS AND EXPERIMENTAL RESULTS

*Magnus Langseth, Torodd Berstad and Per Kr. Larsen
Department of Structural Engineering
The Norwegian Institute of Technology, Norway
and
Arnfinn Jenssen
Norwegian Defence Construction Service, Norway*

Abstract

Model tests have been carried out to study the plugging capacity of thin steel plated structures of grade St52-3N subjected to circular blunt ended large mass projectiles in the low velocity regime ($v_i < 50$ m/s). To extend the parametric range of this study numerical simulations have been done with LS-DYNA3D. The simulations so far have been carried out to verify the code against the present test results. Good agreement has been found between tests and analyses based on models using shell elements and the quasi-static material properties.

1 Introduction

According to the Norwegian Petroleum Directorate large mass projectiles such as dropped objects and fragments generated by a gas explosion have to be considered in the design of offshore structures.

Based on a survey of possible dropped objects, long rods such as drill-collars are identified as the most dangerous item due to its high kinetic energy and small contact area with the structure during impact. A drill-collar has a mass of approximately 3200 kg, a length of 10 m, a diameter in the threaded pin end of 146 mm and may be dropped from heights up to 40 m.

Fragments generated by a gas explosion can be both primary and secondary fragments and can vary both in shape and size. However, for large mass fragments the response in a steel plated structure will be the same as for dropped objects, consisting of global elastic and plastic deformations combined with a local failure at the impact point. This combined mechanism results in a difficult design situation, and existing design formulas show poor agreement with large mass projectile tests [1] [2]. Furthermore, formulas developed for other mass and velocity regimes are not directly applicable, as the physical behaviour during impact is quite different [3].

Due to lack of knowledge about penetration mechanics in the low velocity regime ($v_i < 50$ m/s) for large mass projectiles, a model test study has been carried out. Rigid body blunt ended projectiles have been fired against thin steel plates of grade St52-3N to study the plugging capacity of such targets. The

primary variables have been the plate thickness, mass of projectile and support conditions.

Based on these results and basic principles of mechanics a design model has been proposed to calculate the plugging capacity of thin steel plates subjected to large mass projectiles [4] [5]. However, to extend the parametric range of this model and to get a better understanding of the physical mechanisms present during impact, numerical simulations have been done with LS-DYNA3D [6]. The simulations so far have been carried out to verify the code against the present test results. The comparison is made for simply supported plates and clamped plates equipped with stringers.

The experimental results have been published in ref [7]. However, as a basis for the present comparison between the experimental results and LS-DYNA3D calculations, a short summary of the most important findings from the experiments will be given.

2 Experimental studies

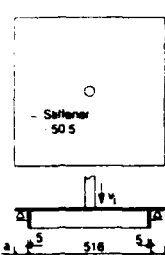
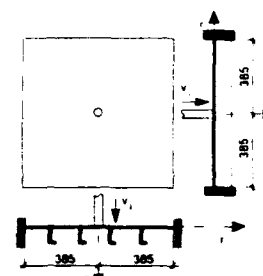
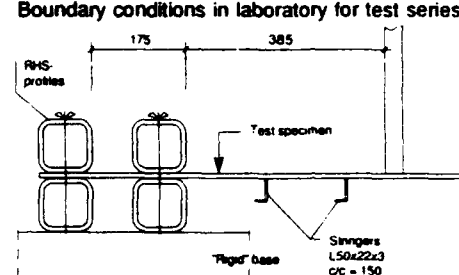
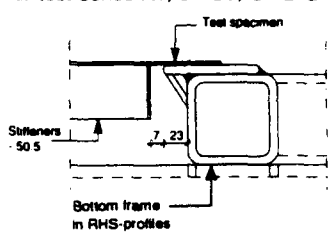
2.1 Test program

All tests were carried out in scale 1:4 using replica modelling. As structural model for the impacted structures was chosen clamped plates with and without stringers (test series DM) and simply supported hatches (test series A1, B1-3, C1-2) of the type used in the wellhead area on a platform for simultaneous drilling and production, Table 1. The hatches consisted of a square steel plate reinforced with rectangular transverse stiffeners along all four sides.

For the present tests the projectile was modelled as a rigid body with a flat ended circular nose. Throughout the tests the diameter of the projectile was taken as $d = 36.5$ mm.

The dynamic tests were performed by means of a pneumatic accelerator consisting of a reservoir of compressed air and an accelerator tube. The reservoir operated at a pressure up to 7 bar and allowed a 50 kg mass to be accelerated to an impact velocity of 40 m/s. For each combination of target geometry and projectile mass, a sequence of tests were carried out. By

Table 1 - Test program and specimen geometry

Test series	Plate geometry		Projectile mass M_p (kg)	Test specimen geometry and boundary conditions		
	h(mm)	a (mm)				
A1	4,6,8,10	52	49.54	Test series A1, B1-B3, C1-2 	Test series DM 	
B1	4,6,8	52	18.86			
B2	4,6,8	52	34.62			
B3	6,8	52	26.00			
C1	4,8	137	49.54			
C2	4,8	242	49.54			
DM	4,6		49.54	Boundary conditions in laboratory for test series DM 		
Boundary conditions in laboratory for test series A1, B1-B3, C1 and C2 						

Diameter of projectile $d = 36.5$ mm

varying the impact velocity the critical velocity giving plugging of the target was determined.

In addition, a series of static tests were performed in order to study a possible relationship between the dynamic and static plugging capacities. Furthermore, the material properties were determined by means of tests at elevated rates of strain in tension and torsion [8].

The test program, test specimen geometry and support conditions in the laboratory are shown in Table 1. Test series A1 was designed to study the plugging capacity as a function of the plate thickness, while series B1-3 were carried out to investigate the influence of the mass ratio of the projectile to target. Test series C1-2 were included to study the influence of an increased inplane stiffness. Finally, test series DM were included to study the effect of stringers in the free span. As shown in Table 1, the hatches rested on RHS-profiles while the clamped support for test series DM was obtained by clamping the plates between RHS-members bolted to a rigid base.

The projectile was instrumented by strain gauges that were used to record the interface force between projectile and target. Based on this force-time history the displacement of the projectile and consequently the displacement of the plate was generated by double integration. The target plate was instrumented with a total of 24 strain gauges, which were primarily used to determine the strain and strain rate levels in the target during impact. Furthermore, a high speed camera shooting 10000 frames per second made it possible to determine the

deformed shape of the target plate throughout the impact. The impact velocity of the projectile was measured by means of two photocells located immediately above the target.

2.2 Experimental results

The primary information gained from the experiments was the impact velocity at incipient plugging. Fig. 1 shows how the impact velocity was varied in order to bracket the critical velocity. Fig. 2 depicts a typical time history of the interface force between projectile and target for a hatch. As seen, the impact can be divided into a transient and a global mode phase. In the transient phase only inertia forces are present in the plate, as no forces are transmitted to the supporting structure. In the global mode phase the supports are fully activated, and the target behaves almost quasistatically.

A sequence of displacement profiles for a hatch is given in Fig. 3 for five discrete times during the impact. The permanent displacement profile is given as well.

The most significant results of the experimental study were as follows:

- The critical kinetic energy at impact was an increasing function of the plate thickness. Reducing the projectile mass from 49.54 kg to 18.86 kg led to an increased critical energy. However, the critical kinetic energy seemed to approach the static plugging energy when the mass was increased.

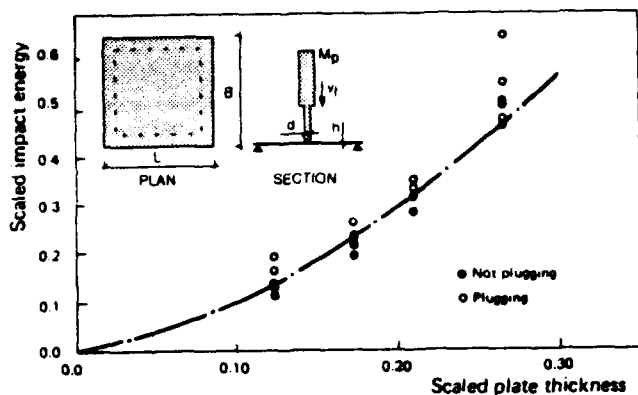


Figure 1 Impact energy at incipient plugging

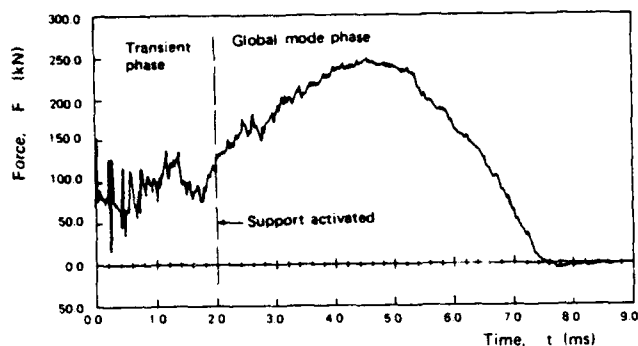


Figure 2 Time history of interface force

- An increase in the inplane stiffness reduced the critical plugging energy.
- Stringers seemed to have no effect on the critical plugging energy.
- Plugging always took place at maximum interface force, and the critical force for each plate thickness was independent of the mass of the projectile and the support conditions.
- A comparison showed that the dynamic force at plugging deviated from the corresponding static one with $\pm 5\%$. The permanent deformations at plugging were quite similar for the static and dynamic tests, even though more energy was required to produce plugging in the dynamic tests. This indicates that the path dependency of the plastic work is important.
- The energy absorption connected to the indentation of the punch into the plate represented less than 10 % of the total absorbed energy at plugging.
- Plastic strain rates up to 40 s^{-1} were measured in the plates. Based on the tensile strain rate data shown in Fig. 4, this gave an increase of the lower yield stress of 30 %, while a reduced strain rate sensitivity was found in the hardening region.

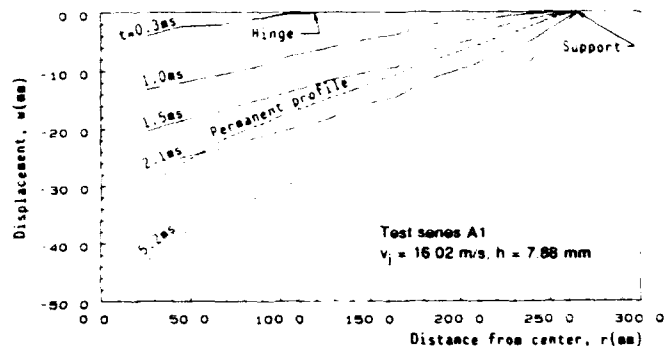


Figure 3 Displacement profiles of target at discrete times

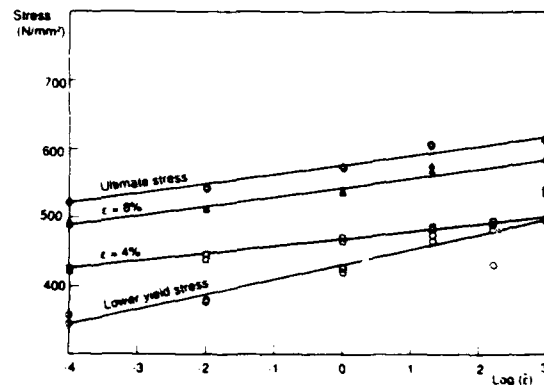


Figure 4 Tests in tension, stress vs strain rate [8]

3.0 Numerical simulations

The comparison between numerical simulations and tests is carried out for the simply supported hatches from test series A1 and B1 and the clamped plates equipped with stringers from test series DM, Table 1.

3.1 Modelling

During an impact large elastic and plastic deformations take place which extend to the supports. Tests have shown that 90 - 95 % of the initial kinetic energy of the projectile is absorbed as global strain energy in the plate and that only a small fraction is spent to push out a plug. This means that the test specimens can be modelled using shell elements and that no account needs to be taken of the local indentation of the projectile into the plate at the impact point.

The Belytschko-Lin-Tsay shell is the default element in LS-DYNA3D due to its computational efficiency and is chosen here. Five through-the-thickness integration points and one integration point in the plan of the element are used. The projectile is modelled as a rigid body using 8-node hexahedron elements.

Fig. 5 shows a view of the finite element model of the test specimens. As seen, the test specimens and projectile are both modelled using two symmetry planes. 144 solid hexahedron

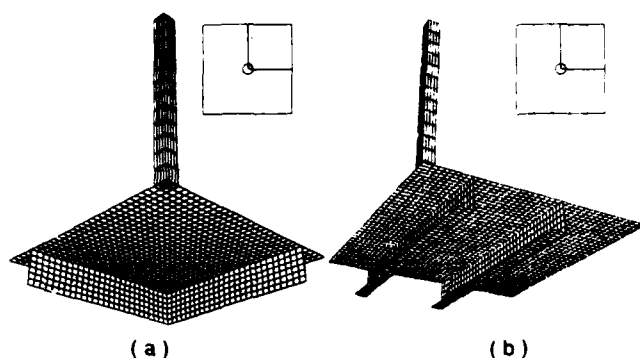


Figure 5 Rear view of finite element models
(a) Hatch, test series A1 and B1
(b) Clamped plate equipped with stringers, test series DM

elements are used for the projectile while 1273 and 2067 shell elements are found to give sufficient accuracy for the loose hatches and clamped plates respectively. This element mesh requires a time step of 1.3 μ s for numerical stability. The support conditions of the test specimens from test series A1 and B1 (Table 1) are modelled as a stonewall that prevents inner penetration of boundary nodes while allowing for separation. Both the stringers and the plate are modelled as clamped for test series DM. Furthermore, the contact between the projectile and plate is modelled as a sliding interface without friction.

Due to the length of the yield plateau for steel grade St52-3N compared to the measured magnitude of the strains in the plates, the plate material is modelled as elastic perfect-plastic. Even if the plate material has shown to be strain rate sensitive, the best fit to the test data is found by using the quasi-static material properties. However, a separate comparison will be shown when the material strain rate effects are modelled by the Johnson and Cook Plasticity Model, using the tensile strain rate data shown in Fig. 4. Also for this case the material is modelled as elastic perfect-plastic.

3.2 Comparison and discussion

When comparing measured and computed time series, it should be noted that no attempt has been made to filter out the oscillations due to travelling stress waves in the projectile for the measured interface-force time series. As the computed values are only available at 0.2 μ s time intervals, the computed histories are in effect filtered.

Test series A1 and B1: Figs. 6-8 show a comparison between the measured and calculated interface force time curves for a representative case when a rebound occurs. Plotted is also the displacement of the plate at the edge of the projectile and good agreement between the measured and calculated data is found. However, the permanent displacement at the center of the plates is too large compared to the measured value. This means that the numerical model is too stiff during the unloading phase of the impact. High-speed camera measurements have shown that this effect may be related to a difference in deformation profiles for test and analysis during impact. Fig. 10 shows a comparison between the measured and calculated deformation

profiles for test no A1-8-7. As seen, the deformation profiles are different during the loading periode of the impact, Fig. 10a, resulting in larger permanent displacements than those for the test, Fig. 10b.

Even if the magnitude of the deformations are different in analysis and test, the deformation patterns are similar during the deformation process. After initial impact, a deformation wave moves radially towards the support. Before this wave reaches the support both test and analysis show that the shape of the deformation pattern is approximately axisymmetric. After this time yield lines extend inwards from the corners. This is shown in Fig. 11, where contour line plots of the computed deformation pattern are given. Fig. 11a shows the deformation pattern before the deformation wave reaches the support, while Fig. 11b depicts the permanent deformation shape. Furthermore, it is worth noting that the impact event in the analyses, as for the tests, is divided into a transient phase and a global mode phase, and that the time when the supports are activated is approximately equal for test and analysis, Figs. 6-9.

Fig. 9 shows a comparison for a case where a plugging failure occurs. As the local indentation of the projectile into the plate has insignificant influence on the global response, the measured and calculated curves are approximately equal until plugging takes place followed by a sudden drop in the measured force-time curve. As plugging always takes place at maximum force, the shell analysis can then be used to determine the onset of plugging when the critical interface force between plate and projectile is known. In ref. [7] the critical interface force for a circular blunt ended projectile is determined based on a mean critical shear stress, $\tau_{cr} = \sigma_u(0.41 h/d + 0.42)$.

In the previous analyses, the quasi-static material properties are used. However, Fig. 12 shows a comparison between test and analysis when the latter is based on the Johnson and Cook Plasticity Model and the strain rate data shown in Fig. 4. For comparison the analysis based on the quasi-static material properties ($\dot{\epsilon} = 10^{-4} s^{-1}$) is shown as well. As can be seen, the inclusion of the strain rate effect increases the stiffness of the plate causing the maximum interface force to be overestimated, while the maximum displacement is underestimated compared to the test data. The increase in stiffness is evident as the response in the plate is mainly controlled by plastic membrane stresses. An increase in the yield stress will then imply an increase in the overall stiffness of the plate.

Test series DM: Fig. 13 shows a comparison between the measured and calculated interface force and displacement histories for a 4 mm thick plate equipped with stringers when a rebound occurs. Good agreement is also here found between test and analysis. However, as for the simply supported hatches, the numerical model is too stiff during the unloading periode, resulting in a larger permanent displacement than for the test. No further discussion will be given to this test series as only the interface force and the permanent central displacement are measured.

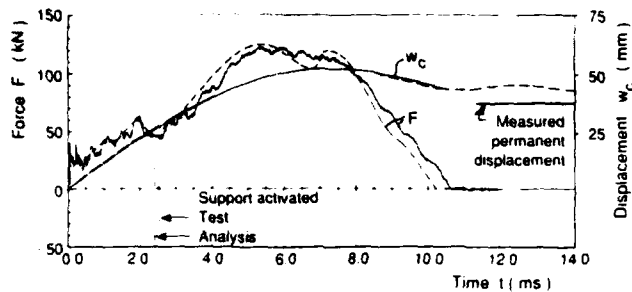


Figure 6 Force and displacement histories
Test series A1, plate A1-4-5
 $v_i = 11.49$ m/s, $M_p = 49.54$ kg, $h = 4.54$ mm
— Test, - - - Analysis

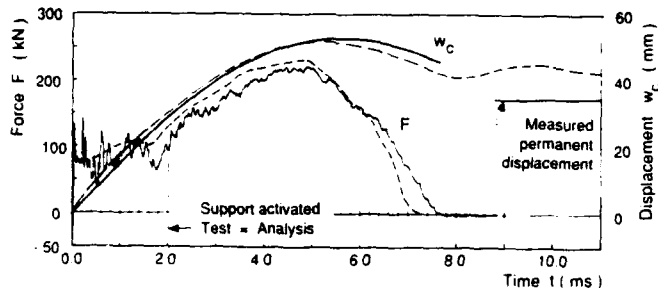


Figure 7 Force and displacement histories
Test series A1, plate A1-8-7
 $v_i = 16.02$ m/s, $M_p = 49.54$ kg, $h = 7.88$ mm
— Test, - - - Analysis

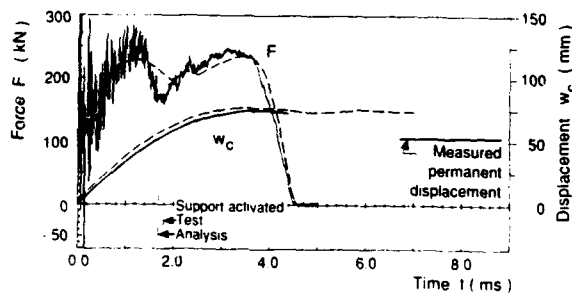


Figure 8 Force and displacement histories
Test series B1, plate B1-8-7
 $v_i = 39.48$ m/s, $M_p = 18.86$ kg, $h = 7.94$ mm
— Test, - - - Analysis

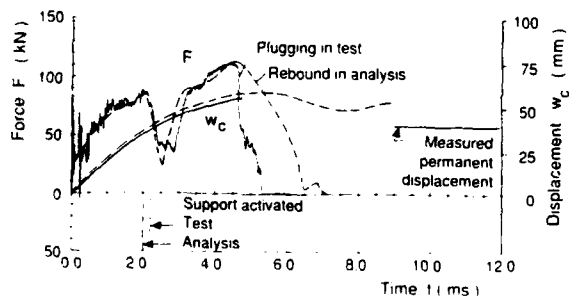
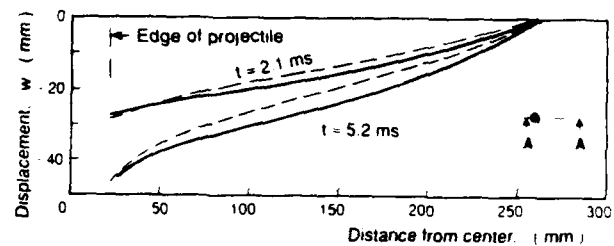
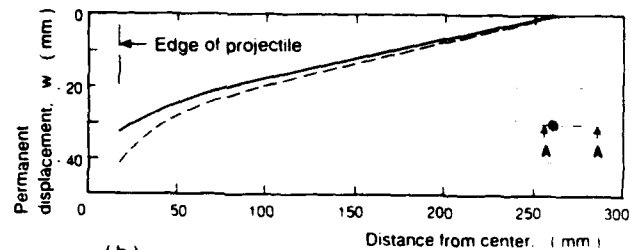


Figure 9 Force and displacement histories
Test series B1, plate B1-4-6
 $v_i = 19.67$ m/s, $M_p = 18.86$ kg, $h = 4.14$ mm
— Test, - - - Analysis



(a)



(b)

Figure 10 Deformation profiles
Test series A1, plate A1-8-7
 $v_i = 16.02$ m/s, $M_p = 49.54$ kg, $h = 7.88$ mm
— Test, - - - Analysis
(a) Deformation profiles at discrete times
(b) Permanent deformation profiles

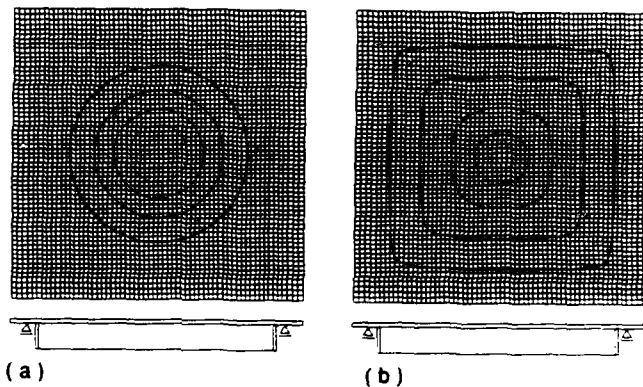


Figure 11 Contour plots of deformation patterns
Test series A1, plate A1-8-7
 $v_i = 16.02$ m/s, $M_p = 49.54$ kg, $h = 7.88$ mm
(a) Time $t = 0.8$ ms
(b) Time $t = 12$ ms. Permanent deformation shape

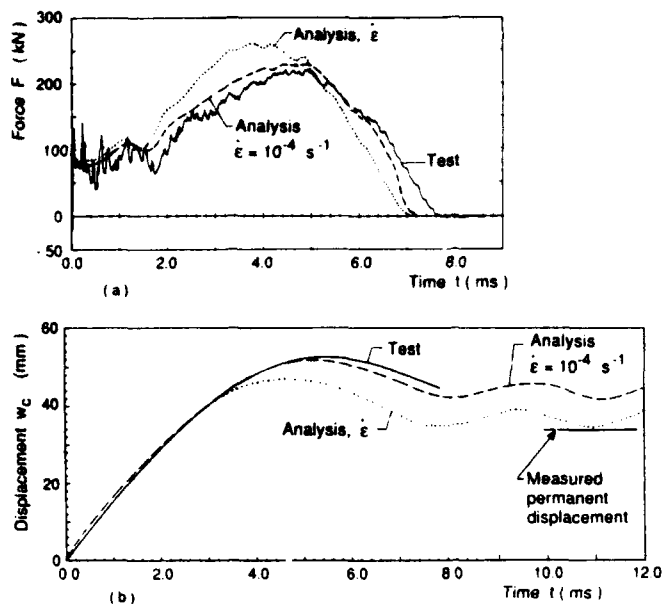


Figure 12 Force and displacement histories
Test series A1, plate A1-8-7
 $v_i = 16.02$ m/s, $M_p = 49.54$ kg, $h = 7.88$ mm
(a) Force-time curves
(b) Displacement-time curves

4 Conclusions

Based on the numerical simulations carried out, good agreement is found between LS-DYNA3D and the test data when using the quasi-static material properties for steel grade St52-3N. The maximum interface force between projectile and plate as well as the maximum displacement at the impact point agree quite well with the test data. This means that a shell analysis can be used for parametric studies to determine the plugging capacity of thin plated structures when a critical interface force between projectile and plate is used as a failure criterion. However, the permanent deformations are overestimated in the analyses. In a design situation these deformations will be of minor interest as a plated structure has to be replaced after an impact from a large mass projectile due to the large plastic deformations which take place.

Notation

a	- overhang
d	- diameter of projectile
F	- interface force between projectile and plate
h	- plate thickness
M_p	- mass of projectile
t	- time
v_i	- impact velocity
w	- displacement of plate
w_c	- displacement of plate at the edge of projectile
$\dot{\epsilon}$	- strain rate
σ_u	- ultimate stress
τ_{cr}	- mean shear stress at plugging

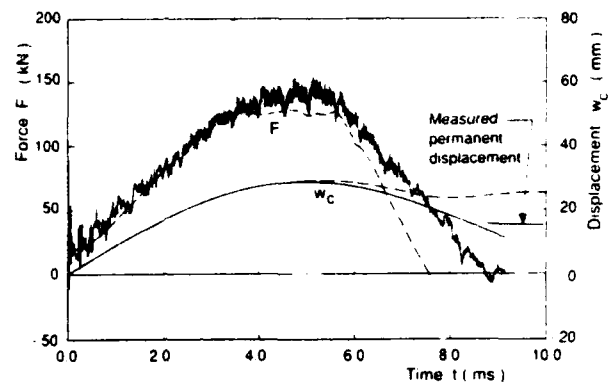


Figure 13 Force and displacement histories
Test series DM, plate DM-4-2
 $v_i = 9.22$ m/s, $M_p = 49.54$ kg, $h = 4.40$ mm
— Test, - - - Analysis

REFERENCES

- Edvardsen, G. and Marley, M.J.: "Dropped Objects. A summary report on damage assessment and energy absorption". Project Report No. 8, Det norske Veritas, Oslo (1983).
- Gjeldsvik, A.: "Mobile Statfjord A Platform. Dropped Object Study". Aker Engineering A/S, Oslo (1977).
- Nielson, A.J.: "Empirical Equations for the Perforation of Mild Steel Plates". Int. J. Impact Engng., Vol. 3, No. 2 pp 137-142 (1985).
- Langseth, M. and Larsen, P.K.: "Dropped Objects. Plugging Capacity of Steel Plates". BOSS'88. Proceedings of the International Conference on Behaviour of Offshore Structures. Trondheim, Norway (Edited by T. Moan, N. Janbu and O. Faltinsen), Vol. 3, 1001-1014. (1988)
- Langseth, M. and Larsen, P.K.: "The Behaviour of Square Steel Plates Subjected to a Circular Blunt Ended Load". Int. J. Impact Engng. Vol. 12, No. 4, pp. 617-638 (1992).
- Hallquist, J.O.: "LS-DYNA3D, Theoretical Manual". Livermore Software Technology Corporation (1991)
- Langseth, M. and Larsen, P.K.: "Dropped Objects - Plugging Capacity of Steel Plates - an Experimental Investigation". Int. J. of Impact Engng. Vol. 3, 289-316. (1990).
- Langseth, M., Lindholm, U.S., Larsen, P.K. and Lian, B.: "Strain Rate Sensitivity of Mild Steel Grade, St52-3N". American Society of Civil Engineers, Journal of Engineering Mechanics. Vol. 117, No. 4, 719-733 (1991)

Design Procedure for Prefabricated Roof Beams for Blast-Resistant Shelters

Larry M. Bryant, Paul F. Mlakar and Brian Campbell

JAYCOR Structures Division
Vicksburg, MS

Captain Richard Reid

AFCEA/RACS
Tyndall AFB
Panama City, FL

ABSTRACT

This paper describes development and validation of a procedure for designing prefabricated blast-resistant beams to form the roof of a protective shelter. The structural system is being considered for rapid construction by intrinsic troop units. The procedure considers several concepts, including conventionally reinforced and prestressed precast concrete, and composite steel and concrete with typical span lengths from 20 to 50 feet. The design procedure relies rational methods of analysis for which calculations may be performed in a spreadsheet. Development of the procedure includes validation by detailed finite element modeling, laboratory tests on prototype beams, and future full-scale field tests.

INTRODUCTION

Changes in the scale and geographic diversity of potential future military involvement favors a different approach to construction of hardened shelters for personnel, aircraft or storage. Required characteristics of these new generation shelters include rapid construction, protection from advanced weapons and concealment. One concept under development consists of an earth-covered shelter constructed with reinforced soil walls and prefabricated roof elements shown in Figure 1.

The roof consists of prefabricated beams containing an integral slab lifted into place after construction of the reinforced soil walls. The prefabricated beams and additional construction materials would be stored at strategic locations worldwide and shipped to the required site(s) when needed. Therefore it is advantageous that the beams be relatively lightweight and wide in order to minimize the overall weight and number requiring transport and erection.

This paper describes development and validation of a procedure for designing the prefabricated roof elements in this concept. One of the goals in developing the design procedure was to keep the computational effort low so that the resulting analysis can be carried out with hand calculator or spreadsheet, or readily programmed for computer. This allows the designer to investigate a wide variety of options or run parametric studies before focusing on a detailed beam design. Validation with more sophisticated models and physical testing confirm the accuracy of the method for predicting the structural response. The design procedure permits analysis of conventionally reinforced concrete, prestressed (pretensioned) concrete and composite steel-concrete, consisting of a solid concrete slab placed upon and integrally connected to a welded plate or box girder.

The design procedure represents a synthesis of existing analysis and design methodologies described in textbooks, technical manuals, journals and concrete and steel codes. The methodology consists of defining the problem constraints and performance criteria, analyzing the dynamic response, and treating additional design considerations. The following discussion describes each of these areas. Validation of the structural calculations and work necessary to finalize the overall design of the protective structure is also briefly described herein.

PROBLEM CONSTRAINTS AND PERFORMANCE CRITERIA

The initial step of the design procedure is definition of constraints and performance criteria for a specific type of shelter and threat. Problem constraints include the geometry of the shelter, blast loading and maximum allowable weight of the beams.

Problem Constraints

Adjacent simply supported beams spanning the short dimension comprise the roof structure of the shelter. This study considered roof spans of 20 and 50 feet. The roof

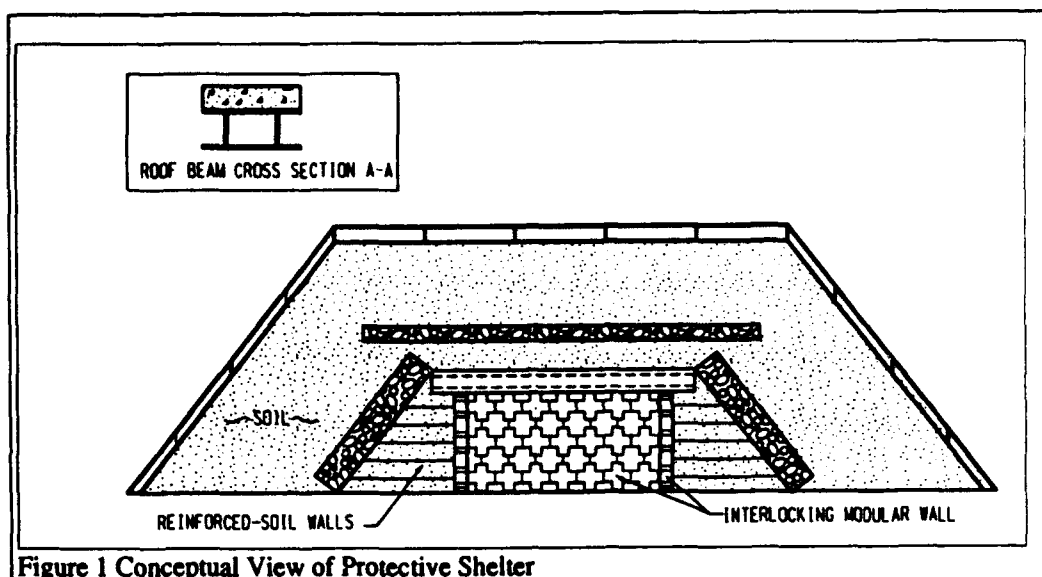


Figure 1 Conceptual View of Protective Shelter

will likely have a covering of soil, burster slab and deflection layer. For purposes of concept comparison, the shelter was assumed to have six feet of overlying soil, contributing to the mass of the system and reducing the available moment capacity of the beam.

Threat assessment and development of design roof loading are not directly addressed in this study. With blast generally representing the critical design case, a uniform distributed pressure with an instantaneous rise time and linear decay (triangular load pulse) approximated the impulse from detonation of a general purpose bomb over the shelter. Penetration or breaching are being addressed by separate design features under development.

Size and weight restrictions associated with transportation and placing the beams using equipment normally available presents another problem constraint. This criterion will likely differ for shelters situated in more remote settings versus locations easily accessible by land or water transport. The latter case could make use of fewer larger beams versus more numerous lightweight beams for shelters in areas with difficult access. Therefore, beam weight represents a problem constraint and affects a number of evaluation criteria described below.

Performance Requirements

Ductility and support rotation commonly measure the ability of a structure to resist dynamic loading. Ductility expresses the ratio of the maximum dynamic deflection to the yield deflection, assuming the beam has an elastic-plastic response. This study adopted a target ductility factor of 6, typical for this type of construction [1]. Support rotation, calculated as the angular rotation of the

beam mid span relative to an end, approximately corresponds to the plastic strain in the hinge. Concrete maintains its ultimate flexural resistance for support rotations up to 2 degrees, whereas achieving support rotation up to 4 degrees requires special reinforcement to confine the concrete or to permit tensile membrane action [2]. This study used a maximum support rotation of 4 degrees, with consideration given to reinforcing the compression zone to give the concrete added ductility.

Evaluation Criteria

It is helpful to identify a set of criteria and associated weighting factors for evaluating various beam designs or concepts. A proposed set of criteria and weights is:

- 1) Fabrication Cost (25%) - Price to initially design and fabricate the beams, including material, labor and capital equipment used in fabrication.
- 2) Handling (15%) - Moving beams between fabrication, storage and erection, including special precautions or equipment.
- 3) Storage (15%) - Addresses long term storage and maintenance requirements such as protection from corrosion, prestress losses and amount of storage space.
- 4) Erection (25%) - Degree of difficulty and resources required to erect the beams in a shelter.
- 5) Reliability (20%) - Level of confidence in design and performance of a given concept or material.

Having established the problem parameters, performance requirements and evaluation criteria, the analysis procedure is described next.

DYNAMIC ANALYSIS METHODOLOGY

In this study a single degree-of-freedom model

approximates the dynamic response of the roof beam. This approach permits analysis of numerous designs due to the moderate computational effort involved and provides sufficient accuracy for structures such as the simply supported roof beams.

A majority of the required calculations for a given concept pertain to determining the flexural resistance and stiffness. A spreadsheet containing the strength and stiffness formulas and numerical integration of the resulting SDOF differential equation was developed to facilitate the analysis.

Calculating the beam's flexural resistance uses the accepted strain compatibility and force equilibrium approach. The procedure generally follows the assumptions and guidelines given in the ACI Building Code [3] and the AISC Manual of Steel Construction [4], with the exception of load and resistance factors. The underlying statistics represented by the load and resistance factors in the codes do not apply to blast resistant design. Thus, the analysis uses load and resistance factors equal to unity in accordance with the general practice for blast resistant design.

The stiffness of a conventional or prestressed concrete beam depends on the extent of cracking it has experienced. As an approximation, the analysis averages the gross and cracked moments of inertia to calculate the stiffness of a concrete beam [2,5]. Computing the stiffness of a composite steel-concrete beam uses transformed-section moment of inertia. Finite element analysis provides a means of validating these assumptions, as described later in this paper.

The design methodology described above relies on the beam attaining its intended flexural response. Other limit states, such as shear failure, must be prevented from governing the beam's ultimate strength.

The design procedure employs two methods to estimate the shear force in the beam. Dynamic reactions obtained from the SDOF calculation consider the dynamic equilibrium of the applied load, resisting moment and inertial force. This approach uses the assumed deflected shape to compute the inertial force and applies to both the elastic and inelastic ranges. The second approach includes the contribution from the higher normal modes since they become increasingly important when calculations involve higher derivatives of the deflection expression, as for shear [5]. Therefore, the analysis uses a simple procedure to compute the shear force using the higher modes over the linear response range of the beam. Shear design is based on the higher of these two results.

In addition to shear, designing and detailing the beam such that flexural response governs includes consideration of:

Conventional or prestressed concrete:

- 1) Web thickness and reinforcement for shear
- 2) Shear and bending of the top flange in the transverse direction
- 3) Effective width of the top flange
- 4) Prestress losses due to shrinkage and creep

Composite steel-concrete:

- 1) Local buckling of the web or flange
- 2) Shear capacity of web
- 3) Shear connectors
- 4) Bearing and intermediate stiffeners

Member sizes are proportioned or checked for conformity with requirements from the relevant portions of the concrete and steel design codes [3,4] including concrete cover, rebar or strand spacing and weld requirements.

VALIDATION OF THE DESIGN PROCEDURE

An initial evaluation of the three concepts considered in this study based solely on estimated fabrication cost favored prestressed concrete and composite over conventionally reinforced concrete. Subsequent evaluation using the above criteria and weights found that the composite steel-concrete beam ranked highest. The composite steel-concrete concept ranked particularly well for each criteria and permitted significant flexibility in individual beam weight.

Keeping the analysis methods intentionally simple required using more detailed methods to check the validity of the key assumptions and calculations. Finite element analysis of several beams for each concept showed good agreement with the static load/deflection response predicted by the design procedure. Load tests of prototype beams serve to further validate the design procedure. In going to each of these levels, greater detail is included in the validation. The following discussion more fully describes some of the finite element results and subsequent static load tests.

Finite Element Analysis

Finite element modeling utilized the nonlinear analysis program ADINA [6] to validate the static resistance functions embodied in the design procedure. Plane-stress two-dimensional elements modeled the steel and concrete portions of the beam while truss elements modeled the shear connectors and longitudinal reinforcing.

The response of a 50 foot conventionally reinforced beam is shown in Figure 2. The load deflection curve depicts the mid span deflection and total applied load computed using the design procedure and predicted by the finite element analysis. The figure also shows the extent of concrete cracking at three stages of loading, starting with the development of flexure cracks and progressing to shear and flexure cracks at intermediate and yield loads.

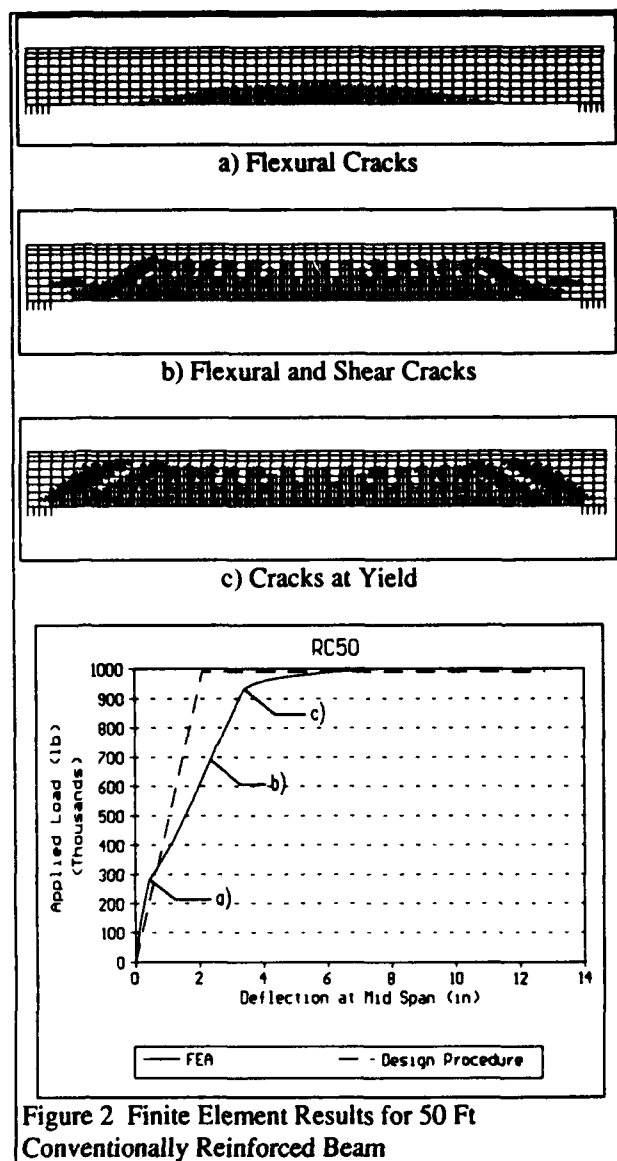


Figure 2 Finite Element Results for 50 Ft Conventionally Reinforced Beam

Figure 3 plots the predicted load-deflection curve for one of the test beams and shows the good agreement between the design procedure and the finite element model. Differences include a slightly less stiff elastic response and positive slope in the plastic region due to the strain hardening behavior of the steel in the model.

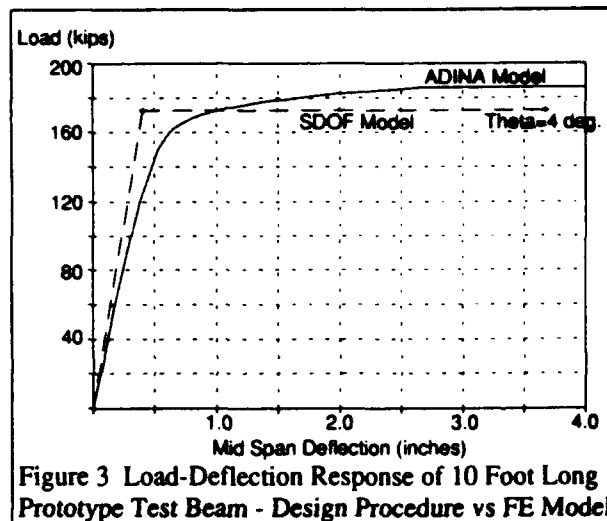


Figure 3 Load-Deflection Response of 10 Foot Long Prototype Test Beam - Design Procedure vs FE Model

The finite element analysis also indicated that achieving an end rotation of 4 degrees requires strains of 2-3% in the concrete and 4-5% in the steel. Concrete typically exhibits only 0.2 to 0.4% maximum usable compressive strain. However, adding confining stress causes concrete to behave in a more ductile manner and greatly enhances its compressive strength. Analytical procedures and experimental results of columns of various sizes and shapes quantify the ductility achieved by using closely spaced rebar cages to create a confined concrete core [7,8,9]. Figure 4 shows the reinforcing used to confine the concrete in the test beams and the resulting stress-strain curve used to derive the ADINA concrete model.

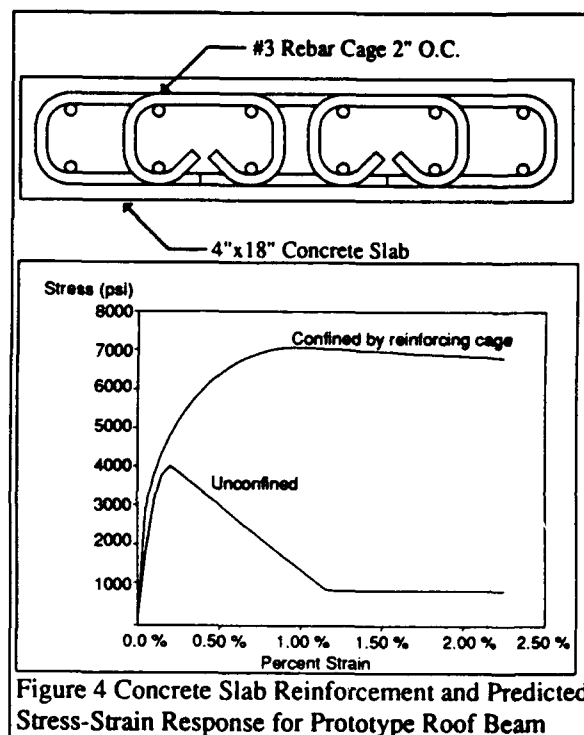


Figure 4 Concrete Slab Reinforcement and Predicted Stress-Strain Response for Prototype Roof Beam

Static Load Tests

Static load tests will further substantiate the predicted strength and stiffness of the composite beam concept and confirm the ability of the overall design to reach the intended flexural response. The design, fabrication and testing of scaled prototype beams is described, though test results are not available in time for discussion herein.

Design of the test beams involved scaling to the capacity of available test devices. The design followed exactly the same procedure as for full-size beams. The 20 foot span is represented by a 1/2 scale 10 foot beam while the 50 foot span is scaled by 1/3 to give a 16 foot beam. Figure 5 shows the configuration of the 16 foot beam. Material used to construct the beams consists of 4000 psi concrete reinforced with 3/8" diameter rebar and 1/4" and 3/8" thick A572 (50,000 psi yield strength) steel plate.

The 10 ft and 16 ft beams both have the same cross-sectional shape, but because of their different lengths and loading, the structural response of the two beams differs. The design triangular pressure pulse for the 20 foot span has a shorter duration and higher pressure than for the 50 foot span. The resulting load duration is about 1/2 of the natural period for the shorter beam, while the longer beam has a load duration of 1/4 of its natural period.

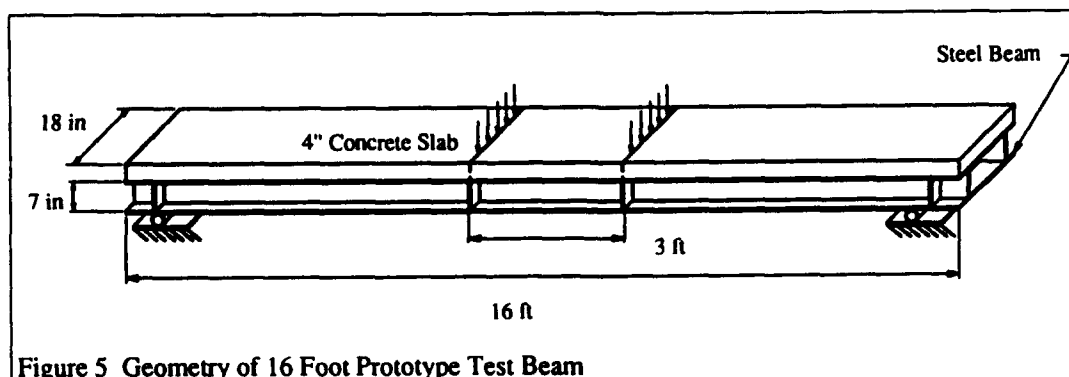


Figure 5 Geometry of 16 Foot Prototype Test Beam

Figure 6 shows the load/deflection response for the 16 foot beam predicted by the design procedure and finite element analysis. While both beams have the same static flexural resistance, the shorter beam is predicted to have a maximum deflection of 3.8 inches and end rotation of 4 degrees. The longer beam is predicted to have an end rotation of 4 degrees and maximum deflection of 6.4 inches. The corresponding ductilities for the short and long beams are 9.0 and 5.5, respectively.

A 150 ton ram will apply two-point loading on 2 foot spacing for the 10 foot beam and 3 foot spacing on the 16 foot beam. Instrumentation consists of 28 strain gages, six displacement gages and a load cell. The strain gage data will validate the design procedure assumptions and

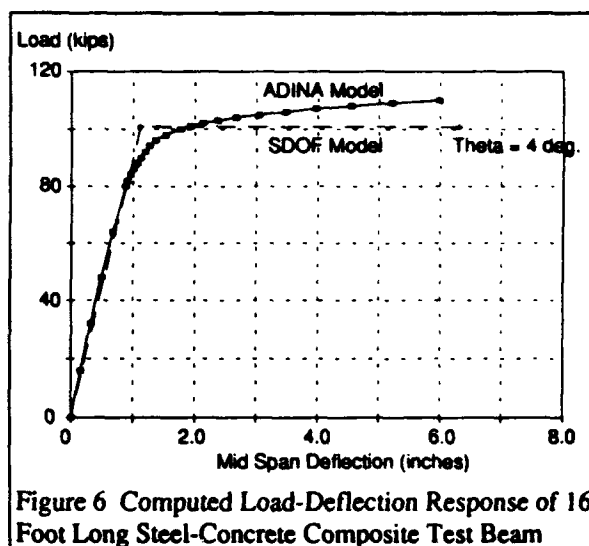


Figure 6 Computed Load-Deflection Response of 16 Foot Long Steel-Concrete Composite Test Beam

ADINA predictions regarding the percentage strain required to achieve the desired ductility and support rotation. Information from gages on the reinforcing bars will confirm the concrete strength and ductility predicted by the analysis.

FUTURE WORK

At the time of writing, the test beams have been fabricated and testing will begin when the concrete reaches its design strength. Analysis of the test results will indicate any modifications or refinements to the design procedure.

The next phase of concept development will integrate the individual components into an overall design of the protective shelter. Analysis and design will encompass the reinforced soil walls, blast doors, mechanical systems, waterproofing, soil cover, burster slab and rubble layer. Physical response modes include forced vibration,

penetration and breaching, considered either separately or in combination. The design will address interaction between the roof beams and reinforced soil walls to determine requirements for bearing and anchorage in rebound. In addition, the design effort will develop standard details to facilitate trouble-free and reliable construction and operation of the shelters.

REFERENCES

1. Protective Construction Design Manual: Resistance of Structural Elements (Section IX), ESL-TR-87-57, Air Force Engineering & Services Center, Engineering & Services Laboratory, Tyndall Air Force Base, Florida, Nov 1989.
2. TM 5-1300. Structures to Resist the Effects of Accidental Explosions Vol IV - Reinforced Concrete Design, Armament, Research, Development and Engineering Center, U.S. Army Armament, Munitions, and Chemical Command, Picatinny Arsenal, NJ, 1987.
3. Building Code Requirements for Reinforced Concrete (ACI 318-89), American Concrete Institute, Detroit, Michigan, 1989.
4. Manual of Steel Construction - Load & Resistance Factor Design, First Edition, American Institute of Steel Construction, 1986.
5. Biggs, J.M., Introduction to Structural Dynamics, McGraw-Hill, 1964.
6. ADINA - Automatic Dynamic Incremental Nonlinear Analysis, ADINA R&D, Watertown, MA, 1992.
7. Mander, J.B., Priestly, M.J.N., and Park, R., "Theoretical Stress-Strain Model for Confined Concrete", J. Struc. Engr., ASCE, Vol 114 No 8, Aug 1988, pp 1804-1826.
8. Mander, J.B., Priestly, M.J.N., and Park, R., "Observed Stress-Strain Behavior of Confined Concrete", J. Struc. Engr., ASCE, Vol 114 No 8, Aug 1988, pp 1827-1849.
9. Saatcioglu, M. and Razvi, S.R., "Strength and Ductility of Confined Concrete", J. Struc. Engr., ASCE, Vol 118 No 6, June 1992, pp 1590-1607.

PROTECTIVE CONSTRUCTION WITH REINFORCED EARTH

Christopher Y. Tuan, Ph.D., P.E.
Senior Engineer

Applied Research Associates, Inc.
Gulf Coast Division
Tyndall AFB, FL 32403

ABSTRACT

The objective of this research is to develop a simple analytical method that characterizes plane shock wave propagation through reinforced earth and the dynamic interaction with modular retaining wall panels. The shock wave was initiated as a velocity boundary condition. The exact solution was obtained by the Laplace transform method. A step-by-step design procedure based on the "limit state" concept is proposed. Because of the impulsive nature of ground shock, the maximum response of the wall panel and reinforced soil system depends mainly on the capacity and rate of energy absorption and dissipation of the system. Therefore, the connection between wall panels and soil reinforcement, and soil reinforcement itself should be ductile beyond the proportional limit. Furthermore, the soil reinforcement should possess a high elastic tensile modulus to minimize the wall panel displacement.

INTRODUCTION

The use of reinforced earth in the construction of retaining walls has received much attention during the past decade. A typical wall can be constructed with interlocking modular panels or blocks connected to soil reinforcement. The layers of soil reinforcement, in the form of sheets or grids placed in a backfill, usually run parallel to the direction of wave propagation. Recent field explosive tests on a reinforced earth shelter conducted in Israel (Raudanski 1990; Reid 1990, 1991) have shown that such shelters can provide good protection from blast loading. Cruciform wall panels attached to horizontal metallic strips in a sandy backfill were utilized in that shelter construction.

Imposing continuity for both stress and displacement at the interface between the soil and structure, Drake and Rochefort (1987) showed that the interface stress can be expressed as

$$\begin{aligned}\sigma_i &= \sigma_{ff} + \rho c_L (V_{ff} - \dot{u}) \\ &= 2\sigma_{ff} - \rho c_L \dot{u}\end{aligned}\quad (1)$$

where ρ is the mass density and c_L the loading wave velocity of the soil, V_{ff} is the free-field particle velocity, σ_{ff} is the free-

field incident stress, and \dot{u} is the velocity of the structure. They also derived the equation of motion for a single-degree-of-freedom (SDOF) structural system, and presented solutions for perfectly plastic and elastoplastic structural responses.

ANALYTICAL MODEL

Figure 1 shows a one-dimensional model for the dynamic interaction between a wall panel and the reinforced earth attached to it. The presence of reinforcement in soil may significantly alter the soil's original mechanical properties. Since soil is not capable of carrying tensile stress, it is assumed in this model that any tension developed in the soil will be taken by the reinforcement and that the soil and wall panel stay bonded at the interface. The shear and bending resistance from connections between the panels has also been included in the analysis.

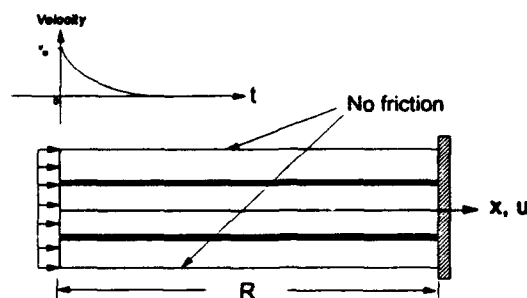


Figure 1. 1-D Model of Shock Wave Propagation Through Reinforced Earth

Governing Equation. The 1D wave equation for the particle displacement, $u(x, t)$, in a homogeneous medium is

$$\frac{\partial^2 u}{\partial t^2} = c^2 \frac{\partial^2 u}{\partial x^2} \quad (2)$$

where c is the wave propagation velocity of reinforced earth. Assuming strain compatibility, the apparent constrained modulus of the reinforced soil can be expressed in terms of the volume ratio of soil reinforcement, V_g

$$K_x = \frac{E_s(1 - \nu_s)}{(1 + \nu_s)(1 - 2\nu_s)}(1 - V_g) + \frac{E_g(1 - \nu_g)}{(1 + \nu_g)(1 - 2\nu_g)}(V_g)$$

$$-V_g(1-V_g) \frac{\left[\frac{E_s v_s}{(1+v_s)(1-2v_s)} - \frac{E_g v_g}{(1+v_g)(1-2v_g)} \right]^2}{\frac{E_s(1-v_s)}{(1+v_s)(1-2v_s)}(V_g) + \frac{E_g(1-v_g)}{(1+v_g)(1-2v_g)}(1-V_g)} \quad (3)$$

where E_s and E_g , and v_s and v_g , are, respectively, the Young's moduli and Poisson's ratios of the soil and reinforcement. The wave propagation velocity can be approximated by

$$c = \sqrt{\frac{K_x}{\rho_o}} \quad (4)$$

and ρ_o is the mass density of the reinforced earth given by

$$\rho_o = \rho_s(1-V_g) + \rho_g V_g \quad (5)$$

where ρ_s and ρ_g are the mass densities of the soil and reinforcement, respectively.

Boundary Conditions. At $x = 0$, the shock wave front, having an initial particle velocity, v_o , arrives at time $t = 0$ and decays exponentially, so that

$$\frac{\partial u}{\partial t}(0, t) = v_o e^{-\alpha t} \quad (t > 0) \quad (6)$$

where α is the particle velocity attenuation rate. The shock front pressure, σ_o , is the product of the impedance of the reinforced earth, $\rho_o c$, and the initial particle velocity, v_o .

At $x = R$, the equation of motion of the wall panel is

$$M \frac{\partial^2 u}{\partial t^2} = -\sigma_x h b - K(u)u \quad (7)$$

where M is the mass of the wall panel, h is the panel height, b is the panel width, and $K(u)$ is the structural stiffness of the wall. Expressing soil stress in terms of the wall panel displacement, Eq.(7) becomes

$$\mu \frac{\partial^2 u}{\partial t^2} + \frac{\partial u}{\partial t} + \frac{K(u)u}{K_x h b} = 0 \quad (8)$$

where

$$\mu = \frac{M}{K_x h b} \quad (9)$$

The unit resistance function, defined as the structural resistance per unit area of wall panel, can be expressed as

$$R(u) = \frac{K(u)u}{h b} \quad (10)$$

The unit resistance function $R(u)$ may be modeled as linearly elastic, elastoplastic, perfectly plastic or by some other appropriate model. However, the high strain rate of a structural system under a strong incident shock would produce perfectly plastic response, if the system were

designed to be ductile. Assuming perfectly plastic wall response, then $R(u) = R_{max} H(t - t_a)$, where $H(t - t_a)$ is a Heaviside step function, $t_a = R/c$ is the arrival time of the shock wave, and the ratio of unit resistance to the constrained reinforced earth modulus becomes a constant

$$\lambda = \frac{R_{max}}{K_x} \quad (11)$$

Initial conditions. The wall panel and reinforced earth system is at rest before the shock front arrives, and thus the initial conditions are:

$$u(x, 0) = 0 \quad (0 \leq x \leq R) \quad (12)$$

$$\frac{\partial u}{\partial t}(x, 0) = 0 \quad (0 \leq x \leq R) \quad (13)$$

Solution. Eq.(2), together with boundary and initial conditions, was solved by the Laplace transform method. The solution for the particle displacement $u(x, t)$ is in the form

$$u(x, t) = \sum_1^{\infty} u_i \quad (14)$$

Keeping only the first five terms and using the variables,

$$t1 = t - \frac{x}{c} \quad (15)$$

$$t2 = \left(t + \frac{x}{c}\right) - 2T \quad (16)$$

$$t3 = \left(t - \frac{x}{c}\right) - 2T \quad (17)$$

$$t4 = \left(t + \frac{x}{c}\right) - 4T \quad (18)$$

$$t5 = \left(t - \frac{x}{c}\right) - 4T \quad (19)$$

$$T = \frac{R}{c} \quad (20)$$

$$m = \mu \alpha c \quad (21)$$

$$p = m + 1 \quad (22)$$

$$q = m - 1 \quad (23)$$

$$\gamma = \frac{1}{\mu c} \quad (24)$$

$$\delta = \mu c^2 \quad (25)$$

the terms on the right hand side of Eq.(14) take the form

$$u1 = 0 \quad (t1 < 0)$$

$$= \frac{v_o}{\alpha} (1 - e^{-\alpha t1}) \quad (t1 > 0) \quad (26)$$

$$u_2 = 0 \quad (t_2 < 0)$$

$$= -\frac{v_o}{\alpha q} \left[p(1 - e^{-\alpha t_2}) - 2m(1 - e^{-\gamma t_2}) \right] - \lambda \left[c \cdot t_2 - \delta(1 - e^{-\gamma t_2}) \right] \quad (t_2 > 0) \quad (27)$$

$$u_3 = 0 \quad (t_3 < 0)$$

$$= \frac{v_o}{\alpha q} \left[p(1 - e^{-\alpha t_3}) - 2m(1 - e^{-\gamma t_3}) \right] + \lambda \left[c \cdot t_3 - \delta(1 - e^{-\gamma t_3}) \right] \quad (t_3 > 0) \quad (28)$$

$$u_4 = 0 \quad (t_4 < 0)$$

$$= -\frac{v_o}{\alpha q^2} \left\{ p^2(1 - e^{-\alpha t_4}) - 4m^2(1 - e^{-\gamma t_4}) + 4mq \left[1 - (1 + \gamma \cdot t_4)e^{-\gamma t_4} \right] \right. \\ \left. + \lambda \left[c \cdot t_4 - \delta(1 - e^{-\gamma t_4}) \right] - 2\lambda \delta \left[1 - (1 + \gamma \cdot t_4)e^{-\gamma t_4} \right] \right\} \quad (t_4 > 0) \quad (29)$$

$$u_5 = 0 \quad (t_5 < 0)$$

$$= \frac{v_o}{\alpha q^2} \left\{ p^2(1 - e^{-\alpha t_5}) - 4m^2(1 - e^{-\gamma t_5}) + 4mq \left[1 - (1 + \gamma \cdot t_5)e^{-\gamma t_5} \right] \right. \\ \left. - \lambda \left[c \cdot t_5 - \delta(1 - e^{-\gamma t_5}) \right] + 2\lambda \delta \left[1 - (1 + \gamma \cdot t_5)e^{-\gamma t_5} \right] \right\} \quad (t_5 > 0) \quad (30)$$

The expressions for the longitudinal normal stress, particle velocity, particle acceleration of the soil medium can be readily derived from Eqs. (26)-(30). Although higher order terms could be added to the solution, the transient response of the reinforced soil system due to shock loading will have been damped out before they become effective. The 1-D model accounts for superposition of incident and reflected waves propagating between the explosion point and the interface, and accommodates Eq. (1) as a special case. The 1-D model gives the same interface stress as that given by Eq. (1) when the soil medium is semi-infinite. The 1-D model is used as the basis to develop a procedure for the design of a modular wall panel and soil reinforcement connection system.

DESIGN CONSIDERATIONS

When the deceleration of the panel by the structural resistance from panel connection and soil reinforcement is less than the deceleration of the incident shock, the interface stress becomes tensile and the wall panel tends to pull the soil reinforcement out from the soil. The soil reinforcement will have to carry the tension developed at the interface. The equation of motion of the wall panel, Eq. (7), becomes

$$M \frac{\partial^2 u}{\partial t^2} + R_{\max} b h + T_g = 0 \quad (31)$$

where T_g is the tension in the soil reinforcement at the interface. If this interface tension is greater than the "pull-out resistance" of the soil reinforcement, slippage will occur between soil and soil reinforcement and the wall panel will become separated from the soil. The confined stiffness or "pull-out resistance" of the soil reinforcement should be used

in the design calculations. Figure 2 shows different characteristics of the confined versus unconfined stiffnesses of CONWED Stratagrid™ 9027 (Farrag et al. 1991).

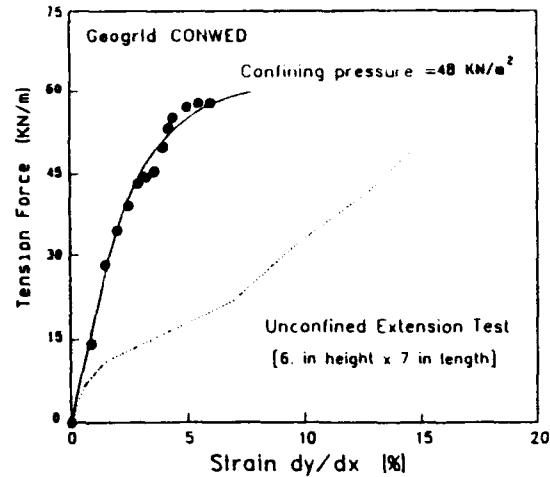


Figure 2. Confined vs. Unconfined Stiffness of a Geogrid

The higher confined stiffness can be attributed to the composite action of the reinforcement with surrounding soil. If the wall panel stays in contact with soil, the connection system is termed "compression-controlled". If the wall panel separates from the soil, the connection system is termed "tension-controlled". Figure 3 shows the relationship between the ratio γ/α and the ratio σ_o/R_{\max} , which can be used to determine whether separation will occur.

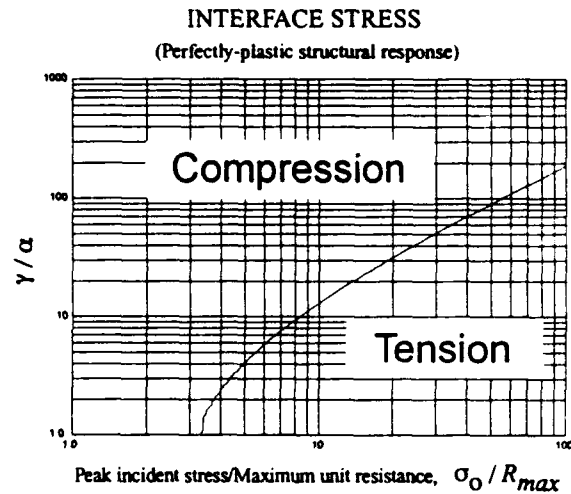


Figure 3. Prediction of Tensile or Compressive Interface Stress

The free-field soil displacement under the shock wave prescribed by Eq. (6) is

$$u_{ff}(t) = \frac{v_o}{\alpha} (1 - e^{-\alpha t}) \quad (32)$$

The maximum wall panel displacement, u_{\max} , for a compression-controlled system is always less than twice the

peak free-field soil displacement. This corresponds to the limiting case of a free soil boundary where $\lambda \rightarrow 0$, $\mu \rightarrow 0$ and $\gamma \rightarrow \infty$. However, a large wall panel displacement may occur for a tension-controlled system. When the wall panel becomes separated from the soil, slippage between soil and soil reinforcement will have occurred. If the soil reinforcement tension at the interface is assumed to be a constant, being equal to the smaller of the soil reinforcement yielding force or the dynamic frictional resistance between soil and soil reinforcement, the maximum panel displacement can be determined by solving Eq.(31) numerically. In this case, the unit resistance R_{max} is the combined resistance of the panel connection and soil reinforcement. Figure 4 shows a normalized displacement envelope in terms of σ_o / R_{max} for both compression- and tension-controlled systems.

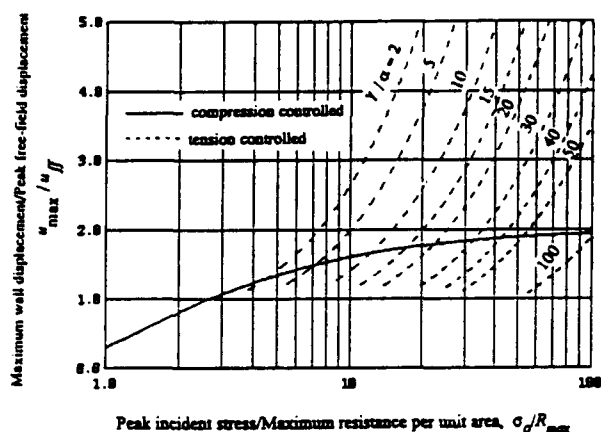


Figure 4 Ratio of Maximum Wall Displacement to Maximum Free-field Soil Displacement

EXAMPLE

A numerical example is given herein to illustrate how the simple 1-D model can be used to determine the normal stress acting on the interface between the reinforced earth and the wall panel and the kinematic response of the wall panel. Furthermore, the effects of wall panel separating from the soil on these response parameters are also presented. The physical parameters used in this example are given in Table 1. Figures 3 and 4 may be used to determine the maximum wall panel displacement rapidly. Using Eq.(3) and the values given in Table 1, the apparent constrained modulus of the reinforced earth, K_x , is computed to be 59,427 psi (410 MPa). Since the soil is very lightly reinforced, the mass density of the soil is not significantly affected by the presence of the reinforcement. The seismic velocity of the reinforced earth, c , is computed to be 1583 fps (482 m/s). Combining Eqs.(9) and (24) yields

$$\gamma = \frac{K_x h b}{M c} \approx 2000 \text{ Sec}^{-1} \quad (33)$$

and $\gamma / \alpha = 25$. The peak normal stress is computed from the free-field particle velocity,

$$\sigma_o = \rho_o c v_o = 230 \text{ psi} \quad (34)$$

and $\sigma_o / R_{max} = 46$. From Figure 3, the connection system falls in the "tension-controlled" region. This means that, during the loading phase, the wall panel is likely to separate from the soil. Using Figure 4, the ratio of maximum wall panel displacement to the peak free-field displacement is found to be approximately 2.5. The peak free-field soil displacement is determined using Eq.(32),

$$u_{ff} = \frac{v_o}{\alpha} = 0.92 \text{ in. (23 mm)} \quad (35)$$

and the maximum wall panel displacement, u_{max} , is $0.92 \times 2.5 = 2.3 \text{ in. (58 mm)}$

Table 1. 1-D Model Parameters for the Example

Parameter (1)	Value (2)
Young's Modulus of Soil, E_s	255 MPa (37,000 psi)
Poisson's Ratio of Soil, ν_s	0.35
Dry Unit Weight of Soil, ρ_s	1765 kg/m ³ (110 pcf)
Young's Modulus of Reinforcement, E_g	1.08 GPa (157,000 psi)
Unit Weight of Reinforcement, ρ_g	963 kg/m ³ (60 pcf)
Poisson's Ratio of Reinforcement, ν_g	0.40
Volume Ratio of Reinforcement, V_g	0.024%
Free-field Soil Particle Velocity, v_o	1.8 m/s (6 fps)
Exponential Decay Rate, α	80 Sec ⁻¹
Length of Reinforced Earth, R	6.1 m (20 ft)
Seismic Velocity of Soil, c	488 m/s (1600 fps)
Unit Structural Resistance, R_{max}	35 kPa (5 psi)
Height of Wall Panel, h	154 cm (5 ft)
Width of Wall Panel, b	180 cm (6 ft)
Weight of Wall Panel, M	1180 kg (2600 lb)

Figure 5 shows that the interface stress is the superposition of the incident stress and the structural unit resistance.

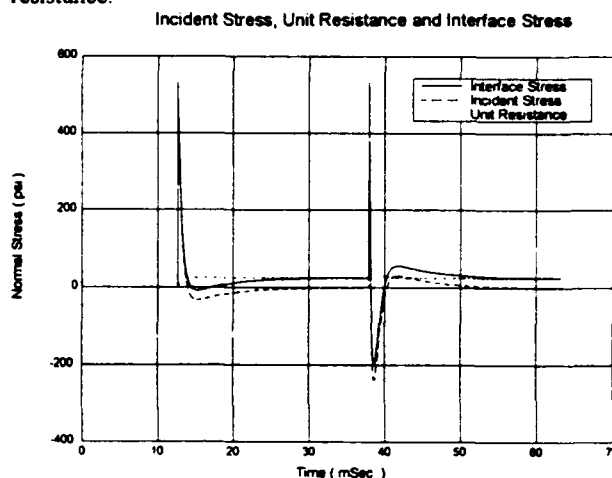


Figure 5. Composition of Interface Stress
In this example, the interface stress becomes tensile at time $t = 14.36 \text{ mSec}$ when the wall panel starts separating from the soil. Eq.(31) becomes effective from that time instant and is solved numerically to determine the maximum wall panel

displacement. Figure 6 shows that wall panel displacement would be significantly underestimated if Eqs.(26)-(30) were used for a "tension-controlled" connection system.

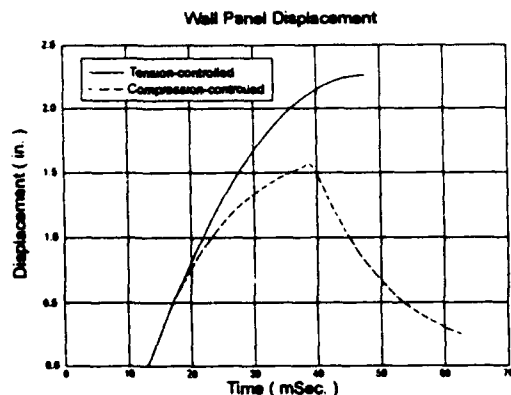


Figure 6. Effect of Panel Separation from Soil on Wall Panel Displacement

LIMIT STATE DESIGN PROCEDURE

Using the above information, a step-by-step design methodology is illustrated herein:

Step 1. Determine the volume ratio of reinforcement in the reinforced soil, V_g .

Step 2. Determine the peak value σ_p and the decay rate α of the free-field normal stress in the reinforced soil due to a given explosion.

Step 3. Conduct limit analyses of the maximum pull-out resistance of reinforced soil.

The resistance of the reinforced soil may become ineffective if sufficient embedment length is not provided to develop the required tensile force in the reinforcement. Due to the high strain rate from a ground shock, an ideal soil reinforcement should possess high tensile modulus, high tensile and impact strength, but most importantly, high ductility. Requirements for minimum embedment length and maximum vertical spacing of reinforcement layers have been developed based on slope stability by Christopher et al. (1990) and Jewell (1990). The maximum pull-out resistance of the reinforced soil is dictated by the following three modes of failure:

- soil shear failure in a zone away from the reinforcement;
- tensile rupture in the reinforcement; and
- bond failure between soil and reinforcement.

The smallest value of these resistances is the maximum pull-out resistance of the reinforced soil.

Step 4. Conduct limit analyses of the maximum resistance of wall panel connection.

Step 5. Determine the maximum wall panel displacement due to the given ground shock

For perfectly plastic structural response, the maximum resistance per unit area of wall panel (or unit resistance), R_{max} , is the sum of the maximum unit resistance of the reinforced soil and that of the wall panel connection. Figures 3 and 4 can then be used to determine the maximum wall panel displacement.

Step 6. Design against breaching of wall panels

The 1989 version Air Force Protective Design Manual provides guidelines for determining structural element thickness and minimum standoff distance to prevent localized breaching. McVay(1988) reported that breaching is likely to occur when the scaled range, $R/W^{1/3}$, is less than 1.3 ft/lb^{1/3}, where R is the standoff in feet and W is the net explosive weight in pounds of TNT. In general, the concrete wall panels are reinforced with welded wire fabric(WWF) made of A82 steel with a minimum yield strength of 64000 psi. For close-in and contact explosions, fibrous concrete may be used as an alternative.

CONCLUSION

The 1-D mathematical model proposed in this study provides a simple method for predicting the dynamic interaction between reinforced earth and wall panels under ground shock loading. The model accounts for superposition of incident and reflected waves propagating between the velocity boundary and the wall panel. The model treats reinforced earth as a linearly elastic and homogeneous medium, and as such cannot model the hysteretic compaction or other plastic behavior of soil under stress wave propagation.

This method of analysis can be applied to earthquake engineering, where the ground motion may be treated as a series of shock waves arriving at the wall at different instants of time. It is anticipated that wall panel will not separate from the soil at low stress level, and therefore, the responses to the different shocks can be superimposed to find the wall response under an earthquake motion.

ACKNOWLEDGMENT

This research was conducted under Scientific and Engineering Technical Assistance (SETA) contract F08635-88-C-0067 with the Air Force Civil Engineering Support Agency, Engineering Research Division (AFCEA/RAC), as part of SETA Subtask 2.14, "Advanced Panel and Connection System for an Airbase Protective Shelter Employing Reinforced Earth."

REFERENCES

- Raudanski, E., Eytan, R., and Sweiry, G.(1990), "Reinforced Soil Ammunition Magazine, Full-scale Tests-1990, Testing Program," Headquarters Israeli Air Force Civil Engineering Division, Engineering and Products Branch.
- Reid, R.A., "Reinforced-Soil Munition Bunker Test," *The Military Engineer*, Vol.82, No.537, August 1990, pp.51-52.
- Reid, R.A., "Full-scale Test of a Reinforced Soil Bunker," *Proceedings of the Fifth International Symposium on the Interaction of Non-nuclear Munitions with Structures*, Mannheim, Germany, April 22-26, 1991, pp.12-16.

Christopher, B.R., et al., Reinforced Soil Structures: Volume I. Design and Construction Guidelines, FHWA-RD-89-043, U.S. Department of Transportation, Federal Highway Administration, McLean, VA, 1990.

Drake, J.L., and Rochefort, M.A., "Response of Buried Structure Walls to Earth Penetrating Conventional Weapons," Dynamics of Structures, ASCE, August 1987, pp.455-468.

Drake, J.L., et al., Protective Construction Design Manual: Groundshock and Cratering, (Section V), ESL-TR-87-57, Tyndall AFB, FL, 1989.

Drake, J.L., et al., Protective Construction Design Manual: Resistance of Structural Elements, (Section IX), ESL-TR-87-57, Tyndall AFB, FL, 1989.

Farrag, K.A., Acar, Y.B., and Juran, I., In-Soil Characteristics and Interface Properties of STRATAGRID 9027, Technical Bulletin GS 101, CONWED Plastics, Roseville, MN, 1991.

Jewell, R.A., "Revised Design Charts for Steep Reinforced Slopes," Proceedings of a Symposium on Reinforced Embankments, Cambridge University, U.K., 1990.

McVay, M.K., "Spall Damage of Concrete Structures," Technical Report SL-88-22, U.S. Army Waterways Experiment Station, Vicksburg, MS, 1988.

Response of Geogrid-Reinforced Soil Subjected to Blast Loading

Capt Richard A. Reid, PE¹; Dr. Robert C. Bachus²,
Kara L. Olen, EIT², and Dr. Ricnard Fragaszy, PE²

¹WL/FIVCS, Tyndall AFB, FL
²GeoSyntec Consultants, Atlanta, GA

ABSTRACT

This paper presents a summary of a comprehensive research program which was developed to evaluate the effectiveness of reinforced soil for blast protective shelters. Following a thorough review of previous investigations, the following three phased experimental program was undertaken: (i) a lab testing program using geogrids subjected to impulse loading; (ii) a numerical modeling program using 3-D dynamic finite element analysis and a two invariant cap model; and (iii) a physical modeling program using 1/30th scale centrifuge models subjected to blast loading. In this paper an overview of results is presented for the successful experimental program, with emphasis on parameters affecting hardened shelter performance.

INTRODUCTION

Protection of sensitive equipment, munitions, communications networks, and high-performance aircraft for military applications is typically accomplished by construction of hardened shelters. Traditionally, these shelters are constructed of reinforced concrete, but may incorporate earthen berms to deflect and reduce blast loads. Recently, the United States Air Force (USAF) has been evaluating the potential use of reinforced soil technology for the construction of protective shelters. The response of geogrid reinforced soil subjected to impulse (i.e., blast) loading has been the subject of recent study.

In 1990, a series of full scale explosive tests were conducted on a reinforced soil munitions bunker by the USAF and the Israel AF to evaluate the survivability of these structures when subjected to conventional weapon effects (Ref. 1). The bunker walls were constructed with conventional reinforced soil as follows. A row of vertical facing panels was placed

at the wall locations. Soil was compacted behind the panel to the level where metal reinforcement strips (inextensible reinforcement) were laid out behind each wall panel and connected to anchors in each panel. The strips were then covered with compacted soil. After completion of the first layer of wall panels, a second course of panels was added and the process repeated. The bunker was tested by detonating general purpose bombs in the soil backfill behind the wall. Deflections of the wall panels were measured. The reinforced soil bunker for these full scale tests showed a high resilience to conventional weapon detonations. Unfortunately, no analysis was conducted in the full scale test program to determine the primary design variables that affect system performance. A comprehensive research effort was subsequently initiated to determine the role of the parameters which influence the response of reinforced soil systems to conventional weapon detonations.

OVERVIEW OF THE RESEARCH PROGRAM

The objective of the research program was to develop validated techniques for evaluating the influence of the parameters that affect the response of reinforced soil to loads from blast waves. The research program was developed to include a three-phased investigation. These included: (i) a laboratory testing program, (ii) a numerical model testing program, and (iii) a physical model (i.e., centrifuge) testing program (Ref 5). Each phase of the testing program was undertaken to provide either complimentary data which could be used in other phases or validating data which could be used to compare results from other phases.

There were several elements of the overall testing program which were common to each phase, and therefore warrant discussion. The program focused on structures which could be used to house aircraft, equipment and/or personnel. These 'structures' were actually 14.8 ft (4.51 m) high reinforced soil walls which can be constructed with an optional roof. The studies focused

primarily on the use of geogrids as the soil reinforcement material. Dry sands were used or modeled in the study. The structure was loaded by use of a blast wave, herein referred to as an impulse load, induced by explosive detonation. The impulse loads have rise times from a few milliseconds (ms) to less than 1 ms; corresponding strain rates in soil exceed several percent per ms. Three geogrid reinforcing materials were selected for evaluation in the lab study. The geogrids were selected based on variations in material composition, structure, and tensile strength. The types of geogrids tested and their properties are shown in Table 1.

A generic geogrid was modeled in the numerical and physical testing studies. A detailed description of each of the three phases is presented in the remainder of this paper. Detailed information on all facets of this research program can be found in reference 5.

Product Name	Manufacture	Structure	Polymer Composition	Ultimate Tensile Strength (kN/m)
UX1500	The Tensar Corporation	Punched Sheet-Drawn	Polyethylene	86.0
Miragrid 10T	Mirafi, Inc.	Woven	Polyester	93.6
Matrex120	The Reinforced Earth Company	Woven	Polyester	181.3

Table 1 (Ref 5)

LABORATORY TESTING PROGRAM

The laboratory testing program consisted of two types of an evaluation of both static and dynamic response. One portion focused on the unconfined response and the other focused on the pullout response of geogrids embedded in soil. Unconfined response testing of the geogrids was performed in general accordance with American Society for Testing and Materials (ASTM) Standard Method D4595-86. Confined response testing was performed in general accordance with ASTM draft Standard Test Method D35.01.87.02. The pullout test device was modified to provide peak loads within tens of milliseconds.

Unconfined Static Tensile Tests: Three unconfined static tensile test were performed on Tensar UX1500, Miragrid 10T and Matrex 120 geogrids at a constant rate

of 10% per minute. Static tensile stress-strain responses of the three geogrids are shown in Figure 1.

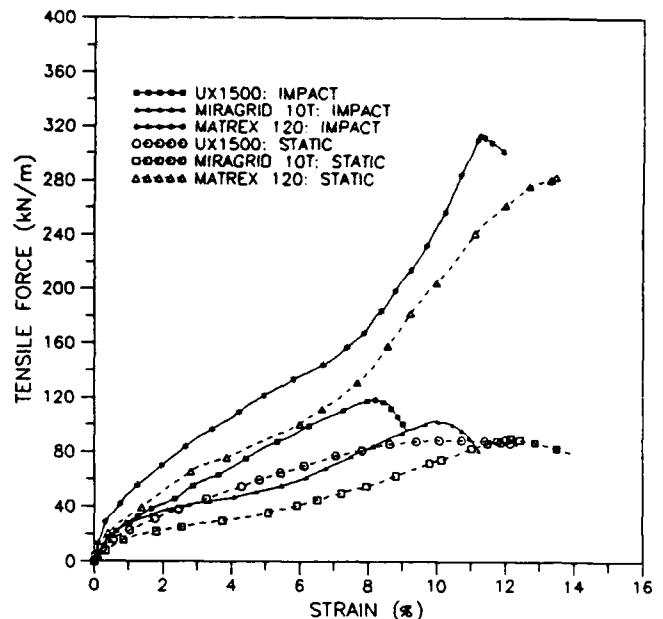


Figure 1 (Ref 5)

Unconfined Impact Tensile Tests: To evaluate the unconfined dynamic strength of the geogrid, the dynamic loading system from the pullout box was used. The results of the three impact tensile tests on Tensar UX1500, Miragrid 10T, and Matrex 120 geogrids are presented in Figure 1 and Table 2. It can be seen from Figure 1 that for all three geogrid products the dynamic tensile strength and dynamic tensile stiffness are higher than the corresponding static properties. The relative increase of tensile strength, defined as ratio of the impact to the static strength, is 33.8, 14.5, and 10.7 percent for Tensar UX1500, Miragrid 10T, and Matrex 120 geogrids, respectively.

Test Series	Geosynthetic Type	Specimen Width (in)	Specimen Length (mm)	Input Kinetic Energy (ft-lb)	Measured Impact Tensile Strength (lb/ft)	Measured Static Tensile Strength (lb/ft)	Relative Increase (%)
DT1	UX1500	4	325	1.81	118.9	88.9	33.8
DT2	Miragrid 10T	3	325	1.81	102.8	89.8	14.5
DT3	Matrex 120	2	325	1.81	213.7	203.3	10.7

Table 2 (Ref 5)

Static Confined Pullout Test Results: Pullout testing consisted of measuring the force necessary to pull the geogrid

specimen out from the confining soil mass.

'Static' pullout tests were defined as the conventional pullout tests in which the specimen is loaded in a displacement controlled manner at a rate of 0.04 in/min (1 mm/min). Conventional static pullout test series were conducted using specimens of each three geogrids in each of two sands to establish six test series. Three test series were conducted in a poorly graded sand (Unified Soil Classification System (USCS) = SP) compacted to a relative density of approximately 80% by hand tamping. The other three test series were conducted in a well-graded silty sand (USCS = SW-SM) compacted to a relative density of approximately 75% by hand tamping at a moisture content of 3.0%. Tests were conducted at a range of confining pressures. Detailed test conditions and results for these six series of tests are presented as Test Series 1 through 6 in Table 3.

Test Series	Geogrid Type	Soil Type	Specimen Length (mm)	Specimen Width (mm)	Normal Stress (kPa)	Soil Compaction		Rate of Pullout (mm/min)	Pullout Resistance (kN/m)	Apparent Friction Coefficient
						D (%)	w (%)			
1	UX1500	SP	100	90	2.1	80	0	1	4.6	1.12
	UX1500		100	90	22.8	80	0	1	47.6	1.06
	UX1500		100	90	26.6	80	0	1	60.7	0.94
	UX1500		100	90	71.1	80	0	1	73.8	0.92*
2	MIRAGRID 10T	SP	100	90	2.1	80	0	1	5.7	1.26
	MIRAGRID 10T		100	90	22.8	80	0	1	48.0	1.06
	MIRAGRID 10T		100	90	26.6	80	0	1	58.6	0.96
	MIRAGRID 10T		100	90	71.1	80	0	1	64.0	0.95*
3	MATREX 120	SP	140	90	2.1	80	0	1	4.8	1.06
	MATREX 120		140	90	22.8	80	0	1	50.6	1.13
	MATREX 120		140	90	26.6	80	0	1	60.3	0.90
	MATREX 120		140	90	71.1	80	0	1	118.1	0.92
4	UX1500	SW-SM	100	90	2.4	75	3.0	1	13.3	2.38
	UX1500		100	90	22.1	75	3.0	1	67.7	1.48
	UX1500		100	90	26.6	75	3.0	1	71.4	0.96*
	UX1500		100	90	71.1	75	3.0	1	143.7	1.32
5	MIRAGRID 10T	SW-SM	100	90	2.4	75	3.0	1	14.0	2.83
	MIRAGRID 10T		100	90	22.1	75	3.0	1	69.3	1.43
	MIRAGRID 10T		100	90	26.6	75	3.0	1	60.6	1.26*
	MIRAGRID 10T		100	90	71.1	75	3.0	1	143.7	1.32
6	MATREX 120	SW-SM	140	90	2.4	75	3.0	1	59.3	1.30
	MATREX 120		140	90	22.1	75	3.0	1	69.6	1.31
	MATREX 120		140	90	26.6	75	3.0	1	69.6	1.31
	MATREX 120		140	90	71.1	75	3.0	1	143.7	1.32
7	UX1500	SP	100	90	2.1	80	0	152	4.8	1.20
	UX1500		100	90	22.8	80	0	152	47.0	1.07
	UX1500		100	90	26.6	80	0	152	72.6	1.02
	UX1500		100	90	71.1	80	0	152	82.6	0.98*
8	MIRAGRID 10T	SP	100	90	22.8	80	0	152	63.2	1.17
	MIRAGRID 10T		100	90	26.6	80	0	152	65.0	1.17
	MIRAGRID 10T		100	90	71.1	80	0	152	82.0	0.97*
	MIRAGRID 10T		100	90	71.1	80	0	152	82.0	0.97*
9	MATREX 120	SP	140	90	2.1	80	0	152	4.8	1.16
	MATREX 120		140	90	22.8	80	0	152	46.6	1.02
	MATREX 120		140	90	26.6	80	0	152	62.0	0.92
	MATREX 120		140	90	71.1	80	0	152	123.6	0.98
10	MATREX 120	SW-SM	140	90	2.4	75	3.0	152	104.0	0.79
	MATREX 120		140	90	22.1	75	3.0	152	104.0	0.79
	MATREX 120		140	90	26.6	75	3.0	152	104.0	0.79
	MATREX 120		140	90	71.1	75	3.0	152	104.0	0.79

Table 3 (Ref 5)

Confined Pullout Testing at Increased Deformation Rate: Three additional series of pullout tests were conducted on the three geogrids in the SP sand at a displacement rate of approximately 6 in/min (152 mm/min) to evaluate the effect of testing rate on the geogrid response. Figure 2 shows comparison of pullout resistance curves at the 0.04 in/min (1 mm/min) rate and those at the 6 in/min (152 mm/min) rate.

It is observed that the peak pullout resistance of each geogrid specimen at these two different displacement rates is almost identical when tested at low confining pressure. As the confining pressure increases, there is an indication that the dynamic pullout resistance may be slightly greater than the static resistance, particularly for the Tensar UX1500 geogrid. Although this affect may be indicative as a rate dependent pullout phenomenon, the response results at the two loading rates are similar. Based on the relatively consistent, yet limited test data, the authors do not believe that these results suggest a significant rate dependency effect.

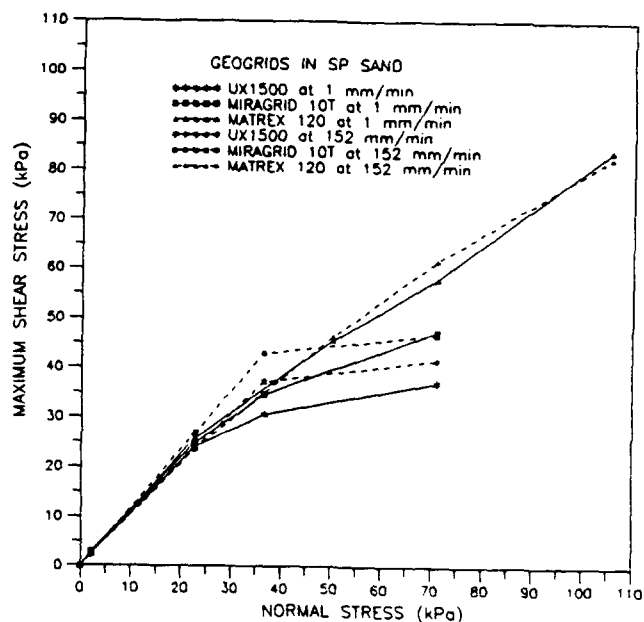


Figure 2 (Ref 5)

Confined Impact Test Results and Comparisons: An impact or dynamic pullout test is one in which the reinforcement is subjected to an impulse load exhibiting a rise time of a few tens of ms. Six series of impact pullout tests on the three geogrids in each of the SP and SW-SM sands were conducted.

Comparison between the impact and static pullout resistances for the three geogrids in the SP sand is shown in Figure 3. For

Tensar UX1500 and Miragrid 10T geogrids, the impact and static pullout resistance curves in the SP sand are almost identical for the range of test normal stresses. However, for the Matrex 120 geogrid, the impact pullout resistance was consistently higher (range from 1 to 15 percent) than the static resistance. For the geogrids in SW-SM sand, the difference between impact and static pullout resistance was insignificant (Ref 5).

Summary: Based on the composite results from all of the pullout test series, the authors suggest that there is, at best, only a slight indication that the pullout resistance demonstrates a rate dependent effect. With the possible exception of the Matrex 120 geogrid in the SP sand, in fact, the results consistently indicate that there is a negligible effect. This lack of rate dependency is supported by the pullout resistance versus deformation response, not presented in this paper due to space limitations but presented in reference 5.

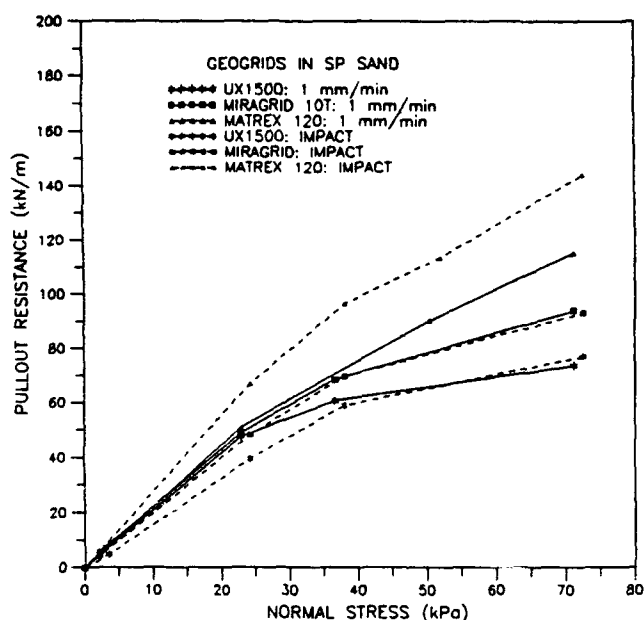


Figure 3 (Ref 5)

NUMERICAL MODELING OF REINFORCED SOIL

Several numerical codes for non-linear finite element or finite difference

analysis are available. These codes have been used for the dynamic analysis of protective structures subjected to weapons effects. However, very few offer soil models of the type appropriate for sophisticated non-linear dynamic analysis. Selection of a code which could implement a realistic soil model was considered essential. The soil model that was determined to be best suited for the present study was the Weidlinger Cap model (Ref 5). This model has been used extensively for ground shock problems, and it is versatile enough to incorporate various effects that were considered important during this study, such as rate effects.

A variety of numerical models were evaluated for their applicability to this study, including ANSYS, ABAQUS, ADINA, and DYNA3D. Of these, DYNA3D was developed specifically for the analysis of blast problems. This non-linear, explicit 3-D finite element code developed by the Lawrence Livermore National Laboratory (Ref 3), also incorporates the Weidlinger Cap model for soil behavior. These characteristics, coupled with the advantage of being currently in use by the USAF and available in the public domain, made DYNA3D the most suitable choice for use in the numerical modeling program.

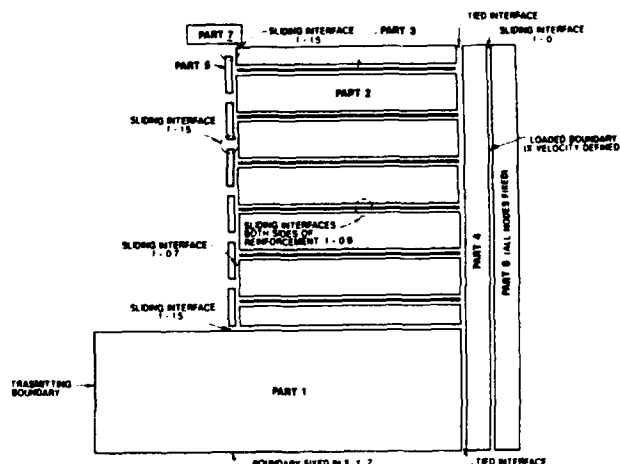


Figure 4 (Ref 5)

For analysis, a prototype structure was modeled. The prototype geogrid reinforced wall was 14.8 ft (4.5 m) high and

contained 6 layers of Tensar UX1600 geogrid, each layer being 14.8 ft (4.5 m) long. Each layer of geogrid was attached to the center of a concrete facing panel 2.46 ft (0.75 m) high and 0.48 ft (14.63 cm) thick. The soil used for both the wall backfill and the foundation was modeled as a clean sand with a friction angle of 35 degrees.

An example of the mesh used for the finite element analysis is shown in Figure 4. This mesh was used in all of fourteen computer runs to evaluate the effect on the performance (i.e., deformation) of the wall face due to variations in the following parameters: reinforcement stiffness and length, weapon size and location, soil/reinforcement friction coefficient, soil stiffness and strength, and constraint of the top of the wall.

The conclusions of the parametric study are summarized as follows:

- Reinforcement stiffness significantly affects the displacements induced by blast loading. Displacements decrease with increasing reinforcement stiffness in the following non-linear fashion: increasing reinforcement stiffness by two orders of magnitude above the stiffness of the baseline model material leads to approximately a 17% decrease in average displacement of the wall facing; decreasing reinforcement stiffness by two orders of magnitude leads to approximately a 40% increase in average displacement of the wall facing.

- Within the range of lengths investigated (14.8 and 10.8 ft (4.51 & 3.29 m)), reinforcement length has little effect on the behavior of the reinforced soil system provided these lengths meet static design criteria.

- The reinforcement is subjected to very high compressive stresses as the blast wave passes through the system. Dynamic tensile stresses in the reinforcement develop after the blast wave has reached the facing.

- Dynamic tensile stresses develop relatively slowly in the reinforcement. Rise times of tens of milliseconds are predicted by the numerical code.

- Reinforcement rupture and excessive deflection were the only observed failure mechanisms. The soil mass and

reinforcement moved as one in response to the blast load, meaning little relative movement between the reinforcement and the soil (i.e. pullout), was observed.

- Weapon size and distance from the wall face are critical parameters which influenced wall behavior much more than any other parameters.

- For a constant soil friction angle, the range of soil/reinforcement interface friction coefficients have a relatively small influence over system behavior (i.e., 0.7-0.9).

- Soil strength and stiffness are very important parameters governing system behavior. Wall panel deformations decrease as soil strength and stiffness increase. This effects appears to be more important than reinforcement stiffness.

- For a given soil, the behavior of the reinforced soil system is very sensitive to placement soil density because of the close relationship between soil density and soil strength and stiffness. Increasing the relative compaction of the soil leads to enhanced wall performance.

PHYSICAL MODELING OF REINFORCED SOIL WALL

Centrifuge modeling of reinforced soil walls subjected to buried blast loading was conducted at Tyndall AFB. Nine, 1:30 scale physical model tests were conducted using Tyndall beach sand, gypsum facing panels and six layers of either steel shim stock or woven nylon netting reinforcement. The steel shim stock was sized to model the steel strip reinforcement used in conventional reinforced soil walls. The properties of the nylon netting approximately modeled the scaled strength and stiffness of Tensar UX1500. The gypsum panel modeled the size and behavior of conventional concrete panels. The explosive was modeled with 3 gm (0.106 oz) of RDX placed at various locations in the backfill behind the reinforced soil mass. Instrumentation included accelerometers placed on selected facing panels and carbon resistance gages placed within the soil mass. Video and high-speed cameras were used to document the tests.

The centrifuge tests were used to evaluate the influence of wall displacement on reinforcement type, length, and stiffness; weapon location; and facing restraint at

the top of the wall. Two of the centrifuge tests were conducted to provide a comparison with numerical predictions. Data collected from the test included: (i) peak wave pressures; (ii) facing panel peak accelerations; (iii) wave velocities; and (iv) permanent wall displacement. The results of the testing indicate the following:

- Peak wave pressures measured in the centrifuge agree well with predicted values (based on CONWEP analysis, Ref 4).

- Based on the limited testing program, centrifuge test results are reproducible.

- Below a minimum length for static stability, reinforcement length is a minimal factor in wall response.

- Reinforcement width and type are significant factors in wall response. The walls with nylon netting performed better than walls with steel shim stock.

- Wall deformations are significantly smaller when top restraint is used, assuming all other factors remain equal.

- Peak pressure, wave velocities, panel displacements, and the effects of wall response to detonator location in the centrifuge tests agree well with the numerical modeling results.

CONCLUSIONS

Laboratory Testing: The laboratory testing has shown that the dynamic unconfined and confined pullout behavior of geogrids in sand, when measured both in terms of load vs displacement and the ultimate pullout resistance, is very similar to the behavior observed with static tests. The dynamic pullout tests subjected the geogrid to a stress path similar to that caused by blast loading. There does not appear to be a significant rate dependency effect for either the unconfined specimen or the geogrid/soil composite specimen.

Numerical Modeling: The numerical modeling tests has shown that soil stiffness, soil friction angle, the presence of top restraint, and reinforcement stiffness significantly affect wall performance. Reinforcement length and soil/ reinforcement interface friction coefficient are relatively less important parameters, provided they are

kept within normal ranges for static stability.

Physical Modeling: The physical modeling testing has demonstrated that reinforcement type and stiffness play a significant role in wall behavior. The importance of a horizontal constraint at the top facing panel has also been demonstrated. Reproducibility of test results and the close agreement between centrifuge test results and numerical predictions provide evidence that centrifuge modeling techniques are appropriate for this class of problems.

This research program has developed some of the first quantitative data on the response of geogrid-reinforced walls to impulse loading. Conclusions were developed showing which of the reinforced soil design variables affect the response of the system to this severe loading regime. Full-scale testing is now in progress at Tyndall AFB to provide validation to the laboratory, numerical, and centrifuge test data presented in this paper.

References

1. Reid, R.A., "Full-Scale Blast Test of a Reinforced Soil Bunker," 5th International Symposium on the Interaction of Non-Nuclear Munitions with Structures, Mannheim, Germany, April 1991.
2. Geotechnical Fabrics Report, Industrial Fabrics Association International, St. Paul, MN, pp. 119-120, December, 1990.
3. Whirley, R.G. and Hallquist, J.O., DYNA3D A Nonlinear Explicit, Three Dimensional Finite Element Code For Solid and Structural Mechanics - User Code, Report UCRL-MA-107254, Lawrence Livermore National Laboratory, CA, May, 1991.
4. Hyde, D.W., ConWep (Conventional Weapon Effects), computer programs, US Army Corps of Engineers Waterways Experiment Station, Vicksburg, MS, February 17, 1988.
5. Bachus, R.C., Fragaszy, R.J., Jaber, M., Olen, K.L., Yuan, Z., and Jewell, R. Dynamic Response of Reinforced Soil Systems, CEL-TR-92-47, Vol 1 & 2, Jun 92.

DIMENSIONING OF HIGH EXPLOSIVE DETONATIONS ON CONCRETE STRUCTURES

Prof. Dr.-Ing. D. Kraus
Dipl. Ing. J. Rötzer

University of German Armed Forces
Department Structural Engineering

1 INTRODUCTION

This contribution continues a paper [5] presented 4 years ago at the Fourth International Symposium. In this report the boundaries for the possibility of a kinematic chain and the fixing of the necessary destruction areas (hinges) were described.

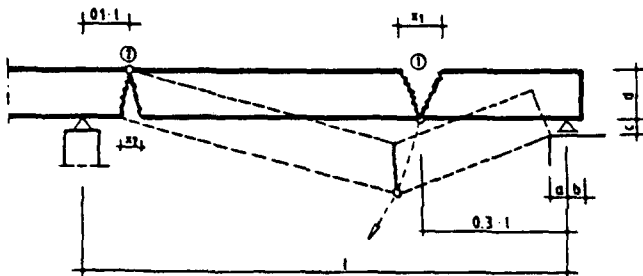


Fig. 1: Arrangement and dimensioning of the necessary hinges

In this contribution the analytical description of the explosion-impact and the behavior of concrete and steel and the coupling of the explosion with the structure are presented.

2 SPATIAL AND TEMPORAL REPRESENTATION OF THE HIGH EXPLOSIVE AND DESTRUCTION PROCESSES

The interaction of a high-explosive detonation upon a reinforced concrete structure can be solved sufficiently through a numerical simulation. The description of impact and detonation processes is possible in a coupled or separated process. For our examination we have been used a coupled solution which can include the correlation between the impact and the reaction of the structure directly.

The used program AUTODYN solves this problem with the method of finite differences

on the basis of an Euler-Lagrange-link. At each timestep the state of equilibrium and the conservation of mass, impulse and energy are satisfied.

In the Lagrange-formulation the nodes, which are describing the investigated medium, are moveable. The grid gets the possibility to deform and distort. In this case the elements may degenerate, so that negative masses or energies can occur. In the Euler-formulation the grid is located in the space and the medium moves through it. In the Euler-Lagrange-connection, the pressure -calculated in the Euler grid - will be act on the structure which is described by the lagrange grid.

3 SIZES OF THE SPATIAL GRIDS AND THE TIMESTEPS

For the spatial grid of the detonation area the size of one element is taken so small, that the highest occurring pressure reaches at least 50 % of the Chapman-Jouguet-pressure.

With the choice of the timestep the following conditions have been satisfied

- the numerical stability of the calculation
- the shockwave must reach each element
- the loss of energy must be limited under a fixed level because the energy-conservation is satisfied approximately.

The two last conditions guarantee the numerical stability of the calculation automatically.

4 DESCRIPTION OF THE MATERIALS

For a practical description of the material strength it is necessary to divide the stresses and strains in a hydrostatic and a deviatoric part.

In a simple approximation the hydrostatic parts represents the volumetric change and

A more exact adaption of the failure criteria to testseries is not worth until the influence of the strain-rate in the range $\dot{\epsilon} = 100[\frac{1}{s}]$ cannot be described yet.

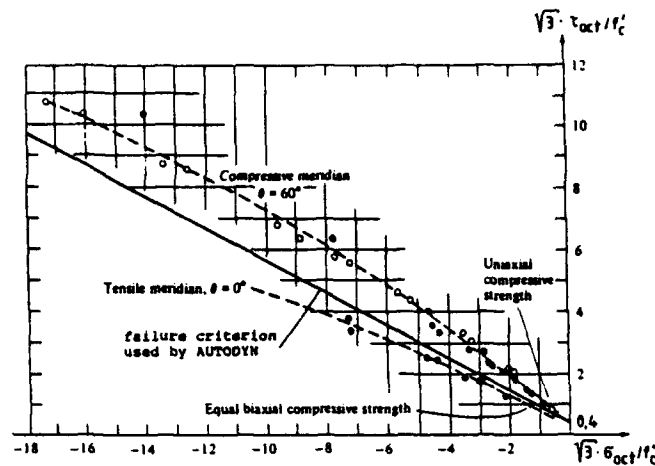


Fig. 3: Failure-criterion [3]

5 COMPARISON OF NUMERICAL CALCULATIONS WITH FIELDTTESTS

The used calculation models and the laws of material are checked for her abilities. This happens by comparing craterdiameter, craterdepth and damage of the lower side of the plate. For our first investigations we used the fieldtests of the "Forschungsinstitut für militärische Bautechnik", Zürich [4].

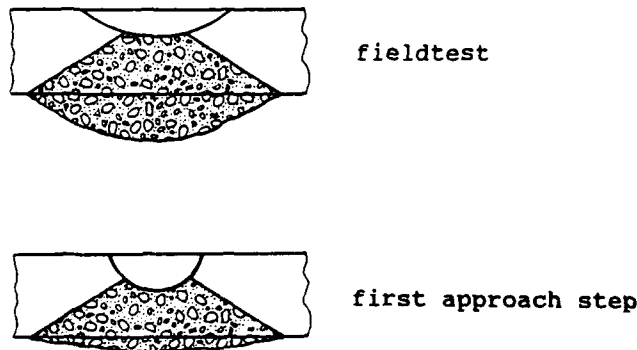


Fig. 4: First approach step

the deviatoric parts represents the plastic behavior, the failure and the strain-rate influence.

The explosive properties are described with the Jones-Wilkins-Lee equation.

$$p = A_j \cdot \left(1 - \frac{w_j}{R_{1j} v_j}\right) \cdot e^{-R_{1j} v_j} + B_j \cdot \left(1 - \frac{w_j}{R_{2j} v_j}\right) \cdot e^{-R_{2j} v_j} + \frac{w_j E_j}{v_j}$$

For characterising the material two fundamental relationships are necessary.

- The equation of state, EOS, which describes the stress-strain-relations.
- The failure-criterion. It determines the maximal possible stresscombination.

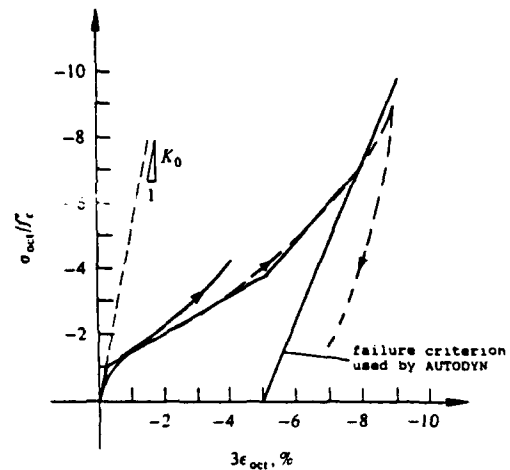


Fig. 2: stress-strain-relation [3]

For the presentation of the EOS we use the pressure-density-relationship. This is similar to the hydrastatic stress-strain-relation. The pressure is equal to the octahedral normal stress σ_{oct} and the density is indirect proportional to the volume.

The failure of the concrete is described by Drucker-Prager with

$$f = \alpha J_1 + \sqrt{J_2} - k = 0$$

6 REFERENCES

- [1] AUTODYN TM, Software for Non-Linear Dynamics, Century Dynamics Incorporated, Users Manual, Oakland 1989.
- [2] Bartlmä, P.: Gasdynamik der Verbrennung, Springer-Verlag, Wien - New York: 1975.
- [3] Chen, W.F.: Plasticity in Reinforced Concrete. Mc Graw-Hill:1982.
- [4] FMB Zürich: Lokale Schadenwirkungen auf armierte Betonplatten bei der Explosion von Sprengladungen und Granaten. Forschungsinstitut für militärische Bautechnik Zürich, FMB 79-13, 1979.
- [5] Kraus, D.: A new Blast Method for Concrete Bridges. Proceedings of the Fourth International Symposium of the Interaction of Non-nuclear Munitions with Structures. Panama City Beach, Florida: 1989.
- [6] Nilson, A.H.: Finite Element Analysis of Reinforced Concrete. American Society of Civil Engineers, New York: 1982.
- [7] Yi, P.: Explosionseinwirkungen auf Stahlbetonplatten. Dissertation TH Karlsruhe: 1991.

THE EFFECTS OF HIGH EXPLOSIVES IN CONTACT WITH REINFORCED CONCRETE SLABS

Lena Lönnqvist

National Defence Research Establishment (FOA)
Sweden

ABSTRACT

A high explosive charge detonated in contact with a reinforced concrete slab causes an essentially different effect than a charge detonated at distance from the slab. If the charge is large enough a hole will be punched, and a cloud of particles will be generated on the back of the slab. At FOA experiments have been done in purpose to find a connection between the weight of a half sphere high explosive charge in contact with a reinforced concrete slab and the diameter of the generated hole. The velocity of the particle cloud has also been measured.

There are several parameters effecting the process, for instance charge characteristics as weight, density and explosive energy, and slab characteristics such as density and strength. By performing dimension analyses relevant parameters have been considered and an equation describing the connection between charge and hole diameter has been adapted to the experimental data.

1. INTRODUCTION - BACKGROUND

At the Swedish National Defence Research Establishment - FOA a dynamic Computer Model for Conventional Weapons Effect in Urban Areas - VEBE, has been developed. VEBE calculates the effects of blast, fragments, fire, smoke and debris on buildings, main systems and humans.

The algorithm for calculating the effects from internal explosions on buildings in VEBE is generated from a more detailed computer code PROMIX (Forsén Jonasson 1989).

PROMIX calculates blast effects on a construction consisting of several cells, for instance a building. First the effects in the room where the bomb detonates are calculated, knowing the deformations and openings the effects in adjacent rooms can be predicted.

A high explosive charge detonated in contact or very close to a reinforced concrete slab causes an essentially different effect than a charge detonated at distance from the slab. Experiments

show that if the charge is large enough a hole will be punched, and a cloud of particles will be generated on the back of the slab.

At FOA effort has been made to find how charge and hole characteristics depend on each other. The reason for this is to be able to predict the leakage of explosive gases to adjacent rooms. Knowing the hole area PROMIX simulations can be done to accomplish this. The simulations can be verified using the test plant for confined explosions constructed at FOA.

The connection between charge and hole diameter is consequently the first part of research leading to improved algorithms for the VEBE-code. The purpose of this studie is to find an equation descibing the relation between a half sphere charge in contact with a concrete slab and the diameter of the generated hole, considering all physical parameters relevant to this case of load.

2. METHOD

A series of experiments has been performed mainly in purpose to find a relation between weight (or diameter) of a half sphere charge and hole diameter.

The relation between charge weight and velocity of the particle cloud has also been studied but not yet analysed.

2.1. MATERIAL

The experiments have been executed in 1/4-scale. Previous work at FOA (Jonasson 1990) shows that using 1/4-scale is valid in this case of load. The length and width of the reinforced slabs were 1000*1000mm², and the thicknesses have been 40, 50, 60, 70 and 80 mm which correspond to slabs used in ordinary Swedish dwelling houses. The strength of the concrete slabs has been recorded with a concrete test hammer (PROCEQ SA Schmidt L) to 38 - 50 MPa. The reinforcement was 2.5 mm ϕ at 75 mm cc's. Two kinds of reinforcement "old" and "new" have been used, simply because of different deliveries. The yield strengths were 450 MPa

(old) and 266 MPa (new). The reinforcement is considered to be of minor importance in this case of comparatively lightly reinforced slabs. One experiment was done in full scale, the slab thickness was in this case 32 cm and the reinforcement 10 mm ϕ at 300 mm cc's Ks400 (410 MPa yield strength and 790 MPa ultimate strength).

2.2. EXPERIMENTS

Totally 28 experiments with charge weights 10 - 1000 g have been executed in 1/4-scale, and one with charge weight 5 kg has been done in full scale.

The explosive used in the experiments was plastic explosive NSP 71 with a density of 1770 kg/m³, an explosion energy of 5.54 MJ/kg, a detonation velocity of 6800 m/s and a calculated detonation pressure of 20,500 MPa.

The measurements of hole characteristics (Figure 1) have been done at 10 points evenly spread around the hole.

To measure the velocity of the generated cloud of particles a board with lines every 10 cm was placed at one of the slab edges, and the experiments were recorded with a high speed camera (frame speed: 4000 frames per second). A sketch of the test setup is shown in Figure 2.

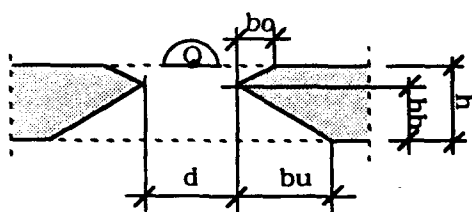


Figure 1: Measured data

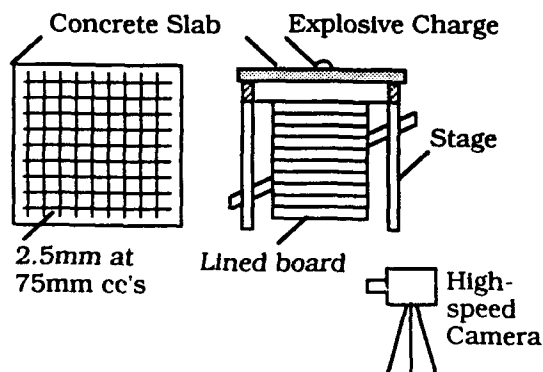


Figure 2: Sketch of the test setup

2.2.1. DIMENSION ANALYSIS - RELATION BETWEEN CHARGE WEIGHT AND HOLE DIAMETER

The objective of the experiments was to find a relation between charge weight and hole diameter. To accomplish this Buckingham's π -theorem (Baker 1973) was applied. According to this all relations between variables in a physical process can be expressed as a function of dimensionless parameters, so called π -terms, that is;

$$F(\pi_1, \pi_2, \pi_3, \dots, \pi_n) = 0$$

where

$$\pi_n = x_1^{q_1} x_2^{q_2} \dots x_n^{q_n}$$

x_1, x_2 and x_n are physical variables relevant to the problem.

q_1, q_2 and q_n are exponents making π_n dimensionless.

By applying Buckingham's π -theorem the problem of how high explosive charges in contact with a concrete slab effects the slab is not solved. But by recording the relevant parameters and performing dimension analysis the way in which charge weight and hole diameter depend on each other can be predicted.

2.2.2. RELEVANT PHYSICAL VARIABLES - RELATION BETWEEN CHARGE WEIGHT AND HOLE DIAMETER

Variables considered to effect the relation between hole diameter and charge weight in the process of high explosives in contact with reinforced concrete slabs are;

Charge parameters:	Symbol:	Unit:	Dimension:
weight	Q	kg	M
density	ρ_x	kg/m ³	L ⁻³ M
explosion energy	K	J/kg	L ² T ⁻²

Concrete parameters:	Symbol:	Unit:	Dimension:
slab thickness	h	m	L
hole diameter	d	m	L
density	ρ_c	kg/m ³	L ⁻³ M
strength	σ	Pa	L ⁻¹ M T ⁻²

(L = length, M = mass, T = time)

Reinforced concrete is a composed material, the total strength of the concrete depend among other things on the cement, the aggregate and the reinforcement. In the dimension analysis all these factors can be put together since they all have the same dimension.

In the case of finding a connection between the weight of a half sphere contact charge and the hole diameter, the strength of the reinforcement is presumed to be of minor importance.

Consequently the strength of the slab in this case is considered to be equal to the cube compressive strength of the concrete.

The number of π -terms is in this case 4 (7 variables - 3 dimensions). There are several sets of π -terms that satisfy the equation;

$$F(\pi_1, \pi_2, \pi_3, \pi_4) = 0$$

one of them is;

$$\begin{aligned} \pi_1 &= \rho_x / \rho_c & \pi_2 &= d/h \\ \pi_3 &= Q/h^3 \rho_c & \pi_4 &= QK \rho_x / h^3 \sigma \rho_c \end{aligned}$$

The function can now be written;

$$d/h = f(\rho_x / \rho_c, Q/h^3 \rho_c, QK \rho_x / h^3 \sigma \rho_c)$$

The only conclusion that can be drawn from this is that if the relation between hole diameter and charge weight only depend on the declared variables the equation for the hole diameter must look like the one above.

To gain our objective a relation between charge weight and hole diameter however this can be adequate.

2.3. RELATION BETWEEN CHARGE WEIGHT AND THE VELOCITY OF THE GENERATED CLOUD OF PARTICLES

To find an equation for the relation between charge weight and the velocity of the generated cloud of particle the physical process of a high explosive in contact with a concrete slab must be comprehensively studied. Most surely charge characteristics as the detonation velocity and detonation pressure and concrete characteristics as acoustic impedance must be regarded. Experiments at TNO (v. Amelsfort Weerheijm 1988) also indicate that the location of the charge in relation to the reinforcement must be considered, and the different modes of failure (cratering and spalling) fully understood. Because of this the experiment data have merely been plotted in a diagram with average cloud velocity on the y-axis and the charge weight on the x-axis (Figure 4).

3. RESULTS

The measured data are presented in Table 1. The presented hole parameters are mean values of 10 measurements evenly spread around the hole. The strength of the concrete is the cube compressive strength recorded with a concrete test hammer.

Table 1: Measured data (see Fig. 1)

Charge:		Slab:						
Q	h	d	bo	bu	hb	hb/h	σ	rein-
g	mm	mm	mm	mm	mm	%	MPa	force-
								old/new
10	40	68	25	24	25	63	38	n
25	"	84	38	32	25	63	38	n
50	"	104	40	38	24	60	38	n
125	"	144	37	40	26	65	50	o
250	"	182	38	48	25	63	43	o
500	"	219	37	42	22	55	39	n
10	50	37	37	66	33	66	44	n
25	"	75	33	52	35	70	44	n
50	"	98	39	50	35	70	44	n
125	"	139	40	56	31	62	48	o
250	"	170	52	61	30	60	42	o
500	"	230	44	65	30	60	40	n
25	60	89	-	-	-	-	46	n
50	"	116	-	-	-	-	46	n
125	"	137	-	-	-	-	46	n
250	"	176	-	-	-	-	48	o
500	"	231	-	-	-	-	44	n
1000	"	293	-	-	-	-	50	o
50	70	97	43	74	48	69	47	n
125	"	130	53	83	48	69	47	n
250	"	186	58	78	42	60	45	o
500	"	224	60	95	47	67	42	n
1000	"	306	60	82	37	53	40	o
50	80	83	52	90	55	69	44	n
125	"	128	60	76	55	69	44	n
250	"	168	69	84	55	69	46	o
500	"	235	62	86	49	61	43	n
1000	"	307	69	81	47	59	42	o
5000	3200	695	-	-	-	-	49	-

3.1. RELATION BETWEEN CHARGE WEIGHT AND HOLE DIAMETER

Dimension analysis has been performed to find the form of an equation describing the relation between a half sphere high explosive charge and the diameter of the generated hole.

The experimental data (Table 1) has been plotted in a diagram with d/h on the y-axis and $QK \rho_x / h^3 \sigma \rho_c$ on the x-axis and a function has been adapted to the datapoints using least squares fit analysis (Figure 3). The obtained equation reads;

$$d/h = 0.919 \ln(QK \rho_x / h^3 \sigma \rho_c) - 1.11$$

3.2. RELATION BETWEEN CHARGE WEIGHT AND THE VELOCITY OF THE GENERATED CLOUD OF PARTICLES

The measured cloud velocities have been plotted in a diagram with the velocity on the y-axis and the charge weight on the x-axis (Figure 4).

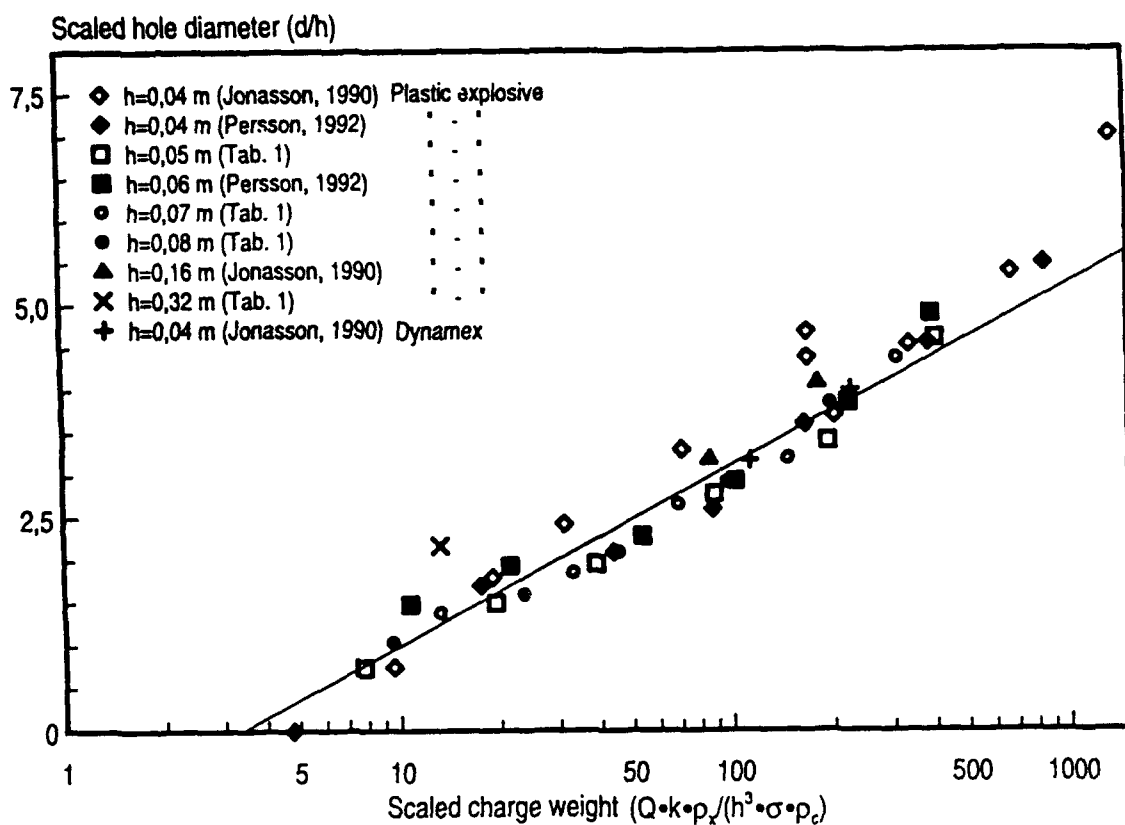


Figure 3: Measured diameters and the adapted function: $d/h = 0,919 \ln(QK\rho_x/h^3 \sigma \rho_c) - 1,11$

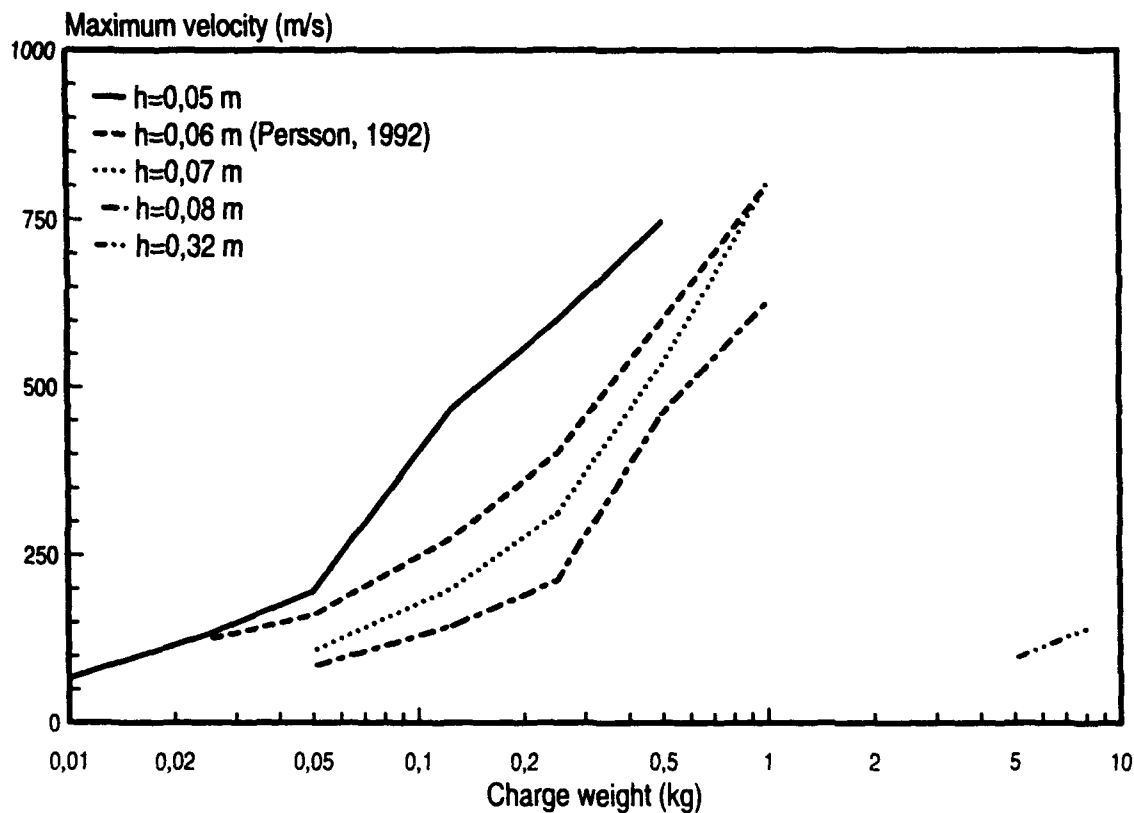


Figure 4: Measured particle cloud velocities

4. DISCUSSION

When a high explosive charge is detonated in contact with a concrete slab a pressure wave propagates in the slab. The propagation velocity of the wave depends on both charge and slab characteristics. The pressure wave is reflected at the free surface at the back of the slab as a tensile wave.

The pressure at the front of the pressure wave causes the concrete to fail if the dynamic compression strength of the concrete is exceeded, and a crater is generated (cratering) at the front/top of the slab. The reflected tensile wave causes the concrete to fail due to tension and concrete fragments are ejected from the back of the slab (spalling). As a result of the cratering and spalling processes a hole is generated in the slab. (This process is more thoroughly described by v. Amelsfort and Weerheijm 1988.)

By applying dimension analysis relevant physical variables for both slab and charge are considered, and an equation describing the relation between charge weight and hole diameter in the case of half sphere charges in contact with reinforced concrete slabs (Figure 3) can be adapted to the experimental data (Table 1).

At FOA (Jonasson 1990) contact charge experiments have been executed with plastic explosive NSP 71 and Dynamex M. Dynamex M has a lower density (1400 kg/m^3), detonation velocity (5000 m/s) and calculated detonation pressure ($8,750 \text{ MPa}$) than plastic explosive NSP 71. An interesting result is that the shape of the punched hole is not the same in the different cases. As shown in Figure 5 in the case of Dynamex M there is no crater at the front/top of the slab which indicates that the dynamic compression strength of the concrete has not been exceeded. In spite of these differences the measured diameters connect to the equation (Figure 3) adapted to the data presented in this paper (Table 1).

An other notable observation is that the quota of h_b and h is approximately the same in all the experiments with plastic explosive NSP 71. The quota is $64\% \pm 5\%$ in 80% of the shots.

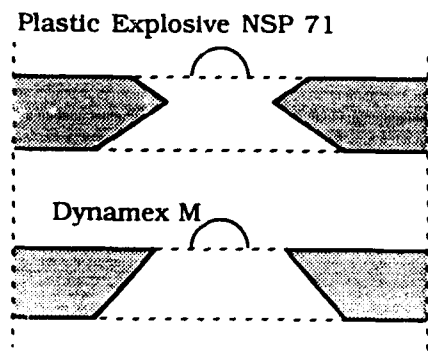


Figure 5: Dynamex M only gives a crater at the bottom of the slab

5. CONCLUSIONS

An equation describing the relation between charge weight and hole diameter in the case of half sphere charges in contact with reinforced concrete slabs can be derived from dimension analysis and adaption of experimental data.

To find a connection between the velocity of the generated cloud of particles and the charge a more comprehensive analysis is required

One reason for finding a relation between charge and hole diameter was, in our case, that knowing the area of the generated hole, the PROMIX code (Forsén Jonasson 1989) can be used to simulate the effect of a contact charge on a construction consisting of several cells. The results of such a simulation can be verified in the test plant for confined explosions constructed at FOA. However a more profound analysis, for instance a continuum dynamic approach, of this case of load is desirable and our research will continue.

6. REFERENCES

1. v. Amelsfort R.J.M., Weerheijm J.
The Failure Mode of Concrete Slabs Due to Contact Charges
TNO Prins Maurits Laboratory
PML 1988-57 Dec. 1988
2. Baker W.E., Westin P.S., Dodge F.T.
Similarity Methods in Engineering Dynamics
Hayden Book Company 1973
3. Forsén R., Jonasson T.
PROMIX A Computer Code for Calculating Building Damage from Internal Explosions
FOA Report C20766-2.3 Sept. 1989
4. Jonasson T.
KONTAKTVERKAN 1 Sprängladdningars kontaktverkan på armerade betong plattor
CONTACT CHARGES 1 The Damage to Reinforced Concrete Slabs from Detonating High Explosive Charges in Contact (in Swedish)
FOA Report C20809-2.6 Aug. 1990
5. Persson J.F.
KONTAKTVERKAN 2 Inverkan av kontaktverkan av sprängladdningar på armerade betongplattor
CONTACT CHARGES 2 (in Swedish)
FOA Report D 20199-2.6 May 1992

ON MODELLING OF SHAPED CHARGE JET INTERACTION WITH SPACED PLATES

Pierre Y. Chanteret

I.S.L. French-German Research Institute of Saint-Louis
P.O. Box 34, 68301 Saint-Louis, France

ABSTRACT

The problem of modelling the interaction of a shaped charge jet with spaced targets has been studied with a particular look at predicting the residual jet velocity on exiting metallic plates. It is shown that an analytical 1D-code is able to predict shaped charge performance against homogeneous steel armor, providing that jet lateral velocities are taken into account. But it is also shown that on perforating a single steel plate, such a code overpredicts the tip velocity of the exiting jet. The interaction between a metallic plate and a high velocity copper cylinder is studied with the use of eulerian hydrocode computations and the amount of projectile length reduction is evaluated as a function of plate thickness. From these computations, a semi-empirical formula is derived and introduced in the analytical shaped charge code. Comparison between experimental and computed jet velocities after perforating ERA sandwiches illustrate the significant improvement obtained with the modified code.

INTRODUCTION

The penetration performance of a shaped charge warhead into homogeneous armor steel may be as high as 8 times its charge diameter. When the shaped charge is initiated at some distance from the target, a metallic jet is formed which stretches before cratering into the armor material. This large penetration capability is due to the fact that the shaped charge jet is a very particular kind of projectile which associates a very high velocity and an extremely large total length. Typical copper jets from modern shaped charges exhibit tip velocities of the order 10km/s with total lengths which may reach 12 charge diameters for the jet portion above 3km/s.

This high velocity regime concerning extremely long projectiles gives the opportunity to predict shaped charge jet penetration by applying the simple penetration model established from the hydrodynamic theory of liquid jets impinging on fluid targets [1]. This theory which is referred as the hydrodynamic theory, stipulates that during jet-target interaction, the strengths and viscosities of the jet and target materials may be neglected with respect to the pressures produced in the crater bottom region. Thus, the penetration process may be considered as the incompressible, inviscid flow of a jet of density ρ_j , with a constant velocity V_j , interacting

with a fluid target of density ρ_t . Considering a system of coordinates moving with the cratering velocity U , the pressure on the two sides of the interface between jet and target must be the same, and the phenomenon being steady state, Bernouilli's equation along axial streamline gives:

$$1/2 \rho_j (V_j - U)^2 = 1/2 \rho_t U^2 \quad (1)$$

From this relation, one obtains an expression for the cratering velocity U :

$$U = V_j / (1 + \sqrt{\rho_t / \rho_j}) \quad (2)$$

which is independent of target strength. In reality, target strength does have some influence on shaped charge performance: it is known that real shaped charge jets achieve a larger penetration into mild steel than into armor steel. This observation is often quoted when stipulating that the assumptions made in the hydrodynamic theory are too crude for accurately predicting jet cratering by the use of equation (2). But this influence of target strength on shaped charge performance does not occur through any significant influence on the cratering velocity U , but through variations on crater diameter values: increasing the strength of the target induces a decrease in the crater diameter value and consequently reduces the number of jet elements which actually hit the crater bottom.

The independence of cratering velocities with regard to target strength has been experimentally verified in [2], where measured cratering velocities have been found to be identical for 5 steel qualities with strengths comprised between .3 and 2.9 GPa.

Furthermore, it is possible to predict the penetration vs standoff performance of any shaped charge with the use of equation (2) as the only cratering formula. As shown in [3] and [4], once the jet characteristics (velocities, mass and break-up times distributions) are known, the penetration depth achievable at a given standoff can be calculated under the condition of knowing the three components of the velocity vector of each jet element. By taking the off axis trajectory of each jet element into account, it appears that some of them strike the target not at the bottom hole but somewhere up the hole profile.

Figure 1 presents some calculated penetration vs standoff curves obtained during a study where jet off axis velocities were experimentally measured for a

given non-precision shaped charge [5]. These curves have been obtained using the following procedure:

- calculation of nominal jet characteristics (mass, axial velocities and break-up times) with an analytical 1D-code;
- calculation of 3D jet elements trajectories from experimentally measured lateral velocities;
- calculation of crater shape as the sum of individual craters created by each jet element. Each individual crater is assumed to be a cylinder with a length given by equation (2) and a diameter given by a proportionality factor relating the crater volume to the jet element energy.

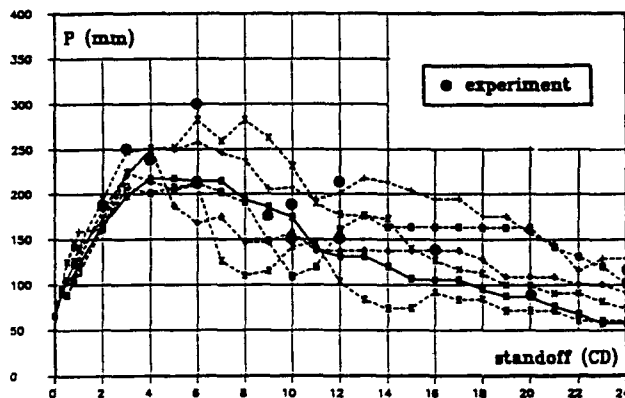


figure 1: Penetration-standoff curves calculated using hydrodynamic theory and measured transversal velocities. (57mm diameter charge, [5])

On this figure, each curve corresponds to calculated penetration depths using one set of lateral velocities measured during one free-flight experiment. It appears that as standoff distances are increased, off-axis displacements become larger, increasing the number of jet elements which hit the crater walls and do not contribute to penetration depth. This kind of calculation appears to provide a reasonable estimate of the overall performance for the given charge.

It remains that several other effects such as compressibility effects, strength effects, multiple impact effects..., have been neglected in equation (2), and an extensive survey of more refined penetration models for shaped charges can be found in [6]. The purpose of this introduction was to show that the discrepancy between predictions of the hydrodynamic penetration theory of ideal jets and real shaped charge performance is mainly to be attributed to jet particles off axis trajectories rather than to the simplicity of equation (2).

JET INTERACTION WITH SPACED PLATES

The jet interaction with targets consisting of armor plates separated by air spaces, can be calculated as the semi-infinite target case. The jet penetration into the first plate is described using a time step procedure: during incremental time dt , the incremental penetration depth dP and consumed jet length dL are obtained from:

$$dP = U dt \quad \text{and} \quad dL = (V_j - U) dt$$

where U is given by equation (2). Due to jet consumption through the plate, the jet tip velocity is continuously reduced; the $V_j(t)$ function is obtained using jet mass conservation and velocity distribution in the jet. Denoting by t_r the time at which the penetration depth is equal to plate thickness e_r , one obtains the exiting jet velocity $V_{jr} = V_j(t_r)$ and the consumed jet length ΔL :

$$\Delta L = \int_0^{t_r} (V - U) dt = \int_0^{e_r} \left(\frac{V - U}{U} \right) dP \quad (3)$$

Subsequent performance into residual armor is then calculated considering a new jet with a new tip velocity V_{jr} which will be denoted as the residual jet velocity.

Now, experience show that using such a procedure will lead to an overestimation of jet residual velocity V_{jr} . Figure 2 presents a double X-Ray picture of a 45mm diameter shaped charge interacting with two steel plates separated by an air space.



figure 2: double X-Ray picture of a jet interacting with two steel plates.

In the experiment shown on figure 2, the two plates are mild steel plates of 10mm thickness separated by an air gap of 45mm; the distance between the charge and the first plate being also equal to 45mm. The jet tip velocity is 8.5km/s and the measured residual tip velocities are respectively 8.0km/s after perforating the first plate and 7.2km/s after perforating the second plate.

The residual velocities predicted by an analytical 1D-code using the previously described algorithm are respectively 8.4km/s and 8.1km/s. Consequently, the jet tip velocity drop through the double plate target is calculated to be 0.4km/s, which is less than one third of the experimentally measured value of 1.3km/s. Such a discrepancy cannot be attributed solely to an inadequate cratering description by equation (2). This is the reason why some eulerian hydrocode computations have been performed with the HULL code [7], in order to get a closer look at the amount of projectile length reduction during hypervelocity plate perforation

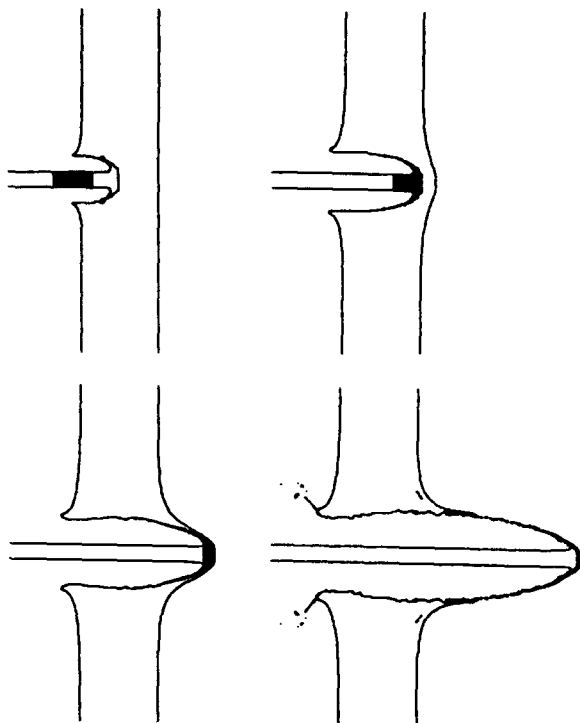


figure 3: HULL computation of a 2mm diameter Cu jet perforating a 10mm RHA plate at 7km/s.

Figure 3 shows four computational pictures of a non stretching 2mm diameter copper jet of semi-infinite length, impacting on a 10mm thick RHA plate at a velocity of 7km/s; the computation has been performed using 20 cells across jet diameter. These four pictures illustrate the phenomenon which is responsible for the jet residual velocity overprediction by the simple analytical perforation model. It can be seen that the second picture on figure 3 corresponds to the time at which the crater bottom displacement is just equal to the plate thickness. According to the simple model, the plate perforation should be completed at this very time, while third and fourth pictures show that the projectile is still

eroding after this time. On the pictures, some lagrangian tracers particles can be seen in the jet, which have been placed in order to make the additional jet erosion visible. In the example shown, this additional jet erosion is somewhat larger than twice the jet diameter.

The hydrocode computations show that two features contribute to this extra jet erosion:

1. when crater depth equals plate thickness, there still exists some target material in front of the projectile which still has to be "perforated";
2. during penetration, a certain amount of jet material is highly compressed in the jet target interface region, and this jet material will "burst out", due to almost instantaneous unloading on exiting the target.

From these simple phenomenological observations, it is clear that the additional jet erosion effect will increase with increasing target thickness, until reaching an asymptotic value when the plate is sufficiently thick for achieving steady state penetration conditions before jet exiting. Hydrocode simulations have therefore been performed for determining the influence of plate thickness on the amount of additional projectile erosion.

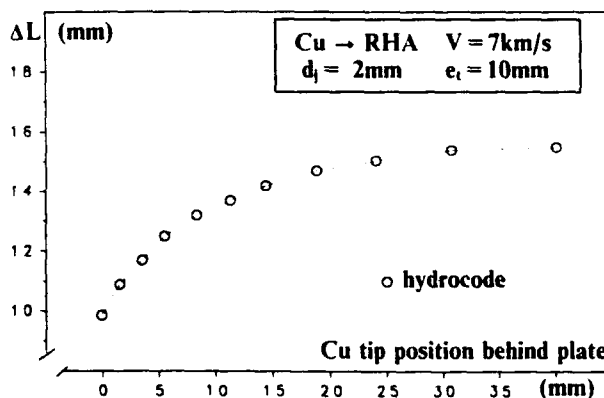


figure 4: hydrocode result of projectile length reduction vs residual jet tip position behind the plate.

Figure 4 shows the computed eroded projectile length as a function of the jet tip position behind the plate, for a 2mm diameter copper jet impacting a 10mm RHA plate at 7km/s. In the following, the computed final projectile length has been defined as the jet residual length at the time when the jet travel through air is equal to 20 jet diameters. The amount of additional jet erosion will then be denoted as ΔL_s and be defined as the difference between the computed projectile final length and the analytically calculated length using equation (3). The results obtained from hydrocode computations for jet additional erosion are presented on figure 5, where a cratering velocity $U=3.5$ km/s (taken from hydrocode computations in a semi infinite RHA target) has been used for defining ΔL_s values. These results have been scaled by the jet diameter d_j and are presented as the influence of scaled RHA plate thickness e/d_j on scaled

additional eroded length $\Delta L_s/d_j$. Most of the computations have been performed for a 7km/s impact velocity and $\sigma = 1.1$ GPa strength steel targets.

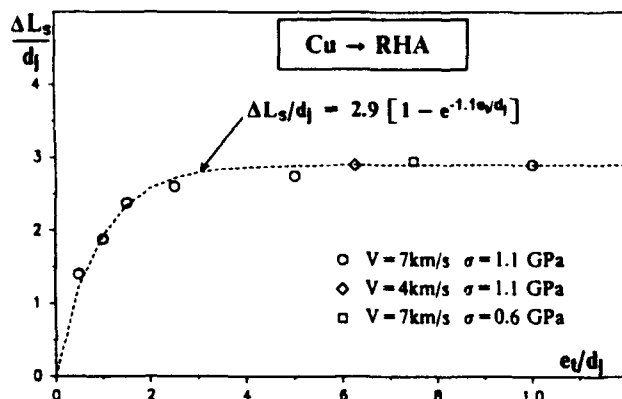


figure 5: computed jet scaled additional erosion as a function of scaled RHA plate thickness.

On figure 5 are also plotted both one hydrocode result for a 4km/s impact velocity and one result obtained for a 0.6GPa strength armor plate. The computed corresponding ΔL_s values show the same tendency as the reference results (7km/s, 1.1GPa), showing that impact velocity -in the hypervelocity range- and target strength do not affect significantly the additional jet erosion. On figure 5 is also plotted the following equation:

$$\Delta L_s/d_j = 2.9 [1 - e^{-(1.1e_j/d_j)}] \quad (4)$$

which fits the hydrocode results and will be used for 1D-code modelling.

MODELLING JET INTERACTION WITH SPACED PLATES

Among the existing analytical penetration models reviewed in [8], no model accounting for the additional erosion effect can be found. It appears that Backofen's "Kernel" model [8], provides an improvement for describing local interaction between penetrator and target: this model allows for a better prediction of crater diameter in thin plates [9], but has still to be further developed for quantitatively predicting jet additional erosion. Reference [10] suggests to reproduce the additional erosion in analytical models by adding extra-layers of a hypothetical superdense material on the rear surface of each spaced plate: adding 1mm of a material with a density one hundred times higher than steel, would allow for predicting jet residual velocities for 60-70mm diameter shaped charges.

In the present work, the results obtained from hydrocode and plotted on figure 5, have been introduced in the analytical 1D-code. Using equations (3) and (4), the consumed jet length ΔL on perforating a plate with thickness e_j is now given by:

$$\Delta L = \int_0^{e_j} \left(\frac{V-U}{U} \right) dP + 2.9 d_j [1 - e^{-(1.1e_j/d_j)}] \quad (5)$$

In the following, one presents several comparisons between calculations and experiments, which show the influence of the ΔL_s term on jet residual velocities predictions. Table 1 presents the results obtained for the experiment previously shown on figure 2: one can see that the use of the additional erosion terms gives a good agreement with experiment.

Table 1

residual velocity V_{jr}	after plate 1	after plate 2
experiment (fig.2)	8.0 km/s	7.20 km/s
1D-code + eq.(3)	8.45 km/s	8.09 km/s
1D-code + eq.(5)	8.05 km/s	7.25 km/s

Similar comparisons have been performed in the case of inclined plates. It is commonly considered that a jet interacting with a plate of thickness e_j under an obliquity α has to perforate an equivalent "line of sight thickness" $e_{eq} = e_j/\cos(\alpha)$, α being measured between jet axis and the normal to the plate. But when looking at the schematic representation depicted on figure 6, one can consider two additional terms corresponding to plate entering and exiting, which may be added to the "line of sight thickness". The following expression:

$$e_{eq} = e_j/\cos(\alpha) + d_j \tan(\alpha) \quad (6)$$

giving the equivalent normal thickness.

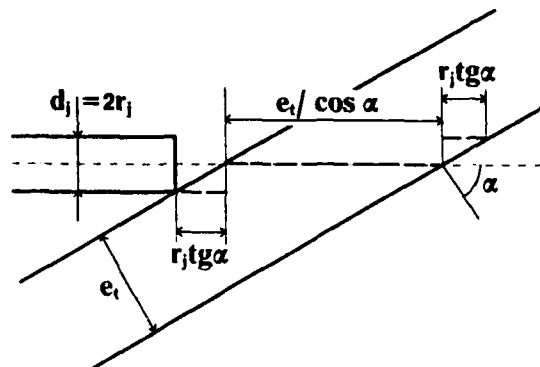


figure 6: schematic representation of the equivalent "line of sight thickness" to be perforated in an oblique plate.

Table 2 shows a comparison between computations and an experimental measurement of the residual velocity of the same jet as for table 1, after perforating two steel plates of 10mm thickness under an incidence of 60°. The distances measured along the jet axis being respectively 90mm between the charge and the first plate, and 20mm between the two plates. These results show the respective influence of eq.(5) and eq.(6). As in the normal impact case, it appears that the correcting terms induce more than 10% reduction of the V_{jr} value and allow for a good agreement with experimental values.

Table 2

residual velocity V_{jr}	V_{jr} after plate 2
experiment	6.67 km/s
1D-code + eq.(3)	7.48 km/s
1D-code + eq.(5)	7.20 km/s
1D-code + eq.(5) + eq.(6)	6.62 km/s

The analytical model has also been used for predicting residual jet velocities after perforating ERA sandwiches. Figures 7 and 8 present some comparisons between 1D-model predictions and experimental jet residual velocities measured for the 45mm previously mentioned shaped charge attacking reactive sandwiches. In all the presented experiments, the sandwiches were made of a 2mm explosive layer embedded between two identical steel plates; the obliquity being 60° and the standoff distance being two charge diameter for figure 7.

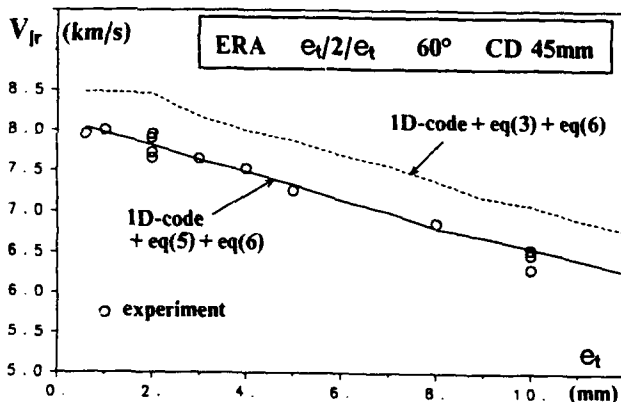


figure 7: residual jet velocities as a function of reactive plate thickness; comparison between experimental results and analytical models predictions.

Considering the small distance between the two reactive plates -about 2 jet diameters along the jet axis- and remembering the hydrocode results plotted on figure 4, it is assumed in the calculations that the first reactive plate induces only 50% of the ΔL_s value given by equation(4). Figure 7 presents the computed residual jet velocities plotted as a function of reactive plates thickness. One can see that the ΔL_s correcting term reduces the residual velocities by about 0.5km/s, giving a very good agreement with experimental values.

On figure 8 are plotted the jet residual velocities as a function of standoff distance for the 45mm charge attacking a given sandwich with heavy plates (10/2/10). On this diagram are also plotted the predictions of the model without any of the two correcting terms. One can see that at low standoff, the effect of correcting terms is larger than 1km/s.

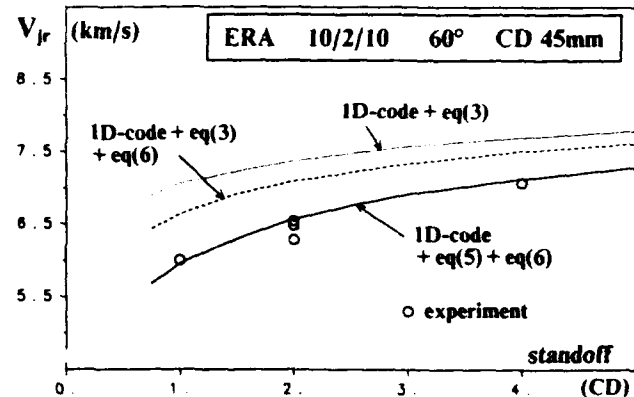


figure 8: residual jet velocities behind a thick plate reactive sandwich as a function standoff distance ; comparison between experimental results and analytical models predictions.

CONCLUSION

It has been shown that the hydrodynamic penetration theory can be used for getting a good estimation of shaped charge performance against homogeneous steel targets, provided to know the lateral velocities of all jet elements. But it has also been shown that such modelling is not suitable against spaced targets and overpredicts the jet residual velocities after perforating metallic plates.

The jet erosion due to perforating an armor plate has been studied using hydrocode computations and the obtained results have been introduced in 1D-computations through a fitting function relating the jet additional erosion and the armor plate thickness. This effect should be further studied, especially for material properties and velocity effects, but the modified 1D-code has already given a notable improvement for predicting jet velocities after perforating reactive sandwiches.

REFERENCES

- [1] G. Birkhoff, D. MacDougall, E. Pugh and G. Taylor, Explosives with lined cavities. J. appl. Physics 19, 563-582, 1948.
- [2] K. Hollenberg, The Penetration of Jets from Shaped Charges in Steel Targets with Tensile Strengths between 30 and 300 kp/mm², German Ministry of Defense Report BMVg-FBWT 75-13, 149-158, 1975.
- [3] J. Smith, Shaped Charge Penetration at long Standoff, AFATL Report TR-81-25, 1981
- [4] S.B. Segletes, Drift Velocity Computations for Shaped Charge Jets, BRL Report ARBRL-MR-03306, 1983

[5] J. Brown, Modelling and Experimental Studies of a Family of Shaped Charges in a European Collaborative Forum, 12th International Ballistics Symposium, San Antonio, 1990

[6] W.P. Walters, W.J. Fils and P.C. Chou, A Survey of Shaped Charge Jet Penetration Models, Int. J. Impact Eng. 7, No3, 307-325, 1988

[7] D.A. Matuska, HULL User's Manual, AFTL Report TR-84-59, 1984

[8] J. Backofen, The effect of Local Target Deformation Motion on Cratering, 12th International Ballistics Symposium, San Antonio, 1990

[9] J. Backofen, Shaped Charge Jet Perforation of Thin Plates-- The "Kernel" Model, 13th International Ballistics Symposium, Stockholm, 1992

[10] J. Brown, The Shaped Charge Jet Attack of Confined and Unconfined Sheet Explosive at Normal Incidence, 11th International Ballistics Symposium, Brussels, 1989

OPTIMIZATION OF SHAPED CHARGES AGAINST CONCRETE TARGETS

Hermann Rösner

Deutsche Aerospace AG - Munitions and Demilitarisation
8898 Schrobenhausen, Germany

ABSTRACT

Utilization of theoretical simulation models allows optimization of Shaped Charge designs not only against steel targets but also against concrete targets. With requirements for borehole volume and borehole diameters at certain depth given the models could be applied easily and yielded important clues for the determination of Shaped Charge design characteristics.

INTRODUCTION

For the bridge destruction system PAM (= Penetration Augmented Munition) a two-stage system consisting of a Forward Shaped Charge (FSC) and a Follow Through Charge (FTC) had been selected as the most promising technical solution (Fig. 1). The requirement for FSC performance is to cut a hole in a surrogate bridge pier target which allows emplacement of the FTC and detonation at an optimal position inside the target.

DASA Schrobenhausen was selected as a subcontractor to ATK, Minneapolis, for the design and engineering work of the FSC and the FTC for the two-stage system because experience was available here from the development of the Anti-Runway-Submunition STABO and from a demonstration of PAM1 at Ft. Polk, Louisiana.

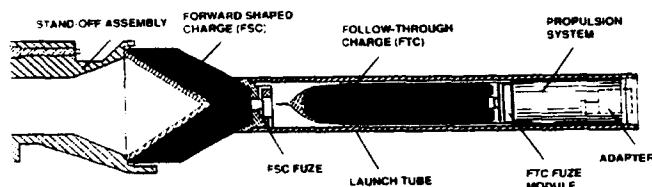


Fig. 1 Penetration Augmented Munition

THEORETICAL INVESTIGATION

From previous comparisons it was well-known that results of simulations and tests were not always in correspondence. One reason for this phenomena lay in a discrepancy between the calculated kinetic energy of the SC-jet (as a measure for hole volume) and that portion of total energy which really interacts with the concrete target. Tests with a typical test set-up (Fig. 2) with a HE mass of 5 kg and a stand-off of 200 mm showed a big crater of the entrance of the borehole which was produced by the energy in the jet tip together with the detonation products. So, an evaluation of the borehole profile and volume created by the jet energy alone was not possible for the first 300 mm of borehole depth (Fig. 3).

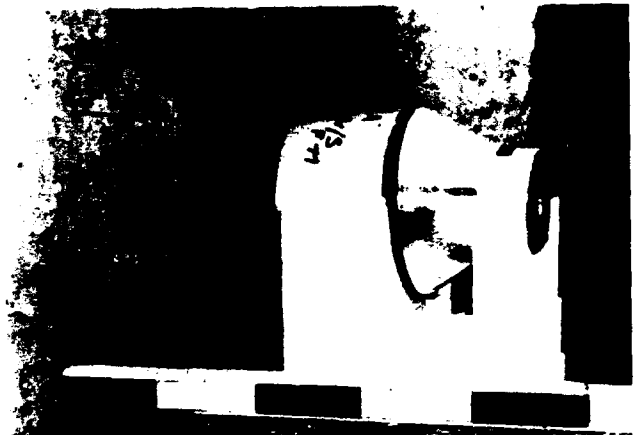


Fig. 2: FSC-Test Set-up

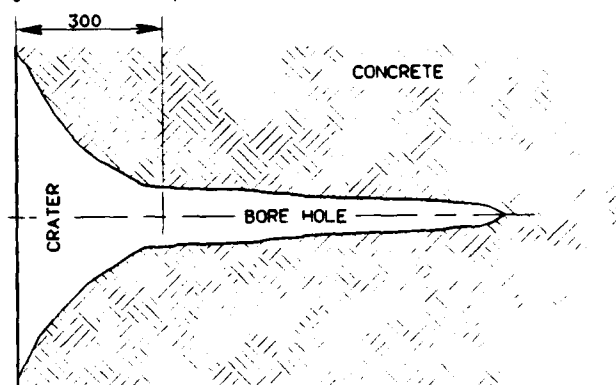


Fig. 3: Typical FSC Result

Furthermore, for the performance of the tandem system the borehole profile over a depth range of 700 ± 200 mm only was relevant as the FTC was to be emplaced in this range. Therefore a better optimization of the FSC could be expected if only the borehole behind the entrance crater would be regarded and optimized. This was the reason to define the so called "energy criterion", which means that only that portion of the total jet energy was considered which contributes to borehole formation beyond the first 300 mm of depth and up to 1000 mm. For the calculation two semi-empirical 1-D codes were employed for the determination of jet properties (DESOB) and for the interaction of the jet with the target (PECO). Jet properties were calculated on the basis of the P.E.R.-theory which is characterized by a hydro dynamic description of the collapse process. Interaction with the target was also described hydrodynamically and material properties as well as lateral velocities of jet particles were taken into account.

Optimization criteria were total borehole depth and the energy criterion, i.e. as explained jet energy consumed between 300 mm and 1000 mm depth in the target. From a greater number of FSC designs seven were selected for further investigation (Fig. 4). Table 1 gives the results of the simulations.

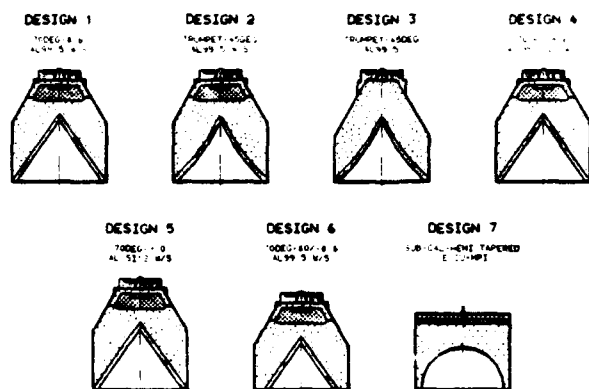


Fig 4 FSC-Designs Ø 185

Design	V_{tip} [m/s]	Energy (crit) [kJ]
1	9.700	1.340
2	10.600	1.570
3	8.200	1.260
4	9.700	1.340
5	9.500	1.340
6	9.700	950
7	-----	-----

Table 1 Simulation results

FXR-TESTS

Following theoretical examination FSCs to the seven designs were fabricated and test fired with FXR diagnostics. Type of HE was TNT/HMX 15/85. The test set-up is shown in Fig. 5 The FXR photos (Fig. 6) were evaluated and four of them are described in detail below. These four designs have been selected for further testing against targets.

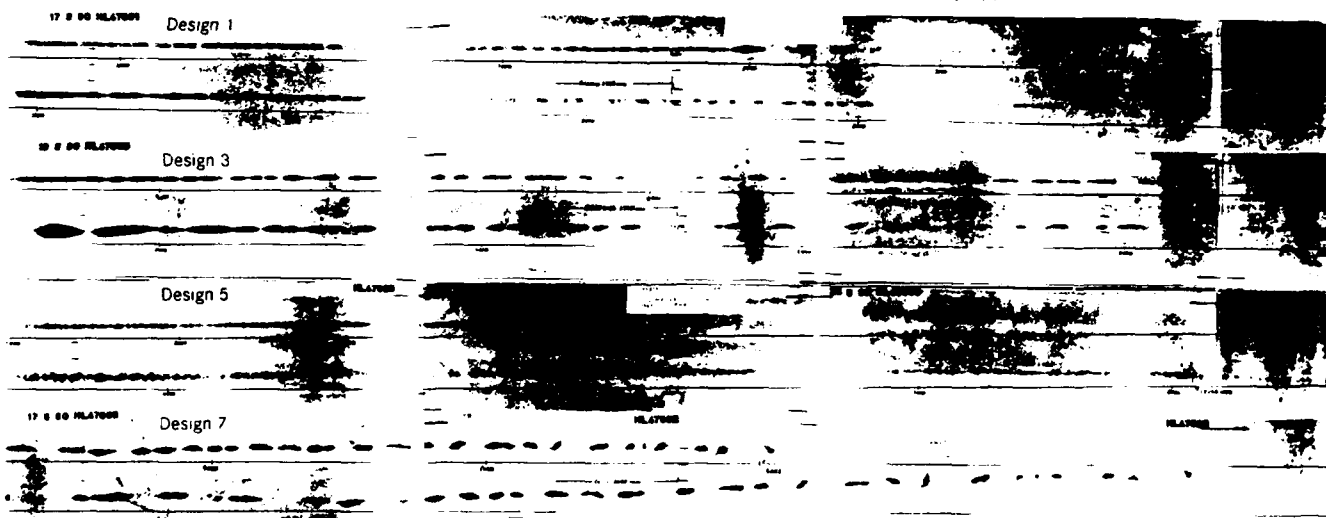


Fig 6 FXR-pictures of FSC-Jets

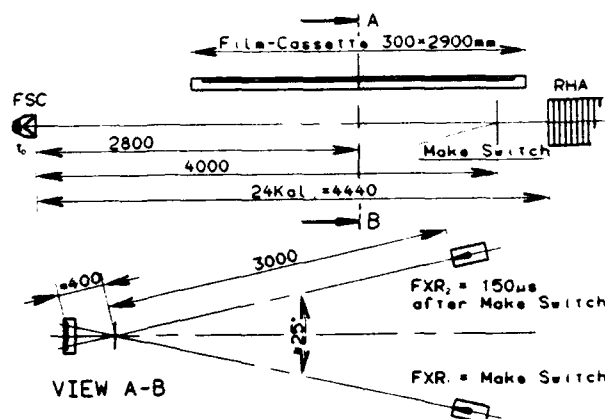


Fig 5 Test Set-Up FSC-FXR

Design 1:

The first visible particle has a velocity of about 9 800 m/s. Three large particles occur over the range from 8 000 to 8 500 m/s. Below 8 000 m/s a particulated jet is found, with the jet for the most part having the appearance of macaroni. This means that it is not a question of small fishes but small tubes which, however, in their cumulative length are indicative of good particulate behaviour. The second flash X-ray shows the jet over the range between 7 500 m/s and 3 300 m/s. The jet is not yet particulate over the range below 3 300 m/s.

Design 3:

With this design peak velocity of 8 600 m/s occur. Compared to the photograph relating to Design No. 1 large particles cannot be determined at the peak of the jet, the particulate effect is very uniform. Here again there is no pronounced macaroni effect, the jet is fully particulate up to a velocity of 2 800 m/s. The apparently final particle of the jet is again in the picture.

Design 5:

In this instance a tip velocity of 8 925 m/s can be evaluated. The contact film, however, has been triggered by particles which must have had a velocity of 12 500 m/s. The jet is seen in its entirety as a shower or an elongated cloud, the tip being relatively thin, thickness around 8 000 m/s, becoming somewhat thinner up to a range of 7 000 m/s and then thickening continually in diameter up to its visible end of about 3 500 m/s. Jet density appears to be constant.

Design 7:

The fastest particles occur with this design at a velocity of 5.900 m/s. A relatively regular particulate effect arose. The particle shape, however, is indicative of severe shear fracture behaviour, i.e. the liner material is certainly not comparable with that of high-performance liners. In addition, it can be seen in this photograph that a certain asymmetry of the jet is present. This could be due to initiation. On account of the flash being triggered by the contact film particles of about 8.000 m/s must have occurred here, too, but are not visible in the picture. The second flash shows the jet over the whole range down to approximately 2.800 m/s.

A remarkable difference is visible of the particle shapes and sizes for the various liner materials pure Aluminum (99.5%), cast Aluminum alloy AISi12 and copper.

The X-ray photographs were evaluated in accordance with the standard used at DASA-Schrobenhausen. Evaluation of the X-ray photographs was performed for both the first photograph, i.e. the exposure with the short delay time, and the second exposure. The results are listed in table 2. It was not possible to perform an evaluation of this kind for Design No. 5. When this variant was detonated, no classical particles were produced; a particle shower and highly distinct disintegration of the jet occurred. Since a continuous jet length is visible in the X-ray photograph, it was not possible to determine a priculation time.

Comparison of velocity and energy from simulation and test shows some minor differences yet still the same trend in relation to the various designs.

Design	V _{tip} (km/s)	Energy (crit) (kJ)	Partic. time (us)	Jet-length (mm)
1	9.8	2.000	295	1650 (9.8 - 4.2)
2	11.0	2.300	218	1680 (11.0 - 4.3)
3	8.6	1.900	416	2290 (8.6 - 3.1)
4	9.8	-----	190	1200 (9.8 - 3.5)
5	8.9 (12.5)	-----	-----	-----
6	10.2	800	182	1040 (10.2 - 4.5)
7	6.0	1.500	358	1220 (6.0 - 2.6)

Table 2: Test results

TESTS AGAINST TARGETS

As mentioned above four of the seven designs were selected on the basis of quantitative and qualitative jet characteristics for further tests. Two each SCs to these designs were fabricated and fired against a reinforced concrete target with a width of 1.53 m. Concrete quality was B55 (German designation) which means a compressive strength of 8.000 psi minimum. The characteristics of the four designs are listed in Table 3.

Design	Description of Design
1	70°- Cone; 8.6 mm; Al 99.5; Waveshaper
3	Trumpet; Al 99.5
5	70°- Cone; 9.0 mm; AISi12; Waveshaper
7	Hemi sub-cal; Copper; MPI-Plate

Table 3: Design characteristics

Test results are to be compared best by means of the plotted borehole profiles (Fig. 7). To measure borehole diameter as a function of depth cylinders with different diameters at steps of 5 mm were pushed into the borehole as deeply as possible, i.e. to the depth of the respective borehole diameter. These measurements were converted into the borehole plots.

Additionally a FTC dummy (Fig. 8) was pushed into the hole and the CG-depth of the HE-charge of the FTC was determined. This gave a more realistic measured for the quality of the holes. The table 4 shows that the best results in terms of C.G.-depth were achieved with design 1 and 5. C.G.-depth for these designs also were markedly above the requirement which was 570 mm.

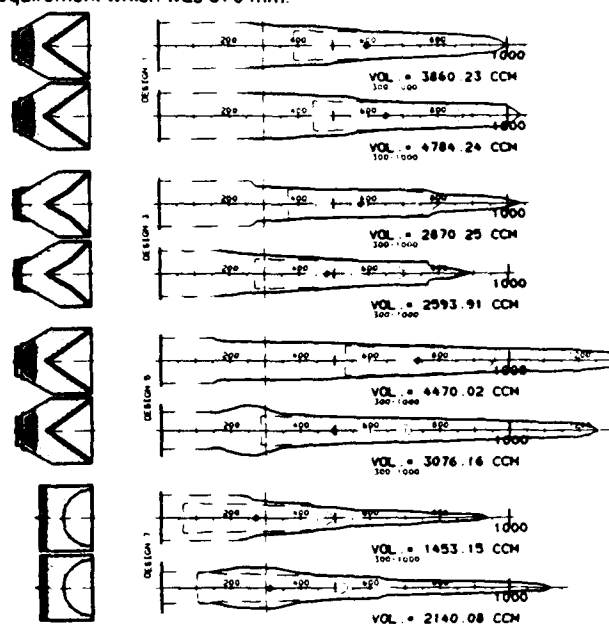


Fig. 7 Bore Hole Profiles

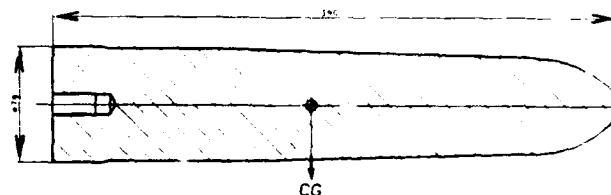


Fig. 8 FTC-Dummy

Design	CG-Depth [mm]	Penetration depth [mm]
1	597 624	1000 1038
3	579 480	1036 892
5	738 495	1301 1252
7	272 312	939 1120

Table 4 CG-Depth of different designs

These designs, although with minor modifications were selected for the next test series. System requirements called for a shorter FSC. Therefore design 1 was reduced in diameter from 185 mm to 175 mm (Concept B) and the liner angle of design 5 was changed from 70° to 80° (Concept A), see Fig. 9. Both concepts had approximately the same length. Characteristics are given in the following Table 5.

Concept	Description of design
A	80° - Cone; 9.0 mm; AISI12, Ø 185, Waveshaper
B	70° - Cone; 8.6 mm; AISI9.5, Ø 175, Waveshaper

Table 5: Design characteristics

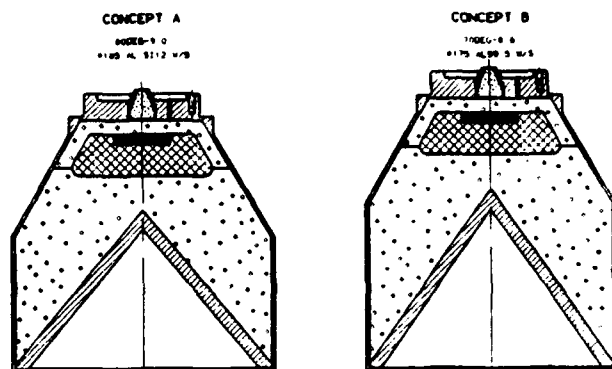
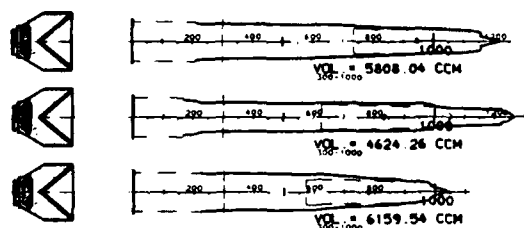


Fig. 9: Selected FSC-Design

Three each FSCs of both concepts were tested against targets as specified for the system. Target compressive strength was above 4.000 psi; vertical rebars were L 11 with 90 mm distance. Both concepts yielded very good results as can be seen from Fig. 10 and Table 6.

CONCEPT A LINER AL SI12, 80°, Ø185, WAVE-SHAPER



CONCEPT B LINER AL 99.5, 70°, Ø175, WAVE-SHAPER

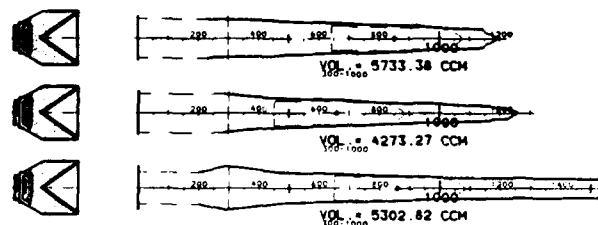


Fig 10: Bore Hole Profiles

Concept	CG-depth [mm]	Penetration depth [mm]	Rebar bedding [mm]
A	944	1222	27
	834	1266	27
	780	1049	31
B	851	1196	11
	660	1262	12
	859	> 1530	15

Table 6: Test results

With both Concepts required C.G. depth (570 mm) was exceeded by far. Due to the higher rebar bending which is essential for initial penetration of the FTC it was decided to follow Concept A for the subsequent steps.

After successful transfer of the necessary technologies the next test series were conducted by our subsidiary CMS in Tampa, Fla. These tests also had very satisfying results.

To simulate the ultimate step in the functional sequence of the system a FTC was hand emplaced into the FSC borehole and fired. The resulting reduction in load bearing capability of the bridge pier which is the ultimate measure for the performance of the system is determined with a code developed by James Ray from WES in Vicksburg, Miss. It determines residual strength of the pier from test data such as amount of concrete blown out or disrupted, rebars form or bent, asymmetry of damage etc.

FEEDBACK

Refinement of theoretical models to enhance their prognostic power and reliability is a continuous concern. An effort like that presented here is an excellent opportunity to feedback test results into the models and thereby calibrate them and achieve a better correspondence with reality.

A somewhat trivial and crude example is the so called volume factor which is the kinetic energy of the jet necessary to create one unit of borehole volume. This factor can be determined from both simulation and test results. In the tests described earlier the volume factor was found to be 360 J/cm³ for the 8.000 psi target and 215 J/cm³ for the 4.000 psi target. Comparison of these figures with these from simulation allows to modify the parameters in the PECO code which control interaction of the jet with target materials of different properties and so to obtain better predictions.

CONCLUSION

Warheads for a sophisticated bridge pier destruction system with tough requirements have been developed successfully. An initial phase of theoretical analysis gave valuable information on promising warhead design characteristics. Thus, effort for subsequent hardware fabrication and test phases could be reduced substantially. A feedback of test results into theory is useful to calibrate and refine the models and, thereby, to increase their reliability.

RESPONSIVE CHARACTERISTICS OF BURIED STRUCTURES SUBJECTED TO IMPULSIVE LOADINGS

Fang Qin

Nanjing Engineering Institute , Nanjing , PRC

ABSTRACT

The response of buried structures to impulsive loadings is determined by an approximate method. The structure is modeled by a three-degree-of-freedom (TDOF) system. The two exterior walls perpendicular to the blast direction are modeled by lumped mass and stiffness. The third DOF is the rigid body motion of the structure. The effect of rigid body motion on the response of the structure is considered and dimensionless responses are predicted for nondimensional parametric variations.

INTRODUCTION

Extensive research in the area of groundshock due to nuclear explosions has resulted in analysis methods which have been successful in predicting the responses of buried structures in simulation tests. These problems are solved by using the numerical method, such as FEM, BEM etc, and simplified analysis methods. These studies show that the deformation of the roof and bottom of the structure is affected by the rigid body motion under the nuclear explosions. [1,2,3] The deformation of the roof and bottom of the structure are usually neglected for simplicity in determining the interaction load on structures and response of structures subjected to this interaction load is predicted. These methods have been used with success for the case of nuclear explosion. Design procedures used for conventional weapons effects are founded in methods developed for designing against nuclear weapon threats. Current method for designing buried protective structures to resist the effects of impulsive loadings due to conventional weapons use a single-degree-of-freedom (SDOF) idealization of the structure. The stresses produced by the weapon, with or without reflection factors, are applied directly to the structure. Simplified SDOF models are usually used to examining the response of the exterior wall near the non-nuclear weapons explosion. In these studies the two principal response mode, the deformation response and the rigid body response are treated separately. [4,5] Reference 6 studies the effect of deformation on the shock response of buried structures.

In this paper, the effect of the rigid body motion

on the deformation response is studied. The TDOF model is used to predict the effect and dimensionless deformation responses are presented for nondimensional parametric variations.

THREE-DEGREE-OF-FREEDOM MODEL

A buried box-shaped structure is subjected to an explosion located at a range R_0 from the nearest surface. Three generic configurations are shown in Fig. (1).

The explosion produces a radially expanding shock wave that propagates through the soil. The stress wave encounters the nearest wall first, which cause the wall deform downward. Then, as the stress wave envelops the structure, it moves as a rigid body.

The fundamental basis for the analysis presented in this paper lies in wave propagation theory and the enforcement of appropriate conditions of continuity of stress and motion at the interface. Formulation for this condition have been widely used by many other researchers successfully for the case of nuclear explosions.

Unfortunately, the free-field stress is not well defined for non-nuclear groundshock problems and these are only limited test data available. Reference 7 provides a semi-empirical expression for the free-field stress based on test data from the early 1970's.

Considering the degree of uncertainty in the definition of the free-field stress, one-dimensional wave propagation theory considering approximate treatment of the localized nature of the loadings, and lumped parameter models are justified at this time in order to gain insight into physical behavior of these systems.

The TDOF model is proposed in this paper. The two exterior wall perpendicular to the blast direction are modeled by lumped mass and stiffness. It is assumed that the two exterior walls parallel to the blast direction have no deformation and move as a rigid body. Therefore, the system has three DOF. They are the deformation of the near wall, $W_n(t)$, the deformation of the far wall, $W_f(t)$ and the rigid body motion of the structure, $W_0(t)$.

The interface pressures acting on the near wall and far wall are

$$P_n(t) = 2p(t) - \rho_n c_n [\dot{W}_0(t) + \dot{W}_n(t) X_n(x, y)] \quad (1)$$

$$P_f(t) = \rho_f c_f [\dot{W}_0(t) - \dot{W}_f(t) X_f(x, y)] \quad (2)$$

where (\cdot) indicates differentiation with respect to time, ρc is the equivalent acoustic impedance of the soil. $X(x, y)$ is the mode of deformation and subscript n and f represent the near and far wall separately. $p(t)$ is the equivalent free-field stress, namely

$$p(t) = \begin{cases} P_m t/t_r, & t \geq t_r \\ P_m \exp(-(t-t_r)/t_r), & t < t_r \end{cases} \quad (3)$$

in which t_r is arrival time of free-field stress, presented by R_0/c and t_r is rise time, about $0.1 t_r$. [7]

Virtual displacement principle is used to formulate the differential equations of motion of the system. The equations of motion of the rigid body and the near and far walls are

$$\ddot{W}_0 + c \dot{W}_0 = 2p(t)/M_0 - \rho_n c_n / M_0 k_{ln} \dot{W}_n + \rho_f c_f / M_0 k_{lf} \dot{W}_f - k_{ln} M_n / M_0 \ddot{W}_n + k_{lf} M_f / M_0 \ddot{W}_f \quad (4)$$

$$\ddot{W}_n + 2 D_n \dot{W}_n + \omega_n^2 W_n = k_{ln} [2p(t)/M_n - 2D_n \dot{W}_0 - \ddot{W}_0] \quad (5)$$

$$\ddot{W}_f + 2 D_f \dot{W}_f + \omega_f^2 W_f = k_{lf} (2 D_f \dot{W}_0 + \ddot{W}_0) \quad (6)$$

where

$$D_i = \rho_i c_i / 2 M_i \quad (i=n, f) \quad (7)$$

$$k_{lmi} = k_{li} / k_{mi} \quad (i=n, f) \quad (8)$$

$$k_{li} = \iint_F X_i(x, y) dF / F \quad (i=n, f) \quad (9)$$

$$k_{mi} = \iint_F X_i^2(x, y) dF / F \quad (i=n, f) \quad (10)$$

$$\omega_i^2 = K_i k_{lmi} / M_i \quad (i=n, f) \quad (11)$$

$$c = (\rho_n c_n + \rho_f c_f) / M_0 \quad (12)$$

$$K_i = \text{stiffness of the wall } (i=n, f)$$

M_0, M_n, M_f = mass per unit area of the total structure, the near wall and far wall respectively.

SOLUTION OF THE DIFFERENTIAL EQUATIONS OF MOTION

Eqs. (4)-(6) are ordinary differential equations of order two. Nondimensional parameters are

introduced so that the results can be applied widely. Set

$$\begin{aligned} \bar{W}_n(t) &= W_n(t) / W_{ns} \\ \bar{W}_f(t) &= W_f(t) / W_{fs} \\ \bar{W}_0(t) &= W_0(t) / W_{ns} \\ \bar{t} &= t / t_r \end{aligned} \quad (13)$$

where W_{ns} and W_{fs} are the maximum deformation of the near and far wall subjected to static load, P_m , respectively. Therefore, eqs. (4)-(6) may be written as follows after introducing dimensionless parameters.

$$\begin{aligned} d^2 \bar{W}_0 / d\bar{t}^2 &= c_1 d\bar{W}_0 / d\bar{t} + c_2 d\bar{W}_n / d\bar{t} + c_3 d\bar{W}_f / d\bar{t} \\ &+ c_4 \bar{W}_0 + c_5 \bar{W}_n + c_6 \bar{W}_f + c_7 p(\bar{t}) \end{aligned} \quad (14)$$

$$\begin{aligned} d^2 \bar{W}_n / d\bar{t}^2 &= a_1 d\bar{W}_0 / d\bar{t} + a_2 d\bar{W}_n / d\bar{t} + a_3 d\bar{W}_f / d\bar{t} \\ &+ a_4 \bar{W}_0 + a_5 \bar{W}_n + a_6 \bar{W}_f + a_7 p(\bar{t}) \end{aligned} \quad (15)$$

$$\begin{aligned} d^2 \bar{W}_f / d\bar{t}^2 &= b_1 d\bar{W}_0 / d\bar{t} + b_2 d\bar{W}_n / d\bar{t} + b_3 d\bar{W}_f / d\bar{t} \\ &+ b_4 \bar{W}_0 + b_5 \bar{W}_n + b_6 \bar{W}_f + b_7 p(\bar{t}) \end{aligned} \quad (16)$$

where

$$\begin{aligned} c_1 &= (2k_{ln} (M_n / M_0) k_{lmn} (D_n / \omega_n) \omega_n t_r \\ &+ 2k_{lf} (M_f / M_0) k_{lmf} (D_f / \omega_f) \omega_f t_r - (c / \omega_n) \omega_n t_r) / s \end{aligned}$$

$$c_2 = c_3 = c_4 = 0$$

$$c_5 = k_{ln} (M_n / M_0) (\omega_n t_r)^2 / s$$

$$c_6 = -k_{lf} (M_f / M_0) (\omega_f t_r)^2 (W_{ns} / W_{fs}) / s$$

$$c_7 = 2 (M_n / M_0) (\omega_n t_r)^2 (1 / k_{lmf} - k_{ln}) / s$$

$$s = 1 - k_{ln} (M_n / M_0) k_{lmn} - k_{lf} (M_f / M_0) k_{lmf}$$

$$c = 2 D_n M_n / M_0 + 2 D_f M_f / M_0$$

$$W_{fs} / W_{ns} = k_{lmf} M_n \omega_n^2 / (k_{lmn} M_f \omega_f^2)$$

$$a_1 = -c_1 k_{lmn} - 2k_{lm}$$

$$a_2 = -2 (D_n / \omega_n) \omega_n t_r$$

$$a_3 = a_4 = 0$$

$$a_5 = -c_5 k_{lmn} - (\omega_n t_r)^2$$

$$a_6 = -c_6 k_{lmn}$$

$$a7 = -c7k_{lmf} + 2(\omega_n t_r)^2$$

$$b1 = (W_{ns}/W_{fs})k_{lmf}[c1 + 2(D_f/\omega_f)\omega_f t_r]$$

$$b2 = b4 = 0$$

$$b3 = -2(D_f/\omega_f)\omega_f t_r$$

$$b5 = c5(W_{ns}/W_{fs})k_{lmf}$$

$$b6 = c6(W_{ns}/W_{fs})k_{lmf} - (\omega_f t_r)^2$$

$$b7 = c7(W_{ns}/W_{fs})k_{lmf}$$

Eqs. (14)-(16) are solved using numerical method. The independent nondimensional parameters are D_n/ω_n , $\omega_n t_r$, M_n/M_0 , h_n/h_f and $\rho_f c_f/\rho_n c_n$, in which h_n and h_f are thickness of the near and far wall repetitively.

NUMERICAL RESULTS AND DISCUSSION

The results of dimensionless deformation of the near wall are presented for commonly used parameters. The nondimensional maximum deformation of the near wall, A_0 , includes the effects of the reflection of incident stress wave on the wall and dynamic property of the system subjected to the reflection load. Hence, A_0

may be defined as the coefficient of the interaction. Effect of the above-mentioned independent nondimensional parameters on the A_0 are shown in Fig. (2)-(6).

The effect of $\omega_n t_r$ on the A_0 is shown in Fig. (2). In Fig. (2), solid curve represents the result obtained by SDOF model and dashed curve is the result of the TDOF model. Comparison of the responses obtained by the TDOF model with those of the SDOF model shows that A_0 is less affected by rigid body motion. The peak deformation of the near wall for the TDOF model is lower than that of the SDOF model by 10%. There are two distinct response regions in Fig. (2). For $\omega_n t_r < 2$, A_0

increases with the increasing of $\omega_n t_r$; For $\omega_n t_r > 2$, A_0 decreases with the increasing of $\omega_n t_r$. When $\omega_n t_r$ equals to 2, maximum response is obtained.

It is shown that A_0 is not affected by M_n/M_0 in Fig. (3).

The effect of D_n/ω_n on the response is presented in Fig. (4). As D_n/ω_n denotes the quantity of soil dampings, the larger the D_n/ω_n , the smaller the A_0 .

Fig. (5) shows that A_0 is not affected by $\rho_f c_f/\rho_n c_n$. The explanation to this may be that

A_0 is insensitive to the rigid body motion.

Therefore, acoustic impedance below the far wall has not influence on the response of the near wall.

The insensitivity of A_0 to the boundary conditions of the structural element is shown in Fig. (6).

Fig. (7) indicates the effect of t_r/t_s on the response of the near wall.

CONCLUSIONS

The results of this study indicate that the peak deformation response of the near wall for the TDOF model is lower than that of the SDOF model by 10%. It is suggested that the response of the near wall due to conventional weapon explosions is predicted by the SDOF model for practical design purpose. The response of the near wall of buried structures is insensitive to the acoustic impedance of the soil below the far wall and the boundary conditions of structural elements.

ACKNOWLEDGEMENTS

The author gratefully acknowledges the contribution of Prof. Qian Qihu. His early work on SMI is very helpful in preparing this paper.

REFERENCES

1. Qian, Qihu, "Computational Principle of Protective Structures", limited publication, 1981. (in chinese)
2. Qian, Qihu, "Practical computational Method for Shallow-Buried Structures Subjected to Nuclear Explosion", limited publication, 1987. (in chinese)
3. Crawford, R. E., Higgins, C. J. and Bultmann, E. H., "The Air Force Manual for Design and Analysis of Hardened Structures", AFWL-TR74-102, Air Force Weapon Laboratory, Kirtland AFB, New Mexico, October 1974.
4. Hinman, E., and Weidlinger, P., "Single Degree of Freedom Solution of Structure-Medium Interactions," Proc. Int. Symp. on the Interaction of Non-Nuclear Weapons With Structures, Mannheim, West Germany, March 9-13, 1987
5. Weidlinger, P., and Hinman, E., "Analysis of Underground Protective Structures," Journal of Structural Engineering, ASCE, Vol. 114, No. 7, July 1988, pp. 1658-1673
6. Hinman, E., "Effect of Deformation on the Shock Response of Buried Structures Subjected to Explosions," Structures under Shock and Impact (edited by P. S. Bulson), 1989, pp 455-465
7. Fundamentals of Protective Design for Conventional Weapons, TM5-855-1, Headquarters, Dept. of the Army, Wash. DC, Nov. 1986

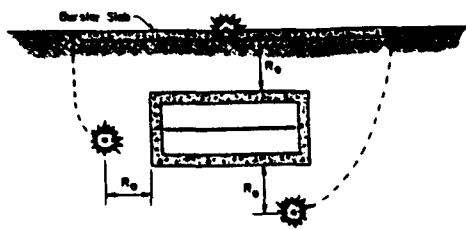


Fig.1 Buried Protective Structure

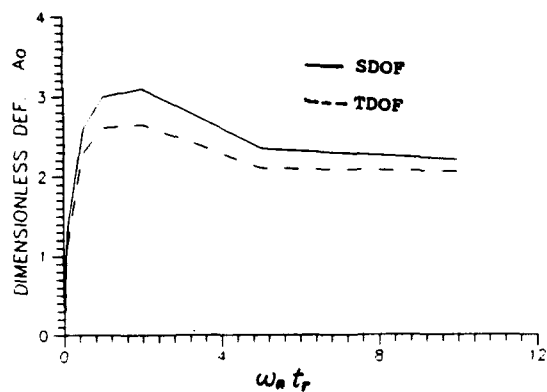


Fig.2. Effect of $\omega_n t_r$ on the Response, A_0

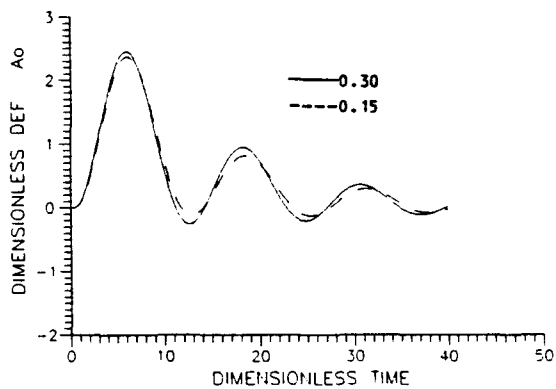


Fig.3 Effect of M_n/M_0 on the Response, A_0

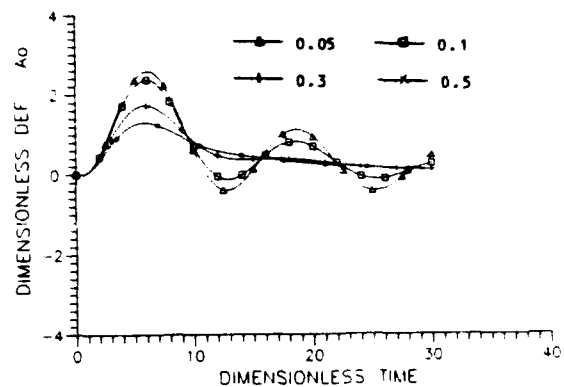


Fig.4 Effect of D_n/ω_n on the Response, A_0

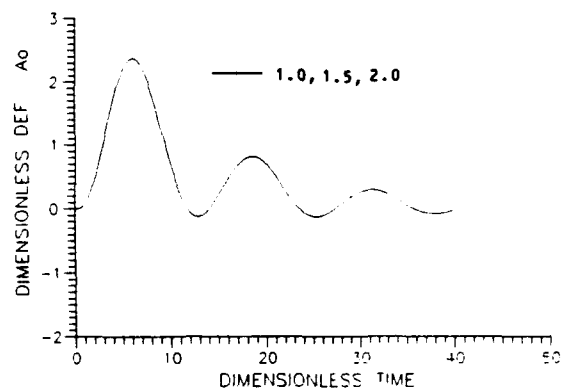


Fig.5 Effect of $\rho_f c_f / \rho_n c_n$ on the Response, A_0

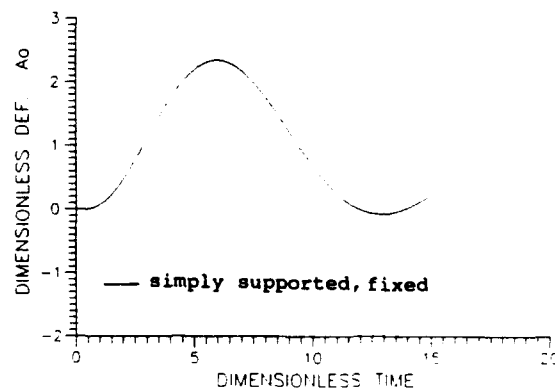


Fig.6 Effect of Constraint Conditions on the Response, A_0

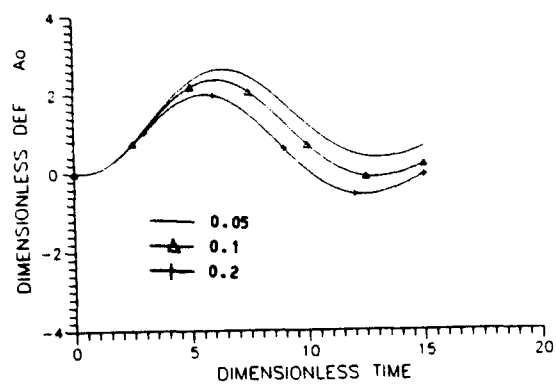


Fig.7 Effect of t_r/t_a on the Response, A_0

FEM IN SATURATED SOIL UNDER EXPLOSIVE LOADING

QiHu Qian Mingyang wang

Nanjing Engineering Institute ,P.R.C.

ABSTRACT

Saturated soil is a three-phase media comprised of particles of solid soil, water and a small amount of closed air. In this paper, motion equations for saturated soil under explosive loading are presented. Dynamic finite element equations in which artificial viscosity is introduced are deduced. The stability and convergence properties in the finite element analysis are preliminary investigated. The law of propagation of explosive wave in the media with a different amount of air are obtained. The comparisons of solutions by FEM and by DEM (Godunov's solutions) are given to verify the effectiveness of the presented method.

1. INTRODUCTION

Some protective structures are buried in saturated soil. One of the characteristics of saturated soil is that it contains a certain amount of closed air. Hence, it is a three-phase medium comprised of particles of solid soil, water and air. The behavior of saturated soil is quite different from that of non-saturated soil even under a small explosive pressure. Tests show that when explosive wave propagates in saturated soil, its velocities of wave front, the pressure and the particles velocities at the wave front are closely related to the content of the air. The methods and

corresponding formula for the calculation of the stresses propagation and the soil-structure interaction in non-saturated soil can't be used in saturated soil. and there are still no such better methods to study the dynamic properties of saturated soil under explosive loading. So it is very urgent to provide a appropriate model and numerical methods for saturated soil.

Tests also indicate that the saturated soil can't be treated as a elastic continuum, therefore the constitutive equations for the saturated soil must be established at first. For simplification, only plane waves under nuclear and chemical explosion are studied in this paper. The problem is regarded as a one-dimensional one, the shear stresses in the media are neglected. The pressure-density equations of three-phase media in saturated soil are deduced from the pressure-density equation of individual phase medium. It shows that the saturated soil is a nonlinear elastic medium. This conclusion is identical to the experimental result [1].

Differential equations of movement are obtained according to dynamics of medium. Nonlinear ordinary differential equations of finite element analysis are established by applying the Galerkin

method and then the differential equations are discredited into nonlinear algebra equations. Artificial viscosity is introduced into the equations to improve the convergence property in the finite element analysis. Many useful results are obtained with FEM. The comparisons of finite element solutions and difference equation solutions are given to verify the effectiveness of presented method. It lays the foundation for the study the dynamic behavior and related topic of saturated soil under explosive loading.

2. BASIC EQUATIONS OF SATURATED SOIL

Assume that the contents of air, water and particles of solid soil in a unit volume of saturated soil are α_1 , α_2 and α_3 respectively, ρ_1, ρ_2 and ρ_3 are the densities of the corresponding medium. c_1 , c_2 and c_3 are voice speeds of the corresponding medium under the condition of initial pressure equals to p_0 .

For $p=p_0$, the density of medium in saturated soil is

$$\rho_0 = \alpha_1 \rho_1 + \alpha_2 \rho_2 + \alpha_3 \rho_3 \quad (1)$$

$$\alpha_1 + \alpha_2 + \alpha_3 = 1 \quad (2)$$

The equations of state for an individual medium of saturated soil are

$$p = p_0 (\rho/\rho_0)^{k_1} \quad (\text{air}) \quad (3)$$

$$p = p_0 + \frac{\rho_2 \cdot c_2^2}{k_2} [(\rho/\rho_2)^{k_2} - 1] \quad (\text{water}) \quad (4)$$

$$p = p_0 + \frac{\rho_3 \cdot c_3^2}{k_3} [(\rho/\rho_3)^{k_3} - 1] \quad (\text{solid}) \quad (5)$$

where, k_1, k_2 and k_3 are the specific entropy of the corresponding medium, generally $k_1=1.4$, $k_2=k_3=3.0$. As the compressibility of a individual medium of saturated soil is different from each other under the pressure, the content of a individual medium

of saturated soil can't be determined. Assuming that the contents of the corresponding media of saturated soil are α_1^* , α_2^* and α_3^* under the pressure respectively, ρ is the density of saturated soil. We can obtain the following equations from Eq.(3) to Eq.(5)

$$\alpha_1^* = \alpha_1 (p/p_0)^{-k_1^{-1}} \quad (6)$$

$$\alpha_2^* = \alpha_2 \left[k_2 \cdot \frac{(p-p_0)}{\rho_2 c_2^2} + 1 \right]^{-k_2^{-1}} \quad (7)$$

$$\alpha_3^* = \alpha_3 \left[k_3 \cdot \frac{(p-p_0)}{\rho_3 c_3^2} + 1 \right]^{-k_3^{-1}} \quad (8)$$

$$\rho = \rho_0 + (\alpha_1^* - \alpha_1) \rho_1 + (\alpha_2^* - \alpha_2) \rho_2 + (\alpha_3^* - \alpha_3) \rho_3 \quad (9)$$

substitute Eq.(6), Eq.(7) and Eq.(8) into Eq.(9),

the equation of state of saturated soil is

$$\rho = \rho_0 \left\{ \alpha_1 \left(\frac{p}{p_0} \right)^{-k_1^{-1}} + \alpha_2 \left[\frac{k_2 (p-p_0)}{\rho_2 c_2^2} + 1 \right]^{-k_2^{-1}} + \alpha_3 \left[\frac{k_3 (p-p_0)}{\rho_3 c_3^2} + 1 \right]^{-k_3^{-1}} \right\}^{-1} \quad (10)$$

The above equations of motion represent the conservations of mass and momentum. In Eulerian description, after neglecting the effect of shear stresses for one-dimensional flow, the equations of motion can be written as

$$\frac{\partial u}{\partial t} + u \frac{\partial u}{\partial x} + \frac{1}{\rho} \frac{\partial p}{\partial x} = 0 \quad (11)$$

$$\frac{\partial \rho}{\partial t} + u \frac{\partial \rho}{\partial x} + \rho \frac{\partial u}{\partial x} = 0 \quad (12)$$

where x -spatial coordinates and t -time,

initial conditions

$$\rho(x, 0) = \rho_0 \quad (13)$$

$$u(x, 0) = 0. \quad (14)$$

$$p(x, 0) = p_0 \quad (15)$$

and boundary conditions

$$p(0, t) = f(t) \quad (16)$$

It is not convenient to solve for Eq.(11) and Eq.(12) which are unsteady and nonlinear equations

However, it is convenient to treat the propagation of plane wave in dense media in the Lagrangian description. To get the equations of

motion in the material coordinates, we introduce a change of coordinates. and set

$$t = t, h = \int_{(0,0)}^{(x,t)} \rho dx - \rho u dt, v=1/\rho \quad (17)$$

(17)The following relations can be obtained from above equations

$$\begin{aligned} \rho \frac{\partial x}{\partial h} &= 1 \quad \frac{\partial h}{\partial x} = \rho \quad \frac{\partial x}{\partial h} = 1/v \quad \frac{\partial h}{\partial t} = -\rho u \\ 1/\rho \frac{\partial p}{\partial x} &= \frac{\partial p}{\partial h} u \frac{\partial u}{\partial x} = \rho u \frac{\partial u}{\partial h} \\ \frac{\partial u}{\partial t} &= -\rho u \frac{\partial u}{\partial h} + \frac{\partial u}{\partial t} \\ \rho \frac{\partial u}{\partial x} &= \rho^2 \frac{\partial u}{\partial h} \quad \frac{\partial \rho}{\partial t} = -\rho^2 \frac{\partial v}{\partial t} \end{aligned} \quad (18)$$

The change of density varying with the propagation distances is not great in the dense media where it contains a small amount of air .Therefore , the density can be approximately regarded as the function of time. that is

$$\frac{\partial \rho}{\partial x} = 0 \quad (19)$$

Substitute Eq.(19) and above identities into Eq.(11) and Eq.(12),we obtain

$$\frac{\partial u}{\partial t} + \frac{\partial p}{\partial h} = 0 \quad (20)$$

$$\frac{\partial u}{\partial h} - \frac{\partial v}{\partial t} = 0 \quad (21)$$

The initial conditions and boundary conditions are

$$\rho(0) = \rho_0 \quad (22)$$

$$u(0) = 0 \quad (23)$$

$$p(0) = p_0 \quad (24)$$

$$p(0,t) = f(t) \quad (25)$$

From Eq.(21), for the specific volume $v=1/\rho$,we obtain

$$\begin{aligned} v=1/\rho_0 \{ & \alpha_1 (p/p_0)^{-k_1} + \alpha_2 \left[\frac{k_2 (p_0-p)}{\rho_2^2 c_2^2} + 1 \right]^{-k_2} -1 \\ & + \alpha_3 \left[\frac{k_3 (p-p_0)}{\rho_3^2 c_3^2} + 1 \right]^{-k_3} \} \end{aligned} \quad (26)$$

Assuming $v=F(p)$,as the result of Eq.(19), $F(p)$ is only the function of time.

3.DYNAMIC EQUATIONS OF FINITE-ELEMENT

(1). artificial viscosity

It may be seen from Eq.(10) that the saturated soil is a nonlinear elastic media. When the

explosive wave propagates in this media, the shock wave will produce. It is very difficult for ordinary FEM to treat the problem of shock wave.

The reason is that the shock wave front is a geometrical surface, physical variables are discontinues functions on this surface . In the sense of physics, the shock wave surface is not a geometrical surface but a surface with certain depth because of the effects of viscosity and dispersion in the medium .Theoretically , if the effects of artificial viscosity and dissipation are adequately introduced into the dynamic equations,above equations can be still used to solve the problem of shock wave.But the thickness of shock wave surface is so small that it is very difficult to choose adequate size of element in the practical calculation. Therefore, the effects of viscosity and dispersion must be enhanced .It requires some effects of dissipation to extend the depth of shock wavefront ,this can be accomplished by introducing the even order deviation term into the dynamic equations. but, the numerical oscillation should not appear. How to dissipate the effects of artificial viscosity and dissipation is a problem needs further discussion .

Assume the artificial viscosity is q , and replace the variation p in Eq.(20) with $p+q$, the equations of motion can be written as

$$\frac{\partial u}{\partial t} + \frac{\partial (p+q)}{\partial h} = 0 \quad (27)$$

$$\text{where, } q = \begin{cases} \gamma \frac{\partial u}{\partial h} & \frac{\partial u}{\partial h} \leq 0 \\ 0 & \frac{\partial u}{\partial h} > 0 \end{cases} \quad \text{and} \quad \gamma = a \rho c \Delta h$$

in which, ρ is the density of saturated soil , c is local voice speed , Δh is the size of element, a is a constant.generally varying from 0.2 to 0.5 .

Consider the following relationship

$$c^2 = dp/d\rho \quad (28)$$

and the state equation (10), eq.(28) can be rewritten as

$$c^2 = \frac{[\alpha_1 (p/p_0)^{-k_1^{-1}} + \alpha_2 (\frac{k_2(p-p_0)}{\rho_2 c_2^2} + 1)^{-k_2^{-1}} + \alpha_3 (\frac{k_3(p-p_0)}{\rho_3 c_3^2} + 1)^{-k_3^{-1}}]}{\frac{\alpha_1}{\rho_1 c_1^2} 2(p/p_0)^{-(1+k_1^{-1})} + \frac{\alpha_2}{\rho_2 c_2^2} 2[\frac{k_2(p-p_0)}{\rho_2 c_2^2} + 1]^{-(1+k_2^{-1})} + \frac{\alpha_3}{\rho_3 c_3^2} 2[\frac{k_3(p-p_0)}{\rho_3 c_3^2} + 1]^{-(1+k_3^{-1})}} \quad (29)$$

For $p=p_0$, we have

$$c_0 = \{1/\rho_0 (\sum_{i=1}^3 \frac{\alpha_i}{\rho_i c_i^2})^{-1}\}^{1/2} \quad (30)$$

and $p_0 = \rho_1 c_1^2 / k_1$

(2) finite-element equations

Introduce the following approximations into

Eq.(27) and Eq.(21)

$$\begin{aligned} u^{(e)} &= u_i^{(e)}(t) \varphi_i^{(e)}(h) \\ v^{(e)} &= v_i^{(e)}(t) \varphi_i^{(e)}(h) \quad (i=1,2) \\ p^{(e)} &= p_i^{(e)}(t) \varphi_i^{(e)}(h) \end{aligned} \quad (31)$$

φ_i is shape function, and it satisfies the following equation

$$\varphi_1 + \varphi_2 = 1$$

Because the specific volume of element $v^{(e)}$ doesn't vary with the distance, we have

$$\begin{aligned} v_i^{(e)}(t) \varphi_i^{(e)}(h) &= v_i^{(e)}(t) [\varphi_1(h) + \varphi_2(h)] = v^{(e)}(t) \\ \text{hence,} \quad v_1^{(e)}(t) &= v_2^{(e)}(t) = v^{(e)}(t) \end{aligned}$$

Substitute Eq.(31) into Eq.(27) and Eq.(21), apply Galerkin method to dynamic equations, and set weight function $w_i = \varphi_i(h)$, we obtain

$$\begin{aligned} \int_e \dot{u}_i^{(e)}(t) \varphi_i^{(e)} dh + \int_e \dot{p}^{(e)}(t) \varphi_i^{(e)} dh \\ - \gamma \int_e u_i^{(e)}(t) \varphi_i^{(e)} dh = 0 \\ \int_e u_i^{(e)}(t) \varphi_i^{(e)} dh - \int_e v_i^{(e)}(t) \varphi_i^{(e)} dh = 0 \end{aligned}$$

By the partial integration methods, and introduce the boundary conditions, the equations of motion

are rewritten as

$$u_i^{(e)}(t) \int_e \varphi_i^{(e)} \varphi_j^{(e)} dh - \dot{p}_i^{(e)}(t) \int_e \varphi_i^{(e)} \varphi_j^{(e)} dh + \gamma u_i^{(e)}(t) \int_e \varphi_i^{(e)} \varphi_j^{(e)} dh = -p_i^{(e)}(t) \varphi_i^{(e)} \varphi_j^{(e)} + \gamma u_i^{(e)}(t) \varphi_i^{(e)} \varphi_j^{(e)} \quad (33)$$

$$u_i^{(e)}(t) \int_e \varphi_i^{(e)} \varphi_j^{(e)} dh - \dot{v}_i^{(e)}(t) \int_e \varphi_i^{(e)} \varphi_j^{(e)} dh = 0 \quad (34)$$

From Eq.(33) we have $\gamma u_i^{(e)}(t) \varphi_i^{(e)} \varphi_j^{(e)} = 0$

for the first element

$$-p_1^{(e)}(t) \varphi_1^{(e)} \varphi_1^{(e)} = -f(t) \varphi_1^{(e)}$$

and for the other element

$$-p_1^{(e)}(t) \varphi_1^{(e)} \varphi_j^{(e)} = 0$$

Assume

$$\begin{aligned} A_{ij}^{(e)} &= \int_e \varphi_i^{(e)} \varphi_j^{(e)} dh \quad \dot{A}_{ij}^{(e)} = \int_e \dot{\varphi}_i^{(e)} \dot{\varphi}_j^{(e)} dh \\ C_{ij}^{(e)} &= \int_e \varphi_i^{(e)} \varphi_j^{(e)} dh \quad \dot{C}_{ij}^{(e)} = \int_e \dot{\varphi}_i^{(e)} \dot{\varphi}_j^{(e)} dh \end{aligned}$$

the Eq.(33) and Eq.(34) can be written as (note the change of footnotes)

$$A_{ij}^{(e)} \dot{u}_j^{(e)}(t) - C_{ij}^{(e)} \dot{p}_j^{(e)}(t) + \gamma A_{ij}^{(e)} u_j^{(e)}(t) = f_i^{(e)}(t) \quad (35)$$

$$B_{ij}^{(e)} u_j^{(e)}(t) - A_{ij}^{(e)} F'(p) p_j^{(e)}(t) = 0 \quad (36)$$

$$f_i^{(e)}(t) = -f(t) \varphi_i^{(e)} \quad (i=1) \quad f_i^{(e)}(t) = 0 \quad (i \neq 1)$$

$$F'(p) = \dot{v}_i^{(e)}(t) / p_i^{(e)}(t)$$

After assembly of the condensed elements, the equations of motion take the form

$$A_{nm} \dot{U}_m(t) - C_{nm} \dot{P}_m(t) + D_{nm} U_m(t) = f_n(t) \quad (37)$$

$$B_{nm} U_m(t) - A_{nm} F'(p) P_m(t) = 0 \quad (38)$$

where

$$\begin{aligned} A_{nm} &= \sum A_{ij}^{(e)} \delta_{in}^{(e)} \delta_{jm}^{(e)} \quad B_{nm} = \sum B_{ij}^{(e)} \delta_{in}^{(e)} \delta_{jm}^{(e)} \\ C_{nm} &= \sum C_{ij}^{(e)} \delta_{in}^{(e)} \delta_{jm}^{(e)} \quad D_{nm} = \gamma \sum A_{ij}^{(e)} \delta_{in}^{(e)} \delta_{jm}^{(e)} \\ f_n(t) &= f_1^{(e)}(t) \quad (n=1) \quad f_n(t) = 0 \quad (n \neq 1) \end{aligned}$$

in which, Δ^e is the Boolean matrix of the "e" element

Consider the difference relationships

$$\dot{U}_m^k = \frac{U_m^{k+1} - U_m^k}{\Delta t} \quad \dot{P}_m^k = \frac{P_m^{k+1} - P_m^k}{\Delta t}$$

$$U_m = (1-\vartheta) U_m^{k+1} + \vartheta U_m^k \quad P_m = (1-\vartheta) P_m^{k+1} + \vartheta P_m^k$$

$$\text{Set} \quad A'_{nm} = A_{nm} / \Delta t$$

and substitute above relations into Eq.(37) and

Eq.(38) the final equations of motion are

$$\begin{bmatrix} A'_{nm} + D_{nm}(1-\vartheta) & -C_{nm}(1-\vartheta) \\ (1-\vartheta) B_{nm} & -A'_{nm} F'(p) \end{bmatrix} \begin{bmatrix} U_m^{k+1} \\ P_m^{k+1} \end{bmatrix} = \begin{bmatrix} f_n \\ 0 \end{bmatrix} + \begin{bmatrix} A'_{nm} - D_{nm}\vartheta & C_{nm}\vartheta \\ -B_{nm}\vartheta & -A'_{nm} F'(p) \end{bmatrix} \begin{bmatrix} U_m^k \\ P_m^k \end{bmatrix} \quad (30)$$

4. PROPAGATION OF EXPLOSIVE WAVE IN THE FREE-FIELD OF SATURATED SOIL

Comparisons of the FEM solutions and Godunov's results are firstly presented for verifying the effectiveness of the FEM.

The parameters used in calculation are

$$\begin{aligned} c_1 &= 340.\text{m/sec} & c_2 &= 1500.\text{m/sec} & c_3 &= 4500.\text{m/sec} \\ \rho_0 &= 2.21\text{e-}6\text{kgf}\cdot\text{sec}^2/\text{cm}^4 & \rho_1 &= 1.2\text{e-}9\text{kgf}\cdot\text{sec}^2/\text{cm}^4 \\ \rho_2 &= 1.\text{e-}6\text{kgf}\cdot\text{sec}^2/\text{cm}^4 & \rho_3 &= 2.65\text{e-}6\text{kgf}\cdot\text{sec}^2/\text{cm}^4 \\ \alpha_1 &= 0.001 & \alpha_2 &= 0.3 & \alpha_3 &= 0.699 \end{aligned}$$

and assume the form of loading is

$$p(t) = \begin{cases} p_{\max}(t/t_{ch}) & t \leq t_{ch} \\ p_{\max}[1 - (t - t_{ch})/(t_* - t_{ch})] & t_{ch} \leq t \leq t_* \end{cases}$$

The value of the parameters in above equations are shown in Fig.1

The mesh for the finite element of one-dimensional problem is shown in Fig.2. The size of element (Δh) and time (Δt) in finite element are 4.5cm and 0.05ms, respectively. The number of element (N) equals to 100. The viscosity coefficient (a) is taken between 0.2 and 0.5, which is varying with the changing air content in calculation procedure, the best value is that the numerical oscillations are not appeared. The viscosity coefficient should be appropriately enlarged with the increasing of the content of air in our numerical experiments.

Comparisons of waveform of the pressure and the particle velocities located at node No.50 are

carried out. The results of the two methods are illustrated in Fig.3 and Fig.4, respectively.

It is shown in Fig.3 and Fig.4 that either the pressures or the particle velocities results with FEM agree with Godunov's solutions. In addition, the numerical experiments also demonstrate that the method presented here takes less computer time and is more effective than Godunov's method.

Now, we investigate the law of propagation of plane explosive wave in the free field of saturated soil with different contents of air. The parameters of medium used in calculation are also taken as above.

Comparison charts of pressure and velocity waveforms for different sections (nodenumber (N) = 1, 40, and 80) in saturated soil ($\alpha_1=0.0, \alpha_2=0.3, \alpha_3=0.7$) are shown in Fig.5 and Fig.6, respectively. The similar comparison charts in saturated soil ($\alpha_1=0.001, \alpha_2=0.3, \alpha_3=0.699$) are shown in Fig.7 and Fig.8

, respectively. It can be seen from Fig.5, 7 and Fig.6, 8 that even a small amount of air in saturated soil can lead to a obvious decrease of pressure and particle velocity. Comparisons in Fig.5, 6 and Fig.7, 8 indicate that with the increase of the distance from the explosive center the pressure and particle velocity in the saturated soil with more air content decay more rapidly than those in the saturated soil with less air content. Fig.9 shows the comparisons of pressure waveforms on the same section (nodenumber (N) = 60) in saturated soil with the different amount of air, the similar comparisons (nodenumber (N) = 90) is shown in Fig.10. Fig.9 and Fig.10

indicate that the explosive waveform in saturated soil vary obviously with the contents of air .Waveform neither the same section nor the different section is alike , the near waveform is of rising time , the far waveform is close to shock wave .The above solutions are identical to the experimental results [1].

5. CONCLUSIONS

The following conclusions are obtained from the above analysis

(1) The FEM with artificial viscosity is adequate for the study of dynamic properties of saturated soil under explosive loading.

(2) The numerical and experimental results indicate that

a. with the increase of the distance from the explosive center,the decay of explosive wave in saturated soil depends the content of air more obviously

b. a small amount of air in saturated can still lead to a obvious decay of maximum pressure and particle velocity.

c. the explosive waveform section with the different content of air in saturated soil is quite different; the waveform neither in the same section nor in the different section is alike . for the loading just like Fig.1, the near waveform is of rising time, the far waveform is close to shock wave.

3. numerical experiments indicate that the FEM presented here takes less computer time and is more effective than the DEM (Godunov's method) . The discussions on this topic will be presented in another paper.

Acknowledgement:The authors are indebted to

prof.TingYing Su who provided the Godunov's solutions for this paper .

REFERENCE

1. Г.М.Ляхов:Основы Динамики взрывных волн в густых и горных породах. 1974
- 2.Graham F.Carey J.Tinsley Oden , <<FINITE ELEMENTS>> FLUID MECHANICS VOLUME VI 1986
- 3.QiHu Qian , <<Calculation principle of protective structure>> 1981

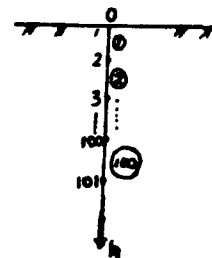
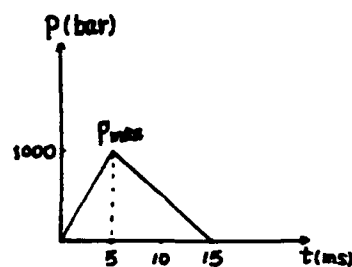


Fig.1 loading of the ground Fig.2 mesh for FE model

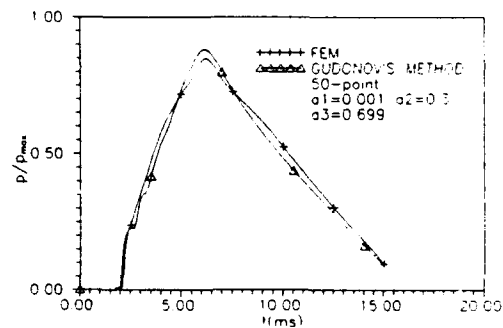


Fig.3 comparison of pressure waveform according to FEM and Godunov's method

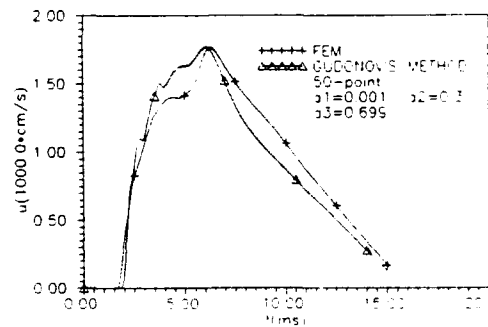


Fig.4 comparison of velocity waveform according to FEM and Godunov's method

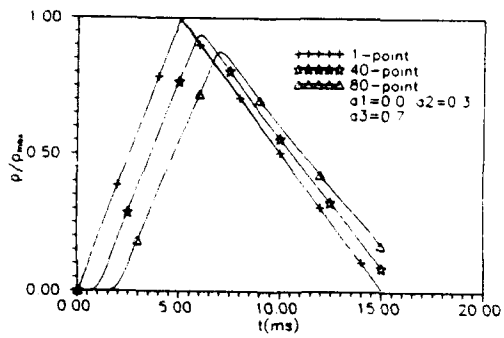


Fig. 5

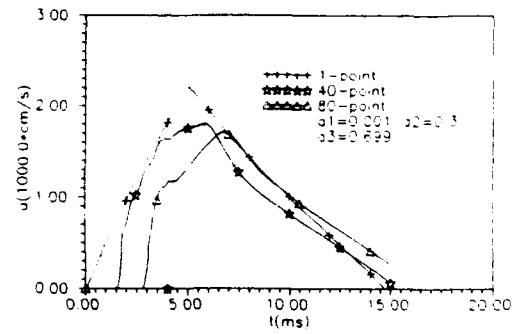


Fig. 8

Fig. 5, 6, 7, 8 comparison of waveform with a different nodenumber

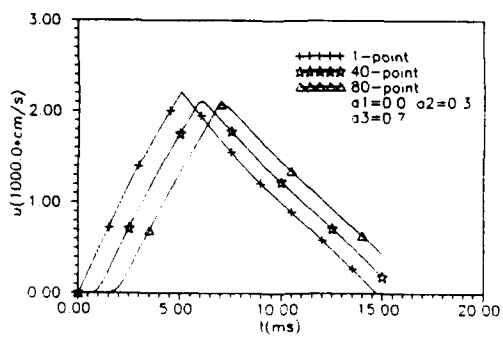


Fig. 6

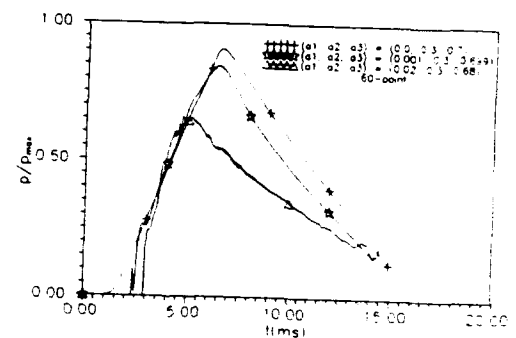


Fig. 9 comparison of pressure waveforms with the different content of air (nodenumber(N) = 60)

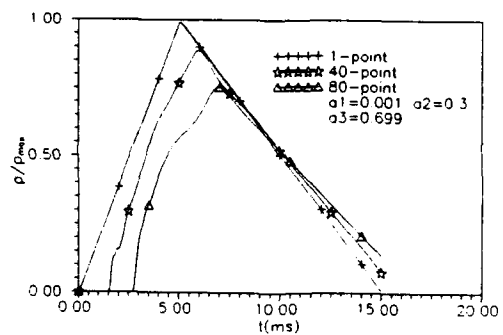


Fig. 7

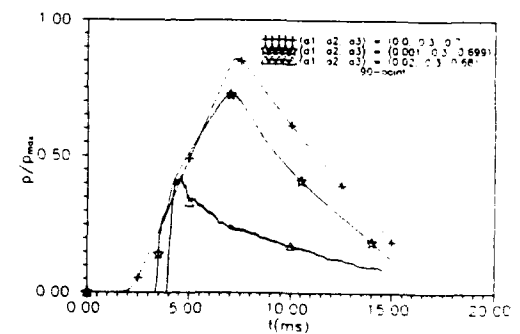


Fig. 10 comparison of pressure waveforms with the different content of air (nodenumber(N) = 90)

MATERIAL PROPERTIES DATABASE SEARCH AND RETRIEVAL PROGRAM

B. R. Phillips, D. E. Barnes, and A. E. Jackson, Jr.*
T. R. Slawson and R. E. Walker**

* US Army Engineer Waterways Experiment Station, Vicksburg, MS

** Applied Research Associates, Inc., Vicksburg, MS

ABSTRACT

A material properties database coupled with a search and retrieval code were developed to provide those within the defense community who are performing ground shock calculations and hardened structure designs and analyses associated with conventional weapons effects with consistent mechanical property data sets for a wide variety of soil and rock materials. The database contains a general description of both structure backfill and undisturbed geologic materials in terms of the project for which the material is associated, the material's location with respect to geologic interfaces, and its classification and composition. The grain size distribution for soils is provided. Mechanical responses of each material are available for a variety of stress and strain boundary conditions. To retrieve information, an interactive PC-compatible, search and retrieval code MPQ was developed. To use the code, the user establishes the bounds for a query involving most all of the variables discussed above.

BACKGROUND

The Geomechanics Division, Structures Laboratory at the US Army Engineer Waterways Experiment Station (WES) conducts high-pressure quasi-static and dynamic mechanical property laboratory tests on soil, rock, and cement-based materials to define their responses to intense transient loadings such as those produced by explosive detonations and high-velocity projectile impact. Standard classification and composition tests are also conducted for correlations and comparisons. Results are analyzed to provide graphical data sets required for fitting the mathematical constitutive models currently used in first-principle weapon effects prediction and analysis codes. The database contains mechanical property recommendations for a wide variety of soil and rock materials associated with numerous high explosive (HE) and conventional weapons effects (CWE) test events as well as hardened facility site characterization studies. It continues to be expanded with current interest focused on effective stress properties for saturated and nearly saturated soils and properties of high-strength cement-based materials being evaluated for use in hardened construction.

To assist in the management and distribution of the mechanical property recommendations generated by WES, a database structure and a query program were developed by Applied Research Associates (ARA) during 1990. The database file format is dBase III Plus (Ref 1). Input and maintenance can be performed using dBase or the file editor included with Clipper, DBU. To access the database, a search and retrieval, or query, code was written in Clipper (Refs 2 and 3), a dBase language compiler. The query program MPQ is designed for users that require information on WES mechanical property recommendations for specific materials. The program allows the user to extract information about a selected material from the database and to plot the available recommended responses for that material. MPQ also allows very broad searches so that information can be obtained for all materials in the database that meet a general description (like "sand" or "clay"). It can be used easily by inexperienced users on commonly available IBM PC-compatible computers. Composite plots of material responses can be made using the DPLOT graphics program, which is part of the HGRAPH library (Ref 4) of graphics programs.

The purpose of this paper is to describe the material properties database in its present format along with the query code MPQ and its use. An example of the use of the code is also presented.

MATERIAL PROPERTIES DATABASE

The Material Properties Database actually consists of three databases linked together as shown in Figure 1. The basic philosophy is to use multiple databases linked by keywords to maintain flexibility in data storage. The general structure consists of the main database MPROP containing general material descriptions and two supporting databases that contain gradation data GRAD and file names for material property plots MPLOTS. These databases are tables of information. Each table consists of records (rows), and each record is subdivided into fields (columns). The fields in a record contain specific information (like "density" or "Unified Soil Classification System designation") for that record. A field may also be a keyword that is used to link the record to additional records in other databases.

Main Database (MPROP)

The MPROP database contains basic information as shown in Table 1 about each material that WES has characterized. The general information includes the project name associated with the material, keyword links to the HE event or series of events associated with the material, site information (layering, water table depth, etc.), material composition (water content, density, etc.), and keyword links to the MPLOTS (mechanical property plots) and GRAD (gradation data) databases.

Plot File Database (MPLOTS)

The MPLOTS database consists of three fields per record. The first field consists of a keyword link (PLOT_KEY) to a record in the MPROP database. The second field is a mechanical property plot file name. The plot file name identifies the file that contains the data required to generate the plot that is described in field 3. Typical data available for each material include:

- a. Isotropic Compression (IC) Test Results in terms of Mean Normal Stress versus Volumetric Strain.
- b. Triaxial Compression (TXC) Test Results in terms of
 - (1) Principal Stress Difference versus Axial Strain,
 - (2) Principal Stress Difference versus Principal Strain Difference, and
 - (3) Failure Envelope as Principal Stress Difference versus Mean Normal Stress.
- c. Uniaxial Strain (UX) Test Results in terms of
 - (1) Axial Stress versus Axial Strain,
 - (2) Mean Normal Stress versus Volumetric Strain, and
 - (3) Principal Stress Difference versus Mean Normal Stress.
- d. Special Strain Path Test Results in a variety of the above mentioned Stress and Strain spaces.

Several plot files may be available for each type of plot listed above based, for example, on the number of confining stresses used in the TXC tests and the peak stress levels achieved during the IC and UX tests. The plot files are ASCII data files that contain the data sets, line types, axes labels, and titles required by DPLOT (Ref 4).

Gradation Database (GRAD)

This database contains the results of a standard sieve analysis of each soil material in the MPROP database. The GRAD database consists of three fields. These fields consist of a keyword link (GRAD_KEY) to a record in the MPROP database. The second field is a sieve size in millimeters, and the third field is the percent of the material by weight passing the sieve size in field 2. Several records (sieve sizes) are available in the GRAD database for every record in the MPROP database that pertains to a soil.

SEARCH AND RETRIEVAL CODE

The MPQ program was developed to assist in the management and distribution of the WES material property data. MPQ is a database query program written in the Clipper programming language that enables the user to easily locate and extract data from the Material Properties Database (MPROP, GRAD, and MPLOTS). MPQ consists of a main module that provides the user with five options and the procedures that perform the operations associated with each option. The five options are:

- (1) Create a query condition.
- (2) Modify the query condition created in Option 1,
- (3) Execute a query based on the conditions from Option 1 or Option 2,
- (4) Generate reports of the information found in Option 3, and
- (5) Exit MPQ.

Query conditions (Option 1) are constructed by specifying information in the query table to any desired extent. The query table consists of twenty-two fields from the MPROP database. The fields used for searching the database are marked by asterisks "*" in Table 1. Text strings are input for character fields, and ranges (upper and lower bounds) are input for numeric fields in the query table. Based on the information contained in the query table, macros are constructed to filter the MPROP database to identify all records that meet the query conditions. If the default query conditions are used for all fields in the query table, all records in the MPROP database are considered matches. If the default value for any field in the query table is used, that field is not used in constructing the search macros. This means that the scope of the query can range from every record in the MPROP database to one record based on the extent of the user specification in the query table.

Option 2 allows the query conditions to be modified to expand or restrict the scope of the query. Option 2 may be selected at any time after Option 1 has been used.

After the query conditions have been specified, the database may be searched by selecting Option 3. All records in the MPROP database are identified that satisfy the conditions of the query.

After searching the MPROP database for all records that match the query conditions, reports may be displayed by selecting Option 4. As each matching record is reported, gradation information in tabular form and mechanical property information in graphical form may be viewed. Gradation data are extracted from the GRAD database by finding all records in the GRAD database in which the GRAD_KEY field matches the GRAD_KEY field in the current record in the MPROP database. Similarly, available mechanical property plots for the current material are identified by keyword links (PLOT_KEY) between the MPROP database and the MPLOTS database. Plotting an individual mechanical property data file from within MPQ is accomplished automatically. Composite plots of mechanical property data files

can also be prepared by exiting MPQ and utilizing the DPLLOT program.

If the reports do not satisfy the user, the scope of the query can be modified by editing the query condition table (Option 2). The database is queried again by Option 3, and data are reported by selecting Option 4 as discussed above.

EXAMPLE

Preceding sections described the structure of the linked databases (MPROP, GRAD, and MPPLOTS) that comprise the Material Properties Database and introduced the function of the MPQ program. This section presents an example query.

To begin, Option 1 is selected, and the Query Table shown in Figure 2 is displayed on the PC screen. Note that all text fields are initially blank and all numeric ranges are zero by default. If the user exits the Query Table without changing the default values, the query conditions are such that all records in the MPROP database are matches when the query is executed.

For the example problem, we will set the query conditions to find all records with the SERIES KEY equal to CONWEB as shown in Figure 3. The CONWEB test series consisted of four tests performed at Fort Knox, KY (Ref 5). After typing CONWEB in the SERIES KEY entry box, the user returns to the main menu. The MPROP database is searched for records that satisfy the query conditions by selecting Option 3 on the Main Menu. After the search of the database is complete, a Query Results screen is displayed showing the total number of records in the database and the number of records that match the query conditions. For this example, the number of matching records for the example query is 4 matches out of the 41 records presently available.

After searching the MPROP database, reports for each matching record can be displayed by selecting Option 4 on the Main Menu. Each report screen displays the information contained in one matching record as shown in Figure 4 (the first record found that matches the example query conditions). In addition, the GRAD database is searched for available gradation data based on the keyword link between the MPROP and GRAD databases. Similarly, the MPPLOTS database is searched to compile a list of file names for mechanical property data for plotting. Messages are displayed on the report screen informing the user about the availability of gradation data and mechanical property plots as shown in the bottom left corner of Figure 4.

A prompt is displayed at the lower right corner of the screen asking the user if he wants to view the gradation data for the current material. The gradation table for this example is shown in Figure 5. Plots of mechanical properties may also be displayed. The menu shown in Figure 6 allows the user to display available mechanical property plots. Figures 7 through 10 are plots of the mechanical properties listed in Figure 6 for record 1 of the example query. A hard copy of each of the plots shown in Figures 7 through 10 may be obtained by a screen dump if desired.

After exiting the mechanical property plotting option, the first record that matched the query conditions is shown. The user may now move to the next record of the report, move back to the previous record of the report (or the last record if the current record is number one), or exit the report option without examining the remaining records. After viewing the remaining records or selecting the exit option on the report screen, the user returns to the main menu. The query conditions can now be modified to begin a new query or the Exit Option can be selected to terminate the MPQ session.

DPLLOT is a stand-alone graphics program that may be used to create overlay plots of several sets of material response data. After running MPQ to identify the data file names containing the desired material response data, DPLLOT can be executed to create overlay plots.

STATUS AND PLANNED MODIFICATIONS

The Material Property Database and computer code MPQ are documented in an evaluation draft report (Ref 6) that was distributed in September 1992 for review by a limited number of government agencies and private contractors. Comments from this evaluation will be incorporated into a final report that is planned for publication and distribution in the early Fall of 1993. This report will be in loose-leaf format to allow for easy updates. We are presently modifying the MPQ code to handle descriptions of cement-based materials and will insert material properties for selected cement-based materials into the database. This modification should be included in the Fall 1993 report. We also plan to continually augment the database with additional property sets for geologic and manmade materials of interest to CWE analysts and designers.

ACKNOWLEDGEMENT

The research reported herein was conducted as a part of the U.S. Army Corps of Engineers (USACE) Hardened Structures Work Package, Work Unit No. AT22-HS-001, "Statistical Evaluation of Dynamic Material Property Variations." The permission from the Office, Chief of Engineers, to publish this paper is gratefully acknowledged.

REFERENCES

1. "dBase III Plus," Version 1.0, Ashton-Tate, Inc, 1986.
2. "Clipper," Summer of 1987, Nantucket, Los Angeles, CA, 1987.
3. "Clipper 5.0," Nantucket, Los Angeles, CA, 1991.
4. Hyde, D. W., "HGRAPH," Version 5.1, US Army Engineer Waterways Experiment Station, Vicksburg, MS, 1990 (unpublished).
5. Hayes, P. G., "Backfill Effects on the Response of Buried Reinforced Concrete Slabs," Technical Report SL-89-18, US Army Engineer Waterways Experiment Station, Vicksburg, MS, September, 1989.

6. Slawson, T. R., and Walker, R. E., "User's Guide for Material Properties Database Search and Retrieval Program," Evaluation Draft, Applied Research Associates, Vicksburg, MS, September 1992; prepared for US Army Engineer Waterways Experiment Station, Vicksburg, MS.

Table 1. Structure for MPROP database.

Field	Field Name	Type	Description
* 1	SER_KEY	Character	Link to SERIES database
* 2	EVENT_KEY	Character	Link to EVENT database
3	PROJ_NAME	Character	Project name
* 4	TYPE_BF_U	Character	Type of material: "BF" = backfill "U" = undisturbed
* 5	SITE_LOC	Character	Site location
* 6	INSITU_L_T	Character	Insitu representation of properties: "L" = live stress "T" = total stress
7	LAY_NUM	Numeric	Layer number
8	DEPTH_TOP	Numeric	Depth to top of layer, meters
9	DEPTH_BOT	Numeric	Depth to bot of layer, meters
10	DEPTH_TGWT	Numeric	Depth from top of layer to water table (positive down)
* 11	WATER_FLAG	Character	Water table flag: "A" = GWT above layer "B" = GWT below layer "W" = GWT within layer
* 12	SAT_FLAG	Character	100% saturation point flag: A, B, or W as in 11
* 13	GEN_DES_M	Character	General description of material
* 14	USCS_CLASS	Character	USCS classification
* 15	WATER_CONT	Numeric	Water content, %
* 16	WET_DEN	Numeric	Wet density, Mg/m ³
* 17	DRY_DEN	Numeric	Dry density, Mg/m ³
* 18	SPECIFIC_G	Numeric	Specific gravity
* 19	P_AIR_VOID	Numeric	Percent air voids
* 20	DEG_SAT	Numeric	Degree of saturation, %
* 21	VOID_RATIO	Numeric	Void ratio
* 22	POROSITY	Numeric	Porosity
23	GRAD_KEY	Character	Keyword link to database
* 24	A_LL	Numeric	Liquid limit
* 25	A_PL	Numeric	Plastic limit
* 26	A_PI	Numeric	Plasticity index
27	COMP_NOTE	Character	Note on compaction
* 28	SEIS_VEL	Numeric	Seismic velocity, m/s
* 29	DET_PROB	Character	Type of properties: "D" = deterministic "P" = probabilistic
30	TXE_S_FACT	Numeric	TXE strength factor
31	PLOT_KEY	Character	Keyword link to plot file database

Notes: 1. * means that this Field can be used in a Query condition by MPQ.
2. If TYPE_BF_U = "U", then fields 6-12 should be populated.

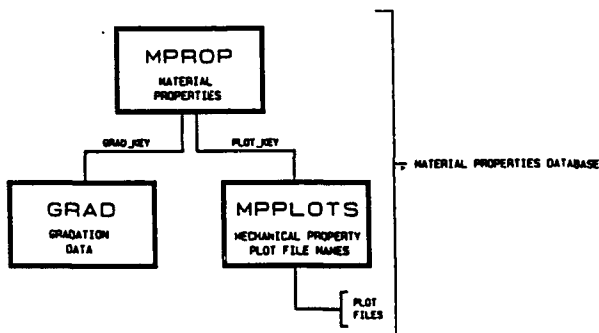


Figure 1. Material Property Database General Structure.

QUERY TABLE

SERIES KEY: EVENT KEY: TYPE_BF_U:

SITE LOCATION:

INSITU_Live_Total: WATER_FLAG: SAT_FLAG:

GENERAL DESCRIPTION OF MATERIAL:

USCS CLASSIFICATION: WATER CONTENT: 0.0 to 0.0

WET DENSITY: 0.00 to 0.00 DRY DENSITY: 0.00 to 0.00

SPECIFIC GRAVITY: 0.000 to 0.000 PERCENT AIR VOIDS: 0.00 to 0.00

DEG. OF SATURATION: 0.00 to 0.00 VOID RATIO: 0.0000 to 0.0000

POROSITY: 0.0000 to 0.0000 LIQUID LIMIT: 0.0 to 0.0

PLASTIC LIMIT: 0.0 to 0.0 PLASTICITY INDEX: 0.0 to 0.0

SEISMIC VELOCITY: 0 to 0 DETERMINISTIC OR PROBABILISTIC:

<ESC to exit>

Figure 2. The Query Table Showing the Default Conditions (Option 1).

QUERY TABLE

SERIES KEY: COMEB EVENT KEY: TYPE_BF_U:

SITE LOCATION:

INSITU_Live_Total: WATER_FLAG: SAT_FLAG:

GENERAL DESCRIPTION OF MATERIAL:

USCS CLASSIFICATION: WATER CONTENT: 0.0 to 0.0

WET DENSITY: 0.00 to 0.00 DRY DENSITY: 0.00 to 0.00

SPECIFIC GRAVITY: 0.000 to 0.000 PERCENT AIR VOIDS: 0.00 to 0.00

DEG. OF SATURATION: 0.00 to 0.00 VOID RATIO: 0.0000 to 0.0000

POROSITY: 0.0000 to 0.0000 LIQUID LIMIT: 0.0 to 0.0

PLASTIC LIMIT: 0.0 to 0.0 PLASTICITY INDEX: 0.0 to 0.0

SEISMIC VELOCITY: 0 to 0 DETERMINISTIC OR PROBABILISTIC:

<ESC to exit>

Figure 3. The Query Table Showing an Entry in the SERIES KEY Field (Option 1).

MPROP DATABASE QUERY PROGRAM REPORT # 1

Project Name: BACKFILL EFFECTS ON RESPONSE OF BURIED REINFORCED CONCRETE SLABS

SITE LOCATION: RODGERS HOLLOW, FORT KNOX, KY

Series Key: COMEB Event Key: COMEB 1 & 2 Type of Matl: BACKFILL

Layer No: 1 Depth to Top & Bottom of Layer (m): 0.00 2.74

Depth from Top of Layer to Water Table (m): N/A GWT Below Layer

100% Sat. Below Layer Rep of Properties: TOTAL

Material: BROWN GRAVELLY CLAY USCS: CL

Water Content (%): 22.5 Densities (g/cc): Wet 1.97 Dry 1.60

Specific Gravity: 2.710 % Air Voids: 4.00 Degree of Saturation: 89.80

Void Ratio: 0.6940 Porosity: 0.4100 Seismic Vel. (m/s): 335

Liquid Limit: 38.0 Plastic Limit: 19.0 Plasticity Index: 19.0

Compaction Note: N/A

Properties are: DETERMINISTIC TXE Strength Factor: N/A

GRADATION DATA ARE AVAILABLE

MATERIAL PROPERTY DATA ARE AVAILABLE

Do You Want Gradation Information? <Y/N> Y

Figure 4. Report Screen.

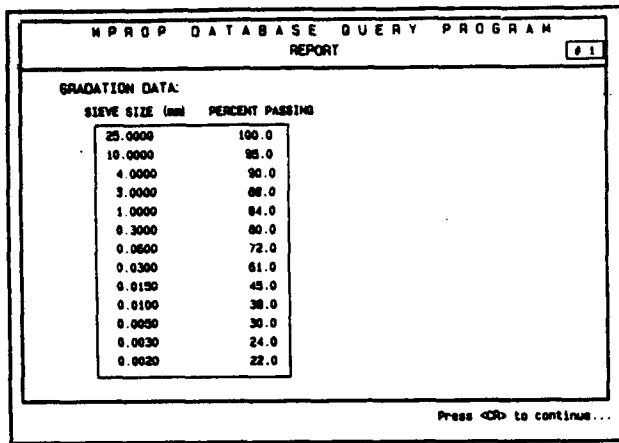


Figure 5. Example Gradation Data Report.

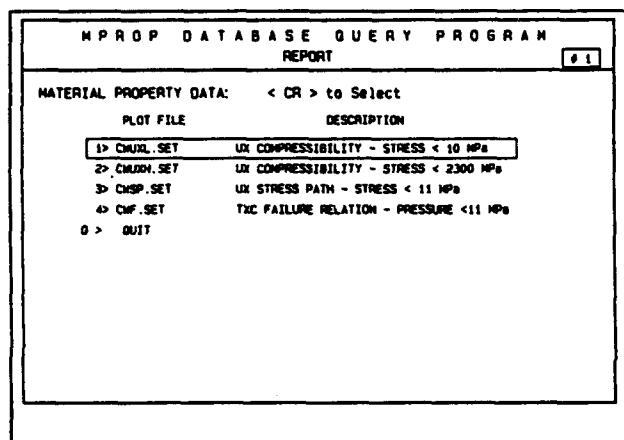


Figure 6. Available Mechanical Property Plots.

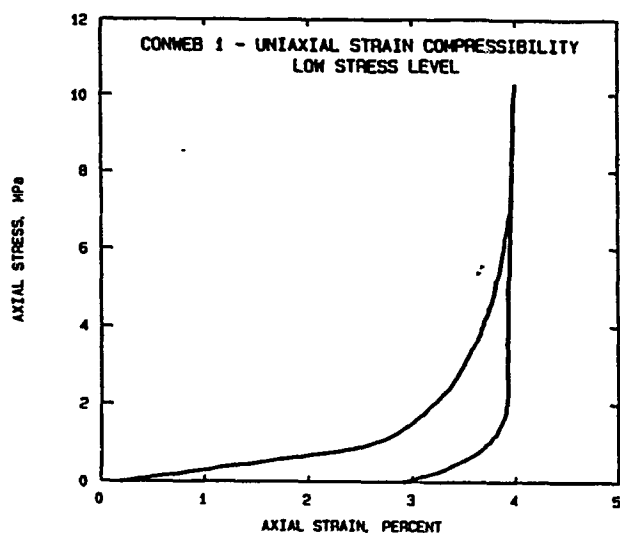


Figure 7. Example Uniaxial Strain Compressibility at a Low Stress Level.

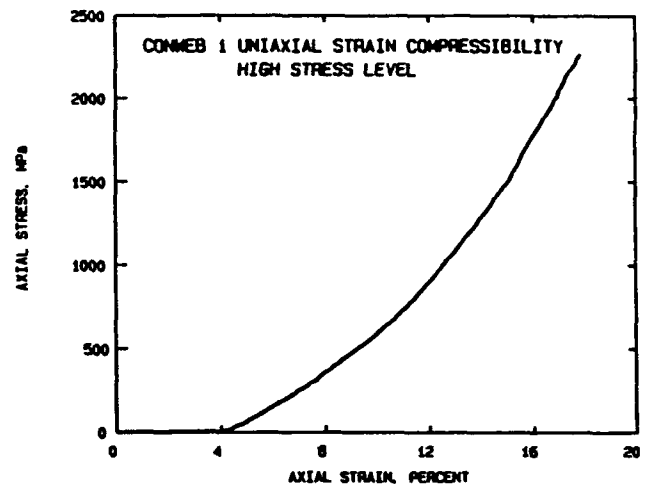


Figure 8. Example Uniaxial Strain Compressibility at a High Stress Level.

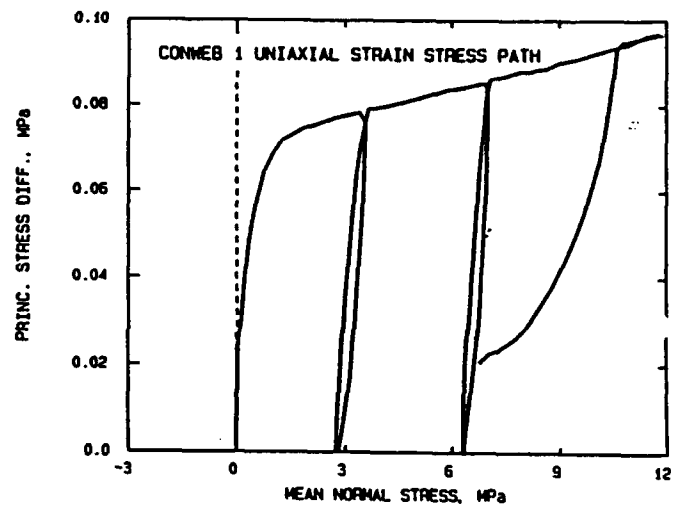


Figure 9. Example Uniaxial Strain Stress Path.

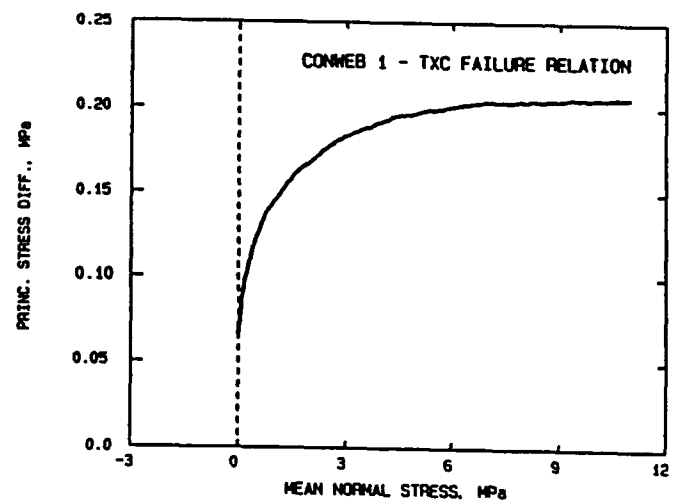


Figure 10. Example Triaxial Compression Failure Relation.

Effective Stress Constitutive Models for Saturated & Partially Saturated Soils

H.D. Zimmerman, Y.M. Ito, J.A. Carney

California Research & Technology, Titan Corporation, Chatsworth, CA

ABSTRACT

California Research & Technology (CRT) has supported the U.S. Army Engineer Waterways Experiment Station (WES) in development and evaluation of material models and numerical simulation techniques for predicting the ground shock environment due to explosive-produced loading conditions from buried conventional munitions. An effective stress constitutive formulation is described which is intended for modeling the response of geologic materials (rocks and soils) subjected to explosive loading. This paper will discuss the advantages of employing such an approach in the modeling of saturated and partially saturated soils. Comparisons of model response for dry, partially saturated and fully saturated conditions and the effects of model response and the importance of shear-volume coupling on calculated ground shock will be presented.

BACKGROUND

Effective stress model formulations were originally developed and implemented into CRT numerical codes (Frederickson, Zimmerman, Carney, 1989) and validated against SRI International lab-scale saturated rock HE experiments (Zimmerman, Carney, & Ito, 1992). This constitutive model has been implemented into the SABER/CWE-family of large-strain finite element codes specifically designed for calculating ground shock from conventional munitions (Akers & Stelter, 1991), (Zimmerman, Shimano, & Ito, 1992).

This effective stress approach involves explicit consideration of the portions of the material stress carried by the porous soil or rock skeleton and by the fluid/gas phase constituents. The effective stress is that portion of the material stress supported by the porous skeleton, and the portion supported by the fluid/gas phase constituents is termed pore pressure. There are several advantages to employing such an

approach in the modeling of saturated and partially saturated geologic materials; 1) Reduced modeling effort and increased model fidelity, 2) Reduction of uncertainty in modeled material response, 3) Extension of modeled response regime beyond regime of laboratory testing or other available data used in model fitting.

EFFECTIVE STRESS CONSTITUTIVE MODEL

Geologic materials are generally multiphase materials, consisting of matter in solid, liquid, as well as gaseous states. The solid portion of such a multiphase material exists as a complex assemblage of particles of various shapes and sizes forming a porous skeleton. The pore volume in this skeleton is occupied by a mixture of fluid and gases.¹ In performing the task of developing a constitutive model for a multiphase geologic materials, it will be seen convenient to break the total stress tensor into two components

$$\sigma_t = \sigma_e + MU \quad [1]$$

where σ_t is the total state of stress of the material,² U is the pressure of the pore air/fluid, M is the matrix equivalent of the Kronecker delta function, and σ_e is termed the effective stress, a measure of the loads carried by the skeleton. This relationship, first proposed in 1923 by Terzaghi implicitly defines the term effective stress as employed herein.

Consider first the case of a porous material loaded in drained conditions. In drained conditions, the pore air and fluid are allowed to drain away, thereby preventing the development of pore pressure. In this case, loads are supported by the solid skeleton alone via a complex state of intergranular stresses. For a control volume containing a statistically relevant number of

¹Gas phase matter will hereafter be referred to simply as "air".

²Compressive normal stresses are positive.

particles, traction's supported by this very complex structural system are characterized by the effective stress tensor alone.

Since effective stress is expressed relative to a volume of material consisting both of solids and pore space, the "average" state of stress in solid material is somewhat higher than the effective stress. The average state of stress of solids in the drained material, σ_s is assumed to be

$$\sigma_s = \sigma_e / (1 - \phi) \quad [2]$$

where ϕ is the (porosity) volume fraction of the material which is occupied by pore space. Note that this relationship assumes that the area fraction of pore space on any plane is equivalent to the volume fraction of the pore space, an assumption which strictly holds only for isotropic materials.

Next consider the case of a saturated porous material, loaded in undrained conditions. Under these conditions, control volume tractions are supported by "partial" stress contributions from solid and pore fluid constituents as follows:

$$\sigma_t = \sigma_s(1 - \phi) + \phi MU \quad [3]$$

Substituting Eq. [1] for σ_t , the average state of stress of the solids in a saturated material in undrained conditions is seen to have an additional contribution from the pore pressure.

$$\sigma_s = \sigma_e / (1 - \phi) + MU \quad [4a]$$

The hydrostatic component of the solid stress is

$$P_s = P_e / (1 - \phi) + U \quad [4b]$$

Where P_s and P_e are the solid and effective pressures, respectively. As in the case of the drained material, the effective stress tensor is again seen to be a measure of the loads carried by the intergranular state of stress in the solid skeleton expressed relative to the entire control volume of material.

Equations [3] and [4] are the first two of three relationships which together define the equilibrium between the material constituents and the external tractions on a control volume. Physically, Eq. [4b] defines the extent which the intergranular state of stress causes the average pressure of solid material

to be higher than the pore pressure. The remaining equilibrium relationship,

$$P_a = P_f = U \quad [5]$$

simply mandates that any air occupying the pore space is in pressure equilibrium with pore fluid. The satisfaction of Eqs. [4b] and [5] is central to the operation of the effective stress constitutive model in the numerical code.

The uncertainties in mechanical response of saturated geologic materials are largely attributable to the uncertainty in response of the porous skeletons since the behavior of the water/gas and solid mineral constituents of geologic materials is quite well understood. Because the effective stress approach considers the role of the skeleton and the constituents explicitly, the portion of the material response which is well understood is automatically included in the modeling.

DEMONSTRATION OF MODEL

Use of the effective stress response requires development of three separate constitutive response models, 1) the dry or drained skeleton, 2) the solid grain, and 3) the fluid behavior. Once the grain and fluid behaviors are fit for a given type of material only its drained response needs to be fit to provide a complete description of the material's constitutive model response. Well-developed constitutive response laws for the water/gas and solid grain (quartz) constituents, are used. No additional fitting of solid or fluid/gas constituents is required to use the effective stress model. After the drained response is developed it can be used to predict material response over all saturation ranges, from totally dry to partially saturated to fully saturated. All that is required is the specification of air filled void or degree of saturation.

Total stress responses (under uniaxial strain) of a 30.5% porous soil at three levels of airfilled void ($\phi_a = 0, 5, \& 30.5\%$) were calculated with effective stress theory (see Figure 1). At low pressures, dry sand, $\phi_a = 30.5\%$, is very hysteretic and relatively strong (i.e. it can support significant stress deviators). For the partially saturated response, $\phi_a = 5\%$, no pore pressure can develop, until all of the air-filled porosity is crushed out (marked as saturation in the figure). Until saturation, all of the load is carried by the drained skeletal response. At saturation, almost all of the load is carried by the pore pressure, and the development of any

significant additional strength is precluded. Because the load carried by effective stress is small, partially saturated sand is relatively non-hysteretic. For the same reason, saturated sand has a low shear bearing capacity and virtually no hysteresis, as indicated in the pressure-strain curve, and stress path. There are several key differences in the dry, and partially/totally saturated responses. Greater volumetric compaction (due to compression of air-filled porosity), accompanied by higher material strength is attained at lower levels of saturation.

It is illustrative to demonstrate the behavior of the effective stress model for partially saturated conditions under a uniaxial strain loading, Figure 2. Note that until air-filled porosity is crushed out (marked as saturation) no pore pressure can develop. The initial volume fraction of air-filled porosity and air filled fraction of pore volume are given by:

$\phi=31.3\%$	Porosity
$S=85\%$	Saturation
$\phi_a=(1-S)\phi=4.8\%$	Air-Filled Void
$1-S=15\%$	Fraction of Air-Filled Porosity

The volumetric strain at the saturation point is in agreement with this value of air-filled porosity as well as the constituent strain. After saturation, most of the load is carried by the pore pressures, effective stress and strength increase only slightly. Neither the grain nor pore response have any hysteresis. Hysteresis in the total pressure is seen to stem from the stiff unloading effective stress modulus.

A shear-volume coupled drained response model that is capable of capturing strain path sensitive hysteresis (Zimmerman et al., 1993) is employed for the skeletal response. Effective stress mechanics with shear-volume coupled treatments of the porous material skeleton are crucial in determining the strength of saturated and partially saturated soils under a wide variety of loading/unloading conditions. The effective strength of saturated materials may be reduced or dramatically increased, depending on the strain path and amount of dilatancy or shear induced compaction that occurs in the skeletal response.

The importance of shear-volume coupling in determining the residual strength is illustrated in Figure 3. Here, the calculated hydrostatic and deviatoric response for uniaxial strain load followed by spherically divergent unload ($d\epsilon_2/d\epsilon_1 = -1$), for drained models with and without shear volume

coupling is presented. The non dilatant model (no shear-volume coupling) is seen to produce *liquefaction* i.e., strength reduces to zero while significant pressures remain in the material. On the other hand, the strain path sensitive model dilates on unload, resulting in *cavitation*, i.e. a loss of pore pressure resulting in all load being carried by the drained skeleton. These affects can drastically effect the duration of free-field velocity waveforms, and peak displacement.

FREE-FIELD GROUND SHOCK

The role of strain path dependent hysteresis on calculated ground shock has previously been investigated in dry soil (Zimmerman et al., 1993). The role of path dependence in an effective stress formulation was investigated here by conducting a series of 1-D spherical fully contained hydrocode calculations of the detonation of 15.4 lbs of C-4 explosive in partially saturated soil.

Calculated free-field displacement waveforms using drained response models with shear-volume coupling (enhanced model) and without shear volume coupling (non-dilatant model) are presented in Figure 4. The non-dilatant model drastically overestimates the duration of the velocity waveform, due to *liquefaction* on unloading. The enhanced model, which retains strength on unloading, significantly reduced the positive phase velocity pulse duration.

CONCLUSION

A multi-phase effective stress constitutive model which can provide better response fidelity when used with drained skeletal formulations that are capable of capturing the dominant physical process of strain path sensitive hysteresis has been presented. The multi-phase effective stress approach is capable of simulating various levels of saturation and important strain path dependent phenomena such as *liquefaction* and *cavitation*, which cannot be predicted by single-phase total stress formulation.

ACKNOWLEDGMENT

The work reported herein was conducted by California Research & Technology Division, Titan Corporation, and the U.S. Army Engineer Watways Experiment Station (WES) for Headquarters, U.S. Army Corps of Engineers under Hardened Structures Research Program Work Units AT22-HS-005 and

AT40-HS-003. The permission from the Office, Chief of Engineers, to publish this paper is gratefully acknowledged.

References

S.A. Akers, & J. Stelter, "SABER-PC/CWE: A Ground-Shock Software Package for The PC" in Proceedings of the Fifth International Symposium on the Interaction of Conventional Munitions with Protective Structures, page N3-N10, NATO Session, Mannheim FRG, 22-26 April 1991

A.A. Frederickson, H.D. Zimmerman, & J.A. Carney, "Effective Stress Constitutive Models for Computational Applications", DNA-TR-89-18, Defense Nuclear Agency, Alexandria, Virginia, December 1989.

K. Terzaghi. 1923. "Die Berechnung der Durchlässigkeitsziffer des Tones aus dem Verlauf der hydrodynamischen Spannungserscheinungen".

H.D. Zimmerman, Y.M. Ito, J.A. Carney, & J.E. Windham, ABSTRACT "Effects of Enhanced Constitutive Models on Calculated Free-Field Ground Shock", Sixth International Symposium on Interaction of Nunnuclear Munitions with Structures, May 1993.

H.D. Zimmerman, R.T. Shimano, & Y.M. Ito, "Early-Time Ground Shock From Buried Conventional Explosives: Users Guide for SABER-PC/CWE", I.R. SL-92-1 Structures Lab U.S. Army Engineer Waterways Experiment Station, Vicksburg, Mississippi, August 1991.

H.D. Zimmerman, J.A. Carney, & Y.M. Ito, "Computational Application of Effective Stress Constitutive Model", DNA-TR-91-192, Defense Nuclear Agency, Alexandria, Virginia, June 1992.

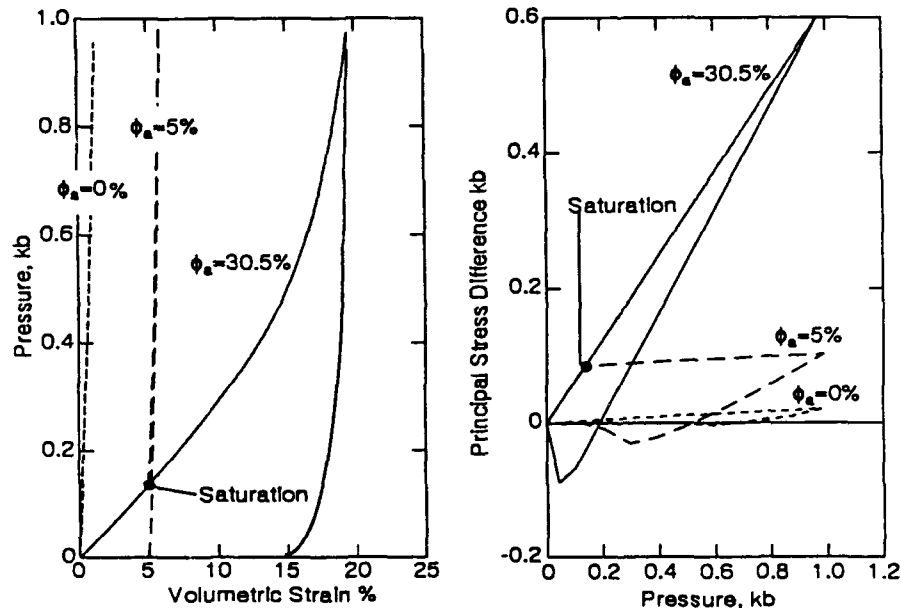


Figure 1. Sand Response obtained with effective stress theory for three air filled void ($\phi_a=0$, 5, and 30.5%) levels for 30.5% porous sand.

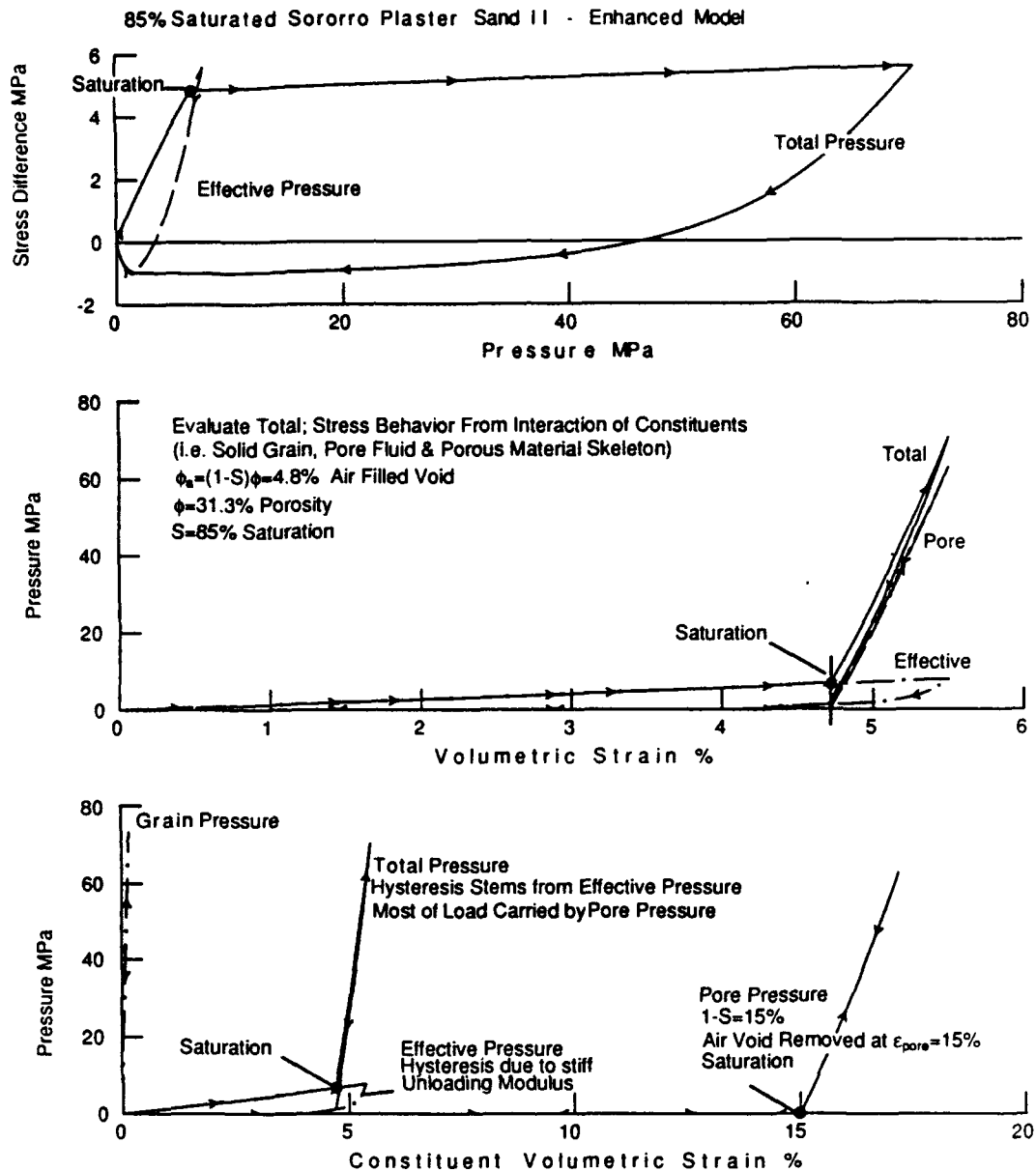


Figure 2. Undrained Uniaxial Strain Response of a 85% Saturated, 31.3% Porous Sand

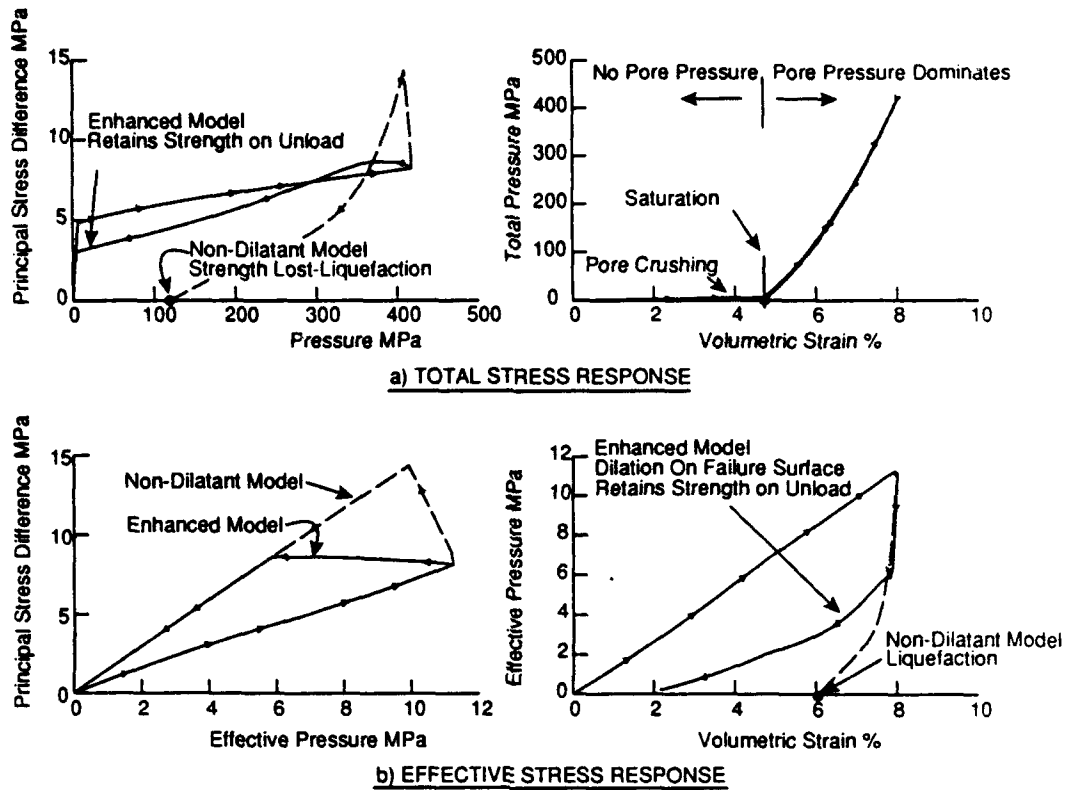


Figure 3. a) Total Stress Response and b) Effective Stress Response for Uniaxial Strain Load Followed by a Spherically Divergent Unloading Path ($d\epsilon_2/d\epsilon_1 = -1$), Showing Effects of Strain Path Sensitive Hysteresis on Residual Strength.

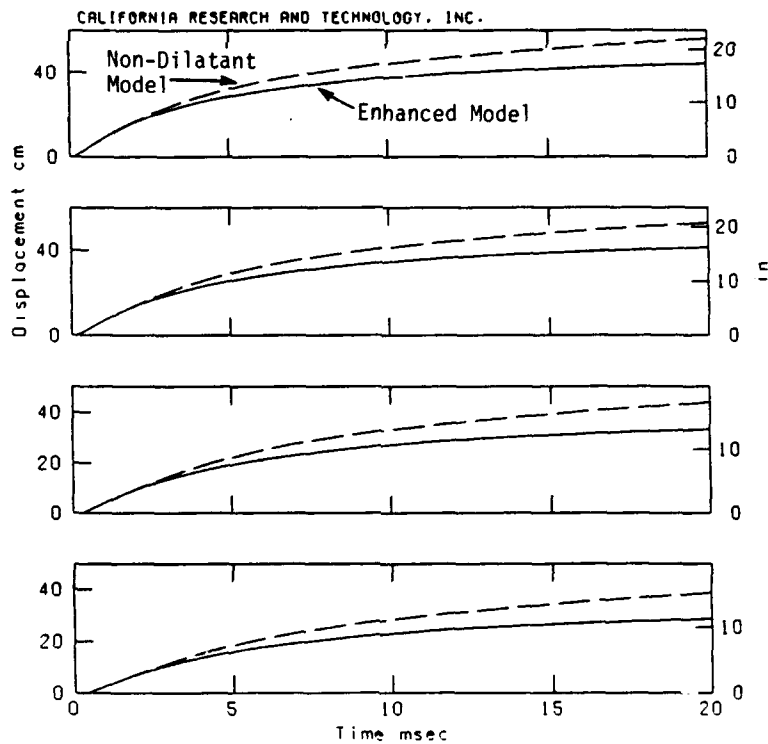


Figure 4. Comparative displacement waveforms, 15.4 lb of C-4 in partially saturated sand using a shear volume coupled and nondilatant model (range = 0.43, 0.46, 0.59, and 0.67 meters from charge CG).

STRAIN-RATE EFFECTS IN UNSATURATED SOILS

by

George E. Veyera, Ph.D.
Associate Professor
Department of Civil and Environmental Engineering
University of Rhode Island
Kingston, RI 02881 USA

Wayne A. Charlie, Ph.D.
Professor
Department of Civil Engineering
Colorado State University
Ft. Collins, CO 80523 USA

C. Allen Ross, Ph.D.
Emeritus Professor
University of Florida
Graduate Engineering
and Research Center
Eglin AFB, FL 32542 USA

ABSTRACT

The Split-Hopkinson Pressure Bar (SHPB) at the AF Civil Engineering and Support Agency, Air Base Survivability Branch (AFCEA/RACS) Tyndall AFB, Florida was used to study the uniaxial stress-strain behavior of compacted moist soils. Soils were subjected to one-dimensional, undrained, confined compression loading at high strain rates (1000/sec and 2000/sec). Three soils, Eglin Sand, Tyndall Sand and Ottawa 20-20 Sand were tested. Each sand was compacted to a constant dry density at varying degrees of saturation between 0% (air dry) and 100% (fully saturated). General features of the uniaxial stress-strain results indicate: a) an initially steep loading portion associated with the initial rise in the loading pulse which appears to be strain rate independent; b) the slopes of each curve are about the same after the initial steep portion up to lock-up; c) the initial saturation affects the point at which lock-up occurs; and d) after lock-up the slope is approximately that of water. Lock-up refers to the sharp increase in the slope indicating a stiffening behavior at some compressive strain after the initial steep loading portion of the curve. The results suggest that the stress-strain response is dominated by the water phase from the lock-up strain and beyond, while the soil skeleton dominates the response from the start of loading up to the lock-up strain. It appears that there may be some strain rate effects, however, the data are insufficient to adequately demonstrate this and further investigations are required.

The research described in this report has demonstrated that the SHPB system is a viable technique for high strain rate dynamic geotechnical testing of unsaturated, saturated and dry soils, and provides a framework for conducting further studies using the SHPB with soils. While the saturation dependent uniaxial stress-strain behavior observed in this study has been theorized and hypothesized in the past by other researchers, these results appear to be the first detailed measurements of this phenomenon for undrained uniaxial confined compressive loadings at high strain rates.

INTRODUCTION

Current empirical relationships for predicting soil pressure as a function of standoff distance from a buried explosive typically have a variation of $\pm 50\%$ or more and use material properties data based on conventional weapons effects in dry soils. However, most soils, whether naturally deposited or placed as select engineered fill, exist with moisture at saturations somewhere between 0% and 100%. The reaction of a structure to a specified loading can usually be determined, however, there are no theoretical, numerical

or empirical methods available for predicting the groundshock energy arriving at a structure in unsaturated soils. This arises from the fact that dynamic load transfer mechanisms in soils are not well defined especially when moisture is present. In addition, there is little if any actual data available for the transient dynamic behavior of unsaturated soils, particularly at high strain rates.

The ability of a soil to transmit applied dynamic stresses (energy) is of particular interest with respect to military protective construction and survivability designs. Typical engineering analyses assume that little or no material property changes occur under dynamic loadings and in addition, analyses do not account for the effects of saturation (moisture conditions) on the stress-strain behavior of soils. This is primarily due to an incomplete understanding of soil behavior under transient loadings and uncertainties about field boundary conditions. Results from field and laboratory tests with explosive detonations in soils have shown that material property changes do in fact occur and that variations in soil stiffness (or compressibility) significantly affect both dynamic and static stress behavior. The research described in this paper is important since there are currently no theoretical, empirical or numerical methods available for predicting the dynamic uniaxial stress-strain response of unsaturated soils from loading environments such as those produced by conventional weapons effects.

Recent research (1-8) using the SHPB facility at AFCEA/RACS to study unsaturated soil behavior has shown that: (a) the presence and amount of moisture significantly affects the dynamic and static response of soil specimens; and (b) the amount of stress transmitted, stiffness, wave speed and compressibility in unsaturated soils varies with the amount of moisture present during compaction. Experimental evidence from a number of researchers suggests that such behavior for both dynamic and static loading conditions can be attributed to variations in soil compressibility and soil microstructure as a result of conditions during compaction including the compaction method used and the amount of moisture present during compaction (1-4, 6-17). While the moisture effects on soil behavior as described above have been observed experimentally, a clear and concise explanation of the phenomenon is not currently available. This is primarily due to the fact that the multiphase behavior of unsaturated soils, the interaction between the individual phases (air, water and solid), and the mechanics of load transfer mechanisms in soils are not well understood.

The research described herein was performed as a part of the 1992 Summer Faculty Research Program (SFRP) (18) to investigate the undrained behavior of unsaturated soils subjected to dynamic confined uniaxial compression loading at high strain rates using the

Split-Hopkinson Pressure Bar (SHPB) at AFCESA/RACS. With reference to this research, the term "dynamic" defines large amplitude, high strain rate loadings as opposed to the low strain oscillatory frequency pulses used in wave attenuation studies. The results of studies such as that described herein will lead to a better fundamental understanding of the load transfer mechanisms and constitutive relationships for unsaturated soils and have direct applications to groundshock prediction techniques including stress transmission to structures.

BACKGROUND

Differences in the stress-strain response for dry and moist soils under both dynamic and static one-dimensional loading conditions have been observed experimentally by a number of researchers at various strain rates. Farr and Woods (19) accurately describe the current state of affairs with regards to the uniaxial stress-strain behavior of soils: "It has long been recognized that the one-dimensional or uniaxial strain response of most soils subjected to high intensity transient loads differs from the response measured under static conditions. As the time to peak pressure decreases, most soils exhibit a stiffening of the loading stress-strain response. The stiffening is usually referred to as a time or loading rate effect. Some researchers (20, 21) have suggested that, as the time to peak pressure approaches the submillisecond range, a drastic increase (up to tenfold) in the loading constrained modulus occurs for partially saturated granular soils under unconsolidated-undrained conditions. The existence of this effect has been the subject of much debate." A number of researchers have attempted to address the controversy surrounding the issue of strain rate effects in both dry and unsaturated soils.

High pressure static uniaxial confined compression tests were conducted on moist specimens of sandy silt at various dry densities by Hendron et al. (22). They observed increases in stiffness with increasing saturation and from their results, concluded that the key variables in uniaxial stress-strain behavior are void ratio and saturation. Wu et al. (23) tested moist silty soils at small strains in the resonant column device and found a significant increase in the dynamic shearing modulus for specimens compacted moist at saturations in the range of from 5 to 20 percent. Whitman (24) indicated that rate effects become very important at submillisecond loading times and theorized that at high saturations, the pore phase of the soil is much stiffer than the soil skeleton (pore fluid compressibility dominates), while at lower saturations the skeleton matrix is stiffer than the pore phase (skeleton compressibility dominates). Jackson et al. (25) conducted unconsolidated-undrained one-dimensional confined compression tests on several different air dry soils at various loading rates and observed loading rate effects at submillisecond loading times, with the constrained modulus increasing by an order of magnitude in going from 0.1 to 1.0 ms rise time to peak stress. Farr and Woods (19) used a modified version of Jackson et al.'s (25) experimental apparatus to conduct similar tests on moist carbonate sand. They observed a progressive stiffening in the stress-strain response with faster loading times to peak stress and noted rate dependent effects occurred even at multi-second loading rates for the carbonate sand.

Limited research has also been conducted using the Split-Hopkinson Pressure Bar to study the uniaxial stress-strain behavior of compacted moist soil under one-dimensional confined compression loading at high strain rates (26-28). The results of these studies indicated that the uniaxial stress-strain response is primarily governed by the initial gas filled porosity of the soil specimen, and that strain-rate effects did not occur at strains less than the initial gas filled porosity. However, it should be noted that the specimen container boundary conditions were not for completely undrained conditions and therefore, this may have had

significant effects on the results. The SHPB at AFCESA/RACS (1-8) has also been used to study stress transmission characteristics of unsaturated soils for conditions of undrained confined uniaxial compression. Detailed information about the SHPB device at AFCESA/RACS and results of recent investigations to study dynamic soil behavior can be found in the references cited above.

EXPERIMENTAL INVESTIGATION

Three different granular soils were tested using the AFCESA/RACS SHPB facility: Eglin Sand (from Eglin AFB), Tyndall Sand (from Tyndall AFB), and Ottawa 20-30 Sand (commercially available from the Ottawa Silica Company). Representative soil samples were randomly obtained for analysis and testing from bulk quantities of each material using standard sample splitting procedures. The Eglin Sand is a medium to fine, angular to subangular Sand with about 7% fines; the Tyndall Sand is a fine, uniform, subangular sand with no fines; and the Ottawa 20-30 Sand is a uniformly graded, subrounded to rounded, medium sand with no fines. Various physical index properties data were obtained for each sand and the results are summarized in Table 1. The compacted void ratios and dry densities utilized in the research are also included in Table 1. A detailed description of specimen preparation and operation of the SHPB is given in References (4,18).

RESULTS AND DISCUSSION

Figures 1, 2, and 3 show typical SHPB uniaxial stress-strain results for the Eglin, Tyndall and Ottawa 20-30 sands, respectively obtained at a strain rate of 1000/sec. Figure 4 shows two high strain-rate tests for pure water obtained at approximately the same strain rates. There are some general features observable in the stress-strain data: a) an initially steep loading portion of the curves which is probably associated with the initial rise in the loading pulse and appears to be strain rate independent; b) the slopes of each curve are about the same after the initial steep portion up to the lock-up strain; c) the initial saturation affects the point at which lock-up occurs (the higher the initial saturation, the smaller the strain required); and d) after lock-up the curves exhibit a stiffening response with a slope approximately that of water (Figure 4). In comparing the test results at different strain rates, it appears that there may be some strain rate effects, however, the data are insufficient to adequately demonstrate this and further investigations are required.

In comparing the three different soils together it can be seen that: a) the slopes of the curves after the initial steep portion are nearly identical regardless of the initial saturation and soil type; b) the initiation of the lock-up strain is somewhat different for each soil at the same saturation; c) lock-up was not developed in the Ottawa 20-30 sand below 80% saturation. Differences in the basic features between the curves when comparing the three different soils are most likely due to differences in grain size characteristics (i.e., size and distribution).

The term "lock-up" as used herein refers to the sharp increase in the slope indicating a stiffening behavior of the stress-strain curve at some compressive strain (after the initial loading portion of the curve). Since the slope is approximately double that obtained for SHPB tests conducted on water (theoretical predictions show that the saturated soil-water mixture slopes are approximately twice that of water due to the density and modulus differences) the lock-up strain represents a condition of full saturation in the soil due to a reduction in void space. Therefore, the results suggest that the stress-strain response is dominated by the water phase (saturated soil-water mixture) from the initiation of the lock-up strain and beyond, while the soil skeleton (unsaturated soil-water

mixture or soil-air mixture if dry) dominates the response from the start of loading up to the lock-up strain. Lock-up was not developed at lower saturations even at large strains, which indicates that insufficient pore space reduction occurred (i.e., not enough compressive strain was developed).

Therefore, larger amplitude stress loadings (higher compressive strains) with longer pulse lengths need to be applied so that the stress-strain response at the lower saturations can be determined.

Table 2 shows a comparison of the approximate measured lock-up strains estimated from the SHPB data (Figures 1, 2, and 3) and the theoretical compressive strain required to reach full saturation (i.e., lock-up). Stress-strain curves for the 2000/sec strain rate were omitted due to length requirements of the paper. The theoretical calculations only account for the amount of air-filled void space in each soil based on initial void space and initial saturation. The theoretical calculations of lock-up generally over estimate the measured compressive strain at lock-up. However, the interaction of the various components of the soil-water mixtures are not accounted for in these calculations. Since the soil-water mixture represents a multi-phase material, a complete description of the problem becomes very complex since in general there are four different interacting components contributing to the bulk response: a) the soil skeleton; b) the pore air, c) the pore water; and d) the individual grain stiffnesses. While the individual stress-strain response of each component can be determined separately, it is their interrelationship that determines the overall behavior. A further complicating factor is that the dominance of any one (or combination) of these components changes depending upon the initial conditions and those during loading (i.e., strain magnitude). However, these interrelationship are not well defined or understood, particularly for transient dynamic loading conditions.

SUMMARY

This investigation sheds some new light (and poses new questions) on the undrained dynamic behavior of unsaturated soils at high strain rates and represents an important first step towards establishing an understanding of this phenomenon. In addition, this research has also demonstrated that the SHPB system is a viable technique for high strain rate dynamic geotechnical testing of unsaturated, saturated and dry soils, and provides a framework for conducting further studies using the SHPB with soils. While the saturation dependent uniaxial stress-strain behavior observed in this study has been theorized and hypothesized in the past by other researchers, these results appear to be the first detailed measurements of this phenomenon for undrained uniaxial confined compressive loadings at high strain rates.

ACKNOWLEDGEMENTS

The authors acknowledge and are very appreciative of financial and laboratory support of the Air Base Survivability Branch, HQ AF Civil Engineering Support Agency, Tyndall AFB, FL.

REFERENCES

1. Charlie, W. A. and Pierce, S. J., (1990), "High Intensity Stress Wave Propagation in Unsaturated Sands," *Report No. ESL-TR-90-12, Under Contract No. F49620-87-0004*, AFESC, Engineering Research Division, Tyndall AFB, FL, Sept., p. 146.
2. Charlie, W. A., Ross, C. A., and Pierce, S. J., (1988), "Split-Hopkinson Pressure Bar Testing of Unsaturated Sand," *Geotechnical Testing Jnl*, GTJODJ, Vol. 13, No. 4, pp. 291-300.
3. Fitzpatrick, B. J. and Veyera, G. E., (1992), "The Microstructure of Compacted Moist Sand and Its Effect on Stress Transmission," *Report No. ESL-TR-92-01 Under Contract Number F49620-88-C005315B5881-0378, AFESC/RDCM*, Tyndall AFB, FL, p. 200.
4. Ross, C. A., (1989) "Split-Hopkinson Pressure Bar Tests," *Report No. ESL-TR-88-2*, AFESC/RDCM, Tyndall AFB, FL, 80 p.
5. Ross, C. A., Nash, P. T., and Friesenhahn, C. J., (1986), "Pressure Waves in Soils Using a Split-Hopkinson Pressure Bar," *Report No. ESL-TR-86-29*, AFESC, Tyndall AFB, FL, July, p. 83.
6. Veyera, G. E., (1989), "Static and Dynamic Behavior of Compacted Unsaturated Sands," *Final Report to US AFOSR Under Contract No. F49620-87-0004*, AFESC/RDCM, Tyndall AFB, FL, Sept., pp. 451, :45-20.
7. Veyera, G. E. and Fitzpatrick, B. J., (1990), "A Specimen Preparation Technique for Microstructural Analysis of Unsaturated Soils," *Final Report to US AFOSR Under Contract No. F49620-88-C-0053*, Bolling AFB, Washington D.C., Sept., 20 p.
8. Wilbeck, J. S., Thompson, P. Y., and Ross, C. A., (1985), "Laboratory Measurement of Wave Propagation in Soils," *Proc. of the 2nd Symp. on the Interaction of Non-Nuclear Munitions With Structures*, P. C. Beach, FL, pp. 460-465.
9. DeGregorio, V. B., (1990), "Loading Systems, Sample Preparation, and Liquefaction," *Jnl. of Geotechnical Engineering*, Vol. 116, No. 4, ASCE, pp. 805-821.
10. Ladd, R. S., (1977), "Specimen Preparation and Cyclic Stability of Sands," *Jnl. of the Geotechnical Engineering Division*, ASCE, Vol. 103, No. GT6, pp. 535-547.
11. Lindholm, U. S., (1971), "High Strain Rate Tests," *Measurement of Mechanical Properties, Vol. V Part 1*, Interscience Publishers, New York, NY, pp. 200-271.
12. Mitchell, J. K., (1976a), *Fundamentals of Soil Behavior*, John Wiley and Sons, New York, NY.
13. Mitchell, J. K., (1976b), "The Influences of Sand Fabric on Liquefaction Behavior," *Report Number S-76-5*, U.S. Army Waterways Experiment Station, Vicksburg, MS, pp. 1-38.
14. Mulilis, J. P., Seed, H. B., Chan, C. K., Mitchell, J. K., and Arulanandan, K., (1977), "Effects of Sample Preparation Technique on Sand Liquefaction," *Jnl. of the Geotechnical Engineering Division*, ASCE, Vol. 103, No. GT2, pp. 91-108.
15. Oda, M., (1972a), "Initial Fabrics and Their Relations to Mechanical Properties of Granular Material," *Japanese Society of Soil Mechanics and Fndtn. Engineers*, Tokyo, Japan, Vol. 12, No. 1, pp. 17-36.
16. Oda, M., (1972b), "The Mechanism of Fabric Changes During Compressional Deformation of Sand," *Japanese Society of Soil Mechanics and Fndtn. Engineers*, Tokyo, Japan, Vol. 12, No. 2, pp. 1-18.
17. Richart, F. E., Jr., Hall, J. R., and Woods, R. D., (1970), *Vibrations of Soils and Foundations*, Prentice-Hall, Inc, Englewood Cliffs, NJ.
18. Veyera, G. E., (1992), "Uniaxial Stress-Strain Behavior of Unsaturated Soils at High Strain Rates," *Final Report RDL 1992 Summer Faculty Research Program*, HQ, AFCEA/RACS, Tyndall AFB, FL, 15 -1: 15-20.

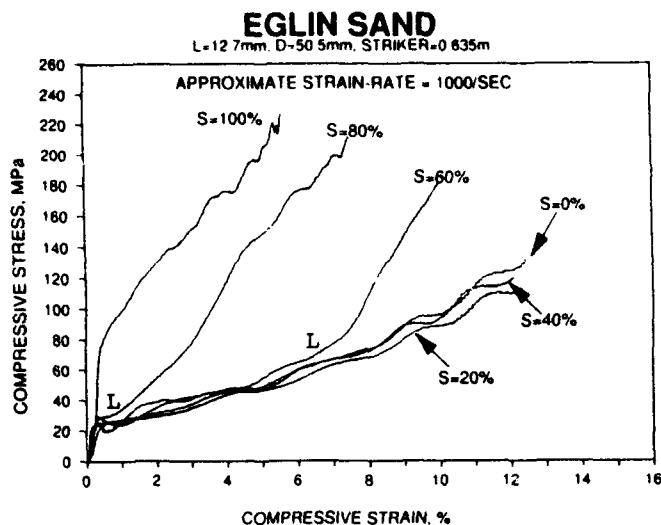


Figure 1. SHPB uniaxial undrained compressive stress-strain response for Eglin Sand as a function of saturation. L denotes approximate lock-up strain for 60 and 80% saturation.

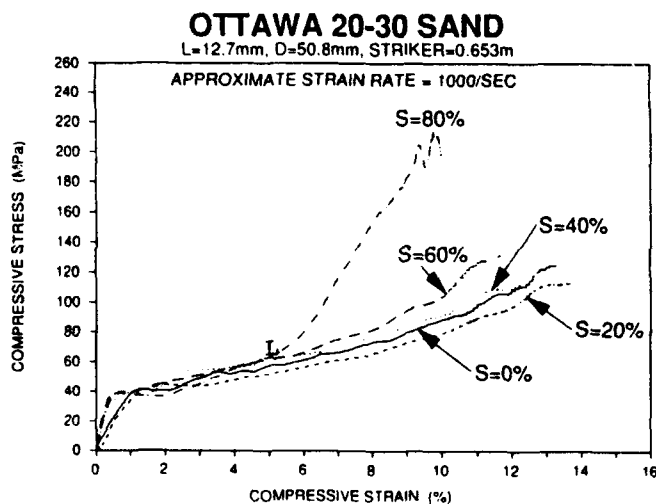


Figure 3. SHPB uniaxial undrained compressive stress-strain response for Ottawa 20-30 sand as a function saturation. L denotes approximate lock-up strain for 80% saturation.

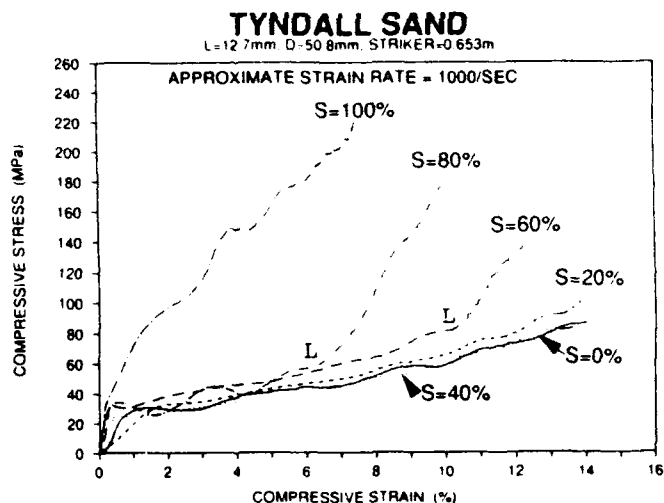


Figure 2. SHPB uniaxial undrained compressive stress-strain response for Tyndall Sand as a function of saturation. L denotes approximate lock-up strain for 60 and 80% saturation.

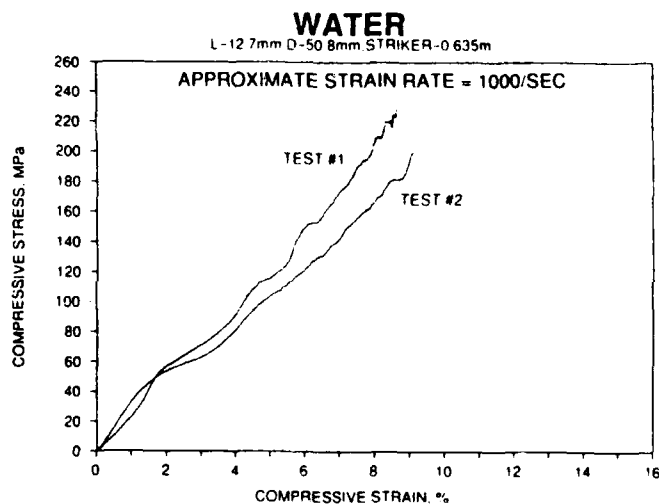


Figure 4. SHPB uniaxial undrained compressive stress-strain response for water.

19. Farr, J. V. and Woods, R. D., (1988), "A Device for Evaluating One-Dimensional Compressive Loading Rate Effects," *Geotechnical Testing Jnl.*, GTJODJ, Vol. 11, No. 4, pp. 269-275.

20. Juang, C. H. and Holtz, R. D., (1986), "Fabric, Pore Size Distribution, and Permeability of Sandy Soils," *Jnl. of Geotechnical Engineering*, Vol. 112, No. GT9, ASCE, pp. 855-868.

21. Whitman, R. V., Miller, E. T., and Moore, P. J., (1964), "Yielding and Locking of Confined Sand," *Jnl. of the Soil Mechanics and Fndtn. Division, ASCE*, Vol. 90, No. SM4, April, pp. 57-84.

22. Hendron, A. J., Davisson, M. T., and Paroloa, J. F., (1969), "Effect of Degree of Saturation on Compressibility of Soils From the Defence Research Establishment, Suffield," *Report No. WES-BPJ68-67*, U.S. Army Waterways Experiment Station, Vicksburg, MS.

23. Wu, S., Gray, D.H., and Richart, F. E., (1984), "Capillary Effects on Dynamic Modulus of Sands and Silts," *Jnl. of the Geotechnical Engineering Division, ASCE*, Vol. 110, No GT9, Sept., pp. 1188-1202.

24. Whitman, R. V., (1970), "The Response of Soils to Dynamic Loadings; Report 26, Final Report," *Contract Report No 3-26*, US Army Waterways Experiment Station, Vicksburg, MS.

25. Jackson, J. G., Ehrgott, J. Q., and Rohani, B., (1981), "Loading Rate Effects on Compressibility of Sand," *Jnl. of the Geotechnical Engineering Division, ASCE*, Vol. 106, No GT8, August, pp. 839-852.

26. Felice, C. W., Brown, J. A., Gaffney, E. S., and Olsen, J. M., (1987), "An Investigation into the High Strain Rate Behavior of Compacted Sand Using the Split-Hopkinson Pressure Bar Technique," *Proc., 2nd Symp. on the Interaction of Non-Nuclear Munitions With Structures*, P.C. Beach, FL, pp. 391-396.

27. Felice, C. W., Gaffney, E. S., Brown, J. A., and Olsen, J. M., (1987), "Dynamic High Stress Experiments on Soils," *Geotechnical Testing Jnl.*, GTJOW, Vol. 1, No. 4, pp. 192-202.

28. Gaffney, E. S., Brown, J. A., and Felice, C. W., (1985), "Soil Samples for the Split Hopkinson Bar," *Proc., 2nd Symp. on the Interaction of Non-Nuclear Munitions With Structures*, P.C. Beach, FL, pp. 397-402.

29. ASTM, (1992), *Annual Book of ASTM Standards - Volume 04.08 Soil and Rock; Dimension Stone; Geosynthetics*, American Society for Testing and Materials, Philadelphia, PA, pp. 160-164.

TABLE 1. Physical Properties of Eglin, Tyndall and Ottawa 20-30 Sands.

	Eglin	Tyndall	Ottawa 20-30
USCS Classification	SP-SM	SP	SP
Specific Gravity	2.65	2.65	2.65
D ₅₀ Particle Size (mm)	0.26	0.19	0.70
^b C _u	3.41	1.18	1.4 ^h
^c C _c	1.29	0.95	1.03
^d Percent passing #100 sieve (%)	12	2	<1
^d Percent passing #200 sieve (%)	7	0	0
^e Maximum dry density (kg/m ³)	1,670	1,630	1,720
^e Minimum dry density (kg/m ³)	1,450	1,450	1,560
Maximum void ratio	0.817	0.817	0.705
Minimum void ratio	0.590	0.621	0.545
Tested dry density (kg/m ³)	1,351	1,645	1,444
Tested void ratios	0.510	0.654	0.545

Note: ^aUnified Soil Classification System (1) ^dU.S. Standard Sieve
^bCoefficient of Uniformity ^eASTM D4253 (29)
^cCoefficient of Curvature ^fASTM D4254 (29)

TABLE 2. Comparison of Approximate Measured Compressive Strains at Lock-Up and Theoretical Compressive Strains to Reach S=100% Based on Initial Void Ratio and Initial Saturation.

S (%)	EGLIN ^a			TYNDALL ^b			OTTAWA 20-30 ^c		
	ϵ^d	ϵ^e	ϵ^f	ϵ^d	ϵ^e	ϵ^f	ϵ^d	ϵ^e	ϵ^f
0	33.8	(g)	(g)	39.5	(g)	(i)	35.3	(g)	(g)
20	27.0	(g)	(g)	31.6	(g)	(i)	28.2	(g)	(g)
40	20.3	(g)	(g)	26.7	(g)	(i)	21.2	(g)	(g)
60	13.5	7.5	6.0	15.8	10.5	(i)	14.1	(g)	(g)
80	6.8	3.0	2.0	7.9	6.5	(i)	7.0	6.0	1.5
100	0.0	0.5	1.0	0.0	0.5	(i)	0.0	?(h)	?(h)

Note: a Eglin sand at initial void ratio = 0.510
b Tyndall and at initial void ratio = 0.654
c Ottawa 20-30 sand at initial void ratio = 0.545
d Theoretical compressive strain (%) required to obtain S=100% based on initial void space and saturation. For S=0%, this represents a condition of zero air voids
e Approximate lock-up compressive strain (%) from SHPB data for strain rate = 1000/sec.
f Approximate lock-up compressive strain (%) from SHPB data for strain rate = 2000/sec
g Unable to obtain lock-up strains using the 0.653 m (25.7 inch) projectile at 690 kPa.
h Unable to obtain reliable data for Ottawa 20-30 sand at S=100%.
i Data not obtained for Tyndall sand at this strain rate.

Effects of Enhanced Constitutive Models on Calculated Free-Field Ground Shock

H.D. Zimmerman, Y.M. Ito, J.A. Carney
California Research & Technology, Titan Corporation, Chatsworth, CA

J.E. Windham
U.S. Army Engineer Waterways Experiment Station, Vicksburg, MS

ABSTRACT

California Research & Technology (CRT) has supported the U.S. Army Engineer Waterways Experiment Station (WES) in development and evaluation of material models and numerical simulation techniques for predicting the ground shock environment due to subsurface detonations from buried conventional weapons. This paper will discuss the development of an enhanced strain path dependent hysteretic constitutive model for computational applications and hydrocode simulations of an instrumented field event; DIPOLE FACADE 2 (a vertically oriented 1/3-scale MK-83 buried bomb containing 15.4 lb of C-4 detonated in high air-filled void sand). Comparisons of model response with and without path dependent hysteresis and the effects of model response on the calculated ground shock will be presented.

BACKGROUND

Results of recent laboratory material property tests (Phillips, 1991a) indicate significant shear-volume coupling for Socorro plaster sand; showing that hysteresis is highly strain path dependent. Shear-volume coupling implies that the deviatoric stress state influences the hydrostatic state via dilation or shear-induced compaction. In the illustration (Figure 1) of strain path dependent hysteresis, ϵ is the strain, the subscripts 1, 2, 3 refer to the principal directions, and v indicates the volume strain. This sand has been extensively employed as the backfill material in a number of recent instrumented conventional munitions field events and has been the subject of laboratory mechanical property tests.

Key aspects of the material response that play important roles in the physics of ground shock propagation are material hysteresis and strength. Hysteresis controls the relative wave speed in

loading, unloading and reloading. These speeds strongly influence the interaction of the ground shock with interfaces (layers, free-surface and structures) and associated relief/reflected signals, and hence the attenuation of shocks. Hysteresis also determines how much energy is absorbed in the form of waste heat, (i.e. energy that no longer contributes to ground shock propagation). Strength is an important factor in determining the total duration of the ground motion and hence peak displacement. While the general character of strain paths developed in ground shock events is known (i.e. uniaxial strain during shock loading followed by spherical divergence on unload), details of the strain path can become very complicated. Shear-volume coupled treatments are thus crucial to modeling material hysteresis in a robust manner.

CONSTITUTIVE MODEL

An enhanced mathematical constitutive model formulation that is capable of capturing the dominant physical process of strain path sensitive hysteresis has been developed. This model employs a strain hardening yield surface and a strain path dependent plastic flow potential. Nonlinear three-invariant Hybrid-Elastic-Plastic models of the type previously developed (Zimmerman et al., 1987) were fit consistent with the WES laboratory mechanical property tests [e.g. uniaxial strain compressibility (Phillips, 1991b) and biaxial strain unloading (Phillips, 1991a)]. At the time the original non-dilatant baseline model was developed (Zimmerman, Carney, Ito, 1991), only uniaxial strain load unload data was available. As strain path dependent mechanical property data became available, model enhancements in terms of shear-volume coupling and strain hardening were implemented. The main model parameters varied are given in Table 1, and represent a step-by-step developmental approach to incorporate greater detail and improvements in both the material constitutive relations and the numerical simulation of ground shock.

Emphasis of model fitting has been on developing model response for uniaxial strain loading and a number of spherically divergent unloading strain paths. Calculated and recommended deviatoric and hydrostatic responses for uniaxial strain load, followed by pure shear unload are presented in Figure 2.¹ The laboratory mechanical property tests exhibit significant shear-induced compaction until the ultimate failure surface is reached, wherein compaction ceases and the material becomes dilatant. Both the baseline (non-dilatant) and baseline-coupled (associated flow) models continue to compress, a trend opposite that observed in the test data.

Hydrostatic and deviatoric responses for a second spherically divergent strain path ($d\epsilon_2/d\epsilon_1 = -0.65$), are presented in Figure 3. Various levels of material hysteresis are predicted by the three models. The fully associated flow model over-predicts both the onset (when the deviatoric state exceeds the failure criterion) and the extent of dilation (i.e. path is unloading volumetrically, however pressure and strength increase as the material walks up the failure surface). This is a result of the magnitude of the plastic strain increment exceeding the volumetric strain increment resulting in a compressive elastic step, i.e.:

$$P(\epsilon_{\text{elastic}}), d\epsilon_{\text{elastic}} = d\epsilon_v - d\epsilon_{\text{plastic}} > 0$$

On the other hand, non-associated flow drastically underpredicts the amount of volume recovery, both pressure and strength rapidly drop. For these and other paths, the enhanced model matches both the qualitative and quantitative material response.

FREE-FIELD GROUND SHOCK

This enhanced constitutive model has been implemented into the SABER/CWE-family of large-strain finite element codes specifically designed for calculating ground shock from conventional munitions (Akers & Stelter, 1991), (Zimmerman, Shimano, & Ito, 1992). Previous research (Windham, Zimmerman, & Ito, 1991), (Zimmerman, Ito, & Windham, 1991) on the influence of geometric asymmetries on the near source ground shock indicated that the environment to the side of the bomb was nearly identical to that of an equal mass spherical source. Thus, for depths of burial

sufficiently deep such that free surface relief effects are of second order, a 1-D spherical fully contained approximation is adequate to simulate the ground shock environment. Earlier experimental and calculational efforts focused on measurement and prediction of early-time ground shock (i.e., duration of a few milli-seconds past peak stress and velocity). This earlier calculational effort employed total stress constitutive models with a non-dilatant flow rule that were fit to uniaxial strain (UX) compressibility and stress path, and peak triaxial compression (TX) failure relations determined from laboratory tests. Calculated ground shock with non-dilatant total stress models was nominally consistent with early-time measurements. During the initial shock loading, the material is predominately in a state of uniaxial strain.

The previous field tests were primarily focused on measuring early-time near source ground shock. Reliable measurements of free-field motions out to the time of peak displacement were not obtained. The DIPOLE FACADE 2 test was specifically designed to obtain late-time motion measurements. This test employed redundant measurements with shock-mounted accelerometers and DX velocity gages at ranges of 1.52, 2.13, and 2.74 meters from the charge CG. These measurements provide a database for evaluating the ability of various models to predict late-time behavior.

The role of strain path dependent hysteresis was investigated by conducting a series of 1-D spherical fully contained hydrocode calculations of the DIPOLE FACADE 2 event. Comparative waveforms (using the three models) and attenuation of peak stress and velocity along the side of the bomb are shown in Figures 4 and 5. At sufficiently high stress levels, predicted attenuation of peak quantities is nearly identical. At these levels, attenuation is dominated by pore crushing, all three models have the same nominal level of hysteresis. As stress levels drop, the effects of strain path sensitive hysteresis starts to be manifested. Attenuation is most rapid in the baseline non-dilatant response. Referring back to the hydrostatic response plot, Figure 3, this model is seen to be the most dissipative. On the other hand, the Baseline-Coupled model (associated flow) is significantly less dissipative. Excessive dilation holds up the pressure pulse on unloading, resulting in the development of larger stress deviations which resists radial flow, reducing the positive phase velocity pulse amplitude. Although the magnitude of the peak particle velocity is lowest for the baseline non-dilatant calculation,

¹Laboratory mechanical property tests employ the small or engineering strain definition of pure shear, $\Delta\epsilon_v = 0$, $\epsilon_v = \epsilon_1 + \epsilon_2 + \epsilon_3$. The actual volumetric strain path is compressive $\epsilon_v = 1 - (1 - \epsilon_1)(1 - \epsilon_2)(1 - \epsilon_3)$.

the amplitude of the overall positive phase pulse is larger. Here the development of large late time stress deviators are precluded due to the rapid hydrostatic unloading.

In terms of dissipation and volume recovery the enhanced model falls in between the fully associated (dilatant) and non-dilatant models, as do the attenuation's. Calculated waveforms (using the path dependent enhanced model) are compared with measured waveforms at three ranges in Figure 6. These enhanced model waveforms match best the peak particle velocity and positive phase duration (displacement).

CONCLUSION

An enhanced mathematical constitutive model formulation that is capable of capturing the dominant physical process of strain path sensitive hysteresis has been developed. The model's ability to better replicate laboratory strain path mechanical property tests has been demonstrated. Previous research indicated that when total stress models without shear-volume coupling were used, the calculated ground shock for CWE test events are nominally consistent with early-time measurements. A predictive capability to also simulate late-time motion has been achieved with the addition of strain path sensitive hysteresis.

ACKNOWLEDGMENT

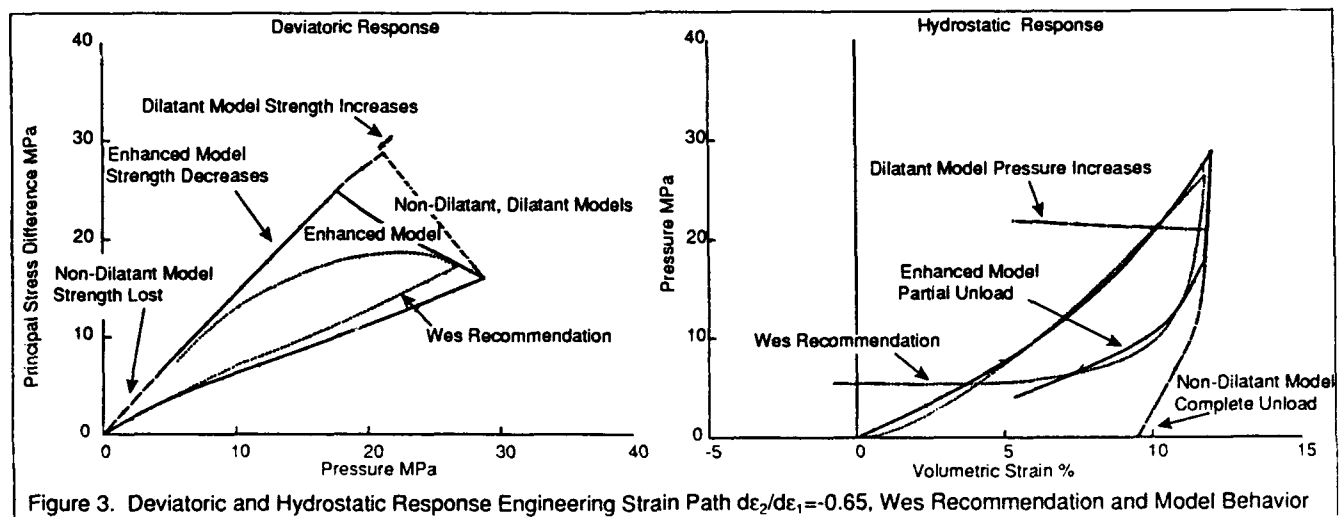
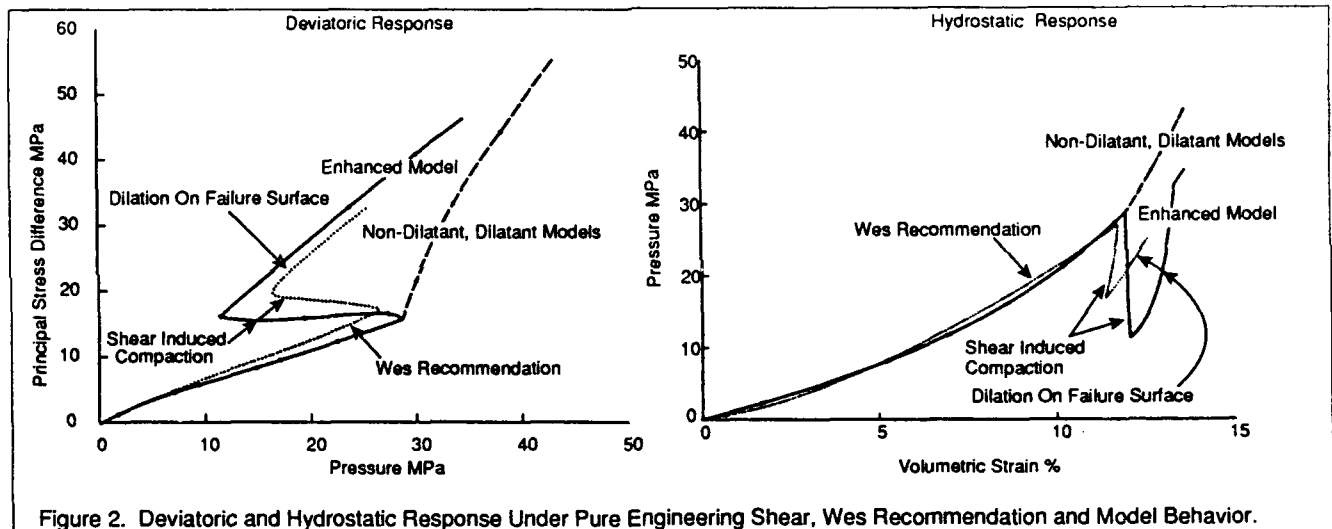
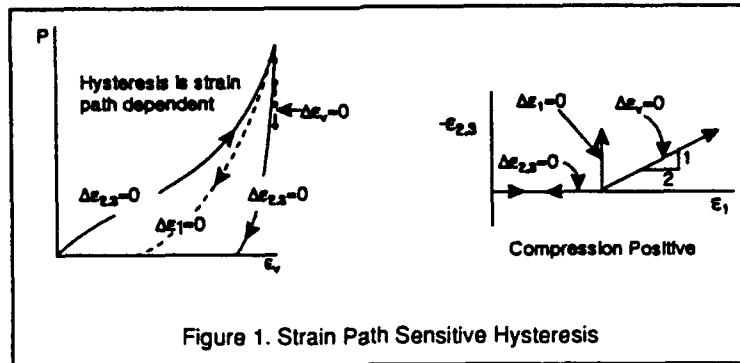
The work reported herein was conducted by California Research & Technology Division, Titan Corporation, and the U.S. Army Engineer Waterways Experiment Station (WES) for Headquarters, U.S. Army Corps of Engineers under Hardened Structures Research Program Work Units AT22-HS-005 and AT40-HS-003. The permission from the Office, Chief of Engineers, to publish this paper is gratefully acknowledged.

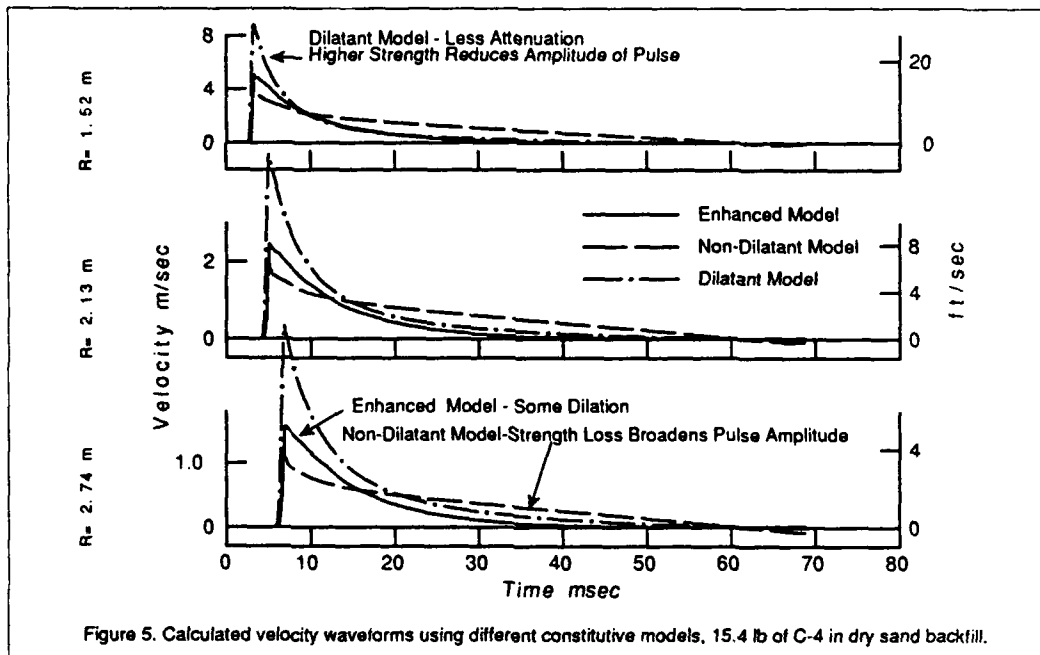
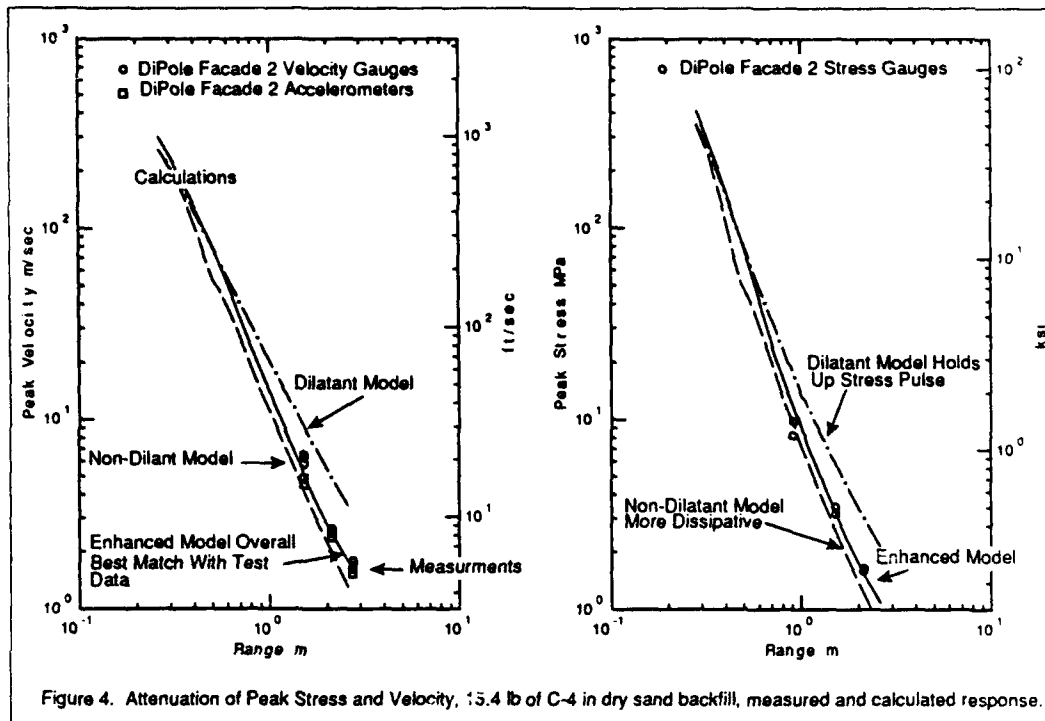
REFERENCES

- S.A. Akers, & J. Stelter, "SABER-PC/CWE: A Ground-Shock Software Package for The PC" in Proceedings of the Fifth International Symposium on the Interaction of Conventional Munitions with Protective Structures, page N3-N10, NATO Session, Mannheim FRG. 22-26 April 1991.
- B.R. Phillips, "Mechanical Property Recommendations for Post-Test Evaluation of MIDNIGHT HOUR 2 Test", US Army Engineer Waterways Experiment Station, Vicksburg, Mississippi, (CEWES-SD-S), "Personal Communications", 6 August 1991.
- B.R. Phillips, "Mechanical Property Recommendations for Post-Test Evaluation of DIPOLE AXIAL Shallow-Buried 1000-lb Bomb", US Army Engineer Waterways Experiment Station, Vicksburg, Mississippi, (CEWES-SD-S), "Personal Communications", January 1991.
- J.E. Windham, H.D. Zimmerman, & Y.M. Ito, "Analysis of Ground Shock Measurements from Shallow-Buried MK83 Bombs", in Proceedings of Instrumentation for Nuclear Weapons Effects Testing Conference, Blast & Shock Session, Vicksburg, Mississippi, 16-19 April 1991.
- H.D. Zimmerman, J.A. Carney, Y.M. Ito, "Cratering and Ground Shock Environment Prediction of Buried 500 lb SAP Bomb in Dry Socorro Plaster Sand: DIPOLE CHAIN 4 Test", CRT 3295-080-01, Submitted to U.S. Army Engineer Waterways Experiment Station, 1991
- H.D. Zimmerman, R.T. Shimano, & Y.M. Ito, "Early-Time Ground Shock From Buried Conventional Explosives: Users Guide for SABER-PC/CWE", I.R. SL-92-1 Structures Lab U.S. Army Engineer Waterways Experiment Station, Vicksburg, Mississippi, August 1992.
- H.D. Zimmerman, Y.M. Ito, & J.E. Windham "Hydrocode Analysis of Ground Shock Environment in Wet Clay Backfill", in Proceedings of the Fifth International Symposium on the Interaction of Conventional Munitions with Protective Structures, page N27-N34, NATO Session, Mannheim FRG, 22-26 April 1991.
- H.D. Zimmerman, M.H. Wagner, J.A. Carney, & Y.M. Ito, "Effects of Site Geology on Ground Shock Environments: Report 1 - Constitutive Models for Materials I2, I3, and W1-W10", SL-87-19 Structures Lab U.S. Army Engineer Waterways Experiment Station, Vicksburg, Mississippi, June 1987.

Model	Hysteresis	Model Parameter	
		Shear Volume Coupling (flow rule)	Failure Surface
Baseline	$f(\epsilon_{max})$	none, (non-dilatant)	Non-Hardening
Baseline-Coupled	$f(\epsilon_{max})$	on Peak TXC surface, (associated)	Non-Hardening
Enhanced	$f(\epsilon_{max})$ & ϵ path	full, (generalized)	Hardening

Table 1. Key Constitutive Model Parameters Varied





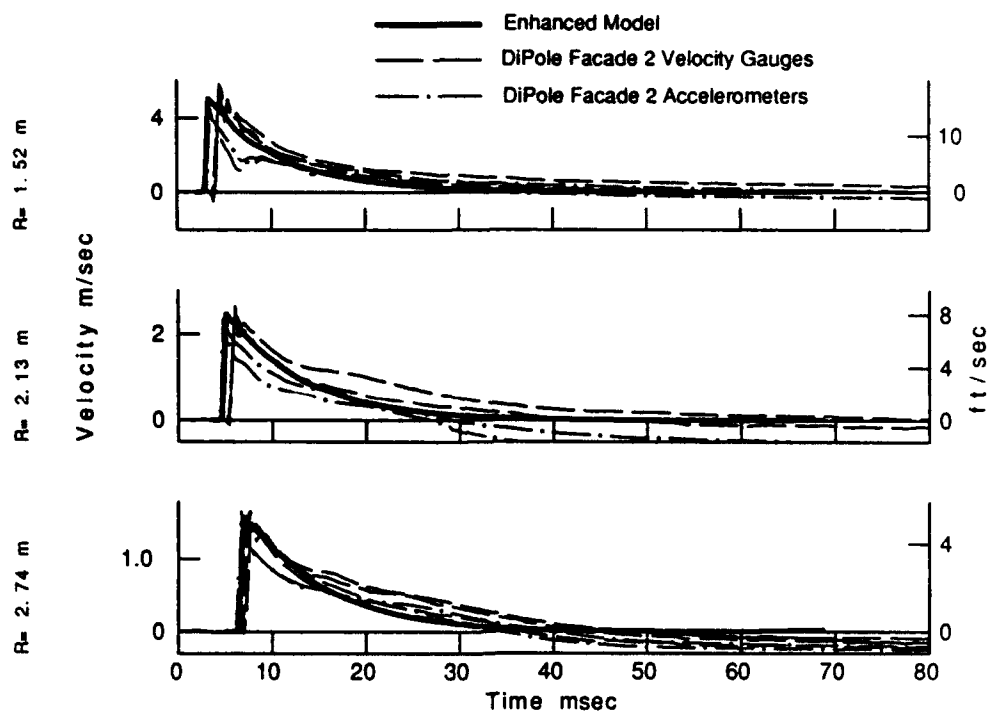


Figure 6. Velocity waveforms, 15.4 lb of C-4 in dry sand backfill, measured and calculated response.

HOW TO SELECT A DESIGN FRAGMENT FOR PROTECTIVE STRUCTURE DESIGN WITH CONSISTENT RELIABILITY

Robert H. Sues and Lawrence A. Twisdale

Applied Research Associates, Inc., Raleigh, North Carolina 27615
Telephone: 919 876-0018

ABSTRACT

In traditional, deterministic protective construction, the structure is designed to withstand the penetration effects of a single "design" fragment. We present here a reliability-based design (RBD) framework that can be used in the design fragment selection process. The RBD methodology differs from the Confidence Level (CL) approach used in current manuals in that the structure designed using the RBD method will protect its contents with a known level of confidence. It has been shown that the CL approach used in current manuals does not directly relate to design reliability or confidence and in fact can sometimes be grossly conservative and sometimes grossly unconservative. The RBD framework is used herein to illustrate the process of developing and applying design charts and tables for a MK82 500-lb GP bomb threat for fragment penetration in concrete.

1. INTRODUCTION

In traditional, deterministic protective construction, the structure is designed to withstand the penetration, perforation, and/or spall effects of a single "design" fragment, where the design fragment is characterized by a specified weight, initial velocity, and shape. Although current manuals recognize the variability in fragment mass (via Mott's distribution), the Confidence Level (CL) approach that is used to select a design fragment does not directly relate to design reliability or confidence since it does not consider the number of impacting fragments (which varies with standoff and target size) and it does not address the inherent variability in the velocity, shape, impact angle and orientation, and spatial distribution of the fragments generated by the cased explosive [Dass and Twisdale, 1987]. In addition, fragment-structure interaction phenomenon can be highly uncertain, that is, fragment ricochet and fragment penetration. In fact, it can be shown that structures designed to resist fragment perforation (or spall) using the current CL approach can sometimes be grossly conservative and sometimes grossly unconservative.

We present here a framework that provides the basis for developing reliability-based design (RBD) charts and tables that can be used in the design fragment selection process. With these charts and tables the designer need not perform complex fragmentation or probabilistic analyses. The RBD methodology differs from the conventional approach in that the structure designed using the RBD method will protect its contents with a known level of confidence. Specification of the design fragment in the RBD approach can consider the variability in each of the fragmentation variables as well as how these variables combine to affect the lethality (load-effect) of a particular fragment. Most importantly, the procedure

considers the number of fragments that impact the structure. This is a key feature of the method since the greater the number of impacting fragments, the greater the chance that fragments more lethal than the design fragment will hit the structure. The RBD framework is used herein to illustrate the process of developing and applying design charts and tables for a Mk82 500-lb GP bomb threat for fragment penetration in concrete. The framework uses the fragment penetration formulas given in the U.S. Air Force *Protective Construction Design Manual* [Drake, et al., 1989], hereinafter referred to as the *PCDM*. Research is underway to tabulate and generalize results for a range of weapons of interest and to develop validated penetration formulas, since the current formulas tend to significantly overpredict penetration depth (lethality) for high-speed fragments generated by modern weapons.

2. OVERVIEW OF RBD FRAMEWORK

The developmental framework for reliability-based selection of a design fragment encompasses the important fragmentation variables (e.g., velocity, shape, impact angle and orientation) as well as the number of fragments that strike the target. The framework accounts for the multivariate nature of penetration by transforming the problem variables into a single load-effect called the fragment lethality variable. Using this transformation and the distributions of the underlying fragment variables, the probability distribution for the lethality variable is computed. Finally, the expected number of fragment hits on the structure is evaluated and the extreme value distribution for the lethality variable is derived. The extreme value distribution is the appropriate distribution for use in designing the structure since it gives the probability that no fragments more lethal than the design fragment will hit the structure. Thus, the design fragment is selected from the extreme value distribution for the lethality variable. Design charts and tables can be developed for a range of cases to aid in the selection of the design fragment so that the designer need not perform any probabilistic computations. Also, the probability that one or more fragments that are more lethal than the design fragment will hit the target (i.e., in addition to the probability that no fragments more lethal than the design fragment impact the structure) can be obtained in closed form. More details on the methodology are documented in Twisdale, Sues, and Lavelle [1992].

3. RBD PROCEDURE

Using the developmental framework a step-by-step design procedure has been developed. The steps in the design procedure are illustrated in the flow chart of Figure 1.

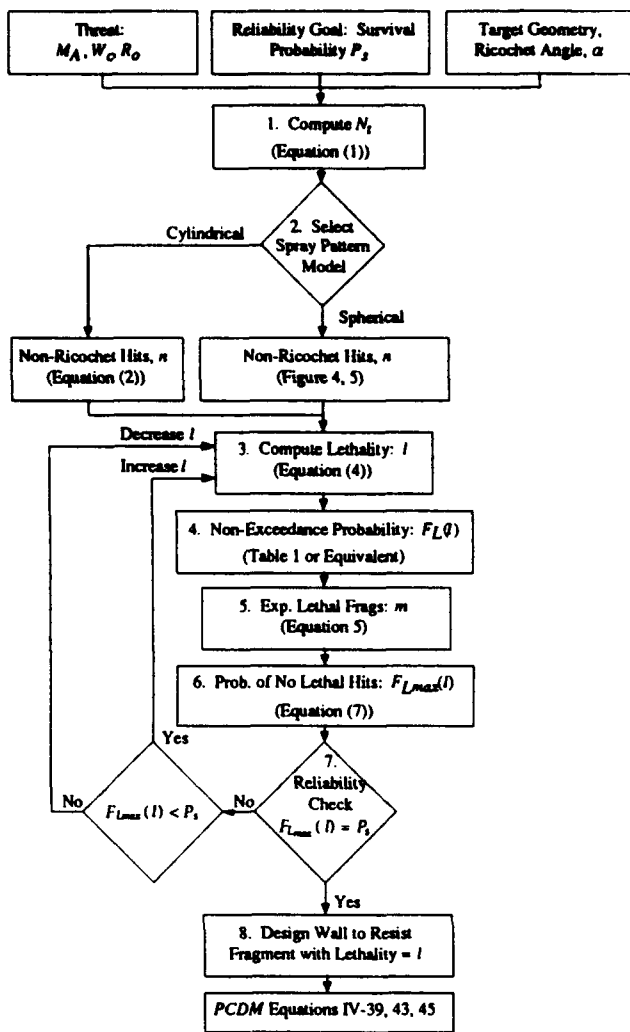


Figure 1. Flowchart for Reliability-Based Selection of a Design Fragment.

Step 1. The first step is to evaluate the expected number of fragments generated by the threat weapon. This number can be obtained from arena test data or can be estimated using the following formula from the PCDM:

$$N_i = \frac{W_c}{2 M_A^2} \quad (1)$$

where W_c is the bomb casing weight, and M_A is the fragment weight Mott probability distribution parameter (values of M_A for various weapons are given in a number of design manuals including the PCDM).

Step 2. The second step is to compute the expected number of fragments that hit the structure without ricocheting. The cylindrical spray pattern is most appropriate when the bomb length to standoff ratio is relatively large and for weapons having narrow beam sprays. For a cylindrical spray pattern, the problem is as depicted in Figure 2 and the number of non-ricochet hits is

$$n = N_i \frac{(\theta_{max}^+ + \theta_{max}^-) y}{2\pi c} \quad (2)$$

where the two angles θ_{max}^+ and θ_{max}^- , and the vertical dimension y are given by

$$\theta_{max}^+ = \min \left[\alpha, \tan^{-1} \frac{w-x}{R_o} \right] \quad (3)$$

$$\theta_{max}^- = \min \left[\alpha, \tan^{-1} \frac{x}{R_o} \right]$$

$$y = \min [c, h]$$

where, as illustrated in Figure 2, w is the width of the target, x is the distance from the edge of the target to the point on the target directly opposite the bomb, h is the height of the wall,

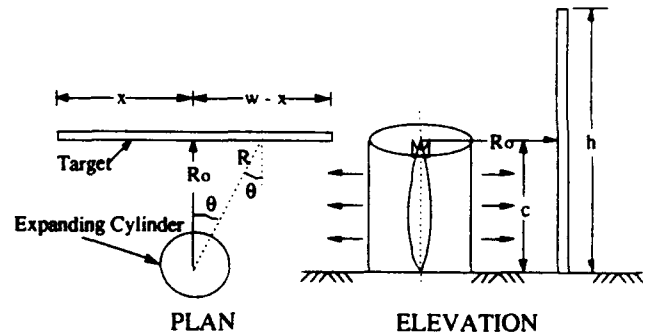


Figure 2. Fragment Non-Ricochet Hit Analysis Assuming a Cylindrical Dispersion Pattern.

and c is the length of the bomb. The angle, α , is the ricochet angle. The fragments that have impact angles, θ (the angle between the normal to the target and the fragment velocity vector), less than α do not ricochet.

The spherical spray pattern is most appropriate for small values of c/R_o (see Figure 2 and for weapons that have less distinct beam sprays). For a spherical spray pattern, design charts have been developed. First the structure is divided into four separate sections with a common corner as shown in Figure 3. The fraction of non-ricochet fragments impacting each section of the structure under the threat at a standoff, R_o is then calculated using the following procedure: (1) Calculate the values of s ($= R_o/a$) and t ($= R_o/b$) where R_o is the standoff distance, a is section length, and b is the section height; (2)

TABLE 1. PRELIMINARY LETHALITY VARIABLE CDF FOR Mk82 500-LB GP BOMB FOR PCDM PENETRATION EQUATION.

$F_L(l)$, Fraction of Fragments with Lethality $< l$	Lethality, l^a ($lb^{0.4} kfps^{1.8}$)
0.01	0.05
0.1	0.33
0.2	0.64
0.3	0.98
0.4	1.4
0.5	1.9
0.6	2.4
0.7	3.2
0.8	4.6
0.9	7.2
0.95	9.6
0.975	13.1
0.99	16.3
0.995	19.9
0.999	26.0
0.9995	29.0
0.9999	37.0

^a Based on PCDM Penetration Equation (Equation (4) herein).

Step 6. For reliability-based design we need the probability that there will be no lethal hits. That is, that there will be no hits by fragments that are more lethal than the design fragment. This probability is evaluated using the hypergeometric function. The probability that there are x hits with lethality greater than the design fragment is:

$$P(X=x) = \frac{\binom{m}{x} \binom{N_t - m}{n - x}}{\binom{N_t}{n}} \quad (6)$$

$$\binom{m}{x} = \frac{m!}{x!(m-x)!}$$

where $!$ is factorial and N_t is the total number of fragments generated by the bomb (computed in Step 1), m is the number of these fragments with lethality greater than the design fragment (computed in Step 5), n is the number of fragments that impact the structure and do not ricochet (computed in Step 2). The probability that no fragments with lethality greater than the design fragment will impact the structure is given by Equation (6) with $x = 0$. Thus,

$$F_{L_{max}}(l) = P(L_{max} < l) = \frac{\binom{m}{0} \binom{N_t - m}{n - 0}}{\binom{N_t}{n}} = \frac{\binom{N_t - m}{n}}{\binom{N_t}{n}} \quad (7)$$

$$= \frac{(N_t - m)! (N_t - n)!}{N_t! (N_t - m - n)!}$$

The design fragment must be selected so that the probability given by Equation (7) is the desired reliability level. Because a general purpose bomb can generate tens of thousands of fragments, some numerical difficulty may be encountered in evaluating the factorials in Equation (7). To avoid the problem two simple approaches are given in Appendix A. (Sues, Twisdale, and Lavelle [1993].)

Step 7. As mentioned above the design fragment must be selected so that the probability given by Equation (7) is the desired reliability level. If the probability obtained in Step 6 is acceptable then we proceed to Step 8. Otherwise we revise the design fragment lethality up if the probability in Step 6 is too small, and go back to Step 4; or we revise the design fragment lethality down if the probability in Step 6 is too big, and go back to Step 4.

Step 8. Design the wall to resist the design fragment using procedures given in PCDM Section VI.D.2. Note that Steps 1 through 7 only address fragment load-effect. Reliability-based capacity reduction factors to account for penetration equation prediction errors and material property uncertainties should also be included in the final design.

4. RELIABILITY-BASED DESIGN FRAGMENT SELECTION EXAMPLE

As an example, we consider the selection of a design fragment for a 12 ft by 12 ft door panel on a protective shelter that must resist penetration of fragments from a 500-lb Mk82 GP bomb at a standoff of 50 ft. A spherical spray pattern and a ricochet angle of 45 degrees are assumed. Pertinent parameters for the Mk82 threat are: $W_c = 311$ lbs, $M_A = 0.067$ lbs^{1/2}, and $c = 7.5$ ft.

First, we compute the expected total number of fragments generated by the bomb. The number of fragments is given by Equation 1 as $N_t = 311/(2) (0.067)^2 = 34640$, where we have rounded to the nearest integer.

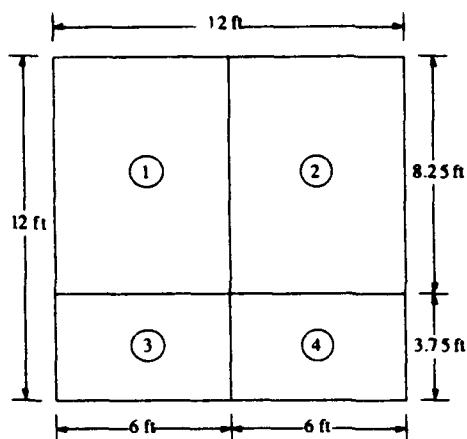
The second step is to compute the expected number of nonricochet hits on the panel. Given the 45-degree ricochet angle, we use the design chart given in Figure 5. Assuming that the bomb is centered horizontally along the wall and that the center of the bomb is at a height of 3.75 ft (i.e., half of the bomb length), the wall can be broken up into four sections. The calculations for the fraction of fragments hitting the panel are summarized in Figure 6. The expected number of nonricochet hits for a 50-ft standoff and spherical spray pattern is 156.

The next two steps are to select a trial design fragment and determine its non-exceedance probability using the preliminary lethality probabilities for Mk-82 bombs given in Table 1. To begin the iterative design process, we select a fragment with lethality greater than 99.9% of the fragments (i.e., the 0.999 fragment with a lethality of 26.0 $lb^{0.4} kfps^{1.8}$).

The expected number of fragments with lethality greater than 26.0 $lb^{0.4} kfps^{1.8}$ is given by Equation (5) as $m = 34640(1 - 0.999)$, or 35 fragments, rounding to the nearest integer.

We now have all of the inputs needed to compute the reliability of the selected design fragment. The probability that no fragments more lethal than 26.0 $lb^{0.4} kfps^{1.8}$ will strike the panel is evaluated using Equation (7) as,

$$P(L_{max} < l) = \frac{(34640 - 35)! (34640 - 156)!}{(34640)! (34640 - 35 - 156)!} = 0.854 \quad (8)$$



Section 1 or 2:

$R_o = 50 \text{ ft}$
 $a = 6 \text{ ft}, b = 8.25 \text{ ft}$
 $s = 50/6 = 8.33, t = 50/8.25 = 6.07$
 $1/4\pi = 0.00154 \text{ (see Figure 5)}$

Section 3 or 4:

$R_o = 50 \text{ ft}$
 $a = 6 \text{ ft}, b = 3.75 \text{ ft}$
 $s = 50/6 = 8.33, t = 50/3.75 = 13.33$
 $1/4\pi = 0.000710 \text{ (see Figure 5)}$

$$n = [(2) \times (0.00154) + (2) \times (0.000710)] \times (34,640) = 156$$

Figure 6. Expected Number of Nonricochet Hits Computation for a 50-foot Standoff and Spherical Spray Pattern.

Thus, the 0.999 fragment almost provides the required reliability of 90%. If we increase the design fragment to $29.0 \text{ lb}^{0.4} \text{ kfps}^{1.8}$ (i.e., the 0.9995 fragment) and repeat the above steps, the resulting reliability is 92.7%. Simple linear interpolation between these points yields a design fragment of approximately $27.9 \text{ lb}^{0.4} \text{ kfps}^{1.8}$ to achieve 90% reliability.

5. DISCUSSION AND NEED FOR FURTHER RESEARCH

The foregoing is a systematic framework for reliability-based selection of design fragments. A validated, robust procedure can be implemented for PC-based design that is significantly better than the outdated CL approach. Final design tables can be developed within this framework as new bomb arena test data become available. New sophisticated data acquisition systems are making it possible to do a much better job of characterizing the fragmentation environment for protective design. In particular, better characterizations of the upper tail of the fragment weight distribution and of the entire fragment velocity distribution are needed, and the correlation between weight and velocity should be studied.

We emphasize that it is necessary to use the raw arena test data, before it is reduced, as presented in manuals such as the JMEM [1990]. The reduced data tables only provide averages and are insufficient for characterizing the distributions, in particular the upper tails required for protective design. In

addition, the current JMEM tables are erroneous for the large weight fragments. The error arises because the new tabular format includes a finer discretization of the large fragment weights than was used in the old format. Finer discretization of fragment weight classes is a needed improvement; however, in fitting the old data into the new format, the JMEM authors have "created data." All of the fragments from the heaviest fragment group in the old table have been lumped in the new table assuming that they all have a weight equal to the average weight of the group. Thus, the new table implies that there is a large number of fragments at this average weight and that no fragments heavier than this were generated. Clearly this is unconservative for protective design.

Finally, we mention that the reliability framework, as presented here, makes it probable that the structure will not be hit by a fragment more lethal than the design fragment. However, the methodology can also be used to compute the probability that the structure will not be hit by any number of fragments more lethal than the design fragment. Thus, for cases wherein more than one fragment penetration would be required to cause damage, selecting the design fragment can be tailored to the specific damage criteria (e.g., allowing one hit more lethal than the design fragment per 100 feet^2 of target area).

6. REFERENCES

Dass, W. C., and Twisdale, L. A., "Comparison of Design Procedures for Fragmentation Effects," *International Symposium on the Interaction of Conventional Munitions with Protective Structures*, Mannheim, FRG, March 1987.

Drake, J. L., et al., *Protective Construction Design Manual*, ESL-TR-87-57, Air Force Engineering and Services Center, Tyndall Air Force Base, November 1989.

Sues, R. H., Twisdale, L. A., Lavelle, F. M., *Addendum to Protective Construction Design Manual, Reliability-Based Design for Reinforced Concrete Structures*, Air Force Civil Engineering Support Agency, 1993.

Twisdale, L. A., Sues, R. H., Lavelle, F. M., *Reliability-Based Analysis and Design Methods for Reinforced Concrete Protective Structures*, Air Force Civil Engineering Support Agency, August, 1992.

7. APPENDIX A - EVALUATION OF THE HYPERGEOMETRIC FUNCTION FOR LARGE NUMBERS.

Selection of the design fragment requires evaluating the equation:

$$F_{L_{max}}(l) = P(L_{max} < l) = \frac{(N - m)! (N - n)!}{N! (N - m - n)!} \quad (\text{A-1})$$

Because a general purpose bomb can generate tens of thousands of fragments, some numerical difficulty may be encountered in evaluating the factorials in this equation. Two approaches are possible to avoid this problem. The first is an approximate close form solution based on Stirling's factorial formula and the second is a simple FORTRAN algorithm that

provides an exact solution yet avoids generating very large numbers that would result in numerical overflow.

Stirling's factorial formula is given as:

$$n! = \sqrt{2\pi} n^{n+1/2} e^{-n} \quad (\text{A-1})$$

Using this formula we can rewrite Equation (A-1) as:

$$\begin{aligned} \ln [P(L_{\max} < 1)] = \ln P^* = & (N - m + 1/2) \ln (N - M) + \quad (\text{A-2}) \\ & (N - n + 1/2) \ln (N - n) \\ & - (N + 1/2) \ln N - (N - m - n + 1/2) \ln (N - m - n) \end{aligned}$$

and finally, the probability given by Equation A-1 is given as:

$$P(L_{\max} < 1) = e^{\ln P^*} \quad (\text{A-3})$$

Stirling's formula is highly accurate for large numbers and becomes exact as n approaches infinity. Even for factorials as small as 10, the error is less than 1 percent.

An exact FORTRAN algorithm that avoids generating very large numbers that would result in numerical overflow is given below. It takes advantage of the fact that, after dividing out common multiples in the numerator and denominator, exactly m multiplications must be performed in both the numerator and denominator. That is, after dividing common multiples, Equation (A-1) becomes:

$$\begin{aligned} P(L_{\max} < 1) &= \frac{(N - n)(N - n - 1)(N - n - 2) \dots (N - m - n + 1)}{(N)(N - 1)(N - 2) \dots (N - m + 1)} \\ &= \left(\frac{N - n}{N} \right) \left(\frac{N - n - 1}{N - 1} \right) \left(\frac{N - n - 2}{N - 2} \right) \dots \left(\frac{N - m - n + 1}{N - m + 1} \right) \quad (\text{A-4}) \end{aligned}$$

The algorithm for evaluating the above equation is:

```
A = N - n
B = N
C = 1.0
DO I = 1, m
  C = C * A/B
  A = A - 1
  B = B - 1
END DO
```

Reliability-Based Safety Factors for Ground Shock Loads in Protective Construction

R. H. Sues, J. L. Drake, and L. A. Twisdale

Applied Research Associates, Inc., 6404 Falls of Neuse Rd., Ste. 200, Raleigh, NC 27615
Telephone: (919) 876-0018

ABSTRACT

To develop survivable buried structure designs, we must first predict ground shock loads on the structure and then apply load factors to ensure an appropriate margin of safety. This paper presents such tabulated load factors as a function of design reliability (survivability) — the greater the design reliability the greater the load factor. Detail of the methodology used to derive the load factors and for use in making site-specific reliability-based predictions are also given; along with a presentation of the ground shock database used in the research.

1. INTRODUCTION

Ground shock loading is a highly variable conventional weapons effect. This variability is due to the complex multiphase composition of geologic materials and their inherent spatial variability. To develop survivable buried structure designs, we must first characterize the uncertainty in predicting free-field ground shock and then develop load factors to ensure an appropriate margin of safety. In this paper we analyze the sources of uncertainty in predicting ground shock from a conventional weapons explosion and present reliability-based load factors for free field velocity and stress that can be used in protective design. The load factors have been derived for use with the ground shock prediction methods given in the Air Force Protective Construction Design Manual [Drake, *et. al.*, 1989], hereinafter referred to as the *PCDM*.

To characterize ground shock prediction uncertainty, it is important to consider and quantify both the model prediction error and the model parameter (*i.e.*, geologic descriptors) uncertainties. Model prediction error has both a systematic component and a random component. Model parameter uncertainties have both prediction error and random components. Uncertainties are quantified by analysis of ground shock data.

2. *PCDM* DETERMINISTIC GROUND SHOCK PREDICTION MODEL

The *PCDM* prediction model for peak free-field velocity and stress from bombs detonating on or within the soil near a structure is given as (*PCDM* Equations (V-11) and (V-10)):

$$V_o = f \cdot 160 \cdot \left(\frac{R}{W^{1/3}} \right)^n \quad (1)$$

$$P_o = \frac{\rho_o C_1 V_o}{144} = f \cdot \rho_o C_1 \cdot \frac{160}{144} \cdot \left(\frac{R}{W^{1/3}} \right)^n \quad (2)$$

where P_o = peak pressure, *psi*; f = coupling factor for near-surface detonations; C_1 = loading wave velocity, *fps*; R = distance to the explosion, *ft*; W = charge weight, *lbs*; V_o = peak particle velocity, *fps*; ρ_o = mass density, *lb-s²/ft⁴*; n = attenuation coefficient; and

$$C_1 = \max \left\{ \frac{kc}{c} + SV_o \right. \quad (3)$$

where $k = 0.06$ for clay; $k = 1.0$ for sand; c is the seismic velocity; $S \approx 1/\epsilon_o$ for partially saturated soils; and $S = 0.0$ for fully saturated soils (ϵ_o = irreversible volumetric compaction behind the wave front).

3. RELIABILITY-BASED DESIGN PROCEDURE

The magnitude of the load factors, λ , for reliability-based prediction of free-field ground shock depends on the variability in the geologic material at the site and the detail to which the site has been characterized. Thus, the load factors are site specific and should, strictly speaking, be computed on a case-by-case basis. We present in the following a reliability-based model that can be used to make site-specific predictions. However, because most protective design situations fall in a limited range of cases we are able to provide, at the conclusion, generic load factors for typical cases. These generic factors are applicable for preliminary design. For final design of mission critical structures we recommend that the site specific prediction model be used.

The site-specific reliability-based peak free-field velocity and stress predictions are obtained, respectively as:

$$V_{oR} = \exp \left[E[\ln V_o] + \Phi^{-1}(R) \times \sigma_{\ln V_o} \right] \quad (4)$$

$$P_{oR} = \exp \left[E[\ln P_o] + \Phi^{-1}(R) \times \sigma_{\ln P_o} \right] \quad (5)$$

where R is the desired reliability level, $E[\]$ denotes expected value (mean), σ denotes standard deviation, and Φ is the standard normal function. Values for the standard normal function can be obtained from Table 1. Equations 4 and 5 assume that the free-field velocity and stress are lognormally distributed. This is a good assumption since, as we will show below, the model prediction error is lognormally distributed and dominates the total prediction uncertainty.

TABLE 1. STANDARD NORMAL FUNCTION FOR USE IN SITE-SPECIFIC FREE-FIELD GROUND SHOCK RELIABILITY CALCULATION.

R	$\Phi^{-1}(R)$
0.05	-1.65
0.10	-1.28
0.25	-0.67
0.50	0.00
0.75	0.67
0.90	1.28
0.95	1.65

The statistics in Equations 4 and 5 are the mean and standard deviation of the natural logarithm of the free-field velocity and stress, respectively and are obtained as:

$$E[\ln V_o] = E[\ln \xi] + \ln 160 - E[n] \ln(R/W^{1/3}) \quad (6)$$

$$\sigma_{\ln V_o}^2 = \sigma_{\ln \xi}^2 + [\ln(R/W^{1/3})]^2 \sigma_n^2 \quad (7)$$

$$E[\ln P_o] = E[\ln \rho_o] + E[\ln C_1] + E[\ln V_o] - \ln 144 \quad (8)$$

$$\sigma_{\ln P_o}^2 = \sigma_{\ln \rho_o}^2 + \sigma_{\ln C_1}^2 + \sigma_{\ln V_o}^2 + 2 \text{COV}[\ln \rho_o, \ln C_1] \quad (9)$$

where $\text{COV}[\]$ denotes covariance, ξ is the model prediction error random variable, and all other symbols are as defined for Equations (1) and (2) earlier. The scaled range term $R/W^{1/3}$ is treated as a deterministic quantity (*i.e.*, specified threat), however it is straightforward to extend the approach to treat this quantity probabilistically.

4. MODEL PREDICTION ERROR

The database used for quantifying the model prediction error is a collection of both published and unpublished free-field velocity and stress measurements [Drake, *et al.*, 1989]. The data are shown in the plots of Figures 1 and 2. The geologic conditions and shot names are shown on each plot.

The model prediction error can have both a systematic and a random component. The systematic component is the bias in the model (*i.e.*, a systematic under or over prediction at some range) and the random component is the unexplained variation of measured ground shock about the prediction model (*i.e.*, the scatter of the data). Since the prediction model is linear with scaled range in the log-log space, the random component of the model prediction error is the variability (or scatter) of the data about the linear regression in the log-log space. This is pure error that cannot be accounted for by systematic adjustment to the model. The systematic error is the difference in the prediction and the linear regression.

a. Random Component

To quantify the random component of the model prediction error, the data are grouped by soil type (*i.e.*, groups for which the same model parameters are used) and analyzed by linear regression in log-log space. The data and the regression lines are shown in Figures 1 and 2 for free-field velocity and free-field stress, respectively. The random component of the model prediction error is now characterized

by the distribution of the natural log of the prediction error ratio. The prediction error ratio, ξ , is evaluated for each data point as the ratio of the observed ground shock (velocity or stress) to the value given by the regression line. For linear regression in the log-log space this is proportional to the regression residual. Table 2 shows the standard deviation of the natural log of ξ for each soil type, for both the velocity and stress data. The expected value of the natural log of ξ (not shown) is 0 for all cases because the regression line is an unbiased model. The table also shows the results of the hypothesis test for lognormality of ξ .

TABLE 2. VARIABILITY OF LOG-PREDICTION ERROR RATIO ($\ln[\xi]$).^a

Soil Type	Free-Field Velocity		Free-Field Stress	
	St. Devi. $\sigma_{\ln \xi}$	Hypothesis: Reject Lognormal?	St. Devi. $\sigma_{\ln \xi}$	Hypothesis: Reject Lognormal?
a. Dense Wet Sand	0.32	No	0.48	No
b. Loose Wet Sand	0.31	Marg.	0.28	No
c. Sandy Clay & Loess	0.33	No	0.45	No
d. Dry Sand	0.17	No	0.36	No
e. Wet Clay	0.08	No	0.39	No
f. Sand (Varied Wet to Dry)	0.15	No	0.04	No
g. Wet Loess	-	-	0.32	No
h. Shaley-Clay, Clay-Shale	-	-	0.31	No

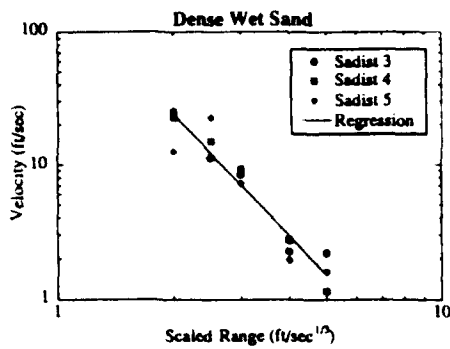
^a $\ln(\xi)$ = Natural logarithm of prediction error ratio.

$\xi = \frac{\text{Observed Ground Shock}}{\text{Regression Model Prediction}}$

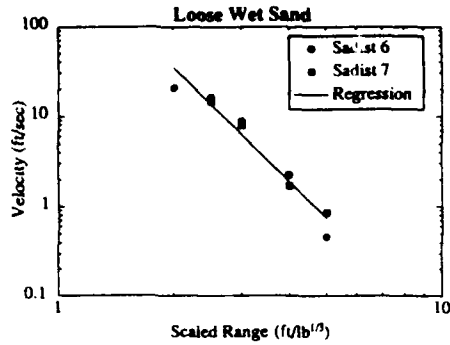
Since peak free-field stress is simply $\rho_o \times C_1$ times free-field velocity, we use the free-field velocity data to quantify the random component of the model prediction error. The larger data scatter for free-field stress is due to greater sensitivity of free-field stress to spatial variation of the geologic parameters ρ_o and C_1 . Since this additional uncertainty is highly site specific, we will treat it as a parameter uncertainty.

There are three main contributors to the free-field velocity model random prediction error (*i.e.*, factors that are not accounted for in the model): (1) bomb-to-bomb variability (*i.e.*, repeatability of experiments at a single site); (2) site-to-site differences for sites that fall into a single category (*e.g.*, all dry sand sites are not the same); and (3) spatial variability of velocity attenuation within a single soil type.¹ Not all sources of uncertainty are adequately represented for each of the soil types. For example, for case f in Table 2 we have only one shot, so that bomb-to-bomb and site-to-site variability is not represented. Hence, we estimate the random component of the model prediction using only those cases wherein we have

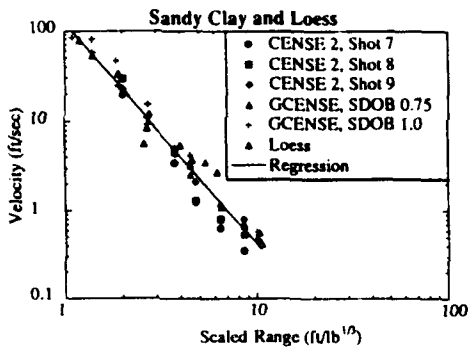
¹ Random measurement error can also add to the data scatter, however, we have not attempted to remove the measurement error component in this analysis.



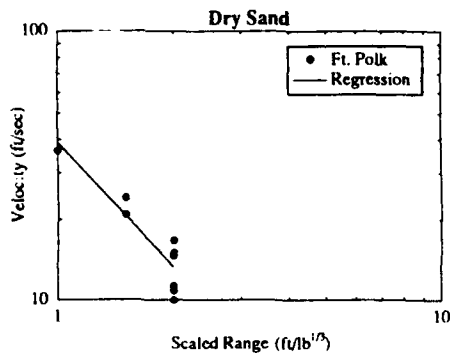
a. Dense Wet Sand - Sadist 3, 4, 5.



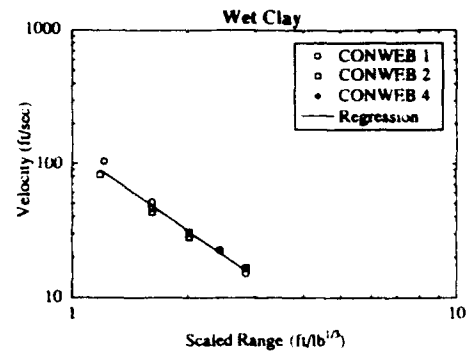
b. Loose Wet Sand - Sadist 6, 7.



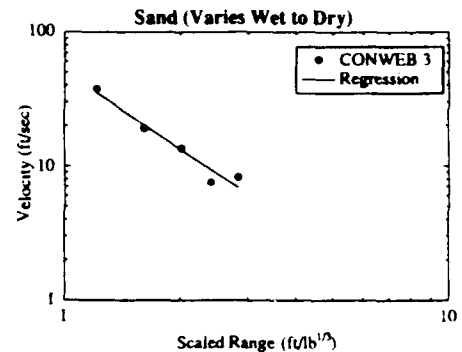
c. Sandy Clay & Loess - Cense 2, Shots 7, 8, 9; Gcense SDOB 0.75, SDOB 1.0; Loess.



d. Dry Sand - Fort Polk.

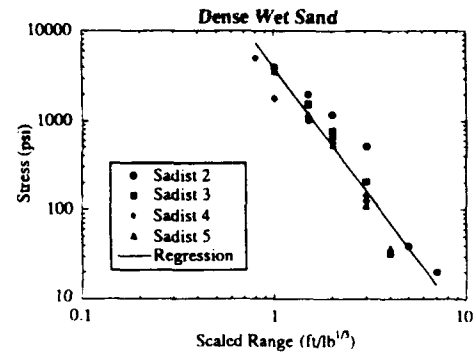


e. Wet Clay - Conweb 1, 2, 4.
Hollow Above Water, Below Water.

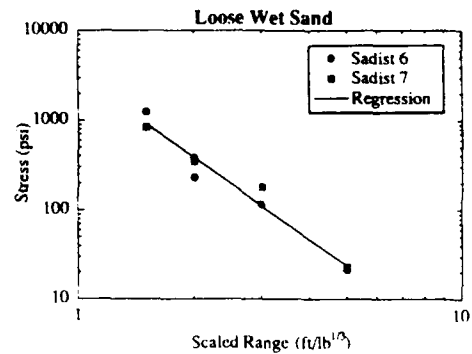


f. Sand (Varies Wet to Dry) - Conweb 3.

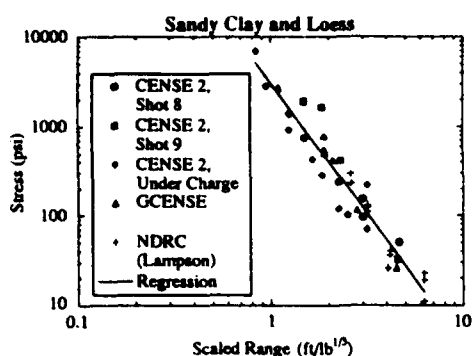
Figure 1. Free-Field Velocity vs. Scaled Range.



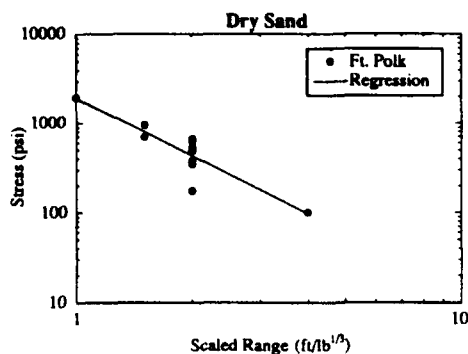
a. Dense Wet Sand - Sadist 2, 3, 4, 5.



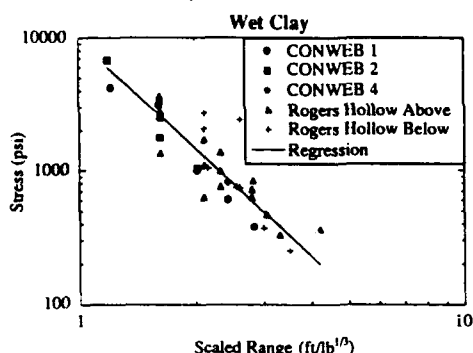
b. Loose Wet Sand - Sadist 6, 7.



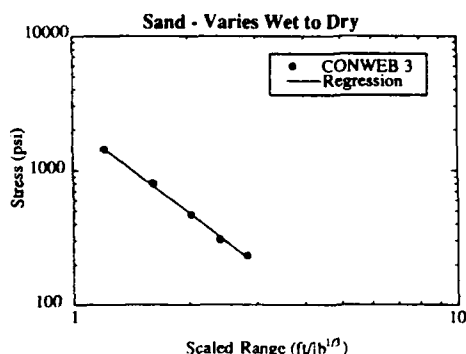
c. Sandy Clay & Loess - Cense 2, Shots 8, 9, Under Charge; Gcense; NDRC (Lampson).



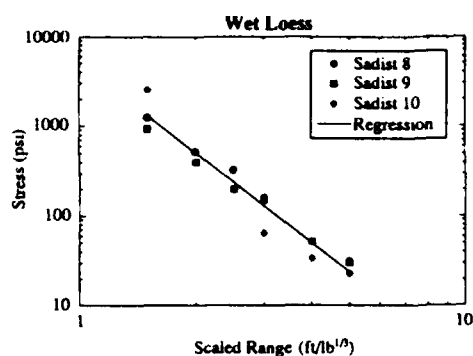
d. Dry Sand - Fort Polk.



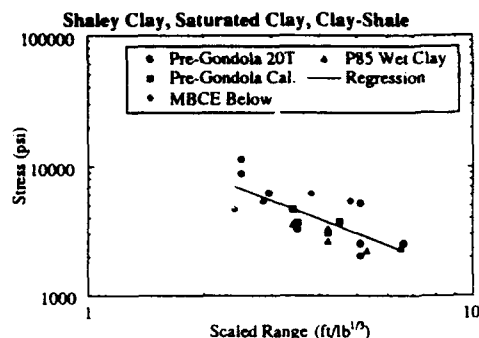
e. Wet Clay - Conweb 1, 2, 4; Rogers Hollow Above Water, Below Water.



f. Sand (Varies Wet to Dry) - Conweb 3.



g. Wet Loess - Sadist 8, 9, 10.



h. Shaley Clay, Saturated Clay, Clay-Shale - P85; Rogers Hollow Below Water; Pre-Gondola Cal; Pre-Gondola 20T, MBCE Below.

Figure 2. Free-Field Stress vs. Scaled Range.

multiple shots -- that is: cases a, b, and c. We do not include case e, even though there were multiple shots, because these shots used an atypical, highly controlled clay material that is not representative of backfill used in protective design.¹

From Table 2, the logarithmic standard deviations of ξ , for the three selected soil cases (a, b, c), vary over a small range from 0.31 to 0.33 and for all three cases we do not reject the lognormal model. Hence, we model the random component of the model prediction error as lognormal with a unit median and conservatively select the logarithmic standard deviation to be 0.35 (slightly larger than the observed 0.31 to 0.33 range).

The model presented above does not attempt to represent any change in the mean and standard deviation of ξ with range. To investigate range variability, we regress ξ on range and $(\xi - 1)^2$ on range. In both cases the R^2 value is very small, indicating that the mean and standard deviation can be modeled as range-independent. Hence, the range-independent model is used herein.

b. Systematic Component

The systematic component of the model prediction error is the difference between the model prediction and the mean of the data. From the analyses performed in the previous section we observe that the mean ground shock is a linear function of scaled range in the log-log space (if it were not then

¹An alternative approach would be to use analysis of variance techniques to separately quantify each uncertainty source.

prediction error would show a significant trend with range). Therefore, the systematic component of the model prediction error is simply the error in selecting the attenuation exponent, n (slope of the model in the log-log space) and the multiplying coefficient of the model. For purposes of the following discussion we will refer to the multiplying coefficient as v_1 . For the *PCDM* free-field velocity model, $v_1 = 160$, as given by Equation 1.

The systematic model error that is due to error in selecting the attenuation exponent (i.e., error in specifying the proper attenuation exponent given that the soil properties are known or well understood) is in addition to the basic parameter uncertainty (due to basic soil property randomness and prediction error) which is the subject of Section 5 to follow. These two sources of error are difficult to separate since we don't have precise soil characterization data for all of the tests. Hence, we will present a procedure for quantifying attenuation exponent uncertainty in Section 5 that combines both sources of uncertainty.

It remains to quantify the systematic component of the model prediction error that is due to the use of a fixed value for v_1 for all soil types. The *PCDM* model is a simplified procedure wherein v_1 is independent of material properties. In actuality, v_1 is a function of the size of the expanded cavity and the expansion velocity, and, therefore, depends on the material density, strength, and compressibility. The simplified *PCDM* procedure addresses this model deficiency by recommending attenuation exponents that compensate for this source of error. Because the compensating affect is range dependent, and was developed to match the ground shock data in the range of interest in protective design (i.e., scaled range of $1.0 \text{ ft/lb}^{1/3}$ to $3 \text{ ft/lb}^{1/3}$), the *PCDM* model should only be used in this range. For most soil types the *PCDM* model tends to overpredict the ground shock loading and is, therefore, design-conservative in the range of interest.

Research is ongoing to correct the design-conservative bias, therefore, we do not propose a systematic adjustment at this time. However, because of the simplified nature of the prediction model, we recommend that additional uncertainty be included to account for the potential systematic error. To quantify this uncertainty, we use a bounding procedure and estimate that conservative 90% bounds on the systematic error, in the scaled range of interest, is from $1/2$ the predicted value to $1 1/2$ times the predicted value. These bounds are approximately fit by a lognormal distribution with unit median and a logarithmic standard deviation of 0.30.

Finally, we combine the random and systematic components of the model prediction error. Since the total prediction error is the product of these two components, the total prediction error, ξ is also a lognormal random variable with unit median, i.e., $E[\ln \xi] = 0.0$ and logarithmic standard deviation given by $\sigma_{\ln \xi} = \sqrt{0.35^2 + 0.3^2} = 0.46$.

5. MODEL PARAMETER UNCERTAINTY

It remains to compute the statistics of the model parameters given in Equations 6-9. Model parameter uncertainty can have both a prediction error component (due to limited testing and site characterization) and a random component (variability in soil properties at the site).

The mean and standard deviation of the attenuation exponent is site specific and can be obtained using the following procedure (see Twisdale, Sues, and Lavelle [1992] for details): (1) Categorize the soil using Table V-1 of the *PCDM* which gives attenuation exponents and other soil properties necessary for ground shock prediction¹; (2) Select the mean value of the attenuation coefficient to be the value recommended in the table. If a range of values is given in the table, select the midpoint of the range²; (3) Quantify the uncertainty in the attenuation exponent as follows: (a) if a range of values is given in the table, assume that this range represents ± 1 standard deviation; (b) if the standard deviation obtained from the above procedure is less than 5% of the mean value, set the standard deviation to 5% of the mean attenuation exponent³.

To evaluate the free-field stress we also require statistics of the mass density, ρ_0 and the loading wave velocity C_1 . Uncertainty in these model parameters results from variability in the soil properties at the site (random component) and uncertainty in predicting the soil properties due to limited testing and site characterization (prediction error component). Both uncertainties will be case specific. For example, for design of a new buried structure located in a well controlled and well characterized backfill, the model parameter uncertainty will be small. However, for survivability assessment of an existing structure wherein the soil properties are not well characterized the uncertainty could be large. As a general rule, even for a well characterized and well controlled site, mass density and seismic velocity can be expected to have coefficients of variation of approximately 5%. Often it is acceptable to estimate the coefficient of variation for mass density and loading wave velocity using judgment since other uncertainties will typically dominate the reliability evaluation. The correlation coefficient (covariance, COV, divided by standard deviation of each variable) of these two variables is taken as 0.9, based on work of Sues and Twisdale [1990].

6. GENERIC RELIABILITY-BASED LOAD FACTORS

For many protective design situations, ground shock predictions are necessary for only a limited range from 1.0 to $3.0 \text{ ft/lb}^{1/3}$. Since model prediction errors will dominate the prediction uncertainty, it is possible to tabulate generic load factors for ground shock prediction. We have tabulated reliability-based load factors for two cases (A and B) that represent two different degrees of uncertainty in the site geologic properties. Case A corresponds to a controlled backfill material typical of protective construction, and Case B corresponds to a site where only limited material property information is available. The reliability-based load factors are derived using the equations given in Section 3 and are tabulated in Table 3.

¹If the soil does not fall precisely into one of the categories, select the two that best describe the site. Assign each category a weighting factor representing the degree of belief for each category. The weighting factors must sum to 1.0. If each category is equally likely, assign each category a weighting factor of 0.5.

²If more than one soil category was selected in Step 1, use a weighted average of the tabulated values.

³If more than one soil category was selected in Step 1, evaluate the total standard deviation using the weighting factors assigned to each attenuation exponent and the standard deviations evaluated in Step 3a.

TABLE 3. FREE-FIELD GROUND SHOCK LOAD FACTORS, λ

Reliability	Free-Field Velocity		Free-Field Stress	
	Case A ^a $\sigma_{\ln v_o} = 0.49$	Case B ^b $\sigma_{\ln v_o} = 0.54$	Case A $\sigma_{\ln p_o} = 0.53$	Case B $\sigma_{\ln p_o} = 0.73$
0.05	0.45	0.41	0.41	0.30
0.10	0.53	0.50	0.51	0.39
0.25	0.72	0.70	0.70	0.61
0.50	1.00	1.00	1.00	1.00
0.75	1.39	1.44	1.43	1.63
0.90	1.87	2.00	1.97	2.55
0.95	2.24	2.44	2.40	3.34

^aCase A: Typical Backfills: $\sigma_n = 0.15$, $\sigma_{\ln p_o} = \sigma_{\ln c_1} = 0.10$
 $\text{COV}[\ln p_o, \ln c_1] = (0.9) (0.10)$
 (0.10) , $R/W^{1/3} = 3.0$
 $\Rightarrow \sigma_{\ln v_o} = 0.49$, $\sigma_{\ln p_o} = 0.53$

^bCase B: High Site Uncertainty: $\sigma_n = 0.25$, $\sigma_{\ln p_o} = \sigma_{\ln c_1} = 0.25$
 $\text{COV}[\ln p_o, \ln c_1] = (0.9) (0.25) (0.25)$,
 $R/W^{1/3} = 3.0$
 $\Rightarrow \sigma_{\ln v_o} = 0.54$, $\sigma_{\ln p_o} = 0.73$

7. SUMMARY OF RELIABILITY-BASED GROUND SHOCK PREDICTION PROCEDURE AND EXAMPLE

Reliability-based analysis for ground shock prediction using the generic load factors consists of the following three simple steps: (1) Evaluate the nominal ground shock values (velocity and/or stress — Equations 1 and 2); (2) Select the desired reliability level based on the mission criteria and then find the corresponding load factor from Table 3; (3) Multiply the nominal ground shock value by the load factor obtained in Step 2. Note that for free-field stress, the load factor is applied to the nominal free-field stress value; do not use the factored velocity to compute the free-field stress.

For site-specific reliability-based prediction, Equations 4 and 5 are used.

To illustrate use of the generic load factors, suppose that we wish to compute a 90% reliability level for free-field stress at a scaled range of $2 \text{ ft/lb}^{1/3}$. The soil is a dense dry sand whose properties will be controlled during construction to have a target density of 104 ft/lb^3 , a seismic wave speed of 1000 fps , and 32% air voids.

The first step is to use Equation (1) to get the nominal PCDM prediction of peak free-field velocity. We select a value for the attenuation exponent, n , from Table V-1 of the PCDM. For a dense dry sand, a range of values is given in the table, i.e., 2.5 - 2.75, and we select the midpoint, or 2.63. The nominal value of the peak free-field velocity is obtained from Equation (1) as: $v_o = 25.8 \text{ fps}$. The next step is to evaluate the nominal peak free-field stress. To evaluate peak free-field stress we multiply the nominal peak free-field velocity by the soil mass density and loading wave velocity. Thus free-field stress is (Equations 2 and 3), $P_o = 626 \text{ psi}$.

Table 3 shows that $\lambda = 1.97$ for 90% reliability and the 90% reliability-based peak free-field stress prediction is $(1.97)(626) = 1233 \text{ psi}$. Thus, to achieve 90% reliability the free-field stress prediction is increased roughly by a factor of 2.

Note, that a more exact analysis using the equations given in Section 3, yields a slightly smaller $\lambda = 1.9$. More complete example applications can be found in Sues, Twisdale, and Lavelle [1993].

8. REFERENCES

Drake, J. L., et al., *Protective Construction Design Manual*, ESL-TR-87-57, Air Force Engineering and Services Center, Tyndall Air Force Base, November 1989.

Sues, R. H., and Twisdale, L. A., "Probability-Based Design Factors," Chapter 8 in, *DNA Manual for the Design Underground Tunnels*, Defense Nuclear Agency, DNA-TR-88-87, July 1990.

Sues, R. H., Twisdale, L. A., Lavelle, F. M., *Addendum to Protective Construction Design Manual, Reliability-Based Design for Reinforced Concrete Structures*, Air Force Civil Engineering Support Agency, 1993.

Twisdale, L. A., Sues, R. H., Lavelle, F. M., *Reliability-Based Analysis and Design Methods for Reinforced Concrete Protective Structures*, Air Force Civil Engineering Support Agency, August, 1992.

Reliability-Based Design Methods for the *Protective Construction Design Manual*

L.A. Twisdale, R. H. Sues, and F. M. Lavelle

Applied Research Associates, Inc., 6404 Falls of Neuse Road, Suite 200, Raleigh, NC 27615
Telephone: (919) 876-0018

ABSTRACT

Reliability-based design methods have been developed for use with the analysis and design procedures in the *Protective Construction Design Manual (PCDM)*. The application of these methods is based on easy-to-use, reliability-based design factors (RBDFs). The research focused on five fundamental areas: (1) airblast and aboveground structure response; (2) groundshock and belowground structure response; (3) fragmentation effects; (4) projectile penetration; and (5) protective structure systems reliability. The scope of the structural response research was limited to reinforced concrete structures; however, the load uncertainty analyses are generally applicable to protective structures of any material. The research also uncovered several areas of significant bias in the analysis methods, which could not be corrected without changes to the fundamental approach in the *PCDM*. RBDFs were not developed for these cases; however, either specific ways to improve the model prediction accuracy were recommended or improved models were provided and demonstrated.

INTRODUCTION

The process of developing RBDFs is illustrated in Figure 1. By conducting research to identify and analyze the uncertainties in load and structural response, the safety margins in the nominal load (E) and nominal capacity (C) can be quantified. Once the research is completed, the analyst/designer does not perform "probabilistic" analysis, but simply uses the resulting probability-based safety factors in a simple design equation for acceptable structural performance

$$\Psi \cdot C > \lambda \cdot E \quad (1)$$

where Ψ = RBDF on capacity and λ = RBDF on load effect. In some cases, a load factor of unity may be appropriate, whereas in others the load and capacity factors may be combined into a single factor. In general, a table of Ψ and λ values are provided corresponding to different levels of design survivability, P_S . A value of P_S is selected consistent with the design requirements, considering the consequences of failure and cost-survivability tradeoffs. A key advantage of the RBD approach is that optimized safety designs can be developed, whereas the traditional approach produces unknown safety margins. Reliability-based methods thus provide the designer with knowledge of the degree of conservatism or unconservatism in the design. The benefits of reliability-based design have been recognized in the structural and geotechnical engineering community and several major design codes are now reliability-based.

Table 1 summarizes several RBD definitions and the three-step procedure for performing reliability-based design. This table emphasizes that reliability-based approaches are particularly relevant to protective construction where the accepted design philosophy has long embraced the concept of limit states for both nuclear and non-nuclear weapon effects. Nonlinear response and local damage are acceptable to some degree, provided that structural integrity is maintained and critical assets are protected. Uncertainties are large due to the extreme load effects and the nonlinear dynamic response behavior of protective structures under these loads. Also, in protective construction it is important to have a quantifiable measure of the confidence that the protective structure will survive the weapon threat. In summary, the philosophy and approaches of protective design fit in ideally to the RBD concept. Concepts of structural reliability theory that pertain to protective construction are discussed by Twisdale, *et al.*, [1988] and also in Section II of the *PCDM* [Drake *et al.* 1989]. The results of the research are given by Twisdale, Sues, and Lavelle [1992] and a summary addendum has been prepared for use with the *PCDM* [Sues, Twisdale, and Lavelle, 1993]. This paper will summarize the approach, list the specific areas where RBDFs have been developed, and identify areas where significant biases in the *PCDM* methods were discovered.

APPROACH FOR DEVELOPING RBD FACTORS

For each design method that we analyzed from the *PCDM*, the approach for developing RBD procedures followed four basic steps. These steps are summarized in Figure 2 as: (1) identify failure modes and limit states; (2) characterize parameter uncertainties; (3) perform the probabilistic response analyses; and (4) perform the reliability assessment. The nominal parameters and models are the prediction equation in the *PCDM* for each load/response failure mode considered. The experimental data provides the linkage between the nominal procedures and the RBD development process. Figure 2 also illustrates that, in addition to RBDFs, there are many additional benefits of the RBD process.

This systematic step-by-step process may lead to one of several results in terms of how well the nominal *PCDM* design procedures perform. If the systematic errors (biases) were acceptably small and the data were sufficient, RBDFs were developed for use with the nominal *PCDM* procedures. If we found marginally acceptable errors and the data were sufficient to update the model parameters, we produced RBDFs for the *PCDM* procedures, using updated parameters. In most of these cases, we qualified the updates to the range of relevant data available. For cases in which the predictions did not agree with the experimental results, we determined if the data and our

understanding of the issues and research resources were sufficient to update the model. If so, we provided an updated or new model, stated necessary limitations, and gave factors for use with it. If not, and if the *PCDM* methods are conservative, we provide qualitative discussion and recommend that no additional factors be used.

An important final point regarding this research is that it has been done following the publication of the *PCDM*. Although in some cases we had access to new data or data not considered in the *PCDM*, the work would have proceeded more smoothly if it had been done in conjunction with *PCDM* development.

SUMMARY OF RBDFs

Table 2 summarizes some key RBD aspects for each conventional weapon effects phenomena considered. Due to space limitations, sample RBDFs are given only for 50% and 90% reliability levels.

Airblast Effects. The approach used to analyze the airblast uncertainties and preliminary RBDFs were described by Twisdale *et al.*, [1991]. The final load factors for incident airblast have changed slightly to reflect the fact that significant differences were noted in the mean prediction errors for the surface tangent and half-buried bombs [Twisdale *et al.*, 1992]. Separate RBDFs were therefore developed for surface tangent and half-buried bombs for reliability levels from 5 to 99 percent. A preliminary set of load factors for normally reflected airblast was also developed, based on the assumption that the *PCDM* method is median centered. Comparisons of the reflected normal pressure to an independent data set [Coltharp *et al.*, 1985] indicate acceptable agreement, although the preliminary factors tend to understate the data scatter. No RBDFs were developed for non-normally reflected airblast since the *PCDM* methodology overpredicts pressures and impulse by factors greater than three.

Above-Ground Structure Response. The single degree-of-freedom (SDOF) response model in the *PCDM* for aboveground wall flexural response was found to be conservatively biased by factors of two to four, when compared to half-scale tests. Sensitivity analyses identified the two largest sources of prediction error bias as reflected impulse (particularly for small standoffs) and flexural capacity (particularly if significant membrane action is likely). An RBD model was developed for breaching of above ground walls, based on dichotomous regression analysis of the *PCDM* equations, using data from McVay [1988]. For spall, the *PCDM* formula is overly conservative and a new, empirically derived spall model was developed for cased bombs. The new RBD spall model reduces both systematic and random uncertainties *vis a vis* the *PCDM* model.

Ground Shock Effects. The uncertainty in predicting ground shock is both site-specific and range dependent. A reliability-based model is developed using the *PCDM* prediction procedure coupled with analysis of free-field velocity and stress measurements from the ground shock database. Generic RBDFs are also developed for scaled ranges of 1.0 to 3.0 $\text{ft/lb}^{1/3}$ for two cases that represent two different degrees of uncertainty in the site geologic properties: a controlled backfill and a site where only limited soil property information is available. The details of the ground shock RBD methodology are discussed in a companion paper [Sues, Drake, and Twisdale, 1993].

Below-Ground Structure Response. The structural model for the flexural response given in the *PCDM* treats the wall as an equivalent lumped mass SDOF spring system and accounts for effects of structure-medium interaction. Comparisons of the model to experimental results indicates that the *PCDM* procedure significantly overpredicts wall response (support rotation). Additional comparisons were made with improved resistance functions and a 2DOF model that accounts for motion of the reaction structure. The 2DOF model with improved resistance function had significantly reduced prediction error and a reduced coefficient of variation for the random error. No recommended RBDFs were developed due to the systematic errors in the *PCDM* model. However, the improved model was recommended for RBD and we believe the 2DOF prediction error statistics are more indicative of full scale structures (even when the SDOF model is used). For breaching failures, the empirical *PCDM* model was found to be applicable only for scaled ranges less than 1.3 $\text{ft/lb}^{1/3}$. Due to the limited data, RBD factors were developed for only three reliability levels: 0.25, 0.50, 0.75.

Fragmentation Effects. The confidence level selection procedure in the *PCDM* design fragment penetration methodology has no direct relationship with the actual structure design survival probability. Analyses performed in Chapter 2 of the *PCDM* and by Sues *et al.*, [1991] demonstrated that the fragment penetration survival probability depends significantly on weapon standoff and target geometry. A preliminary RBD framework for selecting a design fragment was developed in this research. A lethality extreme value distribution is derived and the hypergeometric distribution is used to compute the probability that no fragments with lethality greater than the design fragment will impact the structure. Additional research is needed to tabulate results for use in selecting design fragments. For fragment impulse effects, a table of velocity load factors was developed based on comparisons to JMEM [1990] data. More work is needed to refine and verify an improved procedure.

Penetration Effects. The *PCDM* penetration formula was found to be approximately median centered when compared to 534 penetration tests into semi-infinite concrete. Dichotomous regression formulations of the spall and perforation models indicate that the *PCDM* methods are essentially median centered and unbiased. Analytic RBD models as well as RBDF tables were developed for both effects. The *PCDM* residual velocity model was compared to 45 test records and found to significantly overpredict actual residual velocities. In addition to these RBDFs, velocity load factors that account for uncertainty in striking velocity were developed for projectile penetration, perforation, and spall.

PROTECTIVE STRUCTURE SYSTEMS ANALYSIS

Protective structures are designed to defeat multiple weapon effects from a wide range of threats. In addition, because the loading, structural response analysis, and failure analysis will be subject to uncertainty it is often not possible to identify a single critical failure mode. For example, it may not be possible to establish, with certainty, whether a flexural failure from a standoff burst or fragment penetration will dominate. The reliability levels for the RBDFs must be selected so that when the individual failure mode reliabilities are combined, the system reliability meets the structure or facility design criteria. A simplified procedure for performing RBD for a protective system or facility is given in Figure 3. The system reliability objective R_s^* is established based on the mission objectives, considering facility functional performance.

Failure modes are identified using fault trees (see Twisdale, Sues, and Lavelle [1992] for a complete set of generic fault trees). The system reliability model takes into account the failure logic for each performance level, generally reduced to a Boolean expression of AND and OR operators. As indicated in Figure 3, reliability is allocated to each failure mode and RBD is performed for the controlling failure modes using the developed RBD factors. The final step involves a design check to recompute the system reliability, using the model developed in Step 3. Iteration is required if $\hat{R}_i < R_i^*$ or if $\hat{R}_i \gg R_i^*$.

SUMMARY

RBD methods have been developed for many of the design procedures given in the PCDM. Twenty-one tables of design factors have been developed for use with the PCDM methods or for updates to the PCDM methodology. A partial summary of these factors is given in Table 2. Significant biases were found in several of the PCDM design methods. In some cases, RBDFs were not developed due to the fundamental nature of the prediction errors or unknowns. Table 3 summarizes the biases and methodological gaps found in the PCDM methods examined in this research. It is clear that the procedures in the current Air Force PCDM are not risk-consistent. The RBD process provides a focused procedure to identify, characterize, and reduce prediction errors in the analysis and design of protective structures. The resulting RBDFs are easy to use and provide the designer with rationally developed safety factors to produce risk consistent designs.

ACKNOWLEDGMENT

The research was funded by the Air Force Civil Engineering Support Agency (now Wright Laboratory, Airbase Survivability Branch) at Tyndall Air Force Base.

REFERENCES

- Coltharp, D.R., *et al.*, "Semihardened Facility Design Criteria Improvement," Final Report ESL-TR-86-32, U.S. Army WES, Vicksburg, MS, June 1985.
- Drake, J.L., Twisdale, L.A., *et al.*, *Protective Construction Design Manual*, ESL-TR-87-57, Air Force Engineering Services Laboratory, Tyndall Air Force Base, Florida, November 1989.
- JMEM, *Joint Munitions Effectiveness Manual, Air to Surface Weapon Characteristics* (U), USAFTH61A1-3-2, Revision 3, Chapter 3, Change 3, 1990, CONFIDENTIAL.
- McVay, M.K., *Spall Damage of Concrete Structures*, Technical Report, SL-88-22, U.S. Army Waterways Engineering Stations, Vicksburg, Mississippi, January, 1988.

Sues, R.H., Drake, J.L., and Twisdale, L.A., "Reliability-Based Safety Factors for Ground Shock Loads in Protective Construction," *6th Int. Symp. on the Interaction of Non-Nuclear Munitions with Structures*, Panama City, FL, May 1993.

Sues, R.H., Hwang, C-W., Twisdale, L.A., and Lavelle, F.M., 1991. "Reliability-Based Design of R/C Structures for Protection Against Projectiles and Fragments," *Proceedings of the 5th Int. Symp. on the Interaction of Non-Nuclear Munitions with Structures*, Germany, April, 1991.

Twisdale, L.A., Sues, R.H., and Lavelle, F.M., "Reliability-Based Analysis and Design Methods for Reinforced Concrete Protective Structures," Final Report F08635-89-C-0121, Air Force Civil Engineering Support Agency, Tyndall Air Force Base, FL, August, 1992.

Twisdale, L.A., Sues, R.H., Lavelle, F.M., and Miller, D., "Research to Develop Reliability-Based Design Methodology for Protective Structures," *5th Int. Symp. on the Interaction of Conventional Munitions with Protective Structures*, Germany, April, 1991.

Twisdale, L.A., Sues, R.H., and Murphy, C.E., *Assessment of Reliability-Based Design Methodology for Protective Structures*, ESL-TR-88-27, Air Force Engineering and Services Center, Tyndall Air Force Base, Florida, 1988.

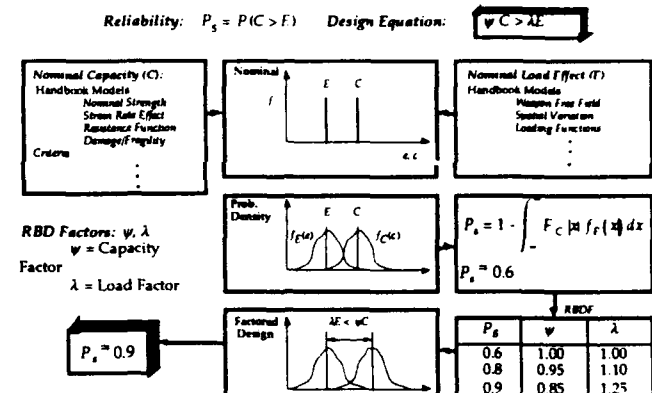


Figure 1. Development of RBD Factors for Use with Nominal Design Methods

TABLE 1. DEFINITION OF RELIABILITY-BASED DESIGN.

Reliability = Probability that the system will perform to its intended function under specified conditions.

Reliability of a protective structure = Probability that the protective structure will perform to its intended function under specified conditions; *i.e.*, the probability of survival to specified weapon threat(s) where survival means that the structural response does not exceed specified design limit states.

Reliability-based design (RBD):

1. Integrally tied to limit states (functional and ultimate).
2. Three-step procedure:
 - i. Identification of all modes of failure.
 - ii. Analysis of uncertainties and determination of reliability for each limit state.
 - iii. Analysis/design for the controlling limit states.
3. **RBD** = Structural analysis/design based on probability-based limit states using factored loads and capacities; permits a quantitative (reliability) measure of assurance of structural performance.

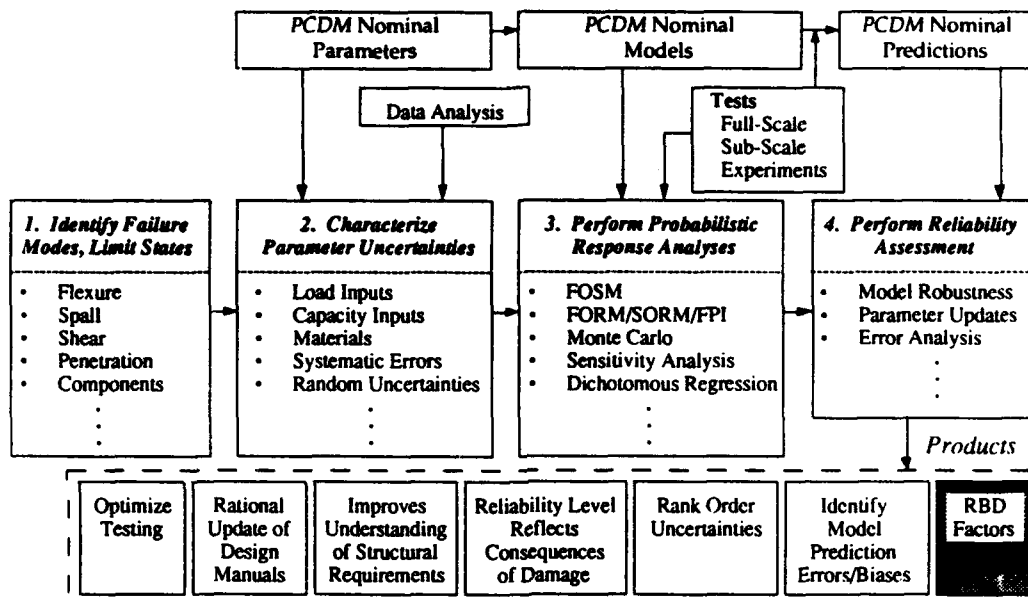


Figure 2. The Four Steps of the RBD Process.

TABLE 2. SUMMARY OF RBD METHODS FOR THE PCDM

Phenomena	PCDM Method	RBDs $P_s=0.50$ $P_s=0.90$	Comments
1. Incident Airblast (i) Pressure - Surf. Tang. (ii) Impulse - Surf. Tang. (iii) Pressure - Half Buried (iv) Impulse - Half Buried	~ Median centered Slightly unconservative Slightly unconservative Slightly unconservative	0.96 1.40 1.12 1.53 1.10 1.60 1.16 1.60	Based on CHEBS data; Range independent; separate factors for surface target and half-buried bombs.
2. Reflected Airblast (i) Normal Pressure and Impulse (ii) Non-Normal Pressure and Impulse	Assumed Unbiased Significantly Overpredicts Significantly Overpredicts	1.00 1.47 Not Developed Not Developed	Preliminary; based on assumption that PCDM is unbiased; combined ideal and nonideal effects assuming independence.
3. Aboveground Wall Flexural Response	Median Centered Conservative	1.00 1.21 New Model Developed 1.00 1.91	Factors of four overprediction when used with the PCDM airblast. Closed form expression developed for design reliability. The new model reduces both systematic and random uncertainties.
4. Breaching of Aboveground Wall	Conservative For Most Soil Types	A: 1.00 1.87 B: 1.00 2.00 A: 1.00 1.97 B: 1.00 2.55	Did not attempt to correct bias. Site-specific RBDs can be developed. Two generic RBDs given for sites A and B, where A = controlled backfill and B = only limited site information available.
5. Spall of Aboveground Wall	Significantly Overpredicts Slightly Conservative	Not Developed 0.95 —	Much better results were obtained for 2DOF model with improved resistance function. PCDM model valid only for scaled range $< 1.3 \text{ ft/lb}^{1/3}$. RBDs developed only for $P_s=0.25, 0.50$, and 0.75 .
6. Ground Shock (i) Free-field velocity (ii) Free-field stress	Conservative or Unconservative Slightly Unconservative	RBD Procedure Developed 1.07 1.22	An RBD method was developed that takes into account weapon standoff and target geometry. Procedure is valid only for structures for which the PCDM equivalent uniform load method is valid.
7. Belowground Wall Flexural Response	~ Median Centered Median Centered Median Centered Very Conservative	1.03 1.23 1.00 1.42 1.00 1.38 0.78 1.00	RBDs were also developed for striking velocity uncertainties for penetration, spall, perforation, and residual velocity.
8. Breaching of Belowground Wall			
9. Fragmentation Effects (i) Fragment Penetration (ii) Fragment Impulse			
10. Penetration Effects (i) Depth of Penetration (ii) Spall (iii) Perforation (iv) Residual velocity			

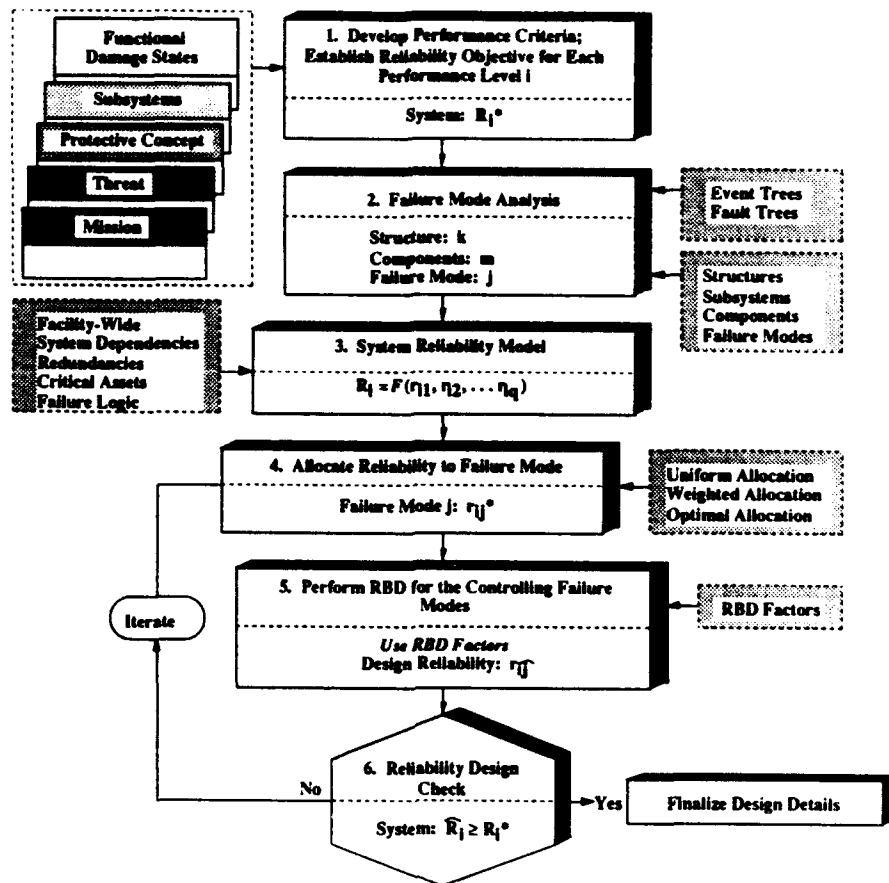


Figure 3. Systems RBD Procedure to Achieve Protective Facility Reliability Objective R_i^*

TABLE 3. BIASES AND METHODOLOGY GAPS IN PCDM METHODOLOGY.

	Conservative	Unconservative	Gap
Airblast and Aboveground Structure Response	<ul style="list-style-type: none"> Non-normal reflection factors Structural element resistance function One-way response model Centerstrip analysis method Cylindrical model for fragment impulse 	<ul style="list-style-type: none"> Free-field impulse Casing factor 	<ul style="list-style-type: none"> Partially buried bombs Spall equation Scale model vs. full-scale behavior for breach and spall
Ground Shock and Belowground Structure Response	<ul style="list-style-type: none"> Free-field velocity for strong and/or stiff materials close in Structural element resistance function 	<ul style="list-style-type: none"> Free-field velocity for weak and/or compressible materials close in Velocity waveform decay for weak and/or compressible materials 	<ul style="list-style-type: none"> Dynamic shear Breaching model very limited Use of same stress and velocity waveform Bomb detonation between burster slab and structure
Fragmentation	<ul style="list-style-type: none"> Fragment penetration formulas Use of standard fragment shape, normal collinear impact, zero rotational velocity Cylindrical spray pattern 	<ul style="list-style-type: none"> Mean fragment velocity 	<ul style="list-style-type: none"> Design fragment selection grossly incorrect Weight distribution for large fragments Fragment loading
Projectile Penetration	<ul style="list-style-type: none"> Penetration for modern high-speed projectiles (e.g., 30 mm A/C cannon) 		<ul style="list-style-type: none"> Residual velocity model very limited Rebar size/spacing

DYNAMIC PROPERTIES OF NOVEL THERMOPLASTIC HONEYCOMB CORE MATERIAL

by

Dr. R.L. Sierakowski
Civil Engineering Department
Ohio State University
Columbus, Ohio 43220 USA

Dr. C. A. Ross
University of Florida
Graduate Engineering
and Research Center
Eglin AFB, FL 32542 USA

ABSTRACT

An experimental investigation of the dynamic properties of novel thermoplastic honeycomb core materials was performed. The new materials, known as NorCore®, consist of a triangular type of honeycomb cell structure with sloping walls which are geometrically interlocked. In the present study, the static and dynamic compressive behavior of three different thermoplastic honeycomb core materials (high impact polystyrene, polycarbonate, surlyn) for several core thicknesses as well as for several initial starting thicknesses of the drawing sheet were studied. The corresponding diameters and heights of the specimens tested were 2 inches by nominally one, two, and three inches respectively. Static tests followed guidelines as set forth in Mil-Std-401B and ASTM Standard C-365. At least three specimens of each configuration were tested following the test procedures noted. Due to the unique cell structure configuration and large air entrainment, these honeycomb core materials show considerable promise as efficient energy absorbing materials. Parameters studied include initial starting draw thickness and free standing height for each of the three thermoplastic core materials studied.

INTRODUCTION

The subject of sandwich construction can be traced historically to the mid-nineteenth century (1). In the broadest context sandwich construction consists of two thin and stiff facing sheets of a dense material separated by a less stiff and strong core material of low density. The core should be stiff in shear in order to ensure that the facing sheets remain separated and flat. In general, the facing sheets take the bending loads while the core is designed to resist the applied shear loads. A commonly used sandwich panel in aircraft structures consists of metal faces with a honeycomb metallic core as shown in Figure 1.

In the present paper, a unique forming method is used to form a light weight sandwich core material. The technique is based upon the principle that when a thermoplastic polymer in either a sheet or extruded form is placed between heated mold surfaces, an adhesion between the polymer and heated platens occurs as the result of the application of a slight amount of pressure. By drawing the platens apart, the viscous polymer flows, extends, and forms a geometric core which is patterned after the design on the mold surfaces. An illustration of the press is shown in Figure 2. Unlike classical parallel wall honeycomb cores, the new material has angular walls with a resultant cell structure that is a function of the expansion height and the mold surface design. A unique feature of the stretched core structure is the increased flexural and shear integrity achieved through the existence of a wide flange area above the periphery of each open cell, obtained through the forming process. This area and the structure of the angular walled honeycomb core material provide new and interesting design possibilities. One important area of application of these stretched

thermoplastic core materials is their better resistance to impact damage. The increased energy absorption obtained with this honeycomb core material is attributed to the peripheral surface area formed during the forming process of the stretched honeycomb core. While some manufacturers data on this material has been reported on in reference (2) and transverse shearing stress data in reference (3), there appears to be less data available on the dynamic properties of this material. In the present paper, a series of static and dynamic compressive tests on three different core materials are reported on. The dynamic tests were conducted using a Split-Hopkinson Pressure Bar with the peak compressive data obtained shown to be a measured function of the original material draw height and web thickness of the core material. In addition, the surlyn core material is shown to exhibit a unique energy absorbing and recovery feature. In support of the static and dynamic test program, high speed pictures of the static and dynamic events have been obtained.

COMPRESSIVE STRENGTH

- Static

The flatwise compressive strength of sandwich cores was determined following ASTM Standard C365 and Mil-Standard 401-B, Section 5. It should be noted that the applicability of these standards to honeycomb cores is premised upon the ligaments/flutes/ribbons being parallel and perpendicular to the core thickness and facings respectively. As previously described herein, the present new honeycomb core structure has ligaments/flutes/ribbons which are at an angle with respect to the core and facing directions. In view of the lack of a directly applicable standard to the configuration studied here, the test specimen geometry as discussed in Mil-Standard 401-B, which in turn refers to ASTM Standard C-365, is used. Thus, for open-celled cores with cell size diameters greater than one-half an inch a minimum cross sectional area of 4 inches squared is recommended as long as at least one unit cell is included within the selected area. In the present tests, two inch diameter specimens were selected for the static tests since a dynamic test specimen size of two inch diameter was the maximum specimen size which could be tested. For each of the static compression tests, data is reported based upon a minimum of three tests per material with specimen core size, and starting thickness of plastic sheet reported (See Table I).

- Dynamic

Dynamic compressive tests of the same size of specimen as used in the static tests, were performed on a Split Hopkinson Pressure Bar (SHPB) as shown in Figure 3. A detailed description of the pressure bar and its operation can be found in Reference (4). Basically, the system operates with a striker bar launched by a spring, pneumatic, or gas driven system which impinges upon an

instrumented incident bar. Compressive pulses are generated in both bars, the length and/or duration of which in the incident bar is twice the wave transit time in the striker bar, and the magnitude of which is directly related to the striker velocity. When the compressive pulse, through the incident bar, reaches the specimen, a part is reflected and a part is transmitted, this due to the characteristic impedance mismatch of the specimen and bar, and also due to any mismatch in the cross sectional areas between the specimen and bar. The cross sectional area and the mechanical behavior of the specimen determine the exact shape of the reflected and transmitted pulses. A record of the strain-time history of the pulses at the incident and transmitter bar stations allow for determining dynamic information occurring at the specimens. The key elements to the pressure bar analysis is knowledge of the dispersive properties of the longitudinal wave speed in the pressure bars in order to shift the pulse in time, using the phase change of the Fourier Components of the wave between the strain gage position and the specimen. Results of the test programs are also shown in Table 1.

RESULTS & DISCUSSION

The relation of dynamic to static compressive strength for the core materials tested are shown in Table I. In an effort to show strain rate effects on stress-strain relations the results of tests of three honeycomb specimens are shown in Figures 4, 5, and 6. Figures 4, 5 show effects of changing the starting thickness on the strength of a polycarbonate honeycomb core. Figure 6 is an example of a polystyrene core material.

In each of Figures 4 and 6, one sees an increase in strength along with a reduction of strain at peak stress, with increasing strain rate. This is typical of many materials with increasing strain rate. What appears to be an increase in Young's Modulus with increasing strain may be deceiving in that the initial portion of the stress strain curve is in the rising portion of the loading pulse. In fact none of the specimens are true SHPB specimens because of their low wave speed. The wave speed of the polycarbonate material was experimentally measured at approximately 500 m/sec (1670 ft/sec).

Uniformity of stress along the length of a SHPB specimen may be achieved in a specimen where a stress wave can make at least five double transits across the specimen during the loading pulse. Using the measured wave speed, a single transit of a 25 mm polycarbonate specimen is 50 μ sec. Since the loading pulse is only 260 μ sec then only about 2.5 double transits are possible. The lack of uniform stress along the specimen length does not negate the measurement of the peak stress of the specimen. However, accurate measurement of the strain is not possible and validity of the stress-strain curve is doubtful.

The mode of failure for both static and dynamic loading was observed to be the same. The initial failure is one of unsymmetric out of plane buckling of the sloping webs. The unsymmetric buckling is present because of the misalignment of the web and the load. The buckling of the web was observed using a low speed video camera for the static case and a ultra high speed image converting camera for the dynamic case.

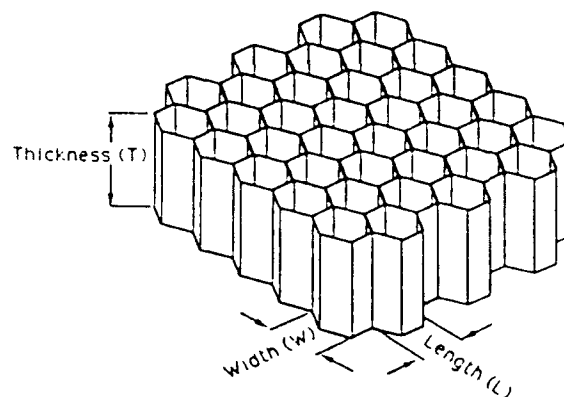


Figure 1. Classical parallel wall honeycomb core.

How NorCore is made

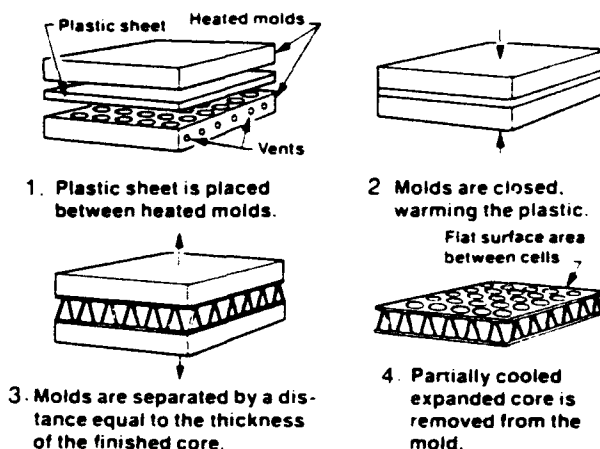


Figure 2. Schematic of fabrication process for NorCore honeycomb core panel.

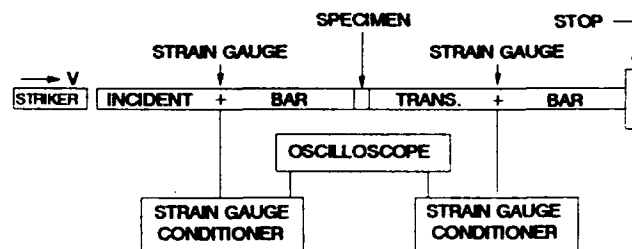


Figure 3. Schematic of a Split Hopkinson Pressure Bar (SHPB).

SUMMARY

All of the novel thermoplastic honeycomb core materials show increased strength with increased strain rate. The dynamic increase factor (dynamic/static strength ratio) is approximately 1.4 for the polycarbonate material, however, the surlyn material exhibited a much higher value of 3.8. In addition the surlyn material exhibits an almost complete return to its original shape after the load is removed. This occurred in both the static and dynamic surlyn tests.

The honeycomb material tested in this study does not show the large energy absorption exhibited by multicell foams at high strain rates.

ACKNOWLEDGEMENT

The authors would like to acknowledge the financial and laboratory support given by the Air Base Survivability Branch, HQ AF Civil Engineering Support Agency, Tyndall AFB, Florida.

REFERENCES

- (1) H.G. Allen, Analysis and Design of Structural Sandwich Panels, Pergamon Press, Oxford, 1969
- (2) E. Phelps and A. Bobkiewicz, "Stretched Polymer Core Offers Unique Advantages", Proceedings Composites Institute, Society of Plastics Industry, 47th Annual Conference, Cincinnati, Ohio, Feb, 1992.
- (3) D.W. Jensen, and C. Schneller, "Transverse Shearing of Novel Honeycomb Cores", Proceedings Advanced Composite Materials in Civil Engineering Structures, Las Vegas, Nevada, Jan, 1991.
- (4) J.A. Zukas, et al, High Velocity Impact Dynamics, John Wiley & Sons, New York, 1990

TABLE I: COMPRESSIVE DATA

NorCore Material	Nominal Thickness mm	Starting Thickness mm	Compressive Strength, MPa		f_{∞}
			Static (f_{∞})	Dynamic (f_{∞})	
Polycarbonate	25	3.2	0.88	1.29	1.47
Polycarbonate	25	4.8	3.45	4.95	1.44
Polycarbonate	48	4.8	0.43	0.52	1.21
Polycarbonate	76	4.8	0.48	0.67	1.40
Polystyrene	51	-	1.43	2.01	1.41
Surlyn	38	3.2	0.14	0.52	3.72

POLYCARBONATE HONEYCOMB

DIA=51mm L=25mm START THICK=4.8mm

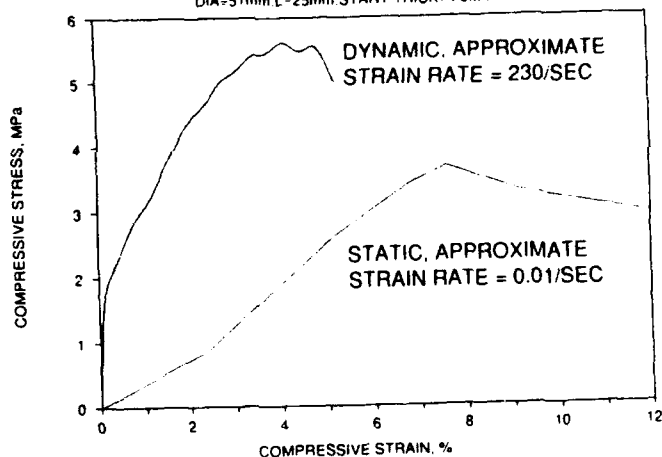


Figure 5. Uniaxial compressive stress-strain response of polycarbonate honeycomb core material with starting thickness of 4.8 mm and core thickness of 25 mm.

POLYCARBONATE HONEYCOMB

DIA=51mm L=25mm START THICK=3.2mm

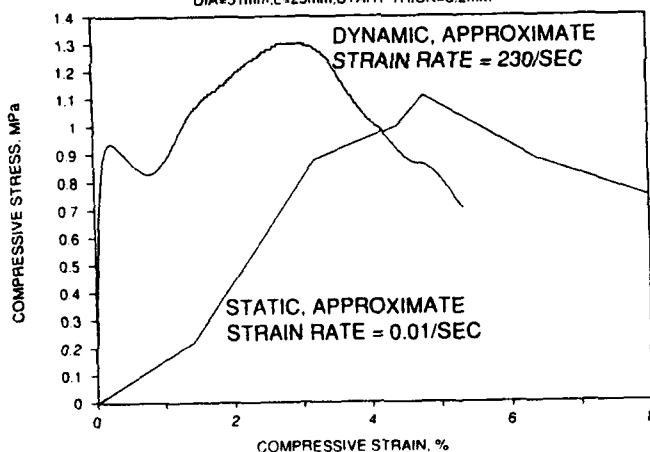


Figure 4. Uniaxial compressive stress-strain response of polycarbonate honeycomb core material with starting thickness of 3.2 mm and core thickness of 25 mm.

POLYSTYRENE HONEYCOMB

51 mm DIA, 51 mm LONG

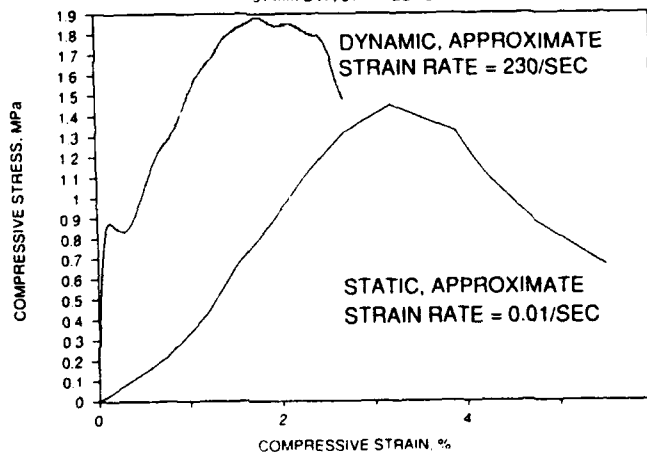


Figure 6. Uniaxial compressive stress-strain response of polystyrene honeycomb core material with unknown starting thickness and 51 mm core thickness.

COMPOSITE MATERIALS - THE FUTURE OF AIRMOBILE SHELTERS

Robert J. Majka

Applied Research Associates
Building 1142, P.O. Box 40128
Tyndall AFB, FL, 32403

ABSTRACT

No bare base shelter exists that will protect personnel and equipment in mobile command and control centers, aircraft maintenance facilities, dining facilities, sleeping and administrative facilities and in any other critical facility from all conventional weapon and chemical/biological weapon effects. At present, bare base facilities consist mainly of soft-walled tents, which provide limited protection against weather and chemical/biological weapons, and tactical shelters which protect only against fragments, low blast overpressures and some chemical/biological weapons. This has an obvious negative impact on the survivability of our mobile forces supporting the United States doctrine of Global Reach/Global Power. A rapid reaction force must be able to transport large amounts of material and supplies directly into the action area, using the least number of aircraft to establish a temporary operating location.

INTRODUCTION

Future airmobile facilities must be simple to erect, provide protection, operate across a full range of climatic conditions, and be recovered with minimum effort. The new Family of Portable Shelters (FOPS) will use state-of-the-art composite technology to provide transportability, survivability, durability and ease of construction/recovery. This paper will review the Air Force requirements and compare those against the most recent advances in materials engineering, shelter geometry, and prefabrication techniques. Air Force shelter requirements are contained in TAF SON 314-88, Survivable Airmobile Shelters [1] and in a draft Operational Requirements Document (ORD), CAF 314-88-I-A, New Family of Portable Shelters (FOPS) [2]. An ORD Working Group meeting was held in February 1992 to establish threat criteria and shelter requirements. Based on these inputs various shelter manufacturers, designers, material producers and fabricators were contacted and meetings/briefings were held. An extensive literature search was conducted through the Technical Information Center, Air Force Engineering Support Center, Tyndall Air Force Base, FL. Additional information was

obtained through organizations such as the American Society for Testing and Materials (ASTM), the Society for the Advancement of Material and Process Engineering (SAMPE), the United States Army's Natick Engineering, Research and Development Center (NRDEC), Natick, MA, Materials Laboratory, Watertown, MA, and the Combat Systems Test Activity, Aberdeen Proving Ground, MD. Information from these meetings and the literature reviewed is contained in a report to Wright Laboratory, Airbase Survivability Section (WL/FIVCS), Tyndall Air Force Base, FL, Survivable Airmobile Personnel Shelter [3]. At the time of the writing of this paper the referenced report was in the review process prior to publishing. It is the intent of this paper to discuss current Air Force requirements and seek information on emerging technologies covering airmobile shelters.

SHELTER REQUIREMENTS

TAF SON 314-88 and the draft ORD address airmobile shelters ranging in size from personnel shelters to aircraft maintenance shelters. Although the shelters differ in size, the requirements are the same for each. Each shelter will be deployed largely by airlift, but also by sea or land systems. The following requirements are included in the TAF SON [1] and draft ORD [2].

1. Each shelter must be rugged, portable, inexpensive and simple to maintain.
2. They should maintain as much similarity in design as possible.
3. Each shelter must be capable of being delivered in a standard shipping/storage container designed for outside storage, and must be compatible with current Material Handling Equipment (MHE), i.e., 463L pallets.
4. Containers must be airliftable on C-141, C-17, and C-130 aircraft. They must be transportable in or as part of sealift containers, or over land on flatbed trailers and/or railcars, and able to withstand the shock loading induced by rail transport.
5. Personnel shelters should require no more than four personnel to erect, and no more than two man-hours per 150

square feet of floor space. Other size shelters should have comparable erection times.

6. Shelters must include suitable and expedient flooring.

7. Flammability should be minimized in all shelters, and material must not produce toxic fumes when burning or melting.

8. Shelters must have the capability to interface with all available utilities.

9. Shelters must be functional throughout the temperature range from -50 °F to +130 °F. This was changed to -60 °F to +150 °F during the ORD Working Group meeting and further revised to say, "The shelters will operate across all climatic conditions".

10. All shelters must be able to withstand winds of 80 mph, with gusts to 100mph. The roof must support a snow load of 10 psf, with a solar load sufficient to raise the outer skin to a temperature of 205 °F. All shelters must withstand the ultraviolet effects of sunshine.

11. All shelters should have adaptation kits for world wide climates, differing conventional weapon protection levels, and differing shelter functions.

12. Shelters require some degree of hardness: splinter protection for the personnel shelter and up to semihardened protection for the aircraft shelter.

13. Shelters should afford chemical/biological weapon protection, and be able to be decontaminated.

14. Shelters must be capable of being coated with camouflage paint or be compatible with existing camouflage systems.

15. Shelters must retain blackout, rain and chemical/biological agent resistance capabilities, yet vent fumes, smoke, steam, and heat.

16. Portable shelters must be operable, maintainable, and repairable in all types of foreseeable conventional warfare environments.

17. Shelters require reliable and maintainable heating and cooling.

18. Shelters must be durable, and capable of withstanding 26 annual cycles of assembly and disassembly.

19. Shelters should be suitable for prolonged use for periods up to one year.

20. Shelters should withstand long-term storage (20 continuous years) with no degradation.

21. Hinges, pins, fasteners, and components requiring maintenance or periodic replacement should be either off-the-shelf or have spares provided with the shelter.

The above requirements are not in priority order. During the ORD Working Group meeting transportability and protection from chemical/biological weapons were placed ahead of the other requirements. Shelters developed under this effort will use the latest collective protection systems. Based on recent military experiences we must be able to deploy a force in a minimum amount of time, using the least number of aircraft possible, and protect that force from the environment and any specified weapon threat.

EXISTING SHELTER TYPES

There are two basic shelter types being considered under this research effort, soft wall or fabric shelters and rigid wall shelters. Fabric shelters are generally lighter in weight and have a higher packing volume ratio than rigid wall shelters. On the other hand rigid wall shelters are usually more durable and can offer better protection against some specified weapon threats. Fabric shelters would require the use of add-on kits to provide weapon effects protection while a rigid wall shelter could use modified wall panels with ballistic material included in the panel construction or an add-on kit similar to the fabric shelter kit.

The typical dimensions of an existing personnel shelter are 20 ft. by 32 ft. (fabric) and 20 ft. by 36 ft. (rigid wall). The TEMPER Tent (Tent, Extendable, Modular, Personnel) is currently used by United States forces for short duration deployments (less than six months). The TEMPER tent is 20 ft. - 6 in. wide and is extendible in 8 foot sections. The older GPM (General Purpose Medium) tent is 16 ft. by 32 ft. MERWS (Modular, Extendable, Rigid Wall Shelter) and EXP (Expandable Personnel Shelter) shelters etc. are used for longer deployments. MERWS is 19 ft. - 10-1/2 in. wide and is extendible in 6 foot sections. MERWS provides a 1200 sq. ft. shelter when used in combination with a two sided expandable ISO (International Organization for Standardization) container or 720 sq. ft. when used alone. The required set up rate for the personnel tents is 75 sq. ft./MH (man-hour).

The older GPM tents use wood poles for support and a heavy cotton duck fabric. They weigh in excess of 500 pounds. The TEMPER tent uses a lighter vinyl-coated polyester fabric and fold-out frame sections made from lightweight aluminum. A common problem in both types of tents is durability. Long duration storage adversely effects the GPM tent. The fabric itself has a tendency to tear or rot and the tie down ropes rot. The wood poles warp or are effected by termites, moisture, etc. The TEMPER tent fabric survives longer in storage and is less effected by moisture and mold. If properly packed the aluminum frames should last for the duration of the deep storage (20 years). The fabric itself, Velcro stripes, and zippers are where the problems have been identified. During recent operations (Desert Shield/Storm) TEMPER tents were the main source for billeting, food service and air transportable hospital facilities. Typically zippers broke, material wore through because of the coarse soil and Velcro material failed to work properly, although this was not as big a problem as the first two items. Solutions are already being worked by personnel at the NRDEC. Within a relatively short time after setting up the TEMPER tents, most units installed wood floors and entrance doors.

The larger shelters used for vehicle maintenance, supply storage, aircraft maintenance, etc. range in size up to the ACH (Aircraft Hangar) that is 76 ft. wide by 125 ft. long

and 25 ft. high at the crest [3]. The ACH is made from aluminum rib sections that are raised by using a block and tackle or with light equipment such as a high reach. There are fabric or rigid aluminum skin panels that are placed between the ribs to form the outer surface. The K-Span shelter is 50-60 ft. wide by generally 100 ft. long. The length can vary depending on the number of arch sections joined together. This shelter is constructed from 24 in. wide galvanized sheet steel that is formed into a 12 in. wide arch after being fed through a K-Span roll-forming machine. Other shelters of similar construction are also available. The required set up rate for the larger shelters is 120MH.

None of the existing shelters mentioned above meet all the requirements stated in the ORD [2] or the TAF SON [1]. They provide an excellent shelter but the emphasis for the new shelter has been placed on protection, ease of erection and recovery, transportability, cost, and a no special equipment requirement. The ORD states that all shelters should be able to survive at the splinter protection level, as a minimum, and up to the semihardened threat level for the aircraft shelters. A detailed description and analysis of each existing shelter system and some recently developed systems is included in Reference 4.

COMPOSITE MATERIALS

Protection can be provided by integral systems or add-on kits. Various fibers and their performance characteristics have been analyzed for use in the shelter components [5]. Kevlar 129, Kevlar KM2, Spectra Fiber, and various S-2 Glass fibers can be used in areas such as ballistic protection. Other fibers such as E-Glass can be used in the structural members. We have also studied several manufacturing methods such as pultrusion, filament winding, and braiding. All may be used to produce various shelter components. A number of upgraded systems are on the market and may meet most of the requirements in the ORD. MERWS is being re-engineered by NRDEC through DBA Systems, Melbourne, FL. The rigid panels are lighter and easier to assemble. A new connection system has been added and the set up rate is now equal to that of the TEMPER tent. Additional research using FRP (fiber reinforced plastic), such as Kevlite, to replace the aluminum skin on a rigid panel and foam insulation or various Owens-Corning insulation systems will further reduce panel weight and increase the insulation efficiency of the panels. Various weapon threats have been analyzed in Reference 5. To protect personnel and equipment in the shelters various protection methods have been analyzed and are discussed in Reference 5. Methods such as box bin revetments, earth berms, reinforced earth, ballistic blankets, and rigid panels were reviewed. The Air Force will determine the threat level for the final design of the shelter systems based on the information in Reference 5 and other operational requirements. Using the specified threat level, panels will be developed for use in either fabric or rigid wall shelters. In addition to weapon effects protection systems floor systems

and entrance doors, for fabric shelters, need to be developed. Composites with characteristics that will improve the performance of shelter components will be used. We must reduce the weight, make the shelters more durable, decrease the complexity of set up and recovery operations, reduce unit costs, and make the shelters survivable.

CONCLUSIONS

Because survivability is a critical requirement we should continue the intensive study of requirements, material behavior, and system configurations. We must accurately define the types and amounts of material required to provide survivability against the specified threats and determine the cost effectiveness of each level of protection. A detailed test series should be developed to effectively evaluate the materials and shelter systems. We must look at the durability of the material and the shelter system. The shelter must be capable of surviving 20 years of storage with minimal maintenance and/or multiple set up and tear down operations. During the review of material for this research effort it was determined that the latest information was not contained in published papers. Many of the new materials identified in this research effort were either proprietary and not yet released to the public or were being analyzed by a very small number of people, usually working for the material manufacturer. This paper is a call for information on materials and shelter systems that will meet the requirements specified by the Air Force. Any information should be forwarded to the author, who is the principal investigator for Airmobile Shelters, or to LT Westmoreland (USN), WL/FIVCS, Tyndall AFB, FL 32403-6001. LT Westmoreland is the Air Force Project Officer for Airmobile Shelters.

REFERENCES

1. Statement of Operational Need for a New Family of Portable Shelters, TAF SON 314-88, Headquarters, Tactical Air Command, HQ TAC/DERX, Langley AFB, VA, 2 November 1990.
2. Minutes of the Requirements Document Working Group, Working Group Meeting, Headquarters, Air Force Civil Engineering Support Agency, Tyndall AFB, FL, 12 March 1992.
3. Majka, R. J., Survivable Airmobile Personnel Shelter, Headquarters, Air Force Civil Engineering Support Agency, Tyndall AFB, FL, February 1992.
4. Twisdale, L. A., Frank, R. A., Lavelle, F. M., Airmobile Shelter Analysis (U), Vol. I, Headquarters, Air Force Engineering Support Agency, Tyndall AFB, FL, November 1992.
5. Twisdale, L. A., Frank, R. A., Lavelle, F. M., Airmobile Shelter Analysis (S), Vol. II, Headquarters, Air Force Engineering Support Agency, Tyndall AFB, FL, November 1992.

Airmobile Shelter Concept Selection Methodology

Francis M. Lavelle and Lawrence A. Twisdale

Applied Research Associates, Inc., Raleigh, North Carolina

ABSTRACT

A decision analysis methodology for screening and selecting air transportable shelter design concepts is presented. A major objective for the new family of portable shelters investigated in this research is to provide some level of either integral or upgradeable protection against fragmenting weapons. The methodology integrates the results of several subsystem trade studies (including shelter hardening studies) into a multi-attribute, multi-objective decision analysis tool for airmobile shelter evaluation.

INTRODUCTION

This paper describes the development and implementation of a multi-objective, multi-attribute decision analysis methodology to evaluate and select design concepts for the new U. S. Air Force (USAF) Family Of Portable Shelters (FOPS). An overview of the FOPS research program and results from the shelter hardening trade studies are presented in two companion papers at this symposium [Twisdale, *et al.*, 1993; and Frank, *et al.*, 1993].

In developing and evaluating new portable shelter concepts, the designer is faced with several design constraints (e.g., air transportability, erectability, etc.) and a wide array of design objectives (e.g., rapid assembly, low weight, durability, survivability, low cost, etc.). Due to the serious conflicts between many of the design objectives, it is not possible to fully maximize each individual design objective. For decision problems involving a limited number of alternatives and objectives, informal judgment-based procedures are often adequate for identifying the best alternatives. However, the complexity of the portable shelter evaluation problem requires a more formal and systematic decision-making process.

The decision analysis tool developed for the airmobile shelter analysis project is called ASEM, for Airmobile Shelter Evaluation Methodology. The model is more general than approaches used in previous shelter studies and eliminates many of the difficulties involved in comparing a wide array of disparate attributes. ASEM quantifies the influences of the design requirements and objectives specified in the FOPS Operational Requirements Document (ORD) on several fundamental, preliminary design decisions. A Summary of the ORD design requirements is provided in Majka [1993]. The key issue investigated in this research is the impact of proposed FOPS hardening objectives on the candidate shelter concepts. For this study, the term *shelter concept* refers to basic design issues such as: general shelter geometry, basic structural system, cladding materials, CWE hardening systems, and logistics features such as transport demand, assembly rate, estimated cost, and relative durability.

SHELTER CONCEPT SYNTHESIS

Sixteen small shelter concepts and eight large shelter concepts are formally assessed in the full research report [Twisdale, Frank, and Lavelle, 1992]. Due to space constraints, the scope of this paper is limited to our evaluation of the eight large shelter concepts. The shelters have nominal unobstructed floor areas of approximately 4800 ft^2 and are intended for use as portable aircraft maintenance hangars.

Shelter Classification Hierarchy. All of the small and large shelter concepts considered in this study fall into the shelter classification hierarchy shown in Figure 1. Since we consider the cladding system to be the principal distinguishing feature of a portable shelter, four major categories of shelters are shown in Figure 1: (1) fabric shelters, (2) rigid-panel shelters, (3) built-up load-bearing wall shelters, and (4) portable shells. Within these classes, we differentiate shelter concepts according to their structural systems (e.g., pole-, frame-, edge-, and air-supported fabric shelters). Due to practical limitations, several shelter classes are unable to provide the large clear spans required for the portable hangar category. The shelter categories represented by the eight candidate large shelter concepts are summarized in the following paragraphs.

Frame-supported fabric shelters are the most prevalent class of fabric shelters. Frame-supported tents retain most of the mobility and cost benefits of pole-supported tents while providing improved structural integrity and permitting the necessary clear spans.

Air-supported fabric shelters eliminate the need for a separate structural support system by using pressurized air to support their fabric skins. Air-supported fabric shelters offer the greatest potential payoffs in terms of shelter mobility (i.e., transportability and rapid assembly). Air-support shelters may be either *passive* or *active*. In passive air-supported shelters such as air beam or dual wall fabric shelters, the air pressure is maintained in sealed bladders. Active air-supported fabric shelters have a single skin, and their interiors are constantly pressurized by mechanical blowers.

Frame-supported rigid panel shelters are highly expandable rigid wall shelters that are shipped in disassembled pieces. The current USAF Harvest Bare family of shelters includes one large-area frame-supported rigid panel shelter, the Aircraft Maintenance Hangar (ACH). The advantages of frame-supported panel shelters generally include strength, stability, maintainability, and habitability; drawbacks include cost and assembly rate.

Built-up, load bearing wall shelters have field constructed load bearing wall systems that function as both cladding and as primary structural elements. Within this class,

the proposed *bin wall shelter* concept incorporates a conventional soil bin expedient hardening system directly into the basic shelter design. A lightweight roofing system such as a truss-supported fabric roof would enclose the structure. The shelter offers significant survivability and is 100% redeployable. The drawbacks of the bin wall shelter are its packing efficiency and slow assembly rate.

The only feasible large-area *portable shell* shelter system identified in our research is the *K-Span* corrugated cylindrical shell system. The K-Span system takes rolled sheet metal and deforms it on-site into a series of circular corrugated sections. The transportability of the K-Span system is reasonably good for a rigid wall shelter, and the structural integrity of the system is sound. Disadvantages of the system include: construction rate, specialized equipment and construction skill requirements, and inability to relocate the shelters.

Large Shelter Concepts. The eight candidate portable hangar concepts selected for consideration in the concept evaluation and selection task are summarized in Table 1. The shelters are classified according to the shelter classification hierarchy presented above. Sketches of the eight portable hangar design concepts along with preliminary estimates of their design attributes (packing ratio, cost, etc.) are provided in Twisdale, Frank, and Lavelle [1992].

TABLE 1. CANDIDATE LARGE SHELTER CONCEPTS.

Concept	Class
1. Frame-Supp. Fabric	Frame-Supp. Fabric
2. Arched Truss/Fabric	Frame-Supp. Fabric
3. Air Beam Hangar	Passive Air-Supp. Fabric
4. Dual-Wall Infl.	Passive Air-Supp. Fabric
5. Air-Supp. Hangar	Active Air-Supp. Fabric
6. Arch Panel Hangar	Frame-Supp. Panel
7. Bin Wall/Fabr. Roof	Load Bearing Bin Wall
8. K-Span Hangar	Portable Shell Struct.

CONCEPT EVALUATION AND SELECTION

Formal decision analysis methodologies are comprised of four basic steps: (1) structuring the problem alternatives and objectives in a clear, well-defined manner, (2) assessing the probable impact of each alternative on each of the design objectives, (3) determining the preferences of the decision maker (DM), and (4) evaluating the alternatives given the information in steps (1) through (3). Several decision analysis methodologies have been applied to shelter development problems. Linear weighted objective decision analysis schemes have been used by Schmidt, *et al.* [1988] in a concept study for portable collective protection shelters, by Johnson [1978] in an evaluation of tent concepts, and by Nickerson [1987] in a concept study for chemically hardened battalion aid stations. Steeves [1987] uses Saaty's analytical hierarchy process to evaluate tent concepts for use in a chemical warfare environment. Seabold, *et al.* [1986] have implemented a cost/benefit/time utility model for shelter selection. We believe that the decision analysis methodology best suited to the shelter selection problem is multi-attribute utility theory [Keeney and Raiffa, 1976]. Figure 2 presents a schematic overview of inputs and outputs for the ASEM multi-attribute decision analysis model.

1. Multi-Attribute Decision Analysis

An attribute is any parameter that can be used to measure the degree to which a specific design objective is achieved. For example, low initial cost is an objective that can be measured in

terms of dollars, and lightweight is an objective that can be measured in pounds. Utility theory provides a framework in which design attributes can be measured, combined, and compared consistently with respect to a decision maker's values and preferences. Based on a scale of 0 to 1, utility quantifies the intrinsic worth that the DM places on a particular attribute or combination of attributes.

As the number of attributes to be considered increases and as the preference set of the DM becomes more complex, a well-defined hierarchical structure for the decision problem becomes necessary. The hierarchical structure documents the relevant objectives and attributes, and explicitly illustrates the interactions between competing design objectives. The hierarchy employed in ASEM is illustrated in Figure 3. Detailed definitions of the objectives and attributes listed in the hierarchy are provided in Twisdale, Frank, and Lavelle [1992].

2. ASEM Preference Sets

The four major shelter objectives in the ASEM decision analysis hierarchy are: (1) high mobility (*i.e.*, transportability and rapid assembly), (2) low initial and life cycle costs, (3) adequate basic shelter performance features (*i.e.*, habitability, durability, etc.), and (4) protection from weapon effects. The first three objectives encompass the traditional objectives typically considered in the design of a portable shelter. In addition to these three objectives, the FOPS ORD specifies both Conventional Weapons Effects (CWE) and Chemical-Biological (CB) survivability objectives. CB protection is generally achieved through careful design of the shelter cladding system details and the shelter HVAC system, design considerations that are beyond the scope of this preliminary design study. Our research focuses on the CWE criteria specified in the FOPS ORD since these requirements will have a significant impact on the basic configuration of the FOPS design concepts.

The relative priorities assigned to the multiple design objectives listed in the shelter evaluation hierarchy are specified in ASEM as scaling constants. Four diverse sets of scaling constants were developed for the ASEM trade studies. In the first preference set, the scaling constants of the four major objectives are based on the results of a survey of AF personnel who attended the FOPS Requirements Working Group (RWG) meeting. In the second preference set, the four first-level objectives are assigned equal scaling constants. These two sets of scaling constants are referred to as the RWG preference set and the Equal preference set, respectively. The third and fourth preference sets are bounding cases: a set in which the scaling constant for survivability has been set to zero, and a set in which the scaling constant for cost has been set to zero. In both cases, the remaining three first-level scaling constants are assigned equal values (*i.e.*, one-third). The third and fourth preference sets are referred to as the No Cost and No Survivability preference sets, respectively.

The lower level scaling constants are assumed to be constant throughout the four preference sets. Since we did not have the opportunity to explore the question of attribute independence with a designated USAF DM (or group of DMs), we have proceeded with the preliminary assumption that the shelter attributes satisfy additive independence.

3. Hardening Upgrade Attributes

Four standard hardening upgrades are considered in the ASEM analyses: (1) a 36-inch thick free-standing soil bin or shelter-supported soil berm, (2) free-standing or shelter-supported aluminum panels with an areal density of 4 *psf*, (3) free-standing or shelter-supported S2-glass reinforced composite panels (4 *psf*), and (4) shelter-supported Spectra ballistic

blankets (4 psf). These four upgrades constitute a representative sampling of the hardening upgrades evaluated in the shelter hardening studies [Frank, Lavelle, and Twisdale, 1993].

The weapon threat selected to evaluate hardness of the four upgrades is a surface burst of a vertically oriented cluster munition at a standoff of 100 ft. Using the fragment hardening analysis results described in Frank, Lavelle, and Twisdale [1993], we quantified the CWE survivability attribute as the expected number of fragment perforation densities per 10 ft² of exposed wall area. Survivability attribute values for the four hardening upgrade configurations are tabulated in the full research report [Twisdale, Frank, and Lavelle, 1992].

4. ASEM Results

Several measures of shelter utility were considered in the research. In this section, present the overall shelter utility results as an illustration. The best-estimate overall utilities of the basic and upgraded shelter concepts are summarized in Figure 4. The plot in these figures illustrate the combined overall utilities of each shelter configuration under the four different preference sets (RWG, Equal, No Survivability, and No Cost). These plots form the primary basis for the shelter recommendations provided in Twisdale, Lavelle, and Frank [1993].

Under three of the four preference sets used in the ASEM studies, the basic and upgraded arch/panel and bin wall hangars are consistently ranked as the leading concepts. The No Survivability preference set is the only case under which the arch/panel and bin wall concepts do not rate the best. When survivability is given little or no priority, the basic air beam and frame-supported fabric shelter concepts excel. However, even under the No Survivability preference set, the basic arch/panel and bin wall hangar concepts are competitive with the fabric hangar concepts. For survivability scaling factors equal to or in excess of the preference levels inferred from the RWG survey, the basic and upgraded arch/panel and bin wall hangar concepts outperform the fabric hangar concepts.

5. Sensitivity Analysis

The ASEM studies indicated that the relative priorities assigned to the survivability and mobility objectives and the curvatures of the packing ratio and perforation density marginal utility functions significantly influence the overall shelter utilities. Sensitivity study results for two of these four factors (survivability priority and median perforation density) are presented below.

Sensitivity to Survivability Priority. Six leading portable hangar design concepts are considered in the survivability priority sensitivity studies: (1) the basic air beam fabric hangar, (2) the basic arch-supported panel hangar, (3) the arch/panel hangar with free-standing 36-inch soil bins, (4) the arch/panel hangar with S2-glass panels on the lower 15 ft, (5) the 12-inch bin wall hangar, and (6) the upgraded 36-inch bin wall shelter. Figure 5 shows plots of overall utility for these shelters as a function of the survivability scaling factor (k_s).

In Figure 5, the mobility, cost, and performance, scaling constants, (k_m , k_c , and k_p , respectively) are assumed to be equal:

$$k_m = k_c = k_p = (1 - k_s)/3 \quad (1)$$

The Equal scaling set used in the ASEM studies is generated when $k_s=0.25$ in Equation (1). Sensitivities were also developed for a second case in which the four scaling constants are assumed to be in the following proportions:

$$\begin{aligned} k_m &= k_p = (1 - 2k_s)/2 \\ k_c &= k_s \end{aligned} \quad (2)$$

When $k_s = k_c = 0.125$ and $k_m = k_p = 0.375$, this second set of constants closely approximate the RWG scaling set.

At low values of k_s , the leading concept under Equal scaling is the basic air beam shelter, but under RWG scaling the basic arch/panel concept is most preferred. At k_s values above 0.12 to 0.14, the 36-inch bin wall concept ranks first under both scaling sets. Note that the mid-range values of k_s produce the lowest points on the overall utility envelope. The intermediately hardened large shelter concepts (i.e., the 12-inch bin wall and the arch-supported S2-glass panel shelter) are fairly insensitive to the survivability scaling factor under both preference sets. Due to the lower perforation density in the 4 psf S2-glass panels, they become the preferred upgrade as k_s increases. Similarly, the S2-glass hardened arch/panel shelter becomes preferred to the basic arch/panel hangar and the basic air beam hangar at k_s values greater than 0.10 to 0.15.

Sensitivity to Single Attribute Utility Function Curvature. Next, we assess the sensitivity of the overall utilities of the leading large shelter concepts to the curvature of the fragment perforation density utility functions. These sensitivities are evaluated through perturbations of the median attribute value (i.e., the value associated with a marginal utility of 0.50). The ASEM results presented in the previous section are based on a perforation density utility function having a median value of 0.2 perforations per 10 ft². Here, we also consider median perforation densities of 0.1 and 0.05. The reductions represent stricter survivability performance requirements in that lower perforation densities will be required to achieve a given level of survivability utility. The results of the median perforation density sensitivity study are shown in Figure 6. The legend in Figure 6 displays the preference set and median perforation density associated with each point. The basic concept number and hardening upgrade configuration for each of the 10 concepts are encoded in the labels on the horizontal axis (e.g., 3BS indicates concept 3, the air beam fabric hangar, in its basic, unhardened configuration).

Within a given preference set (i.e., RWG or Equal), overall shelter utility always decreases as the median perforation density is decreased. The affect of median perforation density on overall utility is slightly greater under Equal scaling than under RWG scaling because survivability receives greater preference under Equal scaling. Shelters with 36 inches of soil protection (i.e., 3SL, 6SL, and 7SL) are unaffected by changes in the median value because their perforation densities are already at the best possible level. Similarly, unprotected shelters are also largely unaffected by changes in the median perforation density because their perforation densities are essentially at the worst possible level. Shelters influenced by variations in median perforation density include those with S2-glass, Spectra, or 12 inches of soil in either their basic or upgraded configurations (1S2, 6S2, 6SP, and 7BS).

If we restrict our attention to the top three RWG large shelter concepts, we observe that the 36-inch bin wall hangar (7SL) rises from fourth to first and the basic arch/panel hangar (6BS) drops from first to second as the median perforation density is reduced below 0.2. The soil hardened arch/panel (6SL) shelter maintains its overall utility and becomes one of the top three large shelter concepts as the median value is reduced. For the Equal scaling preference set, the leading large shelter concepts are all soil hardened and, as a result, are completely insensitive to median perforation density.

In general, decreasing median perforation density significantly affects the overall utility of the intermediately hardened shelters concepts. Therefore, stricter requirements for high probabilities of survival tend to reduce the relative utility of

composites-hardened shelters in comparison to both soil-hardened shelters and unhardened shelters.

CONCLUSION

A multi-attribute decision analysis model for the evaluation of airmobile shelter concepts has been presented. The model is applied in an evaluation of eight candidate portable hangar concepts. Each concept has up to four different CWE hardening upgrade configurations. The decision analysis model is used to quantify the ability of each concept to meet competing objectives under several different sets of decision maker preferences. Detailed interpretations of the ASEM results and recommendations are presented in Twisdale, *et al.* [1992, 1993].

It is clear that the CWE survivability objectives specified for the new family of portables shelters (FOPS) will significantly influence the mobility, cost, and basic performance characteristics of the preferred shelter concepts. Sensitivity studies indicate that strong preferences either for or against CWE survivability objective tend to result in the best overall shelter utilities. This result suggests that some form of selective hardening may be the best design approach for the new FOPS.

ACKNOWLEDGMENT

This research has been supported by the Airbase Survivability section of Wright Laboratories at Tyndall Air Force Base. The USAF contract monitor is Lt. Keith Westmoreland (USN).

REFERENCES

- Frank, R. A., Lavelle, F. M., and Twisdale, L. A., 1993. "Fragment Hardness Analysis of Composite Materials for Airmobile Shelters," *Sixth Int. Symp. on the Interaction of Nonnuclear Munitions with Structures*, Panama City, FL, May 1993.
- Johnson, A. R., 1978. *Comparative Evaluation of Concepts for Tentage*, Natick/TR-78/009, January 1978.
- Keeney, R. L., and Raiffa, H., 1976. *Decision with Multiple Objectives: Preferences and Value Tradeoffs*, J. Wiley and Sons, New York, 1976.
- Majka, R. J., 1993. "Composite Materials -- The Future of Airmobile Shelters," *Sixth Int. Symp. on the Interaction of Nonnuclear Munitions with Structures*, Panama City, FL, May 1993.
- Nickerson, C., 1987. *Concept Study: Mobile Medical Facility for the Chemical Battlefield*, Natick/TR-87/007L, July 1987.
- Schmidt, R. N., et al., 1988. *Collective Protection System Integration Study*, AFWAL-TR-87-2083, January 1988.
- Seabold, R., et al., 1986. *Advanced Base Shelter Evaluation Program (ABSEP)*, NCEL-UG-0009, December 1986.
- Steeves, E. C., 1987. *Evaluation of Design Concepts for Tents with CW Protection Requirements*, Natick/TR-88/023, September 1987.
- Twisdale, L. A., Frank, R. F., and Lavelle, F. M., 1992. *Airmobile Shelter Analysis*, Air Force Civil Engineering Support Agency, Tyndall Air Force Base, FL, Contract F08635-88-C-0067, November 1992.
- Twisdale, L. A., Lavelle, F. M., and Frank, R. F., 1993. "Research to Develop Concepts for a New Family of Airmobile Shelters," *Sixth Int. Symp. on the Interaction of Nonnuclear Munitions with Structures*, Panama City, FL, May 1993.

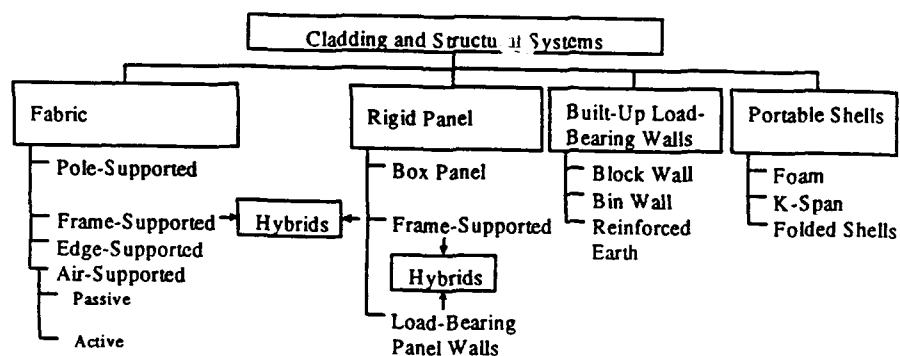


Figure 1. Hierarchy of Shelter Categories.

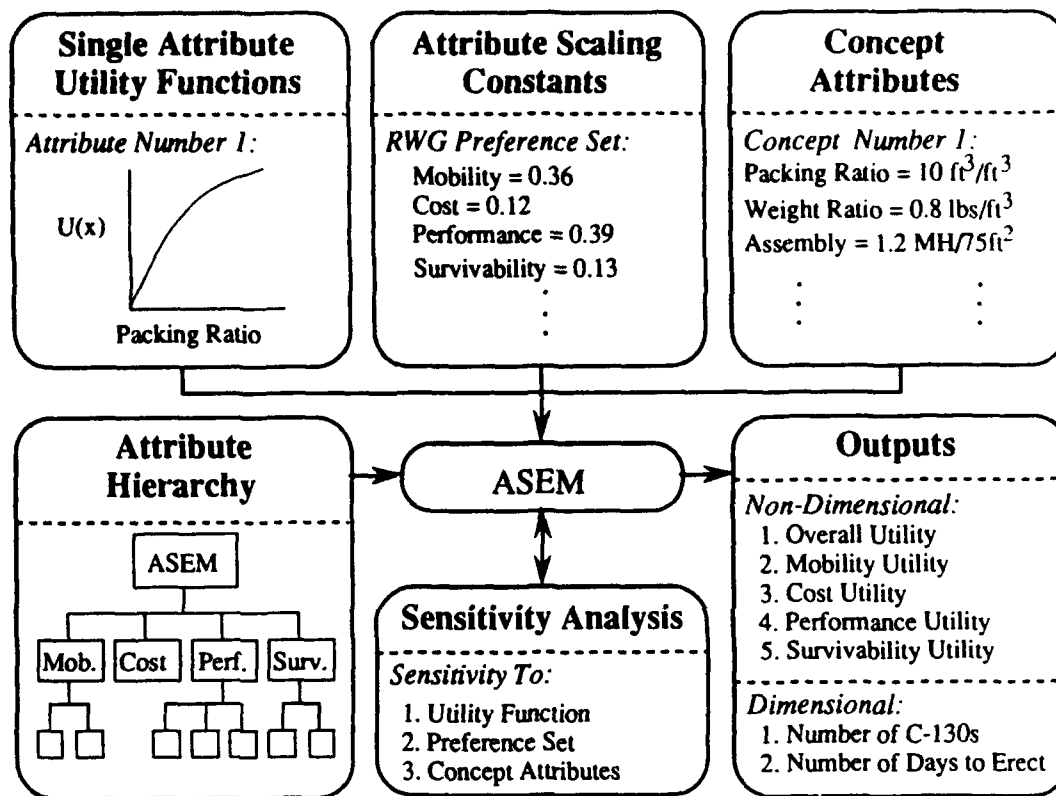


Figure 2. ASEM Inputs and Outputs.

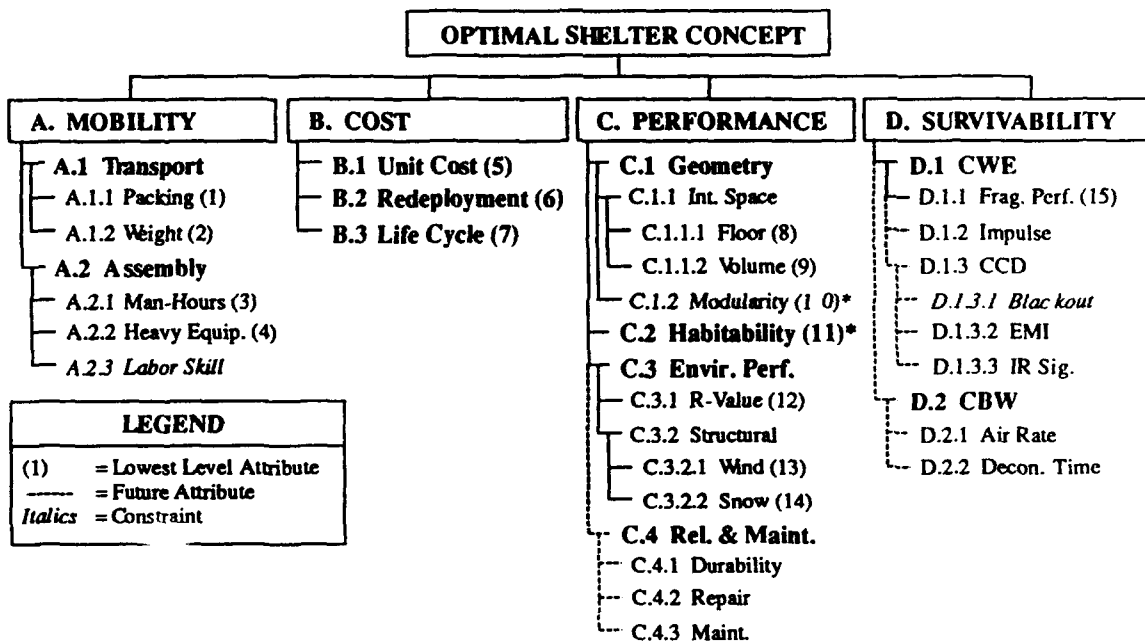
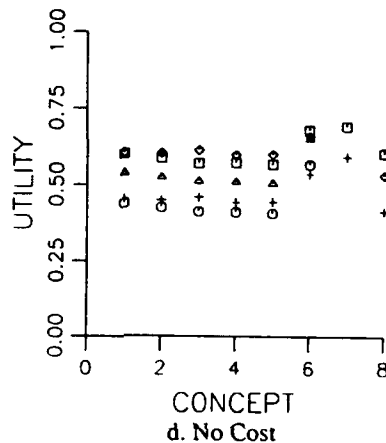
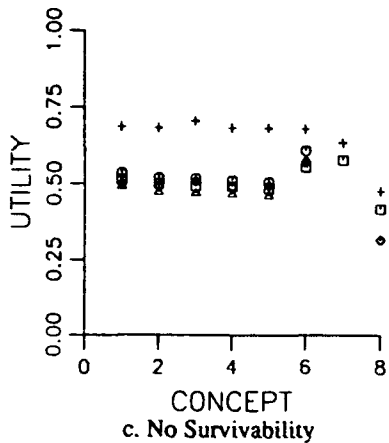
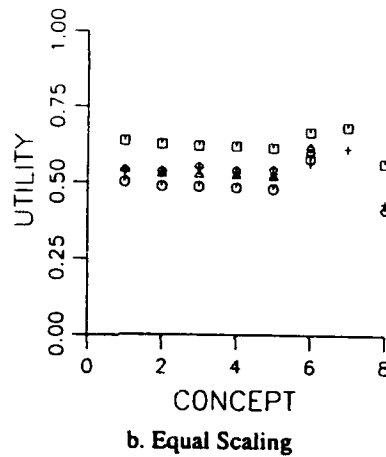
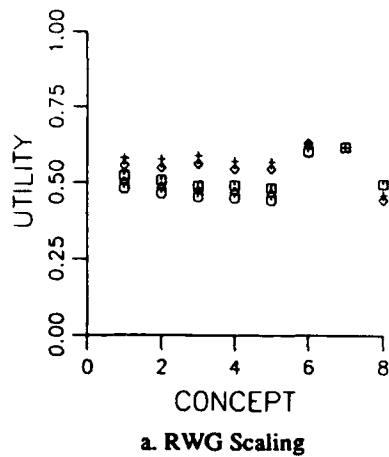


Figure 3. Airmobile Shelter Design Analysis Hierarchy.



- 1 = Frame/Fabric
- 2 = Truss/Fabric
- 3 = Air Beam
- 4 = Dual Wall Infl.
- 5 = Air Supported
- 6 = Arch/Panel
- 7 = Bin Wall/Fabric
- 8 = K-Span

- + = No Upgrade
- = 36" Soil Bin
- = 4 psf Aluminum
- △ = 4 psf S-2 Panel
- ◇ = 4 psf Blanket

Figure 4. Overall Large Shelter Results.

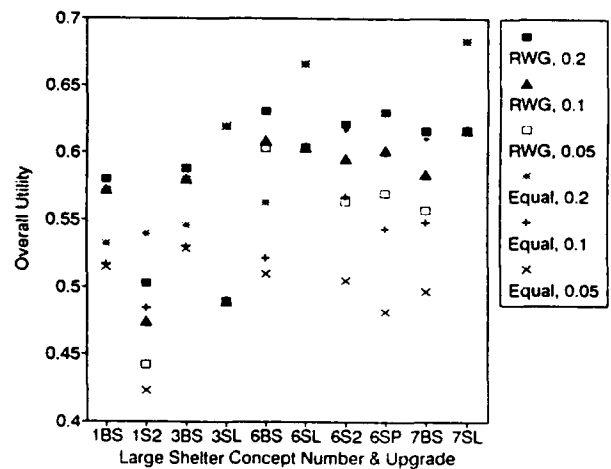
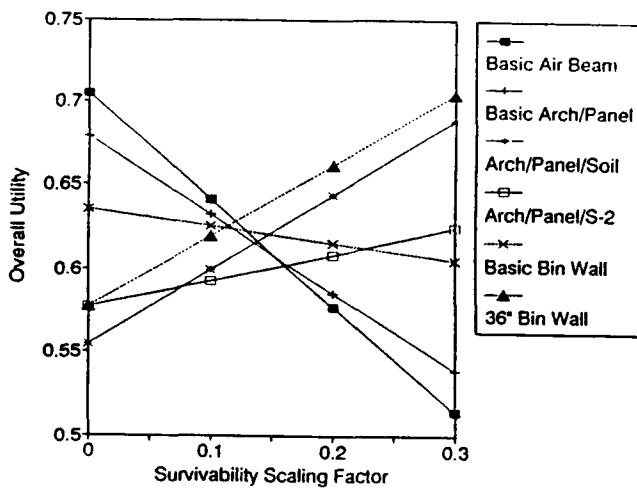


Figure 5. Shelter Sensitivity to Survivability Scaling Factor.

Figure 6. Sensitivity to Median Perforation Density.

Research to Develop Concepts for a New Family of Airmobile Shelters

Lawrence A. Twisdale, Francis M. Lavelle, and Robert A. Frank

Applied Research Associates, Inc., Raleigh, North Carolina

ABSTRACT

This paper summarizes research to develop operational requirements and design concepts for a new family of Air Force portable shelters (FOPS) that provide basic and upgradeable levels of protection from conventional weapons effects. The research focused on identifying and reviewing applicable technology, developing and evaluating shelter concepts, and evaluating the feasibility of hardening the shelters against conventional weapon threats. The basic products included a computational model for quantifying survivability from fragment effects, a multi-attribute shelter selection methodology, recommended shelter/hardening concepts, and a roadmap for shelter development.

INTRODUCTION

Basic USAF doctrine identifies the need for flexibility, responsiveness, and mobility of Air Force tactical forces. The primary purpose of the transportable shelters in the USAF inventory is to provide shelter for rapidly deployed forces in bare base situations and other similar settings. Shelters in the current inventory include Harvest Eagle, Harvest Bare, and Harvest Falcon assets. These shelters will require replacement in the near future, providing an opportunity to develop new shelter designs that provide protection against conventional weapon effects.

Current portable shelters were primarily designed to address three critical design considerations: mobility, operability/maintainability, and cost. Improved operability in high threat areas, specifically protection from chemical-biological warfare (CBW), is an additional design consideration reflected in the more recent additions to the shelter inventory. However, existing shelters offer little or no protection against small arms and fragment threats. Significant advances in materials technologies have occurred since the current shelters were developed, providing the opportunity to incorporate ballistic protection in the new FOPS without unduly compromising shelter mobility. This paper summarizes the results of the initial research project [Twisdale, Frank, and Lavelle, 1992] performed for Wright Laboratory, Airbase Survivability Section, at Tyndall Air Force Base.

METHODOLOGY

The approach to identifying and evaluating the most promising shelter and hardening concepts for FOPS included five basic tasks, as illustrated in Figure 1: (1) Definition of Operational Requirements; (2) Shelter Concept Synthesis; (3) Hardness Analysis; (4) Concept Evaluation, Screening, and Selection; and (5) Trade Studies and Optimization. These five tasks provide for the definition of operational requirements for FOPS; review of relevant technology on portable shelters, materials research, weapon effects, and hardening concepts; the synthesis of this technology into shelter and hardening concepts; and the screening, evaluation, and selection of recommended shelter concepts for follow-on development. The first step in developing a structural design concept for the new shelters is to define the loads the shelter must support. The magnitude of these loads is heavily dependent on the fragment hardening system. Consequently, the structural analysis in this study focused on the hardening methods and loads required to provide Splinter Protection, which was the goal specified in the draft Operational Requirements Document (ORD).

The primary end products of the research effort included recommended shelter concepts and a roadmap for development and testing of the shelters. Additional products of the research were: (1) a working draft ORD, (2) an assessment of current technology with respect to portable shelters and methods for hardening lightweight shelters, (3) an improved methodology for evaluating the survivability of structures for fragment effects, (4) an assessment of the feasibility of hardening FOPS, (5) a multi-attribute decision analysis methodology for evaluating and ranking shelter concepts, and (6) results of preliminary trade and optimization studies.

Task 1: Definition of Operational Requirements. Under this task we developed the operational requirements for FOPS. To formalize the operational needs specified in TAF SON 314-88, we reviewed the current inventory of modular and expandable shelters and visited over a dozen user and support agencies to gather data on current shelter performance, perceived deficiencies, and desired attributes for FOPS. On the basis of our review, we prepared a working draft ORD. We also identified conflicting shelter performance

priorities within the Air Force and recommended that a FOPS Requirements Working Group (RWG) meeting be held to review the draft ORD and form an Air Force consensus on shelter priorities. This meeting was held on 10-14 February 1992. A FOPS survey was subsequently prepared and distributed to the RWG attendees soliciting their comments and inputs on the relative importance of the major shelter requirements. The RWG survey results provided the basis for one of the preference sets used in the shelter evaluation under Task 4.

Task 2: Shelter Concept Synthesis. We reviewed relevant shelter technologies and synthesized possible shelter and hardening concepts through a systematic procedure that included literature reviews; computerized database searches; and visits to relevant laboratories, researchers, and practitioners. The resulting hierarchy of shelters is shown in Figure 2. Based on the results of this technology survey, we developed a total of 24 small and large span shelter concepts for evaluation. For the purposes of this study, the term shelter concept included the following design features: (1) geometry (size and shape), (2) structural system, (3) cladding system (soft- or hard-wall), (4) materials, (5) integral and/or upgraded hardening systems, (6) packaging, (7) assembly characteristics (rate and skill/equipment requirements), and (8) estimated cost. These basic design features encompass key operational issues and constraints for the candidate airmobile shelter concepts that must be quantitatively assessed before detailed design and validation studies of selected concepts can begin.

Task 3: Hardness Analysis. The SON and ORD for FOPS require Splinter Protection as a minimum with Semihardened Protection a goal for high value shelters. Under this task, we developed the necessary analysis tools and performed a preliminary assessment of the feasibility of hardening FOPS against small arms fire and the airblast and fragmentation effects of conventional munitions. Fragmentation, being the controlling weapon effect for lightly protected structures, was the focus of our hardening analyses.

The analysis of fragment hardening feasibility for FOPS required the development and implementation of new analysis models for weapons effects data and perforation resistance. Current design procedures, such as those presented in the *Lightweight Armor Design Handbook* [MTL, 1990] and the *Air Force Protective Construction Design Manual* [Drake, et al., 1989], were inadequate in that: (1) they consider only the fragment weight distribution and do not consider the number of fragments generated or the probability that critical fragments will strike the target at the specified standoff; (2) the weapon characteristics are overly conservative in that they generate larger average fragment weights and higher initial velocities than observed in arena testing; and (3) the methods do not provide a means for evaluating the survival probability stated in the Splinter Protection and Semihardened Protection threat definitions. Use of the traditional fragment analysis procedures

would therefore provide biased and incorrect analyses of airmobile shelter concepts and would not permit evaluation of survival levels vis a vis Air Force specified threats.

The new analysis methodology, termed SAFE (Survivability Assessment for Fragment Effects), models the weapon fragment weights, velocities, and ejection angles based on arena test data for the selected munition. The munition surface is discretized into series of cells and mapped onto the target surface using straight line trajectories. Output quantities calculated include the bomb cell impact points on the target surface; critical fragment weight, impact angle, and striking velocity; and number of perforations. SAFE is used to perform a preliminary assessment of the fragment hardening feasibility for FOPS. As part of this assessment, we developed fragment models for six munitions that represent a spectrum of potential weapon threats for FOPS: (1) a 1000-pound bomb, (2) a 40-mm aircraft (A/C) cannon, (3) a cluster munition, (4) a 152/155-mm artillery round, (5) a 122-mm rocket, and (6) a 250-pound missile. We also developed empirical Thor perforation models for Kevlar KM2, Spectra, and S2-glass fabrics and panels. The detailed models and results are described by Frank, Lavelle, and Twisdale [1993].

Task 4: Concept Evaluation, Screening, and Selection. We developed and implemented the Airmobile Shelter Evaluation Methodology (ASEM) code, a multi-attribute decision analysis tool, for selecting the most promising design concepts [Lavelle and Twisdale, 1993]. There were three major tasks involved in selecting the leading concepts: (1) developing a set of design attributes that accurately characterizes each basic or upgraded shelter concept, (2) evaluating these design attributes, and (3) implementing a decision analysis methodology that models the conflicting design objectives specified in the FOPS ORD. Since the selection of the "best" shelter concept depends on the relative priority or weight assigned to each of the design objectives, we considered four different preference sets: (1) preferences based on a survey of the members of the FOPS Requirements Working Group (RWG), (2) an Equal preference set (i.e., mobility, cost, performance and survivability equally important), (3) a No Cost preference set, and (4) a No Survivability preference set. The latter two cases represent bounding sets in which one major objective is given zero weight and the remaining three are weighted equally.

Task 5: Trade Studies and Optimization. The trade studies and optimization task provided supporting calculations for quantifying the basic and upgraded shelter attributes, preliminary optimization studies on shelter geometry, an assessment of shelter heating and cooling loads, and an analysis of the sensitivity of shelter selection to uncertainties in decision maker preferences.

RESULTS AND CONCLUSIONS

Hardening. Methods considered in the hardness analysis include: integral, field installable upgrades, and field expedient upgrades. Integral hardness is defined as the inherent hardness of the basic shelter and can be provided through the use of ballistic fabrics or panels in the basic shelter design. Field installable upgrades consist of lightweight armors that are added to the shelter in the field. These upgrades can be either shelter supported or free standing. Several ballistic hardened panel concepts suitable for integral or field installable upgrades are proposed in the study. Field expedient hardening upgrades include conventional hardening systems such as soil berms, soil bins, sand bags, and concrete revetments. These hardening upgrades can also be integral (as in the case of bin-wall and reinforced earth shelters) or field expedient. Areal densities considered for the fabric and panel upgrades ranged from 1 to 8 *psf* (16 and 32 *psf* densities were calculated for selected cases) while soil thicknesses were varied from 1 to 4 *feet*.

Although significant hardness levels can be achieved by incorporating modern ballistic composites such as Kevlar, Spectra, and S2-glass, our results show that it is not feasible to integrally harden the entire shelter to Splinter levels of protection. The three composite materials (fabric or panel) provide comparable levels of protection and are generally as effective as twice the areal density of aluminum; however, they are not capable of stopping the large, high-speed fragments generated by the bomb and missile at realistic areal densities. Splinter Protection can be provided for the A/C cannon and rocket at reasonable areal densities, but the areal densities required for the missile and bomb are excessive. These results emphasize the varying severity of the four weapon types encompassed by Splinter Protection and the difficulty in achieving Splinter Protection for the large munitions. Only the soil bin walls and soil berms are capable of providing Splinter level protection at low costs.

The heavy panel weights required for ballistic protection will significantly degrade shelter transportability and erection times. Selective hardening offers an alternative to integrally hardening the entire shelter. Selective hardening concentrates ballistic materials into dedicated "safe" areas that provide very high levels of protection. SAFE results show that by concentrating ballistic composite materials into the lower 2 *feet* of a panel, "Splinter Protection" can be achieved. In practice, providing this "Splinter Protection" over the bottom 2 *feet* will require segmenting the panel height for handling and erection.

Shelter Concept Synthesis and Evaluation. Our concept development approach was to systematically identify a wide range of design alternatives for each of the major shelter subsystems (*i.e.*, geometry, structural system, cladding system, and hardening upgrades). Although we do propose hardening-related shelter design modifications for some of the design concepts (*i.e.*, hybrid panel/fabric claddings and soil-filled

walls), most of the basic concepts assessed in this study are either currently in use or under development. The remaining concepts have either been published previously, or they are portable shelter adaptations of existing construction techniques.

There are significant uncertainties and subjective judgments associated with the ASEM inputs used in the shelter evaluation; however, AF prioritization of the competing shelter objectives stands out as the dominant source of shelter selection uncertainty. The sensitivity analysis results suggest that the RWG preferences fall at or near a cross-over point in the overall utility concepts. A stronger consensus either for or against hardening will produce clear differences in the leading shelter concepts. Without this consensus, we believe that the most effective design solutions will be upgradeable, adaptable shelter concepts. Thus, a major challenge will be to minimize the number of different shelter components so that inventory demands are minimized.

Small Shelter Results. Two concepts appear most frequently at the top of the small shelter overall utility rankings: the basic air beam fabric shelter and the upgraded airmobile Modular Extendable Rigid Wall Shelter (MERWS) configurations. Under two of the four preference sets (RWG and No Survivability), the leading concept is the basic air beam-supported fabric shelter. For the RWG scaling, the air beam is followed by the basic pole-supported tent and the soil bin upgraded airmobile MERWS concept. The third tier of concepts includes the basic dual wall and air-supported fabric shelter concepts as well as the S2-glass panel and Spectra blanket upgraded airmobile MERWS concepts. Under the No Survivability preference set, fabric shelters make up the top five concepts, followed by the basic airmobile MERWS and hybrid MERWS concepts. Under the Equal and No Cost preference sets, the airmobile MERWS concept with the free standing 36-*inch* soil bin upgrade is the highest rated concept followed by six other soil hardened concepts. If soil protected shelter concepts are excluded, the MERWS with shelter-supported S2-glass panels or Spectra blanket upgrades and the basic air beam shelter become the recommended concepts under Equal scaling. Of the non-fabric shelters, the airmobile MERWS concept is the leading overall concept for all four preference sets.

Large Shelter Results. Under three of the four preference sets used in the shelter evaluation studies, the basic and upgraded arch-supported panel and bin wall hangars are consistently ranked as the leading concepts. The No Survivability preference set is the only case under which the arch/panel and bin wall concepts do not rate the best. When survivability is given little or no priority, the basic air beam and frame-supported fabric shelter concepts excel. However, even under the No Survivability preference set, the basic arch/panel and bin wall hangar concepts are competitive with the fabric hangar concepts. For the arch/panel concept, the utilities of soil bin, S2-glass panel, and Spectra blanket upgrade configurations approximately meet or exceed the overall utilities of the basic,

unhardened concept. For the bin wall concept, the only upgrade considered is an increased wall thickness with 36 inches of soil infill. The overall utility of the upgraded bin wall concept is also similar to or better than that of the basic bin wall concept (which has only 12 inches of soil). In both cases, the relative utilities of the hardening upgrades improve as the importance placed on survivability is increased.

SUMMARY AND RECOMMENDATIONS

Hardening. We recommend that the basic shelter be hardened to provide integral protection against small fragmenting munitions and be designed to support field installable or expedient methods against larger weapons. SAFE results show that small areal densities (i.e., 2 to 3 psf) of composite material are effective in stopping fragments from antipersonnel munitions such as A/C cannon fire and cluster munitions and also provide protection from most small arms fire. These areal densities can be easily incorporated into the shelter design and we recommend that this level of protection be provided as an integral feature of the shelter design.

To resist combined airblast and fragment impulses, the structural system must be capable of supporting the dynamic loads imparted via the shelter shell. Shelter concepts with modular load bearing panels, such as MERWS, do not employ a frame as part of the structural support system and must transfer loads through discrete connectors. These shelters are susceptible to collapse by lateral side sway which limits their airblast resistance. Consequently, we recommend modifying MERWS to incorporate a frame structure.

Small Shelter Concepts. For the small shelter, we recommend that the hardened airmobile MERWS concept be the focus of the next phase of the research program. If satisfactory hardening levels cannot be achieved or if the mobility and cost penalties prove to be beyond AF constraints, we recommend that a new generation of unhardened air beam (i.e., pressurized rib) supported fabric shelters be pursued as a high payoff approach to shelter mobility and cost.¹ A low risk alternative fabric concept that rates better with respect to performance and structural reliability is the frame-supported fabric concept. The hardening technology developed under further research for the MERWS system will also be directly applicable to an upgraded frame-supported hybrid fabric/panel concept. Thus, the frame-supported fabric concept should be kept under consideration as a low-risk back-up alternative.

Large Shelter Concepts. For the large shelter, we recommend that the arch/panel and bin wall hangar concepts be studied in parallel. The arch/panel concept is basically an upgraded version of the current Harvest Bare ACH shelter and preliminary design should be relatively straightforward. In

addition, the experimental program for panel hardening is applicable to the arch/panel hangar. Since the preferred portable hangar concept will ultimately depend on whether our estimates for the bin wall design attributes can be met, we also recommend that a preliminary structural design and analysis of the basic and upgraded bin wall concepts be developed. The feasibility of the bin wall concept will be determined by three key issues: (1) the required hardness level, (2) the acceptability of soil-based hardening methods, and (3) the developmental uncertainties associated with the bin wall hangar concept. After a more detailed cycle of design and analysis on the arch/panel and bin wall hangar concepts is complete, a re-evaluation of the two concepts should be performed. As with the small shelter recommendations, the mobility and cost penalties associated with shelter hardening may lead Air Force decision makers to abandon the goal of hardened portable shelters. In this case, the No Survivability preference set would be the most applicable model, and we would recommend that the basic air beam hangar concept be pursued as a high risk/payoff approach to shelter mobility and cost with a low risk back-up alternative being the frame-supported fabric hangar concept.

ACKNOWLEDGMENT

This research has been supported by the Airbase Survivability section of Wright Laboratories at Tyndall Air Force Base. The USAF contract monitor is Lt. Keith Westmoreland (USN).

REFERENCES

- Drake, J. L., et al., 1989. *Protective Construction Design Manual*, ESL-TR-87-57, November, 1989.
- Frank, R. A., Lavelle, F. M., and Twisdale, L. A., 1993. "Fragment Hardness Analysis of Composite Materials for Airmobile Shelters," *Sixth Int. Symp. on the Interaction of Nonnuclear Munitions with Structures*, Panama City, FL, May 1993.
- Lavelle, F. M., and Twisdale, L. A., 1993. "Airmobile Shelter Concept Selection Methodology," *Sixth Int. Symp. on the Interaction of Nonnuclear Munitions with Structures*, Panama City, FL, May 1993.
- Materials Technology Laboratory, 1990. *Lightweight Armors Design Handbook -- Monolithic Armor* (U), MTL-TR-90-40, U.S. Army Materials Technology Laboratory, Watertown, Massachusetts, 1990.
- Twisdale, L. A., Frank, R. F., and Lavelle, F. M., 1992. *Airmobile Shelter Analysis*, Air Force Civil Engineering Support Agency, Tyndall Air Force Base, FL, Contract F08635-88-C-0067, November 1992.

¹The transportability threshold is to be determined in a future revision of the ORD. It is possible that the MERWS may not meet this threshold due to its relatively low packing ratio.

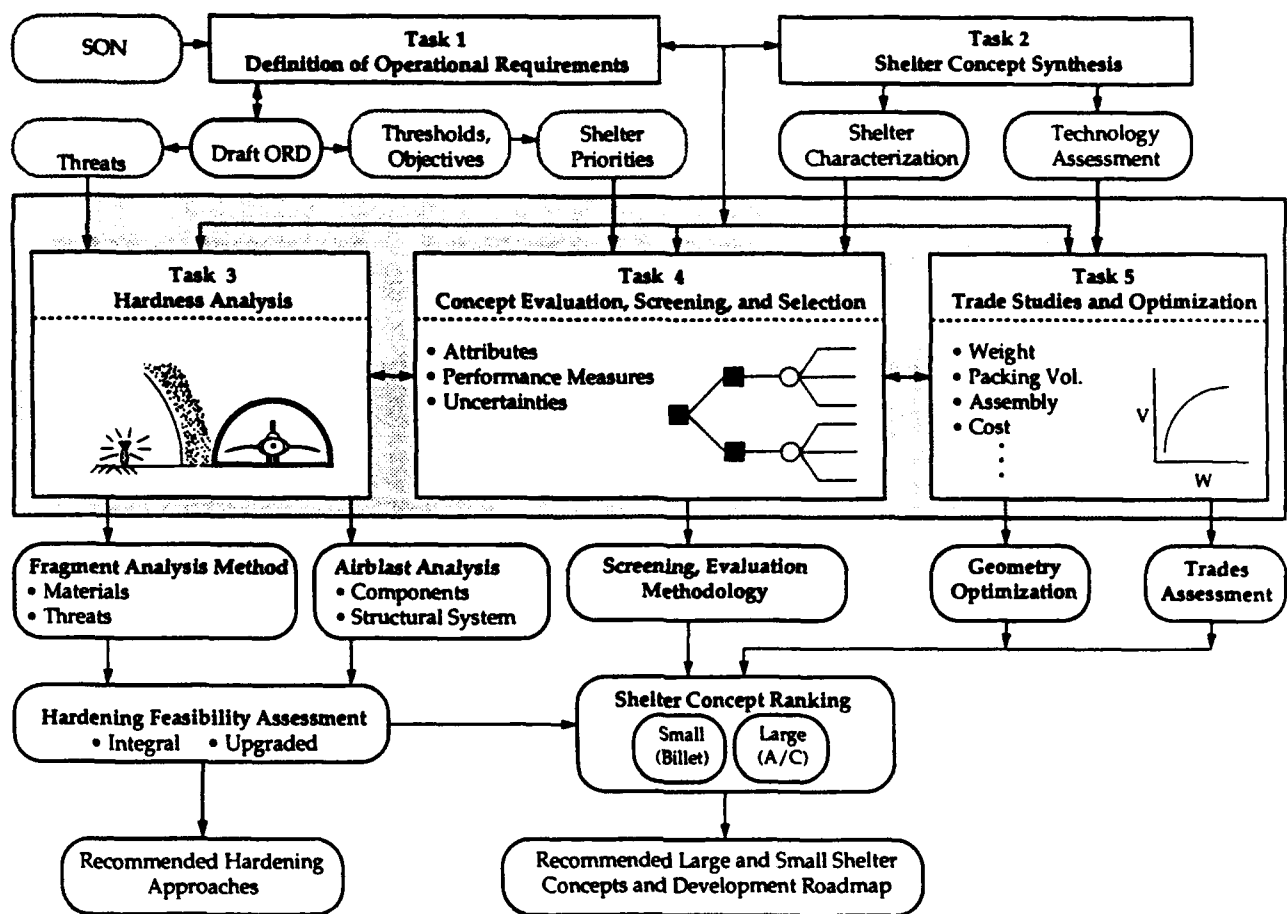


Figure 1. Project Research Tasks and End Products

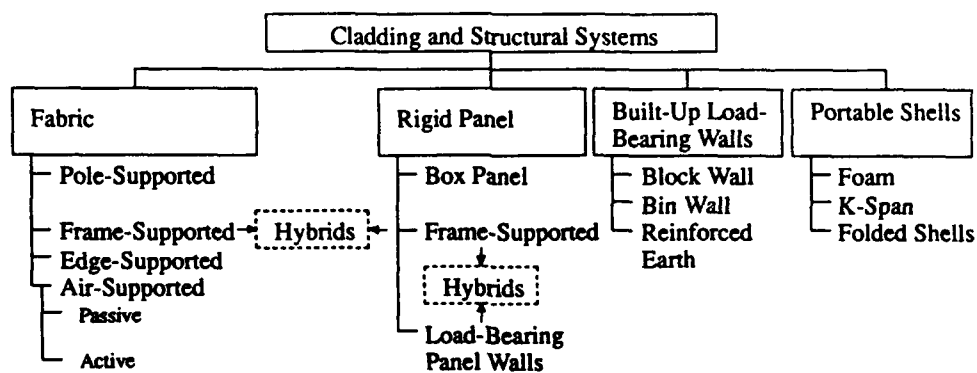


Figure 2. Hierarchy of Shelter Categories.